Measuring and Modeling of Thermodynamic Properties of Alkanol Amin

T. Daneshdar, M.M.Alavianmehr*

Department of Chemistry, Shiraz University of Technology, Shiraz 71555-313, Iran
Email: *bahar.da2018@yahoo.com*

Abstract: In this project, the density and speed of sound of an alkanol amin mixture, 2-anilino ethanol with ethanol is measured by Anton Paar densitometer at atmospheric pressure and temperature rang 293.15-318.15 °K. Then, by using the thermodynamic equation, excessive molar volumes (V_M^E), isothermal compressibility changes (ΔKs) and sound speed changes (Δu) are calculated.

Keywords: Modeling, thermodynamic properties, alkanol amines

I. INTRODUCTION

The thermodynamic properties of pure liquids, especially alcohols have been considered by scientists for many years. Fluid mixing ultrasonic data gave us much information about the nature and force of interaction between atoms and molecules and provide liquid state information. This method cause to understand abnormal alcohol behavior in some conditions [1, 2]. This product is used in multidisciplinary areas like electronic, thermoelectric, chemical, membrane and sensors [3]. Among other alcohols, anilinoethanol is most promising alcohol in research fields because it widely used in anticorrosive coating [4], biosensors [5] and so on [6].

II. METHODS

The pure specimens were injected into the liquid ultrasonic misoNX. The required masses of each substance for each molar fraction carefully determined. In this project for measuring the density and sound velocity, the Anton Paar model DSA 5000M was used. The standard sample is injected into the device using a syringe. After injection, the sample density and the speed of sound in the temperature range 293.15-318.15 °K and intervals of 5 °K at atmospheric pressure were measured and the excess molar volume of some pure and mixture alcohols was calculated.

III. RESULTS AND DISCUSSION

This project is about to calculate values of V_m^E, ΔK_s and Δu of a mixtures at 20 °C. They show an acceptable deviation form the ideal behavior. For example fig.1-3 are relating to measured values of V_m^E, ΔK_s and Δu for mixing ethanol and 2-anilino ethanol in the mole fraction zero to one at 20 °C.
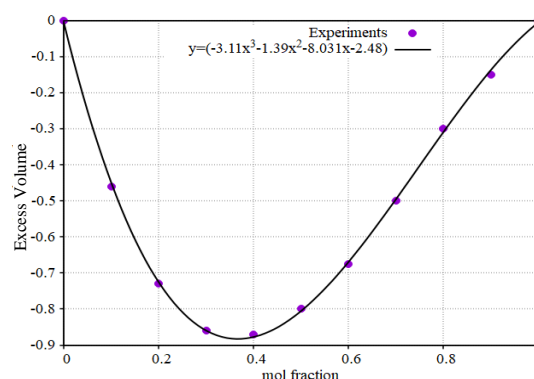

Fig 1.Excess molar volume change of ethanol, 2-anilino ethanol. Points represents experiment data and thick line shows fitted value with Redlich-Kister equation at 20 °C.

In this paper, the excess molar volumes of liquid mixture are calculated by Eq. (1) and fitted to a cubic Redlich-Kister equation by means of vandermond matrix which represented in Eq. (2).

$$V_m^E = \sum_i^n X_i M_i (\rho^{-1} - \rho_i^{-1}) \qquad (1)$$

In which, *X* represents the mole fraction of that sample, ρ is density measured by means of sound velocity and M_i is molecular weight of that substance.

$$V^E = x_2 (1 - x_2) \sum A_n (1 - 2x_2)^n \qquad (2)$$

$$\Delta u = u - \sum_{i=1}^{n} X_i u_i \qquad (4)$$

In this equation A_n represents the coefficients of Redlich-Kister equation for ethanol, 2-anilino ethanol mixture components which reported in table 1.

Table 1. Redlich-Kister coefficients of fitting for ethanol, 2-anilino ethanol.

variable	value
a	-3.1145
b	-1.3978
c	-8.0318
d	-2.4862

The compressibility factor of mixture is calculated by Eq. (3) and represented in fig.2.

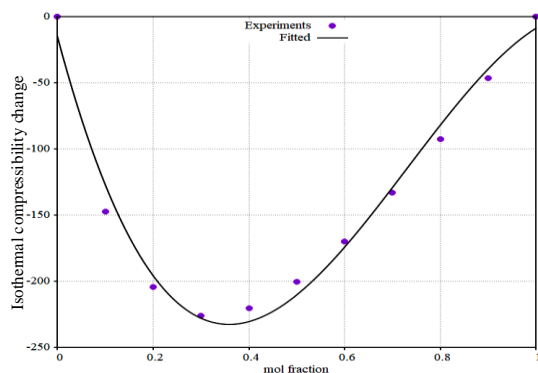$$\Delta K_s = K_s - \sum_{i=1}^{k} X_i K_{s,i} \qquad (3)$$

Fig 2. Isothermal compressibility change of ethanol, 2-anilino ethanol. Points represents experiment data and thick line shows fitted value with a cubic equation at 20 °C.

And the changes in speed of sound for ethanol, 2-anilino ethanol mixture of mixture is as follows and represented in fig. 3.
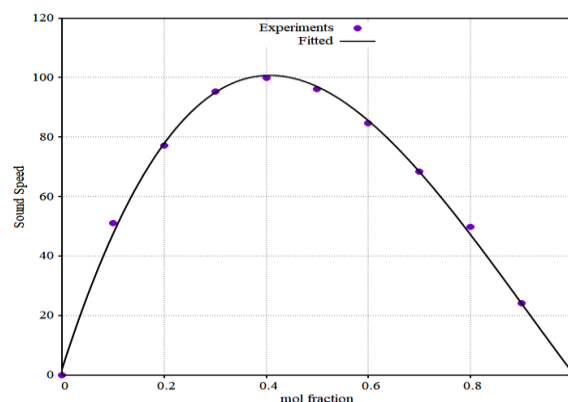

Fig 3. The speed of sound of ethanol, 2-anilino ethanol. Points represents experiment data and thick line shows fitted value with a cubic equation at 20 °C.

IV. CONCLUSION

The volume of fluid and its change depends on the amount of interaction between the molecules inside that fluid. The negative values of V_m^E observed for a system indicate that the interaction of ethanol with a higher alkanol amine is stronger than ethanol-ethanol interaction or alkanolamine-alkanolamine. V_m^E Values for this system increase by temperature. Δk_s decreasing sequence in these mixture is just like the decreasing sequence of V_m values. The observed Δu values for the system are contrary to the shape of V_m^E and Δk_s.

REFERENCES

[1] E. Zorębski, M. Geppert-Rybczyńska,B. Maciej, Journal of Chemical & Engineering Data, 55:pp. 1025-1029. **2009**.

[2] C. Kinart, W. Kinart, D. Chęcińska-Majak,A. Ćwiklińska, Journal of molecular liquids, 109:pp. 19-22. **2004**.

[3] S. Bhadra, D. Khastgir, N. K. Singha,J. H. Lee, Progress in polymer science, 34:pp. 783-810. **2009**.

[4]   A. MirmohseniA. Oladegaragoze, Synthetic Metals, 114:pp. 105-108. **2000**.

[5]   A. Morrin, F. Wilbeer, O. Ngamna, S. E. Moulton, A. J. Killard, G. G. Wallace,M. R. Smyth, Electrochemistry Communications, 7:pp. 317-322. **2005**.

[6]   E. Ahlatcıoğlu, B. Şenkal, F. Yakuphanoğlu,S. A. Mansour, Polymer Engineering & Science, 53:pp. 251-256. **2013**.

Selective Ion Separation Using B-N Doped Graphene Sheet

Maryam Kamal Kandezi[a], _Muhammad Shadman Lakemesari*_
Department of chemistry, University of Zanjan, Zanjan, Iran)
Email: Shadman@znu.ac.ir

Abstract_:_ In this research the ability and mechanism of water desalination in newly designed doped graphene sheet was investigated. Herein, we computationally demonstrate the selective ion separation performance using boron-nitrogen doped nano porous graphene as nano-sponge using in ED desalination process. In this article, in order to prove the selectivity of doped sheet, radial distribution function of species were investigated.

Keywords: water desalination, graphene, doping, Electrical field, selective separation.

I. INTRODUCTION

In this paper, we elucidate the mechanism of separation by B-N doped porous graphene membranes assisted by an external electric field and use it to design an efficient nano-sponge for removing ions from salt-water. In order to elucidate the impact of graphene elemental doping on the efficiency of ion separation, radial distribution function (RDF) of ions with doped atoms were measured and plotted.

II. METHODS

Visual Molecular Dynamics (VMD) was used to construct all initial guesses while MD simulations were performed using the LAMMPS code. The salt-water and B-N doped graphene sheets were first subjected to minimization. All simulations are performed in NVT ensemble at 300 K during 2ns simulation time by using the Nose–Hoover thermostat.

Two-dimensional periodic boundary conditions in the x- and y- directions were then imposed. Intramolecular forces on C, B and N atoms in the doped graphene was described with the Tersoff potential and the forces on water molecules were described with the TIP3P model which has been shown to accurately reproduce the behavior of liquid water.
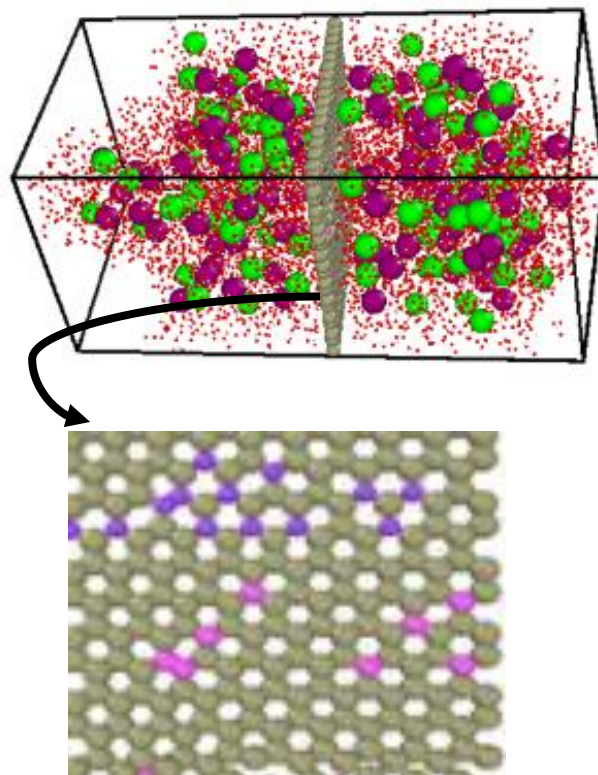

Fig1. Schematic view of simulation

III. RESULTS AND DISCUSSION

There are several peaks in fig1.a and b that show the dispersion of the neighboring shells of Na+ ion at different intervals to the B doped atom, which implies a lack of proper interaction between B and Na+ ion. A similar pattern appears also in Figure 2-B and which reveals a sharp peak around 2.2 Å and broad peaks at about 3-4 Å. Thus, Na+ ion and N-doped sheets can have good interaction and both Na+ and N are well

structured around one another. Clearly, the probability of finding Na^+ ion around N doped region and Cl^- ion around B doped region is high which implies that the N and B can effectively adsorb Na^+ and Cl^- ions, respectively. As above mentioned about the hydration coordination of ions and obtained results for RDFs can yield increasingly good results on separation of salt ions by B and N doped graphene.

Fig.2: a. RDF of B and b. RDF of Na atom with Na and Cl ions.

Equations

Radial distribution function or g(r), also known as the pair correlation functions describes how Na^+ and Cl^- as ions and

atoms in water are spaced apart as a function of distance from a reference. The RDF as a reliable way implies the hydration structure and hydration shell of ions which stated mathematically as below [1][2][3].

$$g(r) = \frac{1}{4\pi N r^2 \rho_0} \sum_{j=1}^{N} \sum_{\substack{i=1 \\ i \neq j}}^{N} \delta(r - r_{ij}) = \frac{1}{2\pi N r^2 \rho_0} \sum_{j=1}^{N} \sum_{i>j}^{N} \delta(r - r_{ij})$$

(1)

IV. CONCLUSION

The similarity of the electronic configuration of N and of Na^+ encourage the latter ions to settle near the N doped site more smoothly than Cl^- ions. On the other hand, the B-doped region favors the passage of the Cl^- anions and limit that of the Na^+ cations. The interactions between the N and B doped pores and Na^+ and Cl^- respectively is, hence, crucial in determining the selective permeability of the doped graphene nano sheet.

REFERENCES

[1] Alkhudhiri and N. Darwish, Desalination, vol. 287, pp. 2–18, 2012.

[2] H. Gao, Q. Shi, D. Rao and Y. Zhang, J. Phys. Chem. C. vol. 121, pp. 22105–22113, **2017**.

[3] M. Misin and M. V. Fedorov, J. Phys. Chem. B. vol. 120, pp. 975–983, **2016**.
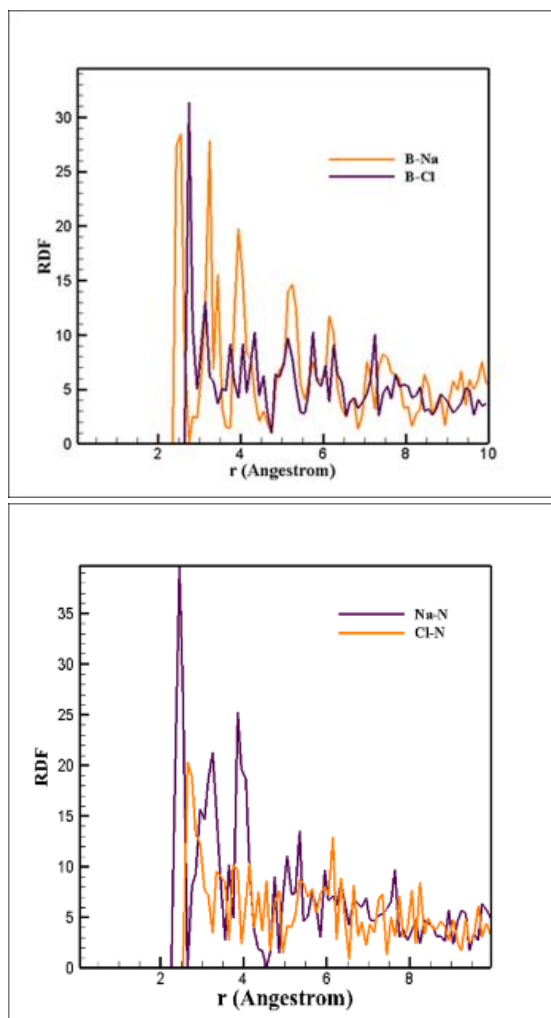
Calculation Young moduli for B-N doped and undoped graphene sheet

Maryam Kamal Kandezi[a], Muhammad Shadman Lakemesari*

Department of chemistry, University of Zanjan, Zanjan, Iran)

Email: Shadman@znu.ac.ir

Abstract*:* In this research the ability and mechanism of water desalination in newly designed doped graphene sheet was investigated. Herein, we computationally demonstrate the selective ion separation performance using boron-nitrogen doped nano porous graphene as nano-sponge using in ED desalination process. In order to investigate the effect of elemental doping on mechanical resistance of doped graphene sheet, Young module of doped sheet was calculated. Overall results of our research indicate that boron- nitrogen doped graphene sheet have a significant potential as desalination Nano-sponge.

Keywords: water desalination, graphene, doping, mechanical strength, Young's modulus.

I. INTRODUCTION

In this paper, we elucidate the mechanism of separation by B-N doped porous graphene membranes assisted by an external electric field and use it to design an efficient nano-sponge for removing ions from salt-water. To investigate the effect of elemental doping on mechanical resistance of doped graphene sheet, Young module of doped sheet was calculated.

II. METHODS

Visual Molecular Dynamics (VMD) was used to construct all initial guesses while MD simulations were performed using the LAMMPS code.
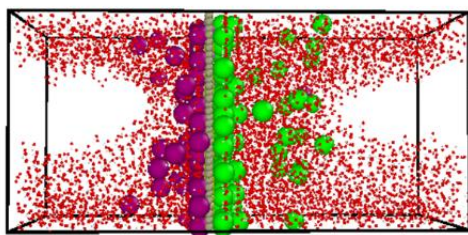

Fig1. Schematic view of simulation box

III. RESULTS AND DISCUSSION

Young's Modulus of B- and N- doped graphene is different from that of a pristine graphene sheet since the presence of defects decreases the structural resistance of sheets. In the Table 1, the forces which overcome the structural resistance of pure and doped graphene sheet are listed. The magnitude of changes in Young's Modulus are not substantial which means that the proposed structures have a relatively good mechanical resistance and, hence, are good candidates for water refinery applications. N are well structured around one another. Clearly, the probability of finding Na^+ ion around N doped region and Cl^- ion around B doped region is high

Table 1. Young's Modulus of pure and B and N doped graphene

Pure graphene			0.088Tpa
BN doped graphene			0.0188Tpa

Equations

The modulus of elasticity, Young's modulus, is the tensile-curve gradient in the linear region (elastic). Hooke's law, which expresses the stress-strain relationship of an object with linear elastic behavior, is defined by the following equation:

$$\sigma_x = E\,\varepsilon_x \rightarrow \varepsilon_x = \frac{\sigma_x}{E}.$$ (3)

In the above relation, σ_x, is the stress on the object along the x-axis, ε_x is the strain (length variation) due to the stress introduced into the axis of the x-axis and the E is the modulus of the elasticity (Young's modulus) [1][2][3].

IV. CONCLUSION

Calculated Young moduli for doped and undoped sheets indicates that the doping has minimal effects on the structural strength of the graphene sheet making the doped graphene an attractive target for future explorations as a base for an efficient membrane desalination technology especially if assisted by external fields.

REFERENCES

[1] Alkhudhiri and N. Darwish, Desalination, vol. 287, pp. 2–18, 2012.

[2] H. Gao, Q. Shi, D. Rao and Y. Zhang, J. Phys. Chem. C. vol. 121, pp. 22105–22113, **2017**.

[3] M. Misin and M. V. Fedorov, J. Phys. Chem. B. vol. 120, pp. 975–983, **2016**.

Section:

Computational Chemistry

DFT Studies of Ethylene Oxide Adsorption on Pristine and Ga-doped Carbon Nanotubes

Tooba Afshari [a]*, **_Mohsen Mohsennia_ [a,b]**, **_Mahdi Rakhshi_ [a]**
[a] Department of Chemistry, University of Kashan, Kashan, Iran
[b] Institute of Nano science and Nanotechnology, University of Kashan, Kashan, Iran
Email: Tooba.afshari@gmail.com

Abstract: Adsorption of ethylene oxide (EO) on the endo- and exo-surfaces of (9,0) and (12,0) zigzag pristine carbon nanotube (CNT) and gallium-doped CNT (CNT-Ga) was investigated using density functional theory (DFT) at M06-2X/6-31++1G** level. The enhanced sensitivity of CNT-Ga towards EO molecule associated with adsorption energies (E_{ad}), Fermi energy level (E_f), band gap energy (E_g), E_g change (ΔE_g) and molecular electrostatic potential (MEP) were calculated and comprehensively analyzed. According to the obtained results, the (9,0) CNT-Ga showed superior sensitivity toward EO and it will be useful in fabrication of new EO gas sensing devices.

Keywords: Adsorption, DFT, Ethylene Oxide, Carbon Nanotube, Gas Sensor

I. INTRODUCTION

Ethylene oxide (EO) is a colorless, flammable and highly reactive gas at the ambient temperature, having a slightly sweet odor [1]. EO (C_2H_4O) is the smallest cyclic ether which has been utilized in some industrial production processes such as solvents, antifreeze, pesticide, sterilization, textiles and pharmaceuticals [2]. Exposure to toxic gas EO molecule may cause to dizziness, convulsions, cataracts, skin allergy, central neuropathy, and cancer [3].

Due to their small size, low power need, high detection sensitivity and low-cost production, the recent sensitive solid-state sensors are widespread devices for detection of hazardous and toxic gases in the environment [4]. In the past decade, due to their high potential to fabricate low-cost portable gas sensors with acceptable sensitivity for the practical gas detection, CNTs-based gas sensors have been widely investigated [5]. The presence of defects and impurities has an important effect on the structural and electronic properties of CNT [6].

In this paper, the adsorption properties of EO on the endo- and exo-surfaces of the (9,0) and (12,0) CNT and CNT-Ga) have been investigated by DFT. The results can be used to develop the further potential applications of the (9,0) CNT-Ga as EO gas sensors.

II. METHODS

All calculations were performed with the Gaussian 09 program package [7] at the level of DFT with meta-hybrid functional M06-2X [8,9] and 6-311++G** basis set [10] to optimize structures, predict energies and describe molecular orbitals of the adsorption complexes. To verify the nature of the stationary point as a minimum or transition structure in obtaining the optimized structures, a frequency calculation was performed. Convergence of calculations is also checked by comparison of the maximum energy and maximum displacement with the corresponding threshold values (1×10^{-6} Ha and 8×10^{-4} Å, respectively).

The E_{ad} of the adsorbed systems is defined as follows:
$$E_{ad} = E_{(adsorbent-EO)} - (E_{adsorbent} + E_{EO}) + E_{BSSE} \quad (1)$$
Where $E_{(adsorbent-EO)}$, $E_{adsorbent}$, and E_{EO} correspond to the energy of the adsorbed systems, the energy of isolated CNT and CNT-Ga and the energy of the free EO molecule, respectively. The E_{ad} values have been corrected by the basis set superposition error (BSSE) [11]. A negative E_{ad} value indicates an exothermic adsorption process. The band gap energy ($E_g = E_{LUMO} - E_{HOMO}$) is the energy difference between the highest occupied molecular orbital (HOMO) and the lowest unoccupied molecular orbital (LUMO) [12].

III. RESULTS AND DISCUSSION

The adsorption of EO molecule on the endo- and exo-surfaces of CNT and CNT-Ga was investigated. The O atom of EO was interacted with C and Ga atoms in endo- and exo-CNT and CNT-Ga respectively. The structure of the isolated EO, systems were optimized using DFT to achieve the lowest energy-level. The optimized diameter for (9,0) CNT is 7.17 Å and (12,0) CNT is 9.33 Å as shown in Fig. 1. When C atom of CNT is replaced by Ga atom, the structure of system is changed, which may be due to the bigger size of Ga compared with C atom.

The calculation results are shown in Table 1. A negative E_{ad} value indicates an exothermic adsorption process. The E_{ad} values of EO on the CNT and CNT-Ga were in the following order: (9,0) CNT-Ga-exo EO>(12,0) CNT-Ga-exo EO>(9,0) CNT-exo EO>(12,0) CNT-exo EO>(9,0) CNT-Ga-endo EO>(12,0) CNT-Ga-endo EO>(9,0) CNT-endo EO>(12,0)

CNT-endo EO. According to the results, the E_{ad} of (9,0) CNT-Ga-exo EO and (12,0) CNT-Ga-exo EO were obtained to be -28.58 and -26.41 kcal/mol, respectively, indicating the strong exothermic adsorption of EO molecule, especially on the (9,0) CNT-Ga. The minimum atom-to-atom distance in the CNT-Ga-exo EO (Ga-O) adsorbed complex systems, which were much shorter than that in the CNT-EO (C-O) and (C-O or Ga-O) systems-endo EO, indicating that there is a covalent bonding between O atom of EO and Ga atom of CNT-Ga. In addition, increasing the diameter of the system was increased the distance and was reduced the E_{ad} (Table 1 and Fig.1).

Table1: Calculated E_{ad} (kcal/mol), E_f, E_g (eV) and $\Delta E_g\%$ for EO adsorption on surface and atom distance between the O and C or Ga in EO and (9,0) and (12,0) CNT and Ga–CNT (Å).

System	d	E_{ad}	E_g	$\Delta E_g\%$	E_f
(9,0) CNT	-	-	1.87	-	-3.71
(9,0) CNT-endo EO	2.71	-0.04	1.91	2.14	-3.71
(9,0) CNT-exo EO	3.40	-1.62	1.90	1.60	-3.67
(12,0) CNT	-	-	2.20	-	-3.48
(12,0) CNT-endo EO	3.02	-0.02	2.21	0.45	-3.47
(12,0) CNT-exo EO	3.43	-1.37	2.22	0.91	-3.43
(9,0) CNT-Ga	-	-	2.19	-	-3.90
(9,0) CNT-Ga-endo EO	3.42	-0.48	2.26	3.20	-3.63
(9,0) CNT-Ga-exo EO	1.95	-28.58	2.34	6.85	-3.38
(12,0) CNT-Ga	-	-	2.38	-	-3.28
(12,0) CNT-Ga-endo EO	3.47	-0.21	2.42	1.68	-3.11
(12,0) CNT-Ga-exo EO	1.97	-26.41	2.50	5.04	-3.01

After the adsorption of EO molecule, the observed E_g change induces a change in the electrical conductivity values, which then generates a recordable electric signal. The E_g of (9,0) CNT-Ga was significantly changed after the adsorption of exo EO (ΔE_g =6.85%). Based on the highest $\Delta E_g\%$ values in Table 1, it can be concluded that CNT-Ga has promising capability to be applied for fabrication of a favorable gas sensor for detection of EO molecules.
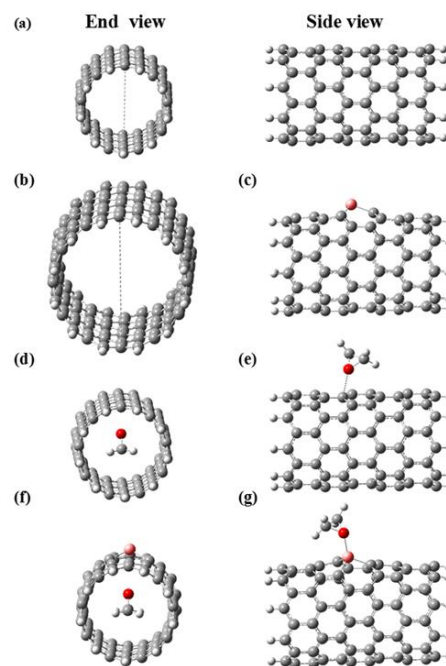

Fig.1: Structure optimized (a) (9,0) CNT, (b) (12,0) CNT, (c) CNT-Ga, (d) CNT-endo EO, (e) CNT-exo EO, (f) CNT-Ga-endo EO and (g) CNT-Ga-exo EO.

The MEP maps of the CNT, CNT-Ga, CNT-Ga-endo EO and CNT-Ga-exo EO systems were calculated, and the results are shown in Fig.2. The bright region in total electron density maps, refers to presence of many electrons which is an active region available for chemical reaction. The graphical results indicated the most electron-deficient regions (blue regions, positive charge) and the most electron-rich regions (red regions, negative charge). From the figure it can be found that there is a strong electron accumulation on the O atom of EO and C atoms of CNTs, whereas electron deficient regions are located on Ga atom of CNT-Ga near interaction sites, which is due to the electronegativity differences between O and Ga atoms.
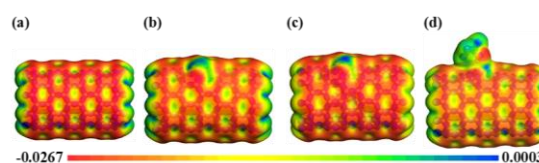

Fig.2: MEP plots for (a) CNT, (b) CNT-Ga, (c) CNT-Ga-endo EO and (d) CNT-Ga-exo EO, Colour ranges, in a.u.

IV. CONCLUSION

According to the obtained results, after adsorption of EO on the CNT and CNT-Ga, the E_g and E_f increase as compared to nanotubes without EO adsorption. The obtained $\Delta E_g\%$ (6.85%) for the CNT-Ga-EO adsorbed complex revealed the significant electrical conductivity change of the CNT-Ga after the EO adsorption, which is a key parameter for sensing purposes. Due to the high E_{ad} of CNT-Ga-exo EO, it could be concluded that EO were chemically bonded to CNT-Ga. The E_{ad} was confirmed that, inter molecular bond CNT-EO is relatively unstable, whereas in the case of CNT-Ga-EO a stable bond was observed. The E_g and E_f rise with increasing the diameter of the nanotube. The E_{ad} declines with increasing of the diameter of nanotube. This behavior revealed that semiconducting properties of nanotubes are reduced by increasing their diameter. The strong binding and high sensitivity of CNT-Ga towards EO can open the new ways for the further potential development of CNT-Ga based gas sensors.

REFERENCES

[1] R. Bashir, B. Afroze, H.F. Zulfiqar, R. Saleem, I. Altaf, F. Saleem, F. Aslam and S. Naz, J. Coll. Physicians Surg. Pak. vol. 26, pp.486-489, **2016**.

[2] S. Rebsdat and D. Mayer, Wiley-VCH Verlag GmbH & Co. KGaA **2001**.

[3] K. Steenland, L. Stayner, A. Greife, W. Halperin, R. Hayes, R. Hornung and S. Nowlin, New. Engl. J. Med. vol. 324, pp. 1402-1407, **1991**.

[4] S. Capone, A. Forleo, L. Francioso, R. Rella, P. Siciliano, J. Spadavecchia, D. Presicce, A. Taurino, J. Optoelectron. Adv. M. vol. 5, pp. 1335-1348, **2003**.

[5] H. Y. Abdullah, Res. Phys. vol. 6, pp. 1146-1151, **2016**.

[6] E. Rahmanifar, M. Yoosefian, and H. Karimi-Maleh, Synth. Met. vol. 221, pp. 242-246, **2016**.

[7] M. J. Frisch, G. W. Trucks, H. B. Schlegel, G. E. Scuseria, M. A. Robb et al. Gaussian 09, Revision B.01. Gaussian, Inc., Wallingford CT; **2009**.

[8] Y. Zhao and D. G. Truhlar, Theor. Chem. Acc. vol. 120, pp. 215-241, **2008**.

[9] S. Grimme, J. Antony, S Ehrlich and H. Krieg, J. Chem. Phys. Vol. 132, pp. 15104-15120, **2010**.

[10] A. D. Becke, Phys. Rev. A, vol. 38, pp. 3098-3100. **1988**.

[11] S. F. Boys and F. D. Bernardi FD. Mol. Phys. vol. 19, PP. 553-566, **1970**.

[12] J. Phillips, Phys. Rev. vol. 123, pp.420-424, **1961**.

Theoretical Study of Carbonic Anhydrase Inhibition by Natural Products

Mina Ghiasi* and Samira Gholami

Department of Chemistry, Faculty of Physics & Chemistry, Alzahra University, 19835-389, Vanak, Tehran, Iran.
Tel: +982188044051-9(2608)
Fax: +982188041344
ghiasi@alzahra.ac.ir
gholamisamira18@yahoo.com

Abstract: Polyamines as important natural products are small aliphatic molecules that increase carbonic anhydrase activity, but new research has shown that they have which recently act as an inhibitor. In the present paper, we used the B3lyp method with the standard 6-31+g* basic set to predict the optimized geometries and interaction energies between polyamines and CA active site.

Keywords: Carbonic anhydrase, DFT, Inhibitor, Spermine.

I. INTRODUCTION

Natural products characterize a simple source for molecular structures bearing a vast array of chemical properties and probably valuable for biomedical objectives such as coumarins and natural products of polyamines. Many bacteria and vagaries are found to be the main cause of the disease, consisting of infectious diseases. This issue generates the polyamines as a significant contributor to make a novel class of antitumor drugs. Some experimental researches recently showed that the polyamines are aliphatic molecules that could raise carbonic anhydrase activity, but a new experimental research indicated that these compounds could act as an inhibitor [1-3]. The aim of this research is to study the interaction between the active site of CA enzyme and polyamine inhibitors by means of density functional theory calculations thermodynamically. This research determines the interaction energies, electronic states, solvent effect and thermodynamic functions.

II. METHODS

The quantum mechanical calculations are performed using the Gaussian program series 2003 [4].It is worthwhile to mention that the geometries of all studied compounds are entirely optimized through density functional theory (DFT), B3LYP method, and the 6-31+G* basis set. The harmonic vibrational frequencies are measured to verify that an optimized geometry properly corresponds to a local minimum, which has only real frequencies.

III. RESULTS AND DISCUSSION

A. The structure of carbonic anhydrase active center, inhibitor and complex between them was entirely optimized with B3LYP method by utilizing a 6-31+G* basis set with no primary symmetry constraints by assuming C_1 point group. By considering the solvent effect (ε=78.9), the optimized geometries of studied compounds in the gas phase re-optimized by utilizing the PCM method.

B. Figures and Tables

Figure 1 illustrates the stability energy diagram in the solvent phase for the inhibition mechanism of one polyamine.
Moreover, the calculated thermodynamic data in the gas and the solvent phase is provided in Table 1. As can be seen from Table 1, it is revealed that the interaction of inhibitor with active center of CA enzyme is energetically exothermic.
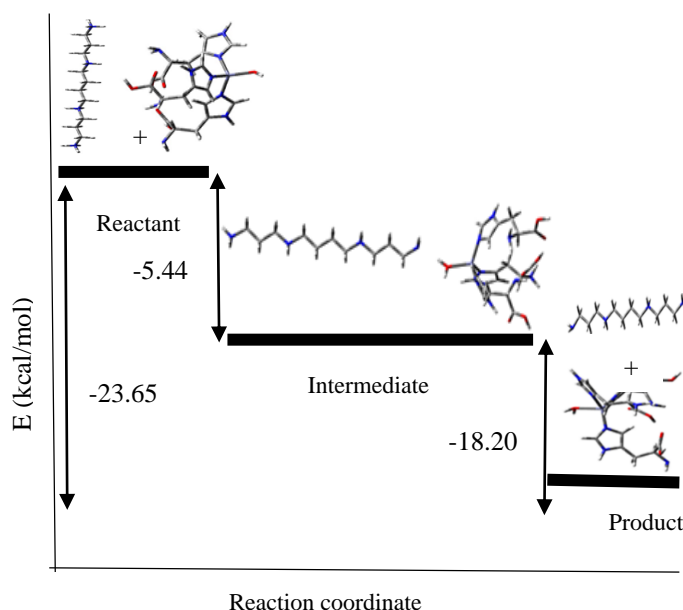

Fig.1: Stability energy diagram in solvent phase
Table1: Thermodynamic information table

data (Kcal/mol)	phase gas solvent	phase
ΔE	-103.60	-23.65
ΔH	-103.60	-23.65
Δ*G*	-112.81	-23.94
Δ*S*	0.030	0.001

IV. CONCLUSION

DFT calculations were performed to investigate the interaction between polyamine inhibitor and active center of carbonic anhydrase. An assessment of the CA active center in the complex under evaluation with the native enzyme indicated that a significant conformational rearrangement was critical in the active site to enable the interacting of the inhibitor. These obtained results may be valuable to make carbonic anhydrase with potential as anti-obesity drugs or other pharmaceutical purposes.

REFERENCES

[1] Casero, R. A., Jr; Marton, L. J. Nature Rev, vol. 6, pp. 373–390, **2007.**

[2] Woster, P. M, Wang, J. Y., Casero, R. A., Jr., Eds., Humana Press: Totowa, NJ, pp 3-24, **2006**.

[3] Peg, A.; Salvi, M.; Mondovi, Med.Chem, vol 11, pp. 2349-2347, **2004**.

[4] Gaussian 2003 (Revision-B), Frisch, M. J.; Trucks, G. W.; Schlegel, H. B.; Scuseria, G. E.; Robb, M. A.; Cheeseman, J. R.; Zakrzewski, V. G.; Montgomery, J. A.; Stratmann, R. E.; Burant, J. C.; Dapprich, S.; Millam, J. M.; Daniels, A. D.; Kudin, K. N.; Strain, M. C.; Farkas, O.; Tomasi, J.; Barone, V.; Cossi, M.; Cammi, R.; Mennucci, B.; Pomelli, C.; Adamo, C.; Clifford, S.; Ochterski, J.; Petersson, G. A.; Ayala, P. Y.; Cui, Q.; Morokuma, K.; Malick, D. K.; Rabuck, A. D.; Raghavachari, K.; Foresman, J. B.; cioslowski, J.; Ortiz, J. V.; Stefanov, B. B.; Liu, G.; Liashenko, A.; Piskorz, P.; Komaromi, I.; Gomperts, R.; Martin, R. L.; Fox, D. J.; Keith, T.; Al-Laham, M. A.; Peng, C. Y.; Nanayakkara, A.; Ghonzalez, C. V.; Challacombe, M.; Gill, P. M. W.; Johnson, B. G.; Chen, W.; Wong, M.; Andres, J. L.; Head-Gordon, M.; Replogle E. S.; Pople, J .A. Gaussian, Inc., Pittsburgh PA, **2003**.

Studying of Interaction of Peptide Adsorbed on Graphene Using Molecular Dynamic Simulation

Sahar Razzaghi[a], Nasser L. Hadipour[a*], Bahar Kharazian[a]

cDepartment of Chemistry, Tarbiat Modares University, P. O. Box 14115-175, Tehran, Iran
*Corresponding Author: (NLH) E-mail: hadipour@modares.ac.ir

Abstract: Molecular dynamics simulation is accomplished to study the binding properties of three aromatic amino acids at their zwitterion state and neutral pH on the surface of graphene. Here, the $\pi - \pi$ stacking and the semi-hydrogen bond formation cause a strong interaction with graphene. We investigate the adsorption energies, center of mass distances, solvent accessible surface area and RMSD to obtain the sequence of these three amino acids in stronger adsorption on graphene. The results revealed that for Tyrosine, the main interaction is between the hydroxyl group and graphene, therefore it's stronger, for Tryptophan the interactions between the nitrogen in the indole ring, and the graphene is the significant interaction so it will be the strongest. These results provide a patronage for using graphene as drug delivery agent for further investigations.

Keyword*:* Amino acids, Force fields, Interaction, Molecular dynamic simulation

I. INTRODUCTION

Graphene, a single layer of sp^2 hybridized carbon atoms arranged in a honeycomb two-dimensional (2D) lattice, has evoked enormous interest throughout the scientific community [1]. Because of its unique structure and geometry, graphene has remarkable physical and chemical properties, including a specific surface area, high intrinsic mobility, high modulus and thermal conductivity, optical transmission and good electrical conductivity [2]. It consists of a layer with π-conjugated structure of six atom rings, offering an excellent capability to immobilize a large number of substances, including metals, drugs, biomolecules and fluorescent probes and cells [3]. Therefore, it is not surprising that graphene has generated great interest in nanomedicine and biomedical applications.

Non-covalent interaction plays an important role in predicting the structures of protein, DNA and RNA [4]. π-π stacking and x-π (x=CH, OH, NH,…) interactions make the complex of amino acids and graphene stable but these interactions at the molecular level are not clearly understood, thus limiting the biological and biomedical applications of graphene. Jing-Yao Qi et.al found that in the adsorption process Leucine molecule adsorbs onto graphene and van der Waals interaction plays an important role [5]. Rajesh R. Naik et. al studied binding of peptide to the planar surface or edge of graphene[6]. In this work we investigate interaction of Tyrosine (Tyr) and Phenylalanine (Phe) and Tryptophan (Trp) with graphene using molecular dynamics simulation to study the adsorption process.

II. METHODS

All calculations were performed using NAMD package. The TIP3P water model[7] and CHARMM force field[8] were used for all simulations. A graphene sheet with a dimension of 42.54 * 36.84 nm^2 was located in the center of the simulation box. In the initial configurations, amino acids were positioned in the 10 Å above graphene surface to ensure that there is enough space to contain several layers of water between the amino acids and the surface. Sodium (Na$^+$) and chloride (Cl$^-$) ions were added to neutralize the system. In all three directions, periodic boundary conditions were set. The potential between atoms in the molecule and surface were represented by a Lennard-Jones 6–12 potential. Cut off of van der Waals interaction was set to 10 Å, and long-range electrostatic interactions were computed with particle Mesh Ewald method with 12 Å cut off [8].

III. RESULTS AND DISCUSSION

In this work, we study interaction of three amino acids Phe, Tyr, and Trp to discover the adsorption details of them on graphene. At first, the structures of amino acids were optimized. After that, amino acids were placed on the surface of graphene at the 10 Å distance. All simulations were done in the NPT and NVT ensembles at a temperature of 300K.

To estimate the equilibrium of systems, RMSD of three amino acids were measured during 20ns of simulation time, which are, drown from Eq.1

$$RMSD(t_1, t_2) = \left[\frac{1}{N} \sum_{i=1}^{N} m_i \left\| r_i(t_1) - r_i(t_2) \right\|^2 \right]^{1/2} \tag{1}$$

where r_i is the position of atom i at time t and N is the total number of atoms in the molecule. Changes in RMSD showed that each amino acid undergoing a conformational change during simulation. The average values for three mentioned amino acids are 0.4Å, 1.1Å, 1.3Å for Trp, Tyr, Phe, respectively.

We calculated the energy of each amino acid after 20ns of MD simulation. The interaction energy, E_{int}, for all the systems is defined as Eq.2

$$E_{int} = E_{graphene/AA} - E_{graphene} - E_{AA} \qquad (2)$$

Where E_{int} is total interaction energy, $E_{graphene/AA}$, $E_{graphene}$ and E_{AA} are the total energy of the graphene/AA complex in water, the potential energy of graphene in water and amino acid in water [4] Results are shown in Table 1.

Table1: Average binding energy

Kcalmol^{-1}	E(graphene + water+ amino acid)	E (amino acid)	E (graphene)	E binding (amino acid-graphene)
Phenylalanin	-32.9	-10.2	-9.1	–13.6
Tyrosine	-29	-5.5	-9.1	–14.4
Tryptophan	-39.5	-12.8	-9.1	–17.6

It is known that aromatic amino acids are adsorbed on the surface with their aromatic rings, the positively charged ammonium groups and the negatively charged carboxylate stay away from graphene surface. The adsorbed amino acids orient their aromatic rings to be parallel with the graphene surface, indicating the main role of π-π stacking interaction. For Phe the side chain adsorbs onto the graphene surface through stacking after optimization, the benzene rings of the Phe and the graphene were not completely parallel or vertical to each other but actually the π-π stacking makes the overall configuration cranked. Interaction of the hydrogen atoms and the benzene ring stabilized the conformers. The nearest equilibrium distances between the graphene and benzene is about 3.7Å. Here benzene stays nearly parallel to the graphene.

In addition, to study adsorption behavior on graphene surface, separation distance between the center of mass of amino acids and the center of mass of graphene surface was calculated during the simulation time. The strongest interaction is for Trp because of the least average value of center of mass distance, which is 4.0Å, and after that Tyr and Phe with 4.1 and 4.4Å.

Solvent accessible surface area (SASA) measured for each amino acid during the simulation time. Trp has the least solvent accessible surface area due to the strongest interaction with graphene that the π-π stacking plays the main role and after that, Tyr and Phe have got more SASA average values as shown in Fig1.
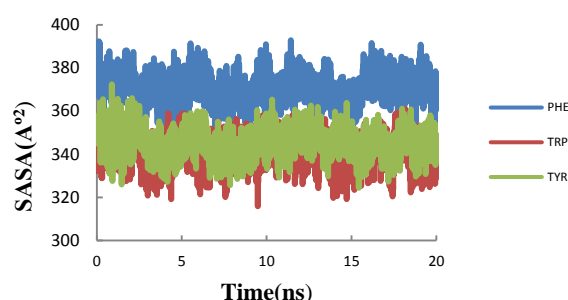

Fig.1: Changes in SASA of Phe, Trp and Tyr over the graphene sheet

IV.   CONCLUSION

Interactions between amino acids with graphene were investigated using molecular dynamics simulation. The simulation results show the chemical structure of amino acids play an important role in adsorption process. Where for Phe the interaction is a weak stacking due to hydrogen binding to benzene. The interaction in Tyr is considered to be between the hydroxyl group and graphene, which is stronger, and for Trp the geometrical orientations show the interaction between the nitrogen in the indole ring and the graphene, which is the strongest.

REFERENCES

[1] J. Liu, L. Cui, D. Losic, Acta biomaterialia, 1742-7061, **2013**.

[2] Y. Zhu, S. Murali , W. Cai , X. Li , J.W. Suk , J.R. Potts ,and R.S. Ruoff, Adv. Mater. 22, 3906–3924, **2010**.

[3] Z.H, J. Zhou, CARBON78, 500-509, **2014**.

[4] C. Rajesh, C. Majumder, H. Mizuseki, and Y. Kawazoe, The J Chem phys, 130, 124911, **2009**.

[5] W. Qin, X. Li, W. Bian, X.J. Fan, J,Y, Qi, Biomaterials 31, 1007-16, **2010**.

[6] S.N. Kim, Z.Kuang, J.M. Slocik, S.E. Jones, Y. Cui, B.L. Framer, J. Am. Chem. Soc, 133, **2011**.

[7] Z.J. Huang, W.B. Yu, THEOCHEM, 758, 195-202, **2006**.

[8] Z.J. Huang, Z.J. Lin, J. Phys. Chem. A. 109,2656-9, **2005**.

Influence of various anions on physicochemical properties ionic liquids based on 1-benzy bis (l-2,3,4,6,7,8,9,10-octa hydropyrimido [1,2-a] azepinium) dication: characterization and DFT calculations

S. Fallah Ghasemi*[a], H. Roohi[a]
(Department of Chemistry, Faculty of Science University of Guilan, Rasht, Iran)
* Email: s.f.gh.1360@gmail.com

Abstract: One of the most attractive characters of DBU-based ionic liquids is that their properties can change with the combination of different anions and various substituents (aromatic or aliphatic alkyl chains groups) which can be linked to DBU rings of their cation, which provides the chances for designing and developing DBU-based ionic liquids with excellent properties In this work, a series of Bn-DBU-based dicationic ionic liquids (DILs) with different anions were investigated by density functional theory (DFT) at M06–2X/6-311++G(d,p) level of theory. The interaction energies, structural parameters and charge transfer (CT) values of [X] [Y1-7]$_2$, ([X]$^{2+}$ = [Bn(DBU)$_2$]$^{+2}$, and Y$_{1-7}$ = CH$_3$CO$_2^-$, PhSO$_2^-$, HCO$_3^-$, HSO$_4^-$, CF$_3$CO$_2^-$, BF$_4^-$ and SCN$^-$) ILs based were explored.

Keywords: Bn(DBU)$_2$; DFT; M06–2X; dicationic ionic liquids; Charge transfer

I. INTRODUCTION

1,8-diazobicyclo[5.4.0]undec-7-ene (DBU) is a strong organic base that has been extensively applied in the base-induced reactions with excellent catalytic activity. The functionalized ionic liquids and task-specific ionic liquids (TSILs) with special functions can overcome this drawback and exhibit the similar basicity to DBU accompanied with the general features of ILs. DBU as a head group are usually used to synthesize the task-specific N-alkylated or arylated ionic liquids via quaternization reaction [1-2]. Compared with the monocationic ILs, the dicationic ILs showed better design ability because different types of substrates could be used to form corresponding cationic part and different functional groups could be also introduced into the spacer [3-4], meanwhile, the anionic moiety might be consisted of different organic and inorganic components.

An increase in the computational power and availability of computational resources has resulted in an increase of publications that use quantum chemical methods to offer theoretical underpinning to experimental data and prediction of physicochemical properties of ionic liquids [5-8]. To the best our knowledge interaction between 1-benzy bis (l-2,3,4,6,7,8,9,10-octa hydropyrimido [1,2-a] azepinium) -based dication ([Bn(DBU)$_2$]$^{2+}$) and CH$_3$CO$_2^-$, PhSO$_2^-$, HCO$_3^-$, HSO$_4^-$, CF$_3$CO$_2^-$, BF$_4^-$ and SCN$^-$ anions has not been characterized and no detailed studies exist on the influence of different anions on hydrogen bonding strength between their constituents. The interaction energy between the [Bn(DBU)$_2$]$^{2+}$ dication and above anions, geometrical parameters and charge transfer values were obtained. An overview of ionic liquids studied in this work is shown in Fig. 1.

II. METHODS

Geometry optimizations and calculation of the property of the ionic liquids were carried out at M06–2X/6-311++G(d,p) level [9].The counterpoise method (CP) [10] was used to correct for basis set superposition error (BSSE) in the calculation of interaction energies. Also, dispersion correction on the interaction energies by M06-2X-D3 functional was explored. To characterize the stationary points and calculation of zero-point vibrational energy (ZPVE) as well as thermochemical quantities, vibrational frequency analysis were performed at mentioned level of theory.

III. RESULTS AND DISCUSSION

The electronic interaction energies for DILs formation of [Bn(DBU)$_2$][Y$_{1-7}$]$_2$, (Y$_{1-7}$ = CH$_3$CO$_2^-$, PhSO$_2^-$, HCO$_3^-$, HSO$_4^-$, CF$_3$CO$_2^-$, BF$_4^-$ and SCN$^-$) ILs in the gas phase are reported in Table1. As can be observed, the range of the interaction energies values with the BSSE, ZPVE and dispersion corrections (ΔE$_c$) is from -213.9 kcal mol^{-1} to -238.8 kcal mol^{-1} in [Bn(DBU)$_2$][Y$_{1-7}$]$_2$ DILs at M06–2X/6-311++G(d,p) level of theory. The results show that the interaction between the dication and the anions in the gas phase is very strong and the strongest interaction is more sensible for the [Bn(DBU)$_2$][Y$_1$]$_2$ DIL with ΔE$_c$ of -238.8 kcal mol^{-1}. The second most stable DIL is the [Bn(DBU)$_2$][Y$_2$]$_2$ one with ΔE$_c$ value of -236.1 kcal mol^{-1}. Based on the corrected ΔEc, the estimated stability order of the ILs formed from interaction between [Bn(DBU)$_2$]$^{2+}$ cation and the anions is [Bn(DBU)$_2$][CH$_3$CO$_2$]$_2$> [Bn(DBU)$_2$][PhSO$_2$]$_2$>[Bn(DBU)$_2$][HCO$_3$]$_2$>[Bn(DBU)$_2$][H

SO_4]>[Bn(DBU)$_2$][CF_3CO_2]>[Bn(DBU)$_2$][BF_4]>[Bn(DBU)$_2$][SCN]. Comparison of atomic charges in DILs shows that formation of the H-bonding accompanies some charge transfer (CT) between anion and dication.The CT values obtained for [X][Y_{1-7}], Y_{1-7} = [CH_3CO_2]⁻, [$C_6H_5SO_2$]⁻, [HCO_3]⁻, [HSO_4]⁻, [CF_3CO_2]⁻, [BF_4]⁻ and [SCN]⁻ DILs are 0.1418, 0.1496, 0.1353, 0.1168, 0.1077, 0.0713 and 0.1082, respectively, in good agreement with the greater interaction energies obtained for the DILs.
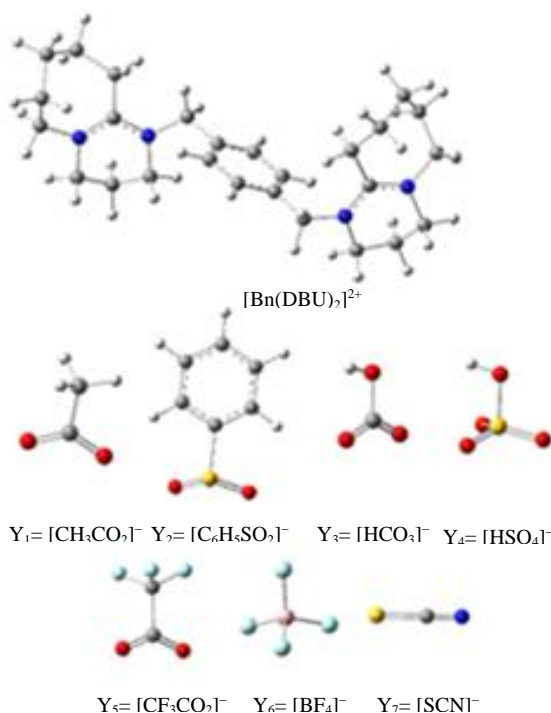

[Bn(DBU)$_2$]$^{2+}$

Y_1= [CH_3CO_2]⁻ Y_2= [$C_6H_5SO_2$]⁻ Y_3= [HCO_3]⁻ Y_4= [HSO_4]⁻

Y_5= [CF_3CO_2]⁻ Y_6= [BF_4]⁻ Y_7= [SCN]⁻

Fig.1 Structures of the isolated [Bn(DBU)$_2$]$^{2+}$ dication and CH_3CO_2⁻, $C_6H_5SO_2$⁻, HCO_3⁻, HSO_4⁻, CF_3CO_2⁻, BF_4⁻ and SCN⁻ anions at the M06-2X/6311++G(d,p) level of theory.

Table1: Interaction energies of [X][$Y_{1–7}$], (X = [Bn(DBU)$_2$]$^{2+}$ and Y_{1-7} = CH_3CO_2⁻, $C_6H_5SO_2$⁻, HCO_3⁻, HSO_4⁻, CF_3CO_2⁻, BF_4⁻ and SCN⁻ DILs at M06–2X/6311++G(d, p) level of theory.

Structure	ΔZPVE	BSSE	ΔE_{elec}	ΔE_{disp}	ΔE_C
[Bn(DBU)$_2$][Y_1]$_2$	3.3	3.1	-240.0	-5.2	-238.8
[Bn(DBU)$_2$][Y_2]$_2$	3.8	7.1	-240.0	-7.1	-236.1
[Bn(DBU)$_2$][Y_3]$_2$	3.2	3.5	-234.3	-5.0	-232.6
[Bn(DBU)$_2$][Y_4]$_2$	3.8	7.3	-229.6	-5.5	-224.0
[Bn(DBU)$_2$][Y_5]$_2$	3.7	4.3	-221.9	-5.6	-219.4
[Bn(DBU)$_2$][Y_6]$_2$	3.5	5.6	-218.4	-5.1	-214.4
[Bn(DBU)$_2$][Y_7]$_2$	2.3	2.4	-214.1	-4.5	-213.9

A. Equations

The interaction energy was determined as the difference between the energy of DIL and the sum of the energies of the corresponding dication and anion as equation (1):

$$\Delta E = E_{(DIL)} - (E_{(dication)} + E_{(anion)}) \qquad (1)$$

IV. CONCLUSION

In this study, we evaluated the effect of various anions (CH_3CO_2⁻, $C_6H_5SO_2$⁻, HCO_3⁻, HSO_4⁻, CF_3CO_2⁻, BF_4⁻ and SCN⁻) on the structural, electronic, thermal and electrochemical characteristics of ionic liquids based on 1-benzy bis (l-2,3,4,6,7,8,9,10-octa hydropyrimido [1,2-a] azepinium) dication ([Bn(DBU)$_2$]$^{2+}$) using computational approach based on quantum chemical methods at M06–2X/6–311++G(d,p) levels of theory. The characteristics such as interaction energy, structural parameters, vibrational frequencies and NBO datas were estimated. The calculated ΔE for the DILs decrease in the order [Bn(DBU)$_2$][CH_3CO_2]$_2$ > [Bn(DBU)$_2$][$C_6H_5SO_2$]$_2$ > [Bn(DBU)$_2$][HCO_3]$_2$ > [Bn(DBU)$_2$][HSO_4]$_2$ > [Bn(DBU)$_2$][CF_3CO_2]$_2$ > [Bn(DBU)$_2$][BF_4]$_2$ > [Bn(DBU)$_2$][SCN]$_2$. The type of anions can undergo effects strong of H-bonding and CT values in [X][Y_{1-7}] DILs. They decreases on going from [Y_1] anion to [Y_7] ones.

REFERENCES

[1] B. Yu, H. Zhang, Y. Zhao, S. Chen, J. Xu, L. Hao and Z. Liu, ACS Catal, 3, 2076-2082, **2013**.
[2] Z. Wang, Z.P. Li, Y. H. Jin, W. Liu, L. H. Jiang and Q. H. Zhang, New J Chem, 41, 5091-5097, **2017**.
[3] D. Fang, J. M. Yang and C. M. Jiao, ACS Catal 1, 42–47, **2010**.
[4] S. K. Tang, G. A. Baker and H. Zhao, Chem Soc Rev, 41, 4030–4066, **2017**.
[5] E. I. Izgorodina, Z. L. Seeger, D. L. A. Scarborough and S.Y.S. Tan, Chem. Re, 117(10), 6696-6754, **2017**.
[6] H. Roohi and K. Ghauri, Journal of Molecular Liquids, 209, 14-24, **2015**.
[7] H. Roohi, H. Iloukhani and F. Rouhani, Journal of Molecular Liquids, 240, 138-151, **2017**.
[8] H. Roohi and R. Salehi, Ionics, 24, 483-504, **2018**.
[9] Y. Zhao and D. G. Truhlar, Acc. Chem. Res, 41, 157-167, **2008**.
[10] S. F. Boys and F. Bernardi, J. Mol. Phys., 19, 553-566, **1970**.

Study of Methane, Ethane and Propane Adsorptions on ZJU-9a Using GCMC Method

Maryam ghaderi[a], Saeid Yeganegi [b]*

Department of Physical chemistry, Faculty of Chemistry, University of Mazandaran, Babolsar, 47416-13534, Iran

* E-mail: Yeganegi@umz.ac.ir

Abstract: In this work, we studied the adsorption of methane, ethane and propane and their mixtures into a MOF porous material, ZJU-9a using Grand Canonical Monte Carlo (GCMC) molecular simulations. Also, the separation of C2/C1 and C3/C1 from their binary mixtures by ZJU-9a was examined. The adsorption isotherms of pure components were studied in different temperatures and pressures. The obtained results revealed that that propane adsorption was higher than that of ethane and methane at 298k and 1 bar, due to the stronger interactions between adsorbate and adsorbent. The calculated isosteric heats of adsorption followed the order $C_3H_8 > C_2H_6 > CH_4$. Moreover, the adsorption selectivity of ZJU-9a toward C2/C1 and C3/C1 binary mixtures reached 17.07 and 109.06, respectively.

Keywords: Metal–Organic Framework, Grand Canonical Monte Carlo, Adsorption, Selectivity, Isosteric heats of adsorption

I. INTRODUCTION

Natural gas, primarily consisting of CH_4, often contains small amounts of heavier hydrocarbons, such as C_2H_6 and C_3H_8 [1]. Nowadays, methane is mainly used as a clean fuel whilst ethane and propane are important raw materials in the petrochemical industry for the production of acetic acid, rubber and plastics [2]. The effective separation of these mixtures has become indispensable because of similar molecular sizes and physical-chemical properties. The conventional cryogenic distillation technology based on different vapor pressures and boiling points of methane and impurities is not efficient due to the high energy consumption [3]. Therefore, porous adsorbents have recently emerged as powerful alternatives to traditional method. In the last two decades, Metal-organic frameworks (MOFs), built from metal ions (metal clusters) connected by organic ligands to form a three or two-dimensional extended network have been recognized as great promising adsorbent for gas storage, separation and catalysis due to distinctive characteristics like large surface area, high porosity, chemically adjustable pore dimension [4-5].

The microporous MOF, ZJU-9a, has the well-known NbO type topology [6]. The activated ZJU-9a exhibits moderately high porosity and the BET surface area [6]. Additionally, it has suitable pore spaces and open copper metal sites which enable ZJU-9a to store large amount of acetylene and methane at room temperature [6]. Hence, these properties encouraged us to study its performance for the storage and separation of light hydrocarbons.

In this work, the adsorption of methane, ethane and propane on ZJU-9a were studied using Grand Canonical Monte Carlo (GCMC) molecular simulations. Furthermore, the selectivity for binary mixture (50:50) of C_2H_6/CH_4 and C_3H_8/CH_4 were appraised to investigate the separation performance of C1 from C2 and C3.

II. METHODS

The grand canonical Monte Carlo simulation (GCMC) was employed to calculate the adsorption of all adsorbate and their mixtures in ZJU-9a. The atomic structure of ZJU-9a came originally from the experimental data [6] after removing solvent molecules. Four unit cells of ZJU-9a (2×2×1) were used to construct the simulation box. Each point of the component isotherm was equilibrated during 10^7 moves followed by 10^7 moves for data collection.

The framework atoms were described here by Lennard-Jones (LJ) and electrostatic potentials. Lennard–Jones parameters between unlike atom types were computed using the Lorentz–Berthelot mixing rules. A LJ cutoff distance of 12.5 angstrom was used for the simulations. A rigid model for MOF was used. The universal force field (UFF) was applied to describe the LJ potential parameters of ZJU-9a [7].

LJ parameters for hydrocarbon were taken from united-atom TraPPE force field [8], in which CHx groups are described as single interaction centers with their own effective potentials.

III. RESULTS AND DISCUSSION

At first, we examined the performance of several force field including UFF, OPLS (All-Atom) and DREIDING to reproduce Duan et al [6] experimental adsorption isotherms of methane at 298K. Although, the agreement between simulated isotherms and experimental ones for universal force field (UFF) was almost close but the agreement in the entire pressure range is not attainable, where the simulation data slightly overestimate the experimental data. This effect could be due to the fact that GCMC simulations consider a perfect crystalline framework, while the real material may contain defects or impurities that cause part of the pore volume unavailable for adsorption [9]. according to Jorge et al work [10], we scaled experimental adsorption isotherms by the ratio of the theoretical over experimental pore volumes which is define as Eq. (1):

$$N^{ideal} = N^{exp} \frac{V_p^{ideal}}{V_p^{exp}} \tag{1}$$

where N^{exp} refers to the raw experimental isotherm on a MOF, N^{ideal} is simulated isotherm on a perfect MOF sample. V_p^{exp} is the experimentally pore volume of the sample and V_p^{ideal} is accessible pore volume of an ideal crystal. For V_p^{exp}, we take the value of 0.887 cm³/gr from Duan et al [6]. For V_p^{ideal}, We calculate 1.25 cm³/gr by RASPA package [11]. We find that a factor of 1.4 gives the best agreement between simulation and experiment data. Adsorption isotherms of pure methane, ethane and propane on ZJU-9a up to 1 bar at 298K were investigated. Fig. 1 displays a comparison of the simulated isotherms of these light hydrocarbons on ZJU-9a. The uptake capacities of ZJU-9a for methane, ethane and propane at 1 bar and 298K are 1.9, 9.52, 10.21 mmol/gr, respectively.

The isosteric heat of adsorption for CH_4, C_2H_6 and C_3H_8 are in the approximately range of 19-17, 33-28 and 38-40 kJ/mol. The isosteric heats of C3 and C2 are higher than

isosteric heat of C1. The higher adsorption heats obtained for the heavier hydrocarbons can be related to the larger interactions between the hydrocarbon molecules and the framework, where C1 has the weakest van der Waals host-guest interactions. The computed selectivities of C_2H_6/CH_4 and C_3H_8/CH_4 are 17.07 and 109.06. As expected, ZJU-9a display higher adsorption selectivity of C3/C1 than C2/C1 which can be attributed to the stronger interaction of C_3H_8 with framework than C_2H_6.
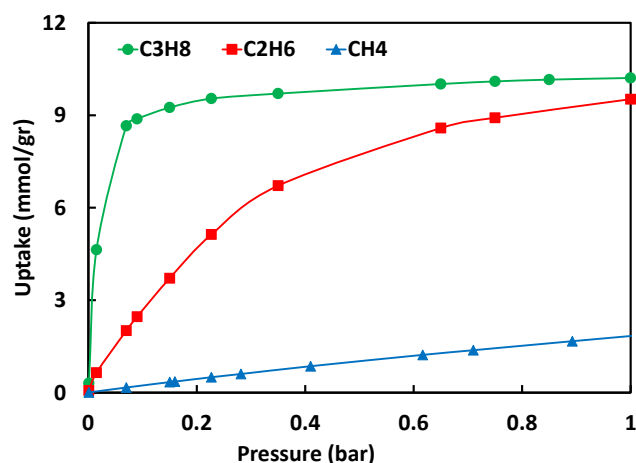

Fig. 1: The adsorption isotherms for C1, C2 and C3 at 298k

III. CONCLUSION

In this work, the adsorption of methane, ethane, propane and their binary mixture on ZJU-9a was studied by GCMC method. The obtained results show that the adsorption capacities and the isosteric heats of this light hydrocarbons followed in order of $C_3H_8 > C_2H_6 > CH_4$, which can be understood in terms of the stronger interaction of propane or ethane with framework compared to methane. Furthermore, calculated adsorption selectivities demonstrated that ZJU-9a is more selective towards propane and ethane over methane.

REFERENCES

[1] R. Shi, D. Lv, Y. Chen, H. Wu, B. Liu, Q. Xia, and Z. Li, Sep. Purif. Technol, vol. 207, pp. 262-268, **2018**.

[2] Y. Zhang, H. Xiao, X. Zhou, X. Wang, and Z. Li, Ind. Eng. Chem. Res, vol. 56, pp. 8689–8696, **2017**.

[3] X. Wang, L. Li, Y. Wang, J. R. Li, and J. Li, Cryst. Eng. Comm, vol. 19, pp. 1729-1737 ,**2017**.

[4] S. Ma, H.-C. Zhou, Chem. Commun, vol. 46, pp. 44–53, **2010**.

[5] Y. He, F. Chen, B. Li, G. Qian, W. Zhou, and B. Chen, Coordin. Chem. Rev, vol. 373, pp. 167-198, **2018**.

[6] X. Duan, H. Wang, Y. Cui, Y. Yang, Z. Wang, B. Chen, and G. Qian, RSC Adv, vol. 5, pp. 84446-84450, **2015**.

[7] A. K. Rappé, C. J. Casewit, K. S. Colwell, W. A. Goddard III, and W. M. Skiff, J. Am. Chem. soc, vol. 114, pp. 10024-10035, **1992**.

[8] M. G. Martin, and J. I. Siepmann, J. Phys. Chem. B, vol. 102, pp. 2569-2577, **1998**.

[9] S. Keskin, J. Liu, R. B. Rankin, J. K. Johnson, D. S. Sholl, Ind. Eng. Chem. Res, vol. 48, pp. 2355- 2371, **2008**.

[10] M. Jorge, M. Fischer, J. R. Gomes, C. Siquet, J. C. Santos,
And A. E. Rodrigues, Ind. Eng. Chem. Res, vol. 53, pp. 15475-15487, **2014**.

[11] D. Dubbeldam, S. Calero, D. E. Ellis, and R. Q. Snurr, Mol. Simul, vol. 42, pp. 81-101, **2016**.

Calculation of Electronic Spectra for Carbazole Derivatives for Applications in Thermally Activated Delayed Fluorescence

F. Mohammadian-Sabet, A. Shayesteh*

School of Chemistry, College of Science, University of Tehran,14176, Iran, Email: ashayesteh@ut.ac.ir

Abstract*:* Thermally activated delayed fluorescence (TADF) offers promise for all-organic light-emitting diodes with quantum efficiencies competing with those of transition-metal-based phosphorescent devices. While computational efforts have so far largely focused on gas-phase calculations of singlet and triplet excitation energies, the design of TADF materials requires multiple methodological developments targeting among others a quantitative description of electronic excitation energetics, fully accounting for environmental electrostatics and molecular conformational effects, the accurate assessment of the quantum mechanical interactions that trigger the elementary electronic processes involved in TADF.

Keywords: OLED، TADF، HOMO، LUMO، TDDFT.

I. INTRODUCTION

OLEDs have many advantages over ordinary light sources such as light bulbs and fluorescence tubes in terms of quality and color adjustment allowing for almost any surface to be used and low electrical energy [1]. While the first generation of fluorescent OLEDs showed a bit of efficiency, the second-generation OLEDs that utilize phosphorescent materials are capable of achieving the maximum light emission theory. But compared to fluorescent OLEDs, phosphorescent OLEDs require expensive metal complexes, and there are limitations in their design and production. Recently, light-emitting diodes have been considered by heat-induced delayed fluorescence (TADF). The new generation of OLEDs has the benefits of both previous generations including the lack of expensive and scarce materials, high flexibility in the design and production of molecules and high efficiency. These compounds provide a promising field for the performance of high-power OLED diodes because they have the ability to convert triplet excitons to singlet excitons. The goal of this project is to predict the absorption wavelengths and the emission of fluorescence diodes with a delayed active heat.

II. METHODS

The geometry optimizations were performed using the ORCA quantum chemistry package [2]. In each case, the structures were optimized at the DFT(B3P86) [3] level using a def2-TZVP basis set [4,5] for all of the atoms except hydrogen, for which a def2-SVP basis was used. The first step in the calculation of the time dependent density functional of the theory (TD-DFT) is on the desired diode. In this study, important transfers and involved orbitals are identified. In the next step, using the CASSCF/NEVPT2 calculations, the energy of the transmissions is determined. Finally, the new diodes are suggested by adding different substitutes and studying the absorption and emission wavelengths.

III. RESULTS AND DISCUSSION

The criterion for our choice in this project is that $S_1 \rightarrow S_0$ electron transmissions are important, but if the transfers $S_2 \rightarrow S_0$ should be very close in energy terms and also have a high intensity. Now, we choose the electron donor groups and the electron acceptor from between carbazole, benzophenone and anthraquinone, respectively and we coordinated together. In examining the important transmissions and involved orbitals, it became clear that even meta and para positions are important.

Electron excited states are divided into two groups: singlet and triplet. The difference between singlet and triplet states are in the spin of electrons, so that the singlet electron ground state and in the excited states where two electrons are in different orbitals, we have the following spin functions for singlet and triplet states that there are 25% singlet and 75% triplet.

$1/\sqrt{2}[\alpha(1)\beta(2) - \alpha(2)\beta(1)]$ singlet   (1)

$1/\sqrt{2}[\alpha(1)\beta(2) + \alpha(2)\beta(1)]$ triplet   (2)

$\alpha(1)\alpha(2)$

$\beta(1)\beta(2)$

It should be noted that the three essential requirements for an OLED-TADF are as follows:

(A) There is a small energy gap between the excited states S_1 and T_1 (less than 0.2 electron volts)

(B) Small Exchange Integral between HOMO and LUMO orbital

(C) The separation and centralization of HOMO or LUMO orbital

As stated in the mandatory clause of a TADF, In Fig.1 the difference in energy between the lower energy level T_1 and the higher energy level S_1 shall be sufficiently small to permit reverse intersection system (RISC) to be carried out at ambient temperature ($T_1 \rightarrow S_1$). The energy difference between these two levels is proportional to the energy converted, which is related to the overlap integral between the two orbital ones responsible for the states of the two levels. Table 1 display an example of λ_{abs}(nm) calculated compositions.
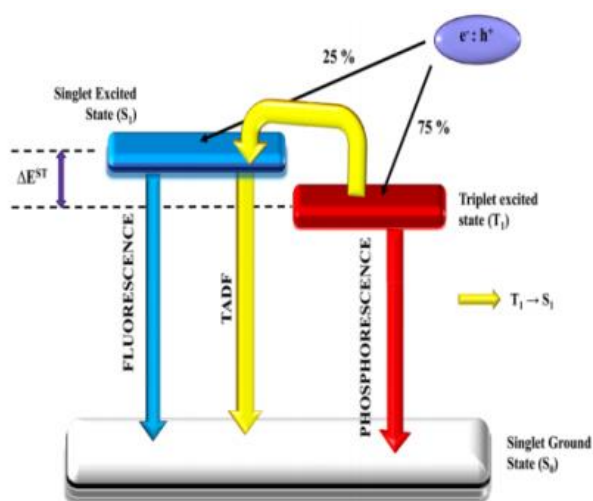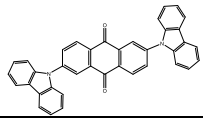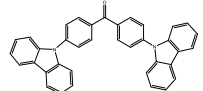

Fig.1: Diagram of first, second and third generation OLEDs

Table1: An example of λ_{abs}(nm) calculated compositions:

Complex	Exp.	TDDFT (B3P86)	NEVPT2	ΔE_{S-T} (eV)
2,6-di(carbazole-9-yl) anthraquinone	444	549	402	0.21
4,4'-di(carbazole-9-yl) benzophenone	340	411	323	0.31

IV. CONCLUSION

In conclusion, this present work can be employed to characterize and design new TADF molecular emitters. The first correlates the overlap and energy gap between the HOMO and LUMO orbitals with the experimental ΔE_{S1-T1}. In most molecules, the fluorescence signal is very weak. Most organic fluorescent molecules have high resonance coupled systems. In this way, the basic molecular framework for organic TADF molecules remains limited to azo-aromatic (such as trizines and oxidazoles), cyanobenzenes, sulfones and spiro flora derivatives [6].

REFERENCES

[1] U. Mitschke, P. Bäuerle, Journal of Materials Chemistry, vol. 10, pp. 1471, **2000**.

[2] Neese, F. Wiley Interdisciplinary Reviews: Computational Molecular Science, vol. 2, pp. 73 – 78, **2012**.

[3] J. P. Perdew, K. Burke, M. Ernzerhof, Physical Review Letters, vol. 77, pp. 3865 – 3868, 1996.

[4] A. Scha¨fer, H. Horn, R. J. Ahlrichs, Chemical Physics, vol. 97, pp. 2571 −2577, **1992**.

[5] F. Weigend, R. Ahlrichs, Physical Chemistry Chemical Physics, vol. 7, pp. 3297 – 3305, **2005**.

[6] S. Y. Lee, T. Yasuda, Y. S. Yang, Q. Zhang, C. Adachi, *Angewandte Chemie International,* vol. 53, pp. 6402-6406, **2014.**

Theoretical Investigation of Vinylogus Anomeric Effects on the Stability of 4-H-4-amino-1-methylpyridin And Its Analogues

Neda Najjari Milani[a]*

[a] Islamic Azad University, arak, Iran, E-mail: milanii.neda@gmail.com

Abstract: In this study, the stability of 4-H-4-amino-1-methylpyridin molecule in planar and bent conformations was investigated in the B3LYP/6-311++G (d,p) level of theory. The Gibbs-Free energy and structural parameters of the molecules were calculated. NBO analysis was used to illustrate vinylogous anomeric effect on the bending of ring. The responsible interactions of this effect were determined. The interaction energy, off-diagonal elements values of their NBO were calculated.

Keywords: 4-H-4-amino-1-methylpyridin, anomeric effects, NBO, ab initio

I. INTRODUCTION

The anomeric effect is originally described as the preference of an electronegative substituent at Cl (the anomeric carbon) of a pyranosides ring to undertake the axial rather than equatorial orientation, in contrast to the predictions based solely on steric grounds[1-4]. One type of this steroelectronic interaction is named vinylogous anomeric effect, extending over four bonds [5]. Two rationalizations to understand the origin of the anomeric effect are electrostatic [6] and hyperconjugation [7] models, which are generally accepted. In this study, we investigated vinylogous anomeric effect in the 4-H-4-amino-1-methylpyridin at the B3LYP/6-311++G (d,p) level of theory, and NBO analysis was used to explain this effect.

II. COMPUTATIONAL METHODS

All calculations were performed with the Gaussian 09 suite program. The standard 6-311++G (d,p) basis set[8-10] was used in the calculations. The population analysis has also been conducted by the natural bond orbital method at B3LYP/6-311++G (d,p) level of theory using NBO 6.0 program under Gaussian 2009 program package.

III. RESULTS AND DISCUSSION

A. Energetic Aspect

Figure 1 presents the structures of 4-H-4-amino-1-methylpyridin molecules in planar and bent conformations. Table 1 shows the Gibbs-Free energy values of these molecules. These values bent form is more stable than planar form in all studied molecules. The Gibbs-Free energy decrease from compound 1 (E=N) to compound 3 (E=As). More stability of the bent conformation is attributed to vinylogous hyperconjugative anomeric effect.

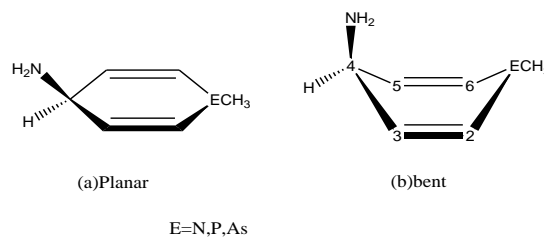(a)Planar   (b)bent

E=N,P,As

Figure 1. 4-H-4-amino-1-methylpyridin molecule in (a) planar and (b) bent conformations.

Table 1. ΔG (in hartree) values of 4-H-4-amino-1-methylpyridin molecule in planar and bent conformations at the B3LYP/6-311++G** level of theory.

	E=N	E=P	E=As
G(bent)	-344.003455	-630.609259	-2523.049213
G(Planar)	-344.003453	-630.60891	-2523.044112
ΔG	3.18	5.56	8.12

B. Structural Parameters

Figure 2 presents the selected structural parameters of the studied molecules. Dihedral angle values reveal that the optimized structure deviates from planar conformation. The ring bending increase in the presence of As compared to N.
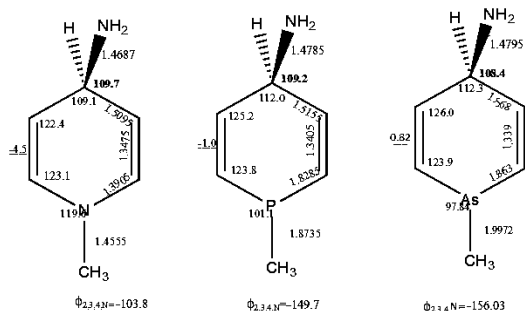
Figure 2. The structural parameters of the optimized 4-H-4-amino-1-methylpyridin molecule in bent conformations. The underline and bold values are dihedral and bond angle, respectively.

C. Natural Bond Orbital Analysis (NBO)

From the natural bond orbital analysis (NBO) viewpoint, the anomeric effect is expressed as resulting from σ (C4-N7) →π*(C2=C3), π (C2=C3) →σ*(C4-N7), σ (E1-C8) →σ*(C2=C3), and σ (E1-C8) →π*(C2=X3) hyperconjugative interactions. Now, in this section, we studied the illustrated bending of the studied molecules based on the calculated parameters like the Stabilization Energies , Off-diagonal Elements (F_{ij}), occupancies and energy of the σ(C4-N7)→π*(C2=C3), π(C2=C3)→σ*(C4-N7), σ (E1-C8)→σ*(C2=C3), and σ (E1-C8)→π*(C2=X3) from NBO analysis. The anomeric effect (AE) values are gathered in Table 3. These values show that anomeric effect (AE) values are larger in the presence of E=N compared to E=As.

Table 3. Stabilization energies (E_2, in kcal mol^{-1}), anomeric effect (*AE*, in kcal mol^{-1}) of 4- H-4-amino-1-methylpyridin molecule in bent conformations at the B3LYP/6-311++G** level of theory.

	E=N	E=P	E=As
E_2 (kcal mol^{-1})			
σ(C4-N7)→π*(C2=C3)	1.80	2.12	2.56
π(C2=C3)→σ*(C4-N7)	5.05	1.63	1.13
σ (E1-C8)→σ*(C2=C3)	1.88	0.94	0.84
σ (E1-C8)→π*(C2=C3)	3.98	2.98	2.18
Anomeric effect(AE)	12.81	7.67	6.71

IV. Conclusion

In this work, we investigated the stability of 4-H-4-amino-1-methylpyridin molecule in planar and bent conformations at the B3LYP/6-311++G (d,p) level of theory. These calculations indicate that:

1. The bent conformation has greater stability than planar conformation in all studied molecules. The greater stability of the bent conformation was attributed to vinylogous hyperconjugative anomeric effect.
2. The anomeric effect is illustrated by Natural bond orbital analysis (NBO). This effect results from σ (C4-N7) →π*(C2=C3), π (C2=C3) →σ*(C4-N7), σ (E1-C8) →σ*(C2=C3), and σ (E1-C8) →π*(C2=C3) hyperconjugative interactions.
3. There is larger anomeric effect (AE) values in the presence of E=N in compared to E=As.

References

1. E. Juaristi and Y. Bandala, in Advances in Heterocyclic Chemistry, 2012, vol. 105, pp. 189-222.
2. E. Juaristi and G. Cuevas, Tetrahedron, 1992, 48, 5019-5087.
3. A. J. Kirby, The Anomeric Effect and Related Stereoelectronic Effects at Oxygen, Springer, Berlin, 1983.
4. R. U. Lemieux, Pure Appl. Chem., 1971, 25, 527-548.
5. A. R. Katritzky, P. J. Steel and S. N. Denisenko, Tetrahedron, 2001, 3309-3314.
6. C. B. Anderson and D. T. Sepp, J. Org. Chem., 1967, 32, 607-611.
7. B. Fuchs, A. Ellencweig, E. Tartakovsky and P. Aped, Angew. Chem. Int. Ed., 1986, 25, 287-289.
8. R. Krishnan, J. S. Binkley, R. Seeger and J. A. Pople, J. Chem. Phys., 1980, 72, 650.
9. A. D. McLean and G. S. Chandler, J. Chem. Phys., 1980, 72, 5639.
10. L. A. Curtiss, M. P. McGrath, J.-P. Blandeau, N. E. Davis, R. C. Binning and J. L. Radom, J. Chem. Phys., 1995, 103, 6104.
11. Najjari Milani N, Ghiasi R, Forghaniha A. (2018). Theoretical investigation of vinylogous anomeric effect on 4-halo-4- H-pyran and 4-halo-4-H-thiopyran molecules. *Sulfur chemistry*, 39(6), 665-673.
12. katritzky AR, Peter Steel J, Sergey Denisenko N. (2001). X-Ray crystallographic evidence for a vinylogous anomeric effectbin benzotriazole-substituted heterocycles. *Tetrahedron, 16*, 3309-3314.

Theoretical Research of Vinylogous Anomeric Effects on the Stability of 4-H-4-triazole-1-methylpyridin And Its Analogues

Neda Najjari Milani[a*]

[a] *Islamic Azad University, arak, Iran, E-mail: milanii.neda@gmail.com*

Abstract: The stability of 4-H-4-triazole-1-methylpyridin molecule in planar and bent conformations was verified in this study by the B3LYP/6-311++G (d, p) level of theory. The Gibbs-Free energy and structural parameters of the molecules were computed. NBO analysis of donor-acceptor (bond-antibond) interactions was used to show vinylogous anomeric effect on the bending of ring. The responsible interactions of this effect were defined. The interaction energy, off-diagonal elements amounts of their NBO were computed.

Keywords: 4-H-4-triazole-1-methylpyridin, anomeric effects, NBO, ab initio

I. INTRODUCTION

The anomeric effect is originally described as the preference of an electronegative substituent at Cl (the anomeric carbon) of a pyranosides ring to undertake the axial rather than equatorial orientation, in contrast to the predictions based solely on steric grounds[1-4]. One type of this steroelectronic interaction is named vinylogous anomeric effect, extending over four bonds [5]. Two rationalizations to understand the origin of the anomeric effect are electrostatic [6] and hyperconjugation [7] models, which are generally accepted. In this study, we investigated vinylogous anomeric effect in the 4-H-4-amino-1-methylpyridin at the B3LYP/6-311++G (d,p) level of theory, and NBO analysis was used to explain this effect.

II. COMPUTATIONAL METHODS

All calculations were performed with the Gaussian 09 suite program. The standard 6-311++G (d,p) basis set[8-10] was used in the calculations. The population analysis has also been conducted by the natural bond orbital method at B3LYP/6-311++G (d,p) level of theory using NBO 6.0 program under Gaussian 2009 program package.

III. RESULTS AND DISCUSSION

A. Energetic Aspect

Figure 1 presents the structures of 4-H-4-triazole-1-methylpyridin molecules in planar and bent conformations. Table 1 shows the Gibbs-Free energy values of these molecules. These values bent form is more stable than

planar form in all studied molecules. The Gibbs-Free energy decrease from compound 1 (E=N) to compound 3 (E=As). More stability of the bent conformation is attributed to vinylogous hyperconjugative anomeric effect.
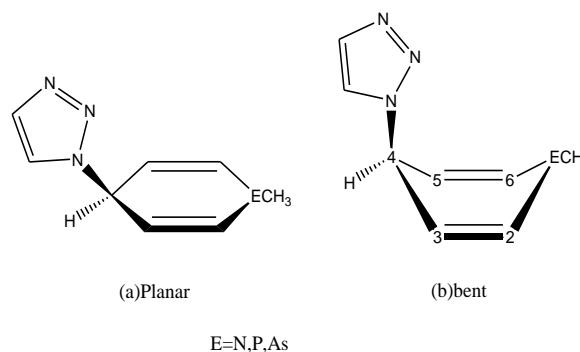

(a)Planar   (b)bent

E=N,P,As

Figure 1. 4-H-4-triazole-1-methylpyridin molecule in (a) planar and (b) bent conformations.

Table 1. ΔG (in hartree) values of 4-H-4-triazole-1-methylpyridin molecule in planar and bent conformations at the B3LYP/6-311++G** level of theory.

	E=N	E=P	E=As
G(bent)	-529.676675	-816.279288	-2708.71503
G(Planar)	-529.675657	-816.277587	-2708.714781
ΔG	1.62228	2.71071	3.96806

B. Structural Parameters

Figure 2 presents the selected structural parameters of the studied molecules. Dihedral angel values reveal that the optimized structure deviates from planar conformation. The ring bending increase in the presence of as compared to N.

C. Natural Bond Orbital Analysis (NBO)

From the natural bond orbital analysis (NBO) viewpoint, the anomeric effect is expressed as resulting from σ (C4-N7) →π*(C2=C3), π (C2=C3) →σ*(C4-N7), σ (E1-C8) →σ*(C2=C3), and σ (E1-C8) →π*(C2=X3) hyperconjugative interactions. Now, in this section, we studied the illustrated bending of the studied molecules

based on the calculated parameters like the Stabilization Energies, Off-diagonal Elements (F_{ij}), occupancies and energy of the σ(C4-N7)→π*(C2=C3), π(C2=C3)→σ*(C4-N7), σ (E1-C8)→σ*(C2=C3), and σ (E1-C8)→π*(C2=X3) from NBO analysis. The anomeric effect (AE) values are gathered in Table 3. These values show that anomeric effect (AE) values are larger in the presence of E=N compared to E=As.
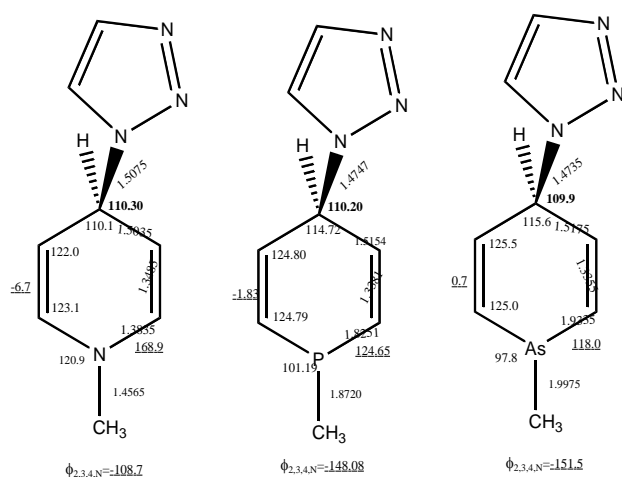

Figure 2. The structural parameters of the optimized 4-H-4-triazole-1-methylpyridin molecule in bent conformations. The underline and bold values are dihedral and bond angle, respectively.

Table 3. Stabilization energies (E_2, in kcal mol^{-1}), anomeric effect (AE, in kcal mol^{-1}) of 4-H-4-triazole-1-methylpyridin molecule in bent conformations at the B3LYP/6-311++G** level of theory.

	E=N	E=P	E=As
E_2 (kcal mol^{-1})			
σ(C4-N7)→π*(C2=C3)	1.47	2.78	3.66
π(C2=C3)→σ*(C4-N7)	7.13	2.65	2.27
σ (E1-C8)→σ*(C2=C3)	1.84	0.84	0.65
σ (E1-C8)→π*(C2=C3)	3.98	2.22	1.62
Anomeric effect(AE)	15.89	8.49	8.2

IV. CONCLUSION

In this study, we verified the stability of 4-H-4-triazole-1-methylpyridin molecule in planar and bent conformations at the B3LYP/6-311++G (d,p) level of theory. These calculations show that:

1. The bent conformation has larger stability than planar conformation in all investigated molecules. The larger stability of the bent conformation was assigned to vinylogous hyperconjugative anomeric effect.

2. The structural parameters amount determines that the optimized structure deviates from planar conformation. The ring bending increase from E= As to E=N.

3. The anomeric effect is showed by Natural bond orbital analysis (NBO). The anomeric effect (AE) amounts increase from E=N to E=As.

References

1. E. Juaristi and Y. Bandala, in Advances in Heterocyclic Chemistry, 2012, vol. 105, pp. 189-222.

2. E. Juaristi and G. Cuevas, Tetrahedron, 1992, 48, 5019-5087.

3. A. J. Kirby,The Anomeric Effect and Related Stereoelectronic Effects at Oxygen, Springer, Berlin, 1983.

4. R. U. Lemieux, Pure Appl. Chem., 1971, 25, 527-548.

5. A. R. Katritzky, P. J. Steel and S. N. Denisenko, Tetrahedron, 2001, 3309-3314.

6. C. B. Anderson and D. T. Sepp, J. Org. Chem., 1967, 32, 607-611.

7. B. Fuchs, A. Ellencweig, E. Tartakovsky and P. Aped, Angew. Chem. Int. Ed. , 1986, 25, 287-289.

8. R. Krishnan, J. S. Binkley, R. Seeger and J. A. Pople, J. Chem. Phys., 1980, 72, 650.

9. A. D. McLean and G. S. Chandler, J. Chem. Phys., 1980, 72, 5639.

10. L. A. Curtiss, M. P. McGrath, J.-P. Blandeau, N. E. Davis, R. C. Binning and J. L. Radom, J. Chem. Phys., 1995, 103, 6104.

11. Najjari Milani N, Ghiasi R, Forghaniha A. (2018). Theoretical investigation of vinylogous anomeric effect on 4-halo-4-   H-pyran and 4-halo-4-H-thiopyran molecules. *Sulfur chemistry*, 39(6), 665-673.

12. katritzky AR , Peter Steel J ,Sergey Denisenko N.(2001). X-Ray crystallographic evidence for a vinylogous anomeric effectbin benzotriazole-substituted heterocycles. *Tetrahedron, 16*, 3309-3314.

Density Functional Theory Calculations of CO_2 Reduction Mechanism on Hybrid Photocatalyst Under Visible Light

S. S. Tafreshi [a]*, A. Z. Moshfegh[b,c], N. H. de Leeuw [d]

[a]Department of Chemistry, Amirkabir University of Technology, Tehran,15875-4413, Iran
[b]Department of Physics, Sharif University of Technology, Tehran, 11155-9161, Iran
[c]Institute for Nanoscience and Nanotechnology, Sharif University of Technology, Tehran, 14588-8969, Iran
[d]School of Chemistry, Cardiff University, Main Building, Park Place, Cardiff, CF10 3AT, UK
Email: s.s.tafreshi@aut.ac.ir

Abstract: Density functional Theory (DFT) calculations have been performed to investigate the electronic structure and photocatalytic activity of a hybrid $Ag_3PO_4(111)/g$-C_3N_4 structure, showing the enhancement of the photocatalytic activity of the $Ag_3PO_4(111)$ surface and g-C_3N_4 sheet under the visible irradiation. The investigation of the reaction pathways for photocatalytic CO_2 reduction on the $Ag_3PO_4(111)/g$-C_3N_4 nanocomposite demonstrate that this heterostructure thermodynamically exhibits a higher selectivity towards CH_4 production than that of CH_3OH.

Keywords: CH_4 and CH_3OH production, density functional theory, graphitic carbon nitride, photocatalytic CO_2 reduction, silver phosphate.

I. INTRODUCTION

Population growth and industrial development result in limiting availability of fossil fuel resources. In addition, as a result of their combustion, CO_2 emissions into the environment and the resulting greenhouse effect have led to significant concerns about climate change. Therefore, conversion of CO_2 to valued products is an important issue in both energy and environmental global concerns. Due to the efficient separation of photo-excited electrons and holes, silver orthophosphate (Ag_3PO_4) possesses excellent photocatalytic properties under visible light. The major problem for practical applications of Ag_3PO_4 is its low structural stability. Several studies have been carried out to improve the stability and thus the photocatalytic activity of Ag_3PO_4 by coupling it with other semiconductors[1].
Graphitic carbon nitride (g-C_3N_4) has been reported as a novel, metal-free layered semiconductor and visible-light-driven photocatalyst for CO_2 reduction[2]. Due to its medium band gap energy (~2.7 eV) and fast charge recombination rate, it is widely accepted that g-C_3N_4 must be coupled with other photocatalysts to enhance its photocatalytic activity[3]. A few studies have focused on combining Ag_3PO_4 with g-C_3N_4 to enhance the photocatalytic activity [4]. Yiming He et al. have

synthesized the Ag_3PO_4/g-C_3N_4 heterojunction, observing enhanced photocatalytic CO_2 reduction, where Ag nanoparticles acted as the recombination center for electrons and holes by a Z-scheme charge carrier pathway[5].
In this investigation, geometrical and electronic properties of the $Ag_3PO_4(111)/g$-C_3N_4 heterojunction photocatalyst have been studied using DFT calculations, to understand charge transfer mechanism at the interface and define the role of Ag nanoparticles as a recombination center of the hybrid $Ag_3PO_4(111)/g$-C_3N_4 in the CO_2 photo-reduction process.
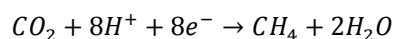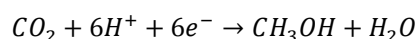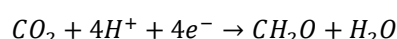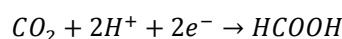
II. METHODS

We have performed electronic structure calculations using DFT as implemented in the Vienna Ab initio Simulation Package (VASP)[6]. The total energy calculations have been performed using the Perdew-Burke-Ernzerhof (PBE) form of the generalized gradient approximation (GGA) with the projector augmented wave (PAW) method[7]. PBE0[8] formalism were applied for the hybrid $Ag_3PO_4(111)/g$-C_3N_4 and ternary $Ag_3PO_4(111)/Ag/g$-C_3N_4 nanocomposites. The g-C_3N_4 monolayer modeled by a 3×3 supercell sits on a 1×1 $Ag_3PO_4(111)$ slab resulting in hybrid $Ag_3PO_4(111)/g$-C_3N_4 photocatalyst with a hexagonal super cell with dimension of 8.287Å and a lattice mismatch of nearly 6%.

III. RESULTS AND DISCUSSION

The side views of the $Ag_3PO_4(111)/g$-C_3N_4 and $Ag_3PO_4(111)/Ag/g$-C_3N_4 interface models used in our calculations, after geometry optimization, are shown in Fig. 1, indicating more interaction at the interface of the ternary composite. There is a shorter distance between g-C_3N_4 layer and $Ag_3PO_4(111)$ surface in the $Ag_3PO_4/Ag/g$-C_3N_4 and a more distorted g-C_3N_4 structure (Fig. 1b), due to the presence of atomic Ag at the interface. The band gap of the hybrid structure is reduced to 2.52 eV (Fig. 2). This could improve photocatalytic activity of the $Ag_3PO_4(111)$ surface and g-C_3N_4 monolayer under visible irradiation. We have

further investigated the mechanism of CO_2 reduction to possible hydrocarbons, catalyzed by the hybrid system. The overall reactions of CO_2 reduction to form HCOOH, CH_2O, CH_3OH and CH_4 using 2, 4, 6 and 8 electrons in the presence of hydrogen are expressed as follows:

$$CO_2 + 2H^+ + 2e^- \rightarrow HCOOH$$

$$CO_2 + 4H^+ + 4e^- \rightarrow CH_2O + H_2O$$

$$CO_2 + 6H^+ + 6e^- \rightarrow CH_3OH + H_2O$$

$$CO_2 + 8H^+ + 8e^- \rightarrow CH_4 + 2H_2O$$

The overall reactions described above include several elementary hydrogenation steps, which are determined by the most stable product at each step, where our calculated reaction energies revealed that the production of CH_4 is the dominant pathway through either formation of HCOOH* or HOCOH* as intermediates.

Our electronic structure calculations of the ternary $Ag_3PO_4(111)/Ag/g$-C_3N_4 nanocomposite revealed that the Ag nanoparticles at the interface of $Ag_3PO_4(111)$ and g-C_3N_4 act as a charge recombination center where the charge transfer occurs, promoting the electron-hole separation in the hybrid $Ag_3PO_4(111)/g$-C_3N_4 system through a Z-scheme mechanism (Fig. 3). Therefore, it can provide to a highly efficient photo-catalyst as supported by experimental measurement [5].
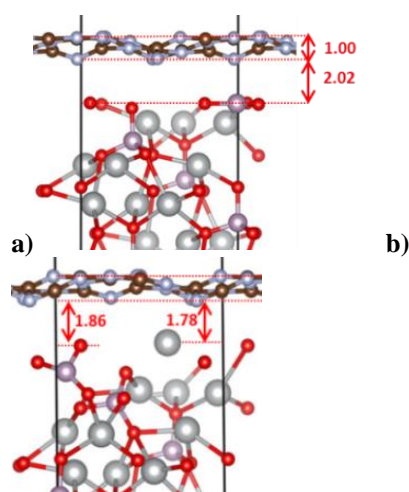
Fig. 1: Side geometries of a) Ag_3PO_4/g-C_3N_4 and b) $Ag_3PO_4/Ag/g$-C_3N_4 interface, after optimization. All values are in Angestrom.
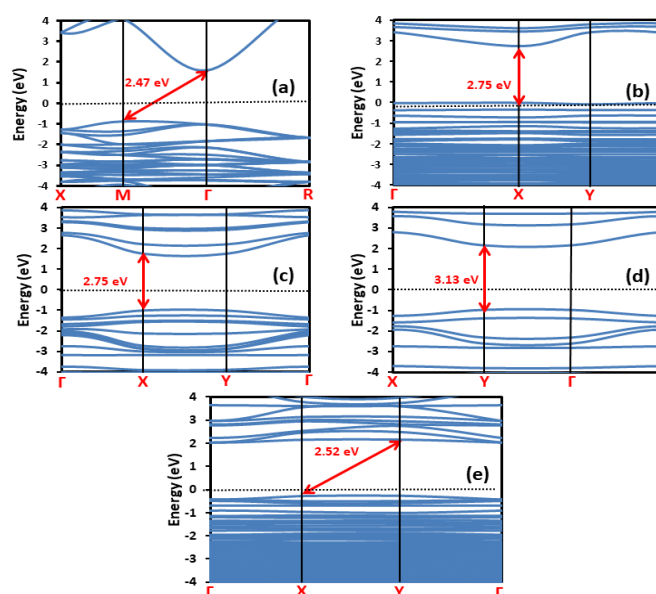
Fig. 2: The calculated band structure of (a) bulk Ag_3PO_4, (b) $Ag_3PO_4(111)$, (c) bulk g-C_3N_4, (d) g-C_3N_4 monolayer and (e) hybrid structure $Ag_3PO_4(111)/g$-C_3N_4.
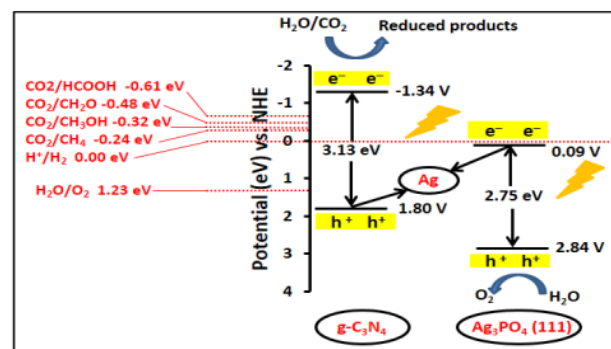
Fig. 3: The calculated Z-scheme charge transfer mechanism of the $Ag_3PO_4(111)/Ag/g$-C_3N_4 hybrid composite under photoirradiation.

IV. CONCLUSION

This study has investigated the electronic properties of the $Ag_3PO_4(111)/g$-C_3N_4 as highly efficient visible light-active photo-catalyst, and its activity towards CO_2 reduction. Due to the Ag(d) and O(p) states, it is forming the upper part of the valence band and C(p), N(p) and Ag(s) the lower part of the conduction band, the band gap of the hybrid material is reduced from 2.75 eV for $Ag_3PO_4(111)$ and 3.13 eV for monolayer of g-C_3N_4 to about 2.52 eV for the hybrid system, as a result enhanced photocatalytic activity of the

Ag$_3$PO$_4$(111) surface and g-C$_3$N$_4$ sheet observed in the visible region. We have also investigated possible reaction pathways for photocatalytic CO$_2$ reduction on the Ag$_3$PO$_4$(111)/g-C$_3$N$_4$ hybrid showing a higher selectivity towards CH$_4$ production than that of CH$_3$OH. Our results revealed that the charge transfer between the Ag$_3$PO$_4$(111) slab and g-C$_3$N$_4$ monolayer occurs through mediation of Ag nanoparticles, thus proposing a Z-scheme mechanism. These results provide in depth understanding of the reaction mechanism in the conversion of CO$_2$ to useful chemicals via an Ag$_3$PO$_4$ and g-C$_3$N$_4$-based hybrid photocatalyst under visible light.

REFERENCES

[1] W. Yao, B. Zhang, C. Huang, C. Ma, X. Song and Q. Xu, *Journal of Materials Chemistry*, 22, pp. 4050-4055, **2012**.

[2] B. Zhu, L. Zhang, D. Xu, B. Cheng and J. Yu, *Journal of CO2 Utilization*, 21, pp. 327-335, **2017**.

[3] Q. Hao, X. Niu, C. Nie, S. Hao, W. Zou, J. Ge, D. Chen and W. Yao, *Physical Chemistry Chemical Physics*, 18, pp. 31410-31418, **2016**.

[4] H. Katsumata, T. Sakai, T. Suzuki and S. Kaneco, *Industrial & Engineering Chemistry Research*, 53, pp. 8018-8025, **2014**.

[5] Y. He, L. Zhang, B. Teng and M. Fan, *Environmental Science & Technology*, 49, pp. 649-656, **2015**.

[6] G. Kresse and J. Furthmüller, *Physical Review B*, 54, pp. 11169-11186, **1996**.

[7] P. E. Blochl, *Physical Review B*, 50, pp. 17953-17979, **1994**.

[8] J. Paier, R. Hirschl, M. Marsman and G. Kresse, *The Journal of Chemical Physics*, 122, p. 234102, **2005**.

Computational assessment of the electro-optical characteristics of $Li_n@B_{12}$ (n=1, 2, 3)

M. Yousefizadeh[a]*, E. Shakerzadeh[b], M. Bamdad[b]
Department of chemistry, shahid Chamran university of Ahvaz, Ahvaz, Iran
Email: Yousofizadehm@yahoo.com

Abstract: In this study, the alteration of the electro-optical properties of B_{12} cluster due to interaction with one, two and three Li atoms is investigated. The first and second-order hyperpolarizabilities of these complexes has been calculated at the CAM-B3LYP/6-311+G(2d) level of theory. The electronic properties of B_{12} cluster is very sensitive to interaction with Li atom. In addition, it is observed that the interaction with Li atom enhances the first and second-order hyperpolarizabilities of this cluster. It is also concluded that the interaction of boron cluster with Li atom, is an effective method to enhance its NLO response and decrease its HOMO-LUMO gap.

Keywords: hyperpolarizability, NLO response, HOMO-LUMO gap

I. INTRODUCTION

Boron is an electron-deficient element with more valence orbitals than valence electrons, which forms a large family of stable cluster structures via multicenter bonding [1, 2]. Among the members of this family, boron clusters' exclusive characteristics such as geometries, physical and chemical properties, as well as their potential applications such as hydrogen storage have been studied by experimentalists and theoreticians [3].

II. METHODS

Structures and relative energies of $Li_n@B_{12}$ ($n = 1, 2, 3$) were optimized without symmetry restriction at the TPSSH/6-31+G(d) level of theory. The first and second-order hyperpolarizabilities of these complexes has been calculated at the CAM-B3LYP/6-311+G(2d) level of theory.

III. RESULTS AND DISCUSSION

All calculations are performed using the Gaussian 09 software. The optimized geometries of the B_{12} and $Li_n@B_{12}$ ($n = 1, 2, 3$) are shown in Figure 1. The adsorptions of one, two and three Li atoms are considered on the surface of these

structures. The HOMO-LUMO gap, i.e. HLG = ($\varepsilon_L - \varepsilon_H$), is used to explore electronic properties of the considered systems and is calculated based on ε_H and ε_L, which are the obtained energies of the highest occupied molecular orbital and the lowest unoccupied molecular orbital, respectively. The nonlinear optical response (NLO) coefficient, which is the magnitude of the total first static hyperpolarizability (β_0), is calculated as:

$$\beta_0 = \left(\beta_x^2 + \beta_y^2 + \beta_z^2 \right) \tag{1}$$

in which,

$$\beta_x = \left(\beta_{xxx} + \beta_{xyy} + \beta_{xzz} \right) \tag{2}$$

$$\beta_y = \left(\beta_{yyy} + \beta_{yxx} + \beta_{yzz} \right) \tag{3}$$

$$\beta_z = \left(\beta_{zzz} + \beta_{zxx} + \beta_{zyy} \right) \tag{4}$$

where $\beta_{xxx}, \beta_{yyy}, \ldots$ are the components of the three-dimensional tensor of hyperpolarizability. The mean second-hyperpolarizability along the molecular axis has been calculated using the following expression, which consist of six distinct compounds at the static limit [4].

$$\langle \gamma \rangle = \frac{1}{5}\left[\gamma_{xxxx} + \gamma_{yyyy} + \gamma_{zzzz} + 2\left(\gamma_{xxyy} + \gamma_{xxzz} + \gamma_{yyzz} \right) \right]$$

The obtained values for the magnitude of first and second hyperpolarizability, i.e. β_0 and $Li_n@B_{12}$ respectively, as well as frontier molecular orbital energies (ε_L and ε_H) and HOMO–LUMO gap are summarized in Table 1.
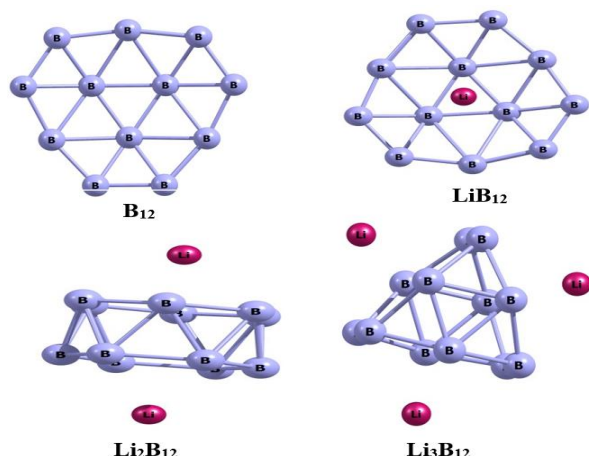
Fig. 1: The optimized structures of the studied compounds.

Table 1: The HOMO (εHOMO), LUMO (εLUMO), HOMO-LUMO gap (HLG) and the HLG variation percentage with respect to pure boron clusters (%ΔHLG), first hyperpolarizability (β_0) and second hyperpolarizability(γ)

	εH $(a.u)$	εL $(a.u)$	HLG (eV)	ΔHLG%	$\gamma_{av} \times 10^5$	β_0
B_{12}	-0.31	-0.09	6.00	-	0.6101	1743.46
LiB_{12}	-0.18	-0.13	1.30	-78.38	1.0059	1211291.08
Li_2B_{12}	-0.16	-0.08	2.17	-63.92	4.0005	0.00
Li_3B_{12}	-0.18	-0.08	2.86	-52.31	3.1819	13148808

The diffuse excess electron usually leads to a large NLO response.

IV. CONCLUSION

The results of the conducted study shows that the interaction with Li tom causes a dramatic decrease of the value of HLG and a dramatic increase of the hyperpolarizability values. These caused effects bring about a notable increase of the nonlinear optical (NLO) response. The achieved results can conclude to some innovative boron-based electro-optical nanomaterials designs.

REFERENCES

[1] E. W. Abel, F. G. Stone and G.Wilkinson, Eds.; Elsevier Science Ltd.: Oxford, U.K., vol. 4, pp. 217-255, **1995**.

[2] R. E. Williams, In Advances in Organometallic Chemistry; F. G. A. Stone and R. West, Eds.; Academic Press: New York, vol. 36, pp. 1-55, **1994**.

[3] L. Wang, J. Zhao, F. Li, and Z. Chen, Chem. Phys. Lett, vol. 501, pp. 16-19, **2010**.

[4] D.P. Shelton, J.E. Rice, , Chem. Rev, vol. 94, pp. 3-29, **1994**.

Investigation of the Heterogeneity Order Parameter of Four Different Imidazolium- And Cholinium-Based Ionic Liquids

S. Hajiyan[a], A. Daneshvar[a*], and M. Moosavi[a]
[a] Department of Chemistry, University of Isfahan, Isfahan, 81746-73441, Iran
Email: a.daneshvar88@yahoo.com

Abstract: The aim of this study is investigation of the cation type effect on the heterogeneity order parameter (HOP) as a structural property in imidazolium- and cholinium-based ionic liquids using molecular dynamics simulation. The results showed that the elongation of the alkyl chain in imidazolium cation and enhancement of the number of hydroxyl group in cholinium cation have reverse effect on the HOP values of cations and anions.

Keywords: Ionic liquid, Molecular dynamics simulation Heterogeneity order parameter, Imidazolium, and Cholinium.

I. INTRODUCTION

Ionic liquids (ILs) are a recent attended class of liquids due to their unique physical properties such as high thermal stability, negligible vapor pressure, non-flammability, high conductivity and low toxicity [1-3]. According to their unique properties the ILs are suitable substituent for volatile organic solvent and can be used as catalyst, extractor, and electrolyte in many industrial applications. The molecular dynamics simulation of the ILs can help us to understand the molecular interactions and its relation to the physical properties. The heterogeneity order parameter (HOP) is a structural property which can give some information about inter molecular interactions of liquids. This parameter was calculated for many ionic liquid systems to clarify the structural changes [4, 5].

In this regards, the HOP parameter of two imidazolium-based and two cholinium-based ionic liquids contains 1-ethyl-3-methylimidazolium [emim]$^+$, 1-butyl-3-methylimidazolium [bmim]$^+$, N-hexyl-N,N-2-dihydroxyethyl-N-methyl ammonium [DHEA]$^+$, and N-hexyl-N,N,N-2-trihydroxyethyl ammonium [THEA]$^+$ cations and tetrachloroferrate [FeCl$_4$]$^-$ anion has been calculated using molecular dynamics simulation.

II. METHODS

In this paper, the studied ionic liquids were modeled using a potential energy function based on the OPLS-AA [6, 7].

The B3LYP density functional with the 6-311++G** basis set have been employed to optimize the structures using Gaussian 09 package. The NBO and the CHELPG methods have been chosen for charge transfer of imidazolium-based and cholinium-based ionic liquids, respectively, due to their lower percentage error between simulated density data and their experimental values in the literature.

All of the MD simulations are done using the LAMMPS molecular dynamics package [8], at T = 298.15 K and at 0.1 MPa. A periodic cubic box containing 216 pairs of ions was used with a 10 Å cut off for non-bonded interactions. Coulombic interactions were handled by the ewald method. A Nosé-Hoover thermostat and barostat [9, 10] were used to control temperature and pressure, with time constants of 0.1 and 1 ps, respectively. The conjugate gradient energy minimization scheme has been used to relax the initial configurations. The isothermal-isobaric (NPT) runs of 5 ns were carried out at the desired pressure and temperature to estimate the HOP of systems.

III. RESULTS AND DISCUSSION

The average HOP is computed by averaging over all N_s sites of interest as the following equation

$$\hat{h} = \frac{1}{N_s} \sum_{i=1}^{N_s} \sum_{j=1}^{N_s} exp\left(-r_{ij}^2 / 2\sigma^2\right) \quad (1)$$

where r_{ij} is the modulation of the vector r_i - r_j corrected with the periodic boundary conditions, and $\sigma = L/N_s^{1/3}$, in which L is the side length of the cubic simulation box. Wang and Voth shows that for some ideal systems the HOP approaches a constant value of 15.5 ± 0.2 after $N > 125$ with considering the periodic boundary conditions [11]. Accordingly, more deviation from 15.5 value shows more heterogeneity. Herein, we calculated HOP for different sites of four studied ILs. The results have been sown in Table 1 and Fig. 1.

Table 1. The HOP values for anion and cation sites of the studied ILs.

	[emim][FeCl$_4$]	[bmim][FeCl$_4$]	[DHEA][FeCl$_4$]	[THEA][FeCl$_4$]
Anion	11.08	10.78	12.42	11.38

Cation	11.04	10.71	10.99	12.44

As the results show, the elongation of the alkyl chain residue of cations in imidazolium-based ILs causes they prefer to aggregate. Accordingly, the heterogeneity of cations increases and the HOP decreases. This result is in contrast with cholinium-based ILs in which the increasing of the number of the hydroxyl group in the cations makes a spherical hindrance for aggregation. So, the HOP values of cations in these ILs increase with increasing the number of   –OH groups of cations and makes a homogenies system.

It is interesting that the HOP values of anion have the same procedure in both class of studied ILs. In fact, the increasing of the alkyl chain length in imidazolium cation and the number of hydroxyl group in cholinium cation causes a decrement in HOP values. So, the anions prefer to aggregate and makes a heterogeneous structure.
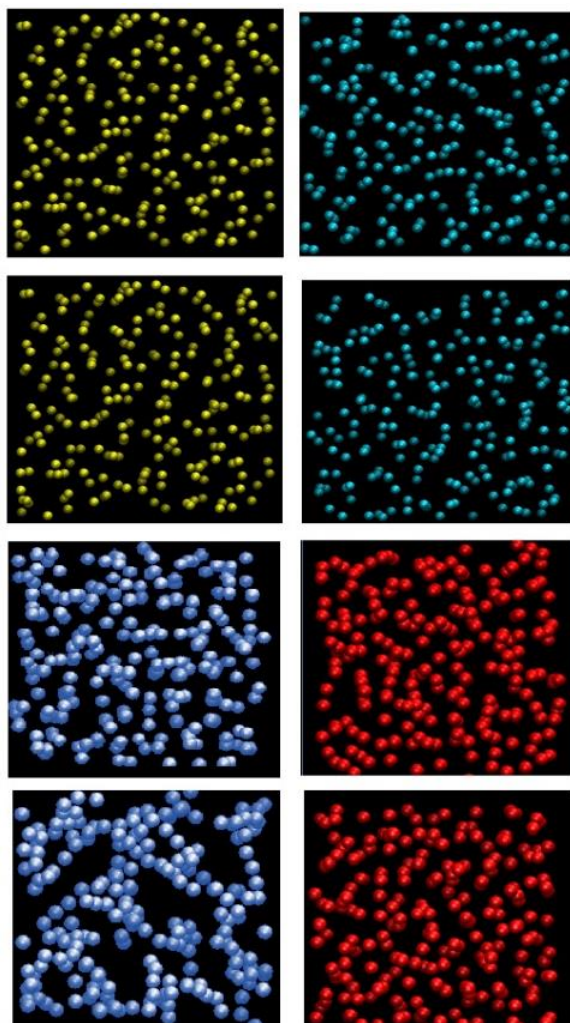

Fig.1. One snapshot of the studied ILs in simulation boxes. The sequence of ionic liquids from top to down is as follow [emim][FeCl$_4$], [bmim][FeCl$_4$], [DHEA][FeCl$_4$], and [THEA][FeCl$_4$]. Anions and cations were placed in left and right, respectively.

IV. CONCLUSION

In this paper, the heterogeneity order parameter of four different imidazolium- and cholinium-based ILs have been studied using molecular dynamics simulation. The results showed that the elongation of the alkyl chain in imidazolium cation and enhancement of the number of –OH group in cholinium cation makes anion prefer to aggregate. While, the HOP values of cation show a reverse procedure. The imidazolium cation makes heterogeneous structure when the alkyl chain length increases, while the cholinium cation makes a homogeneous structure when the number of hydroxyl group increases.

REFERENCES

[1] M. J. Earle, et al. Nature, 439, 831, **2006**.
[2] R. A. Sheldon, et al. Green Chem., 4, 147-151, **2002**.
[3] A. Daneshvar, and M. Moosavi, Ind. Eng. Chem. Res., 55, 6517-6529, **2016**.
[4] Y. Ji, et al. J. Phys. Chem. B**,** 117, 1104-1109, **2013**.
[5] Y. Wang, J. Phys. Chem. B, 113, 11058-11060 **2009.**
[6] J. N. Canongia Lopes, et al. J. Phys. Chem. B**,** 108, 2038-2047, **2004.**
[7] S. V. Sambasivarao, and O. Acevedo, J. Chem. Theo. Commput.**,** 5, 1038-1050, **2009.**
[8]   S. Plimpton, J. Comput. Phys.**,** 117, 1-19, **1995.**
[9]   S. Nosé, J. Chem. Phys.**,** 81, 511-519, **1984.**
[10] W. G. Hoover, Phys. Rev. A**,** 31, 1695-1697, **1985.**
[11] K.-T. Chang, and C.-I. Weng, J. Appl. Phys**,** 100, 043917, **2006.**

Analysis of the Spatial and Radial Distribution Functions of Ionic Liquids with Different Cations

S. Hajiyan[a], A. Daneshvar[a*], and M. Moosavi[a]

[a] Department of Chemistry, University of Isfahan, Isfahan, 81746-73441, Iran

Email: a.daneshvar88@yahoo.com

Abstract: The aim of this study is founding the probability of the presence of the anion around the most probable site of the cations of [DHEA][FeCl$_4$] and [bmim][FeCl$_4$] ionic liquids using molecular dynamics simulation. According to the RDF and SDF analysis, it is found that the anion-N interaction in [DHEA][FeCl$_4$] and anion-imidazolium ring interactions in [bmim][FeCl$_4$] are most probable. It can be due to the stronger electrostatic and π-π interactions in these sites.

Keywords: Ionic liquid, Molecular dynamics simulation Spatial distribution function, Radial distribution function.

I. INTRODUCTION

Ionic liquids (ILs) are used as solvents for synthesis and catalysis [1], electrolytes [2], lubricants [3] and media for the formation and stabilization of nanoparticles [4]. Their physical, chemical and electrochemical properties make them suitable for an enormous range of applications [5], ranging from the petrochemical industry [6] to the nuclear industry [7] and in many diverse applications. There is a great interest in ILs because of their special properties. They are good solvents for both organic and inorganic liquids over a wide range of temperature, not volatile, highly negligible vapor pressure, thermally stable, non-flammable, polar, weakly coordinating solvents and less toxic than usual organic solvents.

Investigation of the properties of ILs using molecular dynamics (MD) simulation becomes an interesting topic for researchers, recently. Some of the important properties of ILs are density, viscosity, diffusion, transport number, electrical conductivity, ionicity, etc. The study of the structural properties of ILs is an attracted topic in physical chemistry. In this paper, the structural properties of two ILs with different cations have been studied using MD. Accordingly, the spatial distribution function (SDF) and radial distribution function (RDF) of N-hexyl-N,N-2-dihydroxyethyl-N-methyl ammonium tetracholoroferrate [DHEA][FeCl$_4$] and 1-butyl-3-methylimidazolium tetracholoroferrate [bmim][FeCl$_4$] ionic liquids have been simulated.

II. METHODS

In this paper, the studied ionic liquids were modeled using a potential energy function based on the OPLS-AA [8, 9].

The B3LYP density functional with the 6-311++G** basis set have been employed to optimize the structures using Gaussian 09 package. The NBO and the CHELPG methods have been chosen for charge transfer of imidazolium-based and cholinium-based ionic liquids, respectively, due to their lower percentage error between simulated density data and their experimental values in the literature.

All of the MD simulations are done using the LAMMPS molecular dynamics package [10], at $T = 293.15$ K and at 0.1 MPa. A periodic cubic box containing 216 pairs of ions was used with a 10 Å cut off for non-bonded interactions. Coulombic interactions were handled by the ewald method. A Nosé-Hoover thermostat and barostat [11, 12] were used to control temperature and pressure, with time constants of 0.1 and 1 ps, respectively. The conjugate gradient energy minimization scheme has been used to relax the initial configurations. The isothermal-isobaric (NPT) runs of 5 ns were carried out at the desired pressure and temperature to estimate the SDF and RDF of the studied systems.

III. RESULTS AND DISCUSSION

The radial distribution function (RDF) is an important function which gives the probability of finding a pair of atoms at a given distance, and can be used to characterize the local structure of a fluid. To obtain insights into the intermolecular interactions of the studied ILs, several site-site RDFs for the cations and anions were computed. The RDF plots for [DHEA][FeCl$_4$] and [bmim][FeCl$_4$] at T=293.15 K and 0.1 MPa have been illustrated in Fig. 1. This figure shows, the interaction of the center of mass of anion (Fe atom) with the first and last hydrogens (H5 and H10) of the alkyl chain residue of cation for [DHEA][FeCl$_4$]. Also, the interaction of Fe atom and hydrogens of imidazolium ring and alkyl chain of cation in [bmim][FeCl$_4$] is illustrated in Fig. 1. As it is clear, the interaction of the Fe-H5 in [DHEA][FeCl$_4$] is stronger than Fe-H10 and also has higher g(r) peak. It can be due to the more preference of the anion for placing around the highest site of cation with the most positive charge density (N atom). Also, Fig. 1 shows that the interaction of Fe-H1 and Fe-HA in the cation of [bmim][FeCl$_4$] are stronger than Fe-HC. It demonstrates that the anion-imidazolium ring interaction is

more probable than anion-alkyl chain. It can be due to the π-π interaction of Fe atom in anion and the ring of cation.

Although, the RDF plots give useful information about the local structure of fluid, for the visualization of the spatial arrangement of the involved molecules the other functions i.e. spatial distribution functions (SDFs) may be used. The SDFs give the probability of finding an atom in the three-dimensional space around a central molecule. The SDFs of each ILs have been calculated via Travis package and visualized by the VMD program and illustrated in Scheme 1. The results of SDF analysis illustrates that the probability of anion around the nitrogen atom of [DHEA]+ and imidazolium ring of [bmim]+ is greater than the alkyl side chains. This is in agreement with the result obtained by the RDF plots.
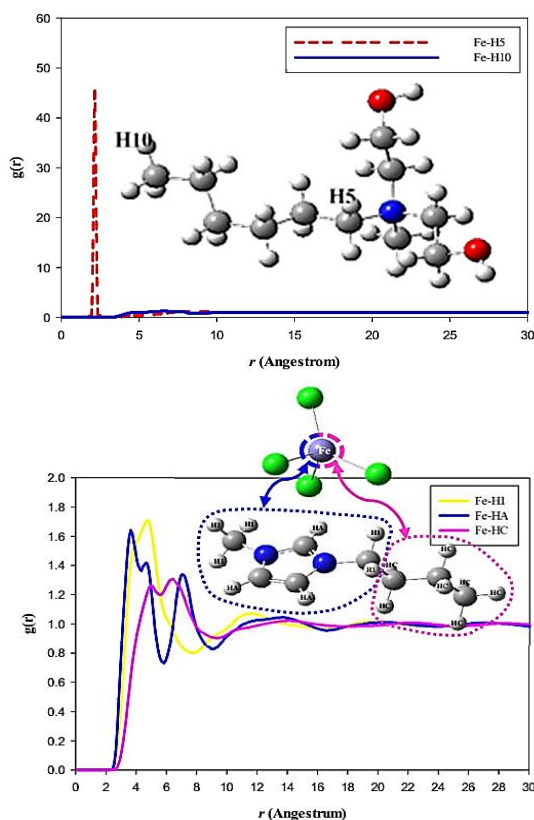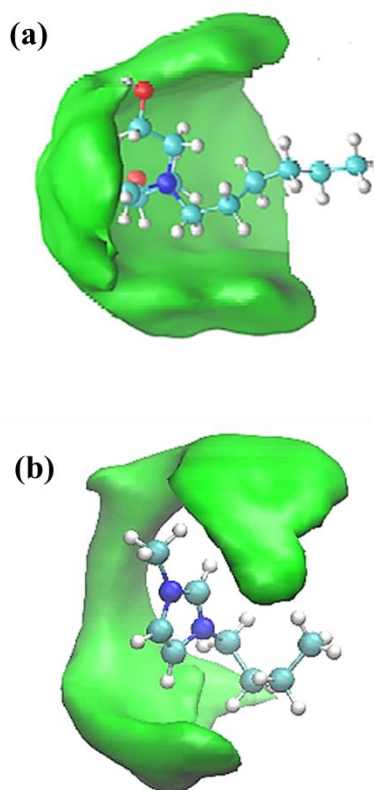

Fig. 1. The RDF plots of anion and hydrogen atoms of (top) [DHEA][FeCl₄] and (down) [bmim][FeCl₄].

Scheme 1. Spatial distribution of anion around (a) [DHEA]+, and (b) [bmim]+ cations at 293.15 K and 0.1 MPa.

IV. CONCLUSION

In this paper, the structural properties such as spatial distribution function and radial distribution function of two different IL namely [DHEA][FeCl₄] and [bmim][FeCl₄] have been obtained using molecular dynamics simulation. The results showed that the anion prefers to placed around the high positive charge density site of [DHEA]+ and π-donor imidazolium ring of [bmim]+. Both RDF and SDF plots confirm each other, well.

REFERENCES

[1] T. Welton, Chem. Rev. 99, 2071–2084, **1999.**
[2] D.R. MacFarlane, et al. Phys. Chem. Chem. Phys. 12, 1659–1669, **2010.**
[3] S.D.A. Lawes, et al. Lett. 37, 103–110, **2010.**
[4] K. Ueno, and M. Watanabe, Langmuir, 27, 9105–9115, **2011.**
[5] R.D. Rogers, K.R. Seddon (Eds.), Ionic Liquids as GreenSolvents: Progress and Prospects, ACS Symposium

Series, 856, American Chemical Society, Washington D.C., **2003.**

[6] M.J. Earle, et al. Green Chem. 2, 261–262, **2000.**

[7] D. Allen, et al. Green Chem. 4, 152–158, **2002.**

[8]   J. N. Canongia Lopes, et al. J. Phys. Chem. B, 108, 2038-2047, **2004.**

[9]   S. V. Sambasivarao, and O. Acevedo, J. Chem. Theo. Commput., 5, 1038-1050, **2009.**

[10] S. Plimpton, J. Comput. Phys., 117, 1-19, **1995.**

[11] S. Nosé, J. Chem. Phys., 81, 511-519, **1984.**

[12] W. G. Hoover, Phys. Rev. A, 31, 1695-1697, **1985.**

The Effect of Cation Type and Temperature on the Transport Properties of Some Room Temperature Ionic Liquids

A. Daneshvar[a*], S. Hajiyan[a], and M. Moosavi[a]

[a] Department of Chemistry, University of Isfahan, Isfahan, 81746-73441, Iran

Email: a.daneshvar88@yahoo.com

Abstract: In this paper the viscosity and electrical conductivity of four different ILs have been calculated using molecular dynamics simulation at different temperatures. As it was expected, the enhancement of temperature makes a decrement in the viscosity and increment in electrical conductivity of the studied ILs. From the simulated properties, it is concluded that the main effective parameter in the viscosity of the cholinium-based ILs is the spherical hindrance. While, the intermolecular interaction is the domain effect in the viscosity of the ILs containing imidazolium cation.

Keywords: Ionic liquid, Molecular dynamics simulation, Transport property, Spherical hindrance, and Intermolecular interactions.

I. INTRODUCTION

Ionic liquids (ILs) have attracted considerable attention during recent years. Contrary to molecular solvents, ILs are composed of ions only (organic cations and organic or inorganic anions) [1, 2]. The possibility of choosing different cations and anions in the chemical structures of ILs causes changes in their physicochemical properties such as viscosity, density, electrical conductivity, etc. Among the physicochemical properties of the ILs, transport properties have an important role in their industrial applications.

Since, the synthesis of the ILs are expensive, the computational method can be a low cost and suitable manner for studying their properties. Accordingly, in this work, we simulate the transport properties such as viscosity and electrical conductivity of some ILs with different cation. The effects of temperature and cation type have been studied using molecular dynamics (MD) simulation. The studied ILs contains N-hexyl-N,N-2-dihydroxyethyl-N-methyl ammonium [DHEA]⁺, N-hexyl-N,N,N-2-trihydroxyethyl ammonium [THEA]⁺, 1-ethyl-3-methylimidazolium [emim]⁺, and 1-butyl-3-methylimidazolium [bmim]⁺ cations and tetracholoroferrate [FeCl₄]⁻ anion.

II. METHODS

The studied ionic liquids were modeled using a potential energy function based on the OPLS-AA [3, 4]. The B3LYP density functional with the 6-311++G** basis set have been employed to optimize the structures using Gaussian 09 package. The NBO and the CHELPG methods have been chosen for charge transfer of imidazolium-based and cholinium-based ionic liquids, respectively, due to their lower percentage error between simulated density data and their experimental values in the literature.

All of the MD simulations are done using the LAMMPS molecular dynamics package [5], in temperature range of 298.15 to 453.15 K and at 0.1 MPa. A periodic cubic box containing 216 pairs of ions was used with a 10 Å cut off for non-bonded interactions. Coulombic interactions were handled by the ewald method. A Nosé-Hoover thermostat and barostat [6, 7] were used to control temperature and pressure, with time constants of 0.1 and 1 ps, respectively. The conjugate gradient energy minimization scheme has been used to relax the initial configurations. The isothermal-isobaric (NPT) runs of 40 ns were carried out at the desired pressure and temperature to estimate the transport properties of the studied systems.

III. RESULTS AND DISCUSSION

Trusty and direct tool for the calculation of viscosity in the case of ILs is Green-Kubo method. In this method, the shear viscosity is calculated from the time integral of the pressure tensor auto correlation function (PTACF) using the Green-Kubo relation [8],

$$\eta(t) = \frac{V}{k_B T} \int_0^t \left\langle P_{\alpha\beta}(t_0) P_{\alpha\beta}(t + t_0) \right\rangle dt$$

where V is the volume of the simulation box, T is the temperature, and k_B is the Boltzmann constant. $P_{\alpha\beta}$ denotes any of the three off-diagonal elements of the pressure tensor and the brackets indicate that the average must be taken over all time origins t_0 at equilibrium.

The electrical conductivity depends on the number and mobility of the free ions in the fluid and can be derived from

the self-diffusion coefficients of ions in the liquids. Since, the Nernst-Einstein equation [9] showed a good applicability for predicting the electrical conductivity of ILs in some previous studies [10-12], we used this equation to calculate the electrical conductivity of the studied MILs at different temperatures as follow

$$\sigma = \frac{Ne^2}{Vk_BT}\left(Z_-^2 D_- + Z_+^2 D_+\right)$$

In this equation, N denotes the Avogadro's number, e is the electronic charge, V is the volume of the system, k_B is the Boltzmann constant, and Z_- and Z_+ are the formal charges on the anion and cation, respectively. D_- and D_+ are the diffusion coefficient of cation and anion which calculated using MSD (mean square displacement) simulations.

The temperature dependence of the viscosity has been given at Table 1 for different studied ILs. As these table shows the viscosity decreases with increasing temperature as we expected. The intermolecular interactions and spherical hindrance are two effective parameters on the viscosity of liquids. These two parameters increase with increasing the number of hydroxyl groups and elongation of alkyl chain in cation of ILs. It is interesting that the viscosity of the cholinium-based ILs decreases with increasing the number of –OH group in cation, while the elongation of the alkyl chain in imidazolium cation increases the viscosity. This phenomenon demonstrates that the spherical hindrance has domain effect on the viscosity of cholinium-based ILs, while the more effective parameter on the viscosity of the imidazolium-based ILs is intermolecular interactions.

Table 1. The simulated viscosity at different temperatures and at 0.1 MPa for the studied ILs.

T(K)	η(mPa.s)	T(K)	η(mPa.s)
[DHEA][FeCl$_4$]		[emim][FeCl$_4$]	
293.15	410	293.15	21.6
313.15	345	313.15	18.6
353.15	206	353.15	13.4
403.15	129	403.15	10.8
453.15	86	453.15	8.7
[THEA][FeCl$_4$]		[bmim][FeCl$_4$]	
293.15	198	293.15	41.3
313.15	155	313.15	27.1
353.15	97	353.15	11.0
403.15	72	403.15	9.5
453.15	54	453.15	7.3

The electrical conductivity is the other simulated transport property, which has reverse relation to the viscosity of liquids.

Computational Chemistry | 30

Fig. 1 shows the electrical conductivity versus temperature for four different studied ILs. As this figure shows, the electrical conductivity increases with increasing temperature. It can be due to the weakening of the intermolecular interactions with temperature enhancement which leads to lower viscosity.
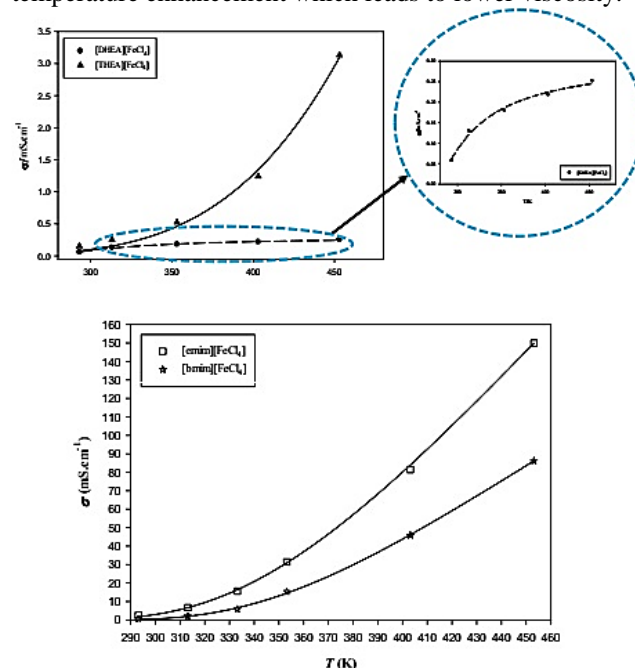

Fig. 1. The electrical conductivity versus temperature for the studied ILs.

IV. CONCLUSION

In this study, the transport properties such as viscosity and electrical conductivity of cholinium- and imidazolium-based ILs have been simulated at different temperatures. The results showed that the spherical hindrance has domain effect on the viscosity of cholinium-based ILs compared to the intermolecular interactions. While, the viscosity of the imidazolium-based ILs is more affected by the intermolecular interactions. Since, the viscosity and electrical conductivity have reverse relation, the electrical conductivity of the studied ILs decreases with increasing viscosity.

REFERENCES

[1] S.-A. Choi, et al. Renew. Energy, 65, 169-174, **2014**.
[2] E. D. Hazelbaker, et al. J. Phys. Chem. B, 116, 9141-9151, **2012.**
[3] J. N. Canongia Lopes, et al. J. Phys. Chem. B, 108, 2038-2047, **2004.**
[4] S. V. Sambasivarao, and O. Acevedo, J. Chem. Theo. Commput., 5, 1038-1050, **2009.**

[5] S. Plimpton, J. Comput. Phys.**,** 117, 1-19, **1995.**

[6] S. Nosé, J. Chem. Phys.**,** 81, 511-519, **1984.**

[7] W. G. Hoover, Phys. Rev. A**,** 31, 1695-1697, **1985.**

[8] D. J. Evans, and G. P. Morriss, Statistical Mechanics of Nonequilbrium Liquids. Academic, London: **1990**.

[9] I. McDonald, and J. Hansen, Theory of Simple Liquids. Academic Press, London and New York: **1986**.

[10] S. U. Lee, et al. Chem. Phys. Lett. *406*, 332-340, **2005**.

[11] C. Rey-Castro, and L. F. Vega, J. Phys. Chem. B**,** 110, 14426-14435, **2006.**

[12] C. Rey-Castro, et al. Fluid Phase Equilib**.** 256, 62-69*,* **2007.**

Separation and Diffusion of Helium from Defective Graphene
A comparative DFT study

Seyedeh Shabnam Daryabari*a, Javad Beheshtianb, Sakineh Mansouric

a Department of Chemistry, Faculty of Science, Islamic Azad University, Center Tehran Branch, Tehran;
shabnam_daryabari1388@yahoo.com

b Department of Chemistry, Faculty of Science, Shahid Rajaee Teacher Training University, P.O. Box: 16875-163, Tehran, Iran;
J.Beheshtian@SRU.ac.ir

c Department of chemistry, Faculty of Science, Islamic Azad University, Central Tehran Branch, Tehran;
sak.mansouri@iauctb.ac.ir

Abstract: Helium is one of the noble gases that widely used in the industry due to its unique properties. The main sources of helium in the planet were air and natural gas reservoirs. The concentration of helium in the air is low and Extraction of helium from the air is not feasible economically. To this end, extensive research has been devoted to the development of new techniques that can reduce costs and reduce the complexity of implementation and control. in this work, we used defected graphene doped with F, B and H atoms for Diffusion of Helium.

Keywords*:* Defect Graphene, DFT, Diffusion, Helium, Quantum Dots.

I. INTRODUCTION

Gas separation such as hydrogen separation is very important for the study of a new clean energy technique [1]. A lot of materials have been developed to pursue the gas separation [2-3]. Traditional systems for gas separation in industry consume a significant energy cost [4] and cause environmental problems. The use of the membrane system [5] as an efficient separation for the gas mixtures without any phase change obviously reduces the energy cost compared to traditional systems, so it may become a powerful material for the gas separation. For this work, we studied separation and diffusion of helium from defective graphene using Gaussian 09 package.

II. METHODS

We investigated the defected graphene doped with F, B and H atoms are Gr.F3H3(1-a) and Gr.B3H3(fig1-b) for diffusion He. The properties and interaction of He on graphene sheet were studied by means of first principles based on density functional theory (DFT). Finally, diffusion and scanning of He was investigated. All DFT calculations performed using Gaussian 09 package and the M062X/6-31G* computational level of theory.

III. RESULTS AND DISCUSSION

In First, helium was placed in the center of the defected graphene and optimized. The interaction energy was calculated. These optimized compounds were used to pass helium from the cavity center. Calculation of the scan at the M062X / 6-31G * level was carried out in order to penetrate the helium from defective graphene using Gaussian09 software. All scans are carried out from -4 to 4 Angstroms, in each case a zero point is considered on the screen passing through the center of graphene (4 angstroms on both sides of the center). For Gr.B3H3, there was less interaction between helium and sheet, thus there was a greater possibility of passage. Results of the NBO analysis and the electronegativity of the atoms in the cavity center, confirmed that the suitable case for the passage is Gr.B3H3.
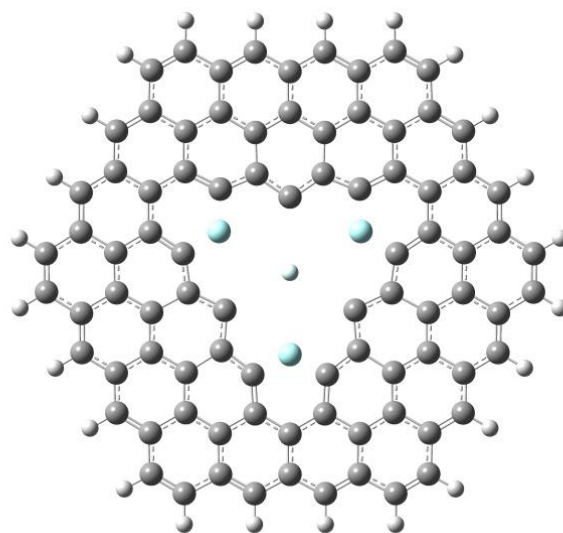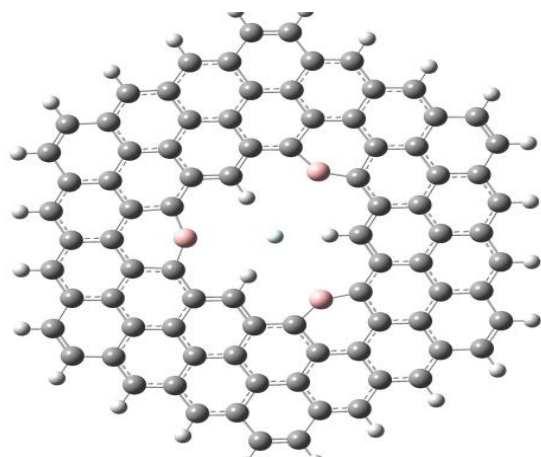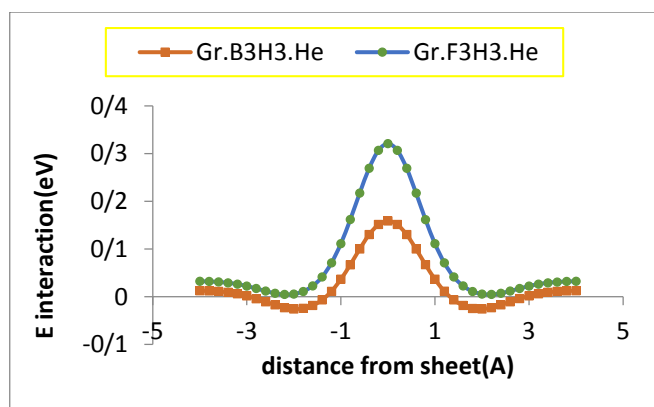

Fig.1-a: Gr.B3H3 + He

(5) Freemantle, M. Chem. Eng. News, 83, 49–57. **2005**

Fig.2-b: Gr. B3H3 + He

IV. CONCLUSION

In this study, the investigation of the propagation of helium from two defective graphene was carried out. Results analysis was performed with NBO to be selected for better penetration and separation. Considering the importance of helium in the industry, it is expected that more studies will be done in the future.

REFERENCES

(1) Sedigh, M. G.; Onstot, W. J.; Xu, L.; Peng, W. L.; Tsotsis, T. T.; Sahimi, M. J. Phys. Chem. A, 102, 8580–8589. **1998**

(2) Williams, J. J.; Wiersum, A. D.; Seaton, N. A.; D€uren, T. J. Phys. Chem. C, 114, 18538–18547. **2010**

(3) Guo, H.-C.; Shi, F.; Ma, Z.-F.; Liu, X.-Q. J. Phys. Chem. C, 114, 12158–12165. **2010**

(4) Kluiters, S. C. A. Status Review on Membrane Systems for Hydrogen

Separation; Energy Research Centre of the Netherlands: Petten, The Netherlands, **2004**.

Computational Chemistry | 33

Electric Field Effect on the Interaction of Helium with Defected Graphene Sheet: A DFT Study

Seyedeh Shabnam Daryabari*[a], Javad Beheshtian[b], Sakineh Mansouri[c]

[a] Department of Chemistry, Faculty of Science, Islamic Azad University, Center Tehran Branch, Tehran;
shabnam_daryabari1388@yahoo.com
[b] Department of Chemistry, Faculty of Science, Shahid Rajaee Teacher Training University, P.O. Box: 16875-163, Tehran, Iran;
J.Beheshtian@SRU.ac.ir
[c] Department of chemistry, Faculty of Science, Islamic Azad University, Central Tehran Branch, Tehran;
sak.mansouri@iauctb.ac.ir

Abstract: Graphene doping with heteroatoms improves their catalytic activity than the reactions required to store or convert energy. As a result, the study tries to classify defects, emphasize their importance, and introduce common ways to study and identify them, and propose new ways to build new nutrient-based devices, such as graphene defect. The presence of an electric field in defective graphene compounds is an emerging field of research with many potential applications in the industry, such as gas purification, gas sensors, batteries and fuel cells.

Keywords: Defect graphene, DFT, Electric Field, Helium, quantum dots

I. INTRODUCTION

Since its discovery in 2004 [1] graphene has received a great deal of attention, because it offers a lot of possibilities for practical applications [2, 3, 4].

Defects are often the first concern in the real application of monolayer materials. Vacancy defects, which are readily induced by laser irradiation and electron beam, are almost inevitable in the fabrication and processing of monolayers, and sometimes, small defects are introduced purposively for specific applications [5]. Due to the importance of the band gap in conductivity, the purpose of this study is to investigate the gap in presence of electric field and creating defect and doping with the nitrogen atoms in the structure. Since the perfect graphene has zero-gap, by applying these cases, the value of gap will change. The next aim is to investigate the effect of increasing the field on the structure.

II. METHODS

We designed a porous graphene (fig1) and doped them with N (Gr.N3). we studied the interaction of Helium on central defective graphene sheet in present of several electric field were investigated by means of first-principles based on density functional theory. All DFT calculations performed using Gaussian 09 package at the M062X/6-31G* computational level of theory.

III. RESULTS AND DISCUSSION

The interaction energy of Helium on central defective graphene sheet in presence of electric field were investigated. Results of calculations were shown in table1. Our results show that the He interaction energy value on doped graphene and band gap decrease when electric field rises.

Table1: Results of calculations of Gr.N3+He in several fields

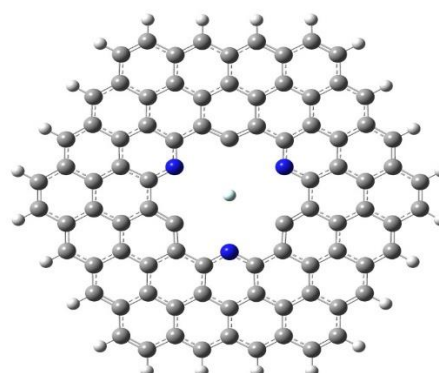|	E interaction (eV)	HOMO	LUMO	Gap (eV)
Gr.N3.He.NO FIELD	-0.051	-0.19	-0.096	2.67
Gr.N3.He z+10	-0.051	-0.19	-0.097	2.65
Gr.N3.He z+20	-0.061	-0.19	-0.096	2.67
Gr.N3.He z+30	-0.06	-0.19	-0.096	2.67
Gr.N3.He z+100	-0.059	-0.19	-0.095	2.66

Fig.1: Optimized structure of Gr.N3 + He

A. Equations

$$E_{interaction} = E_{sheet + atom} - E_{sheet} - E_{atom} \qquad (1)$$

IV. CONCLUSION

In this work, using density functional theory (DFT) calculations, the eﬀect of field were investigated on graphene sheet doped with N atoms.

According to the table1, the electric field can affect the amount of band gap and this can be effective conductivity.

Due to the effect of the defect and the presence of the field in graphene, it is possible to change the amount of band gap. The relationship between band gap and conductivity can be a precursor to further studies on these compounds to improve the conductivity and semiconductor devices that are produced in the future.

REFERENCES

[1] K. S. Novoselov, A. K. Geim, S. V.Morozov, D. Jiang, Y. Zhang, S. V. Dubonos, I. V. Grigoneva, A. A. Firsov, Science.vol. 306 ,pp.666, **2004**

[2] A. G. Geim, K. S. Novoselov, Nature Mater.vol. 6 ,pp.183, **2007**

[3] A. K. Geim, Science ,vol.324 , pp.1530, **2009**

[4] A. H. C. Neto, F. Guinea, N.M. R. Peres, K. S. Novoselov, A. K. Geim, Rev. Mod. Phys. vol.81,pp.109,**2009**

[5] Brumfiel, G. Nature , vol.495, pp.152–153,**2013**

QM study the inhibitory effect of Bisulfite Ion on inhibition of carbonic enzyme

A. Larijani*

Department of chemistry,Faculty of physics & chemistry,Alzahra University,Vanak,Tehran,Iran
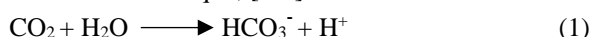*Tel: +9100826353*
Email:Azarlarijani7@gmail.com

Abstract: The theory of density function, a theory in the framework of quantum mechanics to study the electron structure with basic set B3LYP/6311++G** computation has been used to optimized the structures of bisulfite ion and complex between these inhibitors with active site of α-CA enzyme. The anion of bisulfite is coordinate to the zinc as five ligand in intermediate complex.Acoording to calculated results thiocyanate and isothiocyanate with more negative thermpdynamic functions are more effective than the others drugs to control some dieses like of cancer. PCM method used for solvent effects in all calclutions.

Keywords: Anionic inhibitor, Anti-cancer, Carbonic anhydrase, DFT.

I. INTRODUCTION

A family of ubiquitous zinc metalloenzymes known as carbonic anhydrase (CAs) is catalyzed the hydration of carbon dioxide (CO_2) to bicarbonate ion and proton, a simple but essential reaction. Eq. 1, [1-3].

$$CO_2 + H_2O \longrightarrow HCO_3^- + H^+ \tag{1}$$

This enzyme (CA) peresnt in prokaryotes and eukaryotes

And encoded to five classes: α-CAs, β-CAs, γ-CAs, δ-CAs and ζ-CAs [4,5]. In higher vertebrates, including humans, 14 α-CA isozymes have been described with very different tissue Distributions[6,7].The zinc metal ion (Zn^{2+}) in all α-CAs has essential role for catalysis [8-10].According to X-ray crystallographic data, the metal ion is situated at the bottom of a deep active center cleft, being coordinated by three histidine residues (His94, His96 and His119) and a water molecule or hydroxide ion [11-15] (Fig1).

II. METHODS

All calculations were performed at the level of relativistic density functional theory (DFT) using the B3LYP/6-311++G** method. Ab initio calculations were carried out with the Gaussian program series 2003[17]. The harmonic vibrational frequencies, spin density and partial charges in the present of the water solvent have been done by using PCM model.
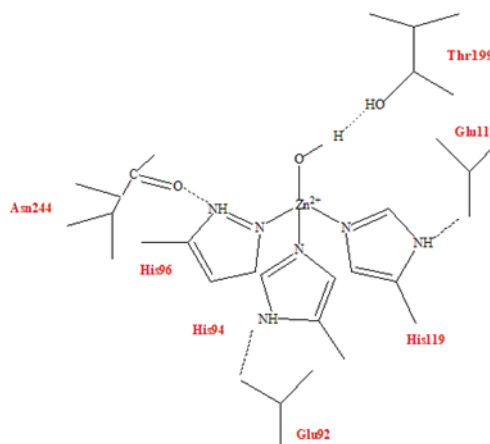
Fig.1:Crystallographic structure of isomer II α-CA

III. RESULTS AND DISCUSSION

Bisulfite ion , like many inhibitors, replace the water molecule. Figure 2 shows a demonstration of this type of carbon dioxide deterioration by this ion. It is probale that an equilibrium exist between the trigonal bipyramial and the tetrahedral species of the metal ion from the active site of the enzyme.
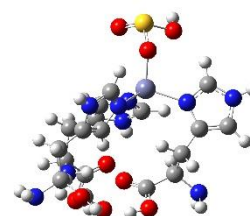
Fig.2: Anionic inhibitor bisulfite ion added metallic metal and the geometric shape of the tetrahedral and trigonal bipyramidal.

According to thermodynamic equation, $\Delta G = \Delta H - T\Delta S$, the $\Delta G°r$ was calculated. Table1.

Table1: Calculation of thermodynamic functions:

Anion Inh	ΔE(Sol) Kcal/mol	ΔH°	ΔG	ΔS
HSO_3	-35.31 (-69.91)	-29.49	-16.88	-0.0618

IV. CONCLUSION

In this paper, the structure of carbonic anhydrase active center was fully optimized at B3LYP method using 6-311G** basis set with no initial symmetry restrictions and assuming C_1 point group. Since, in the presence of the inhibitor, an enzyme-inhibitor complex forms, So, different complexes between active site of CA enzyme and anionic inhibitor were fully optimized at B3LYP level by using 6-311G** basis set with no initial symmetry restrictions.

As the results indicate, substitution of anionic form of inhibitors in place of water molecule at the active center of CA enzyme is energetically exothermic, $\Delta E_{reaction}$ = -35.31 kcal/mol. In conclusion anionic inhibitors as a new class of inhibitors is good candidates for the development of novel anticancer drugs with few side effect.

REFERENCES

[1] Bertini I, Luchinat C. Acc Chem Res. 16(8):272–9. **1983**.
[2] DN. Silverman. Can J Bot. 69(5):1070–8,**2007**.
[3] DW. Christianson,CA. Fierke. Acc Chem Res.;29(7):331–9,**1996.**
[4] C. Capasso, CT. Supuran. J Enzyme Inhib Med Chem. 29(3):379–87,**2014**.
[5] S. Akin, H. Ayaloglu, E. Gultekin, A. Colak, O. Bekircan, Bioorg Chem. 83;170–9,**2019**.
[6] SJ. Dodgson, RE. Forster. J Appl Physiol. 60(2):646–52.**2017**.
[7] D. Hewett-Emmett.29–76,**2012**.
[8] WS. Sly. (1982):95–104,**2012.**
[9] Purkerson JM, Schwartz GJ.Kidney Int. 71(2):103–15,**2007**.
[10] S. Parkkila, C. Supuran, A. Innocenti,S. Monti,G. Simone, M.Hilvo . Curr Pharm Des .;14(7):672–8,**2008**.
[11] A. Bottoni,CZ. Lanza, G. Miscione Pietro, D. Spinelli. J Am Chem Soc. 2004;126(5):1542–50, **2004**.
[12] JY. Liang , Biochemistry;26(17):5293–301,**1987**.
[13] S. Lindskog . J Mol Catal.;23(2–3):357–68,**1984**.
[14] S. Lindskog . Pharmacol Ther.74(1):1–20, **1997**.
[15] A. Solá M, Lledós,M. Duran,J. Bertrán. J Am Chem Soc.;114(3):869–77,**1992.**

[16] Bioorganic & Medicinal Chemistry Letters 14 ,3327–3331,**2004**.
[17]. Frisch MJ, Trucks GW, Schlegel HB, Scuseria GE, Robb MA, Cheeseman JR, Zakrzewski VG, Montgomery JA, Stratmann RE, Burant JC, Dapprich S, Millam JM, Daniels AD, Kudin KN, Strain MC, Farkas O, Tomasi J, Barone V, Cossi M, Cammi R, Mennucci B, Pomelli C, Adamo C, Clifford S, Ochterski J, Petersson GA, Ayala PY, Cui Q, Morokuma K, Malick DK, Rabuck AD, Raghavachari K, Foresman JB, cioslowski J, Ortiz JV, Stefanov BB, Liu G, Liashenko A, Piskorz P, Komaromi I, Gomperts R, Martin RL, Fox DJ, Keith T, Al-Laham MA, Peng CY, Nanayakkara A, Ghonzalez CV, Challacombe M, Gill PMW, Johnson BG, Chen W, Wong M, Andres JL, Head-Gordon M, Replogle ES, Pople JA (2003) Gaussian 2003 (Revision-B). Gaussian, Inc., Pittsburgh PA.

Preparation of Water Soluble Single Walled Carbon Nanotubes:
Study of the Chirality Effect Insights from Molecular Dynamics Simulations

L. Tohidifar, N. L. Hadipour*

Department of Chemistry, Faculty of Fundamental Sciences, Tarbiat Modares University, Tehran, P. O. Box 14115-175, Iran,

Email: Hadipour@modares.ac.ir

Abstract*:* Single-walled carbon nanotubes (SWCNTs) have become one of the best carriers for drug delivery because of their huge surface, size scale, and high cellular uptake. The SWCNTs dispersion in aqueous conditions and rending their biocompatibility require proper surface functionalization by various biomolecules such as proteins and peptides. Recently a biologically compatible peptide (named PW3 with the sequence of NH_2-Trp-Val-Trp-Val-Trp-Val-Lys-Lys-COOH) has been introduced as a good candidate for modification of carbon nanotubes due to its high affinity toward the exterior surface of these nano-carriers. In order to optimize the PW3 modification of SWCNT, the effect of chirality SWCNT on the "PW3/SWCNT" complex solubility was investigated using molecular dynamics (MD) simulations. It was revealed that the PW3 functionalized carbon nanotubes of zigzag and chiral types were suitable for drug delivery due to the higher solubility at 310 K. Lys amino acids and their side chains could significantly contribute in the system solubility.

Keywords: Single-walled carbon nanotube, Chirality, Peptide, MD simulations

I. INTRODUCTION

The unique properties of single-walled carbon nanotubes (SWCNTs) suggest their potential in multiple disciplines such as microelectronics, composite material, sensors, energy storage, and biomedicine. Proper surface functionalization by various biomolecules such as proteins and peptides is the key approach to facilitate CNTs dispersion in aqueous conditions and rending their biocompatibility [1]. Recently, Barzegar and co-workers' [2] showed that a biologically-compatible peptide, named PW3 with the sequence of NH2-Trp-Val-Trp-Val-Trp-Val-Lys-Lys-COOH could be introduced as a novel candidate for non-covalent functionalization of SWCNTs for design of appropriate SWCNT-based biomolecule carriers. In addition to protein/peptide nature, engineering of SWCNTs non-covalent functionalization by the nano-carriers morphology could provide a platform for sufficient surface modification of SWCNTs and further nano-biomedical applications. For example, the chirality, diameter, and length

of SWCNT are introduced as essential three factors that could govern the adsorption behavior of amino acids on SWCNT side-wall. In the present work MD simulations of PW3 non-covalent modification of SWCNT were examined to determine the effect of chirality SWCNT on the "PW3/SWCNT" solubility which tend to design and optimize a suitable SWCNT-based carrier for biomedical applications.

II. METHODS

The armchair (6,6), chiral (7,5), and zigzag (10,0) tube structures, having the length of 26 Å, were acquired by Nanotube Modeler software 1.7.3, JCrystalSoft [3]. The 3-D structure of our target peptide was constructed and minimized by Hyperchem 7 software [4].The complexe of PW3 peptide and SWCNT was solvated in a water (TIP3P model) box under periodic boundary condition (PBC). All MD simulations were carried out by NAMD 2.9 package [5] in the *NPT* ensemble (Nosé-Hoover thermostat/barostat) at 310 K for 200 ns. The widely-used force field parameters of CHARMM 27 were utilized in all the MD simulations [6].

III. RESULTS AND DISCUSSION

As already mentioned, proper surface functionalization is the key approach to facilitate SWCNTs dispersion in aqueous conditions and render their biocompatibility [7]. In the current work, PW3 peptide was selected as a novel candidate for nano-carrier functionalization and three subsystems were considered for "PW3/SWCNT" complex: "PW3/Armchair SWCNT", "PW3/Chiral SWCNT" and "PW3/Zigzag SWCNT" whose solubility was evaluated by solvent accessible surface area (SASA) calculated through using the formula:

$$SASA = \sum \left[\frac{R}{\sqrt{R^2 - Z_i^2}} \right] . L_i . D \qquad (1)$$

$$D = \frac{\Delta Z}{2} + \Delta' Z \text{CNT} \qquad (2)$$

SASA is the surface area of a biomolecule which is accessible to contact with solvent [56]. SASA of an atom is introduced as the area on the surface of a sphere with radius R, on each point of which the solvent molecule center can be placed in contact with this atom without penetrating any other atoms of the molecule. The radius R is introduced by the sum of the van der Waal's radius of the atom and the considered radius of the solvent molecule. L_i and Z_i are the length of the arc drawn on a given section i and the perpendicular distance from the center of the sphere to the section i, respectively. ΔZ denotes the spacing between the sections, and $\Delta' Z$ is $\Delta Z/2$ or $R - Z_i$, whichever is smaller. Summation is over all of the arc drawn for the given atom [58]. According to the Fig. 1, average values of the SASA for "PW3/SWCNT" complex in the case of zigzag and chiral SWCNTs were ~730 and 640 Å², respectively, at 310 K. While for armchair structure the corresponding value was obtained ~ 480. The higher values for the zigzag and chiral nanotubes in comparison to the armchair SWCNT confirmed that "PW3/SWCNT" system had more available surface area to interact with water molecules. The solubility of "PW3/SWCNT" complex may be attributed to the heteroatoms of amino acids in PW3 structure oriented away from the SWCNT and located toward the aqueous phase. Among the amino acids of PW3 peptide, Lys is a polar residue. Hence its side chain can significantly contribute in the system solubility. Based on Figure 2b, the interactions of Lys residues with water molecules in the
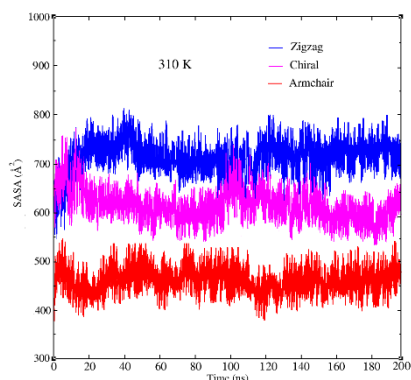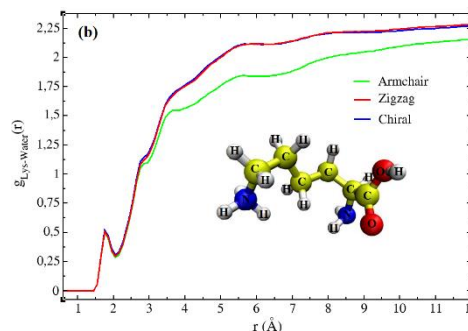

Fig. 2: Comparison of the RDFs between Lys residues of PW3 peptide and water molecules around them in the considered complexes, containing armchair, chiral and zigzag tubes at 310 K.

In order to study the geometry of SWCNT-Lys interactions, we calculated the distances between the several atoms of this polar amino acid and SWCNT surface. The average value of these atomistic distances quantitatively confirmed the close orientation of Lys with respect to the sidewall of SWCNT in the case of armchair system as supported by above discussion. Based on these results, the distances between armchair SWCNT atoms and H1, O1, H2, H3, and H4 atomic sites of polar chain of Lys were estimated around 3.46, 3.12, 3.32, 2.85, and 2.83 Å, respectively (Fig. 3). The mentioned distances changed to 2.99, 5.4, 3.63, 6.3, and 7.4 Å, for zigzag system resulting in the reduction of Lys tendency to outside surface of zigzag SWCNT which led to change in its alignment. Also in the case of chiral SWCNT, Lys chains were located far away from the tube.

Fig. 1: Comparision of solvent accessible surface area (SASA) of "PW3/SWCNT" complex with three kinds of SWCNT structure at 310 K.

zigzag and chiral systems were stronger than that of the armchair complex. In these systems, the Lys amino acids preferred to be exposed to the solvent surface; while in the armchair system, Lys residues tended to disperse around SWCNT and locate at a close distance from SWCNT sidewall so that the strongest interaction between PW3 peptide and SWCNT was resulted for armchair system as shown in Fig. 2

Fig. 3: The schematic view of the alignment of Lys residues around armchair SWCNT at 310 K. The distances between several atoms of this amino acid and SWCNT surface are provided.

Hydrogen bonding was another parameter which has been recognized as an important interaction in the nature and many biochemical processes such as solubility. At this stage, formation of the intermolecular hydrogen bonds between PW3 functionalized armchair, zigzag, and chiral SWCNTs and water molecules was traced. Based on these results, the number of hydrogen bonds in the zigzag and chiral complexes

was higher than the armchair system (10 and 9 for zigzag and chiral, respectively, and 4 for armchair) hence these systems will exhibit higher water-solubility.

IV. CONCLUSION

Functionalization of SWCNTs by surfactant molecules like peptides can be a promising approach to enhance their dispersion in aqueous media. In this research we discussed about SWCNT structure effect on the modification of SWCNT by PW3 peptide. Based on the SASA calculations hydrogen bonding analysis, zigzag and chiral SWCNTs showed higher solubility and had more available surface area to interact with water molecules compared to the armchair structure which tend to design and optimize a suitable SWCNT-based carrier for biomedical applications. RDF results confirmed the significant contribution of Lys amino acids and their side chains in the system solubility.

REFERENCES

[1] A. Antonucci, J. Kupis-Rozmyslowicz and A. A. Boghossian, ACS Appl. Mater. Interfaces, Vol. 9, pp. 11321-11331. **2017**.

[2] A. Barzegar, A. Mansouri and J. Azamat, J. Mol. Graphics. Model, Vol. 64, pp. 75-84, **2016**.

[3] http://www.jcrystal.com/products/wincnt/, Nanotube Modeler, JCrystalSoft Ed., 2004–2005.

[4] M. Froimowitz, Biotechniques Vol. 14, pp. 1010–1013, **1993**.

[5] L. Kalé, R. Skeel, M. Bhandarkar, R. Brunner, A. Gursoy, N. Krawetz, J. Phillips, A. Shinozaki, K. Varadarajan and K. Schulten,
J. Comput. Phys, Vol. 151, pp. 283-312, **1992**.

[6] A.D. MacKerell, D. Bashford, Bellott, R.L. Dunbrack, J.D. Evanseck, M.J. Field, S.Fischer, J. Gao, H. Guo, S. Ha, D. Joseph-McCarthy, L. Kuchnir, K. Kuczera, F.T.K.Lau, C. Mattos, S. Michnick, T. Ngo, D.T. Nguyen, B. Prodhom, W.E. Reiher, B.Roux, M. Schlenkrich, J.C. Smith, R. Stote, J. Straub, M. Watanabe, J.Wiórkiewicz-Kuczera, D. Yin, M. Karplus, J. Phys. Chem. *B*, Vol. 102, pp. 3586-3616, **1998**.

Electric Field Effect on the Adsorption of Li, Na, Mg and Ca on Silicene sheet: A DFT study

Zahra Hasanzadeh Tazeh Gheshlagh *[a], Javad Beheshtian[b], Sakineh Mansouri[c]

[a] _Department of Chemistry, Faculty of Science, Islamic Azad University, Central Tehran Branch, Tehran; Hasanzadeh.206z@yahoo.com_
[b] _Department of Chemistry, Faculty of Science, Shahid Rajaee Teacher Training University, P.O. Box: 16875-163, Tehran, Iran; J.Beheshtian@SRU.ac.ir_
[c] _Department of chemistry, Faculty of Science, Islamic Azad University, Central Tehran Branch, Tehran; Sak.mansouri@iauctb.ac.ir_

Abstract: Using DFT calculations, we investigate the effect of absent and present of an electric field of adsorption defective silicene doped with Lithium (Li), sodium (Na), calcium(ca) and magnesia (Mg) atoms. Our results would present a new worthwhile strategy to study new structures silicene-based devices. The absent and present of an electric field in defective silicene compounds is an important aim of research with many potential applications in the industry, such as transistors, batteries and fuel cells.

Keywords: Electric Field, Silicene, Doping, DFT.

I. INTRODUCTION

Silicene with a buckled layer structure has high surface area and enough space for the adsorption of Li, Na, Mg and Ca atoms [1]. For this reason, we investigated theoretically the creation of double vacancies silicene sheet with doping. In this paper, we focused on these important issues for silicene-based structures in electric applications [2]. It proposed that absent and present of vertical electric field can affect energy of Li, Na, Mg and Ca on doped in defective silicene [3]. The goal of the present work was Comparison interaction energy on Defects in silicene with absent and present of electric field.

II. METHODS

All our density functional theory (DFT) calculations carried out within the generalized-gradient approximation (GGA) [4] for the exchange correlation energy term as implemented in the Dmol3 package [5]. The double numerical plus polarization (DNP) basis set and PBE [4] functional adopted. The k-point meshes for Brillouin zone generated using 6×6×1 Monkhorst-Pack grid [6]. As usual for avoiding interactions of the silicene sheet with its periodic images, a vacuum gap of 60 $°A$ in the z direction used.

III. RESULTS AND DISCUSSION

The interaction energy of Li, Na, Mg and Ca on di-vacancy silicene sheet in presence of electric field were investigated.

the single substitution doping at a di-vacancy (DV-Li, DV-Na, DV-Mg and DV-Ca) the interaction energy value decrease when electric field.
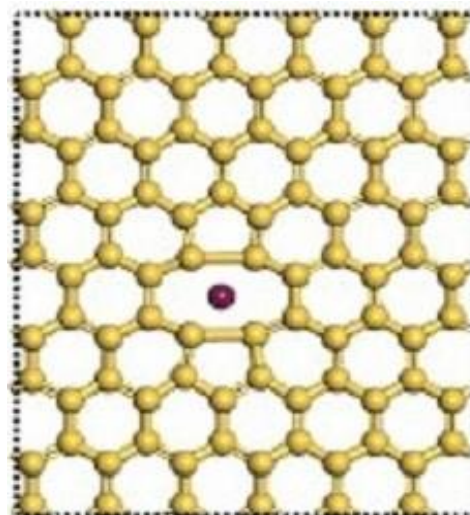
A. Figures and Tables

Fig.1: Optimized structure of di-vacancy (A=Li, Na, Mg and Ca)

Table 1: Interaction energy (E) calculated for the single substitution doping at a di-vacancy (DV-Li, DV-Na, DV-Mg and DV-Ca) in absent and present of electric field.

System	E (eV)	
	Without Electric Field	With Electric Field
DV-Li	-4.06	-2.91
DV-Na	-3.07	-2.42
DV-Mg	-3.19	-2.71
DV-Ca	-4.51	-3.72

B. Equations

As mentioned in the introduction, the following equation can used to describe the interaction energy (E) of structures. where E_{B+A} is the total energy for the optimized equilibrium configuration of double vacancies with A (A = Li, Na, Mg and Ca) atom sited in the vacancy. E_B is the total energy of silicene with vacancy and E_A is total energy of isolated atom in its ground state.

$$E = E_{B+A} - E_B - E_A \qquad (1)$$

IV. CONCLUSION

In this contribution, we theoretically studied the effect of absent and present of an electric field in defective silicene doped with Li, Na, Mg and Ca atoms. According to our results shown in Table1, the electric field can effect on the interaction energy and it can decrease obviously. It noted the absent and present of an electric field played an important role in modulating interaction energy.

REFERENCES

[1] F-H. Du.et al. J. Mater. Chem, vol. A4, pp. 32-50, **2016**.
[2] Berdiyorov, G. R. & Peeters, F. M. RSC Adv, vol. 4, pp. 1133–1137, **2014**.
[3] Dan Zhang. et al. Scientific Reports, vol 6, pp. 23677, **2016**.
[4] J. Perdew, Phys. Rev. Lett, vol. 77, pp. 18-28,**1996**.
[5] Delley, B, J. Chem. Phys, vol.13, pp. 7756-7764, **2000.**
[6] Monkhost, H. J.& Pack, J. D. Phys. Rev, vol. B13, pp. 5188-5192, **1976**.

Quantum Capacitance Effect on silicene sheet doped with N, B and F atoms:

A DFT study

Zahra Hasanzadeh Tazeh Gheshlagh *[a], Javad Beheshtian[b], Sakineh Mansouri[c]

[a] Department of Chemistry, Faculty of Science, Islamic Azad University, Central Tehran Branch, Tehran;
Hasanzadeh.206z@yahoo.com
[b] Department of Chemistry, Faculty of Science, Shahid Rajaee Teacher Training University, P.O. Box: 16875-163, Tehran, Iran; J.Beheshtian@SRU.ac.ir
[c] Department of chemistry, Faculty of Science, Islamic Azad University, Central Tehran Branch, Tehran;
Sak.mansouri@iauctb.ac.ir

Abstract: Supercapacitors are electrical energy storage devices. silicene-based materials are promising materials for use in supercapacitor electrodes. Silicene-based electrodes are superior; on the contrary, a major constraint that prevents their widespread and industrial applications is the limited capacity of their own. It has shown the limiting factor in the total capacity of silicene -based electrodes is the quantum capacity of these materials. In this study, we tried to evaluate the efficiency of silicene derivatives for use in superconductors using DFT calculations, and suggest solutions to improve existing superconductors or to design new superconductors. The efficiency of the electrode consisting of defected silicene with doping B, N, and F with structural defects of double-vacancy studied. The results showed the use of combined configurations of defect and doping in a given specific range has more capacities than the pristine silicene. Briefly, we can design and produce asymmetric and high-capacity supercapacitors with a clever selection of combinations of structural defects and doping.

Keywords: Quantum Capacitance, Supercapacitors, Silicene, Doped.

I. INTRODUCTION

Increasing importance of high-efficiency electrical energy storage for use in electric hybrid vehicles and the use of mobile electronics, research to gain the efficiency of these energy storage devices is developing day by day [1]. supercapacitors are important due to their special features such as good reversibility, high specific capacitance, high rates of charge and discharge, good stability and high cycle efficiency [2]. supercapacitors combine the properties of capacitors and batteries into one device. To earn high capacitance for supercapacitors, it is essential to remember that choice on electrode materials is a key reason [3]. Silicene expected to have potential application of supercapacitor [4]. So, we have studied theoretically to create the double-vacancy silicene sheet, as well as the B, N and F doping of silicene. In this paper, we focused on these important subjects for silicene-based electrode materials in nanoelectronics and supercapacitor applications.

II. METHODS

Calculations carried out with density functional theory (DFT) using a local density approximation scheme, as performed in the Dmol3 package [5]. The generalized-gradient approximation (GGA) for the exchange correlation functional with the parametrization of Perdew − Burke − Ernzerhof (PBE) was used [6]. The double numerical plus polarization (DNP) basis set, 4.4 basis file and Monkhorst-Pack k-point mesh of $(6\times6\times1)$ and (4×4) supercell with a vacuum width of 60 $\mathring{A}$. The calculations done in the following order: First, the system of the pages optimized and then the electron structure of the optimized configuration calculated. In the next step, the DOS data extracted from the got electron structure. DOS data divided into molecular weight systems, the output of which will be DOS per unit weight. DOS data per unit of weight as input entered other numerical calculations, the output of which is differential quantum capacitance. The data earned for differential quantum capacitance, as input, enters another stage, the output of which is the integrated quantum capacitance. In the final step, the data gained from numerical calculations of the integrated quantum capacitance, enters another numerical calculation, the output of which is the stored charge on the pages per unit weight.

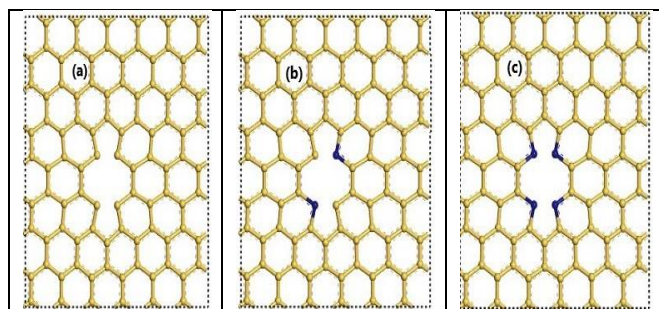## III. RESULTS AND DISCUSSION

A. Figures

Figure 1: Optimized structures of suggested silicene models including (a) di-vacancy (b) doping X (X= N, B and F) with two atoms, (c) doping X (X= N, B and F) with four atoms.
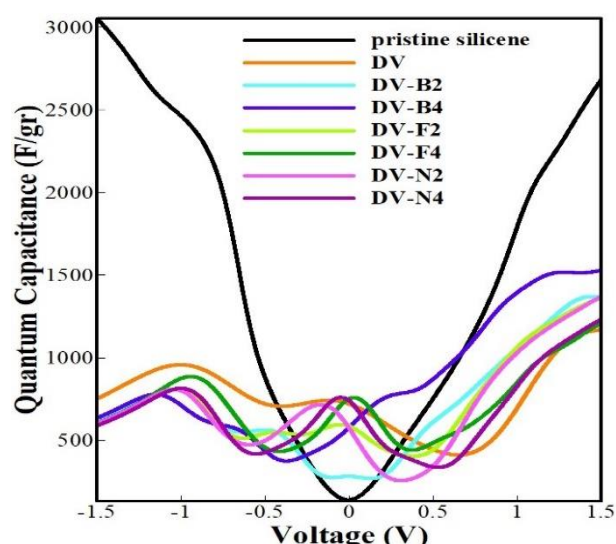

Fig.2: Calculated quantum capacitance of pristine silicene, $DV - B2$, $DV - B4$, $DV - N2$, $DV - N4$, $DV - F2$ and $DV - F4$.

B. Equations

The total capacity of the supercapacitor is considered as a series of two quantum capacitance and a double-layer capacitance.

$$C_t^{-1}(V) = C_Q^{-1} + C_D^{-1} \tag{1}$$

Where total capacitance is C_t, quantum capacitance is C_Q and double-layer capacitance is C_D , respectively [7].

The differential quantum capacitance can be expressed using Equation 2:

$$C_Q^{diff} = \frac{dQ}{dV} = e^2 Dos(-Ve) \tag{2}$$

Where elementary charge is e.

The integrated quantum capacitance can be obtained using Equation 3:

$$C_Q^{int}(V) = \frac{1}{Ve} \int_0^V C_Q^{diff}(V')dV' \tag{3}$$

Eventually, stored charge [8] can be given using Equation 4:

$$C_Q^{int}(V) = \frac{Q}{V} \tag{4}$$

IV. CONCLUSION

In this paper, the electronic properties of defected silicene with doping and vacancies as supercapacitor electrode material studied using density functional theory. The results showed the total capacity that changed by quantum capacity, improved by applying changes in electron properties. The results of the calculations confirmed that doping the defected silicene changes hybridization of the silicon atom connected to the doped atom and changes it. This change of hybridization appears as new states in energies near the Fermi level. In fact, adding number of states in areas near the Fermi level increases the quantum capacity and the total capacity. According our findings in certain ranges, the quantum capacity obtained is higher than the capacity for pristine silicene or defected silicene alone. It is proposed that these results give a good program to advance the supercapacitors electrode materials.

REFERENCES

[1] Liu Y., Qiao Y., Zhang W., Li Z., Ji X., Miao L., Yuan L., Ju X., Huang Y., Nano Energy, vol. 12, pp. 386-393, **2015**.
[2] Brownson, D. A.; Kampouris, D. K.; Banks, C. E, J. Power Sources, vol. 196, pp. 4873-4885, **2011.**
[3] Ni, Z.; Liu, Q.; Tang, K.; Zheng, J.; Zhou, J.; Qin, R.; Gao, Z.; Yu, D.; Lu, J., Nano Lett, vol. 12, pp. 113-118, **2012**.
[4] Shi, L.; Zhao, T. S.; Xu, A.; Xu, J. B., J. Mater. Chem. A, vol. 4, pp. 16377-16382, **2016**.
[5] Delley, B, J. Chem. Phys, vol.13, pp. 7756-7764, **2000.**
[6] J. Perdew, Phys. Rev. Lett, vol. 77, pp. 18-28,**1996**.
[7] Paek E., Pak A.J., Hwang G.S, J. Electrochem. Soc, vol.160(1), pp. A1–A10, **2012**.
[8] Wood B.C.B., Ogitsu T., Otani M., Biener J., J. Phys. Chem. C, vol.118(1), pp. 4-15, **2013**.

Molecular Dynamics Simulation of Ionic Liquid 1-Ethyl-3-Methyl Imidazolium Methyl Sulfate

H. Basouli, F . Mozaffari*

Department of Chemistry, Persian Gulf University, Bushehr, 75168, Iran
Email:hamidehbasouli@gmail.com

Abstract: Molecular dynamics simulations are employed on ionic liquid 1-ethyl-3-methylimidazolium methyl sulfate. The density, diffusion coefficient, radial distribution function and hydrogen bonding are studied that are in good agreement with experiment. Our observations indicated that cation diffusion coefficient is more than that for anion. The hydrogen bond value for C–H group between two nitrogens is more than two others C–H groups in imidazolium ring.

Keywords: Density, Diffusion coefficients, Hydrogen bonding, Modeling and simulation

I. INTRODUCTION

Ionic liquids (ILs) are a new class of non-molecular liquids and the most interesting in science and industry. These compounds are made of ionic species, which include an organic cation with low semmetry and an organic or inorganic anion. The interesting characteristics of these liquids include negligible vapor pressure [1,2], low melting temperature, nonflammability, high ionic conductivity, high thermal stability, and a very rich and complex behavior as solvents [4–7] that can be adjusted by changing the nature of the anion or cation. These incomparable characteristics make them very attractive for applications in the field of green chemistry.

We conduct MD simulations at ambient pressures, over a wide range of temperatures to study the density, radial distribution function, diffusion coefficient, the H-bonding statistics of [Emim][MeSO4]. In this work, the hydrogen bond between different C–H groups of imidazolium ring and oxygen atoms of anion ate investigated. Also, the diffusion coefficients of cation and anion are compared.

II. METHODS

We studied 256 ion-pairs of [Emim][MeSO4] at NPT ensemble via molecular dynamics simulations. In this work, YASP simulation package [8] is used. Berendsen thermostat and barostat used to fix temperature and pressure. [9] The time constant for temperature and pressure couplings were 0.2 ps and 2.0 ps, respectively. All nonbonded interactions were truncated at 1.1 nm and the reaction field correction for the Coulombic interactions [10] with the effective dielectric constant of 30 was comprised. An atomic Verlet neighbor list was used, which was updated every 15 time steps, and the neighbors were included if they were closer than 1.2 nm. The time step for the leapfrog integration scheme was 2.0 fs. The SHAKE algorithm used to constrain all bond lengths and angles . The unlike interactions were computed using the Lorentz–Berthelot mixing rule. Simulations were accomplished for 20 ns to obtain equilibrium configurations. In this work, 1-4 nonbonded interaction strengths were divided by a factor of 2, as is usual in all-atom OPLS-type force fields. The force field parameters for [emim] and [MeSO4] were taken from Zhao and from Lopes, respectively [11].

III. RESULTS AND DISCUSSION

The densities of [emim][MeSO4] over a broad temperature range at P=101.3kpa are calculated and results are reported in Table 1. All equilibrium configurations at lower temperatures were produced by cooling the system down with a temperature step of 10 K in 2 ns. As clearly shown in Table1, the predicted densities of [Emim] [MeSO$_4$] were in good agreement with experimental literature data [12].

Table1: Experimental and calculated density, ρ/kg.m^{-3} and Average Absolute Relative Deviation (AARD) of 1-ethyl3-methyl imidazolium methyl sulfate

Temperature	Density		AARD %
	Experimental[12]	**Calculated**	
273.15		1305.00	
283.15		1295.70	
293.15	1289.48	1286.70	0.21
298.15	1286.02	1288.17	0.17
313.15	1275.76	1270.50	0.41
323.15	1269.04	1261.00	0.63
333.15	1262.40	1254.18	0.65
353.15	1249.28	1237.50	0.94
373.15	1231.40	1221.70	0.79
393.15	1218.10	1206.79	0.93

A microscopic awareness of the local structure around anion and cation can be obtained from radial distribution function, g(r), where r is the distance between a pair of sites. In Figure 1 illustrates the g(r) for, center of mass of (imidazolium) ring-anion, C (between two nitrogens)-anion, N-anion, ring-ring, anion-anion and ring-anion. The g(r) of C–anion indicates a well-resolved double peak structure with maxima at 0.4 nm and 0.6 nm. The first peak is due to the proximity of anions to this C. The second peak is the contribution of anions that are around two other carbons of ring. As expected, the sharp peaks for N-anion and ring-anion were seen. The wide peaks for center of mass of ring–ring and anion–anion were seen. Also, more correlations are observed for anion–anion compared to cation–cation. However, the cation–cation peak starts at shorter distance that is because of the preferentially parallel packings of planar imidazolium rings at short distances.
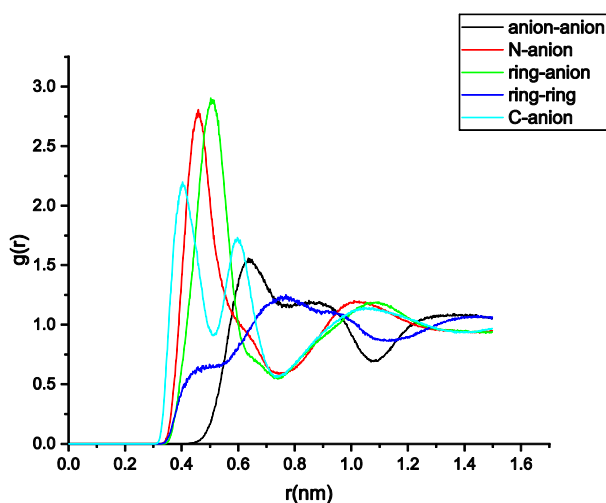

Fig.1: Radial distribution function, g(r), for center of mass of (imidazolium) ring-anion, C (between two nitrogens)-anion, N-anion, ring-ring, anion-anion and ring-anion.

We studied the possibility of hydrogen bond (HB) formation between three polar C-H groups of midazolium ring and oxygen atoms of anion in [Emim][MeSO4]. We have used a set of geometric criteria where two molecules are taken to be hydrogen bonded when the distance between the donor H atom and the acceptor's O atom is less than 0.35 nm and the C−H⋯O angle is larger than 130°. The fraction of bonded C−H⋯O sites for C–H groups between two nitrogens is more than two others C–H groups of imidazolium ring. Also fraction of bonded C−H⋯O sites decreased with increasing

Computational Chemistry | 46

temperature. The orientation survy of ethyle group and the plane of imidazolium ring indicated that ethyle group prefer parallel orientation to the plane of imidazolium ring.

We investigated center of mass mean-squared displacement (MSD) of anion and cation. The MSD is related to the diffusion coefficient through the Einstein relation. Our results indicated that normal Einstein diffusion regime in room temperature establishes after long time ($\approx$ 10 ns). This indicates that cation and anion have relatively long relaxation times. Also, the diffusion coefficient of cation is higher than that for anion.

IV. CONCLUSION

Molecular dynamics simulation at a constant parallel component of pressure of 101.3 kPa, and at different temperatures were employed to investigate the molecular structure and dynamical properties of [Emim][MeSO4].

The g(r) results indicate that more correlation exists between anion–anion compared to cation–cation. However, the distance between cations is shorter than anions that are because of the preferentially parallel packings of planar imidazolium rings at short distances. Our results indicate that relaxation times in [Emim][MeSO4] is long.

REFERENCES

[1] M.J. Earle, J.M.S.S. Esperança, M.A. Gilea, J.N. Canongia Lopes, L.P.N. Rebelo, J.W. Magee, K.R. Seddon, J.A.Widegren, The distillation and volatility of ionic liquids, Nature439 (2006) 831–834.

[2] D.H. Zaitsau, G.J. Kabo, A.A. Strechan, Y.U. Paulechka, A. Tschersich, S.P. Verevkin, A. Heintz, Experimental vapor pressures of 1-alkyl-3-methylimidazolium bis(trifluoromethylsulfonyl) imides and a correlation scheme for estimation of vaporization enthalpies of ionic liquids, J. Phys. Chem. A 110 (2006) 7303–7306.

[3] K.J. Baranyai, G.B. Deacon, D.R. MacFarlane, J.M. Pringle, J.L. Scott, Thermal degradation of ionic liquids at elevated temperatures, Aust. J. Chem. 57 (2004) 145–147.

[4] A.M. Scurto, S.N.V.K. Aki, J. Brennecke, CO2 as a separation switch for ionic liquid/organic mixtures, J. Am. Chem. Soc. 124 (2002) 10276–10277.

[5] K.E. Gutowski, G.A. Broker, H.D. Willauer, J.G. Huddleston, R.P. Swatloski, J.D. Holbrey, R.D. Rogers, Controlling the aqueous miscibility of ionic liquids: aqueous biphasic systems of water-miscible ionic liquids and water-structuring salts for recycle, metathesis, and separations, J. Am. Chem. Soc. 125 (2003) 6632–6633.

[6] J. Łachwa, J. Szydlowski, V. Najdanovic-Visak, L.P.N. Rebelo, K.R. Seddon, M. Nunes da Ponte, J.M.S.S.

Esperanca, H.J.R. Guedes, Evidence for lower critical solution behavior in ionic liquid solutions, J. Am. Chem. Soc. 127 (2005) 6542–6543.

[7] J. Łachwa, I. Bento, M.T. Duarte, J.N. Canongia Lopes, L.P. Rebelo, Condensed phase behaviour of ionic liquid benzenemixtures: congruentmelting of a [emim][NTf2]C6H6 inclusion crystal, Chem. Commun. 23 (2006) 2445 2447.

[8] Müller-Plathe F. YASP: A Molecular Simulation Package. Comput. Phys. Commun. 1993, 78, 77–94.

[9] Berendsen, H. J. C.; Postma, J. P. M.; van Gunsteren, W. F.; DiNola, A.; Haak, J. R. Molecular Dynamics with Coupling to an External Bath. J. Chem. Phys. 1984, 81, 3684−3690.

[10] Allen MP, Tildesley DJ. Computer simulation of liquids. Oxford: Clarendon Press 1987.

[11] Lopes, J. N. C.; Padua, A. A. H.; Shimizu, K. Molecular Force Field for Ionic Liquids IV: Trialkylimidazolium and Alkoxycarbonyl-Imidazolium Cations; Alkylsulfonate and Alkylsulfate Anions. J. Phys. Chem. B 2008, 112, 5039 5046.

[12] Anabela J. L. Costa, Jose M. S. Esperanca, Isabel M.Marrucho, and Luis Paulo N. Rebelo, Journal of Chemical & Engineering Dada, 56, 3433-3441, 2011.

Molecular Dynamics Simulation of Ionic Liquid 1-*n*-Butyl-3-Methylimidazolium Methylsulfate in Contact with a Silica Surface

Z. Khaknejad, N. Golmohammadi, N. Mehdipour*

Department of Chemistry, College of Sciences, Persian Gulf University, Boushehr 75168, Iran

Email: zeynab.khaknejad@gmail.com

Abstract: Molecular dynamics simulations are done to investigate the structure and dynamics of ionic liquid [Bmim][MeSO4] in contact with a silica surface and with vacuum. Alteration in IL structure and dynamics, compared to the bulk sample, at both interfaces are investigated in terms of IL layering, hydrogen bond formation, ion pairing, and electrical conductivity.

Keywords: Molecular Dynamics Simulation, Ionic Liquid, Silica

I. INTRODUCTION

Ionic liquids (ILs) are composed of bulky cations and anions, which remain liquid at ambient temperatures and pressures. Similar to the solution of inorganic salts, ILs consist of cations and anions and are regarded as clean solvents for practical purposes. The existence of bulky cations and anions with asymmetric structures in ILs causes charge distribution on ions, which clearly explains why ILs are liquid at low temperatures. Due to the potential use of ILs as green solvents, there has been a considerable amount of research on then in recent years. Because of their low vapor pressure, ILs are regarded as good replacements for volatile organic solvents in organic synthesis. ILs have also shown great promise for application in heterogeneous systems, such as lubricants, heterogeneous reactions, heterogeneous catalysis, electrochemistry, and fuel cells. However, for these particular applications, a more detailed understanding of the molecular structure of the interface between IL and solid is essential [1].

In general, solid surfaces strongly affect the properties of liquids. The magnitude of solid-liquid interactions and the geometry and surface chemistry of the solid surface have strong influence on the alteration of structure and dynamics of the liquid in contact with the surface [2]. In this work we have done long-time (up to 150 ns) molecular dynamics simulations to investigate structural and dynamical properties of [Bmim][MeSO$_4$] at the silica interface from one side and at the vacuum interface from the other. Our results show that [Bmim][MeSO$_4$ forms organized layered structures at the silica interface. Due to geometrical restrictions, hydrogen

bonding between cation and anion disrupts at the silica surface, but both cations and anions form hydrogen bonds with the silica surface. On the other hand the anions and cations at the vacuum interface more exist in the form of ion pairs. Compared to the bulk sample, the dynamics of IL, investigated in terms of relaxation time for formation/disruption of ion pairs and anion/cation diffusion, is restricted at the silica interface, but is accelerated at the vacuum interface.

II. METHOD

Molecular dynamics simulations were performed for 400 [Bmim][MeSO4] ion-pairs in contact with a silica surface at constant temperature and constant pressure. The silica surface has the structure of α-quartz. All the surface O atoms of the silica surface were saturated with H atoms. The simulations were performed using the simulation package YASP. Temperature and pressure were controlled using a Berendsen thermostat and barostat, respectively. The time constant for temperature and pressure couplings were 0.2 ps and 2.0 ps, respectively. All nonbonded interactions were truncated at 1.0 nm with a reaction field correction for the Coulombic interactions. An atomic Verlet neighbor list was used, which was updated every 15 time steps, and the neighbors were included if they were closer than 1.1 nm. The force field of [Bmim][MeSO$_4$] and silica were taken from the literature [3].

III. RESULTS AND DISCUSSION

The structure of IL at the silica and vacuum interfaces were investigated in terms of a number of properties, including formation of layered structures, hydrogen bonding, orientation of imidazolium ring, and ion pair formation. Our findings indicate that IL forms organized layers at the silica interface. At the silica interface cations keep closer distances to the surface than anions. The vacuum interface is, however, more enriched of the anions. Hydrogen bonding between cations and anions is retarded at close vicinity to the silica surface, but cations and anions form hydrogen bonds with the surface hydroxyl groups. Compare to the anion, the cation's imidazolium ring adhere better to the silica surface; the

imidazolium ring orients parallel to the silica surface. Cations and anions from stable ion pairs at both interfaces. Ion pairing at the vacuum interface is more pronounced than that in the bulk sample.

Furthermore, the dynamics of IL at both interfaces are investigated in terms of hydrogen bond dynamics, reorientation of imidazolium ring, dynamics of ion pair formation/rupture, and anion/cation diffusion at both interfaces. A short-time dynamical property, like hydrogen bond formation, is not noticeably affected at the interface. Only slight dynamic deceleration (compared to that of the bulk sample) is observed at the silica interface and a slight dynamic acceleration is observed at the vacuum interface. However, longer-time dynamical properties like ion pair formation/rupture and anion/cation diffusion are strongly affected at both interfaces. In this case a strong dynamic deceleration is observed at the silica interface, while the dynamics at the vacuum interface strongly accelerates. We have shown the autocorrelation behavior of the continuous correlation function, S(t), for formation/rupture of ion pairs. The results show that more stable ions pairs at the silica interface are formed (compared to the bulk IL). On the other hand, the solvation shells of cations/anions more frequently evolve in the vacuum interface.

We have discussed results from MD simulations of IL [Bmim][MeSO4] on the silica surface. We have found that structural properties of this IL are affected at both interfaces. The effect is more pronounced for larger scale structural properties, like ion pairing. Similarly, the dynamical properties are influenced by the interfaces. The magnitude of dynamic acceleration/deceleration depends on the time scale of the dynamical property of interest. The dynamics is more influenced for a longer-time dynamical property, like ion pair formation or cation/anion diffusion, but is less influenced for a short-time dynamical property, like hydrogen bond formation. Compared to the bulk IL, the dynamics gets accelerated at the vacuum interface. In contrary, the IL has a more restricted dynamics at the silica interface.

REFERENCES

[1] Sh. Maolin, Zh. Fuchun, W. Guozhong, F. Haiping, W. Chunlei, Ch. Shimou, Zh.Yi, and H. Jun, Journal of Chemical Physics, 128, 134504, **2008**.

[2] T. Pal, C. Beck, D. Lessinch, and M. Vogel, Journal of Physical Chemistry, 122, 624-634, **2017.**

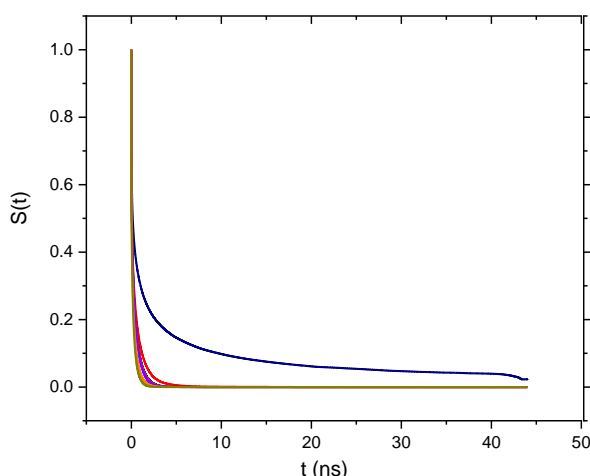[3] A. Afandak, and H. Eslami, Journal of Physical Chemistry, 121, 7699-7708, **2017**.

Fig.1: The continuous correlation function, S(t), for formation/rupture of ion pairs. The blue curve corresponds to the silica interface and the fastest decorrelation curve corresponds to the vacuum interface.

IV. CONCLUSION

Structure and Dynamics in Poly(ethylene terephthalate): Coarse-Grained Molecular Dynamics Simulations

N. Golmohammadi, H. Eslami

Department of Chemistry, College of Sciences, Persian Gulf University, Boushehr 75168, Iran
Email: ngolmohammadi@yahoo.com

Abstract: In this work atomistic simulations of short-chain oligomers of poly(ethylene terephthalate) PET have been done to construct coarse-grained (CG) potentials. The CG modeling has subsequently been employed to simulate long PET chains, of experimentally relevant size, which cannot be relaxed using atomistic simulations. This modeling provides us with an efficient scheme for examining the long-time relaxation behavior of long polymer chains.

Keywords: Molecular Dynamics Simulation, Coarse-Graining, Poly(ethylene terephthalate)

I. INTRODUCTION

PET is the most important polyester, used for many applications such as food packaging for ovenable food trays and beverage packaging, due to its superior barrier properties in comparison with polyolefins, polycarbonates, polystyrene, and other polymers. During the past decades, numerous experimental measurements have been performed to elucidate structural and dynamical properties of PET. Despite this, our understanding on the connection between macroscopic properties of PET and its governing molecular level properties is far from being completely understood. At present, molecular simulation techniques are known as efficient tools for providing a molecular level understanding of macroscopic properties. However, because of its stiff chemical structure, only a few molecular simulation studies are reported on PET [1]. Although atomistic simulations of this type provide us with detailed information on the structural and dynamical properties of PET, however, they are limited to simulation of short polymer chains over a short simulation time. In fact due to limitations in the system size and simulation time, atomistic simulations of long polymer chains are not feasible. This is particularly true for polymers of stiff chemical structure, like PET, which have a long relaxation time.

A solution to this problem is through elimination of a number of degrees of freedom, by lumping a group of atoms in a so-called "super atom" or "CG bead". Normally the fast degrees of freedom (bond stretchings and bendings) are eliminated in the process of coarse graining. The information hidden in such fast degrees of freedom are not necessary for understanding the global properties of polymer. In the process of coarse graining the number of interaction sites (system size) is reduced substantially. Meanwhile elimination of fast degrees of freedoms allows one to choose a longer time step for integration of equations of motion. It is also worth mentioning that grouping a number of atoms in a CG bead softens the CG beads (compared to hard atomistic sites), which artificially accelerates the dynamics in CG models. A combination of afore-cited factors makes CG simulations efficient schemes for simulation of large systems with long relaxation times. Therefore, in simulation of such systems as polymers, with large-scale structural properties (like the radius of gyration, which is of micron size) and long-time dynamical properties (like relaxation of end to end vectors in long chains, which locates within the microsecond domain), CG simulations are regarded as efficient tools for capturing the long-time dynamics and long-scale structure of the system.

II. METHOD

In this work, we use the IBI method to calculate the CG potentials. This is a known procedure, focusing on tuning the structure at the CG with that of the underlying atomistic level. Performing an atomistic simulation, on a very short chain, one can extract target distributions (structure) from this atomistic simulation. Then in an iterative procedure, the CG potentials are tuned in such a way to reproduce the target atomistic distributions. This is regarded as a systematic scheme, trying to keep the structure as close as possible to the underlying atomistic structure. In the IBI, the CG potential is constructed according to the following scheme:

$$U^{(n+1)} = U^{(n)} + \Delta U^{(n)} \tag{1}$$

where

$$\Delta U^{(n)} = k_B T ln \frac{P^{(n)}}{P_{ref}} = U_{PMF}^{ref} - U_{PMF}^{(n)} \tag{2}$$

Here, $U^{(n)}$ is the potential energy at the *n*-th iteration, $k_B T$ is the thermal energy, P is the distribution for a specified degree of freedom, subscript PMF stands for the potential of mean force, and superscript "ref" shows the reference property (obtained from atomistic simulations).

In the IBI, the CG structure is forced toward the atomistic structure by tuning the CG potentials iteratively. In other words, the CG potential is constructed on the top of its

originating atomistic model. This means that many structural features of the atomistic level modeling are preserved in the coarsened model. The procedure described in Eqs. (1) and (2) can be employed to tune all types of potentials/distributions (bonded as well as nonbonded degrees of freedom). The stiffer degrees of freedom are normally tuned in 1-2 iterations. The nonbonded interactions need a larger number of iterations (10-20) to be tuned. As the tuning procedure is done on a small system, this step is not computationally expensive.

The procedure outlined in this section well reproduces the atomistic level structure of the polymer. However, as the CG potentials are much softer than atomistic potentials, the pressure calculated from the virial theorem using such soft potentials does not match with the corresponding pressure obtained in atomistic simulations. To compensate for this effect, a linear ramp to the nonbonded interactions as

$$\Delta U^{pressure} = A(1 - \frac{r}{r_{cut}}) \qquad (3)$$

is introduced. In this equation, A is either a constant, e.g., -$0.1 k_B T$, or can be estimated from the virial expansion [4].

III. RESULTS AND DISCUSSION

In this work, we have adopted three different mapping schemes to develop CG models of PET. The difference between the mapping schemes is in the number of CG beads. Atomistic simulations are done for short chains (tetramers) of PET at high temperatures. From the results of atomistic simulations, we have constructed distributions for different degrees of freedom (reference distributions). The IBI, as explained above, is used to tune the CG potentials for different degrees of freedom. As an example, we have shown in Figure 1 the reference and the IBI-corrected radial distribution functions for two typical distributions. Tuning the CG potentials, we have employed them to run long-time simulations of long PET chains. Because of the long relaxation times of long polymer chains, the CG method is an efficient method for simulation of long chains. Due to the 44 softness of CG potentials and elimination of fast degrees of freedom, the dynamics in CG simulations is artificially accelerated. This artificial dynamic acceleration allows simulation of long chains.

This work is still in progress and the results on the simulation of long PET chains are not complete. Further results on the comparison of statics and dynamics of long PET chains with corresponding experimental and theoretical predictions are to be analyzed.
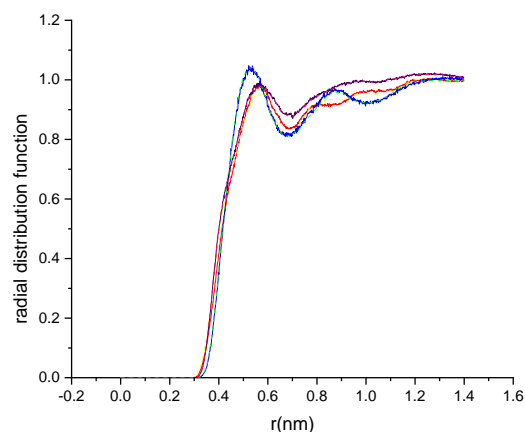

Fig1: Comparison of RDFs for two nonbonded degrees of freedom. The solid and dashed curves indicate the results calculated from atomistic simulation (reference) and CG simulations at 101.3kPa and 470 K, respectively.

IV. CONCLUSION

We have proposed and compared three different mapping schemes for CG simulations of PET. The CG models are constructed based on the structure of the corresponding atomistic level system. In this systematic scheme, the CG model predicts the same structure for the polymer as the corresponding atomistic level resolution. Meanwhile, the number of degrees of freedom reduces substantially and the dynamics gets artificially accelerated. Both factors allow simulation of long chains over long time scales, which is not feasible in atomistic simulations. We have constructed CG potentials for each mapping scheme and are simulating long PET chains. The results on the simulation of long chains (yet to come) will be discussed in terms of the effect of mapping scheme (number of CG beads), CG potential transferability, and capturing long-time relaxation behavior of long chains.

REFERENCES

[1] H.Eslami, and F.Müller-Plathe, Journal of Macromolecules, 42, 8241-8250, **2009.**
[2] B.Bayramoglu, and R.Faller, Journal of Macromolecules, 45, 9205-9219, **2012**.
[3] H.Eslami, H.A.Karimi-Varzaneh, and F.Müller-Plathe, Journal of Macromolecules, 44, 3117-3128, **2011**
[4] V.Ruhle, C.Junghans, A.Lukyanov, K.Kremer, and D.Andrienko, Journal of Chemical Theory and Computation, 5, 3211-3223, **2009.**

Interaction of CO and NO with Heme-Fe^{III} in Gas Phase

M. Aarabi^a, N. Shafizadeh^b, A. de la Lande^c, B. Soep^d and R. Omidyan^{a,}*
^{a}Department of Chemistry, University of Isfahan, 81746-73441 Isfahan, Iran
^{b}ISMO, Université Paris-Sud, CNRS UMR 8214, bat 520, Université Paris-Sud 91405, Orsay Cedex, France
^{c}Laboratoire de Chimie-Physique, Université Paris Sud, CNRS, UMR 8000. 15, rue Jean Perrin, 91405 Orsay Cedex, France
^{d}LIDYL, CEA, CNRS, Université Paris-Saclay, UMR 9222 CEA Saclay, F-91191 Gif-sur-Yvette, France
*Email: r.omidyan@sci.ui.ac.ir

Abstract: The binding energy of CO and NO to isolated *ferric* heme, [Fe^{III}P]$^+$ has been determined in the presence and absence of methylimidazole in 5th axial position, as histidine model at DFT/ADFT levels and compared with experimental results of a cooled ion-trap molecular beam set-up. It is found that the presence of methylimidazole strongly weakens the Fe^{III}–ligand bond and affects the nature of interaction prominently.

Keywords: ferric heme, DFT calculations, ligand binding, ferric porphyrin.

I. INTRODUCTION

The coordination number of heme active site is highly critical for the hemoprotein functions, determining their affinity to ligands and affecting redox potentials. This effect also controls the spin state of heme by nature of axial ligands attaching to Fe^{III} center, in addition to environmental conditions. It is further important to study the coordination effect of the biologically important CO and NO ligands in the naked hemes in presence of a N-methylimidazole (MI) in the 5th axial position, which mimics the coordination of histidine on the affinity of the small molecules CO and NO for heme. Since, it may affect the function of blood hemoproteins, where the heme molecule is attached to the protein by coordination to a histidine residue.

It is hard to observe the 5C hemes in the solution, since H$_2$O (or the solvent) sequentially sticks to Fe center and blocks the axial ligation for other ligands. In such a situation, gas phase experiments provide a controlled approach of sequential addition of ligands in the axial position to the heme, by avoiding the undesirable ligation by H$_2$O or the solvent. Such experiment also allows us to precisely study the intrinsic nature of the interactions, by the help of theoretical calculations. Accordingly, here we have studied and characterized the intrinsic binding properties of the biologically relevant CO and NO molecules to ferric heme in presence and absence of MI in 6th position by using DFT/ADFT calculations compared with experiment.

II. METHODS

The geometry optimizations for all complexes considered in this study were carried out with deMon2k software in the framework of auxiliary DFT (A-DFT) at OPTX−PBE/DZVP-GGA level of theory within the unrestricted Kohn–Sham (UKS) formalism. The GEN-A2 and the larger GEN-A2* auxiliary basis sets have been applied on C and H and also on the Fe, O and N atoms involving in the interaction, respectively. Single-point calculations were then carried out with the Gaussian09 program suite on the optimized geometries at B3LYP/TZP level and the calculated binding energies were corrected by considering the Basis Set Superposition Error (BSSE), zero-point vibrational energy (ZPVE) and the long-range dispersion correction of Grimme (GD3) with Becke−Johnson damping factors (GD3BJ) to B3LYP functional. To get more details about the nature of the interaction, a full topological analysis has been conducted based on the atoms in molecules (AIM) and electron localization function (ELF) approaches by using AIMAll and TopMod programs, respectively.

III. RESULTS AND DISCUSSION

Table 1 presents the ground spin states of the complexes of CO and NO ligands with the [Fe^{III}P]$^+$ and [MI–Fe^{III}P]$^+$ systems derived from EPR, ESR and Mössbauer spectroscopic experiments found in the literature and also, from our theoretical calculations at B3LYP/TZP level. We used Fe^{III} Porphyrin cation ([Fe^{III}P]$^+$) as the model molecular system for theoretical calculations (see Fig. 1.a).

The spin state results collected in Table 1 reveal that NO binding to ferric heme changes the spin state to the low spin S = 0 in both 5C ([Fe^{III}P]$^+$ (S = 3/2) + NO (S = 1/2)) and 6C ([MI–Fe^{III}P]$^+$ (S = 5/2) + NO (S = 1/2)) complexes, respectively, in agreement with the theoretical and experimental results. For CO complexes the situation is different, 5C complex was found in intermediate spin state, S=3/2 the same as bare 4C [Fe^{III}P]$^+$ complex. Thus, CO ligation to ferric heme doesn't change the ground spin state in 5C complex, in agreement with IR-PD spectroscopic results

while for the 6C complex, the high spin state 5/2 is the lowest in energy and a spin crossing is predicted following CO attachment to 5C [MI–Fe^{III}P]$^+$ complex.
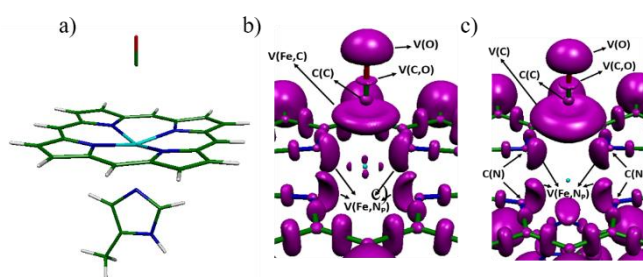

Figure 1. a) Ferric porphyrin model system for [MI–Fe^{III}P–CO]$^+$ complex, b) and c) Selected part of the ELF isosurfaces ($\eta = 0.85$) for 5C and 6C CO complexes, respectively.

Table 1. The calculated and experimental ground spin states and binding energies (in kcal/mol) of the ferric porphyrin complexes.

Complex	Spin state		Binding energy	
	Calc.[a]	Exp.	Calc.[a]	Exp.
[MI-Fe^{III} P]$^+$	3/2	5/2	−33.32	< −51
[Fe^{III} P−CO]$^+$	3/2	3/2	−6.71	−4.63 ± 0.43
[MI−Fe^{III} P−CO]$^+$	5/2	5/2	−0.23	−0.86 ± 014
[Fe^{III}P−NO]$^+$	0	0	−5.03	−24.88 ± 0.71
[MI−Fe^{III} P−NO]$^+$	0	0	−4.62	-
[MP11HH Fe^{III}−NO]$^{3+}$	-	0	-	−3.65 ± 0.17

[a]The binding energies have been calculated at B3LYP/TZP level and corrected by BSSE, ZPE and GD3BJ dispersion term.

Therefore, except for CO, the formation of 5C complexes with MI and NO is accompanied by spin state switching. A half-filled $3d_z^2$ orbital is available for σ donation from ligand which is less efficient than an empty $3d_z^2$ one. Thus, the strength of the ligation to the bare 4C ferric heme is conditioned by the back donation from Fe ($3d_{xz,yz}$), which controls the relative efficiency of the CO and NO ligands. CO donates via C(pσ) to Fe($3d_z^2$), while it accepts the electrons from Fe($3d_{xz,yz}$) in its free π* orbitals.

The theoretical B3LYP/TZP binding energies of CO and NO ligands to the [Fe^{III}P]$^+$ and [MI–Fe^{III}P]$^+$ ferric porphyrin complexes have been compared within Table 1 with the relevant experimental binding enthalpies determined by equilibrium measurements in a low temperature ion trap using the van't Hoff equation in the gas phase. From the results collected in Table 1, it can be rationalized that the weak CO

ligand cannot change the spin state of the ferric porphyrin [MI–Fe^{III}P]$^+$ complex. The MI is strongly attached with a binding energy of −33.32 kcal/mol and thereby a spin crossover is expected from 3/2 in 4C to 5/2 in 5C complex. NO binds more strongly to ferric center in 5C complex with spin crossing, as compared to CO which moderately binds that without spin change.

The results of Table 1 also indicate that MI addition to the 5th position decreases the binding affinity of all 5C complexes. This trend is predominant for 5C/6C ferric CO complexes, where the 5C complex is bound by −6.71 kcal/mol compared to −0.23 kcal/mol for the 6C complex, in agreement with experiments. It seems that the bond strength in 6C complexes is highly influenced by the competition for Fe($3d_z^2$) between the strength of MI (nitrogen sp2 pair), ligand σ donation and π backdonation from Fe($3d_{xz,yz}$) to the π* orbital.

The Fe^{III}-ligand interactions can be characterized by topological analysis of electron density at bond critical points (BCP) of the two interacting atoms via AIM theory and also, the properties of the valence basins V(Fe, Ligand) determined by interpreting the ELF function. The topological properties of AIM for ferric porphyrin systems investigated here are collected in Table 2. It can be seen that the values of ρ_{BCP} and V_{BCP} follow the overall trend [Fe^{III} P−NO]$^+$ > [MeIm−Fe^{III} P−NO]$^+$ > [Fe^{III} P−CO]$^+$ > [MeIm−Fe^{III} P−CO]$^+$ which is the same trend as observed experimentally. Furthermore, a decrease in AIM parameters is happened by addition of MI, pointing to weakening of binding.

Table 2. Topological parameters (in a.u.) at BCP for Fe^{III}-porphyrins considered in this study at B3LYP/TZP level of theory.

Complex	S	ρ_{BCP}	$\nabla^2\rho_{BCP}$	V_{BCP}	H_{BCP}	$\frac{|V_{BCP}|}{|G_{BCP}|}$
[Fe^{III} P−CO]$^+$	3/2	0.047	0.151	−0.051	−0.007	1.149
[MI−Fe^{III} P−CO]$^+$	5/2	0.005	0.013	−0.002	0.000	0.852
[Fe^{III}P−NO]$^+$	0	0.221	1.354	−0.577	−0.119	1.260
[MI−Fe^{III} P−NO]$^+$	0	0.202	1.406	−0.537	−0.093	1.209

The results collected in Table 2 reveal that the calculated value of V_{BCP} in [Fe^{III} P−CO]$^+$ complex dominates the G_{BCP}, and results in the overall negative value of the total energy density, H_{BCP}. Also, the ratio of $|V_{BCP}|/G_{BCP}$ falls into $1<|V_{BCP}|/G_{BCP}<2$. These results exhibit a mixed (largely ionic with significant covalent component) character of Fe^{III}−CO interaction for 5C complex. Interestingly, one can see that the values of ρ_{BCP} and V_{BCP} are decreased when the MI is attached, so that the G_{BCP} dominates the V_{BCP} resulting in positive H_{BCP} value and the ratio of $|V_{BCP}|/G_{BCP}$ becomes <1. The results of the ELF function analysis also confirm this outcome. From the ELF isosurfaces indicated in Figure 1.b and 1.c it is clear

that the bonding V(Fe, C) valence basin in 5C complex would convert to non-bonding V(C) basin when MI is attached, demonstrating the change in covalent character to ionic.

For NO complexes the situation is slightly different. For both complexes with/without MeIm, the H_{BCP} values are negative with a ratio of $|V_{BCP}|/G_{BCP}$ within $1<|V_{BCP}|/G_{BCP}<2$. The analysis of the ELF function also exhibits V(Fe, N) basin for both 5C and 6C complexes, confirming the partially covalency of the interaction. This result indicates that the NO complexes preserve the Fe^{III}-NO bonding nature following the MI addition.

IV. CONCLUSION

High level DFT approaches have been employed to investigate the CO and NO ligation of the *ferric*-Heme system in the presence and absence of methyl-imidazole (MI) as a model of histidine in the 5th axial position and compared to the experimental results, arisen from the cooled ion-trap molecular beam. In agreement with experiment, a dramatic decreasing trend in binding energy has been predicted for the CO/ NO systems in presence of MI. In addition, based on the ELF and QTAIM analyses, a mixed ionic/covalent character has been proposed for the bond nature of CO/NO ligated with [Heme-Fe^{III}] species. Our theoretical results provided essential insights on the nature and mechanism of CO/NO ligation with the 4c and 5c Heme-Fe^{III} systems.

REFERENCES

[1] M. Aarabi, R. Omidyan, S. Soorkia, G. Grégoire, M. Broquier, M.-E. Crestoni, A. de la Lande, B. Soep and N. Shafizadeh, *Phys. Chem. Chem. Phys*, 21, 1750-1760, **2019**.
[2] G. Feraud, M. Broquier, C. Dedonder-Lardeux, G. Gregoire, S. Soorkia and C. Jouvet, *Phys. Chem. Chem. Phys*, 16, 5250-5259, **2014**.
[3] S. J. Grabowski, *Chem. Rev*, 111, 2597, **2011**.

QM Study of Complex Between Acetazolamide Inhibitor and Human α-Carbonic Anhydrase Enzyme

Mina Ghiasi*, Farideh Salari and Mansour Zahedi
Department of Chemistry, Faculty of Physics & Chemistry, Alzahra University, 19835-389, Vanak, Tehran, Iran.
Tel: +982188044051-9(2608)
Fax: +982188041344
*corresponding author: ghiasi@alzahra.ac.ir
Salari.Farideh.93@gmail.com

Abstract: In the present research, the effect of a classical sulfonamide inhibitor, namely acetazolamide on human carbonic anhydrase reaction has been investigated by employing DFT method. Carbonic anhydrase is an enzyme found in red blood cells and many other tissues. Also all thermodynamic functions such as deprotonation enthalpy of inhibitor (ΔH^0), standard enthalpies of complexation, standard entropy of complexation (ΔS_{com}^0) and standard Gibbs free energy of complexation (ΔG_{com}^0) for CA–inhibitor complex are evaluated. The calculated results indicate that deprotonated inhibitor is coordinated to the Zn^{2+} ion and the [enzyme/inhibitor] complex has tetrahedral geometry. According to the calculated thermodynamic functions substitution of sulfonamide group with hydroxyl reduces the tendency of inhibitor to bind to the active center of carbonic anhydrase.

Keywords: Carbonic anhydrase, Acetazolamide, Inhibitor, QM study

I.   INTRODUCTION

CA is an enzyme in red blood cells that catalyzes the conversion of CO_2 and water to (HCO3 $^-$) and (H$^+$) ions. The enzyme was first identified in red bovine tuberculosis in 1933. Since then, in all tissues, plants, algae and bacteria have been scattered. To date, seven families have been known to be CA. All CAs known in animals and humans are alpha [1-3].

Acetazolamide is an anticonvulsant drug that is prescribed by the doctor to control seizures in patients with epilepsy. It is also used in patients with black water to reduce intraocular pressure. Acetazolamide (Diamox) is an inhibitor of carbonic anhydrase enzyme. Therefore, in the kidneys, bicarbonate is excreted, urine increases, and respiratory compensation increases to prevent metabolic acidosis [4].

So in the present research we use the quantum mechanical calculations to investigate inhibition mechanism of acetazolamide, as potent inhibitor of CA from thermodynamic point of view.

II.   METHODS

The complex between carbonic anhydrase enzyme center (CA) and acetazolamide inhibitor has been investigated, based on, B3LYP level, using 6-31G* basis set. All calculations were performed using the Gaussian 2009 software and the GaussView program for visualization.

III.   RESULTS AND DISCUSSION

Structure of active form of carbonic anhydrase II and acetazolamide was fully optimized at B3LYP/6-31G* method. Figure 1 shows the optimized structure of CAII active and acetazolamide molecule. The thermochemical functions of [enzyme/acetazolamide] interactions in the gas phase are reported in Table 1. As the results in Table 1 indicates, interaction of acetazoleamide with active center of CA enzyme is energetically exothermic.

According to ΔG value (ΔG=4.57) the interaction between acetazoleamide and active center of CA enzyme is possible thermodynamically. Because the value ΔG is small in the tempereture room.
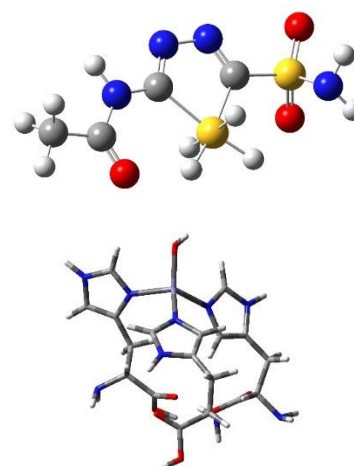

Fig.1: The optimized geometry of acetazolamide (up) and active form of CA active site (down)

Table1: The thermochemical functions of acetazolamide and CAII interactions

inhibitor	ΔE (kcal/mol)	ΔH^0 (kcal/mol)	ΔG_{com}^0 (kcal/mol)	ΔS_{com}^0 (cal/mol.k)
AZA	-13.037	-0.076	4.57	-15.59

IV. CONCLUSION

In this study, we presented a thermodynamic study of inhibition mechanism of CA by acetazoleamide using DFT method. These results showed that AZA have potential as carbonic anhydrase inhibitors.

REFERENCES

[1] S. Sersen, K. Traven, J. Kijun, I. Turel, C.T. Supuran, Journal of enzyme inhibition and medicinal chemistry, Vol. 34, pp. 388-393, **2019**.

[2] C.T. Supuran, Journal of Future medicinal chemistry, Vol. 10, pp. 561-573, **2019**.

[3] S. Del Prete, R. Merlo, A. Valenti, R. Mattossovich, M. Rossi, V. Carginale, & C. Capasso, Journal of enzyme inhibition and medicinal chemistry, Vol. 34, pp. 946-954, **2019**.

[4] C.T. Supuran, Journal of Expert review of neurotherapeutics, Vol. 15, pp.851-856, **2015**.

Anticancer Activity Evaluation of Some 1-hydroxynaphthalene-2-carboxanilide Derivatives Using the Computational Methods

H.S. Delarami[a]*, E. Sanchouli[a], S. Mirjahanshahi[b]

[a]Department of Chemistry, Faculty of Science, University of Zabol, Zabol, Iran
[b]Department of Chemistry, Faculty of Science, University of Sistan and Baluchestan, Zahedan, Iran
Email:hsdelarami@uoz.ac.ir, hsd102012@gmail.com

Abstract: DNA is often major target for the anticancer and antibiotic drugs, therefore consideration of the drug–DNA interaction has an important role in pharmacology. In this study, anticancer properties of some 1-hydroxynaphthalene-2-carboxanilide derivatives were analyzed through its possible interaction with DNA target using molecular docking and quantum mechanical calculations. The docking and quantum mechanics calculations show that the NO_2 derivative has the most affinity to the DNA target, which is in agreement with the previous experimental results. Intercalation of these compounds between the DNA base pairs along with the hydrogen bonds could be responsible for their mechanism of action.

Keywords: 1-hydroxynaphthalene-2-carboxanilides, Molecular docking, DNA, Intercalation, Density functional theory.

I. INTRODUCTION

Since the interaction of small molecules with DNA plays a crucial role in several biological applications including cancer chemotherapy, the evaluation of this interaction recently has drawn the particular attention of several researchers. Investigation of the drug–DNA interaction has a key role in pharmacology because DNA is often the prime target for majority of anticancer and antibiotic drugs. These interactions can inhibit the growth of cancer cells by inhibiting replication or transcription, which leads to apoptosis or cell death [1]. In the present study, some 1-hydroxynaphthalene-2-carboxanilide derivatives (see Fig. 1) were analyzed for its possible interaction with DNA through computational analysis.

II. METHODS

MGL tools 1.5.6 with AutoGrid4.2 and AutoDock4.2 [2] were used to molecular docking calculations between the ligands (1-hydroxynaphthalene-2-carboxanilide derivatives) and DNA sequence obtained from the Protein Data Bank (PDB). The DNA target is an octamer d(GAAGCTTC)2 (PDB ID: 1MTG). The DNA was enclosed in a box with a number of grid points in x×y×z directions, 70×40×70 and a grid spacing of 0.375 Å. The ligands were considered flexible and receptor rigid. The Lamarckian genetic algorithm was used to search for the best conformers. Geometries of ligands were optimized at the M06-2X/6-31G(d,p) level of theory by the Gaussian09 program package [3].

III. RESULTS AND DISCUSSION

Molecular docking is an attractive method that can provide some useful information about the interaction between ligand and target and assist to design new potent candidates. The results of molecular docking calculations clarify the binding modes between the ligands and receptors. The docking results are presented in Tables 1. As seen, the binding energy (BE) value of NO_2 derivative to DNA are the highest, which is in accordance with the previous reported minimum experimental IC_{50} value [4]. Moreover, the quantum mechanics results show that the NO_2 derivative has the highest HOMO energy, smallest LUMO, and smallest energy gap which makes it the most reactive derivative. There are conventional H-bonds and π–π stacking interactions between the ligands and nucleotides of DNA (see Fig. 2).
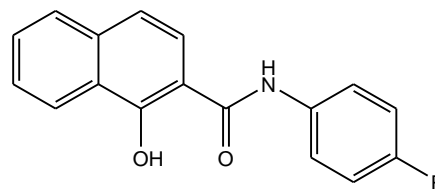
R=Br, CF_3, Cl, F, H, NO_2, OMe

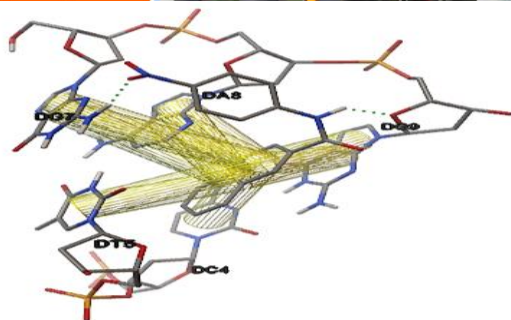Fig.1: 1-hydroxynaphthalene-2-carboxanilide derivatives as anticancer agents.

Fig. 2: Hydrogen bonds and π–π interactions between the NO₂ derivative and the DNA nucleobases.

Table1: The results of docking and quantum mechanical calculation for the interaction of substituted 1-hydroxynaphthalene-2-carboxanilides with DNA receptor.

R	IC50* (μM)	HOMO	LUMO	Gap	BE (kcal mol^{-1})
Br	5.25	-0.219	-0.061	0.158	-6.36
CF₃	4.31	-0.229	-0.064	0.165	-6.04
Cl	9.62	-0.220	-0.061	0.160	-6.25
F	2.49	-0.216	-0.058	0.158	-6.00
H	25	-0.217	-0.056	0.161	-6.06
NO₂	**0.41**	**-0.234**	**-0.085**	**0.149**	**-7.20**
OMe	25	-0.198	-0.053	0.145	-5.74

*The anticancer activity of 1-hydroxynaphthalene-2-carboxanilides described in ref. [4].

IV. CONCLUSION

The interaction mechanism of 1-hydroxynaphthalene-2-carboxanilide derivatives with DNA was investigated by molecular docking method. The results show that NO₂ derivative has the most anticancer activity, as well as experimental results. Based on molecular docking results, it can be concluded that hydrogen bond and the π–π interactions between the ligands and the DNA nucleobases are the major contributor to the potency of inhibition toward DNA targets.

REFERENCES

[1] I. Fukuda, A. Kaneko, S. Nishiumi, M. Kawase, R. Nishikiori, N. Fujitake, H. Ashida, and J. Biosci. Bioeng. vol. 107 pp. 296-300, **2009**.

[2] G.M. Morris, R. Huey, W. Lindstrom, M.F. Sanner, R.K. Belew, D.S. Goodsell, and A.J. Olson. J. Comput. Chem. vol. 30, pp. 2785-2791, **2009**.

[3] M.J. Frisch, et al., Gaussian 09, Revision A.02, Gaussian Inc., Wallingford, CT, **2009**.

[4] Gonec, T. et al. Antimycobacterial and herbicidal activity of ring-substituted 1-hydroxynaphthalene-2-carboxanilides. Bioorg. Med. Chem. vol. 21, pp. 6531–6541, **2013**.

Theoretical Study of Protic Ionic Liquids Composed of *N*- Hexylethylenediaminium Trifluoromethanesulfonate

Abdolhossein Haghani[a,*]

Chemical Engineering Department, Lamerd Higher Education Center,7434167441, Fars, Iran,
Email: Haghani@lamerdhec.ac.ir

Abstract: intermolecular hydrogen bonding interactions, and protonation sites of chelating mono-protic ionic liquids composed of *N*- Hexylethylenediaminium cations with a trifluoromethanesulfonate anion (TFS), forming [HHex][TFS], were studied using DFT calculations with the M06-2X functional and 6-311G(d, p) basis set. The BSSE-corrected interaction energies (ΔE_0^{BSSE}) for all the investigated structures range from -98.3 to -108.3 kcal·mol^{-1}. NBO and AIM analyses were applied to quantify the relative strengths of the hydrogen bonding interactions and to account for their effect on the stability of various molecular structures. The values of ΔE_0^{BSSE} decrease with increasing alkyl chain length and upon introduction of an ethyl branch in the cation. The second-order perturbation energy and electron density indicate that [HAlkyl]1$^+$[TFS] (protonated at the primary amine) are more stable than [HAlkyl]2$^+$[TFS] (protonated at the secondary amine).

Keywords: Protic ionic liquids, chelating amines, intermolecular hydrogen bonding, protonation sites

I. INTRODUCTION

PILs are formed by proton transfer [1,2] from a Brønsted acid (HA) to a Brønsted base (B, Eq. 1). In this study, trifluoromethanesulfonic acid (HTFS, CF$_3$SO$_3$H) was used as the Brønsted acid and *N*-hexylethylenediamines, were used as Brønsted bases.

B + HA→HB$^+$+A$^-$ Eq. 1

The protonated *N*-alkylethylenediaminium cations, which theoretically possess suitable sites for interaction with anion have been studied. H-bonding interactions between the protonated cations, [HAlkyl]$^+$, and TFS$^-$ anions were examined using density functional theory (DFT) [3], natural bond orbital (NBO) and quantum theory of atoms in molecules (QTAIM) [4] calculations. Particular attention was given to the effect of the alkyl chain length and the addition of an ethyl branch on the H-bond strength between cations of three protonated *N*-alkylethylenediamines cations ([HHex-en]$^+$ and TFS$^-$ anion in [HAlkyl][TFS] ion pairs. Moreover, suitable protonation sites on the *N*-alkylethylenediaminium cations were determined from data obtained by DFT calculations.

I. METHODS

The structures of the [HAlkyl][TFS] ion pairs and their corresponding cations and anions were optimized using the GAUSSIAN 09 software package [5]. The M06-2X functional and 6-311G(d, p) basis set were used to optimize all the PILs, while M06-2X with the 6-311++G(d, p) basis set was used to calculate the interaction energy. To examine the nature of the interactions, electric redistribution between the cation and anion in each PIL configuration was calculated by NBO analysis. NBO analyses were performed using the M06-2X/6-311G(d,p) wave function. Topological properties such as electron density (ρ_c), the Laplacian electron density ($\nabla^2\rho_c$), Lagrangian kinetic energy (G(r)), Hamiltonian kinetic energy (H(r)), and potential energy density (V(r)), were calculated using Bader's theory at the M06-2X/6-311G(d, p) level using the AIM 2000 software package.

II. RESULTS AND DISCUSSION

The four stable structures (S1, S2, S3, and S4) and two stable structures (S5 and S6) that were determined are shown in Figure 1 (2-4). It was found that the most favorable H-bonds occur between the N-H of the [HAlkyl]$^+$ cations and the electronegative O atoms in the TFS anion. The bond lengths and angles of the intermolecular hydrogen bonds are shown in Figure 1. It was found that the H···O bond length (1.51–1.64 Å) in [Hhexyl][TFS] is shorter than the sum of the van der Waals (vdW) radii of the bonding atoms (the vdW radii of H and O are 1.20 and 1.53 Å, respectively) and longer than the typical covalent H-O bond length (0.96 Å). The corresponding X-H···O angle (which ranged between 149.9 and 185.8°) is greater than 90.5 °, suggesting the formation of H-bonds between [HAlkyl]$^+$ and [TFS]$^-$. Table 1 shows the absolute energies of the cations, anion, and ion pairs, and the interaction energies between each cation-anion pair corrected by BSSE. Typical interaction energies for IL ion pairs range from -72.0 to -96.0 kcal mol^{-1}. According to the data shown in Table 1, the BSSE-corrected interaction energies ranged from -98.3 to -108.3 kcal·mol^{-1} for the ion pairs. These values are comparable to those of ILs composed of an amino acid-based

anion. As seen in Table 1, the Gibbs free energies of the ion pairs studied herein range from -91.0 to -98.0 kcal·mol^{-1}. These values are comparable with those of ILs such as [X-PhMIM][BF$_4$] (where PhMIM is para-X-phenyl methyl imidazolium, X=NH$_3$, OH, OCH$_3$, CH$_3$, H, F, CHO, CN, and NO$_2$), whose Gibbs free binding energies range from -71.8 to -82.1 kcal·mol^{-1}According to the interaction energies listed above, the PILs in this study are more stable than previously reported ILs. The binding energy decreases with increasing alkyl chain length and upon introduction of the ethyl branch in the cation, with identical anion. Furthermore, as seen in Table 1, the relative interaction energies ($\Delta\Delta E_{int}$, kcal·mol^{-1}) of the [HAlkyl][TFS] ion pair structures S1–S6 calculated by the perturbation method follow the order S2 > S1 > S3 > S4 > S6 > S5 for [HHex][TFS]. For each PIL, stronger interactions were observed in the structures (S1–S4) than in the structures (S5 and S6). The structures of (S1–S4) were shown to be 2–10 kcal·mol^{-1} more stable than other structure for all [HAlkyl][TFS] PILs. This suggests that protonation occurs preferentially at the primary amine of the cation in these PILs.

Table 1. interaction energies (ΔE_{int}, kcal·mol^{-1}), relative energies ($\Delta\Delta E_{int}$, kcal·mol^{-1})

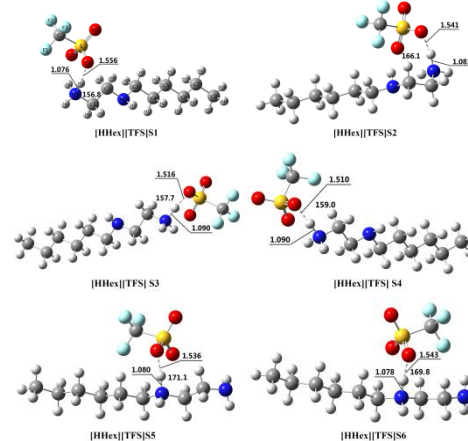| Structures	ΔE_{int}	$^a\Delta E_{int}$ BSSE	$\Delta\Delta E_{int}$	BSSE	ΔZPVE	$^b\Delta E_0$	$^c\Delta E_0$ BSSE
[HHex][TFS]S1	-109.4	-105.4	4.5	4.0	0.3	-108.7	-104.7
[HHex][TFS]S2	-115.5	-109.9	0.0	5.6	0.3	-113.8	-108.3
[HHex][TFS]S3	-107.4	-103.9	6.0	3.6	0.3	-107.1	-103.5
[HHex][TFS]S4	-108.0	-104.1	5.8	3.9	0.3	-107.7	-103.8
[HHex][TFS]S5	-108.0	-102.3	7.6	5.7	0.3	-107.1	-101.4
[HHex][TFS]S6	-108.2	-102.6	7.3	5.6	0.3	-106.6	-101.0

Fig1. Optimized structures of the alkyl cations [HHex]1$^+$, [HHex]2$^+$, and anion [TFS]$^-$.

I. CONCLUSIONS

In this study, chelating PILs composed of *N*-hexyl ethylenediaminium cations and a TFS anion ([HHex][TFS] were studied at the electronic and molecular levels using DFT calculations. Four favorable structures of (S1–S4), wherein protonation occurs at the primary amine (S1–S4), and two favorable structures of S5 and S6, wherein protonation occurs at the secondary amine (S5 and S6), were calculated using the M06-2X functional with the 6-311G(d, p) basis set. Bond lengths and angles of the N-H···O interactions were determined and used for classification of the H-bonding in these compounds. The stability of the ion pairs decreased with increasing alkyl chain length and upon introduction of an ethyl branch in the cation. The interaction energies ranged from -98.3 to -108.3 kcal·mol^{-1} for all PILs studied herein. AIM analysis confirmed that the interactions between the [HAlkyl]$^+$ cation and [TFS]$^-$ anion were partially due to H-bond formation. The $\nabla^2\rho_c$ values were positive, ranging between 0.070 and 0.153 a.u. for all ion pairs. NBO data showed that the second-order perturbation stabilization energies, $E^{(2)}$, for the interactions in structures of S1–S4 were larger than those in structures of S5 and S6. This indicates that protonation occurs preferentially at the primary amine in [HAlkyl][TFS] PILs.

REFERENCES

[1] Yoshizawa, M.; Xu, W.; Angell, C.A. s, *J. Am. Chem. Soc*. **2003**, 125, 15411-15419
[2] Greaves, T.L.; Drummond, J. C., *Chem. Rev*. **2008**, 108, 206-237.
[3] Parr, R. G.; Yang, W. Density-Functional Theory of Atoms and Molecules, Oxford Science, Oxford, **1989**.

[4] Bader, R.F.W. Atom in Molecules: A Quantum Theory, Oxford University Press, New York, **1990**.
[5] Frisch, M. J.; Trucks, G. W.; Schlegel, H. B.; Scuseria, G. E.; Robb, M. A. etc, Gaussian 09, Revision D.01, Gaussian, Inc, Wallingford CT, **2013**.

DFT Calculations of Some Iron Chelators as Antibacterial Inhibitors

Marjan A. Rafiee

Department of Chemistry, Payame Noor University, P.O. Box: 19395-3697 Tehran

Email: rafiee.marjan@gmail.com

Abstract: A series of related 3-hydroxypyridin-4-one hexadentate ligands have been studied. These chelators were found to possess a high affinity for iron(III). In this study, by calculating and comparing of NQCC parameters, the effect of various substituents on three iron chelator was studied and the relation of charge density on atoms with pharmaceutical effects was determined. For this purpose, all considered structures were optimized at B3LYP/6-31$^+$G level using Gaussian09 software, and in continue, the electric field gradient and HOMO/LUMO calculations was performed at this level. The results show Nitrogen atom adjacent to the carbonyl group act as active sites of these chelators, and 1 and 2 have the most reactivity in their pharmaceuitical effects.

Keywords: Ab initio, Charge Density, Gaussian 09, NQR Spectroscopy, Siderophore

I. INTRODUCTION

In recent years, macromolecular iron chelators have received increasing attention as human therapeutic agents[1-3]. These chelators were found to possess high affinity for iron(III). As iron is a critical element to the survival of bacteria, these chelators were predicted to inhibit the growth of bacteria by disrupting of bacterial iron absorption[4-7].

It is essential to know the mechanism of the inhibitory mechanism of the drugs and the introduction of new drug compounds. Theoretical chemistry may be useful to receive this purpose faster and easier.

Some of nuclei have quadrupole moment which is due to asymmetric charge distribution around these nuclei. These nuclei interact with electric field gradient due to other surrounding charges and this interaction is the basis of Nuclear Quadrupole Resonance spectroscopy (NQR). NQR parameters of a nucleus are very sensitive to charge density around it and calculation of these parameters can be used as a useful tool to understanding charge distribution around nulei[8].

II. METHODS

Geometry optimization was performed at the framework of the ab initio approach embedded in the Gaussian 09 program. B3LYP as computational method and 6-31$^+$G as a basis set for all atoms were employed. Using the same level of theory (method/basis set) to calculate EFG for various atoms (in this work: ^{2}H, ^{17}O and ^{14}N) let us predict the EFG qualitatively.

III. RESULTS AND DISCUSSION

In the present work ab initio NQCC computations were performed on a number iron chelators as siderophore inhibitors (Fig. 1) so that a possible relationship between their electronic structure and biological activity could be investigated.

From the expression $\chi = \frac{e^2 Q\, q_{zz}}{h}$, it is clear that the NQCC of nuclei is directly proportional to q_{zz}. In above equation e is charge of electron, Q is the quadrupole moment of nuleus, q_{zz} is z-component of electric field gradient and h is plank constant. Two factors were found to control the value of q_{zz} in a nucleus; charge density on the nucleus and symmetry of EFG around the quadrupolar nucleus. It is obvious that increases in charge density cause the q_{zz}, and consequently increase χ. If charge distribution were spherical, EFG symmetry would increase and q_{zz} and χ would decrease consequently.

Theoretical calculations, particularly calculated NQCCs of quadrupolar nuclei, seem to be proper tools for obtaining a better understanding of the electronic structure of these inhibitors.

The results show that in compound 1 and 2, nitrogen atoms in the vicinity of carbonyl group, have less NQCCs and consequently high charge density and therefore more inhibitory activity of theses compound is related to more ability of these atoms for chelating iron atoms. In other words, these nitrogen atoms are active sits of these compounds for chelating iron and consequently their pharmaceutical effect.

From results of HUMO/LUMO calculations electronic chemical potential (μ), chemical hardness (η), softnes (S) and electrophilicity index (ω) of studied compounds were calculated.

The calculated NQCCs of nitrogen, hydrogen, and oxygen atoms of the above mentioned compounds are reported in Table 1.
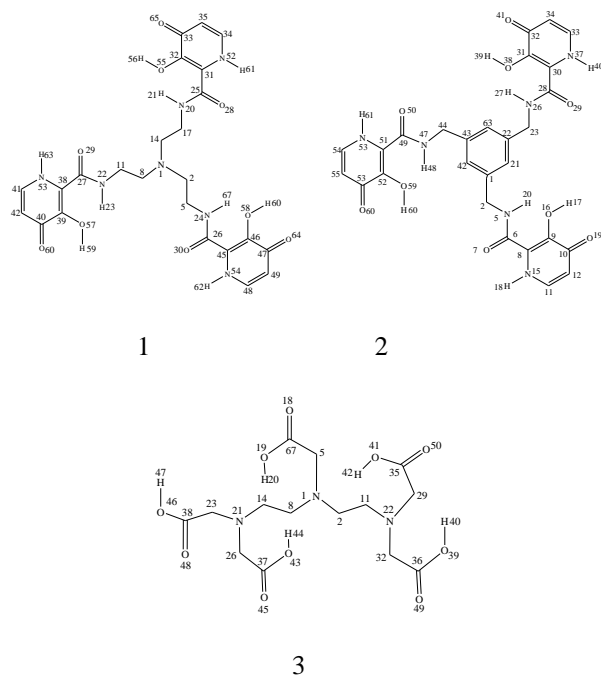
1   2

3

Fig. 1. Chemical structure of studied siderophores

Table 1. Calculated NQCC parameters of quadrupolar nuclei in studied compounds

^{14}N-NQCCs(MHz)			^{17}O-NQCCs(MHz)			^{2}H-NQCCs(KHz)		
1	2	3	1	2	3	1	2	3
N1= ۳/٦	٤/۳٥ N5=	٦/۷۷ N1=	O28= ۸/۰٥	O7= ۷/۸۰	O18= ۸/۸۱	H21= ۱٤۸/۹۰	H21= ۱۲۳/۳٥	H20= ۱٤۹/۹٦
٤/۲٤ N20=	۳/۸۳ N15=	N21= 6.42	O29= ۸/۱۹	O16= ٦/٦۳	O19= ٦/۸۰	H23= ۱٥۰/٦۸	H23= ۱٤۸/۲۳	H40= ۱٥۰/٦۸
٤/۲٤ N22=	٤/۳٦ N26=	N22= 6.11	O30= ۸/۱۱	O19= ۱۰/٦۲	O39= ٦/۹٤	H56= ۱۲۳/٥٥	H56= ۱٥۲/۲۸	H42= ۱٥۰/٦۸
٤/۲۷ N24=	۳/۸۰ N37=		O55= ٦/٦۳	O29= ۸/۱۲	O41= ٦/۹٦	H59= ۱۲۲/۷٥	H59= ۱٥۲/۲۸	H44= ۱٤۹/۹٦
۳/۸۰ N52=	٤/٤۰ N47=		O57= ٦/٦۰	O38= ٦/٦٤	O43= ٦/۸۳	H60= ۱۲۳/٥۹	H60= ۱۲۳/۳٥	H47= ۱٥۱/۳۳
۳/۸۰ N53=	۳/۸۲ N58=		O58= ٦/٦۳	O41= ۱۰/٦۰	O45= ۸/٦۸	H61= ۱٤۸/۰۱	H61= ۱٥۲/۲۸	
۳/۸۱ N54=			O64= ۱۰/٦۱	O50= ۷/۹۹	O46= ۷/۰٥	H62= ۱٤۸/۰۰	H62= ۱٥۲/٦۱	
			۱۰/٦۰ O65=	٦/٦٤ O59=	۸/۹۷ O48=	H63= ۱٤۸/۲۳	H63= ۱۰۸/٦٥	
			O66= ۱۰/٦۱	O62= ۱۰/٦۰	O49= ۹/۱۰	H67= ۱٥۰/۰۷	H67= ۱٥۲/۲۷٦	
					O50= ۸/۹٥			

Table 2. Comparison of calculated reactivity factors of studied compounds

compound	μ	η	S	ω
1	-3.86	1.90	0.26	3.94
2	-3.89	2.03	0.25	3.74
3	-2.88	2.83	0.18	1.46

Comparison of these results in table 2 show that compounds 1 and 2 are more active from 3 and this is in accordance to NQCC results.

IV. CONCLUSION

The results show that Nitrogen atom adjacent to the carbonyl group act as active sites of iron (III)-selective 3-hydroxypyridin-4-one chelators, and 1 and 2 have the most reactivity in their pharmaceutical effects.

REFERENCES

[1] C. Dean, Physical Review, vol. 86, pp. 607-608, 1952.

[2] F. A. Cotton, C. B. Harris, Inorganic Chemistry, vol. 6(2), pp. 376-379, 1967.

[3] C. H. Townes, B. P. Dailey, the Journal of Chemical Physics, vol. 17(9), pp. 782-796, 1949.

[4] H. Budzikiewicz, Current topics in medicinal chemistry, vol. 1(1), pp. 73-82, 2001.

[5] U. Möllmann, L. Heinisch, A. Bauernfeind, T. Köhler, D. Ankel-Fuchs, Biometals, vol. 22(4), pp. 615-624, 2009.

[6] S. Compant, B. Duffy, J. Nowak, C. Clément, E. A. Barka, Applied and environmental microbiology, vol. 71(9), pp. 4951-4959, 2005.

[7] A. Nair, A. A. Juwarkar, S. K. Singh, Water, Air, and Soil Pollution, vol. 180(1-4), pp. 199-212, 2007.

[8] E. A. C. Lucken, Nuclear quadrupole coupling constants. Academic Press, London, Ch. 1-4, 1969.

DFT investigation of the effect of pressure on $Ca(BH_4)_2$ as Hydrogen Storage Material in Fuel Cells

Marjan A. Rafiee

Department of Chemistry, Payame Noor University, P.O. Box: 19395-3697 Tehran
Email: rafiee.marjan@gmail.com

Abstract: Calcium borohydride $Ca(BH_4)_2$ is a potential hydrogen storage material because of its high hydrogen capacity. But, its high thermodynamic stability is undesirable for dehydrogenation operations. Knowing the bonding nature of B and H is necessary for modifying its dehydrogenation process. In this work the charge density distribution in $Ca(BH_4)_2$ is studied. For this purpose, using calculated NQCCs of hydrogen atoms, the electronic structure of α-$Ca(BH_4)_2$ with high pressure forms of $Ca(BH_4)_2$ (β-$Ca(BH_4)_2$ and γ-$Ca(BH_4)_2$)were compared. The results show that in the high pressure phase, hydrogens have greater NQCC and therefore these hydrogens form stronger bond with B.

Keywords: Calcium Borohydride, DFT, Fuel Cell, Hydrogen Storage

I. INTRODUCTION

Hydrides of high hydrogen storage densities with appropriate hydrogenation kinetics are required for fuel cell technology. Complex hydrides have high gravimetric storage valences. For example, $Ca(BH_4)_2$ and $Mg(BH_4)_2$ are favorable materials due to their chance of reversible hydrogen storage [1]. Theoretical hydrogen storage capacity of $Ca(BH_4)_2$ is 11.48 wt %. In dehydrogenation reaction, hydrogen releases from $Ca(BH_4)_2$ with CaH_2 and CaB_6 as dissociation products [2]. Investigation of the thermal decomposition behavior of $Ca(BH_4)_2$ [3] and under vacuum or inert gas flow [4] show that $Ca(BH_4)_2$ transforms from an orthorhombic to a tetragonal structure below 250 °C with a 5.9% hydrogen release. The structural researches at different temperatures and pressures help to identify various structures of the material with better thermodynamic stability. Knowing the bonding nature of boron and hydrogen is necessary for identify its dehydrogenation performance. Nuclear Quadrupole Resonance (NQR) spectroscopy analysis [5] is a technique for further understands the bonding nature of atoms. Quadrupolar parameters are very sensitive to electric charge distribution around quadrupolar nuclei (I > 1/2). Determination of the charge distribution in molecules or complexes can be done by the quantum mechanical approach as an effective method. In this method,

the electric field gradient (EFG) of whole molecular charges can be evaluated at any point in the molecular space. The interaction of EFG and quadrupole moment of quadrupolar nuclei is measured by the nuclear quadrupole coupling constant (NQCC). In the present paper, calculated NQCCs of ^2H nuclei in a unit cell of nanocrystal of $Ca(BH_4)_2$ and some pressure-induced phases of this compound were used to delve the electronic structure and steric factors governing B–H bond strength of these compounds.

II. METHODS

The HF/6-31G* computational model as implemented in the Gaussian software package is an effective method for accurate calculation of ^2H-NQCC tensors[6,7]. In this work the results of NQCC calculations using this model have been reported. The electric field gradient (EFG) at the site of quadrupolar nuclei were calculated to obtain NQCC parameters using Gaussian 09 at HF/6-31G* level of theory. Calculated NQCCs of nuclei are proper way for better understanding of the electronic structure of compounds. NQCC is an appropriate scale for the charge density of atoms. For theoretical calculation of NQCCs, the electric field gradient (EFG) tensor at a nucleus must be calculated. According to NQCC expression, NQCC of nuclei has a direct relation to q_{zz}. q_{zz} controlling factors are Charge density on the nucleus and symmetry of EFG around the quadrupolar nucleus. The importance of NQCCs is that same nucleus in different molecules have different values of the field gradient. Nucleus with higher charge density has greater q_{zz} and consequently larger NQCC.

III. RESULTS AND DISCUSSION

In this work, the calculated NQCCs of hydrogens of pressure-induced phases of calcium borohydride were calculated to determine the relationship between their electronic structures and their hydrogen desorption ability.

The $\alpha \rightarrow \beta \rightarrow \gamma$ transition under high pressure It has been reported for $Ca(BH_4)_2$. (Fig. 1)
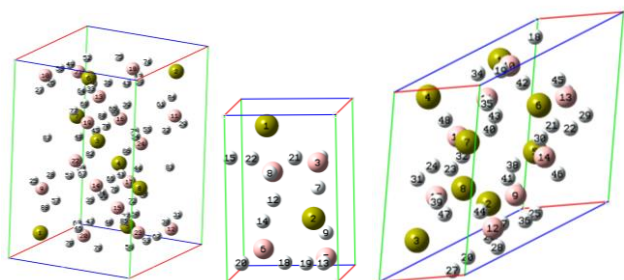
Fig1. Crystal structures of various phases of Ca(BH₄)₂

Table 1. The calculated NQCCs of Hydrogen atoms in considered structures

α -Ca(BH$_4$)$_2$		β-Ca(BH$_4$)$_2$		γ -Ca(BH$_4$)$_2$	
hydrogen	χ$_H$(KHz)	hydrogen	χ$_H$(KHz)	hydrogen	χ$_H$(KHz)
H25	162.024	H7	341.73	H17	179.64
H26	153.56	H8	354.56	H18	36.34
H27	155.85	H9	333.56	H19	39.55
H28	151.48	H10	342.52	H20	264.44
H29	162.02	H11	167.96	H21	281.06
H30	153.56	H12	183.29	H22	271.07
H31	155.85	H13	177.31	H23	292.28
H32	151.48	H14	186.33	H24	280.43
H33	164.54	H15	10.00	H25	280.74
H34	167.80	H16	299.05	H26	203.81
H35	165.62	H17	1.12	H27	189.36
H36	170.15	H18	302.10	H28	274.26
H37	164.54	H19	286.43	H29	157.06
H39	167.80	H20	295.17	H30	159.51
H40	165.62	H21	269.84	H31	150.26
H41	170.15	H22	297.86	H32	160.23
H42	162.45			H33	424.87

The results of Table 1 show that with increasing pressure, phases with a higher density of hydrogen are generated. In other words in (β-Ca(BH₄)₂ and γ- Ca(BH₄)₂) some calculated ²H-NQCCs are very larger than that of normal phase and therefore B-H bond in these phases are stronger than that of normal phase and the high pressure technique is not an useful technique for better dehydrogenation in Ca(BH₄)₂.

IV. CONCLUSION

Based on the information obtained in this research, the quadrupolar parameters of nuclei are a useful tool for understanding the electronic structure of compounds. In β-Ca(BH₄)₂ and γ - Ca(BH₄)₂, hydrogens have larger NQCC and therefore these hydrogens have stronger bonds with B

and easier dehydrogenation is not expected in pressure induced phases of calcium borohydride.

REFERENCES

[1] Ronnebro, E.; Majzoub, E. H. J. Phys. Chem. B 2007, 111, 12045-12047.

[2] Miwa, K.; Aoki, M.; Noritake, T.; Ohba, N.; Nakamori, Y.; Towata, S.; Zuttel, A.; Orimo, S. Phys. ReV.B 2006, 74, 155122.

[3] Kim, J. H.; Jin, S. A.; Shim, J. H.; Cho, Y. W. J. Alloys Compd. 2008, 461, L20–L22.

[4] Aoki, M.; Miwa, K.; Noritake, T.; Ohba, N.; Matsumoto, M.; Li, H. W.; Nakamori, Y.; Towata, S.; Orimo, S. Appl. Phys. A: Mater. Sci. Process. 2008, 92, 601–605.

[5] E. A. C. Lucken, Nuclear quadrupole coupling constants. Academic Press, London, Ch. 1-4, **1969**.

[6] M. A. Rafiee, T. Partooe, Bull. Korean Chem. Soc., vol.32, pp. 208–212, **2011**

[7] M. A. Rafiee , Int. J. Nano Dimens.,vol. 6(3), pp. 289–295, **2015**.

Comparison of the inhibitory effect of thiocyanate and isothiocyanate on inhibition of carbonic enzyme: The DFT study

M. Ghiasi*, A. Larijani

Department of chemistry,Faculty of physics & chemistry,Alzahra University,Vanak,Tehran,Iran
Tel: +982188044051-9(2602) Fax: +982188041344
Email:ghiasi@alzahra.ac.ir
Azarlarijani7@gmail.com

Abstract: The theory of density function, a theory in the framework of quantum mechanics to study the electron structure with basic set B3LYP/6311++G** computation has been used to optimized the structures of thiocyanate and isothiocyanate and complex between these inhibitors with active site of α-CA enzyme. The anions of thiocyanate and isothiocyanate is coordinate to the zinc as five ligand in intermediate complex.Acoording to calculated results thiocyanate and isothiocyanate with more negative thermpdynamic functions are more effective than the others drugs to control some dieses like of cancer. PCM method used for solvent effects in all calclutions.

Keywords: Anionic inhibitor, Anti-cancer, Carbonic anhydrase, DFT.

I.   INTRODUCTION

A family of ubiquitous zinc metalloenzymes known as carbonic anhydrase (CAs) is catalyzed the hydration of carbon dioxide (CO_2) to bicarbonate ion and proton, a simple but essential reaction. Eq. 1, [1-3].

$$CO_2 + H_2O \longrightarrow HCO_3^- + H^+ \qquad (1)$$

This enzyme (CA) peresnt in prokaryotes and eukaryotes

And encoded to five classes: α-CAs, β-CAs, γ-CAs, δ-CAs and ζ-CAs [4,5]. In higher vertebrates, including humans, 14 α-CA isozymes have been described with very different tissue Distributions[6,7].The zinc metal ion (Zn^{2+}) in all α-CAs has essential role for catalysis [8-10].According to X-ray crystallographic data, the metal ion is situated at the bottom of a deep active center cleft, being coordinated by three histidine residues (His94, His96 and His119) and a water molecule or hydroxide ion [11-15] (Fig1).
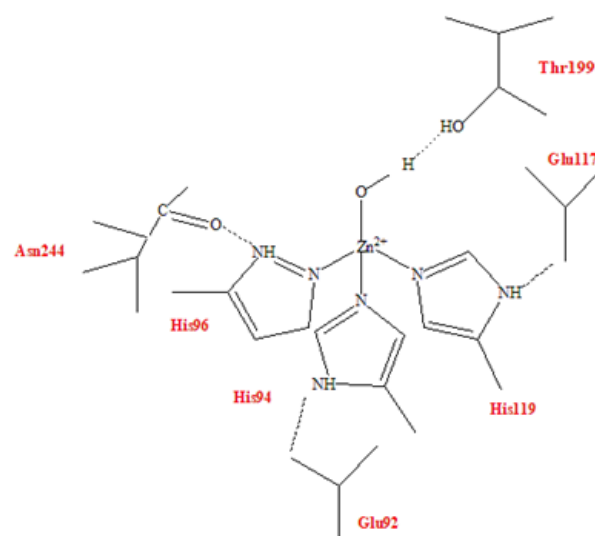

Fig.1: Crystallographic structure of isomer II α-CA

II.   METHODS

All calculations were performed at the level of relativistic density functional theory (DFT) using the B3LYP/6-311++G** method. Ab initio calculations were carried out with the Gaussian program series 2003[17]. The harmonic vibrational frequencies, spin density and partial charges in the present of the water solvent have been done by using PCM model.

III.   RESULTS AND DISCUSSION

Thiocyanate and isothiocyanate, like many inhibitors, replace the water molecule. Figure 2 shows a demonstration of this type of carbon dioxide deterioration by thiocyanate(a) and isothiocyanate(b). It is probale that an equilibrium exist

between the trigonal bipyramial and the tetrahedral species of the metal ion from the active site of the enzyme.
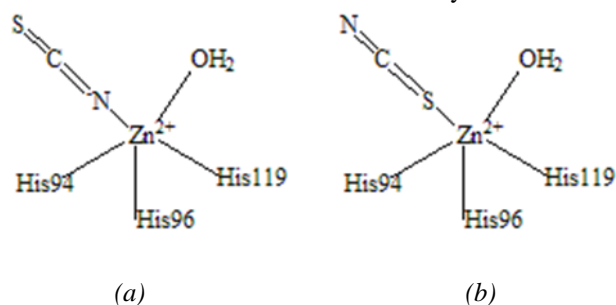

(a) *(b)*

Fig.2: Anionic inhibitor Thiocyanate(a) and Isothiocyanate(b) added metallic metal and the geometric shape of the tetrahedral and trigonal bipyramidal.

According to thermodynamic equation, $\Delta G = \Delta H - T\Delta S$, the $\Delta G^\circ r$ was calculated. Table1.

Table1: Calculation of thermodynamic functions:

Anion Inh	$\Delta E(Sol)$ Kcal/mol	ΔH°	ΔG°	ΔS
SCN	-281.49 (-336.12)	-269.29	-269.80	0.0017
NCS	-213.35 (-343.65)	-201.23	-202.90	0.0053

IV. CONCLUSION

In this paper, the structure of carbonic anhydrase active center was fully optimized at B3LYP method using 6-311G** basis set with no initial symmetry restrictions and assuming C_1 point group. Since, in the presence of the inhibitor, an enzyme-inhibitor complex forms, So, different complexes between active site of CA enzyme and anionic inhibitor were fully optimized at B3LYP level by using 6-311G** basis set with no initial symmetry restrictions.

As the results indicate, substitution of anionic form of inhibitors in place of water molecule at the active center of CA enzyme is energetically exothermic, $\Delta E_{reaction} = -281.49$ kcal/mol by thiocyanate inhibition rather than that of isothiocyanate $\Delta E_{reaction} = -213.35$ kcal/mol.

In conclusion anionic inhibitors as a new class of inhibitors is good candidates for the development of novel anticancer drugs with few side effect.

REFERENCES

[1] Bertini I, Luchinat C. Acc Chem Res. 16(8):272–9. **1983**.

[2] DN. Silverman. Can J Bot. 69(5):1070–8,**2007**.

[3] DW. Christianson,CA. Fierke. Acc Chem Res.;29(7):331–9,**1996.**

[4] C. Capasso, CT. Supuran. J Enzyme Inhib Med Chem. 29(3):379–87,**2014**.

[5] S. Akin, H. Ayaloglu, E. Gultekin, A. Colak, O. Bekircan, Bioorg Chem. 83;170–9,**2019**.

[6] SJ. Dodgson, RE. Forster. J Appl Physiol. 60(2):646–52.**2017**.

[7] D. Hewett-Emmett.29–76,**2012**.

[8] WS. Sly. (1982):95–104,**2012.**

[9] Purkerson JM, Schwartz GJ.Kidney Int. 71(2):103–15,**2007**.

[10] S. Parkkila, C. Supuran, A. Innocenti,S. Monti,G. Simone, M.Hilvo . Curr Pharm Des .;14(7):672–8,**2008**.

[11] A. Bottoni,CZ. Lanza, G. Miscione Pietro, D. Spinelli. J Am Chem Soc. 2004;126(5):1542–50, **2004**.

[12] JY. Liang , Biochemistry;26(17):5293–301,**1987**.

[13] S. Lindskog . J Mol Catal.;23(2–3):357–68,**1984**.

[14] S. Lindskog . Pharmacol Ther.74(1):1–20, **1997**.

[15] A. Solá M, Lledós,M. Duran,J. Bertrán. J Am Chem Soc.;114(3):869–77,**1992.**

[16] Bioorganic & Medicinal Chemistry Letters 14 ,3327–3331,**2004**.

[17]. Frisch MJ, Trucks GW, Schlegel HB, Scuseria GE, Robb MA, Cheeseman JR, Zakrzewski VG, Montgomery JA, Stratmann RE, Burant JC, Dapprich S, Millam JM, Daniels AD, Kudin KN, Strain MC, Farkas O, Tomasi J, Barone V, Cossi M, Cammi R, Mennucci B, Pomelli C, Adamo C, Clifford S, Ochterski J, Petersson GA, Ayala PY, Cui Q, Morokuma K, Malick DK, Rabuck AD, Raghavachari K, Foresman JB, cioslowski J, Ortiz JV, Stefanov BB, Liu G, Liashenko A, Piskorz P, Komaromi I, Gomperts R, Martin RL, Fox DJ, Keith T, Al-Laham MA, Peng CY, Nanayakkara A, Ghonzalez CV, Challacombe M, Gill PMW, Johnson BG, Chen W, Wong M, Andres JL, Head-Gordon M, Replogle ES, Pople JA (2003) Gaussian 2003 (Revision-B). Gaussian, Inc., Pittsburgh PA.

Study of mechanism of hydrogen production from formic acid decomposition on Cu(100) catalyst by using dynamic Monte Carlo

M. Rafiee [a], H. Bashiri*[b]

Department of Chemistry, Faculty of Science, Kashan University of Kashan, Kashan, Iran
Email: *marziehrafiee91@yahoo.com / h.bashiri@ymail.com*

Abstract: In this work, we studied hydrogen production from formic acid decomposition on Cu (100) using dynamic Monte Carlo simulation. A square lattice with the size of 2800×2800 cells has been considered. The surface in our model included top, hollow and two bridge sites. The mechanism, kinetic parameters (activation energy and the pre-exponential factor), details of surface reactions of a lattice-gas model have been obtained by simulation. The simulated kinetics data and experimental data (Temperature programmed desorption) have a good agreement and it confirms the obtained mechanism. So Monte Carlo Simulation is a suitable method to study mechanism and kinetic parameters of reactions.

Keywords: Dynamic Monte Carlo simulation, Mechanism, Hydrogen production, Formic acid, Cu (100)

I. INTRODUCTION

The main energy sources in world are fossil fuels but the using of them leads to environmental pollution and global warming. Therefore researchers are trying to find a clean fuel. Hydrogen is a non-polluting fuel and it has the high energy per unit weight (142 kJ/g) [1]. Hydrogen produces from fossil sources and non-fossil sources.

Formic acid (HCOOH) is as an industrial byproduct and it is low toxicity. It is easy to storage and transfer. Formic acid can be as a good source for hydrogen generation because its hydrogen content is 4.4 wt% [2].

Dynamic Monte Carlo simulation is a method to study mechanism and kinetic parameters of chemical reactions [3]. The mechanism is a set of all elementary reactions. In the Monte Carlo simulation adsorption, desorption, diffusion and reactions are possible events. The time evolution of the reaction system describes by the chemical master equation:

$$\frac{dP_\alpha}{dt} = \sum_\beta (\omega_{\alpha\beta} P_\beta - \omega_{\beta\alpha} P_\alpha)$$

Where, P_α and P_β are the probability of finding the system in configuration α and β, respectively. Also $\omega_{\alpha\beta}$ is the transition probability per unit time that specifies the rate process going from configuration α to configuration β for various elementary events such as adsorption, desorption,

diffusion, reaction and etc. The dynamic Monte Carlo method provides a numerical solution to the Master equation.

Dubois and his co-workers [4] have investigated production of hydrogen by formic acid decomposition on Cu (100) surface. They obtained temperature- programmed desorption (TPD) to analyze surface reactions. In this research the mechanism of hydrogen generation from formic acid on Cu (100) is studied using dynamic Monte Carlo simulation.

II. METHODS

To study mechanism and kinetic parameters of formic acid decomposition on Cu (100), we have used the CARLOS code [5]. It is a computer program that allows us to define of an adlayer, active sites, microscopic reactions, and kinetic parameters. The surface of Cu (100) single crystal was considered as a square lattice of 2800×2800 adsorption sites with periodic boundary conditions. In this computer program, the surface of catalyst was modelled as a collection of active sites. It was assumed that the square lattice contains four adsorption sites per unit cell, one top, one hollow and two independent bridge sites. Each site on a lattice, can be possibly occupied by an adsorbate. In our simulation each step consists of gas species participating in the reaction, different surface sites, activation energy and pre-exponential factor.

III. RESULTS AND DISCUSSION

Temperature programmed desorption (TPD finding) is a good technique in surface science to investigate reaction kinetics. Dubois et al obtained TPD of formic acid decomposition on Cu (100). Formic acid adsorbed at 120 K and 666.61×10^{-6} Pa on empty surface of Cu (100). They found that H_2 and CO_2 are products of formic acid decomposition on Cu (100). In this work, we used dynamic Monte Carlo to simulate mechanism of hydrogen production from formic acid decomposition on Cu (100). To find best mechanism of formic acid decomposition on Cu (100) surface, several mechanisms examined. The best fit with experimental data (TPD) confirms the mechanism and kinetic parameters. In our simulation the details of surface reactions were studied. Activation energies and exponential factors of reactions have been obtained.

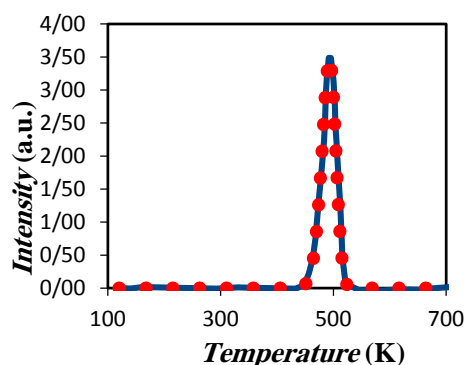Figure 1 shows good agreement between simulated data and TPD of HCOOH decomposition on Cu (100).

Fig.1: The experimental data (solid line) and simulated (dashed line) of temperature programmed desorption spectra of H₂ desorption from Cu (100).

IV. CONCLUSION

In order to investigate mechanism of hydrogen production from formic acid decomposition on Cu (100) we used dynamic Monte Carlo method. Simulation data and experimental data (TPD) were compared to find mechanism and kinetic parameters. The result showed that there is a good agreement between simulation data and experimental TPD spectra. The mechanism and kinetic parameters of elementary reactions have been obtained by using simulation. The details of surface reaction were studied.

REFERENCES

[1] P. Nikolaidis, A. Poullikkas, Renewable and Sustainable Energy Reviews, 67, 597–611, **2017**.
[2]. H. Jeon, Y. Chung, Applied Catalysis B: Environmental, 210, 212-222, **2017**.
[3] T. Bligaard, Journal of Chemical Theory and Computation, 14, 1583-1593, **2018**.
[4] L.H. Dubois, T.H. Ellis, B.R. Zegarski and S.D. Kevan, Surface Science, 172, 385-397, **1986**.
[5] A. Jansen, Physical Review B, 69, 035414, **2004**.

DFT Investigation of Inhibitive Behaviour of Some Phenylurea Derivatives on Steel corrosion

__Hossein Mostaanzadeh__*

Department of Chemistry, University of Qom, Qom, Iran,

E-mail: h.mostaan@qom.ac.ir

Abstract: The use of some phenylurea derivatives as steel corrosion inhibitor was investigated. The correlation between inhibitive effect and molecular structures was studied. Some parameters, such as E_{HOMO}, E_{LUMO}, gap energy (ΔE), electronegativity (χ), global hardness (η) and the fraction of electrons transferred from the inhibitor molecule to the metallic atom (ΔN) were calculated.

Keywords: steel corrosion, inhibitor, phenylurea, density functional theory.

I. INTRODUCTION

Some acidic solutions are used for chemical or electrochemical etching and pickling of several metals. So, corrosion inhibition of metals in acidic media is very important [1,2]. One of the most practical methods for protecting metals against the corrosion is using of organic molecules having functional groups and non-bonding p electrons in their structures as corrosion inhibitors and these methods are suitable progressively general. The inorganic compounds such as chromate, dichromate and nitrate also are used as inhibitors [3]. The toxicity of these compounds, especially organic phosphate and chromate, are recognized about their environmental harmful characteristics [4, 5]. So the use of non-toxic type of novel corrosion inhibitors which do not contain heavy metals is very necessary and important [6]. In this work we study the inhibitive action of some phenylurea derivatives on corrosion behaviour of metals. To clarify which compound has a higher inhibition efficiency on steel, we calculated the proportion of electrons transferred (ΔN), the energy gap ($\Delta E = E_{LUMO} - E_{HOMO}$), global hardness ($\eta$) and electronegativity (χ) of all compounds.

II. COMPUTATIONAL METHODS

Using computational chemistry has important role for screening new corrosion inhibitors [7]. For density functional theory (DFT) calculations the software package; Gaussian 03 is used [8] along with the basis set 6–311++G(d,p). For aqueous phase calculation, the conductor polarized continuum model (CPCM) is one of the most

popular approaches [9]. Some electronic properties of compounds such as the energies of highest occupied molecular orbital (HOMO) and lowest unoccupied molecular orbital (LUMO) have been calculated. By using Gauss View 03 the molecular structures of all compounds were drawn [10]. For determining the atomic charges, the natural bond orbital (NBO) analysis was applied [11, 12].

III. RESULTS AND DISCUSSION

Five constituents of phenylurea were selected and for each constituent, quantum chemical calculations were performed (Fig. 1).
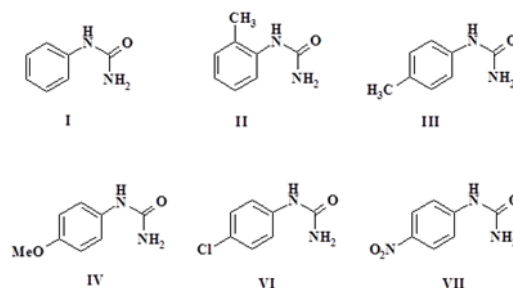

Fig. 1. Chemical structure of all components

The optimized molecular structures and the frontier molecule orbital density distribution (HOMO and LUMO) of six compounds are shown in Fig. 2.
The adsorption of these compounds on the metal surface reduces the surface area available for corrosion. E_{HOMO}, E_{LUMO}, the energy gap ($\Delta E = E_{LUMO} - E_{HOMO}$), and the dipole moment are presented in Table 1. In the most of compounds, LUMO orbitals are localized over the benzene rings. However, as comparison of inhibition efficiency of six components was aim of this study, it seems that quantum chemical calculations can be used to explain the difference in behavior of these constituents. The electronegativity (χ), global hardness (η) and proportion of electrons transferred (ΔN) of compounds are summarized in table 2.
The electronegativity, χ, is the negative of chemical potential and hence given by: $\chi = -\mu \approx -1/2(E_{HOMO} + E_{LUMO})$ The chemical hardness, η is approximated by: $\eta \approx 1/2(E_{HOMO} -$

E_{LUMO}). The number of electrons transferred from the molecule to metal (ΔN), will be given by below equation:

$$\Delta N = (\chi_{Fe} - \chi_{inh})/2(\eta_{Fe} + \eta_{inh})$$

according to the HSAB concept Fe atom is considered as a Lewis acid [13].

	structure	HOMO	LUMO
I			
II			
III			
IV			
V			
VI			

Fig. 2. optimization geometry of six constituents of phenylurea with HOMO and LUMO density.

Table1. HOMO and LUMO Orbital energies, HOMO-LUMO gap energy (ΔE) and electric dipole moments (μ) of Compounds in the gaseous (G) and aqueous (A) phases[*].

	phase	E_{HOMO} (ev)	E_{LUMO} (ev)	ΔE (ev)	μ (D)
I	G	-6.539	-0.909	5.630	3.985
	A	-6.569	-0.807	5.762	5.427
II	G	-6.465	-0.807	5.658	3.920
	A	-6.560	-0.774	5.786	5.417
III	G	-6.358	-0.868	5.490	4.561
	A	-6.410	-0.759	5.651	6.206
IV	G	-6.186	-0.924	5.262	5.316
	A	-6.227	-0.836	5.391	6.962
V	G	-6.607	-1.248	5.359	2.207
	A	-6.554	-1.048	5.506	3.056
VI	G	-7.210	-2.962	4.248	2.991
	A	-6.934	-3.050	3.884	4.152

[*]All quantum chemical parameters calculated at DFT level using the 6-311++G(d,p) basis set.

.

The sum of the hardness parameters act as a resistance and the electronegativity difference between two atoms drives the electron transfer. In order to estimate ΔN, a theoretical value $\chi_{Fe} \approx 7.0$ eV for the electronegativity of bulk Iron and the global hardness of $\eta_{Fe} \approx 0.0$ were used. In metallic bulk the ionization energy (I) and the electron affinity(A) are equal because they are softer than the neutral metallic atoms [14].
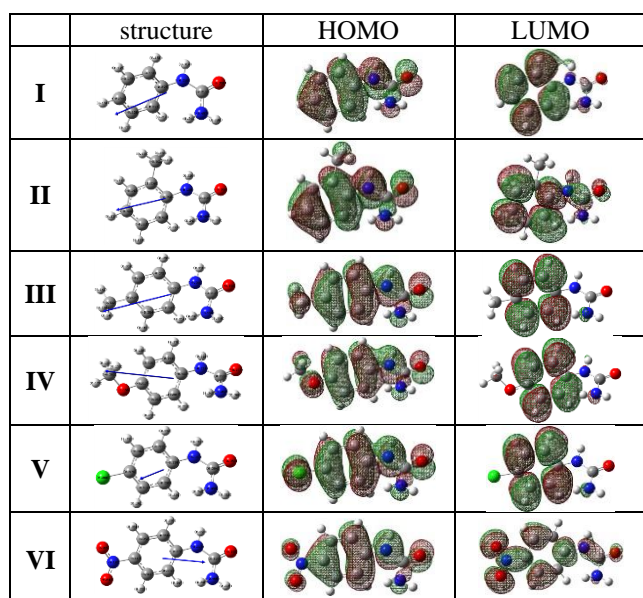
Table 2. Electronegativity (χ), global hardness (η) and proportion of electrons transferred (ΔN) of compounds.

Comp.	phase	χ	η	ΔN
I	G	3.724	2.815	0.582
	A	3.688	2.881	0.575
II	G	3.636	2.829	0.595
	A	3.667	2.893	0.576
III	G	3.613	2.745	0.617
	A	3.584	2.825	0.605
IV	G	3.555	2.631	0.655
	A	3.531	2.695	0.644
V	G	3.927	2.679	0.574
	A	3.801	2.753	0.581
VI	G	5.086	2.124	0.451
	A	4.992	1.942	0.517

Between all compounds, the fraction of electrons transferred ΔN, will be highest for **IV**. Therfore we think that inhibition efficiency of **IV** is better than other compounds, Moreover **IV** has less Electronegativity (χ). On the other hand the lowest value of ΔN is shown for **VI** that contain p-NO$_2$ group. The schematic adsorption behavior of compounds on steel surface is represented in Fig. 3.
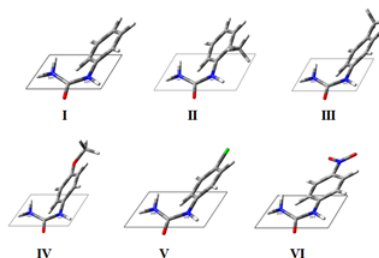

Fig 3. The schematic representation of the adsorption behaviour of compounds on steel surface.

The HOMO orbitals of inhibitor are the sites at which nucleophilic attack take place and represent the active centers, with the maximum ability to bond to the metal surface. According to dipole moment direction, negative local charge and density of HOMO orbitals, it should be expected that the interaction of π molecular orbitals of carbonyl group and lone pair electron of nitrogen atoms in

compounds with p-orbitals of Fe atoms increases adsorption of contituents on the surface of steel . As can be seen from Fig. 3, thus perpendicular orientation of phenyl rings on the metal surface are possible. It seems that the high negative charge of carbonyl and nitrogen (see table 3) also help to increase the inhibition efficiency of compound IV related to the other compounds.

Table 3. Natural Charges (e) for atoms.

I	Natural	II	Natural	III	Natural
12N	-0.66	10N	-0.66	11N	-0.65
15O	-0.66	13O	-0.66	14O	-0.65
16N	-0.84	14N	-0.84	15N	-0.84
IV	Natural	V	Natural	VI	Natural
11N	-0.66	11N	-0.65	11N	-0.63
14O	-0.66	14O	-0.65	14O	-0.63
15N	-0.84	15N	-0.84	15N	-0.83

IV. CONCLUSION

The results of quantum calculations of six phenylurea derivatives revealed that compounds IV because of higher fraction of electron transfer (ΔN) have higher inhibition corrosion in phenylurea substituents.

REFERENCES

[1] H. Ashassi-Sorkhabi, B. Shabani, B. Aligholipour, D. Seifzadeh, Appl. Surf. Sci. 252 (2006) 4039.

[2] M. Abdallah, Corros. Sci. 46 (2004) 1981.

[3] M.G. Fontana, Corrosion Engineering, 3th edition, McGraw-Hill, Singapore, 1986.

[4] J. Sinko, Prog Org Coat. 42 (2001) 267.

[5] S.E. Manahan, Environmental Chemistry. 6th edition,Lewis, Boca Raton, 1996.

[6] E.E. Oguzie, Corros Sci, 50 (2008) 2993.

[7] A. Kokalj, Electrochim. Acta 56 (2010) 745.

[8] M.J. Frisch, et al, Gaussian 03, Revision C.02, Gaussian, Inc.,Wallingford CT (2004).

[9] V. Barone, M. Cossi, J. Phys. Chem. A, 102 (1998), 1995.

[10] Gauss View, Version 3.0, Gaussian Inc., Pittsburgh, PA, 2003.

[11] A.E. Reed, F. Weinhold, Chem. Rev. 88 (1998) 899–926.

[12] H.B. Schelegel, Ab Initio Methods in Quantum Chemistry, John Wiley, New York, 1987. pp. 249–286.

[13] K.F. Khaled, M.A. Amin, Corros. Sci., 51 (2009) 1964.

[14] K. Babic-Samardzija, C. Lupu, N. Hackerman, A.R. Barron, J. Mater. Chem. 15 (2005) 1908.

Molecular Dynamics Simulations of amino acid ionic liquids

Sahar Shokri^a, Rahmat Sadeghi^b*

^a*Department of Chemistry, University of Kurdistan, Sanandaj, Iran, Email:* sahar.shokri.ch@gmail.com
^b*Department of Chemistry, University of Kurdistan, Sanandaj, Iran, Email* rsadeghi@uok.ac.ir

Abstract: We have carried out the molecular dynamics (MD) simulation to support the experimental results and to describe the microstructure and dynamic properties of the synthesized amino acid ionic liquids (AAILS). MD simulation has been used in order to calculate densities (d) radial distribution function (RDFs), combined distribution functions (CDFs), spatial distribution functions (SDFs), mean-square displacements (MSD), and self-diffusion coefficient (D_i). The density of simulation data is in good agreement with experimental data.

Keywords: Amino acid ionic liquids, Molecular dynamics simulation, Radial distribution functions, Spatial distribution functions, Combined distribution functions.

I. INTRODUCTION

Ionic liquids (ILs) have novel characteristics such as media in the field of catalysts, biomass processing, metal extraction, and organic synthesis since they are a matter of attention in recent years. The properties of the Ionic liquids can be tuned by a combination of different cations and anions as well as by incorporating the functional groups into the structure of the ion [1]. Knowing the structure and microscopic characteristics of ionic liquids are helpful for creating new ionic liquids for different applications. MD simulation is a suitable computational method to investigate the properties of molecular systems. These findings helped to explain the behavior of ILs [2].

II. METHODS

To study the dynamical behavior of AAILs, [C10mim]Gly, [C10mim]Ala and [C10mim]Val were formed. We carried out MD simulation utilizing the large-scale atomic/molecular massively parallel simulator (LAMMPS) package[3]. The simulation models consisted of 200 pairs of cations and anions with periodic boundary condition in all directions. To validate the computational simulation, a comparison of computational models with experimental results was done at different temperatures. The MD simulations based on the AMBER force field was used [4]. The electrostatic long-range interactions were computed using the particle-particle particle-mesh method. The minimum-energy geometry of the

isolated ions was calculated by using ab initio geometry optimizations at B3LYP/6-311++G** level of theory using the Gaussian 03 program [5]. The atomic partial charges were obtained by using the restrained electrostatic potential (RESP) method at the B3LYP/6-311++G** level of theory [6]. To do these simulations, firstly, the initial boxes configurations were prepared randomly and the energy minimizations of the structures were performed using the conjugate gradient algorithm. Secondly, the systems were allowed to equilibrate for a time period of 2 ns at 1 atm under isothermal-isobaric (NPT) ensemble. At last, NVT ensemble simulations were obtained from the final configuration of NPT simulation for 22 ns.

III. RESULTS AND DISCUSSION

A. To better understanding of the interaction structure of the existing species, we have obtained the Partial Radial Distribution Function (PRDFs) of oxygen and nitrogen atoms of the anion, and hydrogen atoms of the cation. The labels of the atoms in the cation and anions and calculated PRDFs are shown in Figures 1 (a and b). The strong peaks at 2 Å indicate the powerful interactions between H1 of the cation and oxygen and nitrogen atoms of the anions. The second peaks which exist in longer distances have low intensities. It is remarkable that the Coulombic interactions are long-range interactions and can be effective at a long distance. The coverage influence of the internal shells as well as increasing the radial distance reduces the peak intensity.

B. Figure 1c presents the various view sides of three-dimensional spatial distribution functions of the anions around the cation. These measurements are in agreement with the received RDFs.

Combined Distribution Function (CDF) were measured. The CDFs made of the RDF and the Angular Distribution Function (ADF). Figure 4 shows that there are the powerful H-bonds between the anion and cation and furthermore three peaks between H1 and O atoms, and two separate peaks between H1 and N atoms in the combined distribution function can also be seen
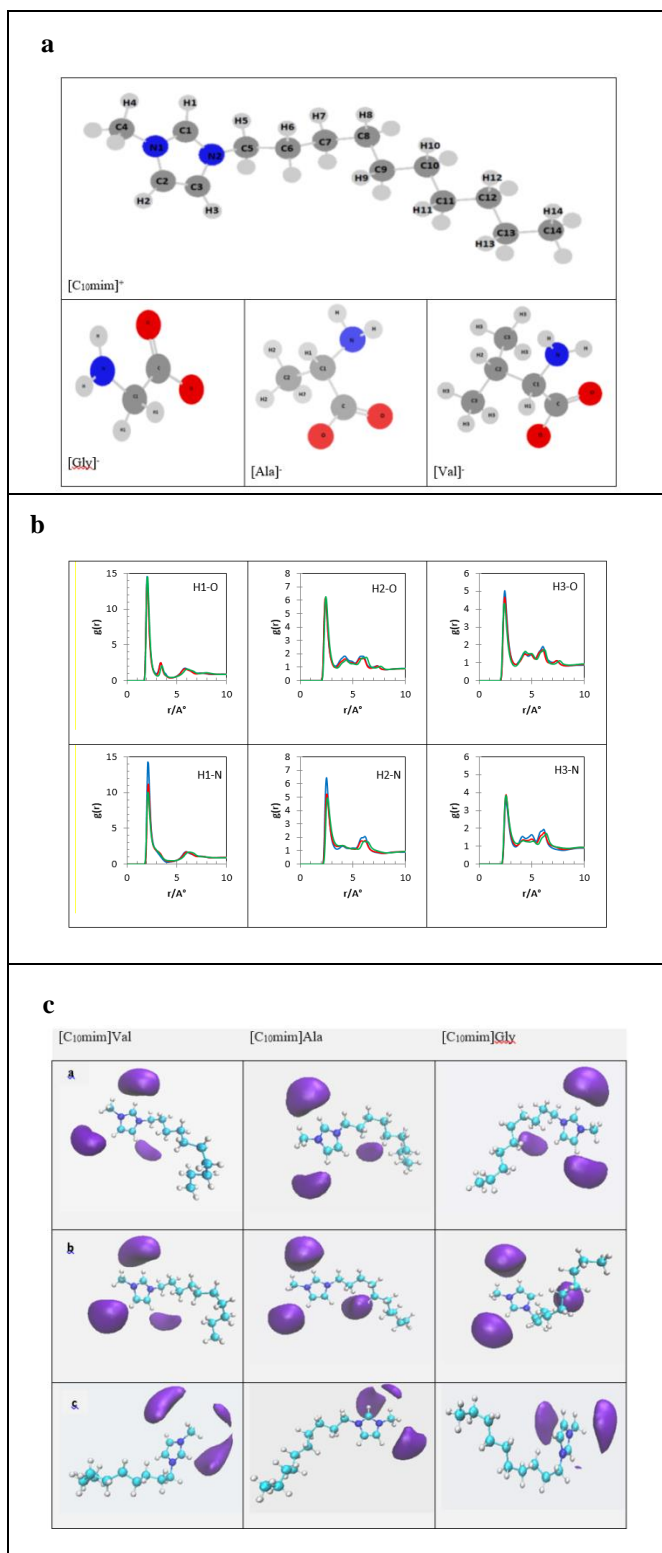
Fig.1 (a) The labels for the atoms in the cation and anions.
(b) Partial Radial Distribution Functions (PRDFs) of oxygen and nitrogen atoms of the anions and hydrogen atoms of the cation. The color codes are as follows: gly (green), ala (red) and val (blue).
(c) Spatial distribution functions of the anions around the selected hydrogen of the cation, H1 (a), H2 (b) and H4.

IV. CONCLUSION

In this work, molecular dynamics simulation was taken out to study molecular structure and intermolecular interactions. The SDFs and RDFs were calculated from MD simulations. The results showed that the anions are strongly associated around the H1 in the imidazolium ring, and the aggregates between the cations formed through alkyl tails. From the RDF results, anions firmly interact with the cation imidazolium ring. The CDFs were employed to demonstrate the strength of hydrogen bonding. The results indicated strong hydrogen bonds between nitrogen and oxygen of anions and the cation. The calculations of Transference numbers have shown that the anion mobility is further than the cation, and in comparing between of the anions, we also were observed that the valinate mobility was less than the other anions.

REFERENCES

[1] Armand, Michel, Frank Endres, Douglas R. MacFarlane, Hiroyuki Ohno, and Bruno Scrosati.In Materials For Sustainable Energy: A Collection of Peer-Reviewed Research and Review Articles from Nature Publishing Group, pp. 129-137. **2011**

[2] Köddermann, Thorsten, Dietmar Paschek, and Ralf Ludwig. ChemPhysChem 8, no. 17, pp. 2464-2470, **2007**.

[3] Plimpton, Steve. Journal of computational physics 117, no. 1, pp. 1-19, **1995**.

[4] Cornell, Wendy D., Piotr Cieplak, Christopher I. Bayly, Ian R. Gould, Kenneth M. Merz, David M. Ferguson, David C. Spellmeyer, Thomas Fox, James W. Caldwell, and Peter A. Kollman. *Journal of the American Chemical Society* 117, no. 19 pp. 5179-5197, **1995**.

[5] Frisch, MJea, G. W. Trucks, HBea Schlegel, GE W. Scuseria, M. A. Robb, J. R. Cheeseman, J. A. Montgomery et al. "Gaussian 03, revision C. 02. **2008**.

[6] Bayly, Christopher I., Piotr Cieplak, Wendy Cornell, and Peter A. Kollman. *The Journal of Physical Chemistry* 97, no. 40, pp. 10269-10280, **1993**.

Substitution effects on philicity of 1,3-diarylphosphole-2-ylidenes based on DFT method

S. Akhondi[a], A. Shiri[a]*
[a] Department of Applied Chemistry, Malayer University, Malayer 65719-95863, Iran
Email:amshiri@gmail.com

Abstract: Substitution effects on reactivity and philicity of 1,3-diarylphosphole-2-ylidenes was assessed using the following calculations: global electrophilicity (ω) and nucleophilicity (*N*) for philicity with the Gaussian 09 package using density functional theory (DFT) at B3LYP/6-311++G** level. Calculations showed that *P*-Heterocyclic carbene with NH_2 group at para position of aryl substituent, had the highest nucleophilicity.

Keywords: P-Heterocyclic carbenes, Electrophilic substitutions, Philicity, Density functional theory

I. INTRODUCTION

Carbenes are divalent and neutral species with six electron carbon atoms having two unshared electrons. Classical carbenes are inherently unstable and considered as highly reactive transient intermediates in chemical processes [1]. It is guessed that carbene carbon to be an electrophilic species due to having six electrons, but many papers, have shown that the reactivity of these compounds being strongly dependent on substitutions attached to them. For example $(CH_3O)_2C$: and $(Me_2N)_2C$: are both nucleoplilic in character [2,3]. 2p-2p π bonding of "vacant" carbenic p orbital of these carbenes with electron pairs of the adjacent Me_2N and CH_3O groups is reason of this property.

N-heterocyclic carbenes (NHC) are one group of carbenes, the representative botteled and stable species of which is 1,3-di(adamentyl)imidazol-2-ylidene (Ida), first reported by Ardengue et al.; both steric and electronic effects are said to be the reasons of their stability [4]. These species then much were taken into consideration from researchers [5-6]. In addition, various applications were found for them, such as organometallic compounds, medicinal and polymerization uses [7-8]. Su and Chuang predicted that triplet ground state of vinilidenes with NHCs skeleton be stable [9]. Recently, we have predicted substitution effects on philicity and reactivity of 1,3-diimidazol-2-ylidenes using DFT method [10]. *P*-Heterocyclic carbenes (PHC) are phosphorous analogues of NHCs [11]. In this study, we investigated computationally philicity of 1,3-diarylphosphole-2-ylidenes using DFT method (Scheme 1).

Theoretical global electrophilicity scale, ω, defined recently by Parr et al. has been used for obtaining this parameter [12]:

$$\omega = \mu^2/2\eta \qquad (2)$$

Here η is the chemical hardness and μ is the electronic chemical potential.

1a: X=NH_2	
1b: X=OH	
1c: X=OCH_3	
1d: X=CH_3	
1e: X=H	
1f: X=F	
1g: X=Cl	
1h: X=Br	
1i: X=CHO	
1j: X=CN	
1k: X=NO_2	
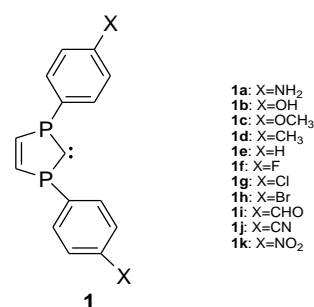
Scheme 1**.** Structure of 1,3-diarylphosphole-2-ylidenes.

II. METHODS

Calculation were optimized with Gaussian 09 program by Density Functional Theory at B3LYP level of theory with 6-311++G** basis set. This method has provided acceptable results to predicting philicity of these species. All the structures of 1,3-diarylphosphole-2-ylidenes were determined to be minima by applying real frequency calculations. Chemical potential μ, η and the additional electronic charge ΔN_{max} were obtained using:

$$\mu = -(IP + EA)/2 \qquad (3)$$

$$\eta = IP\text{-}EA \qquad (4)$$

$$\Delta N_{max} = -\frac{\mu}{\eta} \qquad (5)$$

III. RESULTS AND DISCUSSION

As substituents has an important effect on philicity, it is mainspring for us to investigate such an effect for 1,3-diarylphosphole-2-ylidenes using DFT method.
As seen in Table 1, low σ-withdrawing and high π-electron-releasing effects of X=NH_2 (ω=1.65 eV, entry 1) make this species to be the most nucleophile of these PHCs (**1**).

Carbenes with greater ω values from 3.55 eV for X=CHO to 3.82 eV for X=NO_2 showing the electrophilic character. That is, for X=NO_2 the corresponding carbene is suggested to be the most electrophilic species, displaying the greatest ΔN_{max} and μ values (1.5 eV and -5.10 eV, respectively).

Table 1. Philicity values of 1,3-diarylimidazol-2-ylidene (**1**) obtained based on DFT parameters.

Entry	X	Carbene	η(eV)	N(eV)	ΔN_{max}	μ(eV)	ω(eV)
1	NH_2	1a	3.71	4.11	0.94	-3.50	1.65
2	OH	1b	3.85	3.73	0.99	-3.82	1.90
3	OCH_3	1c	3.81	3.85	1.24	-4.72	2.923
4	CH_3	1d	3.78	3.69	1.01	-3.82	1.93
5	H[*]	1e	3.94	3.33	1.26	-4.96	3.12
6	F	1f	3.89	3.53	1.08	-4.20	2.27
7	Cl	1g	3.83	3.29	1.30	-5.00	3.26
8	Br	1h	3.82	3.29	1.12	-4.27	2.38
9	CHO	1i	3.62	3.01	1.40	-5.07	3.55
10	CN	1j	3.72	2.84	1.29	-4.79	3.08
11	NO_2	1k	3.40	2.67	1.50	-5.10	3.82

IV. CONCLUSION

In this paper, calculation based on DFT, has determined that substituents have dramatic effects on reactivity and philicity of 1,3-disubstituted-diphosphole-2-ylidenes. The highest nocleoplilicity of **1a** and the highest electrophilicity of **1k** may be attributed to positive resonance effect (+R) of NH_2 group and electron withdrawing effect of NO_2 group respectively.

REFERENCES

[1] D. Bourissou, O. Guerret, F. P. Gabba, and G. Bertrand, Chem. Rev., vol. 100, pp. 39-91, **2000.**

[2] R. A. Moss, Acc. Chem. Res., vol. 13, pp.58-64, **1980.**

[3] W. Sander, and E. Kotting,R. Hubert, J. Phys. Org. Chem., vol. 13**,** pp. 561-568, **2000.**

[4] A.J. Arduengo, R. L. Harlow, and M. Kline, J. Am. Chem. Soc., vol. 111**,** pp.361-363, **1991.**

[5] M. N. Hopkinson, C. Richter, M. Schedler, and F. Glorius, Nature, vol. 510, pp. 485-496, **2014.**

[6] F. E. Hahn, and M. C. Jahnke, Angew Chem Int Ed, vol. 47, pp.3122-3172, **2008.**

[7] K. Oisaki, Q. Li, H. Furukawa, A. U. Czaja, and O. M. A. Yaghi, J. Am. Chem. Soc., vol. 132, pp. 9262-9264, **2010.**

[8] A. J. Boydston, K. A. Williams, C. W. Bielawski, J Am. Chem. Soc. vol. 127, pp.12496-12497, **2005**

[9] M-D. Su, Ch-Ch. Chuang, Theor. Chem. Acc. vol, 132, pp. 1360, **2013.**

[10] A. Shiri, A. Khorrammabadi-zad and Z. Siahpur, Monatshefte für Chemie -Chemical Monthly, **2018**.

[11] D. Martin, Baceiredo, A. Gornitzka, H. Schoeller, and W. W. Bertrand, Angew. Chem., vol. 117, pp, 1728-1731, **2005.**

[12] R. G. Parr, L. V. Szentpaly, and S. Liu, J. Am. Chem. Soc., vol. 121, pp, 1922-1924, **1999.**

Development of Optimized Potentials for Liquid Simulation All-Atom (OPLS-AA) Force Field to Sarin Nerve Agent

L. Ebrahimi[a,b,*], A. Khanlarkhani[a], M. R. Vaezi[a] and M. Babri[b]

[a]_Nanotechnology and Advanced Materials Department, Materials and Energy Research Center, Karaj, Postal code: 31787-316, Iran_

[b]_Defense Chemical Research Lab (DCRL), Karaj, Postal code: 31585-1461, Iran_

Email: *chemistry8084@gmail.com

Abstract: In this work, the OPLS all-atom model was developed for sarin (GB). Intramolecular bonding parameters and Lennard–Jones nonbonding parameters were taken from the OPLS all-atom force field databases. Partial charges were determined by ab initio calculations at HF/6-31g(d) level. Average errors in comparison with experimental data are less than 2% and 6% for densities and heat of vaporization, respectively. The comparison of intramolecular bonding parameters obtained from molecular dynamics (MD) simulation and quantum mechanical (QM) calculations showed that these results are well consistent with each other. The results indicated that OPLS-AA force field can be used as an accurate and reliable model in molecular simulation studies of sarin.

Keywords: force field, sarin, density, heat of evaporation, molecular dynamics simulation

I. INTRODUCTION

Molecular dynamics simulation is one of the useful tools for studying compounds at the atomic scale, and as long as there is an appropriate field of field, useful information could be extracted based on the roles of intramolecular and intermolecular interactions. In fact, in molecular dynamics simulations, the most important step is finding a suitable potential or force field which has the great importance in accuracy of calculations [1-2]. Most force fields have a similar form including harmonic bond stretching and angle bending, Fourier series for torsional energetics, and Coulomb plus Lennard-Jones terms for intermolecular and intramolecular non-bonded interactions [3].

The objective of this study is to find a suitable force field for sarin (Fig. 1) to investigate the absorption mechanism of this compound on graphene using a molecular dynamics simulation. Sarin is one of the most dangerous chemical warfare agent, belongs to the group of organophosphate nerve agents. Because of the high toxicity of these compounds, molecular simulation is well suited to direct study of them.
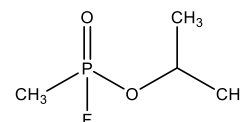

Fig. 1: The structure of sarin.

In this study, the all-atom force field developed which is based on OPLS all-atom [3,4] suggested by Jorgensen et al. It is expressed as the function form which is shown in "Eq. 1" where the potential energy function of the form governs bond stretch, bond angle, dihedral torsion, Lennard-Jones potential and Coulomb interaction. In all-atom model, the force field is applied to each of the atoms instead of a group of them. According to the authors' information, no report has been found that investigated the OPLS all-atom for sarin. In this study, molecular dynamics simulations have been done in liquid and gas phases and the results were compared with experimental data and also quantum mechanical calculations.

$$V(r^N) = \sum_{bonds} \frac{1}{2} k_b (r - r_0)^2 + \sum_{angles} \frac{1}{2} k_\theta (\theta - \theta_0)^2 +$$
$$\sum_{tortions} \{ \frac{V_1}{2} [1 + cos(\emptyset)] + \frac{V_2}{2} [1 - cos(2\emptyset)] + \frac{V_3}{2} [1 + cos(3\emptyset)] + \frac{V_4}{2} [1 - cos(4\emptyset)] \} +$$
$$\sum_{i=1}^{N-1} \sum_{j=i+1}^{N} \{ 4\varepsilon_{ij} [(\frac{\sigma_{ij}}{r_{ij}})^{12} - (\frac{\sigma_{ij}}{r_{ij}})^6] + \frac{q_i q_j e^2}{r_{ij}} \} f_{ij} \quad (1)$$

$$f_{ij} = 0.5 \ if \ i,j \ are \ 1,4; \ otherwise, f_{ij} = 1.0$$

II. METHODS

For simulation of sarin in liquid phase, 250 GB molecules were distributed in a cubic box with a side length of 37 Å. To eliminate surface effects, periodic boundary conditions applied in all directions. Electrostatic interactions were calculated using particle-mesh Ewald method [5-6], whereas non-bonded van der Waals interactions were modeled by a Lennard–Jones potential with a cut-off distance 12 Å. The simulation was first equilibrated for 0.5 ns using Langevin dynamics under canonical (*NVT*) ensemble at 298 K and 293 K. Energy minimization was performed to avoid steric clashes for initial structure. Then, sampling was done in isothermal-

isobaric *(NPT)* ensemble at 298 K and 293 K at pressure of 101.3 KPa for 1.5 ns using Langevin barostat. For simulation of sarin in gas phase, one GB molecule was placed in the center of a very large cubic cell. The system was initially equilibrated for 0.1 ns followed by a 0.5 ns production run. A time step of 1 fs was used to integrate the equation of motion. All MD simulations were carried out by NAMD package [7].

All bonding and non-bonded parameters are derived from available OPLS database [8-9]. Quantum mechanics calculations were used to obtain partial charges of each atom as well as intra-molecular parameters. Optimized geometry was obtained from ab initio calculations at the HF/6-31g (d) level. Partial charges were generated by performing a CHELPG analysis from ab initio calculations at the HF/6-31g (d) level. QM calculations were done using Gaussian 09 [10]. LJ parameters and partial charges are listed in Table 1.

Table1: Parameters for non-bonded interactions of sarin.

GB	ε (kCal/mol)[a]	σ (Å)[a]	q (e)[b]
C	0.066	3.500	-0.402*,0.452**,-0.271***
H	0.030	2.500	0.116•, -0.02••, 0.068•••
P	0.200	3.740	0.963
OP	0.210	2.960	-0.538
OT	0.140	2.900	-0.441
F	0.060	2.900	-0.228

a: data were taken from OPLS-AA force field [8, 9]
b: data were calculated from QM
∗ site adjacent to phosphorus, ∗∗ site adjacent to oxygen,
∗∗∗ site adjacent to carbon
• site adjacent to (C)-P, •• site adjacent to (C)-O, ••• site adjacent to C-(C)
OP: site adjacent to phosphorus, OT: site adjacent to phosphorus and carbon

III. RESULTS AND DISCUSSION

At first, the structural parameters such as bond lengths and bond angles of one GB molecule in the gas phase which was exported from MD simulation, were compared with the QM structural optimization results. The data are shown in Tables 2 and 3. As can be observed from these findings, the results are well consistent with each other, and also the results of bond lengths are well consistent with experimental data.

Table 2: The comparison of bond lengths of sarin obtained from MD and QM studies with experimental data.

GB	C-H	C-P	P-OP	P-F	P-OT	OT-C	C-C
r (Å) (MD)	1.08	1.86	1.47	1.53	1.63	1.40	1.51
r (Å) (QM)	1.08	1.79	1.45	1.56	1.57	1.45	1.52
r (Å) Experimental[a]	1.09	1.84	1.50	1.54	1.63	1.43	1.54

OP: site adjacent to phosphorus, OT: site adjacent to phosphorus and carbon
a: the data were taken from ref [11]

Table 3: The comparison of bond angles of sarin obtained from MD and QM studies.

GB	H-C-H	H-C-P	C-P-OP	C-P-F	C-P-OT	OP-P-F	OP-P-OT
θ (°) MD	108.6	107.4	121.3	105.7	99.4	106.9	114.4
θ (°) QM	108.7	109.8	117.8	102.0	103.9	112.2	116.3

GB	F-P-OT	P-OT-C	OT-C-H	OT-C-C	H-C-C	C-C-C	C-C-H
θ (°) MD	108.3	125.4	112.1	108.1	111.3	112.6	108.0
θ (°) QM	102.7	123.7	107.4	107.7	110.5	113.3	110.2

OP: site adjacent to phosphorus, OT: site adjacent to phosphorus and carbon

For calculating the theoretical densities of sarin at K 298 and K 293, the average volume of this compound was extracted from pure liquid MD simulation, using VMD software. Then, using the equation ρ = m/v, the density of sarin was calculated and compared with the experimental values [11] (Table 4). The results show that the OPLS model predicts the density of sarin with an error of 0.78% and 1.51% at 298 K and 293 K, respectively, compared to the experimental data.

Table 4: Liquid densities predicted for sarin compared to experimental data.

compound	ρ (g/ml³) Theoretical @ 298 K	ρ (g/ml³) Experimental @ 298 K	ρ (g/ml³) Theoretical @ 293 K	ρ (g/ml³) Experimental @ 293 K
GB	1.0802[a]	1.0887[b]	1.0854[a]	1.1020[b]

a: predicted from OPLS force field, b from ref [12]

The heat of evaporation, *ΔHvap*, was calculated by "Eq. 2".

$$\Delta H_{vap}(T) = E_{gas}^{potential}(T) - E_{liquid}^{potential}(T) + RT \quad (2)$$

In this equation, $E_{gas}^{potential}$ and $E_{liquid}^{potential}$ are the potential energies in the gas and liquid phases, respectively. Both of the potential energy terms are obtained through molecular simulations. R is gas constant and T is required temperature. The comparison of the theoretical result with experimental data is shown in Table 5. The results indicated that the OPLS model could predict the heat of evaporation of sarin with an error of 5.84% at 298 K.

Table 5: Heat of evaporation predicted for sarin compared to experimental data.

compound	Heat of Evaporation (kCal/mol) Theoretical @ 298 K	Heat of Evaporation (kCal/mol) Experimental @ 298 K
GB	12.277[a]	11.600[b]

a: predicted from OPLS force field, b from ref [13]

IV. CONCLUSION

The findings of this study indicated that the OPLS-AA could be a suitable model for future MD simulation of sarin. The results showed that the OPLS model predicts the physical properties of sarin like density and heat of evaporation with the average error of less than 2% and 6% compared to experimental data. The investigation of intramolecular parameters such as bond lengths and bond angles also demonstrate that there is a well-consistency between the results of molecular dynamics simulation and quantum mechanical calculations.

REFERENCES

[1] N. Sokkalingam, G. Kamath, M. Coscione, and J. J. Potoff, The Journal of Physical Chemistry B, 113, 10292–10297, **2009**.

[2] S. Chen, S. Yi, W. Gao, C. Zuo, and Z. Hu, Journal of Computational Chemistry, 36, 6, 376-384, **2015.**

[3] W. L. Jorgensen, D. S. Maxwell, J. Tirado-Rives, Journal of the American Chemical Society, 118, 11225-11236, **1996**.

[4] W. L. Jorgensen, J. Tirado-Rives, Journal of the American Chemical Society, 110, 1657-1666, **1988**.

[5] T. Darden, D. York, L. Pedersen, The Journal of chemical physics, 98, 10089-10092, **1993**.

[6] U. Essmann, L. Perera, M. L. Berkowitz, L. G. Pedersen, The Journal of chemical physics, 103, 8577-8593, **1995**.

[7] J. C. Phillips, R. Braun, W. Wang, C. Chipot, K. Schulten, Journal of computational chemistry, 26, 1781-1802, **2005**.

[8] L. S. Dodda, I. Cabeza de Vaca, J. Tirado-Rives, W. L. Jorgensen, Nucleic acids research, 45, W331-W336, **2017**.

[9] L. S. Dodda, J. Z. Vilseck, J. Tirado-Rives, W.L. Jorgensen, The Journal of Physical Chemistry B, 121, 3864-3870, **2017**.

[10] M. J. Frisch, G. Trucks, G. Scuseria, M. Robb, J. Cheeseman, G. Scalmani, V. Barone, B. Mennucci, G. Petersson, Gaussian 09, revision A. 1, Gaussian Inc. Wallingford CT, 27,34, **2009**.

[11] J. E. Huheey, E. A. Keiter, R. L. Keiter, O. K. Medhi, Inorganic chemistry: principles of structure and reactivity, Pearson Education India, **2006**.

[12] R. E. Langford, Introduction to weapons of mass destruction: radiological, chemical, and biological, John Wiley & Sons, **2004**.

[13] U. Army, Potential Military Chemical/Biological Agents and Compounds, released as FM 3-11.9, MCRP 3-37.1 B, NTRP 3-11.32, and AFTTP (I) 3-2.55, January, **2005**.

Investigation of the Structure and Dynamics of Sarin Adsorption on Graphene Surfaces using Molecular Dynamics Simulation

L. Ebrahimi[a,b,*], A. Khanlarkhani[a], M. R. Vaezi[a] and M. Babri[b]

[a]*Nanotechnology and Advanced Materials Department, Materials and Energy Research Center, Karaj, Postal code: 31787-316, Iran*

[b]*Defense Chemical Research Lab (DCRL), Karaj, Postal code: 31585-1461, Iran*

Email: *chemistry8084@gmail.com

Abstract: In this work, the structural and dynamical properties of adsorption of sarin (GB) on graphene (GRA) surfaces as well as examining the effect of the number of graphene layers was studied by molecular dynamics simulation. For this purpose, mass density and orientational distributions and mean-square displacements analyses have been done. Structural analysis showed formation of a solid-like layer of 6 Å thick related to different orientations of GB molecules near all GRA surfaces with a density of about 2.2 times as large as that of the bulk. Mean square displacement (MSD) study demonstrates that the mobility of GB molecules on the surfaces are decreased, and there is no important difference between GRA surfaces.

Keywords: sarin, graphene surfaces, adsorption, molecular dynamics simulation

I. INTRODUCTION

Sarin is a chemical warfare nerve agent which irreversibly blocks the enzyme acetylcholine esterase, responsible for the hydrolysis of the neurotransmitter acetylcholine. The blocking of acetylcholinesterase results in the accumulation of acetylcholine in synapses and neuromuscular junctions lead to a collapse in the central nervous system and finally death [1-2]. The structure of sarin is depicted in Fig. 1.
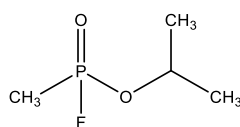
Fig. 1: The structure of sarin.

The aim of this essay is to study the interaction of sarin with intact graphene surfaces from atomistic point of view. The effect of increasing the number of graphene layers up to three layers on adsorption mechanism is also investigated. To achieve this goal, single-layer graphenen (GRA1), bilayer graphenen (GRA2) and three-layer graphene (GRA3) were utilized as the adsorbents. In our pervious study [3], we found that GRA1 could be a suitable adsorbent for sulfur mustard (a blistering agent). So, we extended our investigations to sarin nerve agent. There are also some reports which indicate that graphene is widely used as an adsorbents for different organic and inorganic compounds [4-6].

In this study, structural properties of the adsorption is considered by mass density and orientational distributions of GB molecules in liquid state near GRA surfaces. The dynamic behavior of adsorbed molecules is examined through mean-square displacements of GB molecules near the surfaces and into the bulk (i.e. regions far from GRA surfaces). To date, no research has been found that surveyed the atomic-level insight of adsorption of GB on GRA surfaces. These studies could be useful for making advanced filters and decontamination strategies against these extremely toxic compounds.

II. METHODS

In this work, all-atom OPLS model [7] was used for liquid GB [8-9] and graphene layers [10]. All GRA surfaces with dimensions of 50×40 Å^2 were considered in the middle of separated cubic boxes with their basal planes parallel to *xy*-plane. 630 GB molecules were equally distributed on both sides of each simulation box with periodic boundary conditions applied in all directions. The typical size of the simulation boxes were adjusted to $52.1 \times 43.0 \times 63.2$ Å^3 for GRA1, $52.1 \times 43.0 \times 66.5$ Å^3 for GRA2 and $52.1 \times 43.0 \times 69.9$ Å^3 for GRA3. The simulations were performed under

canonical (*NVT*) ensemble at 298 K using a Langevin dynamics method. The particle-mesh Ewald method [11-12] was applied to calculate electrostatic interactions, whereas non-bonded van der Waals interactions were modeled by a Lennard–Jones potential with a cut-off distance 12 Å. The systems were initially equilibrated for 5 ns with 1000 step energy minimization at first, followed by a 5 ns production run. A time step of 1 fs was used to integrate the equation of motion. All MD simulations were carried out using NAMD package [13].

III. RESULTS AND DISCUSSION

In order to study the structures and adsorption preferences of GB molecules on GRA surfaces, mass density and orientational distributions were used. Fig. 2 compares the mass density distributions along the surface normal *z* axis at 298 K. As can be observed in this figure, a high-density zone or a solid-like layer (adsorption layer) with the atomic thickness of about 6 Å is formed near all surfaces. The mass density of adsorption layer is 2.2 times as large as that of the bulk of GB for all surfaces. Away from the high-density zone ($z > 20$ Å), the effect of the surfaces become insignificant and GB molecules behave as the bulk of liquid GB. The calculated mass density in the bulk region was estimated as 1.09 g/cm^3, which is in good agreement with experimental value [14]. The integration of the area under the adsorption layer also indicates that the number of the adsorbed GB molecules is approximately the same in this zone. The results show that increasing the number of graphene layers up to three layers has no special effect on the structures formed on the GRA surfaces.
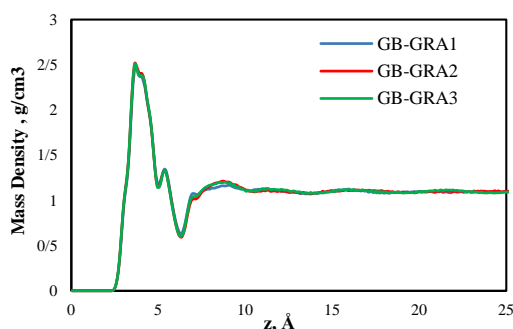
Fig. 2: Mass density distributions along the surface normal *z* axis for GB molecules on GRA surfaces at 298 K.

For exporting the orientational distribution, the orientation angle (α) is defined as the angle between the normal vector (the *z* axis) perpendicular to GRA surface and the vector of dipole moment of GB molecule. Fig. 3 shows the orientational distribution of GB molecules in the adsorption layer near GRA1 surface. Fig. 3 indicated that there are two peaks in this distribution, one peak centered at 51° correspond to $0° < α < 75°$ and the other centered at 131° related to $105° < α < 180°$. There is also a small peak centered at 90° representing parallel orientation of GB molecules. These results showed that GB molecules have different orientations on GRA1 surface. The same results obtained for GRA2 and GRA3, and the data is not shown here.
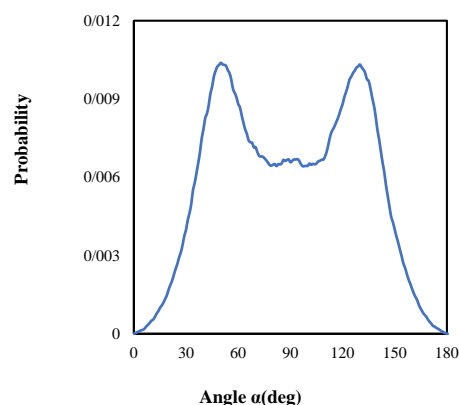

Fig. 3: Orientational distribution of GB molecules in the adsorption layer of GRA1.

To understand the motion of GB molecules toward GRA surfaces, MSD of GB molecules near all surfaces (adsorption layer) and also into the bulk were calculated. Fig. 4 shows the MSD of GB molecules on GRA surfaces. The MSD of bulk GB is given for comparison. The obtained results indicate that MSD of GB molecules near the surfaces is lower than the bulk. It means that there is enough strong interaction between GB and the surfaces, cause restriction on molecular mobility of GB molecules on adsorbents. The comparison of the MSD of GB on GRA surfaces indicate that there is no significant difference between GRA1, GRA2 and GRA3 surfaces. It is also important to note that MSD$_z$ (the data is not shown here) of GB molecules near the surfaces is considerably lower than total MSD which indicates that the adsorption of GB molecules on the surfaces decrease the movement of GB in *z* direction, so there is low tendency of GB molecules in the adsorption layer to leave GRA surfaces and all the surfaces
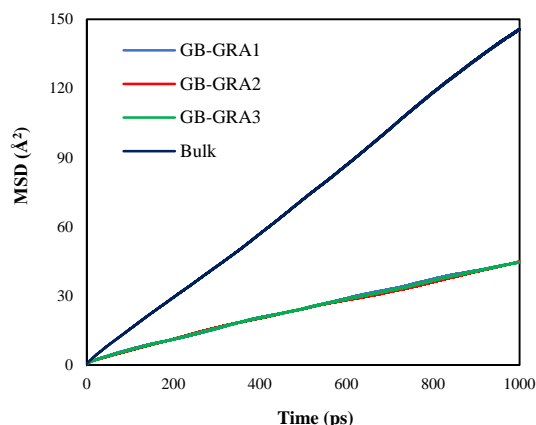
have the same behavior.

Fig. 4: MSD versus time interval for GB molecules on GRA surfaces.

IV. CONCLUSION

This research extends our knowledge about using graphene surfaces as suitable adsorbents for chemical warfare agents. In this article, we focused on the structure and dynamics of sarin adsorption on graphene surfaces based on molecular dynamics simulation. The results showed that a high density zone is formed near GRA surfaces which is related to different orientations of GB molecules. The strong interaction between GB and GRA surfaces caused to decrease the mobility of GB molecules on GRA surfaces. The findings showed that GRA surfaces could be good adsorbents for nerve agents and, also indicated that increasing the number of graphene layers till three layers has no special effect on the adsorption mechanism of GB near GRA surfaces.

REFERENCES

[1] J. E. Chambers, S. F. Oppenheimer, Toxicological Sciences, 77, 185–187, **2004**.

[2] W. P. Schecter, Anesthesiol. Medical Clinics of North America, 22, 579-590, **2004**.

[3] L. Ebrahimi, A. Khanlarkhani, M. R. Vaezi, M. Babri, Computational Materials Science, 152, 355–360, **2018**.

[4] J. G. Yu, Q. Liu, X. H. Chen, X. Y. Jiang, X. Q. Chen, F. P. Jiao, Science of the Total Environment, 502, 70–79, **2015**.

[5] S. Chowdhury, R. Balasubramanian, Advances in Colloid and Interface Science, 204, 35–56, **2014**.

[6] O. Leenaerts, B. Partoens, F. Peeters, Physical Review B, 77, 12, 125416–125421, **2008**.

[7] W. L. Jorgensen, J. Tirado-Rives, Journal of the American Chemical Society, 110, 1657-1666, **1988**.

[8] L. S. Dodda, I. Cabeza de Vaca, J. Tirado-Rives, W. L. Jorgensen, , Nucleic acids research, 45, W331-W336, **2017**.

[9] L. S. Dodda, J. Z. Vilseck, J. Tirado-Rives, W. L. Jorgensen, Journal of Physical Chemistry B, 121, 3864-3870, **2017**.

[10] J. Chen, X. Wang, C. Dai, S. Chen, Y. Tu, Physica E: Low-dimensional Systems and Nanostructures, 62, 59–63, **2014**.

[11] T. Darden, D. York, L. Pedersen, The Journal of chemical physics, 98, 10089-10092, **1993**.

[12] U. Essmann, L. Perera, M. L. Berkowitz, L. G. Pedersen, The Journal of chemical physics, 103, 8577-8593, **1995**.

[13] J. C. Phillips, R. Braun, W. Wang, E. Villa, C. Chipot, R. D. Skeel, K. Schulten, Journal of computational chemistry, 26, 1781-1802, **2005**.

[14] U. Army, Potential Military Chemical/Biological Agents and Compounds, released as FM 3-11.9, MCRP 3-37.1 B, NTRP 3-11.32, and AFTTP (I) 3-2.55, January, **2005**.

Effect of Silver Atom on Bis-GMA Structure: Computational Chemistry Study

M. Dehestani [a]*, S. Pourestarabadi [a,b]
[a] Department of Chemistry, Shahid Bahonar University of Kerman, Kerman, Iran
[b] Young Researchers Society, Shahid Bahonar University of Kerman, Kerman, Iran
Email:

Abstract: In this study, the silver atom has been added to the structure of the Bis-GMA molecule as a monomer used in dental materials, and the effect of this atom on the Bis-GMA electronic properties has been investigated using quantum chemistry calculations through the Fukui function and atoms in molecules (AIM) methods. The results of Fukui functions showed that the presence of silver atoms in the Bis-GMA molecule creates the more reactive sites in reactions, which is related to the position of silver atoms bound to it, and the results of AIM suggest stronger interactions between the Bis-GMA molecules in the presence of silver atoms. Therefore, adding an atom of silver, in addition to generating antibacterial properties in this material, makes the molecule more active and creates stronger interactions at the environment of these molecules.

Keywords: Bis-GMA; Silver; Computational chemistry; Fukui function; Dental material

I. INTRODUCTION

2,2-bis[p-(2'-hydroxy-3'-methacryloxypropoxy) phenyl] propane, that known as Bis-GMA (Fig. 1) is used as dental monomer in dental materials. Rafael Bowen has used this material into composite dental resins [1]. Bis-GMA monomer is widely used in dentistry. Some properties of this monomer are low-molecular weight, less shrinkage, high Young modulus, reduced toxicity due to lower volatility, being not limited working time, having a fast setting time, and having improved color stability [2].

Design of new polymers based on silver coordination can cause new properties such as antibacterial activity. Silver and silver-based compounds are toxic to microorganisms and nowadays known as antimicrobial agent. Currently, silver or silver derivatives are used as biocide agent in antimicrobial ceramics, bone matrices or etc. [3]. In this research, by considering the structure of Bis-GMA and the possibility of adding silver atom to its structure, we have compared the

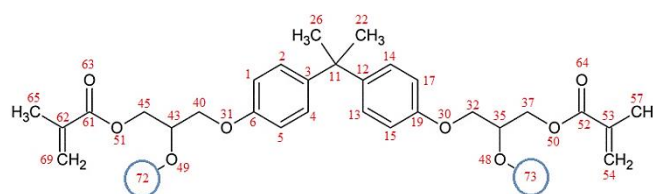properties of the new Bis-GMA and Ag, with the original Bis-GMA monomer.

Fig. 1: Two dimensional molecular structure of Bis-GMA
(Main sites of Bis-GMA were numbered by red color)

II. METHODS

The Bis-GMA structure has two hydrogen atoms bounded to two oxygen atoms (OH groups). Silver ions due to their small size, have the ability to replace these hydrogen atoms (72 and 73 sites in Fig. 1). We here explained the electronic properties and the behavior of the new material with a theoretical review. Here, we examine the silver coordination in the structure of Bis-GMA, and consider the role of this substitution on the properties of Bis-GMA. In this research, the Bis-GMA structure is drawn by GaussView software. Then, computations carried out in the Materials Studio software [4] by DMol3 modules and GGA/PW91 functional method.

In the next step, due to the structure of Bis-GMA and the presence of two hydrogen atoms substitutable by Ag atoms, the following cases were obtained by optimizing the structures after the addition of Ag atom: GMA-Ag formed by reaction of Bis-GMA with one Ag atom and Ag-GMA-Ag formed by reaction of Bis-GMA with two Ag atoms.

After the optimization of structures, the Fukui function and quantum theory of atoms in molecules (QTAIM) analysis were used to compare the active sites of Bis-GMA and nature of interactions between two Bis-GMA molecules.

III. RESULTS AND DISCUSSION

A. Analysis of the Chemical Reactivity through the Fukui Functions

Determination of reactivity of molecules towards other molecules can be considered by Fukui functions. $f_+(r)$, and

$f_-(r)$ are Fukui indices for nucleophilic, and electrophilic attacks, respectively. When a molecule accepts electrons, the electrons tend to go to places where $f_+(r)$ is large because at these locations the molecule is the most able to stabilize additional electrons. Therefore a molecule is susceptible to nucleophilic attack at these sites. A molecule is susceptible to electrophilic attack at sites where $f_-(r)$ is large, because these locations are the regions where the molecule is the most able to stabilize removal electrons [5].

For GMA, the largest value of $f_+(r)$ is for carbon atom at the position 61(C61) and arrangement of $f_+(r)$ for other sites is C52 > H73 ≈ H72 that show GMA is susceptible to nucleophilic attack at sites of C61, C52, H73 and H72, and maximum value of $f_-(r)$ is observed in oxygen atom at the position 30 (O30) that shows GMA is susceptible to electrophilic attack at the position of O30.

For GMA-Ag, the larger value of $f_+(r)$ is observed for Ag72 and then C54 and the largest value of $f_-(r)$ is for O48. The Fukui function results of GMA with one Ag atom show that Ag atom at the position 72 is the most susceptible position to nucleophilic attack and oxygen atom near to Ag atom (O48) is the most susceptible position to electrophilic attack.

In Ag-GMA-Ag, Ag atom at the position 73 has the largest value of Fukui index for nucleophilic attack $(f_+(r))$ and O48 and O49 have the larger value of Fukui index for electrophilic attack. Therefore, the position of reactive electrophilic sites is similar in Ag-GMA and Ag-GMA-Ag and they are located on the O atom bonded to the Ag atom.

B. QTAIM Analysis

In this paper, we encounter three structures, made by GMA, Ag-GMA and Ag-GMA-Ag (Fig. 2), which examine the different modes of dual interaction of these structures with the AIM method.

In the first case, in Fig. 2, two GMA molecules are arranged in the same way as the hydroxyl groups of these two molecules are adjoining, the molecular graph from the computations of AIM method shows that in this case we see the creation of four bond critical points between two molecules include the interaction between two carbon-bound hydrogen (-CH₃) and two oxygen-bound hydrogen (-OH). Two important interactions, the interactions of the two hydroxyl groups shown in Fig. 2 by yellow region, and the two critical points of interest are numbered as 1 and 2.

The electron density and the Laplacian of electron density for the critical points 1 and 2, which are among the hydroxyl groups of the two GMA molecules, were calculated. The positive values of $\nabla^2\rho(r)$ indicate a closed-shell interaction, which indicates a weak interaction between two GMA.

In interaction of GMA with Ag-GMA, at the presence of silver atom at the Bis-GMA molecule, the interaction between two different molecules will be different from the normal GMA, and the interactions are concentrated on the silver atom, which can be seen in the molecular graph of Fig. 2, the Ag atom interacts with hydrogen atom of OH group in the 4 point and CH₃ groups in the 4' point (interaction between GMA and Ag-GMA).

The study of all the possible interaction between GMA, Ag-GMA and Ag-GMA-Ag shows that the interaction between hydrogen and Ag atoms is closed-shell ($\nabla^2\rho(r) = +0.008$) and interaction between two adjacent Ag atoms is covalent type ($\nabla^2\rho(r) = -0.02$).

In general, the study of the molecular graph of AIM, for different states of interaction between GMA, Ag-GMA and Ag-GMA-Ag, and the electron density and the Laplacian of electron density data suggest a stronger interaction between the Ag-GMA-Ag molecules, and if the ratio of Bis-GMA molecules with Ag atoms is increased, the stronger interaction will be create.
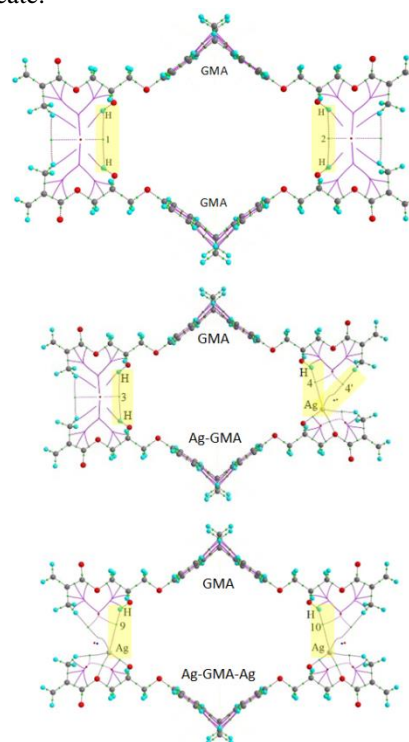

Fig. 2: Molecular graphs of interaction in GMA systems

IV. CONCLUSION

Bis-GMA with two hydroxyl hydrogen was coordinated by two silver atoms instead of the hydrogen atoms. Then optimized probable structures were considered using Fukui

functions and QTAIM. In chemical density functional theory, the Fukui functions are the key regioselectivity indicators for electron-transfer controlled reactions. The comparison of the reactive sites of Bis-GMA, before and after the Ag atom addition, shows the creation of more active sites at the Ag position especially in Ag-GMA structure (Bis-GMA with one Ag atom). To study the nature of interactions using QTAM method, the AIM molecular graph and the Laplacian of electron density show covalent interaction in system of Ag-GMA-Ag (two silvers atoms added to GMA) is stronger than closed-shell interaction between hydrogen atoms of OH groups of Bis-GMA.

REFERENCES

[1] R. L. Bowen, Dental filling material comprising vinyl silane treated fused silica and a binder consisting of the reaction product of bis phenol and glycidyl acrylate, Patent number: 3066112, **1962**.

[2] G. Furtos, M .Tomoaia-Cotisel, and C. Prejmerean, Particulate Science and Technology, vol. 31(4), pp. 332-339, **2013**.

[3] A. Tăbăcaru, C. Pettinari, F. Marchetti, C. Nicola, K. V. Domasevitch, S. Galli, N. Masciocchi, S. Scuri, I. Grappasonni, M. Cocchioni, Inorganic Chemistry, 51(18), pp. 9775-9788, **2012**.

[4] Dassault Systèmes BIOVIA, Material Studio, v7.0, San Diego: **2013**.

[5] P. Chattaraj, Fukui Function, in Chemical Reactivity Theory, CRC Press, **2009**.

Density Functional Study of two Heterodiazocine Molecular Photoswitches

M. Zare*, S. Heliche

Department of Chemistry, Faculty of Science, Shahid Chamran University of Ahvaz, Ahvaz, 43337, Iran
Email: m.zare@scu.ac.ir

Abstract: We utilize DFT functionals (B3LYP and CAM-B3LYP) for obtaining the equilibrium geometries and optical properties of two heterodiazocine molecular photoswitches. We also investigate the effect of THF solvent on the geometry and stability of the molecular isomers. The results show that the compact **Z** isomers are more stable than the elongated **E** configuration. The solvent corrected energies do not differ significantly from the uncorrected values. The long range corrected CAM-B3LYP functional is more suitable than the B3LYP to reproduce the experimental UV spectra.

Keywords: Computational Chemistry, DFT, Diazocines, Molecular Photoswitch.

I. INTRODUCTION

Photochromic molecules, which can be switched between two isomeric forms with different colors, structures, or functional properties by light at characteristic wavelength, are expected to find application as optical memory and logic devices, or as molecular motors and machines [1]. Diazocines (bridged azobenzenes) are particularly interesting switchable compounds [2]. The reversible photoconversion between their **Z** and **E** isomers is illustrated in Scheme 1. Here, we study the geometrical, electronic and optical properties of two heterodiazocines (**1** and **2**).

Scheme 1.
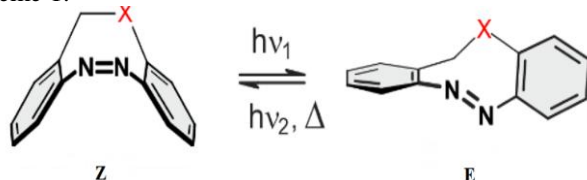
X: O (**1**) and S (**2**)

II. METHODS

All Density Functional Theory calculations have been performed in Gaussian 09. We use B3LYP and CAM-B3LYP DFT functionals with conjugation basis set 6-311++G(d,p) for optimizing the geometry, calculating the vibrational frequencies to check the nature of the stationary points and time dependent DFT (TD-DFT) calculations. Solvent effects are taken into account using a Polarizable Continuum Model with the Integral Equation Formalism variant (IEFPCM) as implemented in Gaussian [3].

III. RESULTS AND DISCUSSION

The optimized structures of both isomers for **1** and **2** obtained with the B3LYP/6-311++G** are shown in Fig. 1. The optimized structures from B3LYP and CAM-B3LYP are very similar (see Table 1). The significant distinction between **E** and **Z** isomers is the C–N–N–C dihedral angle (τ). The values of the dihedrals are listed in Table 1. The **1E** and **2E** isomers are elongated (τ= 142.8° and 151.4° respectively), whereas the **1Z** and **2Z** isomers are bent (τ= 7.4° and 3.6° respectively). Such a large-amplitude structural changes
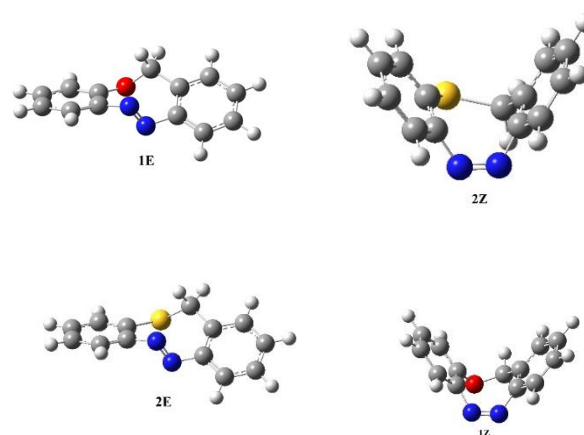

Fig. 1: Optimized structures of studied heterodiazocine at B3LYP/6-311++G**.

between their elongated (**E**) and more compact (**Z**) forms may be of particular interest.

The calculated energies of diazocines **1** and **2** are listed in Table 2. The **Z** configuration is predicted to be more stable for both **1** and **2**. The **1Z** and **2Z** are energetically more stable by ca. 10 and 4.7 kcal.mol^{-1}, respectively. To account for solvent effects a solvent correction for tetrahydrofuran (THF) was performed on the optimized structures of diazocines **1** and **2**. The solvent corrected relative energies are a bit more than uncorrected values (Table 2). It is noteworthy that the CAM-B3LYP relative energies do not differ significantly from the B3LYP values.

Table 1: The calculated C–N–N–C dihedral angle (Degree).

	B3LYP		**CAM-B3LYP**	
	E	**Z**	**E**	**Z**
1	142.8	7.4	143.5	6.9
2	151.4	3.6	151.9	3.6

Table 2: Calculated energies of the **Z** and **E** isomers of the investigated diazocines **1** and **2** and relative energies without and with solvent (THF) correction. Solvent corrected values are in bold.

Method	Isomer	E /Hartree	E_{rel} /kcal.mol^{-1}
B3LYP	1Z	-686.226325 **-686.234652**	0 **0**
	1E	-686.209997 **-686.216943**	10.25 **11.11**
	2Z	-1009.209173 **-1009.216619**	0 **0**
	2E	-1009.20174 **-1009.208521**	4.66 **5.08**
CAM-B3LYP	1Z	-685.868203 **-685.876894**	0 **0**
	1E	-685.852015 **-685.859198**	10.16 **11.10**
	2Z	-1008865092 **-1008.872917**	0 **0**
	2E	-1008.857606 **-1008.864647**	4.70 **5.19**

The results of the TD-DFT calculations performed at the B3LYP/6-311++G** and CAM-B3LYP/6-311++G** levels of theory are shown in Table 3 and compared with the experiment. The predicted values by CAM-B3LYP are in excellent agreement with the experimental results.

Table 3: Calculated transitions and oscillator strengths (f) of the **Z** and **E** isomers of the diazocines **1** and **2** (in THF). Experimental absorption wavelengths (λ exp.) are also included.

Method	Molecule	Isomer	λ cal. /nm	f	exp.(nm)
TD-B3LYP	1	E	528.54	0.049	490
			302.85	0.2107	
		Z	433.54	0.0098	404
			326.47	0.0888	
TD-CAM-B3LYP	1	E	489.95	0.026	490
			274.41	0.1803	
		Z	415.41	0.0072	404
			279.11	0.0995	
TD-B3LYP	2	E	575.54	0.0428	522
			385.7	0.0117	
		Z	430.42	0.0117	404
			324.62	0.1234	
TD-CAM-B3LYP	2	E	526.71	0.0245	522
			315.53	0.0197	
		Z	412.77	0.0087	404
			278.74	0.1477	

IV. CONCLUSION

We have investigated the utilization of two different DFT functionals for obtaining the equilibrium geometries, the vibrational frequencies and the optical properties of **E**/**Z** diazocine photoswitches. Calculations were performed both in vacuum and in the THF solvent. It was found that both functionals correctly predicted the more stable configuration (**Z**). The analysis of the optical properties show that the long range corrected CAM-B3LYP functional is appropriate to reproduce the experimental UV spectra.

REFERENCES

[1] R. Siewertsen, H. Neumann, B. Buchheim-Stehn, R. Herges, C. Näther, F. Renth and F. Temps, J Am. Chem. Soc, vol. 131, pp. 15594–15595, **2009**.

[2] M. Hammerich, C. Schütt, C. Stähler, P. Lentes, F. Röhricht, R. Höppner and R. Herges, J. Am. Chem. Soc, vol. 138, pp. 13111–13114, **2016**.

[3] S. T. Olsen, J. Elm, F. E. Storm, A. N. Gejl, A. S. Hansen, M. H. Hansen, J. R. Nikolajsen, M. B. Nielsen, H. G. Kjaergaard, and K. V. Mikkelsen, J. Phys. Chem. A, vol. 5, pp. 896−904, **2015.**

Study of the Structure of the Peptides Stabilized by the Hydrogen-Bond Surrogate Approach Using Molecular Dynamics Simulation

N.Mehdizadeh darban [a, b], S.Jalili [c] *

[a ,b] *Department of Chemistry, Faculty of chemistry, K.N. Toosi University of Technology, Tehran, Iran;*
n.mehdizade@email.kntu.ac.ir
[c *] *Department of Chemistry, Faculty of chemistry, K.N. Toosi University of Technology, Tehran, Iran;*
Fax: +98 21 22853650; Tel: +98 21 22853649; sjalili@kntu.ac.ir

Abstract To study the path of biological reactions peptides are used from the secondary and tertiary structures of peptides that have an important role in the equilibrium of protein-protein interaction (PPI) inhibitors. Different methods are used to stabilize peptides the method of hydrogen bond surrogate is a unique way to stabilize the peptides, because this method (HBS) while stabilization the peptides keep side chains stable, which can be modified to control attachment and peptide interactions. HBS method create the peptides by forming large 16 - membered rings, and we used three groups' disulfide, thioether, olefin for the stability of the α-helix and β-sheet statures. [8]. In this paper, we examine the structure of peptide β-hairpin stabilized peptide structures, using GROMACS and analysis of RMSD, Gyration, Hydrogen bond interactions with the environment and in terms of stability and structural properties.

Keywords: β-hairpin, Hydrogen bond surrogate, Gyration, RMSD, H-bond

I. INTRODUCTION

Peptides that fold than stable secondary and tertiary structures have become strong tools to mimic molecular identification epitopes and modulate protein-protein interactions (PPIs) to probe biological pathways.[1,4] A range of stabilization program have been validated for efficient secondary(β-strand[4,5]) and tertiary structures (β-sheets [7]) as well as non-regular structures. [4] Protein-protein interactions (PPIs) are involved in most cellular procedure and effect biological functions through proximity-induced changes of protein property such as enzymatic activity, subcellular localization, and binding properties. So the modulation of PPIs is considered an encouraging strategy towards next-production therapeutics. [1]

Modulators of PPIs are important for the explanation of biological processes and are considered engaged candidates in drug growth. [1, 7, 8] In many cases, small molecular scaffolds used in standard drug design failed to provide active and selective PPI inhibitors. Given the large and often shallow interplay spaces of PPIs and the reality that most small molecular drugs target well-specific space of enzymes or receptors. Peptide models β sheets have been a main space of study over the past decade. There has been significant prosperity in create peptide sequences that from β hairpin [1-5] and the extension of such systems to three- and four-stranded antiparallel-sheet models. The hydrogen bond surrogate (HBS) approach is unique among these strategies in that the resulting peptides retain all side chains to allow desirable effects. In the HBS approach, a main chain hydrogen bond is replaced with an isosteric covalent linkage, [5, 6, 7] Because only a main chain hydrogen bond is replaced, all side chains can be operate to control binding affinity and specificity. [5, 6]

II. METHODS

The simulations were supported out by using the GROMACS package of programs. We have performed simulations with the CHARMM27 force filed. This force field is used for biological parameters such as proteins, nucleic acids, lipid and carbohydrates. This force field has expanded in the field of drugs. We chose the HP7 β - hairpin sequence and destabilized different HP7Δ and HP7Δ with an HBS linking the N - and C - termini (HP7Δ- HBS). [8]

III. RESULTS AND DISCUSSION

Analysis of molecular dynamics simulation trajectory:
The β-hairpin HP7 was simulated using GROMACS version 4.6.5. To gauge the dynamics and stability of each system, RMSD profile, gyration, and intermolecular H-bonds were analyzed from the resultant MD trajectories using GROMACS package of programs. Having achieved an appropriate, equilibrium and the results of these simulations are compared using a vast range of parameters and measurements and are detailed as follows:

Stabilization: To availability the dynamic stability of HP7, RMSD profile for backbone residues were generated and plotted against time scale of 30 ns. As apperceive from the graph, the backbone RMSD of HP7, HP7Δ and HP7Δ-HBS state followed 30 ns of simulation. The HP7 system possesses a significant structural deviation of Root Mean Square

Deviation (RMSD) in HP7Δ, there are more than two other structures, while it's stable in HP7Δ-HBS of graphs. We can conclude that binding of HBS can stabilize structure of the HP7.

Protein compactness and folding: To analyze the overall compactness of protein an attempt was made to calculate the radius of gyration. [8]A relatively steady value of Rg over time shows that a HP7Δ-HBS is stably folded to check this, radius of gyration time graphs have been plotted for the structure. After initial fluctuations, the Rg in three state maintains a relatively steady value this indicated that HP7Δ-HBS is having better value of Rg. This indicates that HP7Δ-HBS increases its compactness through its advancement towards simulations.

Hydrogen bond analysis: Hydrogen bonds are indispensable for in molecular recognition as well as overall stability of a protein and its structures. [8] Inter molecular hydrogen bonds were analyzed for the β-hairpin HP7. The investigation illustrated that all the structures variable number of intermolecular hydrogen bonds. The analysis showed overlap hydrogen bonds in the structure HP7Δ-HBS and this is indicative of a stable structure HP7.
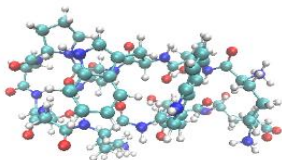
Fig.1: An ensemble of the 20 lowest-energy HP7Δ-HBS conformations derived from Monte Carlo simulations with NMR-derived torsion angle
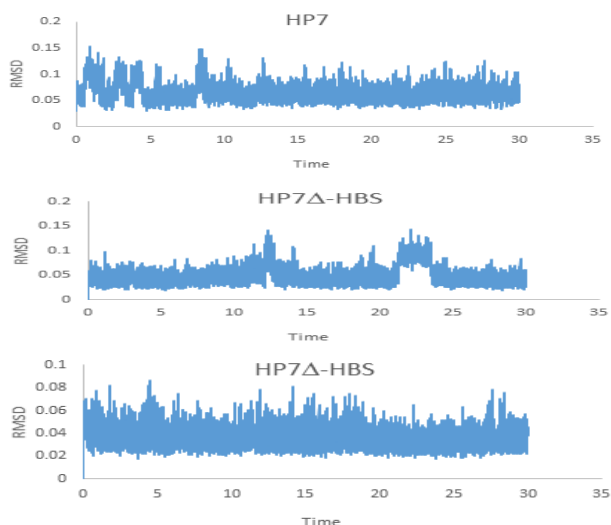
Fig.2: RMSD of atomic positions from the minimized and equilibrated structure averaged over 30 ns MD simulations.
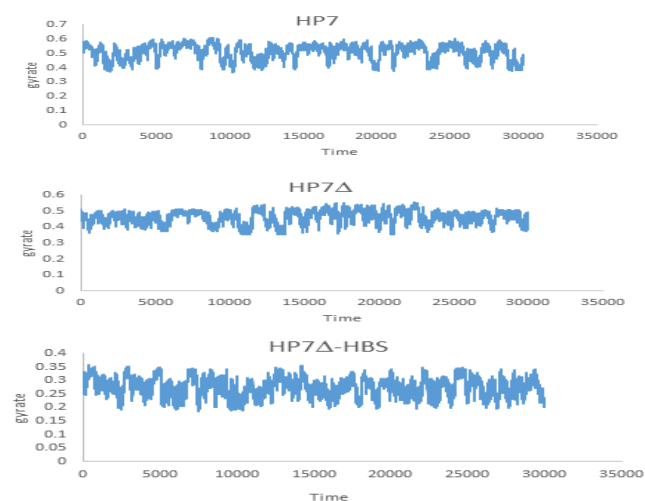
Fig.3: Radius of gyration as a function of Time for the different peptide ensembles simulated.
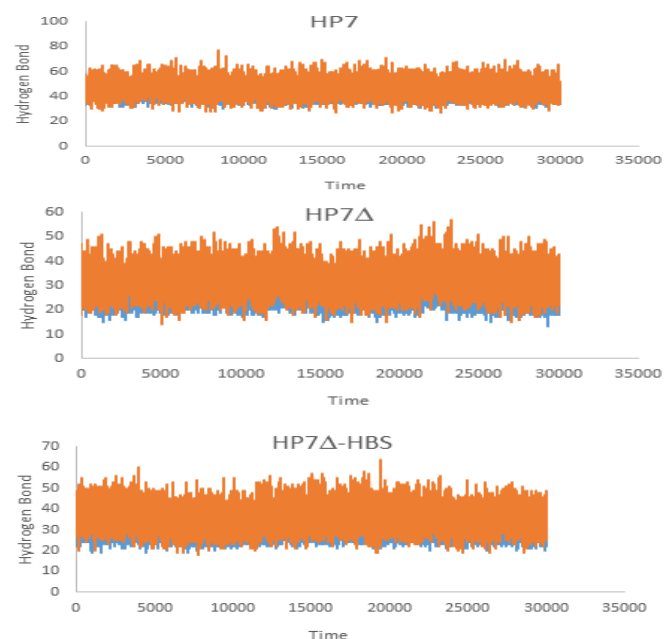
Fig.4: Number of Hydrogen-bonded peptide residue for Hp7 peptide.

IV.   CONCLUSION

According to the results, these calculations confirmed our hypothesis. So computational analysis show that contrast to native PPIs that are optimized for overall function in their biological context and designed proteins receive focused optimization for target protein binding affinity and property . It is thus practical that binding epitopes extracted from these proteins will have higher initial affinities and need less optimization. According to the analyses (RMSD, Gyration,

Hydrogen bond) the structure of HP7Δ - HBS is more stable than other states. The β - hairpin HBS approach described here replaces only an internal hydrogen bond that cannot join in molecular identification, all main - and side - chain functional groups from the original β - hairpin can be Compound and optimized for binding affinity and property. An increasing number of designed proteins that use β - hairpins or β - sheets for molecular identification of targets may encourage further growth of β - hairpin PPI inhibitors

REFERENCES

[1] Chang, Y. S., Graves, B., Guerlavais, V., Tovar, C., Packman, K., To, K.-H., Olson, K. A., Kesavan, K., Gangurde, P., Mukherjee, A., Baker, T., Darlak, K., Elkin, C., Filipovic, Z., Qureshi, F. Z., Cai, H., Berry, P., Feyfant, E., Shi, X. E., Horstick, J., Annis, D. A., Manning, A. M., Fotouhi, N., Nash, H., Vassilev, L. T., and Sawyer, T. K. (2013) Stapled α−helical peptide drug development: A potent dual inhibitor of MDM2 and MDMX for p53-dependent cancer therapy, Proc. Natl. Acad. Sci. USA 110, E3445.

[2] Kushal, S., Lao, B. B., Henchey, L. K., Dubey, R., Mesallati, H., Traaseth, N. J., Olenyuk, B. Z., and Arora, P. S. (2013) Protein domain mimetics as in vivo modulators of hypoxia-inducible factor signaling., Proc. Natl. Acad. Sci. U S A 110, 15602-15607.

[3] Moellering, R. E., Cornejo, M., Davis, T. N., Bianco, C. D., Aster, J. C., Blacklow, S. C., Kung, A. L., Gilliland, D. G., Verdine, G. L., and Bradner, J. E. (2009) Direct inhibition of the NOTCH transcription factor complex, Nature 462, 182.

[4] Peraro, L., Zou, Z., Makwana, K. M., Cummings, A. E., Ball, H. L., Yu, H., Lin, Y.-S., Levine, B., and Kritzer, J. A. (2017) Diversity- Oriented Stapling Yields Intrinsically Cell-Penetrant Inducers of Autophagy, J. Am. Chem. Soc. 139, 7792-7802.

[5] L. Huang, F. Hofer, G. S. Martin, S.-H. Kim, Nat. Struct. Mol. Biol. 1998, 5, 422 – 426.

[6] C. Kiel, L. Serrano, C. Herrmann, J. Mol. Biol. 2004, 340 ,1039 – 1058

[7] T. A. Hill, N. E. Shepherd, F. Diness, D. P. Fairlie, Angew. Chem. Int. Ed. 2014, 53, 13020 – 13041; Angew. Chem. 2014, 126, 13234 – 13257.

[8] L. Nevola, E. Giralt, Chem. Commun. 2015, 51, 3302 – 3315.

Theoretical Study of Oxime Derivatives containing Quinoxaline.

Kh. Shekoohi*

(Department of Chemistry, Darab branch, Islamic Azad University, Darab 7481783143-196, I. R. Iran)
E-mail:sh.shekoohi@gmail.com

Abstract: In this research, The new synthesized compounds by Quantum theoretical calculation are studied. The cyclization of *o*-phenylendiamine with *O*-oxime ether adducts led to synthesis of new analogues of quinoxaline compounds. The density functional theory (DFT) methods have used to determine the geometrical properties, UV, highest occupied molecular orbital (HOMO) and the lowest unoccupied molecular orbital (LUMO) analysis and molecular electrostatic potential (MEP) of these compounds.

Keywords: *O*-oxiem, Quinoxaline, MEP, DFT.

I. INTRODUCTION

The *O*-alkylation of oximes is very important in medicinal chemistry since *O*-oxime ether derivatives are prominent structural motifs found in numerous pharmaceutically active compounds. Several well-known drugs with various chemotherapeutic activities contain an oxime ether moiety in their molecular structures[1].

DFT methods have been widely used as verification of experimental measurements for biological systems . Several experimental and molecular modeling studies have been reported on the electronic structure of Quinoxalines derivatives[2,3] , while there are few theoretical studies on the electronic structures, quantum descriptors and biological activities of them.

II .METHODS

The quantum chemical calculations of the compounds **5a**, **5b**, **5c**, **5d**, were carried out by using Gaussian 09 Rev. A 11.4 software programs on a Pentium IV/4.28 GHz personal computer. The structure of title compound shown in table1.The molecular structure of the title compounds in the ground state was optimized using DFT method (functional PBE1PBE) with the 6-31+G* basis set[4] in a solvent water. The Polarized Continuum Model (PCM)[5] was used for calculations of the solvent effect. Without any constraint on the geometry the energies of the mentioned molecules were minimized, whole intramolecular forces were brought to zero. The Frontier Molecular Orbital (FMO) analysis and electronic properties such as energies HOMO and LUMO orbitals, HOMO-LUMO energy gap (Eg), ionization potential (*I*), electron affinity (*A*), global hardness (*η*), electronegativity (*χ*), electronic chemical potential (*μ*),

electrophilicity (*ω*), chemical softness (*S*) were estimated using the E_{HOMO} and E_{LUMO} energies using the PBE1PBE/6-31+G* level of theory.

III. RESULTS AND DISCUSSION

FMO Analysis and Electronic Properties of the Compounds 5a-d.The HOMO and LUMO are known as the frontier molecule orbitals (FMOs) that participate in electronic properties, optical properties, UV spectrum and chemical reactions [30,31]. We used FMO analysis and the electronic properties of compounds **5a-d** by means of PBE1PBE/6-31+G* level of theory. The calculated results are reported in Table2.

Table1: The structure of study compounds.

Compounds	№	Structure[a]
propan-2-one O-((1,2,3,4-tetrahydroquinoxalin-2-yl)methyl) oxime	5a	
(Z)-butan-2-one O-((1,2,3,4-tetrahydroquinoxalin-2-yl)methyl) oxime	5b	
(Z)-acetophenone O-((1,2,3,4-tetrahydroquinoxalin-2-yl)methyl) oxime	5c	
benzophenone O-(1,2,3,4-tetrahydroquinoxalin-2-yl)methyl oxime	5d	

The E_{HOMO} and E_{LUMO} are related to the ionization potential ($I=-E_{HOMO}$) and the electron affinity ($A=-E_{LUMO}$), respectively [7]. The global hardness (*η*), electronegativity (*χ*), electronic chemical potential (*μ*) and electrophilicity (*ω*) [6], chemical softness (*S*) parameters are calculated with the following equations:

$$(\eta=I-A/2), (\chi=I+A/2), (\mu=-(I+A)/2), (\omega=\mu^2/2\eta), (S=1/2\eta)$$

In which values of these parameters are reported in Table 2. The global hardness (*η*) parameter is related to the Eg and defined as measurement from the resistance of an atom or a

group of atoms to charge transfer[7]. A molecular structure with a small Eg has a high chemical reactivity, low kinetic stability and is a soft molecule; whereas a hard molecular structure has a large Eg .The global hardness values of molecules **5a**, **5b**, **5c** and **5d** are 1.60 eV, 1.57 eV, 1.08 eV and 1.01 eV , respectively. The highest global hardness value is observed for **5a**; therefore, it is the hardest molecule compared to other molecules. Electronegativity (χ) parameter is a measure of the power of an atom or a group of atoms to attract electrons and the chemical softness (*S*) describes the capacity of an atom or a group of atoms to receive electrons.

MEP maps show the electronic density and are used in detection of the negative and positive electrostatic potentials regions for electrophilic attacks and nucleophilic reactions. The difference of the electrostatic potential at the surface is shown by different colors. The colors of the MEP maps are red (electron rich), orange (partially negative charge), yellow (slightly electron rich site), blue (positive charge), and green (neutral). The MEP surfaces of the molecules **5a-d** were computed by theoretical calculations using the PBE1PBE/6-31+G* level of theory (Fig. 1).

Table2: The calculated electronic properties of the compounds **5a-d** using PBE1PBE/6-31+G* level of theory.

Property	5a	5b	5c	5d
HF (Hartree)	-706.09	- 745.35	- 897.604	- 1089.10
Dipole moment (Debye)	3.3034	3.3887	3.1030	3.6624
E_{HOMO} (eV)	-4.30	-4.30	-4.32	-4.42
E_{LUMO} (eV)	-1.09	-1.15	-2.16	-2.39
Eg (eV)	3.21	3.15	2.16	2.03
I (eV)	4.30	4.30	4.32	4.42
A (eV)	1.09	1.15	2.16	2.39
χ (eV)	2.69	2.72	3.24	3.40
η (eV)	1.60	1.57	1.08	1.01
μ (eV)	-2.69	-2.72	-3.24	-3.40
ω (eV)	2.26	2.36	4.86	5.72
S (eV)	0.31	0.32	0.46	0.49

As we can see from the Fig. 1, the negative sites of the compounds **5a**, **5b**, **5c**, **5d**, **5e** are mostly focused on phenyl ring of quinoxaline (ring a); therefore, these site have the high electron density and they are suitable for electrophilic attack. The parts of the molecules **5c**, **5d** are pale red or

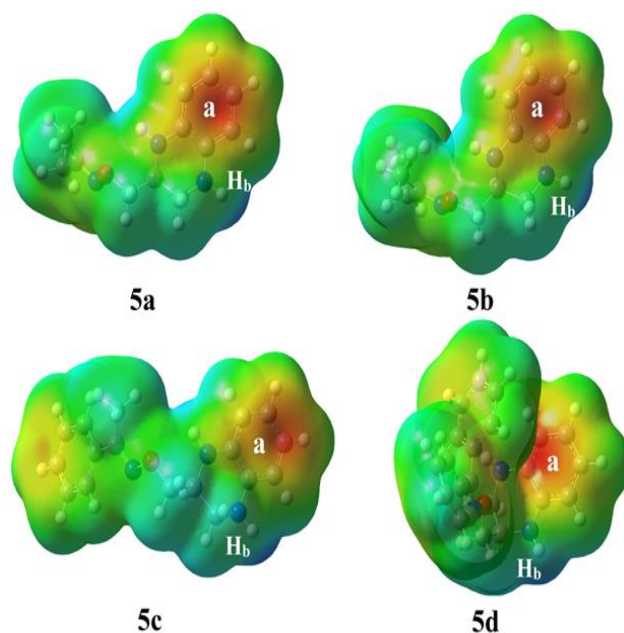orange color that show regions with partially negative charge such as phenyl rings.

Fig.1: MEP maps of the molecules 5a-e computed using the PBE1PBE/6-31+G* level of theory

The positive sites of the title compounds are mostly focused on H_b of N-H in quinoxaline. Also, the regions with green color show areas with zero potential and neutral sites such as the hydrogen atoms of the phenyl rings and the saturated C-C bonds.

Electronic Structure and Excited States of the Compounds 5a-5d

Theoretical absorption spectra of molecules **5a**, **5b**, **5c**, **5d** were calculated in the solvent water using the TDPBE1PBE/6-31+G* method. We computed 20 excited states for title molecules by TD-DFT calculations. According to the computed results, the strongest signal in electronic absorption spectrum of the molecule **5a** is observed at λ_{max} = 232 nm with oscillator strength f = 0.23 . The charge transfer at λ_{max} = 232 nm is relevant to the first excited state $S_0 \rightarrow S_{19}$ with seven electron configurations such as H-1→L+2 (19%), H-1→L+4 (29%), H-1→L+5 (27%), H-2→L+2 (4%), H-1→L+3 (5%), H-1→L+6 (3%), H→L+11 (3%); that the main transition is from HOMO-1 to LUMO+4 (H-1→L+4). The other excited states of **5a** have very small intensity and do not play any role in the formation of electron spectrum of the title compound .The theoretical electronic absorption spectrum of **5a** in the solvent water is shown in Fig. 2.
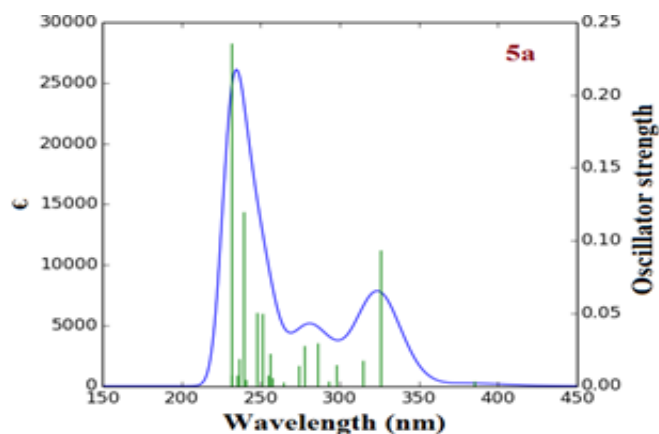
Fig: The UV spectra of the compounds 5a in the solvent calculated by TDPBE1PBE/6-31+G* method

IV. CONCLUSION

Calculations have showed that highest global hardness value is observed for **5a**. The global hardness values of molecules **5a**, **5b**, **5c** and **5d** are 1.60 eV, 1.57 eV, 1.08 eV, 1.01 eV and 0.69 eV, respectively. The highest global hardness value is observed for **5a**; therefore, it is the hardest molecule compared to other molecules.The strongest signals in electronic absorption spectra of the molecules**5a, 5b, 5c** and **5d** are observed at λ_{max} = 232, 240, 296, 281nm.

REFERENCES

[1] M.N Soltani Rad, Z. Asrari, S. Behrouz,G.H Hakimelahi, A. Khalafi-Nezhad, ,.Helv. Chim. Acta. 94 2194-2209, **2011**.

[2] A.Gil, A. Pabón, S. Galiano, A. Burguete, S. Pérez-Silanes, Molecules. 19, 2166-2180, **2014.**

[3] A.G.A El-Helby, R.R. Ayyad, K. El-Adl, H. Sakr, H, Medicinal Chemistry Research, 925, 3030-3046,. **2016.**

[4] S. Chen, B. Mulgrew, and P. M. Grant, Journal, vol. 4, pp. 570-578, **1993**.

[5] R. Soto-Rojo, J. Baldenebro-López,N. Flores-Holguín, D. Glossman-Mitnik, , J. Mol. M odel. 20, 2378-2383, **2014.**

[6] M. Sheikhi, S. Shahab, L. Filippovich, E. Dikusar, M. Khaleghian, , Chinese J. Struc. Chem. 37 1201-1222,**2018.**

[7] S.Shahab, M.Sheikhi, L. Filippovich, M. Khaleghian, E. Dikusar, H. Yahyaei, M. YousefzadehBorzehandani, M., Silicon. 12,2361-2385. **2018.**

Surface Tension of Imidazolium-based Ionic Liquids from Simulation Study

Vahid Sokhanvaran*, Sahar Naderi, Behzad Haghighi

Department of Chemistry, Faculty of Basic Sciences, University of Neyshabur, 9319774446 Neyshabur, Iran.
*Email: v.sokhanvaran@gmail.com

Abstract: Molecular dynamics simulation of the 1-methyl-3-alkyl imidazolium chloride (alkyl= ethyl and pentyl) ionic liquids were performed with an all-atom force field. In this research, physicochemical properties of the ionic liquids, such as density and surface tension were calculated.

Keywords: Ionic Liquids, Physicochemical Properties, Imidazolium, Force Field, Simulation.

I. INTRODUCTION

One of the most important principles of the green chemistry is the elimination of hazardous solvents in chemical research and industry and avoids using toxic solvent and the generation of waste. Ionic liquids as a green solvent have received considerable attention due to their interesting chemical and physical properties [1]. In general, ionic liquids are a group of organic salts that one or both the ions are large, and the cation has a low degree of symmetry [2]. ILs have unique properties such as; wide liquid range with melting point around room temperature, good stability in air and moisture, high solubility including inorganic, organic, polymeric materials, negligible vapor pressure [1] and hydrophobicity which can be changed by simple variations to the structure of the ions [2]. These properties have led to the extension of ionic liquids as environmentally benign solvents for applications in "green chemistry". Furthermore, there is considerable interest in the structural features of IL crystals [3].

1-Alkyl-3-methyl imidazolium ILs are examples of room-temperature ionic liquids, which are exclusively comprised of ions, which have a unique set of properties effectively including zero vapor pressure. For applications such as; lubricants, heat transfer fluids, and in general when considering any scale-up or process design, knowledge of thermophysical properties and in particular transport properties is very important [4]. Understanding basic thermophysical properties of ILs is vital for design and evaluation [5]. Also, understanding the physical properties of ILs using computer simulation is significant for their potential technological applications [6]. The goal of our research is to obtain a unified understanding of the properties of ionic liquids with respect to their underlying molecular structure. Molecular simulation, allows for a molecular-based understanding of large scale properties and thus represents the most powerful tool to draw strategies for the development and use of ionic liquids. Experimental studies of thermophysical properties of ILs have been largely reported [8]. The possibility of designing application-specific ionic liquids by combining different cations and anions, is an attractive feature to both academic institutes and industrial societies [9]. Therefore, in this paper, we evaluated the densities and surface tension of [amim]Cl (ILs) (a=ethyl and pentyl). This particular compound was chosen as it appears to be the ionic solvent for which the widest range of physicochemical properties has been characterized experimentally.

II. METHODOLOGY

Molecular dynamics (MD) simulations have been performed with the MS modeling program version. The simulation box was composed of 64 randomly arranged ion pairs. The usual periodic boundary conditions have been applied. The simulations were carried in the NPT ensemble with a Nose Hoover thermostat maintaining a temperature of 298 K and at 1 atm pressure. In all of the simulations, the cutoff radius was kept to 12.5 Å. The values of Lennard Jones's contribution to surface tensions of ILs are calculated through Fowler, Kirkwood & Buff (FKB) equation.

III. RESULTS AND DISCUSSION

In this paper, we report the density and surface tension of [amim]Cl. At first, we simulated ionic liquids which figure 1 shows that the final structure of [pmim]Cl.
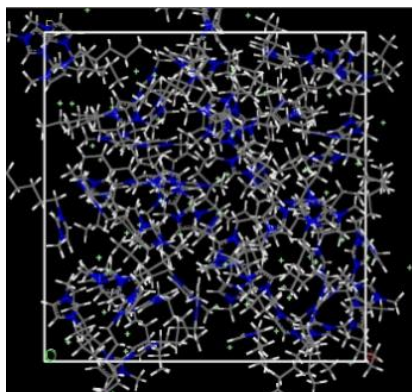
Figure 1: The final simulated structure of [pmim]Cl

In following, the Lennard Jones's contribution to surface tension of two imidazolium-based (ILs) [amim]Cl (a=ethyl and pentyl) were calculated and illustrated in table 1.

Table 1: The calculated values of density and surface tension of ILs.

Ionic liquids	[emim]Cl	[pmim]Cl
d (gr.cm^{-3})	0.969	0.961
γ (mN/m)	2.969	2.827

IV. CONCLUSION

In this work, imidazolium-based ILs with chloride anion were studied by MD simulations using an all atom Force Field. The density and surface tension have been calculated. For the other studied ILs, the calculated density surface tension decrease with an increase the length of alkyl chain.

REFERENCES

[1] A. R. Hajipour, and F. Rafiee, Journal of the Iranian Chemical Society, vol 6, pp. 647-678, **2009**.

[2] M. J. Earle, and K. R. Seddon, Pure and Applied Chemistry, vol 72, pp. 1391-1398, **2000**.

[3] A. E. Bradley, C. Hardacre, J. D. Holbrey, S. Johnston, S. E. J. McMath, and M. Nieuwenhuyzen, Journal Chemistry of Materials, vol 14, pp. 629-635, **2002**.

[4] D. Rooney, J. Jacquemin, and R. Gardas, Topics in Current Chemistry, vol 290, pp. 185-212, **2010**.

[5] C. P. Fredlake, J. M. Crosthwaite, D. G. Hert, S. N. Aki, and J. F. Brennecke, Journal of Chemical & Engineering Data, vol 49, pp. 954-964, **2004**.

[6] Y. Wang, W. E. I. Jiang, T. Yan, and G. A. Voth, Accounts of Chemical Research, vol 40, pp. 1193-1199, **2007**.

[7] C. Krekeler, and L. Delle Site, Phys. Chem. Chem. Phys, vol 19, pp. 4701-4709, **2017**.

[8] A. Bhattacharjee, J. A. Coutinho, M. G. Freire, and, P. J. Carvalho. Journal of Solution Chemistry, vol 44, pp. 703-717, **2015**.

[9] H. Khakan, and S. Yeganegi, Journal of Physical Chemistry B, vol 121, pp. 7455-7463, **2017**.

H₂ and CO₂ Adsorption on Zeolitic Imidazolate Framework-1: GCMC Simulations

Vahid Sokhanvaran*, Atefe Dovlatabadi, Behzad Haghighi

Department of Chemistry, Faculty of Basic Sciences, University of Neyshabur, 9319774446 Neyshabur, Iran.
*Email: v.sokhanvaran@gmail.com

Abstract: In this work, the adsorption of hydrogen and carbon dioxide molecules on the ZIF-1 at room temperature and high pressures have been simulated employing Grand Canonical Monte Carlo (GCMC) method. Some important physical amounts such as; adsorption isotherms were investigated. Our simulation results show that ZIF-1 exhibited average loading of 4.7 (H_2) per unit cell and 5.4 (CO_2) per unit cell at 100 atm, and 298 K, respectively.

Keywords*: Adsorption, Carbon dioxide, GCMC simulations, Hydrogen, Zeolitic imidazolate frameworks.

I. INTRODUCTION

In recent years, Zeolitic imidazolate frameworks (ZIFs) as a new subfamily of porous materials has been synthesized and characterized [1]. ZIFs with zeolite topologies, containing of transition metals for example: Zn or Co that are linked to imidazolate ligands. These frameworks have attracted much interest for membrane-based gas separation because of their thermal and chemical stabilities and ultramicropores (less than 5 Å) [2]. Also, ZIFs have a pore size topology similar to zeolites, and offer a larger variability, obtained by replacing the linker with various kind of organic moieties.

ZIFs demonstrated a considerable affinity to carbon dioxide, and have being considered as viable substrates for carbon dioxide removal from gas flows [3]. Hydrogen with properties likes abundance and higher gravimetric energy density is an excellent candidate for the replacement of existing carbon-based energy sources [4]. ZIFs have increased considerable attention for many applications, e.g., in domains such as gas adsorption, sensing, encapsulation and controlled delivery, and fluid separation [5].

Understanding the behavior of gas adsorption on ZIFs is significant for the design and development of potential applications of ZIFs offered for these porous materials. Knowing how species are adsorbed in the pores of these materials is a prerequisite for considering new metal-organic frameworks (MOFs) in separation applications [6]. Molecular simulation techniques represent a relevant and essential investigation tool to study of adsorption and to gain a deeper insight into microscopic-level information of

phenomena and can play an important role in complementing experimental studies on MOFs [7]. GCMC simulation technique, plays an important role in characterizing the adsorption phenomena without the need for the expensive and time consuming experiments. Therefore, the purpose of this study is to calculation of H_2 and CO_2 adsorption at 298 K and 0-100 atm high pressure on ZIF-1 by GCMC molecular simulations.

II. METHODS

The grand canonical Monte Carlo (GCMC) method was used to calculate the adsorption isotherms. GCMC simulations were performed to calculate the adsorption of the H_2 and CO_2 at 298 K. Absolute adsorption isotherms for ZIF-1 systems were computed up to 100 atm using GCMC simulations as implemented in the MS modeling software. We use rigid frameworks with the framework atoms in ZIF fixed in their experimentally determined crystallographic positions, and the standard force fields such as UFF. All of the calculations were performed with a simulation box corresponding to 8 unit cells, $2 \times 2 \times 2$ for ZIF-1 with typically 15×10^6 Monte Carlo steps. The Ewald summation was used for calculating the long range electrostatic interactions and the short range non-bonded contributions were calculated with a cut-off distance of 10 Å. Periodic boundary conditions were applied in all three dimensions.

III. RESULTS AND DISCUSSION

At first, we computed hydrogen and carbon dioxide adsorption on ZIF-1 at 298 K and up to high pressure (Figure 1).

As shown in figure 1, ZIF-1 can adsorb 1.1 per unit cell carbon dioxide at 1 atm and with the pressure increased to 100 atm, its uptake capacity can reach as high as 5.4 per unit cell. The adsorption loading of H_2 on ZIF-1 was found to be 4.7 and 0.7 per unit cell at 1 and 100 atm, respectively. These results indicate that the adsorption amount of CO_2 on ZIF-1 is higher than that of for hydrogen. Both of isotherms show type I behavior, which is a typical characteristic of nanoporous materials.
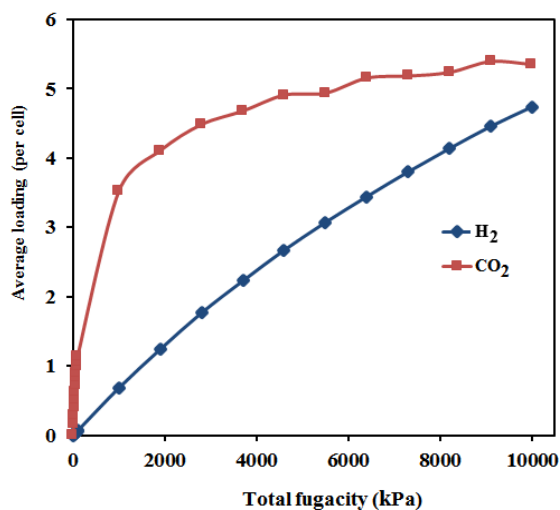
Figure 1: The simulated H_2 and CO_2 adsorption on ZIF-1 at 298 K up to high pressure.

IV. CONCLUSION

In summary, by using GCMC simulations, the adsorption of H_2 and. CO_2 on the ZIF-1 were calculated. The adsorption isotherms of gases clearly revealed that the adsorption capacity of CO_2 was higher than those of H_2 at ambient temperature and pressures up to 100 atm.

REFERENCES

[1] H. Bux, F. Liang, Y. Li, J. Cravillon, M. Wiebcke, and J. Caro, Journal of the American Chemical Society, vol. 131, pp. 16000-16001, **2009.**

[2] P. Nian, Y. Li, X. Zhang, Y. Cao, H. Liu, and X. Zhang, Journal of the American Chemical Society, vol. 10, pp. 4151-4160, **2018.**

[3] A. Battisti, S. Taioli, and G. Garberoglio, Microporous and Mesoporous Materials, vol. 143, pp. 46-53, **2011.**

[4] L. Bouëssel du Bourg, A. U. Ortiz, A. Boutin, and F. X. Coudert, Journal of APL materials, vol. 2, pp. 124110, **2014.**

[5] E. Atci, I. Erucar, and S. Keskin, The Journal of Physical Chemistry, vol. 115, pp. 6833-6840, **2011.**

[6] V. Sokhanvaran, and S. Yeganegi, ChemPhysChem, vol. 17, pp. 4124-4133, **2016.**

[7] S. Yeganegi and V. Sokhanvaran, Adsorption, vol. 17, pp. 4124-4133, **2015.**

Exploring binding of some 4H-benzo[g][1,2,3]triazolo[5,1-c][1,4]oxazocine derivatives with calf thymus DNA using computational methods

E. Sanchooli[a]*, H.S. Delarami[a], S. Mirjahanshahi[b]
[a]Department of Chemistry, Faculty of Science, University of Zabol, Zabol, Iran
[b]Department of Chemistry, Faculty of Science, University of Sistan and Baluchestan, Zahedan, Iran
Email: esmael.sanchooli@gmail.com

Abstract: Heterocycles 4H-benzo[g][1,2,3]triazolo[5,1-c][1,4] oxazocines was exhibited high anticancer activity against human breast cancer cell line (MCF-7). In this study, some these derivatives were considered for its possible interaction with calf thymus DNA (CT-DNA) as a target for the treatment of cancer using molecular docking and quantum mechanical calculations. Hydrogen bonding interactions of these compounds with the amino acid residues of CT-DNA active site could be responsible for their mechanism of action. This study can provide better insight into the understanding of the toxicity of the drugs at the molecular level.

Keywords: Oxazocine, Molecular docking, DNA, intercalation, Density functional theory.

I. INTRODUCTION

DNA is a favorite target for the development of cancer chemotherapeutics and many of the most effective clinical agents are DNA interactive. Interaction of small molecules with DNA has attracted more attention [1]. Tricyclic heterocycles such as 4H-benzo[g][1,2,3]triazolo[5,1-c][1,4]oxazocines was exhibited high anticancer activity against cancer cell lines including human cervix cancer cell line (HeLa), human prostate cancer cell line (DU145), human breast cancer cell line (MCF-7) and human breast adenocarcinoma epithelial cell line (MDA-MB-231) [2]. In the present study, some these derivatives (see Figure 1) were analyzed for its possible interaction with calf thymus DNA (CT-DNA) through molecular docking analysis.

II. METHODS

MGL tools 1.5.6 with AutoGrid4.2 and AutoDock4.2 [3] were applied for molecular docking calculations between the oxazocine derivatives a-f and CT-DNA obtained from the Protein Data Bank (PDB). The DNA target is staphylococcus aureus gyrase B (PDB ID: 1BNA). A blind docking was performed for the recognition of the active sites of receptor. The grid size was set at 70×76×126 Å in the x-, y-, and z-axes respectively, with 0.375 Å grids spacing to cover the whole receptor. The ligand/receptor was considered flexible/rigid. The Lamarckian genetic algorithm was applied to search for the best conformers. Geometries of ligands were optimized at the B3LYP/6-31G(d,p) level of theory by the Gaussian09 program package [4].

III. RESULTS AND DISCUSSION

Molecular docking is widely used technique for prediction of protein–drug interactions that can help in better understanding of bioactivity mechanism. This method clarifies the binding modes between the ligand and receptor and assist to design new potent drug candidates. The interaction energies (BE) between oxazocine compounds and amino acid residues of 1BNA active site and the previous experimental antibacterial activity (MIC_{50}) are presented in Tables 1. As seen, the BE value of compound **b** to receptor is the highest, which is in agreemnet with the lowest IC_{50} value [5]. There are conventional H-bonds interactions between the ligands and amino acid residues of CT-DNA.
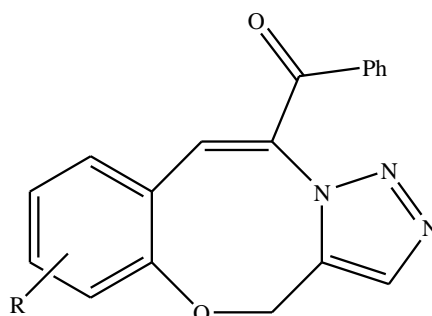

Fig.1: Chemical structure of oxazocine compounds used in this study.

Table1:

No.	R	IC50* (μM)	BE (kcal mol^{-1})
		MCF-7 cell line	
a	H	2.46	-8.97
b	**8-Br**	**1.73**	**-9.04**

c	8-Cl	4.81	-7.88
d	6-OMe	1.81	-8.16
e	8-OMe	9.69	-8.06
f	6-OEt	10.21	-7.91

* The anticancer activity of oxazocine compounds a-f described in ref. [2].

IV. CONCLUSION

The interaction of oxazocine compounds with CT-DNA was considered using the molecular docking method. The results are in good accordance with the previous experimental results. This study can be useful for better understanding of bioactivity mechanism.

REFERENCES

[1] K. Gurova, Future Oncol. vol. 5, pp. 1685-1704, **2009**.

[2] K.N.V. Sastry, S.R. Routhu, S.G. Datta, N. Nagesh, B.N. Babu, J.B. Nanubolu, C.G. Kumar, R.A. Maurya and A. Kamal, Org Biomol Chem. vol. 14, pp. 9294-9305, **2016**.

[3] G.M. Morris, R. Huey, W. Lindstrom, M.F. Sanner, R.K. Belew, D.S. Goodsell, and A.J. Olson. J. Comput. Chem. vol. 30, pp. 2785-2791, **2009**.

[4] M.J. Frisch, et al., Gaussian 09, Revision A.02, Gaussian Inc., Wallingford, CT, **2009**.

Permeation of Curcumin and Its Derivatives through the DPPC Model Membrane: A Molecular Dynamics Simulation Study

D. Mohammad-Aghaie, H. R. Zareie*

Department of Chemistry, Shiraz University of Technology, Shiraz 71555-313, Iran

Email: d_aghaie@sutech.ac.ir

Abstract: Curcumin (bis-α,β-unsaturated β-diketones), the main component of the turmeric plant, has therapeutic and preventive effects for many diseases, including cancers and diabetes. In this study, we deal with some novel anti-diabetic curcumin derivatives, synthesized and investigated provisionally by Yousefi *et. al.* [1]

Both normal molecular dynamics and umbrella sampling simulations were performed on studied curcumin derivatives, to investigate their permeation through the DPPC model membrane. The potential of mean force (PMF) along the chosen reaction coordinate was calculated for each ligand, while the free energy (ΔG) was derived then from PMF. A meaningful correlation was observed between the inhibitory activity of studied curcumin derivatives against α-amylase and α-glucosidase (reported in Ref. 1) and their PMF profile, in which the one with lowest calculated PMF has less experimentally reported inhibitory activity.

Keywords: Curcumin, Molecular Dynamics Simulation, Umbrella Sampling, Potential of Mean Force.

I. INTRODUCTION

In recent years, many efforts have been done to synthesize and discover new derivatives of curcumin family. Our chosen curcumin derivatives were recently synthesized by Yousefi and co-workers and their inhibitory action against porcine pancreatic α-Amy was justified.[1] These four derivatives, named L2-L5, are listed in Table-1 and represented in Fig. 2: Electron surface potential of curcumin derivatives. A (L2), B (L3), C (L4), D (L5).1 and 2. At first, equilibrium molecular dynamics (MD) simulations were performed on studied curcumin derivatives to determine whether these types of molecules cross the DPPC membrane model. Due to the large free energy barrier in the equilibrium MD simulations, no detectable penetration was observed.

Table-1: IUPAC names of four curcumin derivatives.

| Label	IUPAC NAME
L2	7-((E)-4-Hydroxy-3-methoxystyryl)-6-((E)-3-(4-hydroxy-3-methoxyphenyl) acryloyl)-5-phenyl-1H-pyrano[2,3-d]pyrimidine-2,4(3H,5H)-dione
L3	7-((E)-4-Hydroxy-3-methoxystyryl)-5-(4-chlorophenyl)-6-((E)-3-(4-hydroxy-3-methoxyphenyl)acryloyl)-1H-pyrano[2,3-d]pyrimidine-2,4(3H,5H)-dione
L4	7-((E)-4-Hydroxy-3-methoxystyryl)-6-((E)-3-(4-hydroxy-3-methoxyphenyl) acryloyl)-5-(3-nitrophenyl)-1H-pyrano[2,3-d]pyrimidine-2,4(3H,5H)-dione
L5	7-((E)-4-Hydroxy-3-methoxystyryl)-6-((E)-3-(4-hydroxy-3-methoxyphenyl)acryloyl)-5-(1H-indol-3-yl)-1H-pyrano[2,3-d]pyrimidine-2,4(3H,5H)-dione
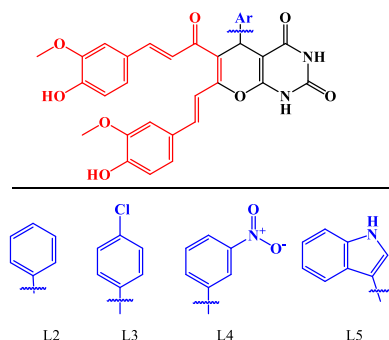
Fig. 1: Chemical structures of synthesized ligands. Different chemical moieties as phenyl, chlorophenyl, nitrophenyl and indolyl were used as the variable aryl (Ar) group in structure of the synthetic inhibitors L2–L5, respectively. (Fig. from Ref. [1])
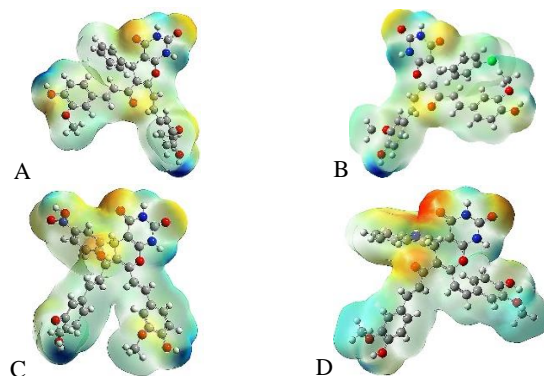

Fig. 2: Electron surface potential of curcumin derivatives. A (L2), B (L3), C (L4), D (L5).

Later, in a series of umbrella sampling simulations, the bias potential was implemented to overcome this free energy barrier and get access to the regions of phase space, being not accessible in normal MD simulations. In umbrella sampling, bias potentials along a reaction coordinate drive a system from one thermodynamic state to another. The intermediate steps are covered by a series of windows, at each of which an MD simulation is performed. From the sampled distribution of the system along the reaction coordinate, the change in free energy in each window can be calculated. The windows are then combined by the weighted histogram analysis method (WHAM) to extract the PMF and calculate the free energy. All calculations and analyses were carried out with the Gromacs simulation package [2].

II. METHOD

Unbiased MD Simulation:

The equilibrium molecular dynamics simulation, without any biasing potential was performed on each ligand to find out whether these molecules are able to cross the DPPC model membrane or not. To obtain the optimized geometries of L2-L5 structures, the Gaussian computational package was utilized. On the other hand, the equilibrated DPPC model membrane, with 64 lipids in each layer was taken from the Tieleman's website.

For each ligand, first the NVT and NPT equilibrium simulations were performed for 100 and 200 ps respectively. Later the systems were subjected to the production MD simulations for 500 ns in NPT ensemble. Close look at the final structures revealed that the high free energy barrier prevented the ligands to penetrate and cross the DPPC membrane.

Biased MD Simulation:

In the biasing or Umbrella Sampling Simulations, in order to force the ligands to overcome the free energy barrier and cross the membrane bilayer, the harmonic potential of 1000 kJ/mol/nm^2 was applied on them, along the reaction coordinate (z-direction, normal to the bilayer). This way a series of configurations were generated along the reaction coordinate, where later 25 frames were extracted from the trajectory at the desired center of mass spacing. Umbrella sampling simulation was performed for 10 ns on each configuration to restrain it within a window corresponding to the chosen center of mass (COM) spacing. Finally the WHAM analysis was utilized to extract the PMF and calculate the ΔG for L2-L5 curcumin derivatives.

III. RESULTS AND DISCUSSION

The most common analysis in umbrella sampling simulations is the extraction of PMF, mainly through the Weighted Histogram Analysis Method (WHAM), included in GROMACS as the wham utility. The value of ΔG is simply the difference between the highest and lowest values of the PMF curve, as long as the values of the PMF converge to a stable value at large COM distance.

Fig. 3 represents the PMF curves for L2-L5 ligands, analyzed by the WHAM method, where the horizontal axis shows the reaction coordinate (z), along which the PMF has been calculated. The zero value in this axis corresponds to the membrane's COM. As shown in Fig. 3, when the L2-L5 molecules approach the bilayer membrane, first they travel through the water layer, adjacent to the bilayer, where the PMF value remains almost constant. By pulling towards the bilayer COM, these molecules experience different moieties, namely the polar DPPC head group, consisting of Choline, phosphate, and carbonyl groups and finally the non-polar hydrocarbon tails.

The global minimum for all curves is around the phosphate group of DPPC molecules, by which the L2-L5 ligands have the most strong interactions. There are also some local minima in each curve, where the ligand molecules are likely to be trapped in normal (unbiased) MD simulations. This is the reason behind the inability of L2-L5 molecules to cross the membrane bilayer in unbiased simulations. In this respect, in umbrella sampling simulations, a bias (an additional energy term) is applied to the systems to ensure efficient sampling along the whole reaction coordinate. The well depth in the PMF curves corresponds to the equilibrium position of the curcumin derivatives in the lipid bilayer. From the interaction point of view, going deeper into the center of DPPC bilayer is less favorable, so the free energy increases dramatically. Finally when the compounds reach the Bilayer COM, the free energy becomes zero.

Having deepest valleys in the PMF curves, shows the stronger effective interactions of L4 and L5 derivatives, with the DPPC's phosphate group. This can be attributed to their greater ability to localize the molecule's overall electron density on their functional groups, hence acting as better electron donating compounds. According to the experimental results, reported in Ref. 1, L4 and L5 are weaker inhibitors in comparison to L2 and L3. In order to act as an inhibitor, the ligand first should cross the membrane and enter the cell's interior. It seems that stronger interactions of L4 and L5 with DPPC's head group, prevents them from penetrating into the membrane, so decreasing their inhibitory activity. On the other hand, L2 and L3 have weaker interactions with the

phosphate group and act as better inhibitors, so in total the curcumin derivative with lower calculated PMF has less inhibitory activity.
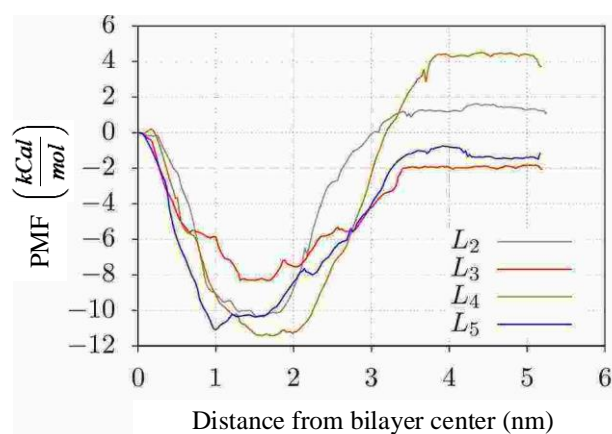

Fig. 3: Potential of mean force curves, for L2-L5 derivatives.

REFERENCES

[1] A. Yousefi, R. Yousefi, F. Panahi, S. Sarikhani, A. R. Zolghadr, A. Bahaoddini, A. Khalafi-Nezhad, International journal of biological macromolecules, 78:pp. 46-55. **2015**.

[2] M. Abraham, D. Van Der Spoel, E. Lindahl,B. Hess, the GROMACS development team, GROMACS user manual version 5.0. 7. Accessed. **2015**.

Molecular Dynamics Simulation Study on the Interaction of Apo-Transferrin with Neomycin

E. Mohammadinezhad[a]*, M.R. Housaindokht[a,b], F. Janati-Fard[a]

a Biophysical Chemistry Laboratory, Department of Chemistry, Faculty of Science, Ferdowsi University of Mashhad, Mashhad, 9177948974, Iran
b Research and Technology Center of Biomolecules, Faculty of Science, Ferdowsi University of Mashhad, Mashhad, 9177948974, Iran
E-mail: e_mohammadin@birjand.ac.ir

Abstract: The interaction of apo-transferrin (apo-Tf) with neomycin was investigated under physiological conditions. Molecular dynamics (MD) simulations study is believed to be an excellent help to perceive the influence of the binding of neomycin on the conformational changes of apo-hTF. The analysis of the RMSF values revealed that the structure of apo-Tf has undergone significant changes in the presence of neomycin. The radius of gyration of the protein becomes larger upon the addition of target indicating a less compact structure and partial unfolding of apo-hTF in the presence of neomycin. The obtained results could open a new pathway in pharmaceutical studies.

Keywords: Transferrin, Neomycin, Interaction, Binding, Simulation

I. INTRODUCTION

Neomycin is an aminoglycoside antibiotic widely used in clinical therapy of serious infections. It inhibits the growth of both gram-positive and gram-negative bacteria. It is also applied as a preventive measure for hepatic encephalopathy and hypercholesterolemia. Neomycin is used to treat gastrointestinal infections of some animals by the oral route and to treat mastitis by intramammary administration [1]. Therefore, the interaction of antibiotics such as neomycin with the plasma proteins is crucial to the health of humans and animals.

Human serum transferrin (hTF) is a single-chain glycoprotein containing around 630 amino acids which are arranged in two similar lobes: the N-terminal (hTFN) and the C-terminal (hTFC) lobes. It reversibly binds two Fe(III) ions, and is the main component in blood for the transport of Fe(III) [2-4]. In the apo-form (apo-hTF) the protein is in the 'open conformation', while upon binding two Fe III ions, forming what we may describe as holo-hTF, the protein adopts a structure which is often designated by 'closed conformation'. In blood serum only 30% of transferrin remains in holo-form while 70% stays in its apo-form (apo-Tf) and can be applied for binding various targets at the same specific sites [5]. Here, we studied the interaction of

neomycin with apo-transferrin using molecular dynamics (MD) simulation.

II. METHODS

MD simulations were performed by GROMACS 5.1.2 and OPLS-AA forcefield was used to parameterize the topology of the protein atoms. The topology parameters of neomycin were built by the LigParGen Server. The solvated system was neutralized by adding sodium ions to the simulation box. Energy minimization was performed using the steepest descent method, followed by the conjugate gradient method. MD simulation (equilibration), the solute (protein, counter ion, and drug) was fixed and the position-restrained dynamics simulation of the system proceeded. Finally, the full system was subjected to 100 ns MD.

III. RESULTS AND DISCUSSION

The root mean-square fluctuation (RMSF) value is a measure of the residue flexibility which shows the deviation between the position of a particle and some reference positions. High flexible domains indicate high fluctuations and therefore these domains can change the structure of protein to the unfolded state [6].

The RMSF of apo-hTF in the absence and presence of neomycin were presented in Fig. 1. It was observed that the fluctuations of apo-hTF in the absence of neomycin are lower than in the presence of neomycin. As shown in Fig. 1, there are regions, including residues 100-160, 250-315 and 345-400 that show essential differences and high flexibility in apo-hTF upon binding neomycin. These results indicate that ligand binding is often associated with changing in conformational structure of apo-hTF.

The average structures of the enzyme were examined. In Fig 2. carton representation of some residues of protein in the absence of ligand was compared with those in the presence of ligand. In these regions, the secondary structure of protein changed and the alpha helix-coil transformation occurred.
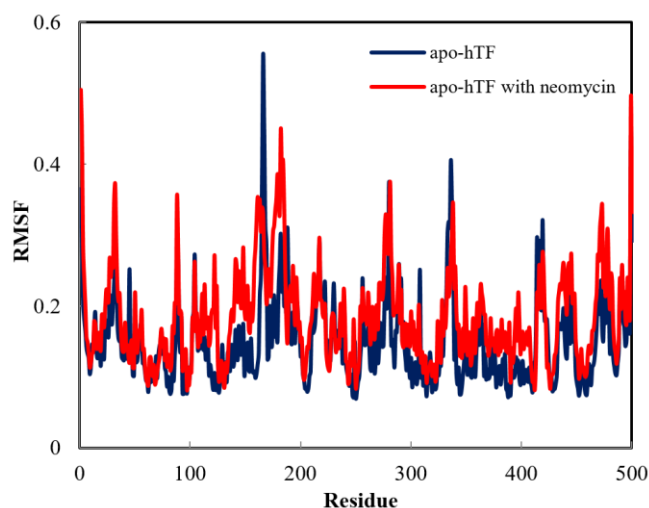
Fig.1. Root mean square fluctuation (RMSF) values of apo-hTF in the absence and presence of neomycin.
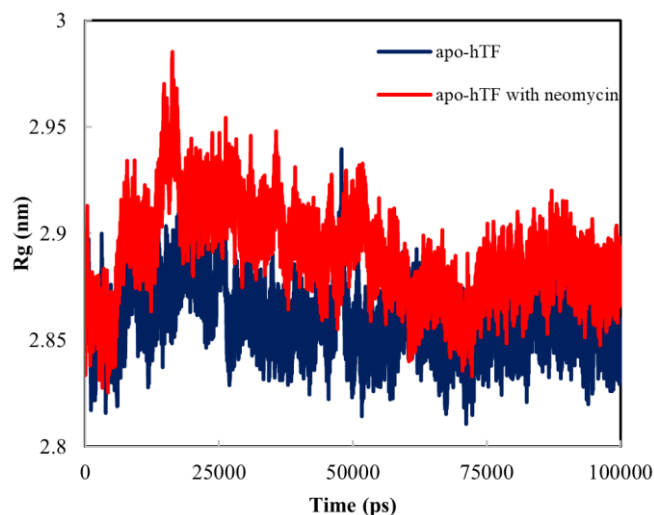

Fig.3. Radius of gyration (Rg) values of apo-hTF in the absence and presence of neomycin.

Fig. 2. Aligned structures of amino acids (110-120) left and (270-275) belonging to apo-hTF in the the absence and presence of neomycin are colored green and red, respectively.

Radius of gyration (Rg) describes the equilibrium conformation of a total system, which could be as an indicator of protein structure compactness [7]. Fig. 3 displays the gyration radius variations for apo-hTF over the simulation time scale. It could be clearly seen that the radius of gyration of apo-hTF becomes larger upon binding of the ligand implying a less compact structure, conformational changes in the structure of protein and partial unfolding of apo-hTF after the simulation.

IV. CONCLUSION

In the study presented here, the interaction between apo-hTF and neomycin was studied by MD simulation technique. The results of the RMSF analysis were in agreement with Rg analysis implied that neomycin can interact with apo-Tf, with affecting the secondary structure of the protein. It is hoped that the present study will open the new approaches for the development of efficient delivery pharmaceutical systems.

REFERENCES

[1] C.B. Cleveland, D.E. Francke, W.M. Heller, J.A. Kepler, G.P. Provost, M.J. Reilly, AHFS Drug, Information, pp. 5167, **1990**.

[2] Z. Ghanbari, M.R. Housaindokht, M.R. Bozorgmehr, M. Izadyar, Journal of Theoretical Biology, vol. 404, pp. 73-81, **2016**.

[3] S. Mehtab, G. Gongalves, S. Roy, MFA. Santos, MJ. Romao, T. Jakusch, T. Kiss, JC. Pessoa, Interaction of vanadium(lV) with human serum apo-transferrin. J Inorganic Biochemistry, vol. 121, pp. 187-195, **2013**.

[4] RW. Evans, X. Kong, RC. Hider, Iron mobilization from transferrin by therapeutic iron chelating agents, BBA - Gen Subjects, vol. 1820, pp. 282-290, **2012**.

[5] Z.M. Qian, H. Li, H. Sun, K. Ho, Targeted drug delivery via the transferrin receptor-mediated endocytosis pathway, Pharmacological Reviews, vol. 54, pp. 561-587, 2002.

[6] S. Shinde, M. Mol, V. Jamdar, S. Singh, Molecular modeling and molecular dynamics simulations of GPI14 in leishmania major: insight into thecatalytic site for active site directed drug design, Journal of Theoretical Biology, vol 351, pp. 327-46, 351,37–46, **2014.**

[7] F. Janati-Fard, M.R. Housaindokht, H. Monhemi, Journal of Molecular Catalysis B: Enzymatic, vol. 134, pp. 16-24, **2016**.

Study of adsorption and separation of CO₂ and H₂S in nanoporous carbon model by GCMC

*Zahra Zarifnia[a], Saeid Yeganegi [b]**

Department of Physical chemistry, Faculty of Chemistry, University of Mazandaran, Babolsar, 47416-13534, Iran

E-mail: z.zarifnia@stu.umz.ac.ir

E-mail: yeganegi@umz.ac.ir

Abstract*:* nanoporous carbon models were constructed for the study of adsorption of H₂S and **CO₂** and separation of H2S/ CH₄ and **CO₂**/CH₄ using Grand Canonical Monte Carlo simulation (GCMC). The models differ in height of channels and cavities**.** we compare our results with experimental values show that our models have higher selectivity values. We found that the vicinity of walls and available volume are two important factors that controls uptake values in low and high pressure respectively.

Keywords*:* Nanoporous carbon, Grand Canonical Monte Carlo, Adsorption, Selectivity

I. INTRODUCTION

Nowadays due to the industrialization of cities, the use of fossil fuels has increased dramatically [1]. Natural gas because of low emissions of greenhouse gases and particulate matter after combustion has an ideal substitute for fossil fuels [2].

Raw natural gas contains different impurities such as carbon dioxide, hydrogen sulfide, nitrogen and water depending on the location of gas fields [3]. CO_2 decreases the heat content of natural gas [4], H₂S is toxic for the human body. Acidic gas reacts metals and causes to high corrosion in pipeline and devices [5], they increase the greenhouse gas emission. However, before using it on a commercial scale, it has to meet several specifications [6].

There are several methods for sweetening NG such as membrane separation, chemical conversion, ionic liquid adsorption, and nanoporous materials, but carbon-based nanoporous material is the most attractive candidate for room temperature due to low cost, no toxicity, high availability, low weight, adjustable pore volume, high porosity, and surface area, good chemical and thermal stability.

In this work, we constructed nanoporous carbon models consist of channels and cavities. Adsorption of H2S and CO2 and their selectivities from binary mixtures were investigated by the Grand Canonical Monte Carlo simulation (GCMC) at 298.15 K.

II. METHODS

The models created by using an in-house FORTRAN program which made appropriate bend and cusp on a graphene sheet. The models differ in the height of channels and cavities. For example, the height of channels in series-5 models are 5 Å and the height of cavities were the ratio of the height of the channels, series-7, and series-9 models were made similarly.

The adsorption isotherms and separation selectivities of gases were obtained by Grand Canonical Monte Carlo simulation (GCMC). Lennard–Jones cross interaction parameter were calculated by Lorentz-Berthelot mixing rules. Periodic boundary conditions were applied in all Cartesian directions. The adsorption selectivity of component i versus j was calculated as Eq. (1):

$$S_{i/j} = \frac{(x_i/x_j)_{pore}}{(x_i/x_j)_{bulk}}$$

Where x_i denotes the molar fraction of component i, and $(x_i/x_j)_{pore}$ and $(x_i/x_j)_{bulk}$ refer to the pore and bulk properties, respectively.

Peng-Robinson of state (PR Eos) was used for converting the input pressures to fugacities. The standard Ewald summation method was used to calculated electrostatic interaction. Table 1 shows the atomic potential parameters and partial charges used in this works.

Table 1: the potential parameters used for simulations

Atom	σ (Å)	ε/KB (K)	q (e)	Refrence
C (model)	3.4	28	-	[7]
C (CH₄)	3.4	55.055	-0.66	[8]

H (CH₄)	2.65	7.901	+0.165	
C (CO₂)	2.80	27	+0.70	[9]
O (CO₂)	3.05	79	-0.35	
S (H₂S)	3.72	250.0	-0.248	[10]
H (H₂S)	0.98	3.9	+0.124	

III. RESULTS AND DISCUSSION

Adsorption isotherms for CO_2 and H_2S were calculated at 298.15K and different pressures for nanoporous carbon models using Grand Canonical Monte Carlo (GCMC) simulation. Fig. 1 shows the adsorption isotherms of CO_2 in 3 models at 298.15 K.
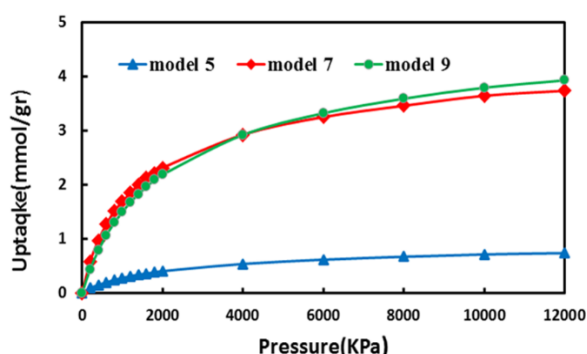

Fig. 1: The adsorption isotherms for CO_2 at 298 K

As illustrated in Fig. 1 model 5 has the lowest amount of CO_2 loading due to the small height of the channel in model 5 which prevents molecules from entering the channel.

The amount of adsorption in models 7 and 9 are similar to each other. At low-pressure range, the loading amounts in model 7 are greater than that of model 9 because of the deeper overlap of potential resulting from the vicinity of two walls of channels. At high-pressure region, model 9 has greater values of loading than model 7, which can be referred to the larger available volume control of the loading amounts. The amount of adsorption in models 7 and 9 are similar due to competition to mentioned factors.

We calculated adsorption values of CO_2 as 0.5772, 3.3965, 2.6142 for model 5, 7, 9 respectively at 298.15 K and 100 kPa, and Yang et al calculated 1 for CNT(10,0), 1.5 for CNT(12,0), 2.4 for CNT(13,0), 2.35 for CNT(14,0), 2.25 for CNT(16,0)[11] at same conditions. We investigated the adsorption of H_2S in the mentioned models at 298.15 K and range 0-2000 kPa. In all pressure ranges, model 5 has the lowest uptake. Uptake of CO_2 in model 7 is greater than model 9 at a pressure lower than 300 kPa, in the rest of the pressure

model 9 has the greater value of loading than model 7. We calculated excess values for comparison. The excess value for H_2S at 303 K and 1600 kPa were calculated 1.5264, 6.2417, 6.6787 for model 5, 7, 9 respectively and Wang et al calculated 1.97 for CNT(6,6), 5.41 CNT(10,10) [12]. In this work the percentage of compounds of sour gas of Sarakhs was used. We calculated $S_{H2S/CH4}$ and $S_{CO2/CH4}$ for models 5, 7 and 9 in the ternary mixture at 298.15 K and 500 kPa, SCO2/CH4 values are 23.57, 62.48, 18.7979 for 5, 7, 9 models, respectively. Yeganegi and Gholampour calculated the same parameter 2.1 for slit-0 and 3.9 for slit-2 at 298.15 K and 500 kPa [13]. Model 7 has the highest value of selectivity, which can be contributed to the vicinity of two walls in the channels that results larger attraction between CO_2 and channels walls. The calculated selectivities in model 5 is greater than model 9 due to the small height of channel in model 5 doesn't allow any molecule adsorbs, in contrast to model 9, CO_2 and CH_4 adsorbed, therefore selectivity decrease. We calculated SH2S/CH4 are 109.23, 537.8099 and 85.8213 for model 5, 7, 9 respectively at 298.15 K and 1000 kPa, Yeganegi and Gholampour obtained 2.9 for slit-0 and 5.6875 for slit-2 at same conditions [13].

IV. CONCLUSION

In the present study, we used the GCMC method for study the adsorption behavior of pure CO_2 and H_2S and CH_4/ CO_2 /H_2S in the ternary mixture for nanoporous carbon models at 298.15 K and different ranges of pressure. The effect of height of channels was studied to obtain the best height of channel for models.

The results show that model 5 has the lowest adsorption and selectivity value in all ranges of pressure for each case of the studied gas molecules. Despite model 7 has the greatest selectivity in all range of pressure, similar adsorption behaviors have been observed for 7 and 9 Models.

REFERENCE

[1] J. H. Zhang, B. X. Shen, H. Sun and J. C. Liu, Pet. Sci. Technol, vol. 29, pp. 48-58, **2011**.

[2] L. Liu, D. Nicholson, S. K. Bhatia, Chem. Eng. Sci, Vol. 121, pp. 268-278, **2015**.

[3] G. Lei, Ch. Liua, Q. Lic, X. Xu, Fuel, Vol. 182, pp. 210-219, **2016**.

[4] R. Sitthikhankaew, S. Predapitakkun, R. W. Kiattikomol, S. Pumhiran, S. Assabumrungrat,and N. Laosiripojana, Energy Procedia, Vol. 9, pp. 15-24. **2011**.

[5] K. L. Bae, H. Milford, Frost, P. Rayan, S. Punnathanam, L. Broadbelt, J. T. Hupp and R. Q. Snurr, Langmuir, vol. 24, pp. 8592-8598, **2008**.

[6] I. Skarmoutsos, G. Tamiolakis, and G. E. Froudakis, J. Phys. Chem. C, vol. 117, pp. 19373-19381, **2013**.

[7] J. C. Palmer, J. D. Moore, T. J. Roussel, J. K. Brennanb and K. E. Gubbins, Phys. Chem. Chem. Phys , vol.13, pp 3985–399, **2011**.

[8] A. P. Lyubartsev, O. K. Forrisdahl, and A. Laaksonen, J. Chem. Phys. Vol. 108, pp 227- 233, **1998**.

[9] V. Sokhanvaran and S. Yeganegi, Chem. Phys. Chem, vol. 17, pp. 4124-4133, **2016**.

[10] S. K. Nath, phys. Chem. B, vol. 107, pp. 9498-95.4, **2003**.

[11] T. Yang, L. Lu, S. Wang, W. Cao, Mol. Simul, vol. 43 , pp 1-11, **2017**.

[12] W. Wang, X. Peng, D. Cao, Environ. Sci. Technol, vol. 45, pp. 4832-4838, **2011**.

[13] F. Gholampour, S. Yeganegi, Chem. Eng. Sci, vol. 117, pp. 426-435, **2014**.

Dispersion-Corrected Density Functional Study of two Acylhydrazone Molecular Photoswitches

M. Zare*, S. Heliche

Department of Chemistry, Faculty of Science, Shahid Chamran University of Ahvaz, Ahvaz, 43337, Iran
Email: m.zare@scu.ac.ir

Abstract*:* We assess quantum chemical calculations, mostly based on density functional theory, on acylhydrazones, in ground and excited states. The solvent effects on the geometry and stability of the molecular isomers have been investigated. We find that the *Z* isomers are more stable than the *E* configuration both in vacuum and solvent. The long range corrected CAM-B3LYP functional is more suitable than the B3LYP to reproduce the experimental UV spectra.

Keywords: Acylhydrazone, DFT, Grimme's dispersion corrected (D3), Photoswitches, TD-DFT.

I. INTRODUCTION

Photoswitches are a class of chemical compounds that can reversibly be converted from one state, or isomer, into another with light. The photochromic molecules undergo photoswitchable behaviour such as ring-opening and -closing and isomerization around double bonds [1, 2]. Molecular photoswitches presented large variety of potential applications in information storage, photopharmacology, controllable drug transport and release, single-molecule localization microscopy, photogated electrical devices, selective dual-channel imaging, acidic sensing materials [3]. A new class of molecular photoswitches based on hydrazone compounds are attracting increasing interest due to their facile synthesis, modularity, functional diversity, and fatigue resistance. The *E−Z* isomerization of C=N bonds in hydrazone under light irradiation has been known for long time (Fig.1), but the (*Z*)-isomer is often very unstable and is inappropriate for photoswitches [3]. Very recently, Yuan and Zheng [3] reported new acylhydrazones with high *E−Z* conversion efficiency. Here, we study the geometrical, electronic and optical properties of two acylhydrazones **1** and **2** (Fig.1).
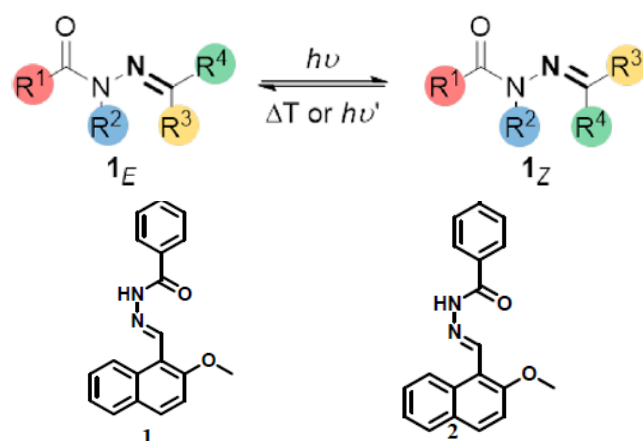
II. METHODS

All Density Functional Theory calculations have been performed in Gaussian 09. In this work the dispersion corrected density functional theory (DFT-D3) for all ground state calculations and time-dependent density functional theory (TD-DFT) methods with the same functional for excited states. We employed the B3LYP and CAM-B3LYP functionals with conjugation 6-311++G(d,p) basis set for optimizing the geometry and calculating the vibrational frequencies. No imaginary frequency is found, confirming that the geometries are true local minimum on the potential energy surface. Solvent effects are taken into account using a Polarizable Continuum Model with the Integral Equation Formalism variant (IEFPCM) as implemented in Gaussian.

Fig.1: Isomerization scheme and structure of acylhydrazone photoswitches.

III. RESULTS AND DISCUSSION

The optimized structures of both isomers for **1** and **2** at the B3LYP/6-311++G** level shown in Fig.2.
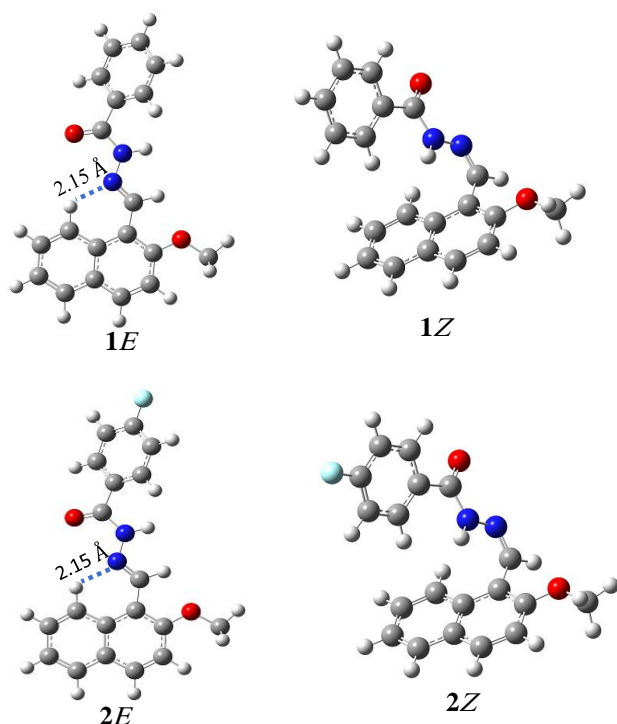
1*E*   **1***Z*

2*E*   **2***Z*

Fig. 1: Optimized structures of studied acylhydrazones at B3LYP/6-311++G**.

Table 1: Calculated energies of the *Z* and *E* isomers of acyldrazone compounds **1** and **2** and relative energies without and with solvent (DMSO) correction. Solvent corrected values are in bold.

Method	Isomer	E /Hartree	E_{rel} /kcal.mol^{-1}
B3LYP(D$_3$)	1*Z*	-993.878366 **-993.897217**	0 **0**
	1*E*	-993.878149 **-993.896523**	0.14 **0.44**
	2*Z*	-1093.148003 **-1093.166918**	0 **0**
	2*E*	-1093.14743 **-1093.166163**	0.36 **0.47**
CAM-B3LYP(D$_3$)	1*Z*	-993.347215 **-993.366623**	0 **0**
	1*E*	-993.346543 **-993.365418**	0.42 **0.76**
	2*Z*	-1092.60007 **-1092.619527**	0 **0**
	2*E*	-1092.599059 **-1092.618286**	0.63 **0.78**

The *E* isomers are approximately planar, whereas the *Z* isomers are non-planar. An intramolecular hydrogen bond between imine nitrogen and the nearest hydrogen of the benzo moiety is observed for *E* isomers (2.15 Å for both **1** and **2**) but no intramolecular hydrogen bond is found for *Z* isomers.

Table 2: Calculated transitions and oscillator strengths (*f*) of the *Z* and *E* isomers of the acylhydrazones **1** and **2** (in DMSO).

Method	Molecule	Isomer	λ cal. /nm	f	λ exp. /nm
TD-B3LYP	1	*E*	399.96	0.7641	365
			292.88	0.5799	
			270.1	0.179	
		Z	348.9	0.2363	294
			283.33	0.1788	
			256.11	0.1739	
TD-CAM-B3LYP	1	*E*	348.54	0.7754	365
			243.5	1.2308	
			211.5	0.0997	
		Z	305.6	0.3203	294
			235.04	1.5333	
			206.11	0.3443	
TD-B3LYP	2	*E*	399.6	0.76	365
			319.63	0.1688	
			292.73	0.176	
		Z	348.78	0.2357	294
			296.05	0.0846	
			282.86	0.1729	
TD-CAM-B3LYP	2	*E*	349.84	0.7797	365
			243.51	1.2247	
			203.54	0.4854	
		Z	305.88	0.3199	294
			240.34	0.3467	
			235.54	0.4854	

Experimental absorption wavelengths (λexp.) are also included.

The calculated energies of two acylhydrazones are shown in Table 1. The *Z* configurations are more stable than *E*, which is consistent with experimental results [3]. The solvent corrected relative energies are more than uncorrected values.

Table 2 shows the absorption bands and oscillator strengths for the first three excited states of **1** and **2** compound at the B3LYP/6-311++G** and CAM-B3LYP/6-311++G** levels of theory and compared with the experiment. The results of the CAM-B3LYP are in agreement to the experimental values.

II. CONCLUSION

We utilize two different DFT functionals for obtaining the equilibrium geometries, the vibrational frequencies and the optical properties of *E*/*Z* acylhydrazone photoswitches. Calculations were performed both in vacuum and in the DMSO solvent. It was found that both functionals correctly predicted the more stable configuration (*Z*). The analysis of the optical properties show that the long range corrected CAM-B3LYP functional is appropriate to reproduce the experimental UV spectra.

REFERENCES

[1] A. Beharry, and G. A. Woolley, Chem. Soc. Rev., vol. 40, pp. 4422–4437, **2011**.

[2] W. ski, J. Beierle, H. Kistemaker, W. Velema, and B. Feringa, Chem. Rev., vol. 113, pp. 6114–6178, **2013**.

[3] Y. Yuan, and Y. Zheng, ACS Appl. Mater. Interfaces, vol. 11, pp. 7303–7310, **2019**.

Thermal Expansion Coefficient of sI Clathrate Hydrates by Molecular Dynamics Simulation

Hakime Ghafari[a], Hossein Mohammadi-Manesh[a]*
[a]Department of Chemistry, Faculty of science, Yazd University, Yazd, P.O. Box 89195-741, Iran
*Email:mohammadimanesh@yazd.ac.ir

Abstract: We perform molecular dynamics simulations for the structure I (sI) clathrate hydrates of linear molecules Acetylene (C_2H_2), Carbon disulfide (CS_2) and Carbonyl sulfide (OCS) under a wide range of pressure and temperature conditions. Systems studied include sI binary clathrate hydrates of C_2H_2 (large 14-sided cage, L) + CH_4 (small 12-sided cage, S), CS_2 (L) + CH_4 (S) and OCS (L) + CH_4 (S). The simulations were started with guest molecules positioned at the cage center of the hydrate. Two water models, the SPC/E and TIP4P/ice, were used in the simulations. We focus on the calculation of the lattice parameters of the three hydrates and their dependence on temperature. The slope of the lattice parameters against temperature use to calculation isobaric thermal expansion.

Keywords*:* Clathrate hydrate, MD simulation, Lattice parameter, Isobaric thermal expansion

I. INTRODUCTION

Clathrate hydrates are non-stoichiometric crystalline inclusion compounds which the host in the crystalline structure contains cavities, holes or channels that guest atoms or molecules with appropriate size are trapped [1]. Clathrate hydrate form at low temperature and high pressure and have different application such as cool energy storage [2], natural gas storage and transport [3], gas sequestration [4], seawater desalination [5]. In almost all of the previously mentioned applications, the understanding of thermodynamic properties such as lattice parameters of the clathrate hydrates and derivative properties namely, the thermal expansion coefficient are essential. Moreover, experimental researches [6-8] and theoretical studies [9, 10] have been carried out in order to investigate effect of type and size guest, structure of cages and number of the guest molecules in the cages on the lattice parameter and thermal expansion clathrate hydrate. In this paper, we perform the MD calculations in order to study the effect of the linear guest molecules on the thermal properties of clathrate hydrate.

II. COMPUTATIONAL DETAILS

The initial coordinates of the water oxygen atoms in the sI clathrate are taken from clathrate X-ray crystallography [11] and the initial positions of the water hydrogen atoms were chosen to be consistent with the ice rules while simultaneously minimizing the total dipole moment of the sI unit cell. Guest molecules are initially placed in the center of the cages and their positions are equilibrated during the simulation. Snapshots of C_2H_2 guest molecule in a large sI clathrate cage from two perspectives are shown in Fig. 1.

In the simulations, $3 \times 3 \times 3$ replica of the sI clathrate hydrate unit cell with 46 water molecules is used. To equilibrate the initial configurations of each clathrate, isotropic NpT molecular dynamics simulations with the Nose´–Hoover thermostat–barostat algorithm [12, 13] with relaxation times of 0.1 and 1.0 ps, respectively were performed using the DL_POLY molecular dynamics program version 2.18. Columbic Long-range interactions were calculated using the Ewald summation method and all interatomic interactions in the simulation box were calculated within a cutoff distance of R_{cutoff}=15 Å. Simulations in NpT ensembles for each clathrate hydrate by 270 ps with an equilibration time of 70 ps are performed.
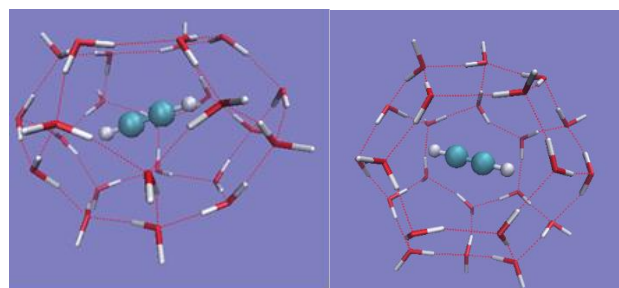

Fig. 1: Snapshots of a large sI clathrate cage with a C_2H_2 guest molecule at 200 K (part left). The same configuration as part left seen from above (part right).

III. RESULTS AND DISCUSSION

We are considered the lattice parameter as a function of temperature for C_2H_2, CS_2 and OCS guest molecules in temperatures 50-250 K at ambient pressure that shown with SPC/E and TIP4P/ice water model in Fig. 2. In all of case, we observe that the lattice parameters increase as the temperature increases. The lattice parameter is predicted for

three clathrate hydrate to be larger for TIP4P/ice than SPC/E simulation.

The slopes of the lattice parameters as a function of temperature appear similar. The slope of this Figure is related to thermal expansion (α) that this property were obtained according to the following definition, where a is lattice parameters, Å :

$$\alpha = \frac{1}{a}\left(\frac{\partial a}{\partial T}\right)_{P,n} \tag{1}$$

If α as a function of temperature is assumed to be:

$$\alpha = a_1 + a_2(T - T_0) + a_3(T - T_0)^2 \tag{2}$$

By separation of variables and integration we obtained Eq. 3:

$$\ln\left(\frac{a}{a_0}\right) = a_1(T - T_0) + \frac{a_2}{2}(T - T_0)^2 + \frac{a_3}{3}(T - T_0)^3 \tag{3}$$
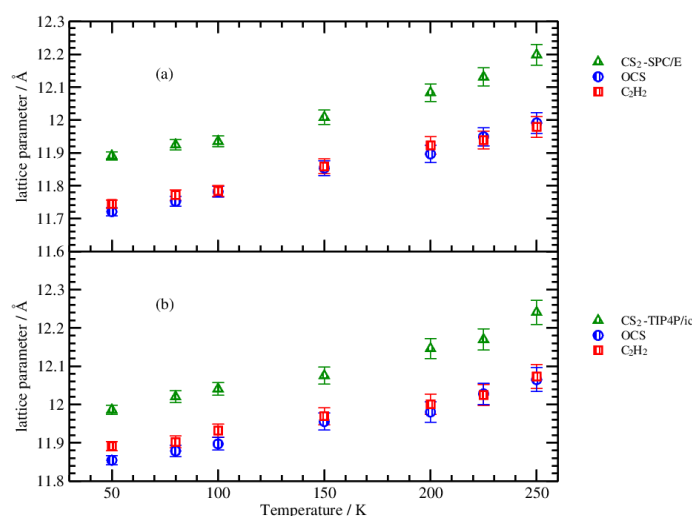
Fig.2: Lattice parameters for sI clathrate hydrates of the C_2H_2, CS_2 and OCS as a function of temperature with (a) SPC/E and (b) TIP4P/ice water model water model at atmospheric pressure.

Where a_0 is the lattice parameter at a reference temperature T_0. Expansion coefficients of Eq. (3) (a_1, a_2, a_3) have obtained by fitting the curve of ln (a/a_0) against ($T-T_0$) in third order polynomials. The coefficients a_1, a_2, a_3 for C_2H_2, CS_2 and OCS guest species in clathrate hydrate using SPC/E and TIP4P/ice water model at atmosphere pressure given in Table 1.

Table1: Coefficients for the third order polynomial fits of the lattice parameter of the C_2H_2, CS_2 and OCS hydrate as a function of temperature using both the SPC/E and TIP4P/ice water potentials.

SPC/E	a_1 (×10⁻⁵)	a_2 (×10⁻⁷)	a_3 (×10⁻⁹)	R^2
C_2H_2	5.76	9.994	-4.530	0.9979
CS_2	8.40	-0.0468	3.564	0.9991
OCS	11.58	-4.902	3.505	0.9996
TIP4P/ice				
C_2H_2	7.39	-6.281	4.712	0.9939
CS_2	11.41	-13.51	9.371	0.9999
OCS	9.05	-6.254	4.465	0.9989

The thermal expansion of C_2H_2, CS_2 and OCS guest species for both pressure can be calculated by expansion coefficient given in Table 1 and Eq. 2 for SPC/E and TIP4P/ice water model.

IV. CONCLUSION

In this work, we performed MD simulation to study thermal properties of sI hydrates including C_2H_2 (L) + CH_4 (S), CS_2 (L) + CH_4 (S) and OCS (L) + CH_4 (S) guest molecules with the TIP4P/ice four-site and SPC/E water potentials. We have presented the dependence of lattice parameters and thermal expansions on temperature for guest molecules that are different in size and chemical nature.

The following general observations can be made:

- The TIP4P/ice model, often predicts larger lattice parameter and smaller thermal expansion than SPC/E potential.
- The lattice parameter for all of three clathrate hydrate increases as the temperature increases.
- The lattice parameters for CS_2 (L) + CH_4 (S) binary hydrate are larger than the lattice parameters for OCS (L) + CH_4 (S) and C_2H_2 (L) + CH_4 (S) hydrates.

REFERENCES

[1] E.D. Sloan Jr, C. Koh, Clathrate hydrates of natural gases, 3rd ed.; CRC Press, Taylor & Francis Group: Boca Raton, FL, **2008**.

[2] Y. Bi, T. Guo, T. Zhu, L. Zhang, L. Chen, Energy Convers. Manage, vol. 47, pp. 2974, **2006**.

[3] J. S. Gudmundsson, M. Parlaktuna, A. A. Khokhar, SPE Prod. Facil, vol. 9, pp. 69, **1994**.

[4] Y. Park, D. Y. Kim, J.-W. Lee, D.-G. Huh, K.-P. Park, J. Lee, H. Lee, Proc. Natl. Acad. Sci. U.S.A., vol. 103, pp. 12690, **2006**.

[5] J. Javanmardi, M. Moshfeghian, Appl. Therm. Eng., vol. 23, pp. 845, **2003**.

[6] T. Ikeda, S. Mae, O. Yamamuro, T. Matsuo, S. Ikeda, R.M. Ibberson, J. Phys. Chem. A, vol. 104, pp.10623-10630, **2000**.

[7] S. Takeya, M. Kida, H. Minami, H. Sakagami, A. Hachikubo, N. Takahashi, H. Shoji, V. Soloviev, K. Wallmann, N. Biebow, Chem. Eng. Sci., vol. 61, pp.2670-2674, **2006**.

[8] K. Hester, Z. Huo, A. Ballard, C. Koh, K. Miller, E. Sloan, Thermal expansivity for sI and sII clathrate hydrates, J. Phys. Chem. B, vol. 111, pp.8830-8835, **2007**.

[9] V.R. Belosludov, T.M. Inerbaev, O.S. Subbotin, R.V. Belosludov, J.-i. Kudoh, Y. Kawazoe, Supramol. Chem., vol. 2, pp. 453-458, **2002**.

[10] H. Jiang, K.D. Jordan, C. Taylor, J. Phys. Chem. B, vol. 111, pp. 6486-6492, **2007.**

[11] T.C. Mak, R.K. McMullan, Polyhedral clathrate hydrates. X. Structure of the double hydrate of tetrahydrofuran and hydrogen sulfide, J. Chem. Phys., vol. 42, pp. 2732-2737, **1965**.

[12] W.G. Hoover, Canonical dynamics: equilibrium phase-space distributions, Physical review A, vol. 31, pp.1695, **1985**.

[13] S. Melchionna, G. Ciccotti, B. Lee Holian, Hoover NPT dynamics for systems varying in shape and size, Mol. Phys., vol. 78, pp.533-544, **1993**.

DFT Study of Novel Drug Delivery Systems Comprising Nanoparticles Based on Chitosan Nanoparticles/Graphene Oxided/Folic Acide For Deliver Targeted of The Chemotherapy Drugs.

Seyede Mahtab Hosseini[a*], **azim soltanabadi**[b], **Majid Abdouss**[a] , **Saeedeh Mazinani**[c]

[a]*Department of Chemistry, Amirkabir University of Technology, 424 Hafez Avenue, P. O. Box 15875-4413, Tehran, Iran.*
[b]*Faculty of Chemistry, Razi University, University Avenue, Taq-e Bostan, Kermanshah*
[c]*New Technologies Research Center (NTRC), Amirkabir University of Technology, Tehran, Iran*
Email: 55hossini55@gmail.com

Abstract: The optimized geometries, electronic structures, of Graphene Oxided (GO) and Nanoparticles Graphene+Oxided+Folic Acide (GOF) were investigated using density functional theory (DFT) calculations. This study was carried out using computerized calculations of Gaussian program in Becke 3-parameters Lee-Yang-Parr (B3lyp/6-31g level GO and GOF in gas phase. Also the stability, highest occupied molecular orbital (HOMO) and lowest unoccupied molecular orbital (LUMO) levels, chemical hardness, and electrophilicity properties of GO and GOF calculated and compared each other's.

Keywords: DFT, Nanoparticles, HOMO, LUMO

I. INTRODUCTION

In recent decades, significant advances have been made in drug delivery systems that have more effective drug therapies. Nanoparticles can be used frequently as drug delivery due to its great bioavailability, control release and less toxic properties .graphne oxide (GO) was prepared from purified natural graphite according to a modified Hummer's method. GO have been extensively used as some of the most favourable biomaterial for biomedical application due to their unique propertices such two-dimensional planar structure with sp^2 hybridized carbon atoms, large surface area, chemical and mechanical stability and good biocompatibility [1-3]. We study a novel drug delivery systems comprising nanoparticles based on chitosan nanoparticles/graphene oxided/folic acide for deliver targeted of the chemotherapy drugs. Chitosan has properties such biodegradability, biocompatibility, antibacterial, nontoxic and anti-infective activity [4,5]. First graphene oxide is synthesized and then chitosan nanoparticle is grafted to graphene oxide by chemical interaction and Folic

acid was then loaded onto carriers of chitosan nanoparticle / graphene oxide and drug release was investigated on nano carriers.

II. METHODS

The quantum chemical calculations were used to predict the equilibrium geometry of of Graphene Oxided (GO) and Nanoparticles Graphene+Oxided+Folic Acide (GOF). The geometry optimization and electronic properties calculations were performed at the Becke's three parameter hybrid method with LYP correlation (B3LYP) [6, 7] level of DFT with 6-31+G basis set for all atoms. All calculations are carried out using the Gaussian 09 suites of program. The optimized structure of the GO and GOF in the gas phase are shown in Fig 1a and b respectively.

III. RESULTS AND DISCUSSION

Figure 1a and ab shows that the optimization structure of Graphene Oxided (GO) and Nanoparticles Graphene+Oxided+Folic Acide (GOF). Fig 1a show that the geometry optimization of GO molecule is flat, which, after increasing chitosan on both sides of graphene oxide, chitosans molecules bend up and down (Fig 1b). Several quantities such as HOMO-LUMO gap (Egap), global (or chemical) hardness (η), chemical potential (μ) and electrophilicity (ω), can be calculated within this framework. They calculated using information on HOMO and LUMO and dipole moment. The calculated values of the HOMO and the LUMO energies (in eV) and gap between them for this material are reported in Table 1. By comparing the dipole moment between GO and GOF, we conclude that the bipolar moment of GO is greater than GOB. A small HOMO-LUMO gap in atomic units automatically means small excitation energies to the excited
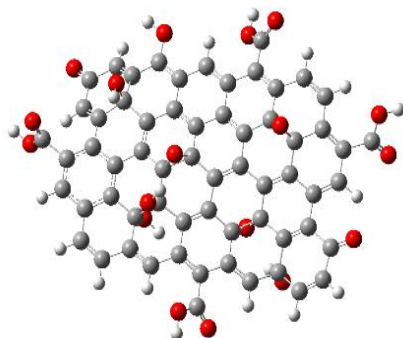
states. Therefore GOF is more conductive than GO (Table 1). Also, EHOMO is the first vertical ionization energy and ELUMO the electron affinity of the molecules.
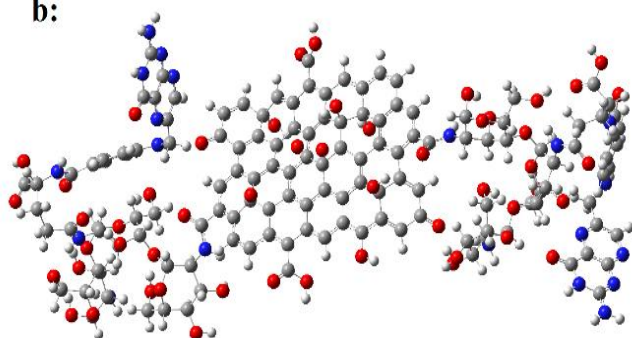
a:

b:

Fig.1 Structures of (a) GO, (b) GOF optimized at B3LYP/6-31++G(d,p) level of theory..

Table1. Quantum molecular description calculated for GO and GOF obtained by B3LYP/6-31G level in gas phase

Indices	GO	GOF
HOMO (a.u.)	-0.320	-0.0009
LUMO (a.u.)	-0.112	0.004
HLG (EHOMO-ELUMO) (a.u.)	0.208	0.0049
Hardness ($\eta = \frac{EHOMO-ELUMO}{2}$) (a.u.)	0.216	0.0024
Chemical Potential ($M = \frac{1}{2(EHOMO+ELUMO)}$) (a.u.)	6.513	17.305
Electrophilicity ($\omega = \frac{-M^2}{2\eta}$) (a.u.)	98.192	61114.89
$\Delta N_{max} = \frac{-M}{\eta}$ (a.u.)	-30.152	-7063.26
Dipole moment (Debye)	6.5134	17.3058

IV. CONCLUSION

In this work, we perform geometry optimization and electronic structures of GO and GOF by density functional theory. The result show that the geometry optimization of GO molecule is flat and dipole moment of GO is 6.5134 debye While the dipole moment of molecule GOF is 17.3058 debye. The high Dipole-Moment causes the GOF to be better dissolved in water and polar solution. Also, chemical hardness in GOF was lower than GO. So according to electrophilicity and ΔN_{max} parameter, GOF is a softer acid than GO. In terms of chemical reactivity, it can be concluded that soft molecules will be more reactive than hard molecules for uni-molecular reaction such as isomerization and dissociation. This can be useful for future pharmaceutical researches, since this action can cause interesting medicinal properties.

REFERENCES

[1] S. Priyadarsini, S. Mohanty, S. Mukherjee, S. Basu, M. Mishra, Journal 8:123–137, **2018**.

[2] Y. Teng Fong, C. Chen, and J. Chen, Journal, 7, 388, **2017**.

[3] M. Hirata, T. Gotou, Sh. Horiuchi, M. Fujiwara, M. Ohba, Journal, 42 2929–2937, **2004**.

[4] K. Divya, M. S. Jisha, Journal, Volume 16, Issue 1, pp 101–112, **2018**.

[5] A. Francesko and T. Tzanov, Journal, 125:1-27, 2011.

[6] A. Becke, AD Becke,), *J. Chem. Phys.,* vol. 98, p. 5648, **1993**.

[7] C. Lee, W. Yang, and R. G. Parr, *Physical review B,* vol. 37, p. 785, **1988**.

[8] Chattaraj PK, Chakraborty A, Giri S. Net Electrophilicity.
J Phys Chem.113,10068-74. **2009**

[9]. Parr RG, Szentpály LV, Liu S. Electrophilicity index. J Am
Chem Soc.;121:1922-4. **1999**

Local Microscopic Structure of the Biocompatible Cholinium Glycinate Ionic Liquid

M. H. Kowsari[a]*, F. Khorrami[a]

Department of Chemistry and Center for Research in Climate Change and Global Warming (CRCC), Institute for Advanced Studies in Basic Sciences (IASBS), Zanjan, 45137-66731, Iran

Email: mhkowsari@iasbs.ac.ir and mohammad.kowsari@gmail.com

Abstract: Atomistic molecular dynamics simulations have been used to study the local structure and hydrogen bonds (H-bonds) in the neat cholinium glycinate ionic liquid (IL), [Cho][Gly]. The microscopic structural details has been determined by calculation of the radial, spatial, angular, and combined distribution functions. For more local structural clarity, the main relative orientations of the nearest neighbors have been investigated. We observed that the adjacent [Cho]$^+$ cations are often antiparallel relative to each other, while in the cationic trimer, a perpendicular orientation is also distinguished. [Gly]$^-$ has the role of a bridge between two [Cho]$^+$ cations in the liquid phase.

Keywords: Cholinium glycinate, Distribution functions, Ionic liquids, Molecular dynamics.

I. INTRODUCTION

Despite the unique properties of common ILs, they exhibit some limitations, including potential toxicity, high cost and viscosity, and poor biodegradability. Thus, it is necessary to synthesize the green ILs from renewable bio-resources. In 2005, Ohno *et al.* [1] have proposed a class of ILs based on 1-ethyl-3-methylimidazolium cation, [emim]$^+$, and amino acid-derived anions, [AA]$^-$. The [Cho][AA] ILs were synthesized and introduced by Liu et al. in 2012 [2]. They also reported a very good enhancement of the enzymatic hydrolysis of microcrystalline cellulose and rice straw after pretreatment using the [Cho][Gly] IL.

On one hand, amino acid ILs (AAILs) have unique physicochemical properties such as the traditional ILs. On the other hand, they have important features of biocompatibility, very good biodegradability, and reasonable cost. However, in general, AAILs show relatively high viscosity and low diffusivity as a drawback in many practical applications. This limitation is eliminated for the [Gly]$^-$-based ILs which have the lowest viscosity among AAILs with the same cation counterions. The structural and dynamical properties of some AAILs have been reported based on molecular dynamics (MD) simulations during the last decade [3].

II. METHODS

MD Simulation has been performed in the isothermal−isobaric ensemble (*NpT*) with the temperature of 353 K and the pressure of 1.0 atm using the DL_POLY 2.18 software for 180 ion pairs of [Cho][Gly] in the simulation box. The force field parameters of the [Cho][Gly] IL have been taken from the work of Aparicio et al [4]. The run-time is 10 ns and data saving interval is every 1 ps in the trajectory file.

Periodic boundary conditions have been employed and electrostatic interactions were calculated using the Ewald summation method. A radius potential cutoff (15 Å) has been used for considering the short ranged van der Waals interactions. The Newton's equations of motion have been integrated by using the Verlet leapfrog algorithm with a time step of 1 fs. The Nosé–Hoover method has been applied for maintaining temperature and pressure with coupling constants of 0.2 and 1.0 ps, respectively.

III. RESULTS AND DISCUSSION

Microscopic structural analysis of ILs based on the investigation of the preferred arrangement of the nearest neighbors help to understand more insight about the origin of unique properties of these neoteric liquids. Therefore, we have studied the structural details of the pure IL. Radial distribution function (RDF) based on both the atomic site-site and center of mass (COM) of species pairs, angular distribution function (ADF), combined distribution function (CDF), spatial distribution function (SDF), and snapshots of equilibrated simulation box is used to obtain clear insight regarding the structural features of pure [Cho][Gly] IL.
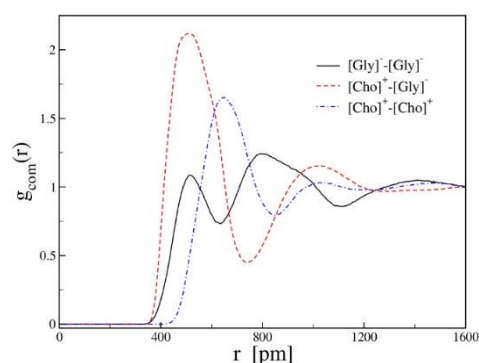

Fig.1: The ion-ion COM RDFs of [Cho][Gly] at 353 K.

The computed COM RDFs between the ionic species of pure IL [Cho][Gly] were depicted in Fig. 1. According to Fig. 1, the cation-anion COM RDF (denoted by a red dash line) is characterized by an intense peak at ~ 5 Å and its height is more than that of other COM RDFs. The higher intensity of the ([Cho]$^+$–[Gly]$^-$) RDF peak reflects stronger electrostatic interaction between opposite charge ions. Moreover, this cation-anion RDF is well defined up to the second solvation shell which confirms the long-range electrostatic interactions in the IL [Cho][Gly] up to 12 Å. The first peak of cation-cation COM RDF (denoted by a blue dot-dash line) is located at ~ 7 Å. A comparison of the peak location shows that the first cation-cation COM RDF peak is located in much longer distances than that of the cation-anion COM RDF. There are two weak peaks for the anion-anion COM RDF (denoted by a black solid line) at ~ 5 and 8 Å. According to the relative intensities of COM RDFs, it is inferable that the anion-anion structural correlation is weaker than that of cation-anion and cation-cation structural correlations. It should be noted here that as expected the oppositely charged ions play significant role in structural correlations of IL [Cho][Gly]. This result is in good agreement with the previous results. However, we would emphasize here about the importance of the [Cho]$^+$–[Cho]$^+$ local structural correlations in the formation of whole liquid structure of [Cho][Gly].

In addition, the cation-anion and cation-cation structural correlations are investigated through computation of the selected site-site RDFs that related to the possible H-bonding. More RDF analysis shows a significant structural correlation between the hydroxyl hydrogen of [Cho]$^+$ and the carboxyl oxygen of [Gly]$^-$ which implies a main cation-anion (H$_O$–O$_A$) H-bonding in IL [Cho][Gly]. Our future structural analysis showed the adjacent [Cho]$^+$ cations are often antiparallel relative to each other, while in the cationic trimer, a perpendicular orientation is also distinguished. Current simulation also is represented that [Gly]$^-$ has the role of a bridge between two [Cho]$^+$ cations in the liquid phase.

IV. CONCLUSION

Local structural correlations and H-bonding in [Cho][Gly] IL are investigated by focusing on the nearest neighbor ionic species. We hope that deeply understanding of the local structure of ILs help us in better design of processes involve these complex liquids and determine the relationship between the structure, interaction, and dynamic behavior of these liquids.

REFERENCES

[1] K. Fukumoto, M. Yoshizawa, and H. Ohno, *J. Am. Chem. Soc.*, vol. 127, pp 2398-2399, **2005**.

[2] Q-P. Liu, X-D Hou, N. Li, M-H. Zong, *Green Chem.*, vol. 14, pp. 304-307, **2012**.

[3] M. H. Kowsari, S. Alavi, B. Najafi, K. Gholizadeh, E. Dehghanpisheh and F. Ranjbar, *Phys. Chem. Chem. Phys.*, vol. 13, pp. 8826-8837, **2011**.

[4] S. Aparicio, M. Atilhan, *J. Phys. Chem. C*, vol. 116, pp. 12055-12065, **2012**.

DFT Calculations and Theoretical Investigations of an innovative Lead(II)-nitrite metal-ligand compound

Babak Mirtamizdoust[a]*, **Faeze Mojtabazade[b]**

[a] Department of Chemistry, Faculty of Science, University of Qom, Qom, Islamic Republic of Iran.
[b] Department of Chemistry, Faculty of Sciences, Tarbiat Modares University, Tehran, Islamic Republic of Iran
Email:babakm.tamizdoust@gmail.com

Abstract: By B3LYP, the geometry of innovative lead (II) metal-ligand compound with methyl-2-pyridincarbaldehyde-4-isonicotinohydrazide Schiff base ligand and nitrite anion has been optimized and by DFT method, the electronic structure of the compound has been determined. The structural data shows a stereo active electron-lone-pair may occupy a hole in the coordination sphere around the Pb^{2+}. The computation shows that for per unite; the compound has 108 occupied molecular orbitals. The highest occupied molecular orbital of the compound is mostly localized on oxygen and nitrogen of the Schiff-base moiety and oxygen atoms of the nitrite counter ion consists of lead (II), while the lowest unoccupied molecular orbital almost delocalized on entire atoms of the Schiff-base moiety and the calculated gap is 3.423 eV.

Keywords: Lead(II), Coordination compound, DFT calculation, theoretical investigation.

I. INTRODUCTION

Recently, metal-organic coordination compounds are of interest due to the diverse structural motifs they may present and the potentially useful properties they may possess [1]. The coordination configuration of metal ions, the geometric characteristics of organic ligands as spacers, metal-ligand ratios, solvents, the feature of counter-anions, the reaction conditions and so forth are some of the numerous factors affecting the assembly of these coordination compounds [2]. The selective sensing and chelating of toxic heavy metals, such as Pb(II), is exceedingly important because of their economic, environmental, and biological roles [3]. Lead(II) has an electronic structure of $[Xe]4f^{14}5d^{10}6s^2$. Due to relativistic effects, which are at a maximum in Au(I) but also operative in other close 6p metals such as lead, the 6s orbital is contracted and stabilized. This stabilized 6s pair reduces its participation in the chemistry of the element (becoming an "inert-pair"), and this explains why inorganic lead forms compounds in a lower oxidation state (less by two) than would be expected from its group number [4]. Theoretical modeling has become an important tool to characterize coordination compounds. Density functional theory has emerged as a handy and cost-effective tool for investigating metal complexes [5]. Herein, The geometry of Pb(II) coordination compound, has been optimized using the B3LYP density functional model, the electronic structure has been determined by the density functional theory (DFT) method. Calculated coordination sphere parameters show a stereo active electron-lone-pair may occupy a hole in the coordination sphere around the Pb^{2+}.

II. METHODS

The geometry of the complex has been optimized by using B3LYP density functional model. In these calculations, we used the 6-311++G** basis set for all carbon, nitrogen, oxygen and hydrogen atoms. For the lead atom, the LanL2DZ valence and effective core potential functions were used. All DFT calculations were performed using the Gaussian 09 program package. The electronic properties such as highest occupied molecular orbital (HOMO) energy, lowest unoccupied molecular orbital (LUMO) energy and frontier molecular orbital coefficients have been calculated. The molecular sketches of all compounds were drawn using Gauss View 03. The natural bond orbital (NBO) analysis which suggested by Reed et al. [6] was applied to determine the atomic charges.

III. RESULTS AND DISCUSSION

The optimized molecular structure of lead (II) coordination compound with methyl-2-pyridin carbaldehyde-4-isonicotinohydrazide Schiff base ligand and nitrite anion showed in figure 1.
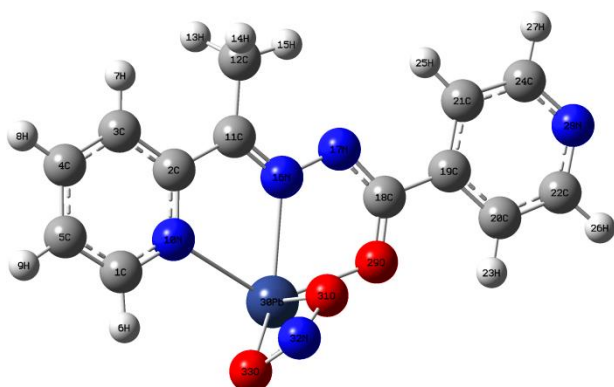

Fig 1.Optimized molecular structure of compound **I**.

The calculated selected bond longs and angles and listed in Table 3. This arrangement shows a stereo active electron-lone-pair may occupy a hole in the coordination sphere around the Pb^{2+}. Table 4 listed selected calculated vibrational data of coordination compound.

The calculated muliken and natural Charges (e) for atoms and orbital energies for HOMO, LUMO, HOMO-LUMO gap energy and dipole moments of Compound listed in tables 2 and 3.
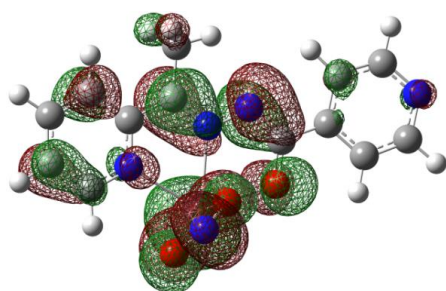
Fig 2.The highest occupied molecular orbital (HOMO)
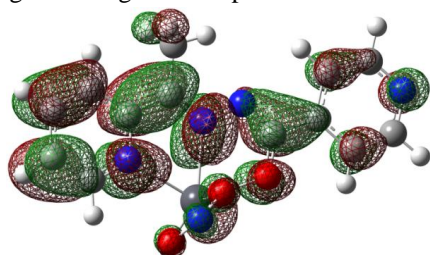
Fig 3.The lowest unoccupied molecular orbital (LUMO)

Table 1. Selected calculations bond distances (Å) and bond angles (degrees) for compound.

Parameter	B3LYP
C8–O3	1.274
N2–N3	1.354
Pb1–N2	2.423
Pb1–O3	2.303
Pb1–N1	2.569
Pb1–O1	2.302
Pb1–O2	2.791
Pb1–O3–C8	117.74
Pb1–N2–N3	117.14
O3–Pb1–N2	66.75
N1–Pb1–N2	65.26
O1–Pb1–O2	47.90
Pb1–O3–C8–N3	4.42

Table 2.Muliken and Natural Charges (e) for atoms.

I	Muliken	Natural
10N	0.094	-0.544
16N	0.247	-0.364
17N	-0.220	-0.434
28N	-0.047	-0.443
29O	-0.227	-0.788
30Pb	0.847	1.348
31O	-0.167	-0.578
32N	-0.151	0.362
33O	-0.196	-0.463

Table3. Orbital energies for HOMO, LUMO, HOMO-LUMO gap energy (ΔE) and dipole moments (μ) of Compound in the gaseous (G) phase*.

Compound	$E_{HOMO}(ev)$	$E_{LUMO}(ev)$	ΔE(ev)	μ(D)
	-6.382	-2.959	3.423	9.1652

*All quantum chemical parameters calculated at DFT level using the B3LYPmethod.

Table 4.Selected calculated vibrational data (cm^{-1}) for compound.

Assignment	Calculated
ν (C-H) aliphatic	3028
ν (C-H) aromatic	3149

δ (C-H)	577
ν (CC) rings vibration	1347-1630
ν (NO$_2$)	1433
ν (CO)	1532
ν (Pb-N) pyridine	649
ν (Pb-N) aliphatic	687
ν (Pb-O) carbonyl	435
ν (Pb-O) nitrite	275

Figures 2 and 3 showed the highest occupied molecular orbital and lowest unoccupied molecular orbital of optimized structure. The NBO charges of lead (II) and of the coordinated atoms were also calculated. The positive charge of the lead (II) ions was 1.348 The charges of the coordinated nitrogen atom of the Schiff-base ligands was -0.544, -0.364 and -0.443, respectively, the coordinated oxygen atoms of the nitrite was -0.578 and -0.463.whereas the coordinated oxygen atom of the Schiff-base ligands was -0.788. The computation shows that complex has 108 occupied molecular orbitals (MOs) per unit. The value of the energy separation between the highest occupied molecular orbital (HOMO) and the lowest unoccupied molecular orbital (LUMO) was calculated. Figures 2 and 3 showed the HOMO and LUMO for the lead(II) complex. As will be seen the HOMO of the title complex is principally localized on four nitrogen and one oxygen atoms of the Schiff-base ligand and two oxygen atoms of the nitrite anion including lead(II), whereas the LUMO is approximately delocalized on all atoms of the Schiff-base ligand. The calculated HOMO–LUMO gap is 3.423 eV.

IV. CONCLUSION

The geometry of innovative Pb (II) metal-ligand compound with methyl-2-pyridincarbaldehyde-4-isonicotinohydrazide Schiff base ligand and nitrite anion has been optimized by B3LYP, and by DFT method, the electronic structure of the compound has been determined. The structural data shows a
Computational Chemistry | 122

stereo active electron-lone-pair may occupy a hole in the coordination sphere around the Pb^{2+} on lead (II). The computation shows that complex has 108 occupied molecular orbitals (MOs) per unit. The highest occupied molecular orbital of the compound is mostly localized on oxygen and nitrogen of the Schiff-base moiety, and oxygen atoms of the nitrite counter ion consists of lead (II), while the lowest unoccupied molecular orbital almost delocalized on all atoms of the Schiff-base moiety. The calculated gap is 3.423 eV.

REFERENCES

[1] R.Chakrabarty ,P.S.Mukherjee,P.J.Stang,Chem.Rev.111 (2011) 6810–6918.

[2] C.L. Cahill,D.T.de Lill,M.Frisch, CrystEngComm 9(2007)15–26.

[3] L. M Engelhardt, B. M. Furphy, J. M. Harrowfield, J. M. Patrick, A. H. White, Inorg. Chem. 28(1989)1410.

[4] L. Shimonni-Livny, J. P. Glusker, C. W.Bock, Inorg. Chem. 37(1998)1853.

[5] T. W. Hambley,L. F Lindoy, J. R. Reimers, P. Turner, G. Wei, A. N. Widmer, Cooper, J. Chem. Soc., Dalton Trans. (2001) 614.

[6] A.E. Reed, F. Weinhold, Chem. Rev. 88 (1998) 899–926.

Theoretical investigation of inhibitors of HIV

*R. Adhami[a], M. Dehestani [a] *, , L. Zeidabadinejad [a]*
Department of Chemistry, Shahid Bahonar University of Kerman, Kerman, Iran
Email: dehestani2002@yahoo.com

Abstract: The interactions between inhibitors with active space of HIV have been analyzed employing B3LYP/6-31g(d) level of theory. The interaction energies between inhibitors with active space of HIV were considered. The calculations show that in all cases interaction between inhibitors with active space of HIV have been performed. The thermodynamic descriptors of the complexes of inhibitors with active space of HIV have been evaluated. Chemical properties of these compounds were studied using highest occupied molecular orbital (HOMO) and lowest unoccupied molecular orbital (LUMO) global hardness, electronic chemical potential and global electrophilicity power.

Keywords: HIV, Inhibitors, Active space, Density functional theory

I. INTRODUCTION

Human immunodeficiency virus infection and acquired immune deficiency syndrome (HIV/AIDS) is a spectrum of conditions caused by infection with the human immunodeficiency virus (HIV) [1]. Following initial infection, a person may not notice any symptoms or may experience a brief period of influenza-like illness [2]. Typically, this is followed by a prolonged period with no symptoms [3]. As the infection progresses, it interferes more with the immune system, increasing the risk of developing common infections such as tuberculosis, as well as other opportunistic infections, and tumors that rarely affect people who have uncompromised immune systems [4]. These late symptoms of infection are referred to as acquired immunodeficiency syndrome (AIDS). This stage is often also associated with unintended weight loss. New HIV inhibitors have been synthesized by Famiglini and *et.al* [5]. Theoretical calculation is an acceptable method, which includes the effects of electron correlation in quantum chemistry. Using theoretical calculations at a lower cost compared to the experimental methods, one can study and investigate the new molecules that are being considered. Hydrogen interactions play an important role in the stability of inclusion complexes. There is a lock of useful information about the nature of interaction between inhibitors with active space of HIV and their active sites. To gain a deeper understanding of the interaction, the present theoretical study on this biological system has been done.

Computational Chemistry | 123

II. METHODS

All calculations were performed using Gaussian 09 package [6] For the isolated species and complexes, we have used B3LYP/ 6-31g(d) level theory to study the geometric, electronic, and vibrational properties. The corresponding frequency calculations were carried out at the same level to make sure that the optimized structures are minimal. The initial structure of inhibitors were drawn with Gauss view software. The stoichiometric ratio of 1:1, is considered for the interaction between initial structures of the inhibitors with active space of HIV. Various aspects of the interactions of the inhibitors with active space of HIV, including the frontier molecular orbital (HOMO and LUMO) calculations were also performed on the studied system. Physical properties, such as global hardness (η), electronic chemical potential (μ), global electrophilicity power (ω) of these compounds, were investigated.

III. RESULTS AND DISCUSSION

The main goal of this work is to characterize the electronic and structural nature of the interactions between inhibitors and HIV. The optimized structures of inhibitors are depicted in Fig. 1.

The interaction energies between inhibitors and active space HIV are reported in Table 1. The negative complexation energy indicates that interactions are thermodynamically favorable.

Table 1: Interaction energy of complexes of 1-4 (in hartree).

Complex	1	2	3	4
$E_{interaction}$	-0.1845	-0.2987	-0.2130	-0.2060

From these results, it concludes that the cavity of HIV is a good candidate to accept inhibitors. The optimized complexes of inhibitors with active space of HIV are shown in Fig. 2.

To clarify the nature of the electronic transitions within interactions inhibitors with active space of HIV, using the molecular properties such as the orbital energies, we can calculate the molecular properties such as the chemical potential (μ) as:
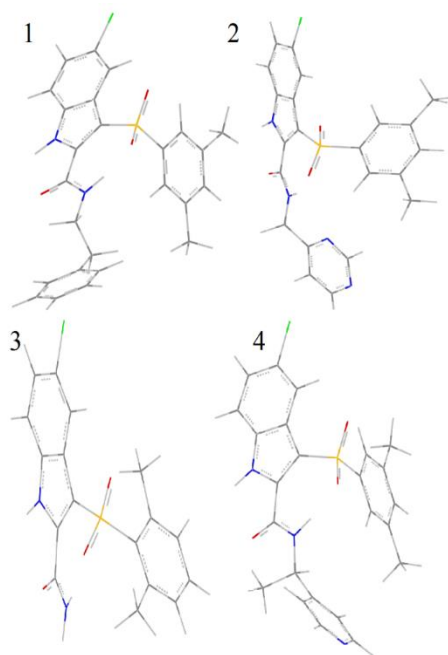
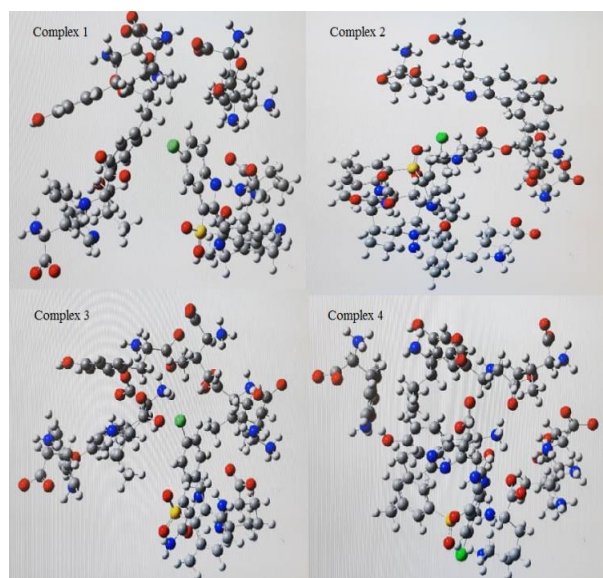Fig. 1: Optimized structures of inhibitors.

Fig. 2: Optimized complexes of inhibitors 1-4 with active space of HIV.

$$\mu = \frac{(I+A)}{2} \tag{1}$$

The hardness (η) as

$$\eta = -\frac{(I-A)}{2} \tag{2}$$

and global electrophilicity index (ω) as

$$\omega = \frac{\mu^2}{2\eta} \tag{3}$$

Where I is the ionization potential, and equal to ΔE_{HOMO}, A is electron affinity and can be expressed as: $A = \Delta E_{LUMO}$.

The energy level of the boundary molecular orbitals provides useful information on the chemical reaction indicator. Therefore, we can discover that how inhibitors interact and where is the active sites in active space of HIV. The LUMO–HOMO gap (E_g), dipole moment (D), μ, η and ω for the stable and interactions are presented in Table 2. The complexes of 1-4 are stable. These values describe the transfer of electron charge from the HOMO to the LUMO orbital, which affects the activity and structure of the electronic of the inhibitors. The relatively high values of LUMO–HOMO indicate that these compounds present high chemical stability. These results were in proper matching with the complexation energy, and the chemical potential of less than zero represents a spontaneous reaction. The chemical potential of less than zero represents a spontaneous reaction. The electrophilicity is a descriptor of the reactivity that allows a quantitative classification of the global electrophilic nature of a molecule within a relative scale. According to the definition, this index measures the tendency of chemical species to accept electrons. A more reactive nucleophile is characterized by lower μ and ω values, and then a good electrophile is characterized by high μ and ω values.

Table 2: Chemical descriptors of complexes of 1-4 (in hartree).

Complex	E_{gap}	S	ω	μ	η
1	4.4847	0.4459	3.3712	-4.0423	2.2423
2	6.3402	0.3154	4.0762	-5.0849	3.1701
3	4.5307	0.4414	3.7843	-4.1407	2.2653
4	4.4651	0.4479	3.8321	-4.1365	2.2325

IV. CONCLUSION

We have studied the structural, and topologic properties of the molecular complexes between active space of HIV and inhibitors 1-4 at B3LYP/ 6-311+G(d,p) level of theory. The results of the obtained theory are very well suited to the experimental studies. Due to done calculations, inhibitors have good interaction with active space of HIV. The chemical descriptors show that there is charge transfer between inhibitors and active space of HIV.

REFERENCES

[1] J. Coffin, A. Haase, J.A. Levy, L. Montagnier, S. Oroszlan, N. Teich, H. Temin, K. Toyoshima, H. Varmus and P. Vogt, Science, vol. 232, pp. 697-685, **1986**.

[2] K.E. Nelson, M.L. Clements, P. Miotti, S. Cohn and B.F. Polk, Ann. Intern. Med. vol. 109, pp. 383-388, **1988**.

[3] E.G. Chadwick, G. Chang, M.D. Decker, R. Yogev, D. Dimichele and K.M. Edwards, Pediatr. Infect. Dis. J. vol. 13, pp. 206-211, **1994**.

[4] A.T. Rodriguez-Penney, J.E. Iudicello, P.K. Riggs, K. Doyle, R.J. Ellis and S.L. Letendre, AIDS Patient Care STDS, vol. 27, pp. 5-16, **2013**.

[5] V. Famiglini, G. La Regina, A. Coluccia, S. Pelliccia, A. Brancale, G. Maga, E. Crespan, R. Badia, E. Riveira-Muñoz and J.A. Esté, J. Med.Chem., vol. 57, pp. 9945-9957, **2014**.

[6] M. Frisch, G. Trucks, H.B. Schlegel, G. Scuseria, M. Robb, J. Cheeseman, G. Scalmani, V. Barone, B. Mennucci, G. Petersson, Wallingford, CT, vol. **19**, pp. 227-238, **2009**.

The Structure Study of the Water molecules in a Transmembrane Cyclic Peptide Nanotube : A Molecular Dynamics Simulation

Samaneh baranipour[*a,b] , *Jaber Jahanbin Sardroodi*[a,b] and **Alireza Rastkar Ebrahimzadeh**[a,c]

a: Molecular Simulation Laboratory, Azarbaijan Shahid Madani University, Tabriz, Iran

b: Department of Chemistry, Azarbaijan Shahid Madani University, Tabriz, Iran

c: Department of Physic, Azarbaijan Shahid Madani University, Tabriz, Iran

* correspounding Author, E-mail:samaneh.barani90@gmail.com

Abstract: In this study, molecular dynamics simulation was used to explore the structural characteristics and the transport performance of water molecules of cyclic peptide nanotubes (CPNTs). MD simulation was used to explain how the hydrophobic modification of functional group affects the structure, channel volume, interior affinity, and transportation behavior of water in CPNTs. Pressure-driven water flow through CPNTS Different sequences ranging from 10 to 50 nm is simulated. We show CPNTs modified by replacing L-Glycine or D- Glycine groups with an L- Alanine or D-Alanine has a negligible effect on the resulting mass flow rate.

Keyword *:* Molecular Dynamics Simulation(MD)، Cyclic peptide nanotubes (PNTs) ،Glycine amino acids، Alanine amino acids

I. NTRODUCTION

The transport of ions such as potassium , sodium and molecules into and out of cells can occur by different mechanisms, such as ion channels, pores, carriers. ion channels are remark- able systems that have the ability to selectively pump necessary chemicals and signals through cell walls at rates that are orders of magnitude faster than inorganic pores with near perfect selection[2-1]. The ion channel can be considered as pores in the phospholipid membrane that minimizes the inherent repulsion between water-soluble molecules and the hydrophobic lipid environment[3]. In addition, the ion channel creates highly compatible and complex functional structures for the transport of ion or water in membranes [4]. This considerable complexity is perhaps the most important challenge that chemists have encountered in designing synthetic ion channels or transporters. Nevertheless, the fundamental features used by Nature to achieve this formidable task, such as size exclusion, ion hopping, hydrogen bonding, and hydrophobic or hydrophilic interactions, afford a vast resource to inspire the design and construction of artificial ion

channels and carriers. peptide nanotubes (PNTs) are a class of synthetic nanomaterials formed by the self-assembly of closed peptide rings with an even number of alternating D- and L-amino acid residues. In recent years peptides have emerged as powerful tools for the design of novel nanobiomaterials because of their exceptional characteristics based on their unique folding and self-assembly properties. In the other words Peptide nanotubes are tubular structures formed by peptide components. cyclic peptide nanotubes (CPN) are a subclass of this type of material formed by stacking of cyclic components and one of the main advantages of these systems is the rigorous control of the internal diameter. Such artificial systems can mimic the biological functions of natural transmembrane channels more suitable than single-wall carbon nanotubes (SWNTs) and others. Water permeation through nanochannels has been the topic of theoretical and experimental studies for many years. For some biological channels, such as Gramicidin C (GC) permeation of water plays the primary function. Molecular dynamics (MD) simulations are widely used to investigate water transportation through the channels, since the movement of every single water molecule can be closely monitored in the simulations.

I. METHODS

In this study, in order to study the effect of hydrophobicity of residues on the interaction of a cyclopeptides nanotube with water, we simulated two hexa-cyclo peptids nanotube composed from Glycine and Alanine amino acids.

The Two dimentioanl structures of the considered peptides were prepared by the help of protein code of Tinker suite of software package and named as CP1 for (GLY)8 and CP2 for (ALA)8.

The CHARMM27 force field and the TIP3P water model were employed for all the MD simulations.

The Nose´-Hoover Langevin piston method was used to maintain the pressure of the MD simulation box at 1 bar during simulation runs, and Langevin dynamics was used to control the temperature. all the MD simulations were performed with NAMD2.9 package along 50 simulation time with 1 fs time steps. Analysis and visualization were made using the molecular graphics program VMD 1.9.3.

The temperature was controlled at 310 K. then MD simulation data of the system were collected during another 50 ns.

II. RESULTS AND DISCUSSION

In this work , in order to study the effect of hydrophobicity of residues on the interaction of a cyclopetid with water, we first simulated two types of cyclic peptide nanotube models (CPNT models) composed from Glycine and Alanine amino acids. The canonical ensemble (NVT) was used to simulate these two types of nanotubes, whereas the NPT ensemble was used to model nanotubes/solvent systems to allow for control over pressure.

The initial structures of the nanotube was changed by the Glycine functional group, which This process disrupted the inner symmetrical structure. As a result, the internal diameter was reduced from 10.3 Å in Alanine – CPNTs to 7.5 Å in Glycine - CPNTs.

Thus, in this work, the designed model for describing the effect by hydrophilic functional group in CPNTs including structural catachrestic such as hydrogen bonds number and transport behavior is convincing.

sequence of channel amino acids Channel size were the dominant factors in water transport performance.

To investigate the effect of amino acid sequencing changes with hydrophobic functional group modification, the interaction of water molecules with channel and structural parameters of CPNTs were fully investigated.

As mentioned ,this research was undertaken to enhance the diffusivity of water molecules by adjusting the hydrophilicity of a common CPNT.

The energy parameters such as van der Waals (vdW) and Coulombic energy were studied.

As the energy charts of structures are shown in Fig. 2, VDW energy is used by hydrophilic functional groups that are used to modify CPNTs.

The GLY hydrophilic amino acid nanotube showed the highest value, indicating that this structure is heavily influenced by the water molecules inside the nanotube.

MD simulation and Hydrogen bond analysis indicated that modification of the nanotubes can be an effective tool

for investigating the behavior of water near nanotubes and exploring the nature of water flow through CPNTs.
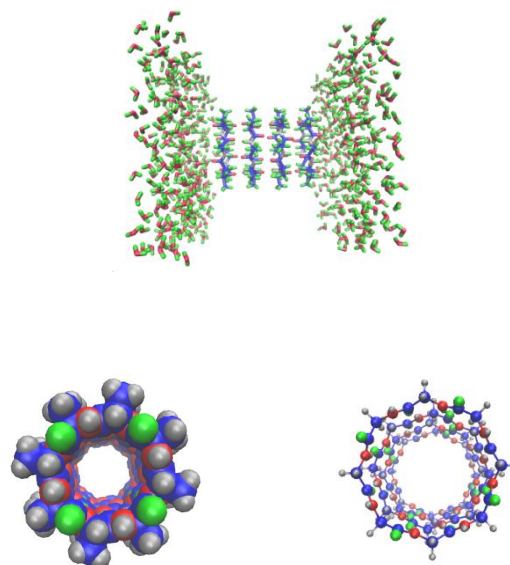
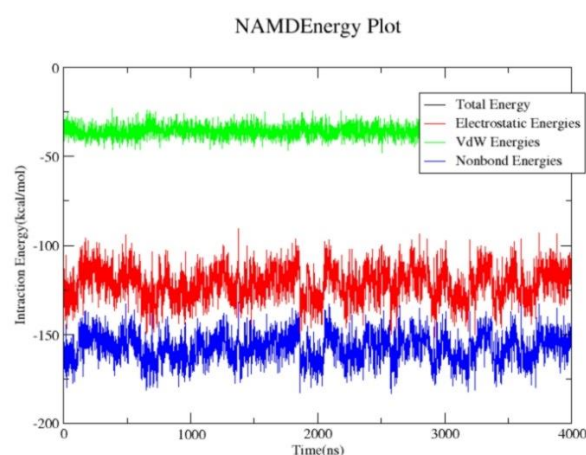Fig.1 The resultant configuration consisting of CPNTs Designed after 50 ns simulated

Fig.2 The interaction energy via van der Waals (vdW) and Coulombic energy comparisons.
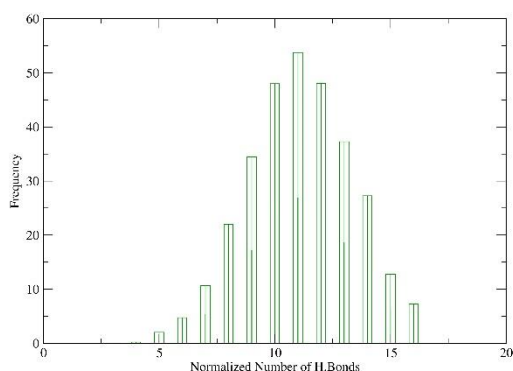
Fig. ٣ The distribution of the hydrogen bonds between the CPNT and water molecules

III. CONCLUSION

The results have been analysed of the transport behavior inside nanotubes show that the considered peptide nanotubes possesses a good potential for the passing of different molecules . Furthermorecyclo peptide can be used as building block for building ion channel.

REFERENCES

[1] S. Chen, B. Mulgrew, and P. M. Grant, Journal, vol. 4, pp. 570-578, **1993**.
[2] J. U. Duncombe, Journal, vol. 10, pp. 34-39, **1995**.
[3] C. Y. Lin, M. Wu, J. A. Bloom, I. J. Cox, and M. Miller, Journal, vol. 10, pp. 767-782, **2001**.

[4] Ghadiri, M. R.; Granja, J. R.; Milligan, R. A.; McRee, D. E.; Khazanovich, N. Nature 1993, 366, 324.

Theoretical investigations of copper ion selectivity by new fluorescent chemo sensor based on carbazole-Schiff

N. Dehghani[1], M. Arabieh[2] B. Ghalami Choobar[3]*

1 Department of Chemistry, , University Campus2, University of Guilan. Rasht, Iran
2 Nuclear Science and Technology Research Institute, Tehran, Iran
3 Department of Chemistry, Faculty of Science, University of Guilan,Rasht, P.O. Box: 19141, Iran
E-mail:B-ghalami@guilan.ac.ir

Abstract: In this work the most practicable complexes formed between Mn(II), Fe(II), Co(II), Ni(II), Cu(II) and Zn(II) cations and 2-Amino-3-((Z)-((9-hexyl-9H-carbazol-yl)methylene)amino)maleonitrile. Since there was no crystallographic data for this ligand, an auxiliary molecule that was the most similar molecule to the original ligand was selected to determine the computational level and its X-ray data was used. Geometry optimization of auxiliary molecule was carried out using B3LYP functional by 3-21G, 6-31G, 6-31G(d), 6-31+G(d), 6-31+G(d,p), 6-31++G(d,p), 6-311++G(d,p) basis sets without any symmetry constrain. The construction parameters of the optimized molecule were compared with the crystallography data. The mean absolute deviation (MAD) between DFT calculated results and those of the crystallographic data were determined. The B3LYP/6-31+G(d) computational level was selected as the best level with the least computational cost for complexation reaction. Formation of the complex in three modes was investigated and the best site of coordination was determined. The geometry optimization and frequency calculations was performed at B3LYP/6-31+G(d) level of theory in the gas phase then thermo-chemistry results, were improved via single point energy (SPE) calculations at higher level of theory. Polarized Continuum Model (PCM) was used to model the solvent medium. Thermo-chemistry data in the solution were collected at the B3LYP/6-31+G(d) computational level.

Keywords*:* AIM, Complexation, DFT, 2-Amino-3-((Z)-((9-hexyl-9H-carbazol-yl)methylene)amino)maleonitrile

I. INTRODUCTION

Copper is one of the fundamental trace elements for animals and humans. Average copper requirement of the human organisms is limited to 2 to 5 milligrams per day. Researches show that discrepancy of this element causes many diseases. There are many traditional and novel methods to identifying Cu^{2+} such as atomic absorption spectroscopy, electrochemical methods, fluorescence techniques (Fluorescent chemo sensor). Among various suggested methods latest approach has some advantages such as independence to advanced equipment and skilled operator, simplicity of sample preparation, high sensitivity, high speed and low- cost. There are many experimental and theoretical investigations on chemo sensor for copper ions. For example Tian and coworkers synthesized new Cu (II) florescent sensor with high selectivity and sensitivity with 4.7 nM detection limit. According to their allegation this ionophore can distinguish between Cu^+ and Cu^{2+} in real water sample. They confirmed their results by fluorescence spectrometry, TD-DFT and DFT calculation. Most recently Wang et al synthesized a new fluorescent chemo sensor based on Schiff base (2-Amino-3-((Z)-((9-hexyl-9H-carbazol-3-yl) methylene) amino) maleonitril) for simplicity this structure is named "maleo" throughout the manuscript. (See figure 1) Maleo was shown to have high ability for Cu (II) selection among first row transition metals. In this study we are going to use computational chemistry method to find more details on the complexation reaction between Cu (II) and maleo chemo sensor. Finally the complexation of some of the others transition metals and maleo are discussed and compared with Cu (II)/maleo system..

II. COMPUTATIONAL DETAILS

Geometry optimizations and thermochemistry calculations of complexation reaction between (2-Amino-3-((Z)-((9-hexyl-9H-carbazol-3-yl) methylene) amino) maleonitril) (briefly: maleo) and (Mn(II), Fe(II), Co(II), Ni(II), Cu(II) and Zn(II) performed at B3LYP/6-31+G(d) level of theory in both gas phase and solution phase. Solvent medium was modeled by PCM model in acetonitrile. Single point energy calculations were carried at the B3LYP/6-311++G(3df,2pd) level of theory. these calculations were performed by general atomic and molecular electronic structure system (GAMESS) program. Graphical representation was performed by Chemcraft package.

III. RESULTS AND DISCUSSION

To determine the computational level an Auxiliary molecule (See Figure 1) was used. That is because absence crystallographic data for maleo in scientific references. The only difference between this molecule and maleo is in their side alkali chain. DFT method with the use of B3LYP hybrid density functional utilized to optimize the auxiliary molecule and its structural parameters were compared with X-Ray data.

In order to examine the complexation reaction maleo was optimized at the B3LYP/6-31+G (d) level of theory in the gas phase. Complexation of six divalent cations with optimized ligand was considered in three probably modes at the same level of theory. Optimization and frequency calculation of eighteen complexes was done in the gas phase without any symmetry constrain. The electronic and the Gibbs free energy differences of complexation reaction $\Delta E = E\_Product - E\_Reactant$ and $\Delta G = G\_Product - G\_Reactant$ were calculated, then zero point energy (ZPE) and Basis set superposition error (BSSE) corrections was performed on them. These results are listed in table 1. It can be seen mode number two has been formed the most stable complex for all of the cations. Table 2 shows that nitrogen atoms (N45 and N47) in the mode number two form stronger interactions with cations. Among six divalent cations the most stable complex is related to Cu2+ with $\Delta E = -343.95$ kcal/mol which is increased to -319.36 kcal/mol, -281.75 kcal/mol, -259.54 kcal/mol, -251.97 kcal/mol and -215.79 kcal/mol in Ni2+, Co2+, Zn2+, Fe2+ and Mn2+ complexes respectively. Hereinafter nature of interaction between cations and two donor atoms (N45 and N47) of ligand considered.

After determination of the best mode of interaction between maleo and cations thermochemistry calculation carried out to find more stable complex among Mn2+, Fe2+, Co2+, Ni2+, Cu2+ and Zn2+. Optimization and frequency calculation of complexation reaction for six divalent cations at the B3LYP/6-31+G (d) was made previously, single point energy calculations (SPE) were done on mentioned minimized structures to correct the obtained electronic energy. This calculation were done at the B3LYP/6-11++G (3df, 2pd) level of theory "high level" in the gas phase.

Gibbs free energy differences of complexation reaction at three computational levels presented in figure 3. It shows that all complexes take part in spontaneous reactions due to negative ΔG values which [CuL] 2+ complex with more negative result has formed the most stable complex at three levels of theory.

To study the solvent medium thermochemistry of complexation reaction was evaluated on gas phase relaxed

reactants in both B3LYP/6-31+G (d) level of theory and single point energy calculation with 6-311++G(3df, 2pd) basis set was done to correct the results. Computations performed using polarized continuum model (PCM) with UAKS atomic radii with acetonitrile as a solvent.
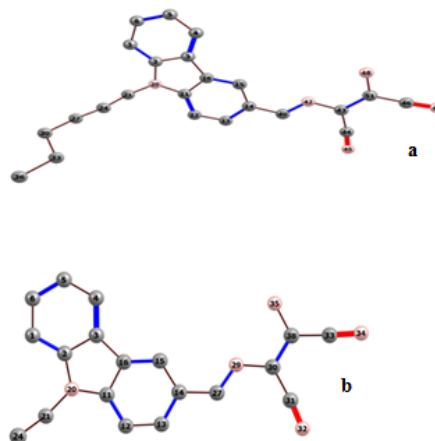

Fig.1: a: original ligand b: auxiliary molecule

Table 1. The electronic and the Gibbs free energy differences of complexation reaction of six divalent cations with consider ligand in three probable modes at the B3LYP/6-31+G(d) level of theory in the gas phase. All values are in kcal/mol.

Different modes	Delta $E^{ZPE+BSSE}$			Delta G		
	1	2	3	1	2	3
[MnL]$^{2+}$	-199.92	-215.79	-206.54	-193.32	-208.39	-200.74
[FeL]$^{2+}$	-228.64	-251.97	-221.65	-222.56	-244.95	-215.56
[CoL]$^{2+}$	-259.59	-281.75	-254.16	-254.35	-275.28	-248.91
[NiL]$^{2+}$	-291.67	-319.36	-292.07	-286.88	-303.02	-277.24
[CuL]$^{2+}$	-320.36	-343.95	-315.22	-316.07	-337.40	-310.54
[ZnL]$^{2+}$	-255.79	-259.54	-251.90	-250.56	-252.87	-245.99

IV. CONCLUSION

According to calculations B3LYP/6-31+G(d) is proper level of theory to study transition metal complexes. Thermochemistry calculation at this level of theory for

complexation reaction of maleo and Mn(II), Fe(II), Co(II), Ni(II), Cu(II) and Zn(II) shows that Cu2+/Maleo is the most stable complex in gas phase and solution phase with acetonitrile as a solvent.

REFERENCES

[1] Dehghani N, Ghalami-Choobar B, Arabieh M, Dezhampanah H. Theoretical insight to the complexation of some transition metals with cryptand. Structural Chemistry. 2019:1-14.

[2] Yin J, Bing Q, Wang L, Wang G. Ultrasensitive and highly selective detection of Cu2+ ions based on a new carbazole-Schiff. Spectrochimica Acta Part A: Molecular and Biomolecular Spectroscopy. 2018;189:495-501.

[3] Varadwaj PR, Marques HM. The physical chemistry of coordinated aqua-, ammine-, and mixed-ligand Co2+ complexes: DFT studies on the structure, energetics, and topological properties of the electron density. Physical Chemistry Chemical Physics. 2010;12(9):2126-38.

Molecular Dynamics Investigation of Gramicidin-C Peptide as antibacterial drug in DMPC Bilayers

Samaneh baranipour[*a,b] , *Jaber Jahanbin Sardroodi*[a,b] and **Alireza Rastkar Ebrahimzadeh**[a,c]

a: Molecular Simulation Laboratory, Azarbaijan Shahid Madani University, Tabriz, Iran
b: Department of Chemistry, Azarbaijan Shahid Madani University, Tabriz, Iran
c: Department of Physic, Azarbaijan Shahid Madani University, Tabriz, Iran
* correspounding Author: E-mail:samaneh.barani90@gmail.com

Abstract: The most membrane peptide use as antibacterials produced by one species of microbe (Bacillus brevis). developing the antimicrobial peptides are recently focused on Pharmacists , since they serve as antibacterials in prevailing over drug resistance by eliciting the disruption of microbial membrane. Still, there are lots of challenges to bring up the structurally stable and functionally efcient antimicrobial peptides. This study analyzes the structural stability and the functional activity of gramicidin-C peptide in lipid bilayers membrane, thereby demonstrating its potent antibacterial activity against antibiotic-resistant micro-organisms. To investigate the structural stability and functionality of gramicidin C, we performed dynamic analysis VMD-1.9.3 package . The structure and lateral pressure profile of the 1,2-dimyristoyl-sn-glycero-3-phosphatidylcholine (DMPC) lipid bilayers in the absence and presence of gramicidin C (GC) are studied by molecular dynamics simulation. In the absence of detailed structural and biophysical/biochemical characterization of protein/lipid interactions, Molecular dynamics (MD) simulations are able to provide a key tool, for probing the interactions of lipids with membrane proteins. In conclusion, gramicidin-C peptide has defnitely demonstrated adequate structural stability and functionality and this work will need to be considered in peptide-based drug discovery.

Keywords: Antibacterials peptide(ABP) , Gramicidin C, molecular dynamics simulation (MD)

I. INTRODUCTION

Increase in resistance of Antibacterials drugs has been a major threat to human lives and immense challenge to researchers [1-2]. Antibacterials product or Antibacterials peptides have fascinated the world for the last decade as a potential natural means of therapeutics with microorganism are the most dependent development since the time of its discovery[3].

Despite the new discovery of antibacterials peptides, the functionality and stability of peptides have varied tendency [4]. Gramicidin C a transmembrane antibacterials peptide,

has characteristic features of therapeutic drugs. This compound is an antibacterial peptide that creates specific ion channels for mononal cations in the membrane [1].

The GC has the amino acid sequence that consists of alternating L- and D-amino acids following the formula: FVA[1] GLY ALA DLE ALA DVA VAL DVA TRP DLE TYR DLE TRP DLE TRP ETA[2] . Due to the alternating L- and D-amino acid sequences of gC, is able to transport potassium and sodium ions across artificial and natural membranes by forming a water-filled pore, approximately 7 Å in diameter.

II. METHODS

In this study, we therefore carried out a series of molecular dynamics Simulation of lipid bilayers in the absence and presence of GC to investigate the effects of GC on the membrane structure and effects of lipid on the GC channel structure and the permeability of ions through the channel pole of GC in the membrane.

We adopted lipid molecule, 1,2-dimyristoyl-sn-glycero-3-phosphatidylcholine (DMPC) for these MD simulations and investigated the structural stability between the GC and surrounding membrane. The lipid molecules commonly have a polar phosphatidylcholine (PC) in the headgroup and two long fatty acyl hydrocarbon chains. These lipids also have two ester carbonyls at the linkage of two hydrocarbon chains to the headgroup. We have carried out the MD simulations of DMPC lipid bilayer in the absence and present of GC for 50 ns, by using NAMD package with CHARMM-36 force field.

At the end of simulation, Several structural properties, such as Radial distribution function (RDF), Number of H.Bonds , Intraction Energy and Bilayer thickness, were analyzed to assess the mutual interactions of protein and lipid molecules.

III. RESULTS AND DISCUSSION

To understand the effect of the Gramicidin sequence mutation on the behavior of water transport, the hydrogen bonds between g-C and water molecules were discussed. The

---

[1] N-FORMYL-L-VALINE

[2] ethanolamine

distribution of the hydrogen bonds between the g-C and water molecules in molecular model is presented in Fig. 2. From the observations of this model, the hydrogenbond distributions were obviously altered When the channel sequence amino acids have been mutated.
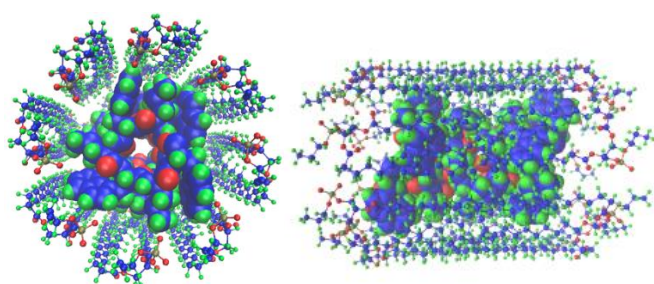

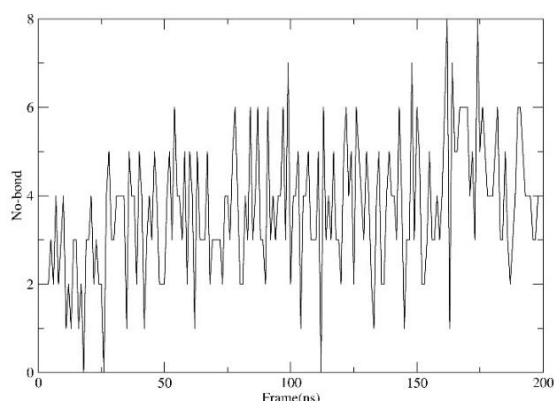**Fig.1:** g-C combination of membrane association of peptide interaction .

Fig. 2 The distribution of the hydrogen bonds between the g-C and water molecules

In other words, the areas modified by the mutation process apparently accelerated the transport of water from Gramicidin. Furthermore, Several structural properties, such as Root mean square deviation (RMSD), Radius of gyration (Rg), Radial distribution function (RDF), Area per lipid (APL) and Bilayer thickness, were analyzed to assess the mutual interactions of protein and lipid molecules. Radial distribution function and hydrogen bonds (1) of water molecules in the Gramicidin and (2) between the peptide backbone and water molecules in the Gramicidin also verified it perfectly.
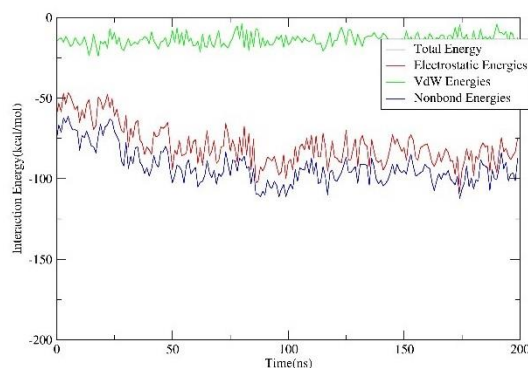
Fig.3 The interaction energy via van der Waals (vdW) and Coulombic energy comparisons.

IV. CONCLUSION

A general analysis of the parameters obtained from molecular dynamics simulation shows that C-Gramicidin peptide has a greater potential than antimicrobial peptides and it is an effective way to eliminate microorganisms.

REFERENCES

1. Gold HS, Moellering RCJ (1996) Antimicrobial-drug resistance.
2. N Engl J Med 335(19):1445–1453 2. Ventola CL (2015) The antibiotic resistance crisis. Pharm Ther 40(4):277–283
3. 3. Liou J-W, Hung Y-J, Yang C-H, Chen Y-C (2015) The antimicrobial activity of gramicidin a is associated with hydroxyl radical formation. PLoS One [Internet] 10(1):e0117065 4. Arenas I, Villegas E, Walls O, Barrios H, Rodríguez R, Corzo
4. G (2016) Antimicrobial activity and stability of short and long based arachnid synthetic peptides in the presence of commercial antibiotics. Molecules 21(2):225.

Molecular Dynamics Simulation of Aqueous Solutions of a Hydrophilic Room Temperature Ionic Liquid

M. H. Kowsari*, S. M. Torabi

Department of Chemistry and Center for Research in Climate Change and Global Warming (CRCC), Institute for Advanced Studies in Basic Sciences (IASBS), Zanjan, 45137-66731, Iran
Email: mhkowsari@iasbs.ac.ir and mohammad.kowsari@gmail.com

Abstract: Classical molecular dynamics (MD) simulations were used to probe the structural properties of neat 1-butyl-3-methylimidazolium nitrate [bmim][NO$_3$] ionic liquid (IL) and its mixture with water at different concentrations. We have tried to provide a comprehensive picture of the effect of water concentration in the structural properties of the [bmim][NO$_3$] IL. The existence of a complex network of interactions between cations, anions, and water molecules has been proven. The results showed that the anion-water interaction played a major role in water/ IL structure and respective interactions.

Keywords: Aqueous solutions, 1-butyl-3-methylimidazolium nitrate, Hydrophilic ionic liquids, Molecular dynamics.

I. INTRODUCTION

On the one hand, the presence of water in ILs has some disadvantages for the applications of these compounds in both industry and laboratory. For example, the presence of water significantly diminishes the broad electrochemical window known for pure ILs, such that the practical usability of ILs in electrochemical devices is still under debate. On the other hand, many positive aspects of the role of water on the application of ILs in industry and biology are appeared, such as interesting related applications have discussed by Ohno et al. in 2012 [1].

In recent years, it is reported daily growing the number of applications of the IL/water mixtures. Economical utilization of aqueous solutions of ILs (versus the neat ILs) can help to solve the high-cost challenge for commercialization of some of the IL-related technologies. In addition, adding water reduces the (high) viscosity of ILs which is necessary to implement of ILs efficiently at the industrial scale, especially for low temperature applications.

IL-water mixtures are promising separation media for bioactive compounds. Hydrated ILs involve a small amount of water have been used effectively as good solvents for proteins [2].

The molecular origins of the tunable properties of an IL-water mixture with x_w are generally not fully understood and described on a rigorous MD study. In addition, demonstrating the microscopic structural details of such mixtures is a poorly understood aspect.

The [bmim][NO$_3$] IL is one of the hydrophilic ILs that absorbs a considerable amount of atmospheric moisture over a short period of time.

In this study, we obtain some microscopic details of the local structure and microheterogeneity of the [bmim][NO$_3$]/water binary mixture at different x_w's on the basis of the time-averaging of the relative locations of the nearest-neighbor ions and water molecules using MD simulation. The possible structural correlations and their complex relation with the interparticle interactions were understood by calculating the radial, spatial, angular, and combined distribution functions.

II. METHODS

We performed all-atom MD simulations on pure [bmim][NO$_3$] IL and its binary mixtures with water. The water mole fractions (x_w) were set at 0.00, 0.10, 0.25, 0.50, 0.70, 0.80, 0.90, and 1.00. The force field parameters for [bmim]$^+$ and [NO$_3$]$^-$ ions were derived from the nonpolarizable force field developed by Lopes et al. [3]. The SPC model is applied for water. To solve problem of the retardation of translational and rotational behavior of ions in the MD simulation of ILs, the partial charges of the ions were reduced to sub-integer scaling values of $\pm 0.8e$ [4].

The temperature was gradually increased to 600 K. The system was then cooled step-wise to 300 K with intermediate equilibrations at 600, 500, 400, 350, and 300 K in the isothermal–isobaric (NpT) ensemble using the Nosé-Hoover thermostat and barostat. The thermostat and barostat relaxation times were set to 0.2 and 1.0 ps, respectively. Production runs of 10 ns were carried out for the neat IL and IL/water mixtures at 300 K and 1 atm pressure. The calculation of long-range Coulombic forces was performed using the Ewald summation technique. Applied Lennard-Jones pair potential cut off radius is 16 Å and the simulation time step is 1fs. All equilibration and production runs were carried out with the Verlet leapfrog scheme to integrate the equations of motion under the periodic boundary conditions

in all directions using DL_POLY2.18 MD simulation package [5].

III. RESULTS AND DISCUSSION

The center of mass (COM) radial distribution functions (RDFs), g(r), are used to investigate the influence of water addition on the local structural correlations of the different possible pair types (cation-anion, cation-cation, anion-anion, cation-water, anion-water, and water-water).

We describe the probability of the H-bonding interaction between the different pair species present in these systems using the respective RDFs. At first, we do not apply any H-bonding criteria to compute key RDFs, hence, probability of H-bonding interaction computed on the basis of g(r) is always maximum. In the next stage, we used a combined distance/angular distribution function for studying possible H-bonding. The H-bonds are defined according to a length and an angular criteria. The first criterion is the distance between the H atom of the donor group and the acceptor site and has to be less than a limiting value ($\sim$ 3-3.5 Å). The angle formed between the donor, the H, and the acceptor has to be larger than a limiting value (ordinary $\sim 130°$) [6].

The microscopic structure and bulk properties of ILs is a result of the net effect of possible interionic interactions which are the Coulomb and van der Waals forces, and the doubly ionic hydrogen bonds [6]. There are two possible forms of relative orientation of the anions around the imidazolium ring of the cations: *in-plane* and *on-top* conformations. In the *in-plane* conformation, the anion is in the imidazolium ring plane which causes the hydrogen atoms of the ring to interact with the $[NO_3]^-$ (*e.g.*, H-bonding) in such a conformation. In the *on-top* conformation, the anion is located above or below the ring.

We applied the corresponding combined distribution function (CDF) to discover the local cation-anion orientations quantitatively. In addition, we used the respective RDFs and CDFs to explore the cation-cation π-π interactions and the aggregation of the butyl side chains of the neighboring cations in the studied systems. The effect of x_w on these local interactions and the structural correlations between the ions and water molecules are also determined.

IV. CONCLUSION

Current microscopic structural study of aqueous ILs will offer a better understanding of the complex coupling between the structures and interactions in these IL-water solutions. It also help to the better engineering design and the efficiency of IL-water related processes.

REFERENCES

[1] Y. Kohno, H. Ohno, *Chem. Commun.* vol. 48, pp. 7119-7130, **2012**.

[2] K. S. Egorova, E. G. Gordeev, and V. P. Ananikov, *Chem. Rev.* vol. 117, pp. 7132-7189, **2017**.

[3] J. N. C. Lopes, J. Deschamps, A. A. H. Pádua, *J. Phys. Chem. B*, vol. 108, pp. 2038-2047, **2004**.

[4] M. H. Kowsari, S. Ebrahimi, *Phys. Chem. Chem. Phys.*, vol. 20, pp. 13379-13393, **2018**.

[5] W. Smith, T. R. Forester, I. T. Todorov, the DL_POLY Molecular Simulation Package, v. 2.18, Daresbury Laboratory, UK, **2007**.

[6] S. Ebrahimi, M. H. Kowsari, *Phys. Chem. Chem. Phys.*, vol. 21, pp. 3195-3210, **2019**.

Investigation of Thermal Decomposition and Chemical Ionization of N-Aminophthalimide Using Ion Mobility Spectrometry

M. Tozihi*, H. Bahrami, and M. Amiri

Department of Chemistry, University of Zanjan, P. O. Box: 38791-45371, Zanjan, Iran

Email: tozihi@znu.ac.ir

Abstract: Thermal decomposition and chemical ionization of N-Aminophthalimide was studied using ion mobility spectrometry. The instrument was equipped with a continuous corona discharge ionization source in positive mode. In addition to the parent product ion peak, two fragment ion peaks and also several adduct ion peaks were observed in the ion mobility spectrum. The effect of injection port temperature on the intensities of fragment and adduct ion peaks were investigated. Fragment ions were identified using mass-to-mobility correlation with two standard masses.

Keywords: N-Aminophthalimide, Thermal decomposition, Chemical ionization, Ion mobility spectrometry.

I. INTRODUCTION

Ion mobility spectrometry (IMS) is a well-known ion separation technique at ambient pressure. In addition to applications for the identification and measurement of chemical compounds, IMS has an important application in understanding the chemistry of ion-molecule reactions, especially in atmospheric pressure [1]. Generation of final product ions in the reaction region of an IMS is a complicated process whose course depends on the type of ion source. Among different ionization sources introduced for IMS, continuous corona discharge (CD) ionization has attracted lots of attentions. The common reactant ions produced in the CD at atmospheric pressure are hydrated proton, $H_3O^+(H_2O)_n$. Ionization of analyte begins with proton transfer from reactant ions to the vaporized analyte molecules [2]. The transfer of the proton from reactant ions to the analyte molecule happens if the proton affinity (PA) of the analyte is higher than that of water. One common phenomenon usually observed in IMS, especially at low temperatures, is the formation of adduct ions [3].

N-Aminophthalimide (N,N-phthaloylhydrazine; $C_8H_6N_2O_2$) has wide applications in dye and plastic

industries. Its chemical structure consists of one benzene ring and one heterocyclic ring fused together [4]. This compound participates in cycloaddition reactions from its amine group [5].

In the present study, the Thermal decomposition and then chemical ionization of decomposition products of N-Aminophthalimide have been studied in the ionization region of IMS. Protonated N-Aminophthalimide, its decomposition products were assigned in the ion mobility spectra.

II. METHODS

All experiments were performed with a commercial ion mobility spectrometer (IMS-300) made by TOF Tech. Pars Co. (Iran). The cell temperature was set at 170 °C, and the injection port temperature was scanned from 180 to 260 °C. Purified air was used as drift and carrier gases. Drift field was set at 500 V.cm^{-1}.

N-Aminophthalimide purchased from Merck and used without further purification. A 500 ppm solution was made by solving the sample in methanol. 1 mL of the standard solution was loaded into the injection port, and the solvent was allowed to evaporate. To increase the decomposition efficiency of N-Aminophthalimide sample, a delay time of 5 seconds was applied after sample injection.

III. RESULTS AND DISCUSSION

Fig. 1a shows the normal CD-IMS spectrum of N-Aminophthalimide with injection port temperature of 260 °C. From the left to the right, three peaks were observed in the background spectrum, which are originated from hydrated NH_4^+, NO^+, and H_3O^+ reactant ions. As seen in Fig. 1a, one product ion peak (PIP1) was observed for N-Aminophthalimide at drift time of 7.80 ms.

As shown in Fig. 1b, applying the delay time leads to the appearance of new peaks at drift times lower and higher than the PIP1. These peaks are probably originated from thermal

decomposition of the studied sample. Fig. 2 shows the effect of injection port temperature on the intensity of these peaks.
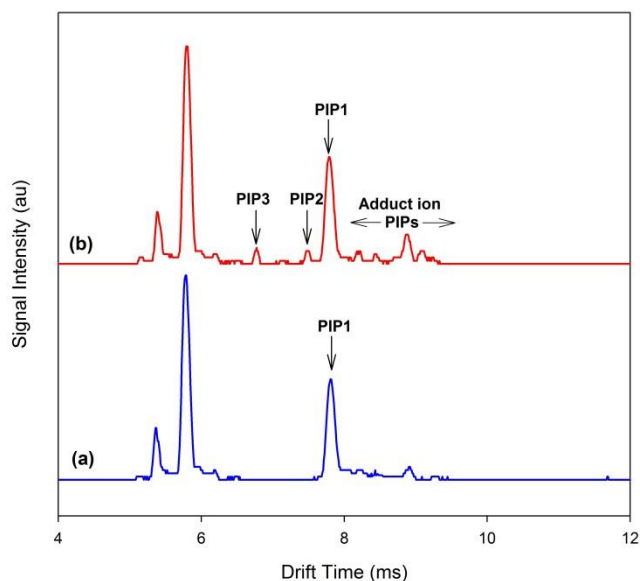

Fig.1: (a) CD-IMS spectrum of N-Aminophthalimide obtained at injection port temperature of 260 °C, and (b) the IMS spectrum obtained with applying 5 seconds post-injection delay time.
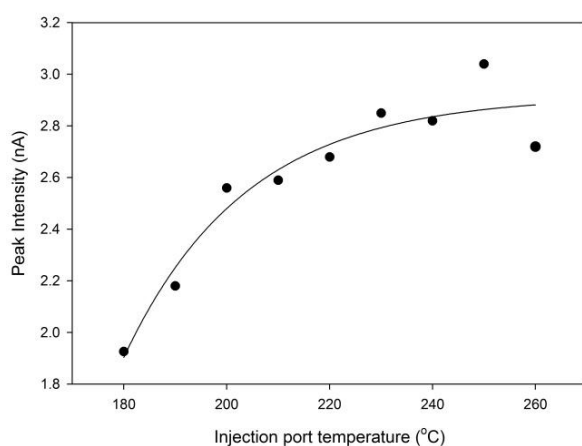

Fig. 2: The sum of the intensities of all PIPs except the PIP1 versus the injection temperature. A post-injection delay time of 5 seconds was applied in all experiments.

As can be seen in Fig. 2, the total intensity of the thermal decomposition product ion peaks increases with increasing

the injection port temperature. It can be concluded that the sample is decomposed in the injection port of the IMS instrument.

The PIPs with higher drift time than the mean peak (PIP1) are probably originated from adduct ions. The identification of these peaks is a complicated process and needs a mass spectrometer coupled to the IMS.

For identification of PIP2 and PIP3, the IMS spectrum of Fig. 1b was converted to the mass spectrum by "two standard mass" method. For this reason, the masses of 54 and 163 amu was considered for the ammonium reactant ion peak ($NH_4^+(H_2O)_2$) and the PIP1 (MH^+), respectively. The converted mass spectrum is shown in Fig. 3.
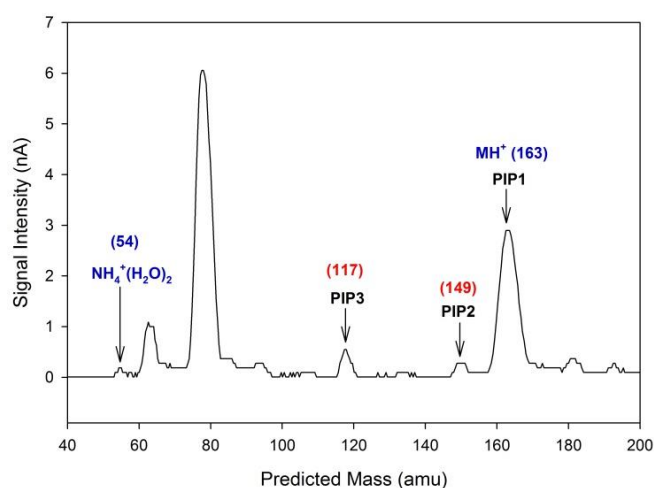
Fig. 3: Mass converted spectrum of N-Aminophthalimide obtained at injection port temperature of 260 ºC and cell temperature of 170 ºC based on two standard masses.

The mass of 149 amu was predicted for PIP2. This peak can be originated from a fragment with the structure of M-NH2, which can be protonated after reaching to the ionization region. The error for this assignment is about 1% that is a little and acceptable error in the two standard mass method. The PIP3 can be assigned to the protonated M-CO2 fragment with exact mass of 119 amu. The elimination of CO_2 has been observed for thermal decomposition of phthalimide compounds [6]. All assigned peaks are listed in scheme 1.
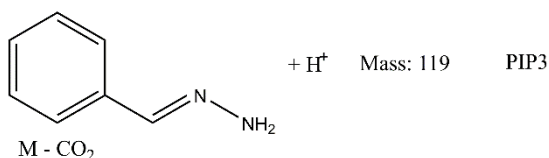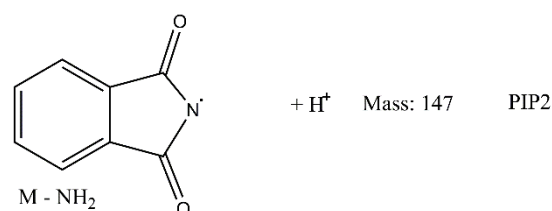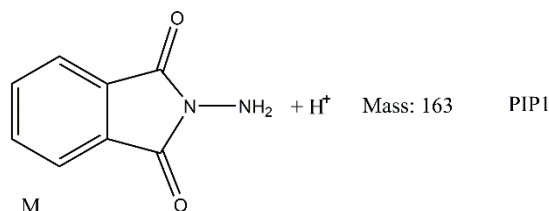
scheme 1

[6] K. Chen, J. C. Mackie, D. Wojtalewicz, E. M. Kennedy, B. Z. Dlugogorski, J. Hazard. Mater., vol. 187, pp. 407–412, **2011**.

IV. CONCLUSION

The results obtained in this study indicated that the IMS technique could be used for studying the thermal decomposition and chemical ionization of N-Aminophthalimide. Also, converting the IMS spectrum to the mass spectrum by using two standard masses assists the identification of the final decomposition products.

REFERENCES

[1] A. J. Bell, K. Giles, S. Moody, P. Watts, Int. J. Mass. Spectrom. Ion Process, vol. 173, pp. 65-70, **1998**.

[2] Y. Valadbeigi, V. Ilbeigi, B. Michalczuk, M. Sabo, S. Matejcik, J. Phys. Chem. A, vol. 123, pp. 313-322, **2019**.

[3] J. Puton, D. Augustyniak, U. Perycz, Z. Witkiewicz, Int. J. Mass Spectrom., vol. 373, pp. 43-49, **2014**.

[4] N. Puviarasan, V. M. Arjunan, S. Mohan, Turk J. Chem., vol. 26, pp. 323-333, **2002**.

[5] D. J. Anderson, T. L. Gilchrist, G. E. Gymer, C. W. J. Rees, Chem. Soc., Perkin Trans. 1, vol. , pp. 550-555, **1973**.

Structural and Dynamical Properties of phenyl propanoic acid Via Molecular Dynamics Simulations

P. Jahanbakhsh-Bonab[a] , _J. Jahanbin-sardroodi[b*]_

a Molecular Simulation laboratory (MSL), Azarbaijan Shahid Madani University, Tabriz, Iran;

E-mail: p.jahanbakhsh@azaruniv.ac.ir

b Molecular Simulation laboratory (MSL), Azarbaijan Shahid Madani University, Tabriz, Iran;

E-mail: jsardroodi@azaruniv.ac.ir

Abstract_:_ Carboxylic acids are commercially important chemicals and are involved in a number of industrially relevant separation processes. This work utilizes molecular dynamics method to simulate phenyl propanoic acid at variety of temperature. Densities, self-diffusivities have been reported for various temperature. The detailed microscopic structure has been discussed in terms of radial distributions, hydrogen bonds and non-bonded interaction energies. The Good agreement was obtained simulated density and experimental data. Radial distribution function was discussed in order to understand the atomistic interactions in these systems. The effects of temperature on the physicochemical, transport and structure properties of acid have been investigated.

Keywords_:_ Phenyl propanoic acid, Molecular Dynamics simulations (MD), Radial Distribution Functions (RDF), Self-Diffusion Coefficient

I. INTRODUCTION

Carboxylic acids are commercially compounds and are used in industrially relevant separation processes. They are used in a variety of fields, such as production of nylon, biodegradable plastics, pharmaceuticals and so on [1]. In order to design for the separation, removal and purification of acids, knowledge of the molecular interaction is necessary.

Carboxylic acids are cross and self-associating species, so experimental data for these acids are scarce [1].

Recently Ramjugernath and et.al [2] used Monte Carlo method in order to evaluated the phase diagram. So far microscopic properties of these systems are not reported. In this paper, we evaluated structural properties such as radial distribution function, spatial distribution function, hydrogen bond network and non-bonded interaction energy as well as dynamical properties such as diffusion coefficient and viscosity were calculated.

II. METHODS

In this study, molecular dynamic simulation was carried out using NAMD package [3]. The partial charges for phenyl propionic acid were obtained from Restricted Electrostatic Potential [4] (RESP) module of CHARMM27 [5]. Firstly, the system was minimized for 1 ns then each of the systems was heated from 0 K to 500K. the system was equilibrated in the NVT ensemble for 4 ns. Subsequently, the production run of 50 ns was carried out in the isothermal-isobar ensemble (NPT) where the temperature and pressure were controlled by Nose-Hoover thermostat and barostat. The particle mesh Ewald method [6] was used for treating long-range electrostatic interactions. The structure of the constituents is given in Figure 1.
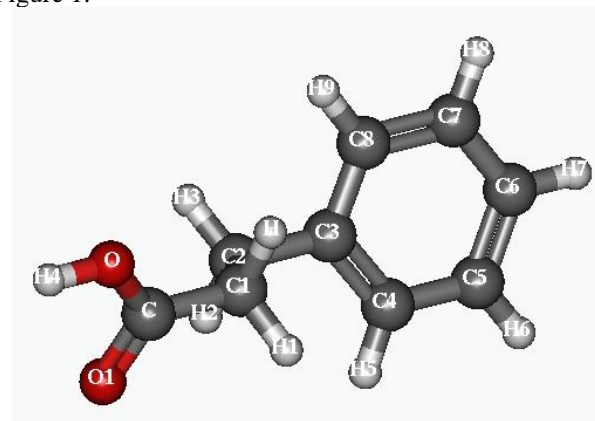

Figure 1. Schematic representation of the molecules of the phenyl propanoic acid.

III. RESULTS AND DISCUSSION
Thermodynamics and transport properties of system

firstly, we calculated density of system at three different temperature (293, 321, 500), that good agreement with experimental data. As results shown in table 1, density of this system decreased with increment of temperature.

Table 1. Simulated density

Temperature (K)	Density (g/cm³)	Diffusion coefficient (A°²/s)
293	1.10007	0.68211
321	1.0776	2.62172
500	0.91081	82.26

The viscosity of this system was measured using by Green-Kubo method which that the value of viscosity decreased with increment of temperature.

Finally, we evaluated diffusion coefficient form the Einstein relation

$$D = \lim_{t \to \infty} \frac{1}{6t} < (r_i(t) - r_i(0))^2 >$$

When beta parameter reached 1. These results shown in table 1. As seen in table 1, self-diffusion coefficient of phenyl propanoic acid increased with increment of temperature.

Structure of properties of systems

A structural analysis was performed for each system at three different temperatures. In order to get insight into the structure of phpr, Site-site radial distribution function (RDF) were evaluated. As represented in figure 2, the atoms H4 and H1 can form hydrogen bonds with oxygen atoms (O1, O). The high and sharp peaks of RDF at short distance for H4-O1 indicated that it has dominate contribution in the formation of hydrogen bonds.
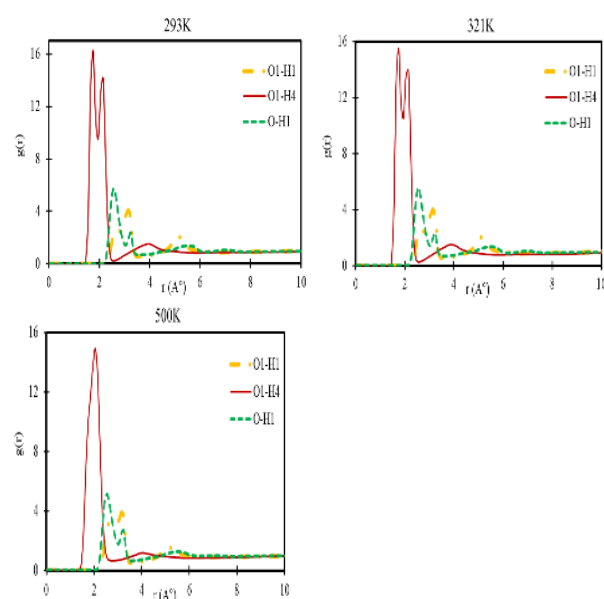
Figure 2. RDF for phenyl propanoic acid at three different temperature (293 K, 321K, 500K)

Figure 3 shows the average interaction energies of this system. The values reported in figure 3 are the electrostatic, van der Waals and sum of them (nonbond). The attractive potential between the phenyl propanoic acid is declining with increasing temperature of systems. The repulsion between them is increasing with increment of temperature.
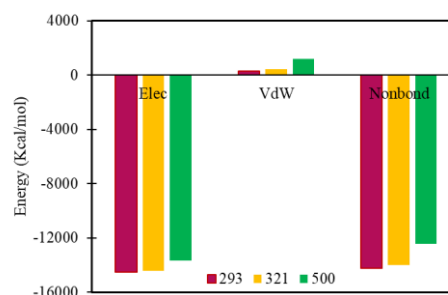

Figure 3. Interaction potential between phenyl propanoic acid at three different temperature (293 K (with violet color) 321 (with yellow color) 500K (with green color)).

Finally, we have quantified the number of hydrogen bonds formed between the phpr molecules. The results shown in figure 4 indicate that, the largest number of hydrogen bond interactions occur between the H4 atom and O1 atoms of phpr molecules. This result confirms the strong peak appeared in 1.8 A⁰ related to H4phpr-O1-'RDF. When tamperature of the system increased the number of hydrogen bonds decreased.
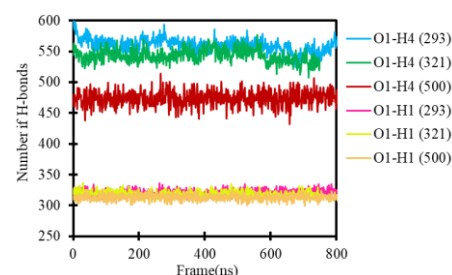

Figure 4. Number of hydrogen bonds per frames.

IV. CONCLUSION

Molecular dynamics simulations performed on phenyl propanoic acid showed very good agreement with experimental densities. Simulating transport properties demonstrated to be a significant task. A structural and hydrogen bond analysis highlighted the importance of phpr-phpr interactions.

In this paper we can calculated thermodynamics properties of phenyl propanoic acid that experimental values were not reported. These data are essential in order to design and operate equipment for the removal,separation, and purification of acides.

REFERENCES

[1]   S. L. Clifford, D. Ramjugernath, and J. D. Raal,
        "Vapour-liquid equilibrium of carboxylic acid
        systems: Propionic acid + valeric acid and isobutyric
        acid + valeric acid," *Fluid Phase Equilib.*, vol. 237,
        no. 1–2, pp. 89–99, 2005.

[2]   S. Clifford, K. Bolton, and D. Ramjugernath,
        "Monte carlo simulation of carboxylic acid phase
        equilibria.," *J. Phys. Chem. B*, vol. 110, no. 43, pp.
        21938–43, 2006.

[3]   J. C. Phillips *et al.*, "Scalable molecular dynamics
        with NAMD," *J. Comput. Chem.*, vol. 26, no. 16, pp.
        1781–1802, Dec. 2005.

[4]   C. I. Bayly, P. Cieplak, W. Cornell, and P. A.
        Kollman, "A well-behaved electrostatic potential
        based method using charge restraints for deriving
        atomic charges: the RESP model," *J. Phys. Chem.*,
        vol. 97, no. 40, pp. 10269–10280, 1993.

[5]   N. Foloppe and J. MacKerell Alexander D, "All-
        atom empirical force field for nucleic acids: I.
        Parameter optimization based on small molecule and
        condensed phase macromolecular target data," *J.
        Comput. Chem.*, vol. 21, no. 2, pp. 86–104, 2000.

[6]   T. Darden, D. York, and L. Pedersen, "Particle mesh
        Ewald: An N· log (N) method for Ewald sums in
        large systems," *J. Chem. Phys.*, vol. 98, no. 12, pp.
        10089–10092, 1993.

Hydrogen bonding in Systems Comprising Chitosan Nanoparticles/poly vinyl alcohol/Erythromycin

Seyede Mahtab Hosseini[a]*, **azim soltanabadi[b]**, **Majid Abdouss[a]** , **Saeedeh Mazinani[c]**

[a]*Department of Chemistry, Amirkabir University of Technology, 424 Hafez Avenue, P. O. Box 15875-4413, Tehran, Iran.*
[b]*Faculty of Chemistry, Razi University, University Avenue, Taq-e Bostan, Kermanshah*
[c]*New Technologies Research Center (NTRC), Amirkabir University of Technology, Tehran, Iran*
Email: 55hossini55@gmail.com

Abstract: The optimized geometries, electronic structures, of Chitosan (CS), tripolyphosphate (TPP) and Nanoparticles/poly vinyl alcohol/Erythromycin (CHE) were investigated using density functional theory (DFT) calculations. This study was carried out using computerized calculations of Gaussian program in Becke 3-parameters Lee-Yang-Parr (B3lyp/6-31g level) TPP, CS and CHE in gas phase. In addition, quantum theory of atoms in molecules (AIM) were applied to analyzed hydrogen bonding (H-bonding) interactions. Also the stability, highest occupied molecular orbital (HOMO) and lowest unoccupied molecular orbital (LUMO) levels, chemical hardness, and electrophilicity properties of CS and CHE calculated and compared each other's.

Keywords: DFT, Nanoparticles, hydrogen bonding.

I. INTRODUCTION

Hydrogen bonds (H-bond) are strong intermolecular forces and are responsible for many of the anomalous physical and chemical properties of liquid materials. Therefore understanding the intermolecular forces between species and the inter- and intra-molecular H-bonding is very significant and help us to better understand the microscopic properties of materials.

The use of nanotechnology in medicine and drug delivery is rapidly expanding. The use of nanoparticles to reduce toxicity and side effects of drugs and increase the medicine penetration into the body. Chitosan (CS) is a natural cationic polysaccharide, and was extensively accepted as a material of drug delivery and protein carriers. It possesses properties such biocompatibility, biodegradability, nontoxicity, antibacterial, anti-infective activity and ability to expedite wound healing, and it has been widely used in medical fields [1, 2]. In the study, chitosan nanoparticles were produced based on the

ionic gelation process of tripolyphosphate (TPP) and CS. We will optimize the size of the nanoparticles in application of drug delivery. A method to product these antibiotic-loaded networks is by electrospinning process. Electrospun nanofibers are explored as drug delivery using erythromycin as a model medicinal. Electrospun nanofibers have been reported to possess great potential for wound dressing as a result of special characteristics such as the high porosity of the nanofibrous membrane and also have a high surface to volume ratio [3-5]. In this study, we present a theoretical investigation of geometrical and electronic structures of systems Comprising Chitosan Nanoparticles/poly vinyl alcohol/Erythromycin. Also we discuss the type and number of hydrogen bonds between chitosan nanoparticles/poly vinyl alcohol/erythromycin.

II. METHODS

The quantum chemical calculations were used to predict the equilibrium geometry of tripolyphosphate (TPP), Chitosan (CS) and Nanoparticles Nanoparticles/poly vinyl alcohol/Erythromycin (CHE).The geometry optimization and electronic properties calculations were performed at the Becke's three parameter hybrid method with LYP correlation (B3LYP) [6, 7] level of DFT with 6-31+G basis set for all atoms. All calculations are carried out using the Gaussian 09 suites of program.

III. RESULTS AND DISCUSSION

Figure 1a and 1b shows that the optimization structure of TPP and Chitosan (CS) respectively.

Figures 2a and 2b show the optimized structure of CHE molecule in two different directions.

According to the figure we can see that CS molecules are located near nanoparticles and formation H-bond.
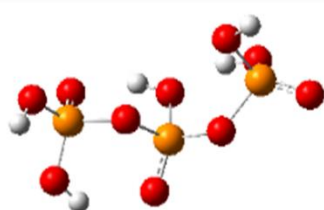
When H-bond is formed, the bond distance is smaller than the sum of the van der Waals radius of X and H atoms, and the angle between them is greater than 90∘. The hydrogen bonds are shown by red line in figure 2. According this figure, it can be seen that the each CS molecule formation one h-bonds with nanoparticles molecule and each APP molecule formation one h-bonds with nanoparticles molecule.

Table 1 shows the N…H, O…H bond length, bond angle and dihedrals angles.

a:

b:

Fig.1 Structures of a: TPP and b: CS optimized at B3LYP/6-31G level of theory.

Table 1. Optimized Bond Lengths and Bond Angles for Chitosan Nanoparticles/poly vinyl alcohol/Erythromycin at B3LYP Level of DFT with 6-31G Basis Set.

A–B	RA–B	A–B–C	∠ABC
232-	1.62	24-247-235	156.1
26-73	1.66	26-73-72	148.2
103-63	1.56	62-63-103	172.9
89-59	1.59	58-59-89	167.4

Computational Chemistry | 143

According this table there are 4 h-bond between CS and APP whit nanoparticles. The formation of 4 hydrogen bonds makes the structure of this molecule very stable and increased its solubility in polar solvents.

a:
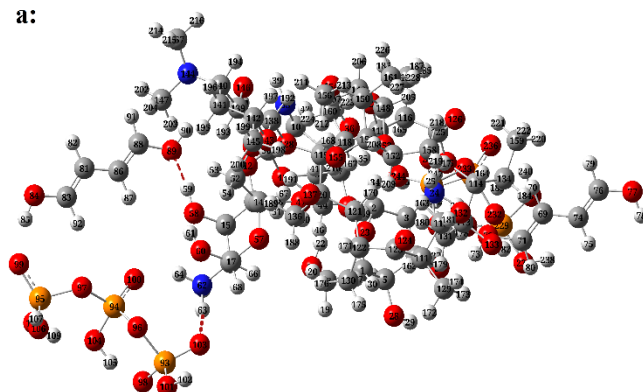
b:
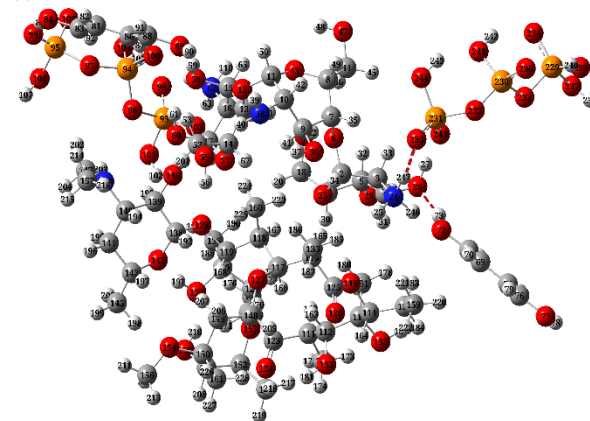
Fig.2 The optimized structure of CHE (two CS and two APP with nanoparticles) molecule in two different directions. at B3LYP/6-31G level of theory.

IV. CONCLUSION

In this work, we perform geometry optimization and electronic structures of TPP, CS and CHE by density functional theory. The formation h-bonds, cause to very stable structure of in this molecule and increased its solubility in polar solvents.

REFERENCES

[1] A. Francesko and T. Tzanov, Journal, vol. 125 pp. 1-27. **2011**

[2] Z.Değim, N. Çelebi, C. Alemdaroğlu, M. Deveci, S. Öztürk, Journal, vol. 8, pp. 343–354. **2011**

[3] M. Rahmani, S. Arbabi Bidgoli, S. M. Rezayat, Journal, vol. 4, pp. 61-70, **2017**.

[4] M. Ganesh, A. Sch Aziz, U. Ubaidull, P. Hemalatha, A. Saravanakumar, R. Ravikumar, M. Peng, E. Choi, H. Jang, Journal, vol. 39, pp. 127–135. **2016**

[5] S. Fatollahipour, A. Abouei Mehrizi, A. Ghaee, M. Koosha, Journal, vol 103, pp. 3852–3862. **2015**

[6] A. Becke, AD Becke,), *J. Chem. Phys.,* vol. 98, p. 5648, **1993**.

[7] C. Lee, W. Yang, and R. G. Parr, J. *Physical review B,* vol. 37, p. 785, **1988**.

DFT Calculation of the Enol Content of Acetone in the Presence of Water Clusters

Z. Tohidi Nafe[*], _N. Arshadi_

(_Department of Science, Zanjan University, Zanjan, Iran_)
Email: _Z.Tohidi@znu.ac.ir_

Abstract_:_ We have reported the effect of small water clusters on keto−enol tautomerization of acetone molecule in gas and liquid phases using DFT method. The results shown that the enol content of acetone is slightly improved by the addition of water molecules. The water clusters could differently stabilize the keto- and enol-forms of acetone. Among them, a cluster of three water molecules increases the enol content more than the other.

Keywords: Enol content, Acetone, Water clusters, DFT methods

I. INTRODUCTION

Keto–enol tautomerization reaction is one of the most important 1,3-hydrogen shift rearrangement that has received considerable attention due to its essential role in chemical and biochemical processes. The value of equilibrium constant of a keto-enol tautomerization reaction (K_{eq} = [Enol]/[Keto]) or enol content of a ketone depends upon the stability of its tautomeric forms. In simple ketones such as acetone the keto-form are usually more thermodynamically stable than the enol-form. It is difficult to determine reliably the enol content of most simple monocarbonyl compounds in solution. Because, the concentration of enol-form is very low and their enol content is very much less than 1, of the order of 10^{-10} [1, 2].

The enol content of acetone, for example, is about 6×10^{-10} at equilibrium [2].

Also, the stability of these tautomeric forms in solution phase depends on dielectric constant, polarity and hydrogen bond-forming ability of the solvent. It seems that, the enol is stabilized in solvents that can act as hydrogen-bond acceptors, while the keto-form is favored in protic solvents acting as hydrogen-bond donors.

Experiments data reveal enol content for simple mono ketones even in pure substances is very low and it is not over the 1-2 %. Also, some theoretical studies of enolization process have been done during the last three decades [3].

An acid or a base can catalyze keto-enol tautomerism process. Water catalyzed Keto–enol tautomerism is called "bifunctional water-catalyzed proton transfer" because in such process water acts both as proton donor and proton acceptor.

II. METHODS

The enol content of acetone in the presence of linear or cyclic discrete hydrogen bonded assembly of water molecules is calculated by using some reported water clusters, Fig. 1[4]. Each assembly is formed from the optimized water cluster and one of the tautomeric forms of acetone.
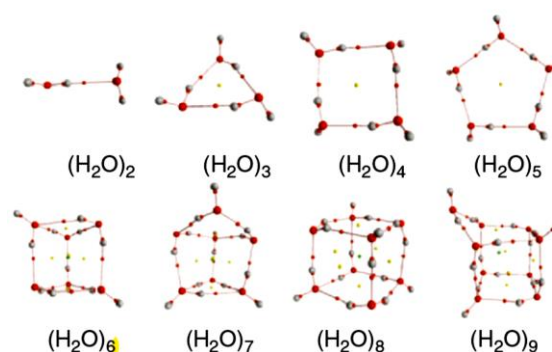

Fig. 1 clusters of water molecules used

At the first, the assembly were optimized by DFT method at B3LYP/6-311++G** level of theory in the gas phase. Then, the calculations were carried out at the B3LYP/6-31+G** level of theory in liquid phase and DMSO as solvent at room temperature. Solvent effects were included using the SM8 solvation model. The enol content (K_e) was calculated based on the thermodynamic properties of the assembly of both tautomeric forms of acetone with the same water cluster by the following equation.

$$Ke = e^{-\Delta G/RT} \tag{1}$$

In which ΔG^0 is the difference in the standard Gibbs free energy of enol- and keto-forms, R is gas constant and T is temperature.

All calculations were carried out using the Spartan'10 software package.

III. RESULTS AND DISCUSSION

The results shown that the enol content of acetone is increased in the persence of one molecule of water or a cluster of water molecules. But, the number of water molecules shows different increasing effects. As it seen, the clusters including 3, 7 and 9 water molecules show more enol content than the others, Table 1.

Table 1 Enol content of acetone in the presence of one to nine water molecule in gas phase at the B3LYP/6-311++G** level of theory

	Assembly	Enol content
I	Acetone	2.2×10^{-10}
II	Acetone + 1 H_2O	3.9×10^{-10}
III	Acetone + 2 H_2O	2.0×10^{-9}
IV	Acetone + 3 H_2O	6.7×10^{-8}
V	Acetone + 4 H_2O	6.3×10^{-10}
VI	Acetone + 5 H_2O	2.4×10^{-9}
VII	Acetone + 6 H_2O	7.5×10^{-9}
VIII	Acetone + 7 H_2O	4.9×10^{-7}
IX	Acetone + 8 H_2O	9.8×10^{-10}
X	Acetone + 9 H_2O	1.1×10^{-8}

The optimized structure of the assembly **VII**, for example, shows a good structural complementarity between the keto-form of acetone and the water cluster, Fig 2. Such an interaction is the main stabilizing effect of one of the tautomeric forms of acetone or both with the cluster of water molecules.
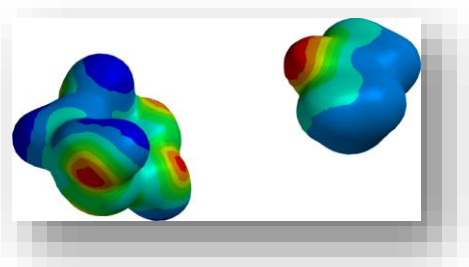

Fig. 2.
Electrostatic potential map of acetone and cluster of six water molecules, it shows the good structural complementarity of both units in the assembly.

IV: REFERENCES

[1] C. Reichardt, W. Thomas, Solvents and Solvent Effects in Organic Chemistry, 4th ed., Wiley-VCH, pp. 123-127, **2011**.
[2] H. Hart, Simple Enols, Chem. Rev., 79, 515, **1979.**
[3] K. Jana, B. Ganguly, DFT Study To Explore the Importance of Ring Size and Effect of Solvents on the Keto–Enol Tautomerization Process of α- and β-Cyclodiones, ACS Omega, 3(7), 8429–8439, **2018.**
[4] S. J. (Ed.) Grabowski, Hydrogen Bonding - New Insights, Springer, **2006**.

Protonation of Gabapentin, ab initio study

M. Tozihi[a]*, **M. R. Zarifiyan[a]**,

[a)]Department of Chemistry, University of Zanjan, P. O. Box: 38791-45371, Zanjan, Iran

Email: tozihi@znu.ac.ir

Abstract In this work the protonation of gabapentin which is antiepileptic drug is investigated theoretically. At first the stable conformers of the molecule have been defined at the B3LYP method and 6-311++G(d,p) basis set. Then two more stable structure were selected to protonation process at the same level of theory. The proton affinity and gas phase basicity obtained 230.333 and 221.825 kJ/mol at 298 K, respectively.

Keywords: Gabapentin, molecular structure, protonation, Proton affinity, Gas phase basicity.

I. INTRODUCTION

Gabapentin or 1-(amino methyl) cyclohexan acetic acid is known as an anticonvulsant and antiepileptic drug. Currently, it is used as decreasing neuropathic pain like headache and backache [1]. Depending on the environment like solvent and pH gabapentin (GABA) exists in neutral form or zuitterions. X-ray Crystallography data suggests that GABA in solid state exists in zouitterionic form [2]. GABA ground stae properties in both zouitterionic and neutral forms have been estimated employing density functional Theory (DFT) [3]. Also, FT-IR, FT-RAMAN and UV-VIS spectra of GABA have been investigated experimentally and theoretically[4]. In this study the protonation of GABA has been investigated in the gas phase, theoretically. Also proton affinity(PA) and Gas phase basisity (GB) of GABA has been reported.

II. METHODS

All calculations were carried out by Guassian 09 package at DFT (B3LYP) level of theory. Polarized triple-zeta 6-311++G(d,p) basis set has been used.

III. RESULTS AND DISCUSSION

GABA includes a 1,1-disubstituted cyclohexan ring, in which carboxyl methyl and amino methyl substituents can interconvert between two orientations, axial and equatorial. Although, the space above the cyclohexan is less crowded, it is predicted the carboxyl methyl group does not place above of the ring in axial orientation in the most stable conformer. 6 stable conformers of GABA were shown in Fig.1 that in GABA5 and 6 conformers carboxyl methyl is in axial orientation. The geometries of these conformers are optimized at B3LYP/6-311++G(d,p) level of theory. Our results are in good agreement with optimized structure in Ref. 3. The electronic energy, zero point energy (ZPE) and relative energies compared to the most stable conformer were reported in Table 1. Our calculation results summarized in Table 1 shows that the electronic energy of the GABA1 (-558.5881892 Hartree) is less than the others, but the Gibbs free energy of GABA5 is found to be lower than that in GABA1 by an amount 0.737 (kcal/mol).
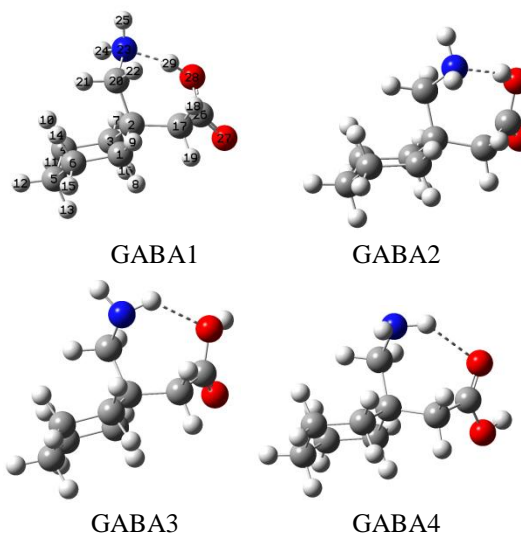
GABA1   GABA2
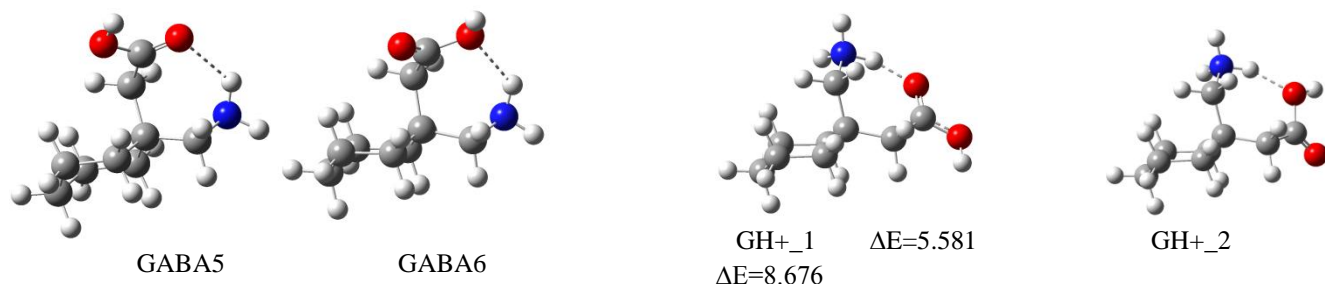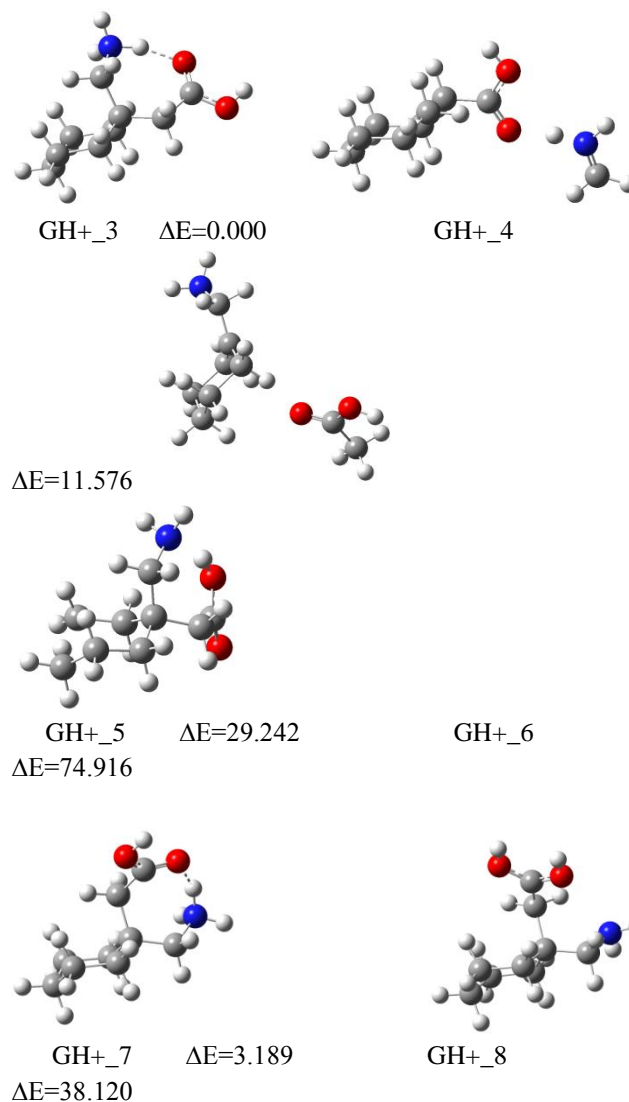
GABA3   GABA4

GABA5   GABA6

Fig.1: six more-low energy conformers of gabapentin at B3LYP/6-311++G(d,p) level of theory

Table1: electronic energy and ZPE, relative energy and Gibs free energy of conformers at B3LYP/6-311++G(d,p) level of theory

conformers	E_{ele}(Hartree)	ZPE (kcal/mol)	ΔE (kcal/mol)	ΔG (kcal/mol)
GABA1	-558.5881892	162.929	0.0	0.0
GABA2	-558.5881761	163.051	0.130	0.302
GABA3	-558.5865883	162.427	0.501	-0.047
GABA4	-558.5854855	162.321	1.087	0.322
GABA5	-558.5876927	162.438	-0.179	-0.737
GABA6	-558.5866518	162.288	0.323	0.313

The tow more stable conformers (GABA1 and GABA5) were selected to protonation. The protonation can occurred from several sits of two conformers. Oxygen of carbonyl and hydroxyl groups, nitrogen of amin group and carbons of methyl and cyclohexane groups. The optimized structures of protonated GABA1 named GH+_1 to GH+_6 were shown in Fig.2. Also GH+_7 to GH+11 in Fig.2 were related to protonated GABA5. Also, relative energy (ΔE) which E is the sum of electronic and ZPE were reported in Fig. 2.

GH+_1   ΔE=5.581   GH+_2
ΔE=8.676

GH+_3   ΔE=0.000   GH+_4

ΔE=11.576

GH+_5   ΔE=29.242   GH+_6
ΔE=74.916

GH+_7   ΔE=3.189   GH+_8
ΔE=38.120

Computational Chemistry | 148

GH+_9   ΔE=16.722   GH+_10

ΔE=25.522
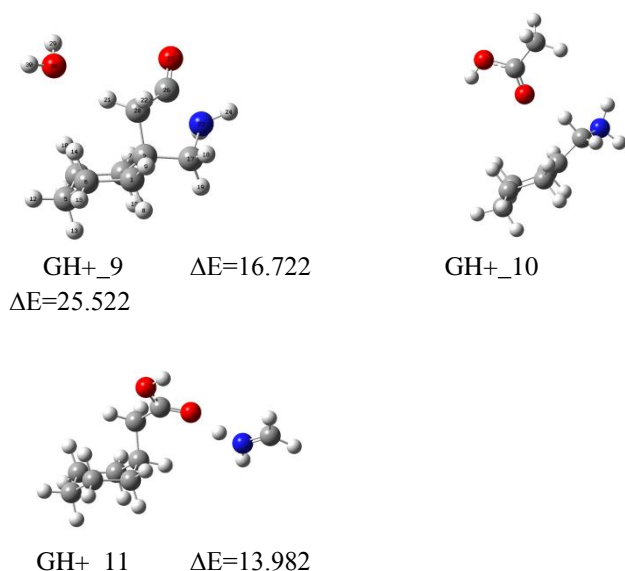

GH+_11   ΔE=13.982

Fig. 2. Optimized structures of protonated GABA1 and GABA5 at B3LYP/6-311++G(d,p) level of theory. ΔE is the relative "sum of electronic and ZPE" to the most stable conformers. All of the relative energies are in (kcal/mol).

It should be mentioned that protonation from some sites leads to migration of proton to nitrogen or other atoms, like GH+_2 and GH+_3 in Fig.2 and some leads to fragmentation of protonated components like GH+_4 and GH+_5 in Fig 2.

It is obvious that, when accepted proton remains on the protonated atoms in optimized structure, topical proton affinity (PA) and topical gas phase basicity can be calculated. PA is defined the negative of the enthalpy change and GPB is estimated as the negative of the Gibbs free energy change of the following proton transfer reaction [5].

$M+H^+ \rightarrow MH^+$ (1)
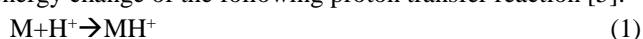
Where M is the neutral molecule and MH^+ is the protonated component. Topical PA (TPA) and topical GB (TGB) were reported in Table 2 for GABA1 and GABA5 conformers.

Table 2. The calculated of topical proton affinity and topical gas phase basicity (kcal/mol) at 298 K.

conformers	TPA		TGB	
	N atom	O of hydroxyl group	N atom	O of hydroxyl group
GABA1	227.791	--- (a)	220.152	--- (a)
GABA5	230.333	194.997	221.825	187.538

(a): migration of H+ to N atom

IV. CONCLUSION

By use of DFT(B3LYP) method and 6-311++G(d,p) basis set 6 stable conformers were obtained. The protonation of two more stable conformers has been occurred from several sits. So, topical PA and topical GB can be calculated. PA of GABA5 conformer changed from 230.333 to 194.997 (kcal/mol) when it was protonated from N atom and O of hydroxyl group sites at 298 K, respectively. It was found that nitrogen atom accepts proton easier than oxygen atom in two selected conformers from the comparison of GPBs. Obtained proton affinity and identify of components from fragmentation of protonated GABA can be used at the peak assignment in ion mobility spectroscopy of gabapentin.

REFERENCES

[1] A. Z. Segal, G. Rordorf, Neurology, vol. 46, 1175, **1996**

[2] A. Jamers, Ibers, Acta. Cryst., vol. C57, pp. 641-643, **2001**.

[3] Spectrochemica Acta Part A: Molecular and Biomolecular Spectroscopy, vol. 109, pp. 298-307, **2013**.

[4] P. S. Ganeshvar, M. Kangaraj, S. Gunasekaran, T. Gnanasambandan, Int. J. Sci. & Eng. Reas. , vol. 7, pp. 8-15, **2016**.

[5] J. C. Rienstra- Kiracofe, *et al.* Chem, Rev., vol. 102, pp. 231, **2002**.

Thermal Efficiency for a Curzon and Ahlborn Engine

M. Bamdad

Department of Chemistry, Faculty of Sciences, Shahid Chamran University of Ahvaz, Ahvaz, 61357-43135, Iran.

E-mail address: mbamdad@scu.ac.ir

Abstract: Usually classical thermodynamics text books are devoted some parts to heat engines and their cycles. Most of these text books pay attention to Carnot cycle and index diagram, therefore the others diagrams and cycles often missed. Although the Carnot cycle has an important role in the evolution of the second law of thermodynamics from historical point of view, the other cycles like Brayton cycle, Otto cycle, Atkinson cycle [1], and recently Curzon and Ahlborn (C-A) cycle [2] are appreciable and must be regarded.

Keywords: Carnot cycle, Heat engine, Thermal efficiency.

I. INTRODUCTION

In a heat engine, heat flows from hot source to cold source spontaneously. Some of the transferred heat (or better energy) changes to work and necessarily some of them transfer to heat sink, which is called degradated. The efficiency of cycle is equal to ratio between the work gains to the heat withdrawn from the hot source. One of the important missions of thermodynamics is the evaluation of efficiency for different cycles. Efficiency of a Carnot engine is maximum and but is not realistic, on the other hand efficiency of Curzon and Ahlborn cycle is more accurate.

II. METHODS

The well-known Carnot cycle consists of four reversible strokes. The cycle can be represented by *P-V*, *T-S* or even *T-V* diagram. The *P-V* diagram (index diagram) is more familiar than the others, but *T-S* diagram is straightforward and instructive that explain as further.

At a Carnot cycle the heat transferred to auxiliary system at first stroke isothermally is $T_h\Delta S$ and heat transferred to cold reservoir at third stroke isothermally is $T_c\Delta S$. Thus, the work transferred to the reversible work source is $(T_h - T_c)\Delta S$ and the coefficient of performance is:

$$\varepsilon_{Carnot} = \frac{(T_h - T_c)\Delta S}{T_h \Delta S} = \frac{dW_{RWS}}{(-dQ_h)} = 1 - \frac{T_c}{T_h} \qquad (1)$$

where dW_{RWS} is reversible work source. It can be shown that ε_{Carnot} is maximum for a Carnot cycle, for any substance that used as working fluid in the engine [3].

III. RESULTS AND DISCUSSION

The Carnot cycle is not real, because all steps in the cycle are reversible. That means a finite amount of work gains at an infinite time of each cycle, therefore the output power becomes zero. Overcoming the problem is possible if a cycle would not be reversible. This approach is followed and published by F. L. Curzon and B. Ahlborn, which cited more than 2100 times. They didn't use a reversible process, and proved C-A efficiency is:

$$\varepsilon_{C-A} = 1 - \left(\frac{T_c}{T_h}\right)^{\frac{1}{2}} \qquad (2)$$

They showed that the C-A efficiency is more compatible to the observed performance of real heat engines rather than the Carnot cycle as shown in Table 1.

Table1: Observed performance of real heat engines. [2]

	t_c (ºC)	t_h (ºC)	ε_{Carnot}	ε_{C-A}	$\varepsilon_{observed}$
Different Power sources	25	565	64.1%	40%	36%
	25	300	48.0%	28%	30%
	80	250	32.3%	17.5%	16%

Recently B. H. Lavenda showed that the efficiency of Curzon-Ahlborn cycle is also applicable for endoreversible engines [4].

IV. CONCLUSION

The Carnot cycle is an ideal cycle that produces maximum thermodynamic performance. In a real engine, thermodynamic efficiency is less than the efficiency that

expects from a Carnot cycle. The difference not only rises by mechanical limitations such as friction, but also comes from the fundamental reason that a real engine does not work reversible. It seems that the C-A performance is more accurate and eligible thermodynamic efficiency for a real engine.

REFERENCES

[1] H. S. Leff, "Thermal efficiency at maximum work output: New results for old heat engines." *American Journal of Physics,* vol. 55, no. 7, pp. 602-610, **1987**.

[2] F. L., Curzon, and B. Ahlborn. "Efficiency of a Carnot engine at maximum power output." *American Journal of Physics,* vol. 43, no. 1, pp. 22-24, **1975**. (2100)

[3] Herbert B. Callen, "Thermodynamics and an Introduction to Thermostatistics." **1998**.

[4] B. H., Lavenda, "The thermodynamics of endoreversible engines." *American Journal of Physics,* vol. 75, no. 2, pp. 169-175, **2007**.

Section:

Computational Drug Design

Evaluating Dopamine Targeting Drugs for Treatment of Schizophrenia By Applying a Practical Java Tool

*P. Amani[a], R. Habibpour[a] ***

a: Department of Chemical Industries, Iranian Research Organization for Science and Technology, Tehran, Iran
Email: Habibpour@irost.ir

Abstract: Computational drug discovery is an effective strategy for economizing drug discovery and development process. Developing drugs for treatment of dopaminergic disorders especially schizophrenia is also very time/cost consuming. Using cApp Java tool we have provided informative physico-chemical data which can enlighten the drug developing process of drug designers.
Keywords: cApp, Drug, Dopamine, Schizophrenia

I. INTRODUCTION

Dopamine is an essential neurotransmitter in the central nervous system that has been implicated in processes as diverse as reward, addiction, control of coordinated movement, metabolism and hormonal secretion [1]. Dysregulation of the dopaminergic system is correlated with diseases such as schizophrenia, Parkinson's disease, depression, attention deficit and hyperactivity disorder [2].

Schizophrenia is a chronic and debilitating neuropsychiatric disorder affecting almost 1% of the world's population. Although the pathology of disorder remain un-resolved, dopamine system dysfunction clearly contributes to the pathophysiology of this disorder [3].

For treatment of Schizophrenia there is a long list of drugs that may be used to reduce symptoms. Evaluating the physicochemical properties of dopaminergic drugs may lead scientist to developing/improving the more valuable drugs [4].

Also, determining and redesigning the PAINS drugs which are polluting the literatures would be a precious achievement. Pan-assay interference compounds (PAINS) are chemical compounds that often give false positive results in high-throughput screens. Baell and et. all have identified rhodanines, phenolic Mannich bases, hydroxyphenylhydrazones, alkylidene barbiturates, alkylidene heterocycles, 1,2,3-aralkylpyrroles, activated benzofurazans, 2-amino-3-carbonylthiophenes, catechols, and quinones as PAINS [5], [6].

II. METHODS

We used cApp Java application [7] to evaluate 52 most common drugs for treatment schizophrenia. The software is intended for the appraisal of compounds with respect to their physicochemical properties, analysis in relation to adherence to likeness rules as well as recognition of pan-assay interference components [1] [8], [6] and cross-linking with identical entries in the PubChem Compound Database.

The result can be seen in a table including seven columns contain information about the physico-chemical properties of the compounds:

- Molecular mass (M)
- Lipophilicity: calculated logP (xlogP)
- Number of hydrogen bond donors (H-Don),
- Number of hydrogen bond acceptors (H-Acc),
- Number of rotatable bonds (rot. bonds),
- Number of rings (ring count),
- Polar surface area (PSA).

The color mapping in these seven columns indicates the compliance with the drug likeness criteria (see Table 1); green color signals compliance, red color shows violation and black color indicates that this property is not part of the criteria set of the drug likeness. The type of likeness criteria selected is displayed as a tool tip for these column headers.

Table1: Criteria for drug, lead and fragment likeness according to [9]

Property	Drug-like (Rule of 5)
Molecular mass	≤ 500 Da
Lipophilicity: calculated logP	≤ 5
No of H-bond donors	≤ 5
No of H-bond acceptors	≤ 10
No of rotatable bonds	n/a
No of rings	n/a
Polar surface area	n/a

- The 10th column indicates whether a molecule contains an entity of a pan-assay interference compound (PAIN).

In the compound appraisal task, cApp conducts SMARTS queries using 480 PAINs substructure filters. The cApp software has subjected a library of 50,000 compounds from the ChemBridge catalogue to PAINs filtering using the same SMARTS filters [7].

III. RESULTS AND DISCUSSION

Lipinski´s rule of five parameters have been determined for selected drugs. According to the mentioned rule, drugs with a molecular weight (MWT) less than 500 Daltons, a calculated log P less than 5, less than 5 H-bond donors, and less than 10 H-bond acceptors were more likely to have better absorption or permeation. Also the drug would have a preferable oral bioavailability if they had 10 or fewer rotatable bonds and a polar surface area equal to or less than 140 Å^2 [10]. The output results due to the assessment of dopaminergic drugs which have been defined for the cApp software are included in table 2.

Table 2: cApp results on Schizophrenia drugs

No	ID	MW (g/mol)	XLogP	H-Don	H-Acc	rot. bonds	Ring count	top.PSA	PAIN
1	Amisulpride (Solian)	369.2	2.5	2	7	7	2	113.6	
2	Amphetamine	135.1	1.8	1	1	2	1	26	
3	Apomorphine	267.1	2.9	2	3	0	4	43.7	catechol_A(92)
4	Aripiprazole	447.1	4.9	1	5	7	4	48.3	
5	Asenapine	285.1	3.4	0	2	0	4	12.5	
6	Benperidol	381.2	4.1	1	5	6	4	58.4	
7	Bifeprunox	385.2	4.9	1	5	4	5	52.7	
8	Blonanserin	367.2	6.1	0	3	3	4	19.4	
9	Brexpiprazole	433.2	5.6	1	5	7	5	77.1	
10	Bromocriptine	653.2	3.9	3	10	5	7	117.9	
11	Butyrophenone	148.1	2.7	0	1	3	1	17.1	
12	Cariprazine	426.2	5.5	1	5	6	3	42.3	
13	Chlorpromazine (Thorazine)	318.1	4.9	0	2	4	3	31.8	
14	Clozapine (Clozaril)	326.1	4.3	1	4	1	4	30.9	
15	Cocaine	303.1	2.3	0	5	5	3	55.8	
16	Dizocilpine	221.1	3.3	1	1	0	4	12	
17	Droperidol	379.2	3.9	1	5	6	4	58.4	
18	Fluphenazine	437.2	4.2	1	4	7	4	55.3	
19	Haloperidol	375.1	4	1	3	6	3	40.5	
20	Iloperidone	426.2	4.1	0	4	8	4	64.8	
21	Ketamine	237.1	2.9	1	2	2	2	29.1	
22	Levodopa	197.1	-2	4	5	3	1	103.8	catechol_A(92)
23	Levomepromazine (methotrimeprazine)	199	3.8	1	1	0	3	37.3	het_thio_666_A(13)
24	Loxapine	327.1	3.8	0	4	1	4	28.1	
25	LSD	323.2	2.4	1	4	4	4	39.3	
26	Lurasidone	492.3	5.2	0	6	5	7	85	
27	Melperone	263.2	3.5	0	2	5	2	20.3	
28	Mescaline	211.1	0.8	1	4	5	1	53.7	
29	Mesoridazine (Serentil)	386.1	3.9	0	3	4	4	68.1	
30	Molindone	276.2	1.2	1	4	3	3	45.3	
31	Monomethyl Phthalate	180	1.6	1	4	3	1	`63.6	
32	Olanzapine (Zyprexa)	312.1	2.8	1	4	1	4	59.1	
33	Paliperidone	426.2	1.8	1	5	4	5	82.2	
34	Perphenazine	403.1	3.9	1	4	6	4	55.3	
35	Phencyclidine	243.2	4.2	0	1	2	3	3.2	
36	Phenothiazine	199	3.8	1	1	0	3	37.3	het_thio_666_A(13)
37	Pomaglumetad Methionil (LY 2140023)	366.1	-3.5	4	9	7	2	201	
38	Prochlorperazine (Compazine)	373.1	4.6	0	3	4	4	35	
39	Promazine	284.1	4.3	0	2	4	3	31.8	het_thio_666_A(13)
40	Promethazine	284.1	4.4	0	2	3	3	31.8	het_thio_666_A(13)
41	Quetiapine (Seroquel)	383.2	2.9	1	5	6	4	73.6	
42	Reserpine	608.3	3.6	1	11	10	6	117.8	indol_3yl_alk(461)
43	Risperidone (Risperdal)	410.2	2.6	0	4	4	5	61.9	
44	Serotonin	176.1	1	3	3	2	2	62	
45	Sertindole	440.2	5.4	1	5	5	5	44	

46	Spiperone	395.2	4.1	1	5	6	4	56.1	
47	Thioridazine	370.2	5.9	0	2	4	4	57.1	
48	Thiothixene	443.2	3.3	0	5	5	4	77.5	styrene_B(8)
49	Trifluoperazine	407.2	4.9	0	3	5	4	35	
50	Triflupromazine	352.1	5.2	0		5	3	31.8	
51	Ziprasidone (Geodon)	412.1	4.2	1	5	4	5	80.2	
52	Zotepine	331.1	5.1	0	2	4	3	37.8	

IV. CONCLUSION

Apomorphine, Levodopa, Levomepromazine, Phenothiazine, Promazine, Promazine, Promethazine, Reserpine and Thiothixene are PAIN drugs and a drug designer should consider the fact that these the effect of these drugs are not genuine and they just give false positive results. However, the other drugs especially those one which have green color data for all the criteria worth to develop and improvement.

Acknowledge

REFERENCES

[1] S. Wang, T. Che, A. Levit, B. K. Shoichet, D. Wacker, and B. L. Roth, "Structure of the D2 dopamine receptor bound to the atypical antipsychotic drug risperidone," *Nature*, vol. 555, no. 7695, p. 269, 2018.

[2] N. D. Harriott, J. P. Williams, E. B. Smith, H. P. Bozigian, and D. E. Grigoriadis, "VMAT2 Inhibitors and the Path to Ingrezza (Valbenazine)," in *Progress in medicinal chemistry*, vol. 57, Elsevier, 2018, pp. 87–111.

[3] P. Li, G. L Snyder, and K. E Vanover, "Dopamine targeting drugs for the treatment of schizophrenia: past, present and future," *Curr. Top. Med. Chem.*, vol. 16, no. 29, pp. 3385–3403, 2016.

[4] J. M. Kane, "Pharmacologic treatment of schizophrenia," *Biol. Psychiatry*, vol. 46, no. 10, pp. 1396–1408, 1999.

[5] J. Baell and M. A. Walters, "Chemistry: Chemical con artists foil drug discovery," *Nat. News*, vol. 513, no. 7519, p. 481, 2014.

[6] J. B. Baell and G. A. Holloway, "daucture filters for removal of pan assay interference compounds (PAINS) from screening libraries and for their exclusion in bioassays," *J. Med. Chem.*, vol. 53, no. 7, pp. 2719–2740, 2010.

[7] P. Amani *et al.*, "A practical Java tool for small-molecule compound appraisal," *J. Cheminform.*, vol. 7, no. 1, 2015.

[8] J. L. Dahlin *et al.*, "PAINS in the Assay: Chemical Mechanisms of Assay Interference and Promiscuous Enzymatic Inhibition Observed during a Sulfhydryl-Scavenging HTS," *J. Med. Chem*, vol. 58, pp. 2091–2113, 2015.

[9] J. Barker, T. Hesterkamp, and M. Whittaker, "Integrating HTS and fragment-based drug discovery," *DDW DRUG Discov. WORLD*, vol. 9, no. 3, p. 69, 2008.

[10] D. F. Veber, S. R. Johnson, H.-Y. Cheng, B. R. Smith, K. W. Ward, and K. D. Kopple, "Molecular properties that influence the oral bioavailability of drug candidates," *J. Med. Chem.*, vol. 45, no. 12, pp. 2615–2623, 2002.

Studying the interaction of phosphodiesterase inhibitors in the treatment of Alzheimer's disease

Raheleh Rahbar Kahkha[*], **Effat Dehghanian, Mehran Feizi Dehnayebi, Khatereh Abdi**

Department of Chemistry, University of Sistan and Baluchestan, Zahedan, Iran

Email:rahilrahbar96@gmail.com

Abstract: Phosphodiesterases are one of the causes of Alzheimer's disease. These enzymes mediate the hydrolysis of adenosine or guanosine monophosphate (cAMP or cGMP) that act as secondary messengers and play a key role in performance and cellular signaling. In this study, some phosphodiesterase (PDE4D) inhibitors have been investigated in the treatment of Alzheimer's disease. Five PDE4D inhibitors were selected and their structures were plotted by gaussview05. Optimization of each ligand was done by Gaussian09 software. The crystallographic Structure of PDE4D was taken from protein data bank (PDB ID:1Q9M). Then, molecular docking was performed by MOLEGRO Virtual Docker software. Compound (1) with the most negative binding energy to PDE4D (-199/569) was selected as the best one for binding to the active site of receptor.

Keywords: Alzheimer, Docking, Phosphodiesterase, MOLEGRO Virtual Docker

I. INTRODUCTION

Alzheimer's disease is a type of functional impairment in the brain that gradually affects memory and other mental abilities such as thinking, reasoning and judgment of the individual. The disease was first recognized by the German psychiatrist Alois Alzheimer in 1906 [1]. Alzheimer's disease is caused by various factors, One of them is phosphodiesterase enzyme. Phosphodiesterases are categorized into Eleven types (PDE1-PDE11), each containing several isoforms. They are a group of enzymes that selectively control the rate of hydrolysis of adenosine and guanosine monophosphate (cAMP or cGMP). Phosphodiesterases 4, 7 and 8 mediate the hydrolysis of cAMP to 5'-AMP, and phosphodiesterases 5, 6 and 9 convert cGMP to 5'-GMP. The other phosphodiesterases perform the hydrolysis of both nucleotides. These two nucleotides play a role in cellular signaling through the regulation of intracellular levels. Phosphodiesterases are Secreted in the brain, and their inhibitors regulate the neural processes by increasing the concentration of cAMP and cGMP in the brain tissue [2]. PDE4D inhibitors are divided into two groups including competitive and allosteric inhibitors. Inhibitors Such as ROFLUMILAST, CILAMILAST and PICLOMILAST are competitive inhibitors, and D-159153, PMNOQ and D-159404 are allosteric inhibitors [3].

Molecular docking is computational method that investigates the interaction between drug and receptor. The use of molecular docking techniques has began since 1980 and is one of the key methods in computational chemistry that is commonly used in drug discovery processes. Valuable information such as ligand-protein binding energy, and the role of each amino acid of proteins or ligand atoms in the interactions are obtained. Also, determining the best orientation of the ligand relative to the active site of the receptor is another important aspects of molecular docking [4].

II. METHODS

In this study, five compounds (Table.1), which are inhibitors of PDE4D, were selected. The three-dimensional structure of these ligands were drawn using the Gauss view05 software. Then, quantum mechanics calculations for structure optimization of these compounds was carried out by Gaussian09 software via employing DFT method at B3LYP/6-31g level of theory. Afterward, molecular docking simulations was performed using MOLEGRO Virtual Docker software with mole dock algorithm. Docking requires the protein and ligand Structure. In this Study, the crystallography Structure of the PDE4D enzyme (PDB ID:1Q9M) was taken from the protein data bank (www.rcsb.org). After preparation of the protein and ligands, docking of each ligand was Carried out with protein**.**

III. RESULTS AND DISCUSSION

Molecular docking simulation of five inhibitors of PDE4D was performed using MOLGRO virtual Docker software. First of all, preparation of protein was carried out, this means that ligands, additional cofactors and water molecules in the crystallographic structure of the protein were removed and hydrogen atoms were added. Three cavities were observed in the active site of PDE4D where the biggest one has a volume of 309 cm^3 and is located in the area between domain I, II. The second and third cavities are 199/68 (cm^3) and 17/408 (cm^3) respectively (figure.1). After simulation, twenty superior conformations were reported by the software, all of which were located in cavity I. The interaction of the best conformation of compound (1) with the amino acids of the

phosphodiesterase enzyme is shown in figure 2. As can be seen, threonine 271 with a fluorine atom and threonine 333 with an oxygen atom of compound (1) form two hydrogen bonds, other important interactions with amino acids are of steric type. The strongest steric interaction belongs to the phenylalanine 372 with the energy -34/9621.

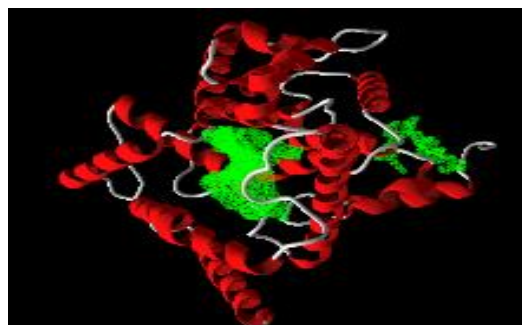Table 1.Phosphodiesterase (PDE4D) inhibitors

Compound	Structure
1	
2	
3	
4	
5	

Fig. 1. Cavity position on phosphodiesterase structure
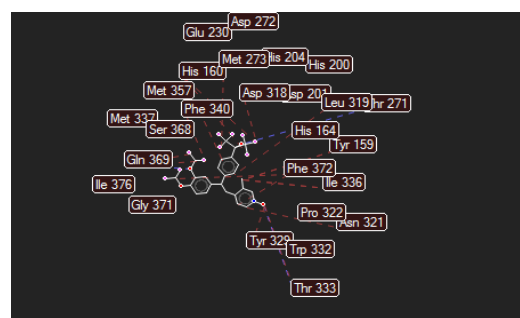
Fig. 2. Two-dimensional diagram for the interaction of compound 1 (best pose) with PDE4D (blue line: hydrogen bound and red line: steric interaction).

Table 2. Docking results of five PDE4D inhibitors.

Compound	Interaction	MOL dock
1	-199.569	-151.326
2	-168.3	-156.759
3	-165.976	-145.81
4	-163.35	-143.492
5	-158.743	-138.658

IV. CONCLUSION

In this Study, the molecular docking of five inhibitors of PDE4D enzyme was performed by MOLEGRO virtual Docker software. Based on the results, all of the compounds were located in the cavity I, which is the biggest one. Compound (1) with the most negative energy was selected as the best compound. It interacts with Thr_{271}, and Thr_{333} via hydrogen bond and shows steric interaction with $Glu_{23}.Glu_{230}$, Tyr_{159}, Tyr_{329}, Trp_{332}, Ser_{368}, Pro_{322}, Phe_{372}, Phe_{340}, Met_{357}, Met_{337}, Met_{273}, Leu_{319}, Ile_{376}, Ile_{336}, His_{204}, His_{200}, His_{164}, His_{160}, Gly_{371}, Glu_{230}, Gln_{369}, Asp_{318}, Asp_{272}, Asp_{201}, and Asn_{321}.

REFERENCES

[1] Mohammadzadeh E, Alipour F, Khallaghi B. Evaluation of spatial memory impairment after intracerebroventricular streptozocin injection in adult rats. Shefaye Khatam. 2014; 2(1).**1995**.

[2] Ana García-Osta*, Mar Cuadrado-Tejedor*, Carolina García-Barroso, Julen Oyarzábal, and Rafael Franco, Phosphodiesterases as Therapeutic Targets for Alzheimer's Disease, 2012; 3, 832-844

[3] Frank Wunder,* Ramona Quednau, Andreas Geerts, Martina Barg, and Adrian Tersteegen Characterization of the Cellular Activity of PDE 4 Inhibitors Using Two Novel PDE 4 Reporter Cell Lines,2013; 10, 3697-3705

[4] Novikov FN, Chilov GG. molecular docking theoretical back ground, practical application and perspectives. Men com 2009;19: 237-242

Docking and virtual Screening for determination of new derivatives of anti-cancer drugs from Quinazoline compounds

E.s. Mousavi*, M. Sargolzai, H. Nikoufard

Physical chemistry, Shahroud University of Technology, Shahroud, 3619995161 , Iran

Email:elahe.s.mosavi@gmail.com

Abstract: The growth and spread of tumors to a great extent depend on the activity of recipients of cell membrane such as EGFR or the recipients of epidermal growth. EGFR plays a key role in most of cell processes involved in the spread of tumor and is indeed a promising objective regarding the treatment of cancer. Some drug combinations have been synthesized in order to control the enzyme of epidermal growth factor that have a considerable linkage energy. Due to the fact that in empirical and laboratory work the linkage mechanism of such drugs to protein is not specified, therefore, with the use of molecular docking, the strength and how the drugs were linked have been examined. The results reveal that the combination of 6-Fluoro-2-(4-fluoro-phenyl)-3-(2-oxo1,2-dihydro-indol-3-ylideneamino)-3H-quinazolin one, concisely; called combination a is considered as the most powerful combination that has been placed as the base, and its similar combinations which include 263 combinations have been examined more. Among these combinations, the combination of N-Cyclopropyl-3-{[2-(4-fluoro-phenyl)-quinazolin-4-yl]-furan-2-ylmethyl-amino}-propionamide concisely; called combination b has been recognized as the most powerful and best new combination.

Keywords: Analysis of linkage point, Epidermal growth fact, Linkage energy, Molecular docking ,Quinazolines.

I. INTRODUCTION

Quinazolines belong to a famous class of heterocyclic compounds displaying a diverse and important range of therapeutic activities. They are used as antihypertensive, antibacterial, antiviral, anti-inflammatory, antidiabetic, anticonvulsant, analgesic and anticancer medications[1]. Many quinazolines were reported as anticancer agents having multi-target features, like epidermal growth factor receptor (EGFR), aldose reductase (AR), dihydrofolate reductase

(DFR), folate thymidylate synthase (FTS) , cyclic guanosine monophosphate (cGMP) phosphodiesterase, erythroblastosis oncogene B2 (erB2) tyrosine kinase, and cellular-sarcoma (c-Src) tyrosine kinase. Other quinazolines yield their anticancer activity by inhibition of DNA repairing system or tubulin polymerization. There are many other derivatives have dual EGFR/tubulin polymerization inhibitors, like amide derivatives and quinoxalines. Gefitinib, lapatinib and erlotinib are well-known anticancer drugs with quinazoline nucleus that target epidermal growth factor (EGFR) protein kinase .Today the scientists are looking for the discovery of drugs that influence the cancer cells directly and as a result do not change other cells. The combination of quinazoline has been researched and the recognition of their new derivatives for treatment purposes has been going on so far[2].

II. METHODS

Firstly, the related enzyme code (epidermal growth factor) was extracted from PDB site that its related code is 1M17, then by the use of chem draw software the molecules of water and ligand have been removed from it and were saved as pdb. Using molecular docking and softwares such as screening molegro the combination of quinazole core is done in such a way that firstly the target protein is selected and optimized, then the combination of quinazole core that were 263 combinations are added to it and is docked using Molegro software. Using the obtained results, powerful combinations will be recognized and will be used for the continuation of the research.

III. RESULTS AND DISCUSSION

After the process of molecular docking by the use of molegro software, based on the obtained results, from among 263 combinations, 20 combinations that have more negative

moldock score were selected for the comparison with combination a.

Figures and Tables

The obtained calculations and results show that the combination b with amino acids Asp831, Thr766, Thr830, and combination a with amino acids Lys721, and Thr830 form a hydrogen bond (Fig.1). The length of linkage and the energy of hydrogen bond linkage formed for combination b with amino acid Asp831 is consecutively equal to 3/02Å and -1/66kcal/mol, amino acid Thr766 is equal to 2/64Å and -2/47kcal/mol and amino acid Thr830 is equal to 3/20Å and -1/44kcal/mol and for hydrogen bond formed between combination a with amino acid Lys721 is equal to 3/36Å and - 1/18kcal/mol and amino acid Thr830 is equal to 2/79Å and -2/50kcal/mol. Also the obtained values of released energy of the linkage for amino acids Asp831, Thr766, Thr830 related to combination b consecutively is equal to -8/74141kcal/mol,-17/0618kcal/mol,-8/88889kcal/mol and for amino acids of Lys721 and Thr830 related to combination a is equal to -15/135kcal/mol and -11/7788kcal/mol. In addition to these results obtained from molecular docking, reveal that combination b has more negative moldock score (Table1). More negative moldock Score means that this combination has more stability, released more energy (is pyrogenic) and links with the active placement of protein with more strength, as a result it has a better and more restraining characteristic in comparison with other combinations.

(a)

(b)
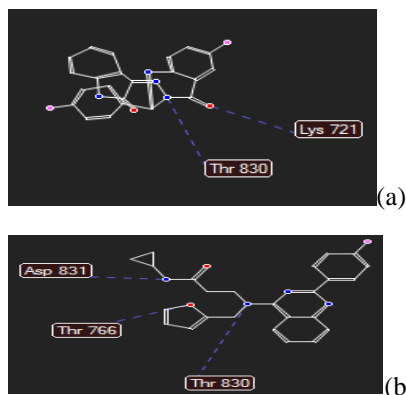
Fig.1: the formed hydrogen bonds between combinations and amino acids related to them a)combination a

b) combination b

Computational Drug Design | 7

Table1: Moldock score and rerank score of 20 superior combination and combination a

Name	MolDock Score(kcal/mol)	Rerank Score(kcal/mol)
combination b		
[00]ZINC37384124	-141.054	-63.2379
[00]ZINC00922174	-134.503	-91.4469
[00]ZINC00922159	-134.338	-48.3965
[00]ZINC06905939	-132.778	-93.0849
[00]ZINC08660865	-132.283	-88.2192
[00]ZINC37383013	-131.526	-68.4292
[00]ZINC37383109	-131.317	-85.4091
[01]ZINC37384124	-130.707	-89.6537
[01]ZINC37383013_1	-130.589	-95.1487
[00]ZINC37383013_1	-130.56	-27.1919
[02]ZINC37384124	-130.513	-66.2664
[00]ZINC27528406	-130.446	-85.6872
[01]ZINC37383109	-130.223	-84.004
[03]ZINC37384124	130.197	-96.5453
[01]ZINC37383013	-128.814	-89.8877
[01]ZINC08660865	-128.413	-41.8434
[02]ZINC12716340	-127.873	-102.488
[01]ZINC12716340	-127.372	-98.922
[01]ZINC00922174	-127.135	-99.0579
[03]ZINC08660865	-126.866	-25.8917
combination a *	-101.806	-47.2056

* combination a was taken from ref [1].

IV. CONCLUSION

In this research by the use of the method of molecular docking the energy linkage and their interactive method for some derivatives of restraining quinazoline was calculated. The

results of this research reveal that combination b has the most powerful linkage energy. combination b provides a more powerful interaction with the linkage point of the related protein because of having 3 hydrogen bonds with amino acids of Thr830, Asp831,and Thr766 in comparison with combination a with two hydrogen bonds with amino acids of Lys721 and Thr830. The purpose of this research is to obtain and use the best combination among the combinations, the best combinations considering their placement in the related protein and use them in the research and the treatment of the diseases such as cancer.

REFERENCES

[1] Z. Mohamed. International journal of molecular sciences, 19.6, pp. 1731, 2018.

[2] M.F, Zayed. M.H,Hassan. Design, synthesis and biological evaluation studies of novel quinazoline derivatives as cytotoxic agents. Drug Res. 63, 210–215, 2013.

Antibacterial evaluation of some synthetic thiazole compounds using the molecular docking study

H.S. Delarami[a]*, E. Sanchouli[a], S. Mirjahanshahi[b]

[a]*Department of Chemistry, Faculty of Science, University of Zabol, Zabol, Iran*
[b]*Department of Chemistry, Faculty of Science, University of Sistan and Baluchestan, Zahedan, Iran*
Email:hsdelarami@uoz.ac.ir, hsd102012@gmail.com

Abstract: Bacterial DNA gyrase is an attractive target for the consideration of novel antibacterial candidates. In this study, some synthetic thiazole derivatives were investigated for its possible interaction with DNA gyrase target using molecular docking and quantum mechanical calculations. Hydrogen bonding interactions of these compounds could be responsible for their mechanism of action. This study assists us to gain a better insight for the rational design of more powerful and selective antibacterial agents.

Keywords: Thiazole, Molecular docking, DNA, intercalation, Density functional theory.

I. INTRODUCTION

Staphylococcus pseudintermedius is responsible for severe and necrotizing infections in humans and animals.

Staphylococcus pseudintermedius is an important problem in medicine as it is a major source of opportunistic infections in companion animals and is responsible for severe and necrotizing infections in humans and animals [1]. Thiazole compounds have been shown to be useful in multiple therapeutic applications including as anticancer, antiviral, and anticonvulsant agents [2]. In the present study, some thiazole derivatives (see Figure 1) were analyzed for its possible interaction with bacterial DNA gyrase through molecular docking analysis.

II. METHODS

MGL tools 1.5.6 with AutoGrid4.2 and AutoDock4.2 [3] were used to molecular docking calculations between the ligands (thiazole derivatives 1-6) and DNA gyrase obtained from the Protein Data Bank (PDB). The DNA target is staphylococcus aureus gyrase B (PDB ID: 3G75). A blind docking was performed for the recognition of the active sites of receptor. The grid size was set at 126×126×126 Å in the x-, y-, and z-axes respectively, with 0.375 Å grids spacing to cover the whole receptor. The ligands and receptor were considered flexible and rigid, respectively. The Lamarckian genetic algorithm was used to search for the best conformers.

Geometries of ligands were optimized at the M06-2X/6-31G(d,p) level of theory by the Gaussian09 program package [4].

III. RESULTS AND DISCUSSION

Molecular docking is a useful technique for prediction of protein–drug interactions and the orientation and conformation of a drug within a receptor. This method clarifies the binding modes between the ligand and receptor and assist to design new potent drug candidates. The interaction energies (BE) between the thiazole compounds and amino acid residues of 3G75 active site and the previous experimental antibacterial activity (MIC_{50}) are presented in Tables 1. As seen, the BE value of compound **6** to 3G75 is the highest, which is in accordance with the lowest MIC_{50} value [5]. There are conventional H-bonds interactions between the ligands and amino acid residues of DNA gyrase, through the N-H groups of ligands.
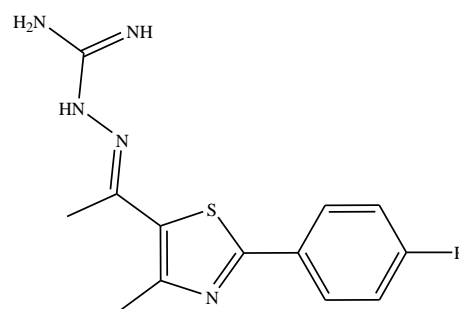

Fig.1: Chemical structure of thiazole compounds utilized in this study.

Table1:

No.	R	MIC50* (μg/mL)	BE (kcal mol⁻¹)
1		0.69	-7.93
2		0.46	-8.90
3		0.48	-8.02
4		1.47	-8.35
5		0.42	-8.07
6		**0.40**	**-10.11**

*Minimum inhibitory concentration (MIC) of thiazole compounds 1–6 described in ref. [5].

IV. CONCLUSION

The interaction mechanism of thiazole compounds with DNA gyrase was investigated by molecular docking method. The results are in good accordance with the previous experimental results. This study can be a useful guideline for efficient drug design.

REFERENCES

[1] N.G. Eckholm, C.A. Outerbridge, S.D. White, J.E. Sykes, vol. 24, pp. 154–161, **2013**.

[2] I. Hutchinson, T.D. Bradshaw, C.S. Matthews, M.F. Stevens, and A.D. Westwell, Bioorg Med Chem Lett. vol. 13, pp. 471–474, **2003**.

[3] G.M. Morris, R. Huey, W. Lindstrom, M.F. Sanner, R.K. Belew, D.S. Goodsell, and A.J. Olson. J. Comput. Chem. vol. 30, pp. 2785-2791, **2009**.

[4] M.J. Frisch, et al., Gaussian 09, Revision A.02, Gaussian Inc., Wallingford, CT, **2009**.

[5] H. Mohammad, P.V. Narasimha Reddy, D. Monteleone, A.S. Mayhoub, M. Cushman, G. Kenitra Hammac, , M.N. Seleem, PLoS One. vol 10, pp, 1-19, **2015**.

Interaction of Polyphenols with Nerve Growth Factor: A Docking Studies

H.Roohi[a], V.Pourghasem[b]*

[a]Department of Chemistry, Faculty of Science, University of Guilan, Rasht, Iran
[b] Department of Chemistry, Faculty of Science, University Campus 2, University of Guilan, Rasht, Iran
Email:vpourghasem89@phd.guilan.ac.ir

Abstract Polyphenols are an important group of phytochemicals that are found in food sources. Flavonoids are large group compounds of polyphenols that are used in diagnosing and treating certain diseases.
In this study, Baicalein(BCL) and Isoharmentin(IHN) was optimized and they have docked to nerve growth factor by genetic algorithm. Results show they have less binding energy and best interaction and more inhibitory constant. It means they can inhibits NGF and they have anti-aging properties.

Keywords: polyphenols, Flavenoids, docking, NGF, anti-aging.

I. INTRODUCTION

Polyphenols are an effective group of phytochemicals that are found in food sources.[1] Several lines of evidence have displayed useful effects of these compounds, [2] and it has frequently been proven that use of foods full of phenolic compounds can decrease the risk of some diseases. [3]. Flavonoids are a kind of organic compounds which play compelling role in a wide spectrum of biochemical and biophysical systems [4, 5]. They are natural compounds that find in plants that display several interesting biological properties.

A number of molecular biological and biophysical chemistry studies have shown that proteins (including enzymes) are mostly the targets for remedial active flavonoids of both natural and artificial sources[6, 7]. But Up to now the quality of interactions of flavonoids with their respective aim proteins have been studied very little at the molecular level.

In this current work, structures was optimized and docked to nerve growth factor. As a result, they are a good inhibitors for anti-aging.

II. METHODS

Baicalein(**BCL**) and Isoharmentin(**IHN**) were optimized at M06-2x/6-311G++(d,p) level of theory in the gas phase using Gaussian 09 package[8]. Molecular docking simulations were carried out using AutoDock 4 software[9], to better understand the structural logical behind the inhibitory activity observed for the studied compounds. Flexible docking was used for flexible inhibitor's ligands and rigid receptor for getting better function. The crystal structure NGF(Nerve Growth Factor), that is a factor for aging, was acquired from the Research Col laboratory for Structural Bioinformatics (RCSB) Protein Data Bank (PDB Code:4XPJ)[10] and was applied throughout the molecular docking study. A grid box of -15.634, 3.669, 12.925 in x, y, and z directions, respectively, in an x, y, and z accommodation of space was defined for the binding site a grid spacing of 0.5 Å. The protein was assumed as rigid.

III. RESULTS AND DISCUSSION

The results of docking for structures **BCN, IHN** showed that these structures have been having more stability and less binding energy with more inhibitory activity in a large cluster. some of these structures' interactions were shown in Figure 1. TYR52, VAL87, PHE53, GLN51 and LYS88, and TRP99 amino acids were participated in the active site. The best inhibition constant and energy is related to these ligands (Table 1). Ligands **BCN** and **IHN** display the H-bond interaction in the active site. The key interaction between docked states and binding site residues were identified using Discovery Studio Visualizer[11].

Table1. Energies and inhibitory constants of ligands

Subunit	Binding energy (kcal/mol)	Inhibitory constant (nM)	Intermolecular Energy (kcal/mol)	Electrostatic Energy (kcal/mol)
BCL	-8.47	620.47	-9.92	-0.11
IHN	-8.85	325.65	-10.64	-0.17

Table2. H-Bonding interaction and π-π interaction Binding length and involved aminoacids

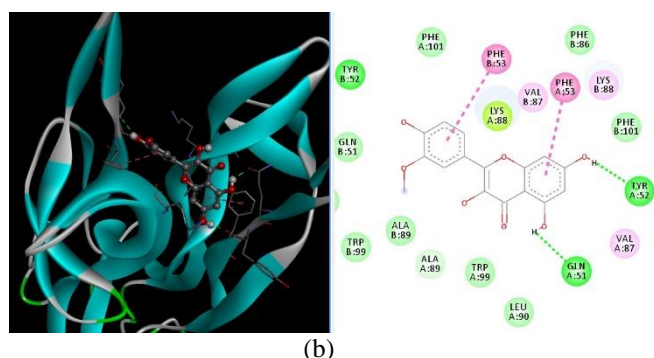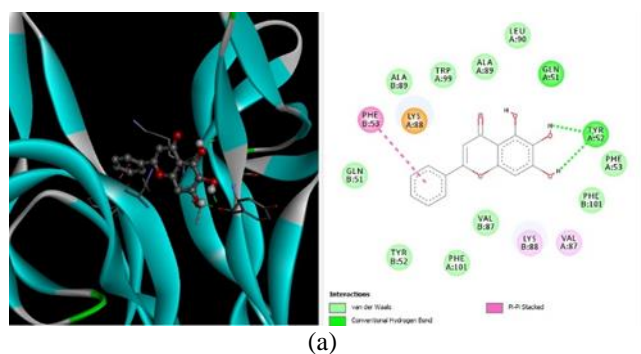| Bonding Length π-π Interaction (Å)	Bonding Length H-bond interaction (Å)
4.47:PHE53	1.80:TYR 52 1.90:TYR52
4.74:PHE53	1.99:GLN51 1.92: TYR52

(a)

(b)

Fig1: Protein ligand-binding site interactions of ligands BCN(a) and IHN(b) with NGF. H-bond interaction was shown in green lines and hydrophobic interactions were identified by other colors. Participating amino acids were shown in 2D structures.

IV. CONCLUSION

In conclusion, the intreraction of two derivatives of flavonoid was investigated with NGF as anti-aging factor. Structures were docked to NGF by Autodock tools. The results show that both of them have the most favored binding energy and they can inhibit the NGF with inhibitorier constant. It showed they have best interaction with NGF.

REFERENCES

[1] C. Manach, A. Scalbert, C. Morand, C. Rémésy, and L. Jiménez, "Polyphenols: food sources and bioavailability," *The American journal of clinical nutrition,* vol. 79, pp. 727-747, **2004**.

[2] J. Shay, H. A. Elbaz, I. Lee, S. P. Zielske, M. H. Malek, and M. Hüttemann, "Molecular mechanisms and therapeutic effects of (−)-epicatechin and other polyphenols in cancer, inflammation, diabetes, and neurodegeneration," *Oxidative medicine and cellular longevity,* vol. 2015, **2015**.

[3] D. Vauzour, K. Vafeiadou, A. Rodriguez-Mateos, C. Rendeiro, and J. P. Spencer, "The neuroprotective potential of flavonoids: a multiplicity of effects," *Genes & nutrition,* vol. 3, p. 115, **2008**.

[4] S. Maini, B. M. Fahlman, and E. S. Krol, "Flavonols protect against UV radiation-induced thymine dimer formation in an artificial skin mimic," *Journal of Pharmacy & Pharmaceutical Sciences,* vol. 18, pp. 600-615, **2015**.

[5] R. Menezes, A. Rodriguez-Mateos, A. Kaltsatou, A. González-Sarrías, A. Greyling, C. Giannaki*, et al.*, "Impact of flavonols on cardiometabolic biomarkers: A meta-analysis of randomized controlled human trials to explore the role of inter-individual variability," *Nutrients,* vol. 9, p. 117, **2017**.

[6] A. F. M. Monteiro, J. D. O. Viana, A. Nayarisseri, E. N. Zondegoumba, F. J. B. Mendonça Junior, M. T. Scotti*, et al.*, "Computational Studies Applied to Flavonoids against Alzheimer's and Parkinson's Diseases," *Oxidative Medicine and Cellular Longevity,* vol. 2018, **2018**.

[7] M. Santi, C. Bouzidi, N. Gorod, M. Puiatti, S. Michel, R. Grougnet*, et al.*, "In vitro biological evaluation and molecular docking studies of natural and semisynthetic flavones from Gardenia oudiepe (Rubiaceae) as tyrosinase inhibitors," *Bioorganic chemistry,* vol. 82, pp. 241-245, **2019**.

[8] M. Frisch, G. Trucks, H. Schlegel, G. Scuseria, M. Robb, J. Cheeseman*, et al.*, "Gaussian 09, version D. 01," *Gaussian, Wallingford,* **2009**.

[9] G. M. Morris, R. Huey, W. Lindstrom, M. F. Sanner, R. K. Belew, D. S. Goodsell*, et al.*, "AutoDock4 and AutoDockTools4: Automated docking with selective receptor flexibility,"

Journal of computational chemistry, vol. 30, pp. 2785-2791, **2009**.

[10] S. Mutahir, M. A. Khan, I. U. Khan, M. Yar, M. Ashraf, S. Tariq*, et al.*, "Organocatalyzed and mechanochemical solvent-free synthesis of novel and functionalized bis-biphenyl substituted thiazolidinones as potent tyrosinase inhibitors: SAR and molecular modeling studies," *European journal of medicinal chemistry,* vol. 134, pp. 406-414, **2017**.

[11] D. S. BIOVIA, "Discovery Studio Visualizer, Release 4.5," ed: Dassault Systèmes: San Diego, CA, **2015**.

Novel p21-Activated Kinase 4 (PAK4) and an effective in *vitro* inhibitor

N. salehi[a], A. bordbar[a]*
Department of Chemistry, Isfahan Universit, 81746-73441, Iran
Email:na_salehi84@yahoo.com

Abstract*:* PAKs have an active role in the body, which makes it a target for cancer that can control cancer. PAK is among the various types of signaling of anecognition expression and has the most relevance to tumor genes, therefore, for many people; there is an understanding of their direct or beneficial effect on disease progression.

Currently, competitive inhibitors of ATP have been studied extensively. KPT-9274 has been considered as an effective drug in pancreatic cancer. It's known as EMT. It has low toxicity and has a great impact as a medicine, and so is the reference of this work.

Keywords: Adenosine triphosphate (ATP), Activated protein kinase(PAK), Inhibitors

I. INTRODUCTION

The cell cycle is regulated by kinases that catalyze the serine-threonine side chain phosphorylation. Kinase are enzymes that carry high-energy phosphate from molecules such as ATP to their substrates.

In the mammals, six different types of serine / threonine kinase have been introduced from the PAK class divided into two major categories I and II. These six members are in the path to the signal of the expression of the oncogene. Category I: PAK1, PAK2 and PAK3.Category II: PAK4, PAK5 and PAK6. PAK4 is a kinase protein of category 2, which is most likely to be linked to a variety of cancers.

PAKs affect the code of cdc42 and ras, which are the key to the regulation of bone cells. Therefore, PAKs play an active role in the growth, proliferation and invasion of cancer cells, which can be used to investigate drug targets and cancer inhibition. Protein kinase inhibitor is a type of inhibitor which inhibits the activity of one or more protein kinases. The interaction between PAK4 and KPT-9274, however, did not impact the kinase activity of PAK4. The interaction disrupts steady-state levels of PAK4 in cell lines and reduces overall PAK4 activity. These compounds are different from other inhibitors because they alter the basal state of the PAK4 protein, inhibiting compounds such as PAK4 and taking a more effective drug.

II. METHODS

Optimization the molecules using the goussiam software can be verified after taking the types of ligands from the Zinc15 data bank

A molecular docking technique using the virtual docker's molegro software done.

The energy results can be found in the molegro molecular viewer software.

In Ligand map, the types of interactions can be observed, including hydrogen bondings with residuals and water, electrostatics, and stereos. In fact, we see the contribution of each of the atoms and energy residues.You can report the number of involved atoms and their type as well as their energy.

III. RESULTS AND DISCUSSION

Computational technique like structure based virtual screening developed primarily in the pharmaceutical or biotechnology industries has been successfully applied for the generation of hit and lead structure candidates. Thus we performed a cascaded pharmacophore matching and docking searching of commercially available library to find chemical leads.

After recognizing and introducing an effective drug(KPT-9274), we selected more of the same ligand for studing. The binding modes of compounds to PAK4 were analyzed using. All of the compounds dopted extended conformations to perfectly fit the PAK4 active site shape and interacted with the surrounding residues in PAK4.

Some of these ligands are listed in Table 1 along with the energy derived from the Docking method.

The high resolution crystal structure of PAK4 with potent ligand ($C_{12}H_{15}N_3O_3S$) was chosen for modeling, and significant result of the cross-docking simulation show in figure1.

As shown in Fig.2, ligand forms three contacts with the hinger region through H-bond interactions with the amino acids and forms charge-charge interaction.

Table1: some energy results from docking

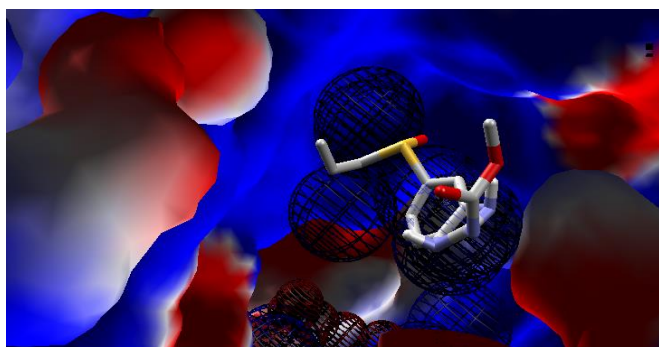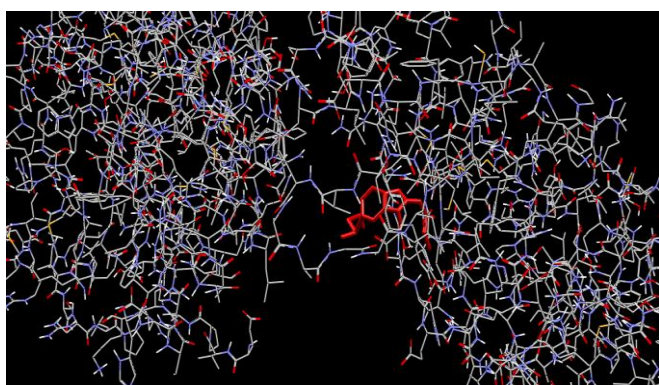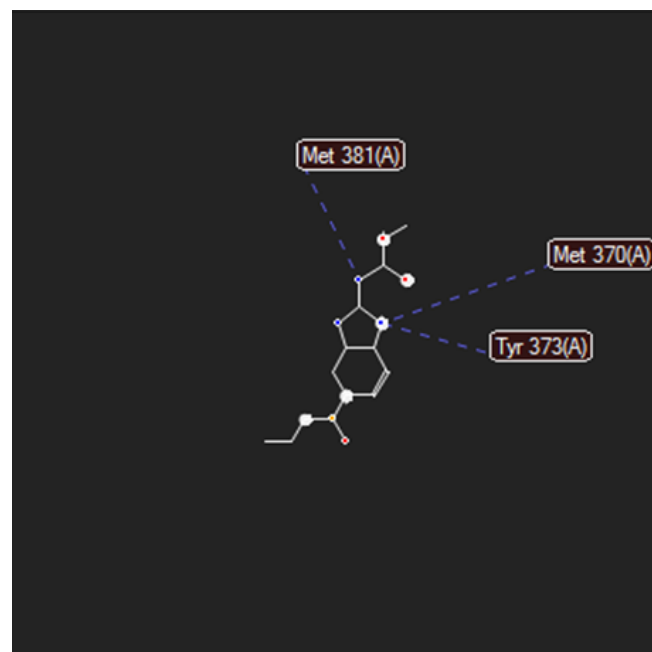| ligand	Number of hydrogen bond (acceptor)	Number of hydrogen bond(doner)	Doking Energy
C12H15N3O3S	2	4	-119.318
C16H12ClNO3	0	4	-100.826
C16H26N2O4	3	4	-97.279

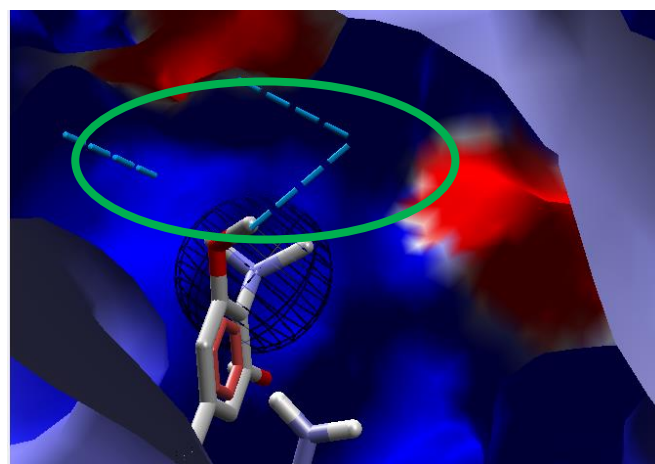Fig.1: A view of the doped molecule in the protein

Fig.**2**: Hydrogen bonds of the molecule (with less energy) with surrounding amino acids

I. CONCLUSION

PAK4 has emerged as an important cancer target, and researchers are considerably interested in developing PAK4 inhibitors as biological markers and leads for developing therapeutics. After a virtual screening of the database, twenty-seven commercially available compounds were selected and assessed. Top ten docked poses for each ligand were retained, with other docking parameters as default settings. The scoring function was used to predict binding energy between compounds and PAK4.

REFERENCES

[1] Amro Aboukameel1, Irfana Muqbil1, j. Mol Cancer Ther, vol:16, pp:76-87, **2017**.

[2] Ruijuan Li, *a* Xiaolin Su, *a* Zheng Chen, RSC Advances, vol: **00**, pp:1-3 **,2013.**

Computational Study of the Inhibition of HIV-1 Protease by RNA Aptamer: Effect of the Form of Dimer and Monomer in Protease

M. Ajamgard[a]*, J.Jahanbin sardroodi[b], A.Rastkar Ebrahimzadeh[c]
[a b,c] *Address: Molecular Simulation laboratory (MSL), Azarbaijan Shahid Madani University, Tabriz, Iran*
Email:mrz.ajam@gmail.com

Abstract*:* HIV-1 protease (PR) is a major drug target in combating AIDS, as it plays a key role in maturation and replication of the virus. All of drugs designed to inhibit enzyme activity by blocking the active site, which exists only in the dimer. An alternative inhibition mode would be required to overcome the emergence of drug resistance through the accumulation of mutations. This might involve inhibiting the formation of the dimer itself. Here, the folding of HIV-1 PR is studied with two simulation models appropriate for folding mechanism studies. All-atom molecular dynamics simulations strongly support the stability of an isolated monomer. Accordingly, the design of dimerization inhibitors should not focus only on the flexible N and C termini that constitute most of the dimer interface, but also on other structured regions of the monomer.

Keywords: Dimer, Molecular dynamics, Monomer, Protease inhibit, RNA aptamer.

I. INTRODUCTION

The human immunodeficiency virus type-1 (HIV-1), a member of retrovirus family, has been a causative organism in an acquired immunodeficiency syndrome (AIDS). One of the important enzymes necessary for the replication of this virus is HIV-1 protease (HIV-1 PR). Thus, searching for HIV-1 PR inhibitors from natural sources has become a promising approach [1]. HIV-1 aspartyl protease (PR) plays a key role in virion morphogenesis, underscoring the effectiveness of protease inhibitors (PI) [2].

Aptamers are short single-stranded RNA or DNA oligonucleotides whose function is to recognize and bind target molecules with high affinity and selectivity [3– 8].

In the present work, we investigate the orientation and interaction between aptamer and two HIV-1 PR (monomer and dimer) by using molecular dynamics (MD) simulation.

II. METHODS

Classical molecular dynamics simulations were performed using NAMD package [9], and visual molecular dynamics

(VMD) [10] was used for visualization and analysis of the trajectories. Structures of HIV-1 protease enzyme in the access number 1HHP [11] and 1HVR [12] was taken from Protein Data Bank (PDB). (http://www.pdb.org/pdb/) (see Fig. 1). 2D structure of the anti-HIV-1 PR RNA aptamer obtained from kinefold (kinefold.curie.fr/). The generated 3D structure with the formed SiMRNA (https://genesilico.pl/SimRNAweb) was used as basis for the MD simulation. We studied mutation aptamer with nucleotide sequencing of CTTAAGTGTAACTTCTCGTAAGTAATTCCCAAGGCT TTTACCTCGGGGTCCT.
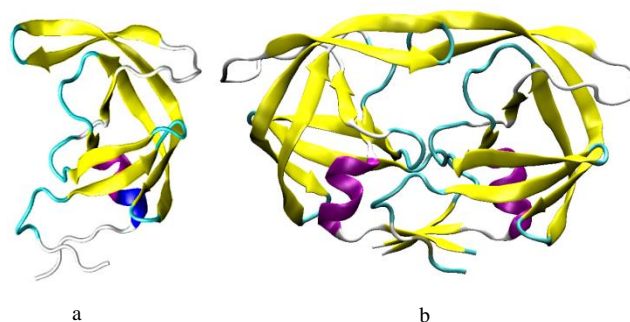
III. RESULTS AND DISCUSSION

Fig.1: New Cartoon of the three-dimensional structure of the aspartyl protease from the HIV-1 PR. a:monomer (1HPP), b: dimer (1HVR)

The interacted residues along with their averaged RMSF values have been collected in Table 1 was calculated for the 5 ns. In dimer protease, one of these clusters is located at the hinge region of the flap, which has been suggested to be an inhibitory allosteric site. This cluster is a representation of the underlying positive side chains of Lysine 41, Lysine 43, Lysine 45, and Lysine 55. Two other clusters formed by Histidine 69 and Lysine 70 as well as Arginine 14 and Lysine 40, may also serve as a potential site for aptamer interactions. In monomer protease, the considered aptamers

interacted the enzyme by the strong attraction of dimer interface, flap tipe.

Table 1: The RMSF values between aptamer and monomer protease in complex in Å are displayed.

Region	Base Range	RMSF [Å] of Complex-HIV-1 PR	RMSF [Å] of HIV-1 PR
flap-tipe	G49	3.37	12.36
	I50	3.37	12.83
	G51	3.25	12.98
	G52	3.24	13.18
dimer interface	P1	2.94	10.99

The structure obtained from the interaction between aptamer and monomer protease at the site is shown in Fig. 2.
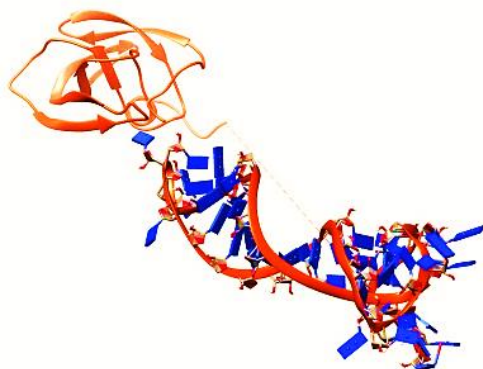
Fig.2: A snapshot of interaction monomer protease with the aptamer at the end of simulation with explicit water molecules.

IV. CONCLUSION

Protease inhibitor drugs have successfully been used as a therapy for HIV-infected individuals to reduce their viral loads and slow the progression to Acquired Immune Deficiency Syndrome (AIDS). Since inhibit enzyme activity by blocking the active site, exists only in the dimer. It was suggested previously that inhibiting the dimerization might overcome the limitation of this mode of inhibition, which suffers from inevitable drug resistance. Binding of HIV-1 PR occurs by association of two folded monomers opens a new venue for inhibiting the enzyme. So, in present work, we

used the monomer shape of HIV-1 PR and we compared it with dimmer mode. A number of parameters, such as the root mean square deviations and the averaged root-mean-square fluctuation, RMSF are monitored during simulation. Our results show that monomeric HIV-1 PR is, in fact, stable and its folding is conditional for the dimer formation. The interacted residues were verified by the help of the averaged RMSF. In monomer protease, the considered aptamers interacted the enzyme by the strong attraction of dimer interface, flap tipe. We can consider it as good targets for inhibitor design.

REFERENCES

[1] N.E.Kohl, E.A.Emini , and W.A. Schleif, Proc. Natl. Acad. Sci. U.S.A, 85, 4686, **1988**.

[2] S. Duclair1, A. Gautam, A. Ellington , and V.R. Prasad, Molecular Therapy-Nucleic Acids, 4, e228, **2015**.

[3] AD. Ellington, JW. Szostak, In vitro selection of RNA molecules that bind specific ligands. Nature, 346, 818–822, **1990**.

[4] LC. Bock, LC. Griffin, JA. Latham, EH. Vermaas and JJ. Toole, Selection of single-stranded DNA molecules that bind and inhibit human thrombin. Nature, 355, 564–566, **1992**.

[5] AD. Ellington, Aptamers achieve the desired recognition. Curr Biol.; 4: 427–429. PMID: 7522916,**1994**.

[6] M. Famulok, Oligonucleotide aptamers that recognize small molecules. Curr Opin Struct Biol.; 9: 324–329, **1999**.

[7] M. Famulok, G. Mayer, and M. Blind, Nucleic acid aptamers from selection in vitro to applications in vivo. Accounts Chem Res, 33: 591–599, **2000**.

[8] F. Radom, PM. Jurek, and MP. Mazurek, J. Otlewski, F. Jeleń, Aptamers: molecules of great potential. Biotechnol Adv.; 31: 1260–1274, **2013**.

[9] J. C. Philips, R. Braun, W. Wang, et al, J Comput Chem, , 26, 1781–1802, **2005**.

[10] W. Humphrey, A. Dalke , and K. Schulten, J Mol Graph, , 14, 33-38, **1996**.

[11] S. Spinelli, Q.Z. Liu, P.M. Alzari, P.H. Hirel, R.J. Poljak,. Biochimie, 73: 1391-1396 (1991).

[12] P.Y. Lam, P.K. Jadhav, C.J. Eyermann, C.N. Hodge, and et.al
Science, 263, 380-384, **1994**.

Effects Of Isoxsuprine On The Catalytic Activity Of Catalase. Kinetics, Interaction Mechanism And Molecular Docking Approach

S. Shahraki*, H. Samareh Delarami
Department of Chemistry, University of Zabol, Zabol, Iran
E-mail: s-shahraki@uoz.ac.ir, somaye_shahraki@yahoo.com

Abstract: The side effects of Isoxsuprine (ISO) on the structure and catalytic function of bovine liver catalase (BLC) were investigated by various spectroscopic and theoretical methods. Enzyme inhibition kinetics showed that ISO inhibited catalase function by mixed-type inhibition. UV–Vis spectra, CD spectroscopy, synchronous and 3D fluorescence confirmed conformational changes in the structure of BLC in the presence of ISO. Fluorescence measurements showed that this drug quenches intrinsic fluorescence of BLC via static quenching mechanism. Thermodynamic parameters revealed that the reaction of ISO with catalase could proceed spontaneously through hydrogen bonds and Van der Waals forces. The molecular docking simulation in the well coherent with kinetics results showed that there is one binding site for ISO on BLC and this drug did not directly bind into the catalase activity site.

Keywords: Catalase; Kinetics; Thermodynamic; Binding Mechanism; Molecular Docking

I. INTRODUCTION

Hydrogen peroxide oxidoreductase or catalase is one of the enzymes that is used to scavenge reactive oxygen species and reduce their deleterious effects. This enzyme has been introduced as a promising therapeutic agent because it can play a protective effect in many pathological conditions, such as atherosclerosis, radiation, viral infection, ischemia-reperfusion syndrome, and tumor progressio. Due to its pivotal role in the antioxidant defense system, the interaction of catalase with small molecules such as drugs has been extensively studie. It has been found that at higher pH and low ionic strength, monomers in catalase not only separate from each other but also loses its conformation and biological activit. So, the structural changes of catalase by small molecules compromised the catalytic activity as well as hampers the antioxidant counterbalance in the cellular system. In this study, bovine liver catalase (BLC) interaction with ISO was investigated. The binding affinity of catalase with ISO are followed by different spectroscopic techniques; from the point of pharmacokinetics, the bond strength is very important because the moderate interaction between drug and protein leads to a faster diffusion rate in the circulatory system to reach target sites. More importantly, this study will be helpful for increasing our awareness of the probably side effects of drugs (such as ISO) for body.

II. METHODS

Catalatic activity of catalase in the presence of ISO was studied spectrophotometrically by detecting of hydrogen peroxide (1.0×10^{-2} M) decomposition at 240 nm. Geometry optimization of ISO was carried out using the Gaussian 09 program package at the B3LYP method. The LANL2DZ effective core potential was used for the heavy atom (I) and a 6-31G(d,p) basis set was used for all other atoms. The 3D X-ray structure of catalase (BLC) (encoded 1TGU) was obtained from the Protein Data Bank (http://www.Znb.org). In this study, molecular docking was performed using MGL tools 1.5.6 including the AutoDock4.2 scoring function to predict the interactions between ligands and receptor. The ligands and receptor were considered flexible and rigid, respectively. The Lamarckian Genetic Algorithm (LGA) method was applied for docking simulations [1, 2]. The number of Genetic Algorithm runs was set to 10. Then, 10 conformations with the lowest binding energy were selected for further analysis. PyMOL software was used to visualize and analyze the docking results [3].

III. RESULTS AND DISCUSSION

Enzyme kinetic mechanism is reflected with special features that allow us to evaluate the type of inhibition of that enzyme. To determine the inhibition mode, the Lineweaver–Burk plots of BLC and ISO-BLC systems were drawn. For this purpose, the BLC inhibition were studied using different ISO concentrations (0, 5 and 10×10^{-7} M) at different concentrations of substrate (H_2O_2: 0.01-0.06 M). The result shows that free BLC, has a higher affinity toward H2O2 as compared to the ISO-BLC system which revealed mixed-type enzyme inhibition mode.

Molecular docking can help to obtain some insight into the interactions of macromolecules with ligands. Then, theoretical evaluation was performed on all chains of BLC. The results for docking of the ISO with BLC are presented in Fig. 1, and Tables 1. As seen, the affinity of isoxsuprine to BLC is –-6.69 kcal mol-1. As shown in Fig. 1, there are six

main conventional H-bonds between isoxsuprine and amino acid residue of His363(D), Arg65(A) and Arg362(D). Detailed analysis of the the best docked pose of ligand showed a π-π stacking interaction between the aromatic ring of His363(D) amino acid and phenyl ring of the isoxsuprine ligand.

Table1: Docking results for interaction between the isoxsuprine complex with BLC

Pose	BE (kcal mol^{-1})	k_i (μM)	vdW+Hbond+ desolv (kcal mol^{-1})	Electrostatic (kcal mol^{-1})	Torsional (kcal mol^{-1})
1	-6.11	33.45	-8.09	-0.70	2.68
2	-5.33	124.25	-7.18	-0.84	2.68
3	**-6.69**	**12.42**	**-8.32**	**-1.05**	**2.68**
4	-5.94	44.47	-7.77	-0.85	2.68
5	-3.53	2570	-5.14	-1.08	2.68
6	-3.89	1400	-6.16	-0.41	2.68
7	-5.38	113.05	-7.24	-0.83	2.68
8	-5.86	50.67	-7.78	-0.77	2.68
9	-6.10	33.64	-7.87	-0.92	2.68
10	-5.44	102.47	-7.28	-0.85	2.68

(A)

(B)

Fig.1: : (A) The BLC binding sites and (B) amino acid residues involved in the interaction of BLC- ISO.

IV. CONCLUSION

From the kinetic point of view, our results showed that the Zn complex inhibits BLC function to some extent via the mixed inhibitory mechanism. Fluorescence study and thermodynamic analysis also suggested that the interaction between catalase and Zn complex was performed through hydrophobic and van der Waals interactions.

REFERENCES

[1] B. Ghalandari, A. Divsalar, M. Eslami-Moghadam, A.A. Saboury, T. Haertlé, M. Amanlou, K. Parivar, Appl. Biochem. Biotechnol. 175, pp. 974–987, 2015

[2] G.M. Morris, D.S. Goodsell, R.S. Halliday, R. Huey, W.E. Hart, R.K. Belew, A.J. Olson, J. Comput. Chem. 19, pp. 1639–1662, 1998.

[3] De Lano, W. L. The PyMOL Molecular Graphics System (2002) ; De Lano Scientific.: San Carlos, CA, USA, ttp://www.pymol.org.
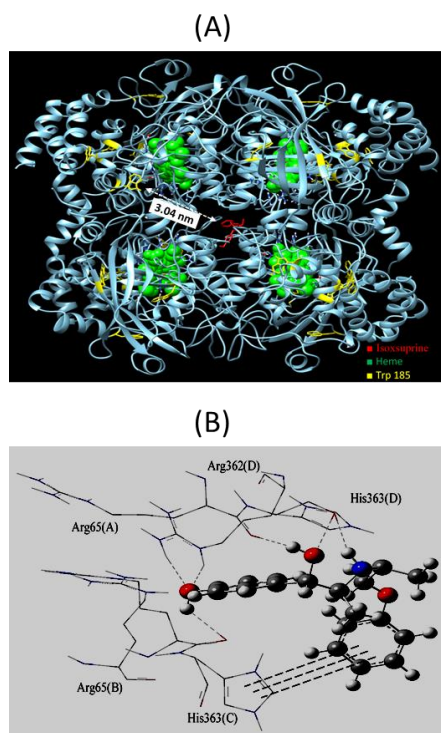
Molecular Docking And Analysis Of Binding Interaction Between Levothyroxine And Bovine Liver Catalase

S. Shahraki*, _H. Samareh Delarami_
Department of Chemistry, University of Zabol, Zabol, Iran
E-mail: s-shahraki@uoz.ac.ir, somaye_shahraki@yahoo.com

Abstract*:* Here, the structure and enzyme activity of bovine liver catalase (BLC) were evaluated in the presence of levothyroxine (LEV) by using spectroscopic techniques and molecular docking simulation. According our results in the kinetics section, LEV inhibited BLC through a mixed-type inhibitory mechanism. Both kinetics and molecular docking results showed that LEV did not directly bind into the activity site of catalase. The interaction of this drug with the cavity of BLC influenced the microenvironment of the enzyme activity site; so the activity of the enzyme is reduced. The structure of the enzyme changes in the presence of the LEV by decreasing α-helix and increasing β-sheet content. Fluorescence quenching of BLC was occurred in the binding interaction via a static mechanism. Thermodynamic and also molecular docking results confirmed that the main forces in the LEV-BLC interaction were hydrogen bonds and Van der Waals forces.

Keywords: Enzyme; Kinetics; Thermodynamic; Molecular Docking

I. INTRODUCTION

Catalase has four subunit heme. There is in this enzyme a heme group with ferric iron within each of identical subunit. Catalase has an important role in body. This enzyme breaks down H_2O_2 to H_2O and O_2 (the catalatic pathway). Levothyroxine ((2S)-2-amino-3-[4-(4-hydroxy-3,5 diiodophenoxy)-3,5-diiodophenyl]propanoic acid, L-thyroxine, LEV) is a synthetic form of thyroxine (the thyroid hormone). When the thyroid gland does not produce enough thyroid hormone, the LEV is used. This drug is applied to treat congenital hypothyroidism (cretinism) and, (enlarged thyroid gland) and also with surgery and radioactive iodine therapy to treat thyroid cancer. The aim of the present study was to determine how LEV may effect on the structure and activity of catalase.

II. METHODS

Catalitic activity of catalase in the presence of LEV was studied spectrophotometrically by detecting of hydrogen peroxide $(1.0 \times 10^{-2}$ M) decomposition at 240 nm. The optimization of geometry in the levothyroxine was done using the Gaussian 09 program package [55] at the B3LYP method. The LANL2DZ effective core potential was used for the heavy atom (I) and a 6-31G(d,p) basis set was used for all other atoms. The 3D X-ray structure of bio macromolecule (BLC) (encoded 1TGU) was obtained from the Protein Data Bank (http://www.Znb.org). In this research, molecular docking was performed using MGL tools 1.5.6 including the AutoDock4.2 scoring function to predict the interactions between ligands and receptor. The ligands and receptor were considered flexible and rigid, respectively. The Lamarckian Genetic Algorithm (LGA) method was applied for docking simulations [1, 2]. The number of Genetic Algorithm runs was set to 10. Then, 10 conformations with the lowest binding energy were selected for further analysis. PyMOL software was used to visualize and analyze the docking results [3].

III. RESULTS AND DISCUSSION

The activity of enzyme increased to 121.3% of the initial level when the concentration of LEV was 1.5×10^{-5} M , and slightly changed with the continuous increase of LEV concentrations $(1.5 \times 10^{-5}$ - 2.5×10^{-5} M). Conversely, the catalytic activity of enzyme decreased to 97.3% with further increase of LEV concentration $(5 \times 10^{-5}$ M). So, it can be said that LEV facilitated the catalytic activity of catalase within the extent of the used concentrations, but this effect was weaker at higher concentration of drug.
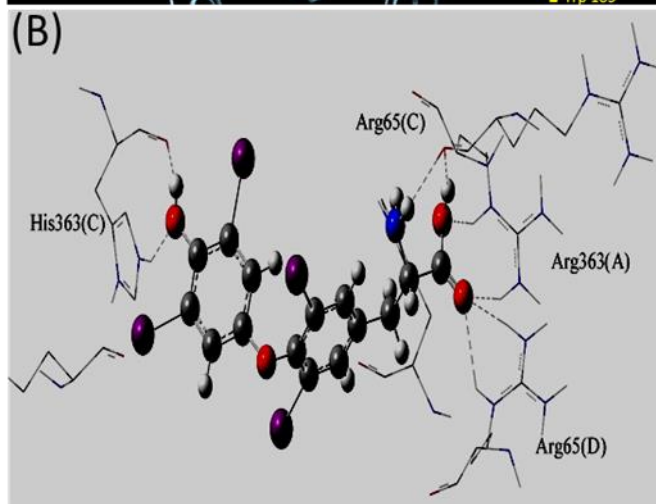
(A)
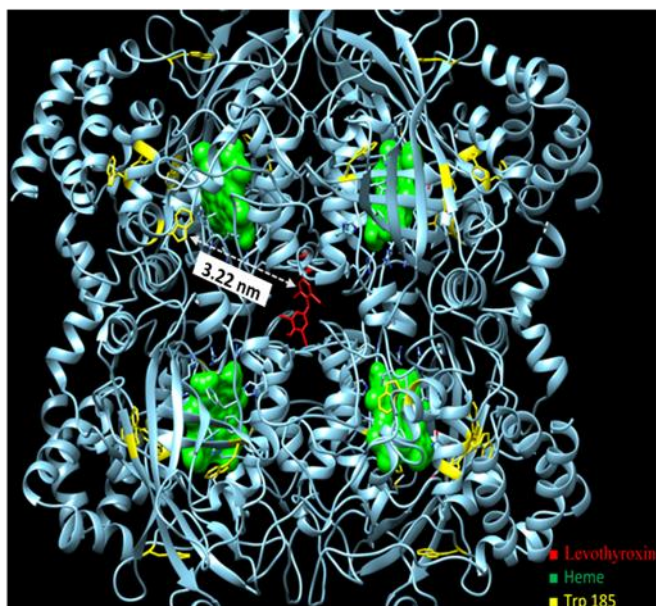
Fig.1: (A) The BLC binding sites and (B) amino acid residues involved in the interaction of BLC- levothyroxine

Table 1. Docking results for interaction between the levothyroxine complex with BLC

Pose	BE (cal mol⁻¹)	k_i (µM)	lW+Hbond+desolv (kcal mol⁻¹)	Electrostatic (kcal mol⁻¹)	Torsional (kcal mol⁻¹)
1	-8.27	0.867	-9.23	-1.43	2.39
2	-7.94	1.50	-8.99	-1.34	2.39
3	-8.17	1.02	-9.09	-1.46	2.39
4	-8.39	0.713	-9.28	-1.49	2.39
5	-8.46	0.627	-9.45	-1.40	2.39
6	-8.70	0.420	-9.68	-1.40	2.39
7	**-8.77**	**0.373**	**-9.74**	**-1.41**	**2.39**
8	-8.55	0.539	-9.46	-1.48	2.39
9	-8.09	1.18	-9.22	-2.78	2.39
10	-8.28	0.851	-9.21	-1.46	2.39

The results for docking of the LEV with BLC are presented in Fig. 1 and Tables 1. As seen, the affinity of LEV to BLC are –8.77 kcal mol-1. As shown in Fig. 1, there are eight conventional H-bonds between LEV and amino acid residues of His363(C), Arg362(A), Arg65(A) and Arg65(D).

IV. CONCLUSION

The interaction mechanism of BLC in the presence of LEV was studied. In the interaction process between BLC and LEV that assigned by spectroscopic and molecular docking techniques, the secondary structure of BLC changed.
Although structural changes are relatively high, enzyme activity does not experience serious effect from.

REFERENCES

[1] B. Ghalandari, A. Divsalar, M. Eslami-Moghadam, A.A. Saboury, T. Haertlé, M. Amanlou, K. Parivar, Appl. Biochem. Biotechnol. 175, pp. 974–987, **2015**
[2] G.M. Morris, D.S. Goodsell, R.S. Halliday, R. Huey, W.E. Hart, R.K. Belew, A.J. Olson, J. Comput. Chem. 19, pp. 1639–1662, **1998**.
[3] De Lano, W. L. The PyMOL Molecular Graphics System (**2002**) ; De Lano Scientific.: San Carlos, CA, USA, ttp://www.pymol.org

Section:

Electrochemistry

An investigation on specific conductivities of the ternary $KCl − [C_6mim][Cl] − H_2O$ system using semi-ideal solution theory at 298.15 K

P. Ghasemi[a], R. Salamat Ahangari[a*]

Department of Chemistry, Faculty of Basic Sciences, Azarbaijan Shahid Madani University, Iran
Email: Pgh.chemist@yahoo.com, R.a.Salamata@gmail.com

Abstract: This work, purposes a specific conductivity studies at 298.15 K for the ternary system $KCl − [C_6mim][Cl] − H_2O$ Measurements were made for both pure solutions and for the mixed solutions with various equilibrium molalities. The experimental results were treated by extended forms of conductivity methods. The values of the specific conductivities were calculated using semi-ideal solution theory.

Keywords: semi-ideal solution theory, binary system, ternary system, conductivity

I. INTRODUCTION

Study of the specific conductivities of mixed electrolyte + ionic liquid are of considerable interest in marine and industrial applications. Binary solutions of chloride salts are important in connection with sea industry. Determination of specific conductivity using semi-ideal solution theory method for systems of $KCl − [C_6mim][Cl] − H_2O$ makes it possible to obtain the properties of a mixed solution with the help of the properties of its pure components. Therefore, we were prompted to determine specific conductivity of the above mentioned $KCl − [C_6mim][Cl] − H_2O$ by semi-ideal solution theory method. In this treatment, the conductivity of a mixed electrolyte + ionic liquid solution can be expressed as [1, 2-3]

$$\ln \sigma = z_1 \ln \sigma_1 + z_2 \ln \sigma_2 \tag{1}$$

σ_i is the specific conductivities of the binary solution $M_i X_i − H_2O$, having the same water activity as that of the ternary solution $M_1 X_1 − M_2 X_2 − H_2O$. z_i is the ratio of the mole fraction in the ternary ideal solution to the mole fraction in the binary ideal solution.

$$z_i = \frac{x_{i,H_2O}^{ideal}}{x_{i,H_2O}^{o.ideal}} \tag{2}$$

$$x_{i,H_2O_{(Li)}}^{o,ideal} = \frac{v_i m_i}{55.51 - c_i v_i m_i^{\circ} + v_i m_i^{\circ}} \tag{3}$$

$$x_{i,H_2O_{(Li)}}^{ideal} = \frac{v_i m_i^{\circ}}{[55.51 - c(v_1 m_1 + v_2 m_2) + v_1 m_1 + v_2 m_2]} \tag{4}$$

Where v is salt stoichiometric coefficient. m_i and m_i° are respectively the molalities of the ith solute in ternary aqueous solution and its binary subsystem of equal water activity.
Using an idealized mixing rule, when the ternary solution is in isopiestic equilibrium with its binary constituents this treatment is known as Zdanovskii's rule [4].

$$m_1 / m_1^{\circ} + m_2 / m_2^{\circ} = 1 \tag{5}$$

II. METHODS

All the measurement were made by Isopiestic and Conductivity methods. The semi-ideal solution theory has been used and the calculations have been done with MATLAB and Excel softwares.

III. RESULTS AND DISCUSSION

Specific conductivities of the ternary system were calculated using the equation (1).

Specific conductivities of the binary MX-H2O, where MX is KCl and were taken from [5,6].

By inspecting figure 1, it illustrates a comparisons of experimental data and the predicted specific conductivity for the ternary solution at 298.15 K. It is realized that the predictions are in good agreement with the experimental results. The results also obviously indicated that the semi-ideal solution theory are suitable to predict the conductivities of the ternary electrolyte solution from the data of their binary subsystems.

The figure 2, illustrates the comparisons of the experimental data and the predictions of the specific

conductivities against the total molality for the ternary solution at 298.15 K.
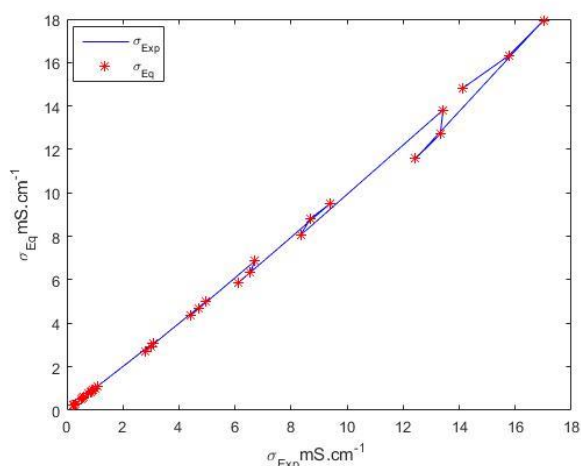

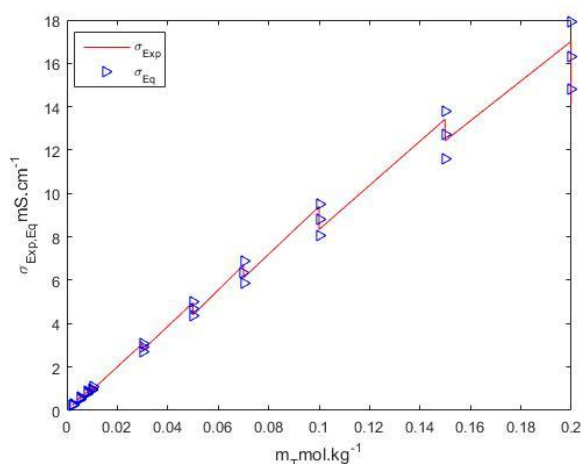Fig.1: Experimental data and the prediction specific conductivities for $KCl - [C_6 mim][Cl] - H_2O$.

Fig.2: Specific Conductivities versus total molality for the ternary system at 298.15 K.

IV. CONCLUSION

The measured specific conductivities were used to check the validity the predictability of the semi-ideal solution theory. The results show that the pseudo semi-ideal-solution theory can provide good results of the Specific conductivity ternary solution of electrolyte + ionic liquid + H2O from the

properties of its binary systems.

REFERENCES

[1] Hu, Y.F., Zhang, X.M., Li, J.G., Liang, Q.Q., "The semi-ideal solution theory. 2. Extension to conductivity of mixed electrolyte solutions", J. Phys. Chem. B, 112(48), 15376-15381 (2008). J. U. Duncombe, Journal, vol. 10, pp. 34-39, 1995.

[2] Zhang, X.M., Hu, Y.F., Peng, X.M., Yue, W.J., "Conductivities of several ternary electrolyte solutions and their binary subsystems at 293.15, 298.15, and 303.15 K", J Solution Chem., 38(10),1295-1306 (2009).

[3] Hu, Y.F., Chu, H.D., "Extension of the simple equations for prediction of the properties of mixed electrolyte solutions to the mixed ionic liquid solutions", Ind. Eng. Chem. Res., 50(7), 4161-4165 (2011).

[4] Zdanovskii, A.B., "Regularities in the property variations of mixed solutions", Tr. Solyanoi Lab.Akad. Nauk SSSR, No.6, 5-70 (1936).

[5] Ruby, Charles E., and Juntaro Kawai. "The densities, equivalent conductances and relative viscosities at 25, of solutions of hydrochloric acid, potassium chloride and sodium chloride, and of their binary and ternary mixtures of constant chloride-ion-constituent content." Journal of the American Chemical Society 48.5 (1926): 1119-1128.

[6] Shekaari, Hemayat, and Sedighehnaz S. Mousavi. "Conductometric studies of aqueous ionic liquids, 1-alkyl-3-methylimidazolium halide, solutions at T= 298.15–328.15 K." Fluid Phase Equilibria 286.2 (2009): 120-126.

Ion-ion and ion-solvent interaction studies on the ternary system: KSalicylate+ Ethanol+ H₂O by Potentiometric Method

M. Ghasemi[a], R. Salamat Ahangari[a]*
Department of Chemistry, Azarbaijan Shahid Madani University, Tabriz, Iran.
Email: Mgh.chemist@gmail.com, r.a.salamata@gmail.com

Abstract: This research focuses on the results of the thermodynamic investigation of the aqueous ternary KSalicylate + Ethanol+ water system, from the sightly low up to moderate concentrations range, by exploiting the potentiometric method at 25 ℃. The deviation from ideality behavior for this system was investigated by determination of KSalicylate mean activity coefficients in the studied ternary (KSalicylate+ Ethanol+ H2O) electrolyte system using ion-selective electrodes (K⁺ ISE, Salicylate⁻ ISE). The electrolyte system was modeled on the basis of the extended Debye-Huckel theory. Finally, the Gibbs free energy of transfer of salts from pure solvent to solvent mixtures was investigated.

Keywords: Activity Coefficients, Gibbs free energy of transfer, Salicylate and Ethanol

I. INTRODUCTION

Electrochemical methods are directly related to the thermodynamic characteristics of solutions containing electrolytes, Therefore, electrochemical cells are the basic tools for laboratory studies and are widely used to measure the thermodynamic parameters of electrolytic solutions. Electrochemical methods, such as potentiometric, directly investigate the physicochemical and thermodynamical properties of ions. One of these properties is the Gibbs free energy of transfer of ions from pure solvent to solvent mixture. The present study performed a measurement on the activity coefficients of the electrolyte with employing ion selective electrodes and using a potentiometric method, Therefore, modeling and analyzing the results with the extended Debye-Huckel model in a mixture of solvents was surveyed .

II. METHODS

Polymeric membrane electrode of salicylate was fabricated in the Lab. and all the measurement were made by potentiometric method. The extended Debye-Huckel equation has been used and the calculations have been done with MATLAB and Excel software.

III. RESULTS AND DISCUSSION

The emf measurements of the following galvanic cells:
K⁺ISE | KSalicylate(m), H2O (1- wt%), Ethanol (wt%)| Salicylate⁻ISE
Here m is the pure molality of salt.
The Nernst equation is as follows:

$$E = E^0 + S \log(m\gamma_\pm) \tag{1}$$

Here E^0 the constant (standard potential) and S the Nerntian slope.
The extended Debye-Huckel equation for 1:1 electrolyte, could be expressed as follows:

$$\log_{10} \gamma_\pm = -\frac{Am^{1/2}}{1 + Bam^{1/2}} + cm - \log(1 + 0.002mM) \tag{2}$$

where A and B are the Debye-Huckel constants , a the ion size parameters, c the ion-interaction parameter and M the average molecular mass of mixed solvent.
the Debye-Huckel constants can be written as follows:

$$A = 1.8247 \times 10^6 d^{1/2} / (\varepsilon_r T)^{3/2} \tag{3}$$

$$B = 50.2901 \times d^{1/2} / (\varepsilon_r T)^{1/2} \tag{4}$$

Here d is the density of solvent, ε_r dielectric constant and T the temperature [1-2-3].
In Figure 1, the activity coefficient versus the molality of potassium salicylate at 298.15K for different weight percentages is plotted.
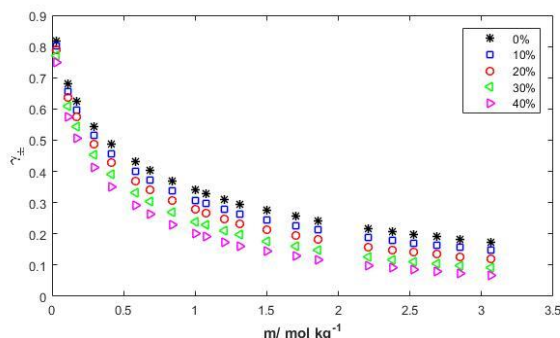
Fig. 1: Activity coeffcients versus molality of KSalicylate in the ternary KSalicylate + Ethanol + Water at 298.15 K

The Gibbs free energy of transfer is is written as follows:

$$\Delta G_t^\circ = -nF(E_s^\circ - E_w^\circ) \tag{5}$$

Here E_s° stands for the standard potential in the mixed solvent and E_w° is the corresponding value in the pure water [4-5].

In Figure 2, The Gibbs free energy of transfer of the electrolyte versus the weight percentages of Ethanol in mixed solvent at 298.15 K is plotted.
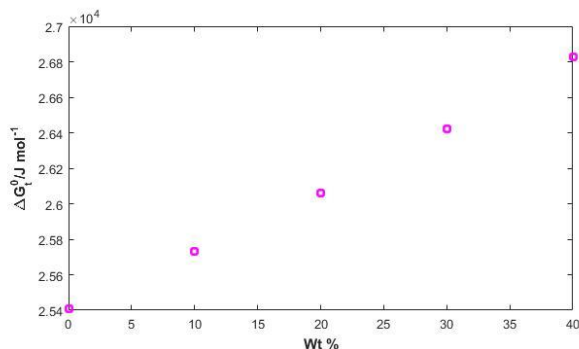
Fig. 2: Gibbs free energy of transfer versus the weight percentages of Ethanol in the ternary KSalicylate + Ethanol + Water at 298.15 K

IV. CONCLUSION

The activity coefficient decreases with decreasing the dielectric constant of the mixed solvent (increasing in weight percentages of Ethanol). And this is related to the solvation of the ions. The Gibbs free energy of transfer increases according to the enhancing of the weight percentages of the mixed solvent, this fact legitimately is an indication of decrease in solvating ability of the mixed solvent.

REFERENCES

[1] F. Hernández-Luis, H.R Galleguillos, M. V. Vazquez, Journal of Chemical Thermodynamics Vol. 36, pp. 957-964, **2004.**

[2] F. Hernández-Luis, E. Amado-González, M. A. Esteso, Carbohydrate research, Vol.338(13), pp.1415-1424, **2003**.

[3] O. M. Gonzilez-Dfaz, L. Fernzindez-Merida, F. Hernández-Luis, and M. A. Esteso, Journal of Solution Chemistry, Vol. 24, pp. 551-563, **1995** .

[4] R.N. Roy, R. A Robinson,R. G. Bates, Journal of Chemical Thermodynamics, Vol. 5, pp. 559, **1973**.

[5] U. N. Dash, D. Satyanarayan ,K .N. Panda, S . C. Rath, S. K. Mohanty, Journal of Thermochimica Acta, Vol. 30, pp. 217-223, **1979**.

Experimental and computational study of the electrochemical oxidation of some urazole species

*Hadi Beiginejad*a, Shadi Paziresha, Hadis Farahania, Shadpour Mallakpourb*
a Department of Chemistry, Malayer University, Malayer, 6571995863, Iran.
bDepartment of Chemistry, Isfahan University of Technology, Isfahan, Iran.
E-mail: h.beiginejad@malayeru.ac

Abstract: In this work, a computational analysis was performed to study the electrochemical oxidation of some urazol species. Cyclic voltammetry was used to obtain experimental results, and the theoretical data were calculated at DFT (B3LYP/6-311G (d,p)) level of theory. In this research effect of the substituent on the oxidation potential and acidity equilibrium constants (K_a) for some urasole species were studied. By the use of ΔG_{tot}, it was indicated that the potential of the electrochemical oxidations of the studied urazoles are dependent on their ΔG_{tot}. The diagram of ΔG_{tot} vs. E_0 was used to estimate the oxidation potential of some other urazole species. The pK_a of the studied urazoles in aqueous solution have been calculated by the use of potential–pH diagrams. ΔG_d of the studied species were calculated, and diagram of ΔG_d vs. pK_a was used to estimate pK_a of the other urazoles.

Keywords: Urazole derivatives, Electrochemical oxidation, Gibbs free energy, Cyclic voltammetry.

I. INTRODUCTION

Amines are widely used in chemistry, biology, medicine and agriculture. Urazole, which is amine species, is a biochemical reagent and has been used to production of some drugs [1]. Electrochemical oxidations of urazole derivatives at various conditions have been studied, and thermodynamic and kinetic information about their reactions were reported [2]. The use of computational analysis in the electrochemical studies of different species has been shown that the computational study can be used to justify the reaction mechanisms [3]. In this work, the electrochemical study of the urasole species (**1-5**) was performed both experimentally and theoretically, and the effect of the substituent on the oxidation potential and the acidity equilibrium constants (K_a) were studied. Cyclic voltammograms of urazole derivatives (**1-5**) at various pHs were recorded and using potential-pH diagrams, E_{p0} (oxidation potential of studied species in pH = 0.0) of them were obtained. Also, ΔG_{tot} of oxidation of the studied spices were calculated with considering a general thermodynamic cycle (Born- Haber cycle). Diagram of E_{p0} versus ΔG_{tot} was used to predict the oxidation potential of other urazole

species (**6-9**). Dependence of pK_a of acids to ΔG of deprotonation (ΔG_d) was studied, and it was reported that pK_a increases upon increasing ΔG_d [4]. The pK_a of urazole derivatives (**1–5**) in aqueous solution has been calculated by the use of potential–pH diagrams. Using a Born-Haber cycle, the ΔG_d of the species were calculated. Drawn graph showed that there is a good correlation between ΔG_d and pK_a. This diagram was used to predict the pK_a of other urazole species (**6-9**).

II. METHODS

Apparatus and reagents

Cyclic voltammetry was performed using an Ivium potentiostat/galvanostat (model vertex). A glassy carbon disk (1.8 mm diameter) used in the voltammetry as a working electrode and a platinum wire was used as the counter electrode. The working electrode potentials were measured vs. SCE. More details described in previously reported article [4].

Computational methods

Density functional theory (DFT), B3LYP level of theory and 6-311G (d,p) basis set, was used to obtain optimized forms of all species in the gas phase. Vibrational frequency analysis of studied species at the mentioned level of theory indicates that there is no negative frequency.

$$\Delta G_{tot} = \Delta G_{gas} + \Delta G_{sol} \qquad \text{(Eq. 2)}$$

Where ΔG_{gas} is the standard Gibbs free energy change in gas phase and ΔG_{sol} is the solvation energy. More details described in previously reported article [4].

III. RESULTS AND DISCUSSION

Fig.1 shows cyclic voltammogram (CV) of 4-phenylurazole (**1**) in water containing phosphate buffer (pH = 3.0) at a glassy carbon electrode. The voltammogram with an irreversible future shows one anodic peak (A$_1$) at 0.58 V vs. SCE, and the A$_1$ peak corresponds to oxidation of **1** to **1ox** (Scheme 1).

The electrochemical behavior shows that the produced **1ox** is unstable and participates in a hydrolysis reaction (Scheme 1).

By the use of changing the scan rate, it was found that in upper scan rates a cathodic peak (C_1) appears at 0.53 V vs. SCE and its current (I_{pC1}) increases upon increasing the scan rate. Recorded CVs of **1** at various pH indicate that the voltammograms shift to the negative potentials by increasing the pH of the solution (Fig. 2). This dependency of the potential to pH is related to the participation of proton(s) in the electrochemical oxidation reaction of **1** to **1ox**.
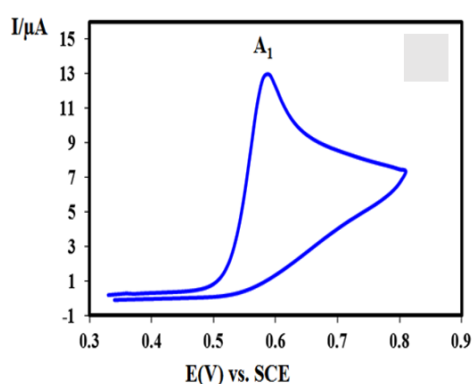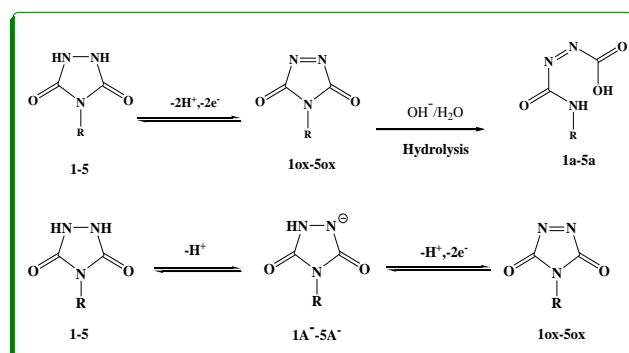

Fig.1: CV 1 mM of 4-phenylurazole (**1**) at a GCE, in phosphate buffer solution (pH = 3.0), scan rate: 50 mV s^{-1}.

Scheme 1. Proposed mechanism for the electrochemical oxidation, ring cleavage and deprotonation of urazole derivatives (**1-5**).

The potential-pH diagram shown in Fig. 2 indicates that the diagram composed of two segments. The reaction that occurs at pHs lower than 5.46 is two-electron, two-proton process, and **1** oxidized to **1ox** in the positive scan. In addition, the reaction that occurs at pHs upper than 5.46 is two-electron, one-proton process, and **1A$^-$** converts to **1ox**. The pK_a obtained in this work for acid/base (**1/1A$^-$**) equilibrium is 5.46. Also, extrapolate of the E_{pA1}−pH diagram in pHs lower than 5.46 indicates that E_{pA1} in pH=0 (E_{p0}) is 0.7648. Similar

studies were performed for other urazol species, and then E_{p0} and pK_a of them were obtained. Thermodynamic study of the electrochemical oxidation of different species indicates that the oxidation potential of species (E_A) depends on the total change in Gibbs free energy (ΔG_{tot}) and E_A increase upon increasing ΔG_{tot}. The ΔG_{tot} can be related with potential via the Eq. 1[5].

$$\Delta G_{tot} = -nF (E_c - E_a) \qquad \text{(Eq. 1)}$$

Where E_c is the oxidation potential of studied species in cathode and E_a is reduction potential of water in anode. By considering the reduction of water as the cathodic reaction for all studied species, ΔG_{tot} is calculated by *Eq.* 2.

$$\Delta G_{tot} = K + nF E_a \qquad \text{(Eq. 2)}$$

E_{p0} (E_{pA1} in pH=0) was considered as the oxidation potential.
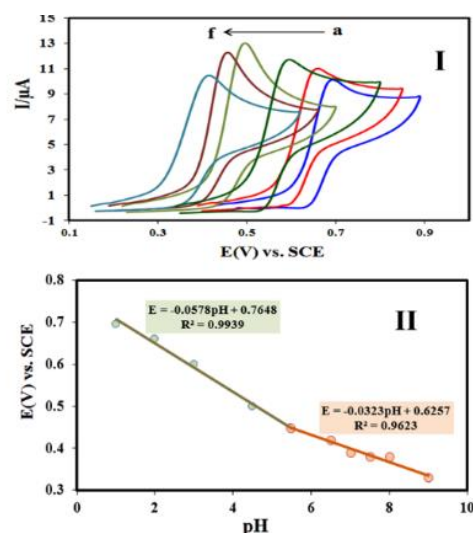
Fig. 2. (*I*) CVs 1.0 mM of **1** in aqueous solution at various pHs. pHs from (a) to (f) are 2.0, 3.0,4.5, 5.5, 6.5 and 7.5, scan rate=50 mV/s. (II) Potential-pH diagram of A_1 peak.
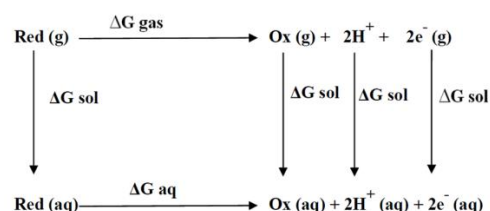

Fig.3. Thermodynamic cycle used to calculate Gibbs free energy.

The plot of calculated ΔG_{tot} versus E_{p0} indicates that there is a good correlation between ΔG_{tot} and E_{p0} of the studied species. The diagram indicates that the species with larger ΔG_{tot} value have more positive oxidation potential. Based on the previous experiences in the relation between ΔG_{tot} and oxidation potential of different species [4] and regular dependence of E_{p0} to ΔG_{tot} for this urazole species (**1-5**), the oxidation potential (E_{p0}) of other substituted species of urazole (**6-9**) were estimated.
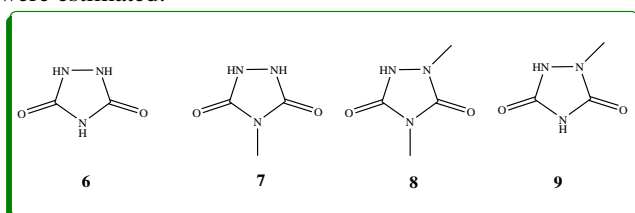
Scheme 2. The structure of urazol derivatives (**6-9**).

Theoretical calculations of pK_a for different organic acids indicate that the pK_a increases upon increasing ΔG_d, and there is a linear relationship between ΔG_d and pK_a [5]. Therefore, ΔG_d was calculated using a Born-Haber cycle. The diagram of calculated ΔG_d versus pK_a was recorded, and it indicates that there is a good correlation between the parameters. The recorded diagram indicated that the pK_a of the studied species increase upon increasing ΔG_d. Dependence of pK_a to ΔG_d and the good correlation of the plot enable us to estimate pK_a of other substituted species of urazole (**6-9**) without performing laboratory research.

IV. CONCLUSION

Electrochemical oxidation of some urazol species was investigated, and the results were analyzed using computational study. It was found that electrochemical oxidation potentials (E_{p0}) of **1–5** are directly dependent on the ΔG_{tot} of the electrochemical oxidation. The diagram of ΔG_{tot} vs. E_{p0} was used to predict the oxidation potential of other urazole species (**6-9**). Also, diagram of ΔG_d vs. pK_a was used to estimate pK_a of the urazole species (**6-9**).

REFERENCES

[1] M. Amir, H. Kumar, S.A. Javed, Eur. J. Med. Chem., vol. 43, 2056-2066, **2008**.

[2] S. Mallakpour, Z. Rafiee, Polymer, vol. 48, pp. 5530-5540, **2007**.

[3] H. Beiginejad, D. Nematollahi, S. Khazalpour, J. Iran. Chem. Soc., vol. 14, pp. 873-882, **2017**.

[4] H. Beiginejad, A. Amani, D. Nematollahi, S. Khazalpour, Electrochim. Acta, vol. 154, pp. 235-243, **2015**.

[5] M. Namazian, S. Halvani, J. Iran. Chem. Soc., vol. 2, 65-70, **2005**.

Diversity of mechanism in the electrochemical study of different electrophiles in the presence of some thiol nucleophiles: thermodynamic and mechanistic study

Hadi Beiginejad* and Faezeh Shirzadi
Department of chemistry, Malayer University, Malayer, 6571995863, Iran.
E-mail: h.beiginejad@malayeru.ac

Abstract: In the current study, the electrochemical oxidation of different electrophiles in the presence of *p*-toluenesulfinic acid and 2-mercaptobenzoxazole as thiol nucleophiles was studied. Mechanistic study of the electrochemical reactions indicates that the electrochemical oxidation of some electrophiles in the presence of the thiol groups have different mechanisms. But some other electrophiles in the presence of both thiol nucleophiles have the same mechanism. The aim of this work is providing an answer to the question of: "why the mechanisms of the electrochemical oxidation of the studied species are different in the presence of different nucleophiles?", and the computational study was used. Thermodynamic investigation shows that when ΔG_{tot} of the electrochemical oxidation of product is less than that of initial species, the electrochemically produced species can be oxidized during controlled-potential coulometry.

Keywords: Controlled-potential coulometry, Cyclic voltammetry, Density Functional Theory (DFT), Total Change of Gibbs free energy (ΔG_{tot}).

I. INTRODUCTION

Electrochemical methods are used to research about biochemical pathways and mechanisms of electroactive species [1]. Due to good selectivity of the electrochemical methods, synthesis of organic species has been done by the use of these methods [2]. The reported results demonstrated that electrochemically produced electrophiles in the presence of different nucleophiles proceed via different mechanisms such as *ECECCC, ECECECE, ECECE, EC, ECE, ECEC*, etc [3]. Why the mechanisms of the electrochemically produced electrophiles are different in the presence of various nucleophiles? To answer this question, the computational study was used.

II. METHODS

Apparatus and reagents: Cyclic voltammetry was performed using an Ivium potentiostat/galvanostat (model vertex) potentiostat/galvanostat. The working electrode used in the voltammetry experiments was a glassy carbon disc (1.8 mm diameter), and platinum wire was used as the counter electrode. The working electrode potentials were measured versus standard Ag/AgCl (all electrodes from AZAR Electrode). All experiments were carried out at room temperature. More details are described in the previously reported paper [3].

Computational study: The geometries of all studied species in the gas phase were optimized at density functional theory (DFT), Bp86 level of theory using the Gaussian 03. The standard 6-31G (d, p) basis set was used for all species. Vibrational frequency analysis was calculated at the mentioned method, and the results indicate that there is no negative frequency. More details are described in the previously reported paper [3].

III. RESULTS AND DISCUSSION

Cyclic voltammogram (CV) of 2,3-dihydroxybenzoic acid (2,3-DHBA) in an aqueous solution containing phosphate buffer (pH=7.0, c=0.2 M) was recorded, which is shown in figure 1. As can be seen, there is a couple anodic (A$_1$) and cathodic (C$_1$) peaks, which correspond to the transformation of 2,3-DHBA (**1**) to its *o*-benzoquinone (**1ox**), and reduction of produced **1ox** to **1** respectively.
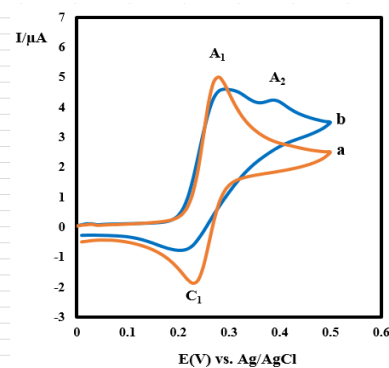

Fig. 1: CV 1.0 mM of 2,3-DHBA (**1**): a) in the absence, b) in the presence 0.25 mM of *p*-toluenesulfinic acid (**4**), in aqueous solution containing phosphate buffer (pH = 2.0). Scan rate: 10 mV s^{-1}

At the same condition, the CV of 2,3-DHBA (**1**) in the presence of *p*-toluenesulfinic acid (*p*-TSA) as a nucleophile was recorded. The CV indicates that the cathodic peak (C_1) decreased and a new anodic peak (A_2) appears in the more positive potentials. To obtain more data, a solution containing 2,3-DHBA (**1**) and *p*-TSA (**2**) was electrolyzed using controlled-potential coulometry (CPC) at the potential of peak A_1. The coulometry was terminated after consumption about two electrons per molecule of **1**. The precipitated product during CPC was analyzed using NMR and IR spectroscopy. According to the results, it can be concluded that the produced **1ox** reacts with **2** leading to the final product **1a**. Because the oxidation of **1a** is more difficult than that of 2,3-DHBA (**1**), the **1a** is produced via an *EC* mechanism. Reported results indicated that, during electrosynthesis process using CPC, if ΔG_{tot} of product is higher than that of starting molecule the electrolysis after consumption $2e^-$ per molecule has been terminated and mechanism of this electrolysis is *EC*. Also, if ΔG_{tot} of the species which produced during coulometry is lower than that of starting molecule, the produced species are oxidized under experimental conditions and the electrolysis have different mechanisms such as *ECE* and *ECECE* [4].
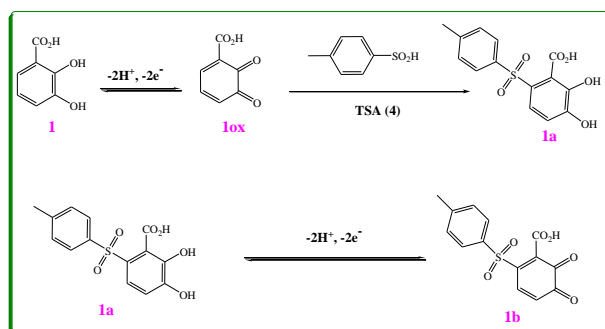
Scheme 1. Proposed mechanism for the electrochemical oxidation of 2,3-DHBA (**1**) in the presence of *p*-TSA (**4**).

ΔG_{tot} of 2,3-DHBA (**1**) and it's corresponding product **1a** were calculated by the use of computational study and is shown in scheme 1. It was found that $\Delta G_{1a} > \Delta G_1$, therefore the oxidation potential of **1a** (E_{p1a}) is positive than that of 2,3-DHBA (**1**), and under the CPC electrolysis conditions the produced **1a** cannot oxidize and the final product (**1a**) is produced via an *EC* mechanism. The electrochemical oxidation of 4-aminodiphenylamine (**3**), quercetin (**4**), 4-methylesculetin (**5**) and 4-(Piperazin-1-yl) phenol (**6**) in the presence of *p*-TSA (**2**) were performed, and the results indicate that related final products are produced via an *EC* mechanism. It can be concluded that in all studied cases, *p*-TSA increased ΔG_{tot} of studied species, and it prevents further electrochemical oxidation during CPC.

Electrochemical oxidation of hydroquinone (**7**) in the presence of 2-mercaptobenzoxazole (2-MB) was studied using voltammetry and coulometry methods. The results indicate that the electrochemical mechanism is *EC*. The calculated ΔG_{tot} of the electrochemical oxidation of **7** and its product (**7a**) indicate that the ΔG_{tot} of the electrochemical oxidation of **7a** is more positive than **7**, therefore the oxidation of **7a** is more difficult than the oxidation of **7** and the final product (**7a**) is formed via an *EC* mechanism. Also, electrochemical oxidation of catechol (**9**) in the presence of 2-MB (**8**) showed that the mechanism is *EC* too.

Electrochemical oxidation of 1-(4-(4-hydroxyphenyl) piperazin-1-yl)ethanone (**10**) has been studied in the presence of 2-mercaptobenzoxazole (**8**) as a nucleophile. A mixture solution of water (containing phosphate buffer, c =0.2 M, pH = 2.0)/acetonitrile (50/50v/v) containing **10** and 2-MB (**8**) was electrolyzed using CPC at the oxidation potential of **10**, and advancement of coulometry was carried out by the use of cyclic voltammetric analysis. It was found that the CPC was terminated when the charge consumption becomes $6e^-$ per molecule of **10**, and **10 d** was produced as a final product via an *ECECE* mechanism. Calculated ΔG_{tot} of **10** and its substituted species (**10a** and **10c**) indicates that ΔG_{tot} varies in the order $\Delta G_{10} > \Delta G_{10a} > \Delta G_{10c} >$. In other word, because ΔG_{10a} is lower than ΔG_{10}, the oxidation of **10a** is easier than the oxidation of the **10** and the produced **10a** oxidized to **10b** during controlled potential coulometry. Also, ΔG_{10b} is lower than ΔG_{10}. Therefore, it should be oxidized under this condition. Accordingly, the electrochemical oxidation of different species in the presence of 2-MB (**8**) have different mechanisms depending on their ΔG_{tot} of the electrochemical oxidation.
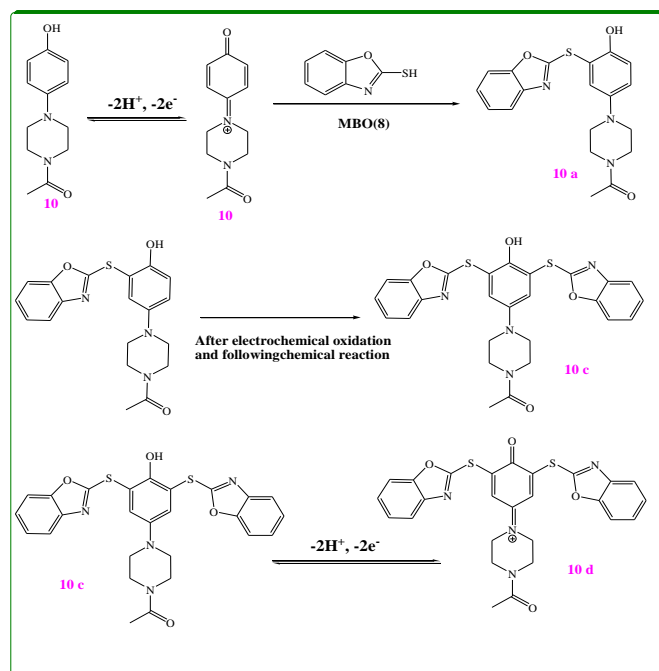
Scheme 2. Proposed mechanism for the electrochemical oxidation of **10** in the presence of **8**.

I. CONCLUSION

In this work, the computational study was used to mechanistic study of the electrochemical oxidation of different electrophiles in the presence of some thiols nucleophiles. The electrochemical study indicates that the electrochemical oxidation of some electrophiles in the presence of both thiol groups have different mechanisms. But some other electrophiles in the presence of the thiol nucleophiles have the same mechanism. Thermodynamic investigation shows that when ΔG_{tot} of the electrochemical oxidation of product is less than that of initial species, the electrochemically produced species can be oxidized during controlled-potential coulometry. In addition, when ΔG_{tot} of the electrochemical oxidation of product is more than that of initial species, the mechanism is *EC*.

REFERENCES

[1] H. Shayani-Jam, D. Nematollahi, Chem. Commun., vol. 46, pp. 409−411, **2010**.

[2] H. Beiginejad, D. Nematollahi, J. Org. Chem., vol. 79, pp. 6326−6329, **2014**.

[3] H. Beiginejad, A. Amani, D. Nematollahi, S. Khazalpour, Electrochim. Acta, vol.154, pp. 235–243, **2015**.

Electrochemical oxidation of some hydroquinone derivatives in the presence of *p*-toluenesulfinic acid: Thermodynamic and Mechanistic studies

Hadi Beiginejad* and Faezeh Shirzadi

Department of chemistry, Malayer University, Malayer, 6571995863, Iran.
E-mail: h.beiginejad@malayeru.ac

Abstract: In this work, electrochemical oxidations of three p-dihydroxybenzene species (tert-Butylhydroquinone, 2,5-dihydroxybenzoic acid and hydroquinone) have been studied. By the use BP86 level of theory and 6-31G(d,p) basis set, the computational data were obtained. Also, to obtain the experimental results, cyclic voltammetry and controlled potential coulometry were used. The results showed that because the potential of the electrochemical oxidation of the species (E_{pA}) is dependence on ΔG_{tot}, E_{pA} increases upon increasing ΔG_{tot}. The ΔG_{tot} of studied species, calculated by the use of a general thermodynamic cycle, were used to mechanistic study of the electrochemical oxidation of the *p*-dihydroxybenzenes in the presence of *p*-toluenesulfinic acid.

Keywords: Cyclic voltammetry, Controlled-potential coulometry, Density Functional Theory (DFT).

I. INTRODUCTION

Electrochemistry methods were used to electrosynthesis, mechanistic and kinetic studies of different species [1]. And thermodynamic and kinetic information about the reactions of organic and inorganic species were obtained using these methods [2]. To electrosynthesis of a vast number of new species, the electrochemical oxidations of dihydroxybenzenes in the presence of nucleophiles were performed [3]. This work shows that the reaction rate of the produced *p*-benzoquinone with nucleophile is dependent on the substituent group on the benzene ring. Also, the reaction site of the reaction depends on the substituent group.

II. METHODS

Apparatus and reagents: Cyclic voltammetry was performed using an Ivium potentiostat/galvanostat (model vertex) potentiostat/galvanostat. The working electrode used in the voltammetry experiments was a glassy carbon disc (1.8 mm diameter), and a platinum wire was used as the counter electrode. The working electrode potentials were measured versus standard Ag/AgCl (all electrodes from AZAR Electrode). All experiments were carried out at room temperature. More details are described in the previously reported paper [4].

Computational study: The geometries of all studied species in the gas phase were optimized at density functional theory (DFT), Bp86 level of theory using the Gaussian 03. The standard 6-31G (p,d) basis set was used for all species. Vibrational frequency analysis was calculated at the mentioned method, and the results indicate that there is no negative frequency. More details are described in the previously reported paper [4].

III. RESULTS AND DISCUSSION

Figure 1, curve-*a* shows cyclic voltammogram (CV) of 1.0 mM of tert-Butylhydroquinone (**1**) in an aqueous solution containing 0.2 M phosphate buffer (pH=2). As can be seen, there are an anodic peak (A_1) in the positive going scan and a cathodic peak (C_1) in the negative going scan. In the positive scan, tert-Butylhydroquinone (**1**) is oxidized to its *p*-benzoquinone (**1ox**), and the A_1 peak corresponds to this electrochemical reaction. In the negative scan, the produced 1ox is reduced to **1** and the C_1 peak corresponds to it (Scheme 1). Nearly unity of a peak current ratio (I_{pC1}/I_{pA1}) indicates that under the experimental conditions, the produced **1ox** is stable at the surface of the glassy carbon electrode (GCE). The CVs of 1.0 mM of hydroquinone (**2**) and 2,5-dihydroxybenzoic acid (2,5-DHBA) at the mentioned conditions are shown in Fig. 1 curves *b* and *c*, respectively. The A_2 and A_3 are related to the electrochemical oxidation of hydroquinone (**2**) and 2,5-DHBA (**3**) to their *p*-benzoquinones (**2ox** and **3ox**).
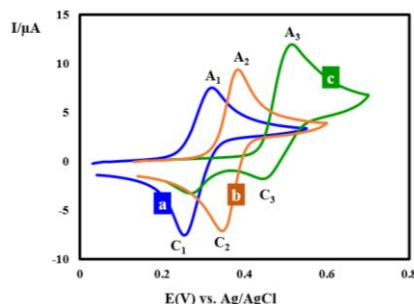

Fig. 1. CVs 1.0mM of: a) tert-Butylhydroquinone (**1**), b) hydroquinone (**2**) and c) 2,5-DHBA (**3**) in phosphate buffer solution (c=0.2 M, pH=2.0); scan rate: 25 mV s⁻¹, t=25 ± 1 °C.

By comparing the CVs, it can be concluded that electrochemical oxidation potential varies in the order $3 > 2 > 1$. Reported results indicate that the value of oxidation potential (E_{pA}) increases upon increasing ΔG_{tot}. Calculated data showed that ΔG_{tot} of the electrochemical oxidation of species (**1–3**) varies in the order $\Delta G_3 > \Delta G_2 > \Delta G_1$. The calculated results indicate that electrochemical oxidation of **3** is harder than **2** and **1**, and the electrochemical oxidation of **2** is harder than **1**. The obtained ΔG are agreed with the electrochemical oxidation potentials of species (**1–3**), which are mentioned above ($E_{p1} > E_{p2} > E_{p3}$).
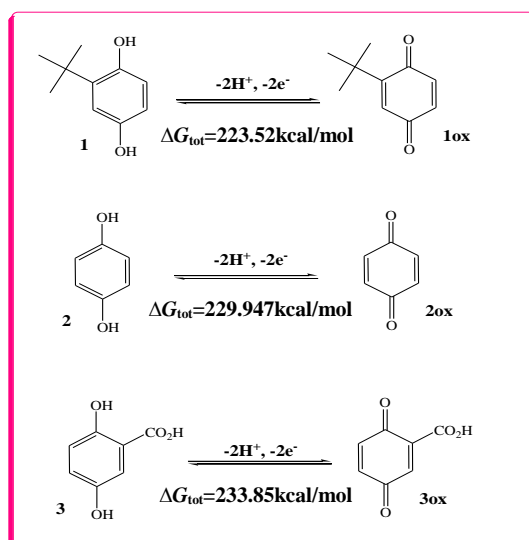
Scheme 1. Proposed mechanism for the electrochemical oxidation of **1-3**.
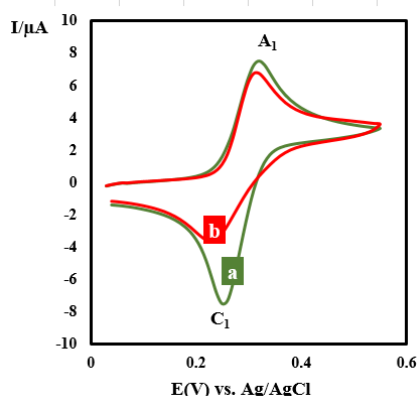
Fig. 2: CV 1.0 mM of **1**: *a*) in the absence, *b*) in the presence 0.5 mM of **4**, in aqueous solution containing phosphate buffer (pH = 2.0). Scan rate: 25 mV s^{-1}.

The CV 1.0 mM of **1** in an aqueous solution containing phosphate buffer (pH=2.0, c=0.2 M) in the absence and the presence of 0.5 mM *p*-toluenesulfinic acid (*p*-TSA) is shown in Figure 2. As shown in the presence of the nucleophile (*p*-TSA), the cathodic peak (C$_1$) decreased. This electrochemical behavior is related to the reaction of the produced **1ox** and nucleophile (*p*-TSA) at the surface of the electrode. In other word, the produced **1ox** is consumed by a chemical reaction with *p*-TSA (**4**). Electrolysis a solution containing tert-Butylhydroquinone (**1**) and *p*-TSA (**4**) was performed at the potential of the A$_1$ peak using controlled potential coulometry (CPC). The results indicate that after consumption of two electrons per molecule of tert-Butylhydroquinone (**1**) the electrolysis was terminated, and the precipitated product was analyzed using NMR.
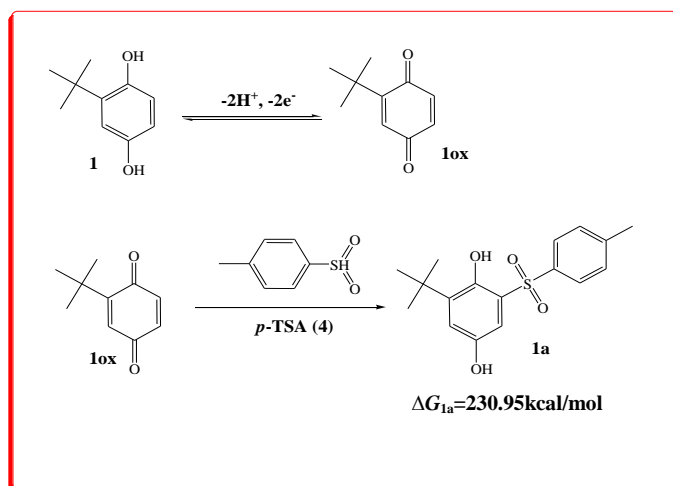
Scheme 1. Proposed mechanism for the electrochemical oxidation of **1** in the presence of *p*-TSA (**4**).

It was found that **1a** as a final product is produced due to reaction between the electrochemically generated **1ox** and **4** (*EC* mechanism). Because the oxidation potential of the produced **1a** is positive than that of **1**, the electrolysis terminated after consumption two electrons per molecule of **1**. Comparing computational results indicates that ΔG_{tot} of **1a** is more positive than that of **1**. This led to the increase of the electrochemical oxidation potential of **1a**, and the oxidation of **1a** is harder than the oxidation of **1**, therefore the final product (**1a**) is produced via an *EC* mechanism. The electrochemical oxidations of both other *p*-dihydroxybenzene species (**2** and **3**) in the presence of **4** were studied too. The results indicate that the final products (**2a** and **3a**) are produced via an *EC* mechanism. Using the current study, it was found that charge on reaction sites has an

influential role on the rate and on site-selectivity of Michael type addition reactions.

II. ONCLUSION

The results of this work show that tert-Butylhydroquinone (**1**), hydroquinone (**2**) and 2,5-dihydroxybenzoic acid (**3**) are oxidized to their *p*-benzoquinone (**1ox−3ox**). The coulometries were terminated after consumption of 2 electrons per initial molecules (**1-3**). The nucleophile (*p*-TSA) reacts with the electrochemical produced *p*-benzoquinones, and the final products (**1a-3a**) are obtained via an *EC* mechanism. Also, the effect of the charge of the reaction site on the rate of the reaction between **1ox−3ox** and **4** was investigated.

REFERENCES

[1] H. Beiginejad, D. Nematollahi, F. Varmaghani, M. Bayat, H. Salehzadeh, J. Electrochem. Soc., vol.160, pp. G3001-G3007, **2013**.

[2] C. Costentin, Chem. Rev., vol.108, pp. 2145-2179, **2008**.

[3] H. Beiginejad, D. Nematollahi, Monatsh. Chem. Vol. 147, pp 329–339, **2016**.

[4] H. Beiginejad, A. Amani, D. Nematollahi, S. Khazalpour, Electrochim. Acta, vol. 154, pp. 235-243, **2015**.

Synthesis and Investigation of Electrochemical Activity of Ni-Co/ poly (p-phenylenediamine) Catalyst Toward Methanol Electrooxidation

R. Azinfar[a] *, A.A. Rostami[a], H. Rostami[a]
[a] *Department of chemistry, University of Mazandaran, Babolsar, P.O. Box 453, Iran*
Email: r.azinfar9069@gmail.com

Abstract: In this study, a facile deposition method was adopted to synthesis Ni-Co/ poly (p-phenylenediamine). The electrochemical activity of the synthesized catalysts was investigated using cyclic voltammetry method. According to the results obtained, current density of Ni-Co/ poly (p-phenylenediamine) with 2-minute deposition time is 9.32×10^{-1} which is higher than current density of poly (p-phenylenediamine), at 5.95×10^{-1} mA/cm^2. The Onset potential shifts to negative values by 185 mV compared to onset potential of the blank sample for methanol electrooxidation. The voltammograms of the prepared electrocatalysts indicated that deposition of nickel and cobalt metallic particles to a blank poly (p-phenylenediamine) carbon paste electrode can enhance the electrochemical activity by lowering the onset potential and increasing the current density and electrochemically active surface area. Comparing electrochemical activity of samples with different deposition times, two minutes can be derived as the optimized amount.

Keywords: Electrocatalysis, Nickle-Cobalt catalyst, Poly(p-phenylenediamine), Methanol electrooxidation

I. INTRODUCTION

There is an increasing energy demand and environmental concern for finding clean, safe and low-cost energy resources [1]. Direct alcohol fuel cells (DAFC) has been received much attention because of high energy conversion efficiency and high specific energy density [2], [3]. The direct methanol fuel cell (DMFC) has numerous advantages such as simple operation and ease of fuel storage [4]. Methanol is safe for storage and transportation and exhibits high energy density in its liquid form [5]. Beside notable progress in fuel cell technology, some drawbacks especially in the case of catalysts remain. High cost and easy poisoning of Pt-based catalyst hindered the practical application of them [6].

To overcome the disadvantages of Pt-based catalysts including insufficient durability, easy poisoning and high cost, several investigations have been carried out to find new replacements [7]. Recently, as alternatives to noble metals, some transition metals such as Ni [8], Co [9], Cu [10] and etc. have been considered to improve the catalytic activity.

It has been proven that nickel, due to its surface oxidation properties, can be used as an effective catalyst for both anodic and cathodic reactions in organic synthesis and water electrolysis [11], [12]. Several studies of electrooxidation of alcohols on Ni have been reported. Most oxidizable organic compounds were found to oxidize at the same potential that coincided exactly at which the surface of the nickel anode becomes oxidized [13], [14].

Ni-Co based electrocatalysts can be considered as promising alternatives of non-precious metals because of their low cost and promoting electrocatalytic activity [15]. The poisoning of intermediate products can be annihilated by the presence of Co and improve electrocatalytic performance [16].

By introducing conductive polymers, a new effective approach has been developed to improve the electrocatalysts performance in order to increase the interfacial properties between electrode and electrolyte. Poly (p-phenylenediamine) is an electroactive polymer of the aromatic diamines' family. The easy synthesis methods and good electrochemical properties of this polymer enabled it to be used in electronic devices such as supercapacitors and batteries [17].

In this work, Ni-Co/poly (p-phenylenediamine) synthesized by a simple electrodeposition and the effect of electrodepositing time on the catalytic activity have been investigated through cyclic voltammetry test.

II. METHODS

Poly (p-phenylenediamine) synthesized through a chemical polymerization [18]. Briefly, p-phenylenediamine dissolved in distilled water and ultrasonicated for 1 hour. Ammonium proxy di-sulphate and hydrochloric acid were added, after ultrasonicating the solution for 4 hours, the polymerization process completed; the resulted precipitation was collected and washed with methanol, distilled water and dried to be used in next steps.

Ag/AgCl electrode, Pt electrode and carbon paste electrodes with 4 mm diameter, were used as counter, reference and working electrode, respectively. In order to provide the working electrode, graphite powder, paraffin

and poly (p-phenylenediamine were mixed thoroughly. A solution of 0.5 molar Nickle chloride hexahydrate, cobalt chloride and boric acid were used as electrodeposition solution. After polishing the carbon paste electrode on a paper, electrodeposition was carried out at 0.3 V potential in 1, 2 and 5 minutes. The metallic shininess on the carbon electrode surface is a sign of successful deposition.

Cyclic voltammetry test was carried out in a 1 molar sulphuric acidic solution of methanol for the purpose of investigating catalytic activity of synthesized catalysts.

III. RESULTS AND DISCUSSION

The cyclic voltammograms of the prepared samples are indicated in figure 1. Voltammogram of a blank sample (without any metallic deposition) is included, compared to other samples. According to figure 1. by adding Ni and Co particles, the methanol electrooxidation improved. Higher oxidation peak and lower onset potential prove that adding these two transition metals to graphite can be an effective way to enhance its activity [19]. It is obvious that deposition of Ni-Co metallic particles can enlarge the redox peaks, which indicate a sharply increased electrochemically active surface areas (ECSAs). By putting the samples into comparison, it can be concluded that the sample prepared in two minutes deposition time has a higher oxidation peak, lower onset potential and higher ECSA. Therefore, the optimized deposition time is 2 minutes. The improved electrocatalytic activity of this sample can be pertinent to the fact that low deposition time is not enough for the depositing of metallic particles. Accordingly, higher deposition time leads to the agglomeration of particles and eventuates in lower catalytic activity.
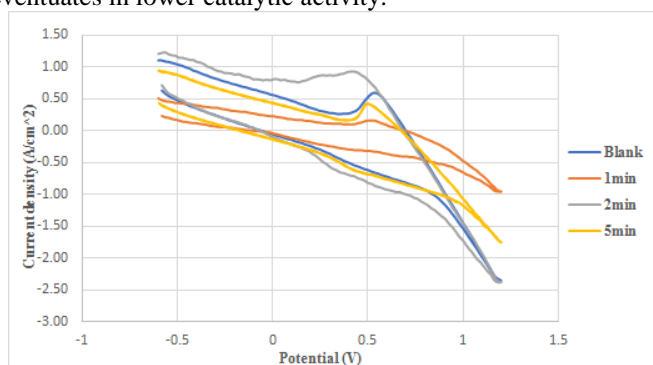
Fig.1: Cyclic voltammograms of Ni-Co/ poly(p-phenylenediamine) in 1 M sulphuric acid/ methanol solution.

IV. CONCLUSION

In this work a simple electrodeposition method was performed to prepare Ni-Co/ Poly(p-phenylenediamine) electrocatalyst. The catalytic activity of Ni-Co/ Poly(p-phenylenediamine) electrocatalyst was investigated using cyclic voltammetry method. Electrochemical results demonstrate that the prepared catalyst has a high activity toward methanol electrooxidation in term of current density, onset potential and electrochemically active surface area, compared to blank sample. Based on the derived results; one can conclude that the Ni-Co/ poly(p-phenylenediamine) sample with 2 minutes deposition time can be a promising catalyst for methanol electrooxidation in methanol fuel cells. Further studies can be carried out in order to optimize the molar ratio of metals and the pH of electrodeposition solution.

REFERENCES

[1] S. Zhao, L. Yan, H. Luo, W. Mustain, and H. Xu, Nano Energy, vol. 47, pp. 172–198, **2018**.

[2] L. An, T. S. Zhao, and Y. S. Li, Renewable and Sustainable Energy Reviews, vol. 50, pp. 1462–1468, **2015**.

[3] Q. Yi, T. Zou, Y. Zhang, X. Liu, and G. Xu, J. Power Sources, vol. 321, pp. 219–225, **2016**.

[4] I. Danaee, M. Jafarian, F. Forouzandeh, F. Gobal, and M. G. Mahjani, J. Power Sources, vol. 33, pp. 4367–4376, **2008**.

[5] L. Gong, Z. Yang, K. Li, W. Xing, C. Liu, and J. Ge, J. Energy Chem., vol. 27, no. 6, pp. 1618–1628, **2018**.

[6] Y. Lu and W. Chen, Chemical Communications, pp. 2541–2543, **2011**.

[7] J. Maya-Cornejo, A. Garcia-Bernabé, and V. Compañ, Int. J. Hydrogen Energy, vol. 43, no. 2, pp. 872–884, **2018**.

[8] G. Li, Q. Yi, X. Yang, Y. Chen, X. Zhou, and G. Xie, Carbon N. Y., vol. 140, pp. 557–568, **2018**.

[9] C. Lo Vecchio, D. Sebastián, C. Alegre, A. S. Aricò, and V. Baglio, J. Electroanal. Chem., vol. 808, pp. 464–473, **2018**.

[10] M. Guo, Q. Tu, L. Wang, Y. Tang, and C. Liu, Int. J. Hydrogen Energy, vol. 44, no. 13, pp. 6886–6895, **2019**.

[11] Y. Zhao et al. Sci. Rep., vol. 5, pp. 1-7, **2015**.

[12] B. Tian, W. Zhen, H. Gao, X. Zhang, Z. Li, and G. Lu, Appl. Catal. B Environ., vol. 203, pp. 789–797, **2017**.

[13] J. Li et al., Adv. Funct. Mater., vol. 26, no. 37, pp. 6785–6796, **2016**.

[14] H. Jin, J. Wang, D. Su, Z. Wei, Z. Pang, and Y. Wang, J. Am. Chem. Soc., vol. 137, no. 7, pp. 2688–2694, **2015**.

[15]   C. Zhang et al., Polyhedron, vol. 117, pp. 661–665, **2016**.

[16]   P. Arunachalam, M. A. Ghanem, A. M. Al-Mayouf, and M. Al-shalwi, Mater. Lett., vol. 196, pp. 365–368, **2017**.

[17]   H. Rostami, A. Omrani, A. A. Rostami, and A. Emamgholizadeh, Ionics (Kiel)., vol. 21, no. 4, pp. 1073–1080, **2015**.

[18]   H. Rostami, A. A. Rostami, and A. Omrani, Electrochim. Acta, vol. 191, pp. 536–547, **2016**.

[19]   Y. Li, X. Zhang, A. Hu, and M. Li, J. Hydrogen Energy, pp. 2–10, **2018**.

Thermodynamic investigation of 1-Butyl-3-Methylimidazolium Bromide Ionic Liquid In Water + DMA Mixed Solvents Based On Conductometric Measurements

F. Haghani Dogahe, B. Ghalami Choobar*

Department of Chemistry, Faculty of Science, University of Guilan,Rasht, P.O. Box: 19141, Iran

E-mail:B-ghalami@ guilan.ac.ir

Abstract: In this research, the ionic conductivity of 1-Butyl-3-methyl imidazolium Bromide in water and DMA mixtures was measured in different mass fractions of DMA mixtures((w/w)% = w_{DMA} / $w_{mixture}$ =0, 10 and 20%) at T = (298.2, 308.2) K. The conductivities data were analyzed by Fuoss Onsager equation. The ion association constant (K_A), limiting molar conductivitiy (Λ_0) was obtained through correlation of experimental data. The estimated parameters were used to compute the standard Gibbs free energy of aggregation (ΔG_A°).

Keywords: Ion association constant, Conductivity, Fuoss Onsager, 1-Butyl-3-methyl imidazolium Bromide , DMA

I. INTRODUCTION

One of the main sources of pollutants is organic solvents released in air and ground waters [1]. As a class of neoteric solvents [2], ionic liquids (ILs) have a unique molecular property, which are composed only of ion. These compounds exhibit many unique physical and chemical properties such as nonvolatility, nonflammability, and recyclable. They are categorized as green solvents [3]. ILs are regarded appropriate average option for some processes such as, solvent for separation, bio catalysis and pharmaceutical synthesis. Many studies on the thermodynamic properties determination of ionic liquids has been reported in literatures [3-4]. However, a literature review indicates that the properties of 1-Butyl-3-methyl imidazolium Bromide ionic liquid in water and DMA ternary mixtures have not been made.

In this work, we present the results in relating to the conductivity of 1- Butyl -3-methylimidazolium bromide, [BMIm]Br, in ternary mixtures of [BMIm]Br + DMA + water. The conductivities data were analyzed by Fuoss Onsager equation to calculate the limiting molar conductivity (Λ_0) and ion association constant (K_A).

II. METHODS

Martini instruments Mi 180 was used to measure the conductance data with a type cell constant of 1.361 cm^{-1}. Data acquisition was carried out via a personal computer and Microsoft office software. The instrument was calibrated with KCl solution before conductometric measurements. The conductivities of ionic liquid solutions were always corrected for the contribution of the solvent. All measurements were performed in a double-walled glass container, and a model GFL circulation water bath with accuracy 0.1 K was used to control the temperature of the test solution. Hamilton syringe 100 µl model CH-7402 Bonaduz with accuracy ±1 µl was applied to take volume in very low quantities. The stock solutions of electrolyte was prepared of ionic liquid, DMA and double distilled water with <2.0 µs·cm^{-1}conductance.

III. RESULTS AND DISCUSSION

The electrical conductivity of [BMIm]Br solutions as function of ionic liquid concentration (mIL) on the mass fractions of (0, 10 and 20%) (DMA/mixture) in aqueous system were measured. Then, molar conductivity of the solutions was determined In Fig. 1. the molar conductivity (Λ) of the ternary system water + [BMIm]Br + DMA were compared with mass fraction 20% at T = 308.2 K. It can be seen that with growing the molal concentration of ionic liquid and mass fraction of DMA, the molar conductivity (Λ) decreased. Limiting molar conductivities (Λ_0) and ion association constants (K_A) of [BMIm]Br in water + DMA mixtures were estimated using the Fuoss-Onsager model in according to the following Eq. (1) [4].

$$\Lambda = \Lambda_{\circ} - [(0.8204 + \frac{10^6}{(\varepsilon_r T)^{3/2}})\Lambda_{\circ} + 82.50/\eta(\varepsilon_r T)^{1/2}]C^{1/2}\gamma^{1/2} + \quad (1)$$

$$(E_1^{'}\Lambda_{\circ} - E_2^{'})C\gamma \ln(6E_1^{'}C\gamma) + LC\gamma - K_A C\gamma\Lambda\exp[-8.405\times10^6\frac{C^{1/2}\gamma^{1/2}}{(\varepsilon_r T)^{3/2}}]$$
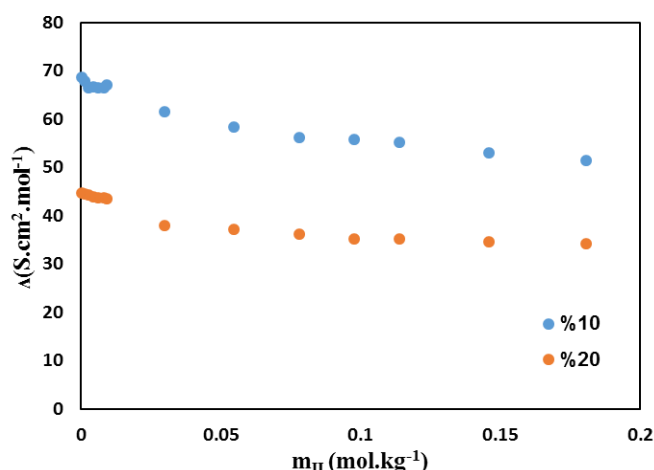
REFERENCES

[1] Kh. Ghandi, Green, Sustainable Chem. 4 (**2014**) 44–53.
[2] J.F. Brennecke, E.J. Maginn, Ionic liquids: AIChE J. 47 (**2001**) 2384–2389.
[3] [3] N. Meine, F. Benedito, R. Rinaldi, Green Chem. 12 (**2010**) 1711–1714.
[4] B Ghalami-Choobar, T Nosrati Fallahkar, Fluid Phase Equilibria 496 (**2019**) 42-60

Fig.1: The plot of the Molar conductivity of [BMIm]Br in DMA + water mixtures as a function m_{IL} in mass fractions 10%, 20% ($w_{DMA}/w_{mixture}$) at T = 308.2 K.

The obtained parameters for [BMIm]Br on DMA mass fractions of 20% ($w_{DMA}/w_{mixture}$) in mixed solvent system were given at T = (298.2,308.2) K in Table 1. It can be seen with increasing the temperature both of the K_A and Λ_0 were increased. In addition, The estimated parameters were used to compute the standard Gibbs free energy of aggregation.

Table1: The obtained parameters for 20% mass fraction (DMA/mixture) at T = (298.2, 308.2) K.

T(K) mol^{-1})	Λ_0(S cm^2 mol^{-1})	K_A(dm^3
298.2	48.63	5.05
308.2	52.69	10.82

IV. CONCLUSION

In this work, molar conductivities, of [BMIm]Br in the [BMIm]Br + DMA + water system were given at T = (298.2 and 308.2) K. Fuoss-Onsager equation was applied to calculate the Limiting molar conductivities and ion association constant. The Limiting molar conductivity and ion association constant values show a increase with temperature increasing.. The Λ_0 value of the IL decrease with increasing the mass fraction of DMA in mixed solvent.

Investigation of Electrochemical Properties of Calcium Manganese Oxide as Supercapacitor Electrode Material

A. Meftahi, S.M. Mousavi-Khoshdel*, S.Rostamnia

Research Laboratory of Industrial Electrochemistry, Department of Chemistry, Iran University of Science and Technology (IUST), Tehran, 1674613114, Iran

Email: *mmousavi@iust.ac.ir*

Abstract: In this study, manganese oxide with quantitative amounts of calcium has been synthesized and its electrochemical performance as supercapacitor electrode material was investigated. Related tests such as charge discharge and cyclic voltammetry were performed. The results indicate that the electrode material exhibited a capacity of 384 F/g at current density of 1 A/g, but the cyclability of the material was not satisfying and 80% of the initial capacity was maintained only after about 200 cycles.

Keywords: Capacitance, Electrode material, Manganese oxide, Pseudocapacitance, Supercapacitor

I. INTRODUCTION

One of the essential demands for devices that need high energy supply is to developing supercapacitors with high energy density. For this purpose, the easiest way is to increase the special capacity of the supercapacitor electrode. In this regard, the point is to find inexpensive and environmental friendly materials. In this study, the energy density has been improved by using metal oxide with outstanding pseudocapacitance behavior. A composite of manganese oxide and calcium has been synthesized and we have investigated its supercapacitor's properties.[1]

II. METHODS

Cyclic voltammetry and Galvanostatic charge–discharge were investigated (KimiaStat 126 battery tester). The impedance test was also taken with Metrohm Autolab

Electrodes preparation method: To prepare the electrode material, the ratio of 80, 10, 10 of synthesized material, active carbon and PTFE were used, respectively. After painting the material on the electrode, we dried it for 10 hours at 80 ° C on the oven.

Preparation of material and electrolyte: A three-electrode electrochemical cell with Ag/AgCl electrode as a reference electrode and platinum electrode as a counter electrode were used. A graphite plate was used to make the electrode. In this test, 1 M sulfuric acid was used as an electrolyte.

III. RESULTS AND DISCUSSION

A. Figures and Tables

Cyclic Voltammetry:

CV curve of calcium manganese oxide electrode was plotted at a scan rates of 2, 10,20,40,80,120,150,200 mV/s in 1M sulfuric acid as an electrolyte, respectively (Fig.1). The curve indicates that this electrode material has pseudocapacitive properties in the potential window of about 0.2-1.2 V, which can be verified through observing redox peak. Anodic and cathodic peaks can be seen at 0.9-0.7 V, respectively. In alkaline earth elements such as calcium, due to lack of multiple valence states, there is no ability to perform redox reactions and as a result, the observed peaks are related to the transition metals (manganese).[1]
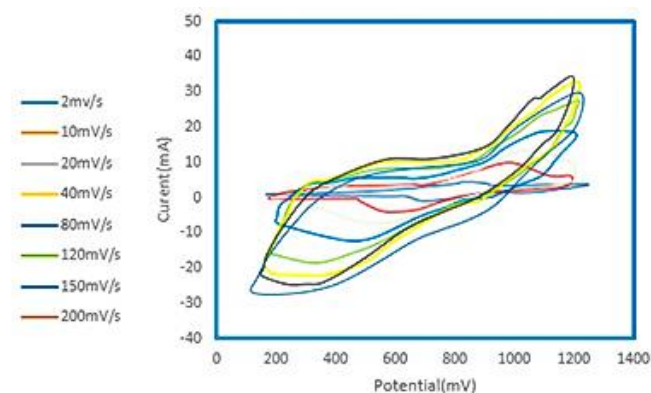

Fig.1: CV curve of calcium manganese oxide electrode at a scan rates of 2, 10,20,40,80,120,150,200 mV/s

Charge –discharge

Galvanostatic curves of the compound are shown in current density of 1, 2, 5, 10, 20, 40 A/g respectively. At current

density of 1 A/g capacity is 384 F/g (Fig.2). Nonlinear curve indicates the pseudocapacitor behavior of this substance. This approach is due to reactions that can be seen in CV curves. It is possible to see the redox peak through CV curve, which is related to manganese oxide. Therefore, the suitability of the above metal oxide is evident due to its pseudocapacitive properties in addition of its electrical double layer supercapacitors behavior.
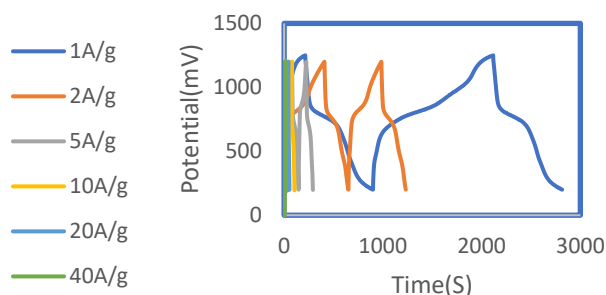

Fig.2: Galvanostatic charge-discharge curves in current density of 1, 2, 5, 10, 20, 40 A/g

Table1: capacity values in different current densities

Current(A/g)	1	2	5	10	20	40
Capacity(F/g)	384	254.7	172.5	151	115	52

Cyclability

After cyclability test, it was found that after 200 cycles, it retained 80% of its initial capacity. Thus, this composite does not show admissible cyclability (Fig.3)
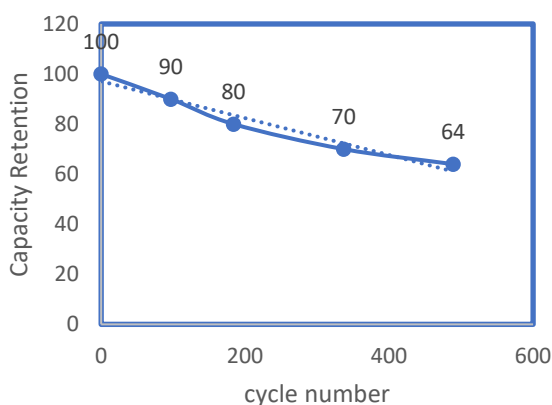
Fig.3: capacity retention curve based on the number of cycles

Impedance

An electrochemical impedance spectroscopy technique was used to further analyze the electrochemical frequency behavior of $CaMnO_2$. Nyquist plot of $CaMnO_2$ drawn (Fig.4). The impedance spectrum includes a semicircle section at high frequencies and a linear section at low frequencies. The semicircle in the high frequencies on the horizontal axis represents (Rs) and (Rs + Rct of the charge transfer resistance) which RS is the electrolyte solution resistance, the internal resistance of the electrode material, and the contact resistance. Rct is the charge transfer resistance of the surface. The slope after the bottom of the semicircle in the low frequency region indicates the diffusion resistance of the electrolyte which we know it by the Warburg impedance (ZW).

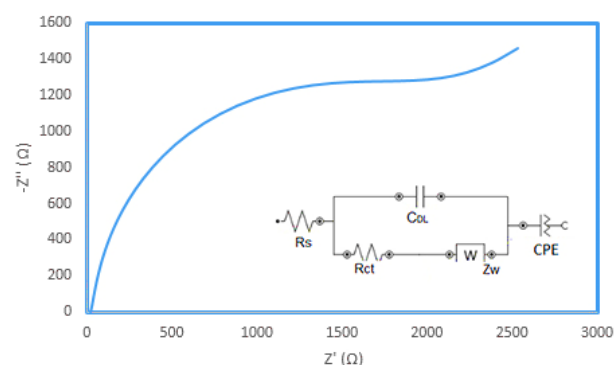The impedance parameters after curve fitting are given in Table 2.

Fig.4: Nyquist plot of $CaMnO_2$

Table2: Fitted data from electrochemical impedance spectroscopy

	Rs(Ω)	Rct(kΩ)	Zw	CPE	C(mF)
$CaMnO_2$	21.3	1.80	0.0064	0.0065	1.24

B. Equations

Specific capacity of the electrode material is calculated using Eq.1. [2]

$$C = \frac{i * t}{v * m} \qquad (1)$$

IV. CONCLUSION

By examining the electrochemical tests of synthesized material, the results indicate a capacity of 384 F/g, which

compared to previous reported works, this electrode material has an acceptable capacity, and in addition, a new and facial method has been used to synthesize this electrode material. [3] But after a cyclability test, it was concluded that, despite its proper capacity, this electrode material does not have a good stability, and after about 200 cycles it reaches to 80% of its initial capacity.

REFERENCES

[1] G. A. M. Ali, O. A. G. Wahba, A. M. Hassan, O. A. Fouad, and K. Feng, "Calcium-based nanosized mixed metal oxides for supercapacitor application," Ceram. Int., vol. 41, no. 6, pp. 8230–8234, **2015**.

[2] S. Alipour and S. M. Mousavi-khoshdel, "Investigation of the electrochemical behavior of functionalized graphene by nitrophenyl groups as a potential electrode for supercapacitors," Electrochim. Acta, **2019**.

[3] C. E. Frey and P. Kurz, "oxides – systematic variations of the calcium," pp. 4370–4379, **2014**.

Determination of the average ionic activity coefficient in aqueous solutions of electrolytic mixtures with a common ion: NaNO₃ + NH₄NO₃, NH₄Cl + LiCl and KBr + KCl

Maryam Abedi

Department of Chemical Engineering, Faculty of Imam Mohammad Bagher, sari branch, Technical and Vocational University (TVU), Mazandaran, Iran.

Email: m.abedi85@gmail.com

Abstract: Ion-Selective electrodes were used to measure the average activity coefficients of specific ions in aqueous solutions of electrolytic mixtures with a common ion for the systems NaNO₃ + NH₄NO₃, NH₄Cl + LiCl and KBr + KCl at a temperature of 298.15 K. These values were obtained by measuring the common ion electrodes potential against an Ag-AgCl single-junction reference electrode filled with 4 mol · kg-1 KCl solution saturated with AgCl. The Henderson equation was used to estimate the value of the liquid-junction potential.

Keywords: Activity of ions; Electrolyte solutions; Ion-selective electrodes; Mixed electrolytes; potentiometric method.

I. INTRODUCTION

The knowledge of the activity coefficients of individual ions is important for the design of equilibrium processes containing electrolyte solutions and in particular for processes involving ion-exchange. At very low molalities m_{ik} of an ion i in aqueous solution k, the Debye-Hückel's equation can be used to calculate single ion activity coefficients of ion i, $\gamma_{i,k}$. However, in many physiological processes and in seawater or salt lakes, the molality of electrolyte in solution is much higher than the range of applicability of the Debye-Hückel equation. In this work, ion selective electrodes are employed to measure the average ionic activity coefficients of ions in a mixture of two salts, different ions of the same charge usually interfere with the response of the electrodes. Thus, this first study of mixed salts, is restricted to the accurate measurement of the activity coefficients of the common ion of two salts, in aqueous solutions containing different counterions. The activity coefficients of the counterions can then be calculated using the mean ionic activity coefficients of both salts present in the solution. junction potential in the final values of ionic activity coefficients. In the potentiometric convention used in this work, we consider a cell of the type [1]:

Reference Electrode | Reference Solution (*r*) ‖ Sample Solution (*k*) | ISE (*i*)

II. METHODS

In this work, we have used the potentiometric method to measure the activity coefficients of single ions in a solution containing two strong electrolytes with a common ion. The electrode potential $E_{i,k}$ of an Ion-Selective electrode sensitive to ion i, measured against an Ag-AgCl reference electrode, immersed in the same solution of molality $m_{i,k}$, of ion i, is related to the ionic activity coefficient $\gamma_{i,k}$ by:

$$E_{i,k} = E_i^0 + S_i \ln(m_{i,k}\gamma_{i,k}) + E_{J,k}$$

The Henderson's equation was used to calculated the liquid junction potential.

III. RESULTS AND DISCUSSION

Average ionic activity coefficients of nitrate at different molalities of nitrate, for molal fractions of sodium at 1,0.75, 0.5, 0.25, and 0, in aqueous mixtures of NaNO₃ + NH₄NO₃, were calculated from potentials of a nitrate Ion-Selective electrode measured against a reference electrode following the method previously described. Similarly, the average ionic coefficients of activity in different molal fractions were calculated for NH₄Cl + LiCl and KBr + KCl solutions. The results and calculations are presented below.

A. Figures and Tables

In the following, an image of the device used to measure the experimental data and the calculated average ionic coefficient of activity is presented.
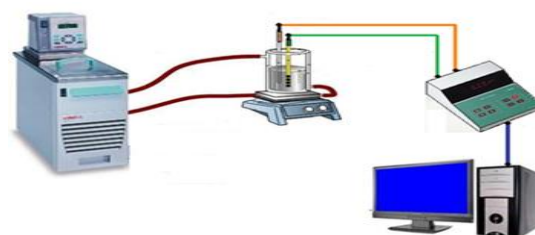
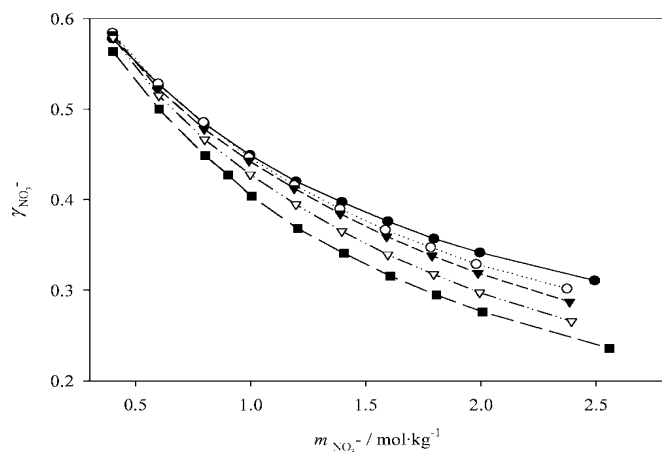

Fig.1: Potentiometric Methods Instrumentation

Fig.2: Variation of average ionic activity coefficients, γ, of nitrate in solutions of $NaNO_3 + NH_4NO_3$

Table1: Average Ionic Activity Coefficients, γ, of the Potassium Ion in Aqueous Mixtures of KBr + KCl

$m/\text{mol} \cdot \text{kg-1}$	γ_{K^+}
0.0020	0.935
0.0043	0.926
0.0059	0.915
0.0081	0.900
0.0120	0.863
0.0302	0.821
0.0705	0.765
0.1008	0.752
0.2014	0.741
0.4002	0.732
0.6001	0.727
0.8005	0.734
0.9892	0.747
1.202	0.759
1.356	0.779
1.542	0.791
1.892	0.835
2.651	0.881
2.911	0.952
3.889	1.116
σ^a	0.01

Table2: Average Ionic Activity Coefficients, γ, of the Chloride Ion in Aqueous Mixtures of $NH_4Cl + LiCl$

$m/\text{mol} \cdot \text{kg-1}$	γ_{Cl^-}
0.0039	0.929
0.0076	0.902
0.0119	0.879
0.016	0.871
0.1860	0.760
0.4736	0.706
0.9788	0.659
1.191	0.649
1.898	0.638
2.854	0.635
3.911	0.670
σ^a	0.005

Table3: Average Ionic Activity Coefficients, γ, of the Nitrate Ion in Aqueous Mixtures of $NaNO_3 + NH_4NO_3$

$m/\text{mol} \cdot \text{kg-1}$	γ_{NO3^-}
0.0019	0.936
0.0044	0.925
0.0059	0.911
0.0083	0.902
0.011	0.881
0.0410	0.861
0.0715	0.764
0.1009	0.762
0.2019	0.681
0.4010	0.562
0.6001	0.527
0.8010	0.464
0.9998	0.432
1.202	0.409
1.391	0.368
1.607	0.349
1.792	0.324
2.002	0.315
2.411	0.295
σ^a	0.017

B. Equations

For the system $NaNO_3 + NH_4NO_3$, average ionic activity coefficients of sodium and ammonium were calculated with

eq 1 using the average ionic activity coefficients, γ_i, calculated with the Harned and Robinson's equations [2]:

$$2\ln \gamma_{NH4NO3}/\gamma_{NH4NO3}° = [2(\varphi_{NaNO3}° - \varphi_{NH4NO3}°) + (am+bm^2)]Y_{NaNO3}+[-1/2bm^2]Y^2_{NaNO3} \quad (1)$$

The average ionic activity coefficients of KCl and KBr in aqueous solution of KCl + KBr were calculated using the Robinson's equations [3]:

$$\log \gamma_{KCl}=\log \gamma_{KCl}° - \alpha_{KCl}m_{KBr} - \beta_{KCl}m_{KBr}^2 \quad (2)$$

IV. CONCLUSION

Average Ionic Activity coefficients of the common ion in aqueous solutions of electrolytic mixtures of $NaNO_3$ + NH_4NO_3, NH_4Cl + LiCl and KBr + KCl at 298.15 K were studied for different molal fractions. The experimental results show that the average activity coefficient of an ion in the presence of different counterions depends on the concentration of all counterions present in the solution. The results also show that the average activity coefficients of the cations in an aqueous solution are different from those of the anions. These effects can be considered as a corollary of the ion-ion and ion-solvent interactions.

REFERENCES

[1] Wilczek-Vera, G.; Rodil, E.; Vera, J. H. On the activity of ions and the junction potential: Revised values for all data. *AIChE J. 50*, 445–462. **2004**.

[2] Harned, H. S.; Robinson, R. A. *Multicomponent Electrolyte Solutions*; Pergamon Press: Oxford, **1968**.

[3] Robinson, R. A. Activity Coefficients of Sodium Chloride and Potassium Chloride in Mixed Aqueous Solutions at 25 Degree. *J. Phys.Chem. 65*, 662–667.**1961**.

Wireless Photoelectrochemical Degradation of Methylene Blue Dye Using a NiCo₂O₄/Cu Photoelectrode

T. Khanahmadlou, M. Lashgari*

Department of Chemistry, Institute for Advanced Studies in Basic Sciences (IASBS), Zanjan 45137-66731, Iran
E-mail: Lashgari@iasbs.ac.ir

Abstract: Dumping of dye pollutants into the environment and its adverse/carcinogenic impact on living organisms is a serious concern for human societies that needs to be resolved by employing a promising sustainable route using a renewable clean energy source. Concerning this green strategy, herein, we demonstrate how using a Schottky junction photoelectrode [NCO/Cu; nickel cobaltite oxide deposited on a copper substrate], methylene blue (MB) [being normally employed as a model dye pollutant in the literature] could be effectively photo-degraded without needing to consume electricity, just by illumination of the setup [photoreactor]. The investigations showed that a significant degradation of dye can be achieved at short illumination periods, particularly in the presence of O_2, serving as an auxiliary traditional oxidizing agent. The photo-degradation phenomenon was discussed in detail from a physicochemical mechanistic perspective, based on the photogeneration of e/h pairs upon the semiconductor surface.

Keywords: methylene blue, non-wired reactors, photoelectrochemical dye degradation, Schottky-junction photoelectrode

I. INTRODUCTION

One of the promising methods to eliminate dye pollutants from aqueous environments is the application of semiconducting materials under illumination of the reactor setup [1]. To this end, the semiconductor compounds can be employed as powder or thin-film electrode [2, 3]. The first approach (photochemical) suffers from difficulty of the separation of the photocatalyst particles from the residual reaction medium, whereas the second one (photoelectrochemical) has successfully resolved this problem. Currently, the photoelectrochemical route which is employed for dye degradation becomes carried out in a two-electrodic [wired] system, by applying a faradic potential bias to the electrode and consuming electricity at the electrode/electrolyte interface [4]. In the present study, however, we introduce a new approach and demonstrate that without applying a potential bias, the photoelectrochemical degradation of dye pollutant could occur in a uni-electrodic [wireless] system/reactor, by introducing an effective thin-film semiconductor electrode fabricated previously in this laboratory [5].

II. METHODS

To carry out the dye photo-degradation tests, a homemade tubular glassy cell (containing 50 cc aqueous solution of 10 ppm methylene blue; pH=5) was employed. The photo-degradation process was performed upon the p-type Schottky junction photoelectrode–already fabricated in this laboratory [5], i.e. NiCo₂O₄ semiconductor thin-film electrodeposited cathodically on a Cu substrate (see Fig. 1, the inset). The photon source was a Xenon lamp with intensity output set at 1 Sun. The UV-Vis. investigations were conducted using a Pharmacia Biotech Ultrospec 3100 spectrophotometer.

III. RESULTS AND DISCUSSION

In this work, the light-induced degradation percent of the methylene blue dye was calculated using spectrophotometric data through "Eq. 1". The results are plotted in "Fig. 1". This figure shows that the presence of NCO/Cu photoelectrode in the reaction medium substantially increases the dye photo-degradation process, and clearly indicates the photo-electro-catalytic activity of the photodevice on acceleration of the process. Moreover, the presence of O_2 has an enhancing effect on improving the photo-degradation phenomenon; according to "Fig. 1", the maximum performance is achieved in the simultaneous presence of photoelectrode and O_2 molecules in the reaction medium. To justify these empirical observations, the following mechanism (Eq. 2-6) could be proposed [6-8]. Briefly, this mechanism is based on e_{CB}^-/h_{VB}^+ entities, being transiently generated under irradiation of the semiconductor (SC) electrode (Eq. 2). Since the photogenerated electron-hole pairs have a redox ability, they could be directly utilized for degradation of dye molecules (Eq. 3) or indirectly consumed (Eq. 4-5) for the generation of reactive oxygen species (ROS; known as oxidizing agent), which in turn eliminate the dye pollutant (Eq. 6).
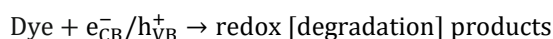
A. Equations

The performance of the photoelectrode to be employed for the degradation of dye pollutant was determined through this formula:
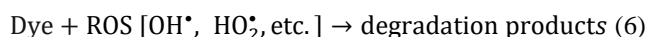
$$P\% = \frac{A_0 - A_t}{A_0} \times 100 \tag{1}$$

Where A_0 is the maximum absorbance recorded around 662 nm, before operation of the reactor (t=0) and A_t is the mentioned quantity measured at a given time under consideration (t).

$$SC + h\nu \rightarrow e_{CB}^- + h_{VB}^+ \qquad (2)$$

$$Dye + e_{CB}^-/h_{VB}^+ \rightarrow redox\ [degradation]\ products \qquad (3)$$

$$h_{VB}^+ + H_2O \rightarrow H^+ + OH^{\bullet} \qquad (4)$$

$$\begin{cases} e_{CB}^- + O_2 \rightarrow O_2^{-\bullet} \\ O_2^{-\bullet} + H^+ \rightarrow HO_2^{\bullet} \end{cases} \qquad (5)$$

$$Dye + ROS\ [OH^{\bullet},\ HO_2^{\bullet}, etc.\,] \rightarrow degradation\ products \qquad (6)$$
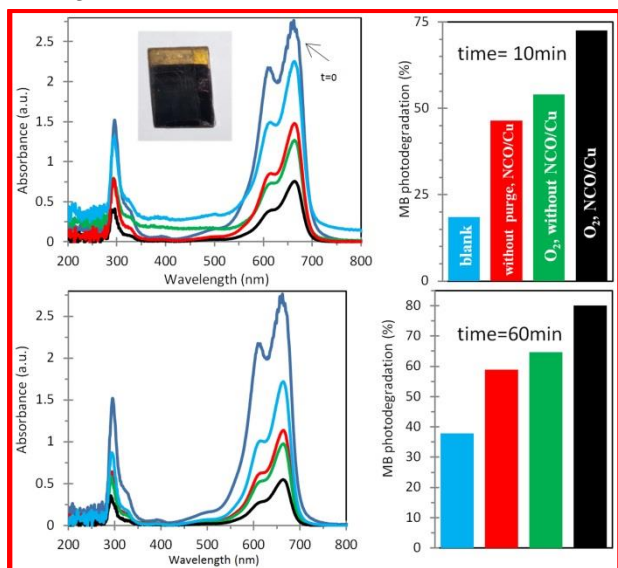
B. Figure

Fig. 1: UV-Vis spectra of methylene blue (MB) aqueous solution (10 ppm) and its photoelectrochemical degradation (percent) upon NCO/Cu device/reactor obtained after 10 and 60 min reaction under different conditions (blue, red, green and black colors indicate the degradation of MB in the absence of electrode without any purge, in the presence of electrode without purge, O_2 presence but in the absence of electrode, and in the presence of oxygen and electrode, respectively).

IV. CONCLUSION

Based on the present study, we can conclude that:

❖ The non-wired photoelectrochemical system, i.e. $NiCo_2O_4/Cu$ photoelectrode is capable to be employed as an effective device (reactor) for photoelectrochemical elimination of methylene blue dye from aqueous solutions.

❖ The presence of O_2 in the reaction medium exhibits a synergistic influence, boosting the degradation process.

❖ The present approach could be employed to other pollutants and photoelectrochemical systems.

REFERENCES

[1] A. Ajmal, I. Majeed, R.N. Malik, H. Idriss, and M.A. Nadeem, RSC Advances, vol. 4, pp. 37003-37026, **2014**.

[2] Y.H. Chen, and K.j. Tu, International Journal of Photoenergy, vol. 2012, pp. 1-6, **2012**.

[3] L. Andronic, and A. Duta, Thin Solid Films, vol. 515, pp. 6294-6297, **2007**.

[4] R. Mei, Q. Wei, C. Zhu, W. Ye, B. Zhou, L. Ma, Z. Yu, and K. Zhou, Applied Catalysis B: Environmental, vol. 245, pp. 420-427, **2019**.

[5] T. Khanahmadlou, and M. Lashgari, 14th Annual Electrochemistry Seminar of Iran, Karaj: Materials and Energy Research Center (MERC), **12-13 Dec. 2018**.

[6] A. Kumar, and G. Pandey, Materials Science & Engineering International Journal, vol. 1, pp. 106-114, **2017**.

[7] M. Lashgari, and M. Ghanimati, International Journal of Energy Research, vol. 39, pp. 516-523, **2015**.

[8] M. Lashgari, and H. Diarmand-Khalilabad, Journal of Electroanalytical Chemistry, vol. 783, pp. 125-131, **2016**.

Wettability of Electrochemically Activated Carbon Cloth

S. Yousefzadeh[a], N. Morovati[a*]

Department of Physics, Faculty of Science, Sahand University of Technology, Tabriz, P.O. Box 51335-1996, Iran
Email:Yousefzadeh@sut.ac.ir

Abstract: Carbon cloths are widely used as conductive, flexible, portable and low-cost substrate in electrochemical applications. In this work, we have reported a one-step electrochemical activation method to improve wettability properties and electrochemical activity of the commercial hydrophobic Carbon cloth (CC). Electrochemically activated carbon cloth (ACC) was readily obtained by simply oxidizing CC in a mixed acid solution under a potential of 3 V for 300 seconds (ACC). Wettability of the ACC was investigated by contact angle method and the results were compared with the CC. This technique is suitable to produce a large scale of the activated carbon cloth.

Keywords: Carbon cloth, Electrochemical Activation, Wettability, Contact Angle

I. INTRODUCTION

Carbon is one of earth abundant elements in world and in recent years, carbon based materials have been widely used in many applied fields due to their unique physical and chemical properties. Carbon cloth as a carbon based material is a stable, conductive, flexible and relative low cost substrate or support in electrochemical applications such as supercapacitors and lithium ion batteries [1]. To enhance hydrophilicity and electrochemical activity, carbon cloth can be treated by physical and chemical technique such as annealing and electrochemical activation [1,2]. Among them, electrochemical activation is simple and rapid method. In this report, we have activated the carbon cloth by oxidation in acidic media. Then, the hydrophilicity and electrochemical activity of the activated carbon cloth was investigated.

II. METHODS

All chemicals were of analytical grade and were directly used without any purification.

The ACCs were obtained by an electrochemical activation method. First, a piece of carbon cloth was cleaned by sonication in water, alcohol and acetone. The electrochemical activation was carried out in a three electrode cell containing Pt as counter electrode, Ag/AgCl electrode as reference electrode and carbon cloth as working electrode and these electrodes were immersed in a mixed acid of HNO_3 and H_2SO_4 with same volume (v:v1:1). Using chronoamperometry technique and under a constant voltage of 3 V for time of 300 sec, carbon cloth was activated. After activation, the obtained ACC was washed with water.

Wettability of the ACC and CC was also investigated by contact angle measurements by dispensing a water droplet on the surface using a syringe.

III. RESULTS AND DISCUSSION

Fig. 1(a,b) shows surface morphologies of the CC in two different scales. Based on scanning electron microscopy (SEM) images, the CC is a textile of carbon fiber with diameter of ~10 µm. By electrochemical activation, the rough surface was obtained for carbon cloth and indicate the modification of the carbon fiber (Fig. 1(c)).
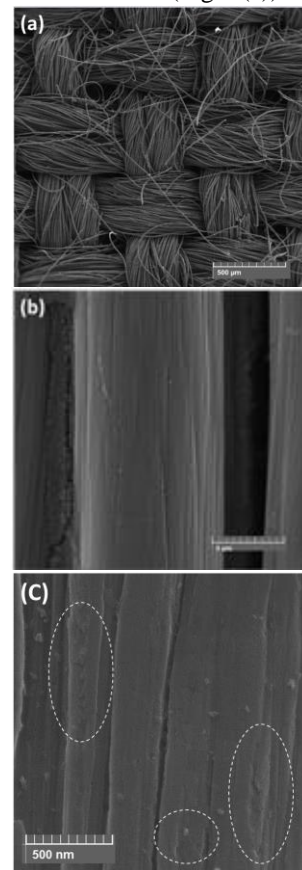

Fig.1: SEM image of (a,b) the CC and (c) the AC.

Pristine CC surface exhibits a hydrophobic property (Fig.2 (a)). The contact angle for this sample was obtained at about 131°. By electrochemical activation, the contact angle of 75° was measured for the ACC sample. Oxidation of CC in acidic medium was introduced hydrophile oxygen functional groups on the CC surface. Electrochemical activity of the CC and AC samples was investigated by linear sweep voltammetry (LSV) measurement that utilized at scan rate of 5 mV/s via three-electrode cell with an Ag/AgCl, a Pt plate and the CC and ACC as the reference, counter and working electrode, respectively. All the electrodes were put into 0.5 M H_2SO_4 electrolyte. The LSV curves for the CC and ACC samples have been illustrated in Fig. 3. It is obvious that the onset overpotential of the ACC electrode is clearly lower than that of CC. Therefore, electrochemical activity can be improved after electrochemical activation and the electrochemical activation method is recommended as a facile, rapid and large output technique for activation of carbon cloth surface in hydrogen evolution reaction.

IV. CONCLUSION

A facile and rapid electrochemical activation method was used to activated. By oxidation of the CC in presence of acids, the ACC with improved wettability was obtained, due to increase of the oxygen functional groups.

REFERENCES

[1] Y. J. Gu, W. Wen, and J. M. Wu, Journal of Materials Chemistry A, vol. 6, pp. 21078-21086, **2018**.
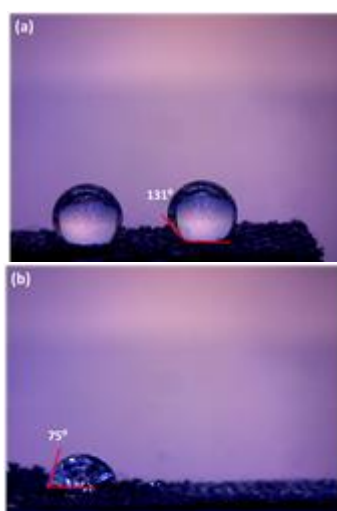[2] W. Wang, W. Liu, Y. Zeng, Y. Han, M. Yu, X. Lu, and Y. Tong, Advanced Materials, vol. 27, pp. 3572–3578, **2015**.

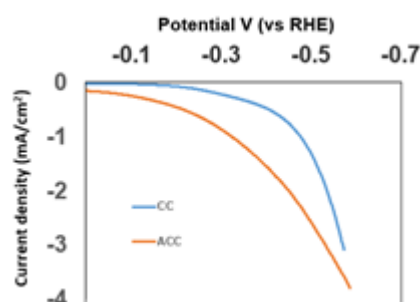Fig.2: Water contact angle of the (a) CC and (b) ACC.

Fig.3: LSV curves of the CC and ACC samples

Experimental and Theoretical Analysis of the Electrochemical Oxidation of 3,4-Dihydroxy-Cinnamic Acid in the Presence of 2-Mercaptobenzimidazole

A. Amani*, F. Yaghoobi

Department of Chemistry, University of Nahavand, Nahavand, Iran.
E-mail address: amani.iran@gmail.com

Abstract*:* Electrochemical oxidation of 3,4-Dihydroxy-Cinnamic Acid (**1**) in the presence of 2-mercaptobenzimidazole (**3**) has been studied by cyclic voltammetry and controlled-potential electrolysis techniques. The results show that 3,4-Dihydroxy-Cinnamic Acid was oxidized to the corresponding *o*-benzoquinone. The formed adduct convert to the corresponding benzo thiazepine derivative *via ECC* mechanism. Furthermore, density functional theory (DFT) study has been used to investigate the enthalpy change (ΔH) of the reaction of species studied here, in the gas phase at the BP86/6-311+G** level of theory.

Keywords: Electrochemical oxidation, Density functional theory (DFT), Caffeic acid, 2-mercaptobenzimidazole, Benzo thiazepines.

I. INTRODUCTION

Electrochemistry techniques provide powerful tools for the study of reaction mechanisms involving electron transfer and afford complementary information. The first technique allows the characterization of the intermediates formed upon electron transfer by their reduction-oxidation pattern [1]. 3,4-Dihydroxy-Cinnamic Acid (**1**) and its naturally occurring derivatives are the main representatives of the hydroxycinnamic and phenolic acids and widely distributed in plants, vegetables, and propolis as simple derivatives such as esters, amides, glycosides, and sugar esters [2]. on the other hand Benzothiazepines have attracted as an important class of heterocyclic compounds in the field of drug and pharmaceutical research. Benzothiazepines are seven member heterocyclic compounds now a day they have received considerable attention and claimed various therapeutic activities and hence, they utilized in drug research [3]. Herein, we report on a facile electrochemical approach for the synthesis of a new benzothiazepines derivative with the electrochemical oxidation of 3,4-

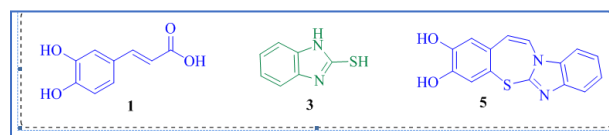Dihydroxy-Cinnamic Acid in the presence of 2-mercaptobenzimidazole.

Figure 1. The structures of 3,4-Dihydroxy-cinnamic acid (**1**), 2-Mercaptobenzimidazole (**3**) and synthesized compound (**5**).

On the other hand in order to confirm the synthesis of **6** as the major product, density functional theory (DFT) study has been used and the enthalpy change (ΔH) of the reaction of species studied here, in the gas phase at the BP86/6-311+G** level of theory obtained.

II. METHODS

Electro-Organic Synthesis of 6:
In a typical procedure, 60 ml of phosphate buffer solution (0.2 M, pH=5.5) in water/acetonitrile (80/20) was pre-electrolyzed at 0.45 V *versus* Ag/AgCl, then 0.20 mmol of **1** and 0.20 mmol of **3** were added to the cell. The electrolysis was terminated when the current decayed to 5% of its original value. At the end of the electrolysis the cell was placed in refrigerator overnight. The precipitated white solid was collected by filtration and washed several times with water. After washing, product was characterized by IR, and MS. All of apparatus and reagents has been described in an earlier paper [4].

Theoretical study:
The Gaussian 09 package [5] was used to perform all of the calculations reported in this work. All structures optimized at the BP86/6-311+G** level of theory. Also, the vibrational frequency analysis calculated at the same level.

III. RESULTS AND DISCUSSION

Cyclic voltammogram of 3,4-Dihydroxy-Cinnamic Acid (**1**) in water (phosphate buffer, $c = 0.2$ M, pH = 2.0)/acetonitrile mixture (80/20 v/v) is shown in Fig. 2 curve a.
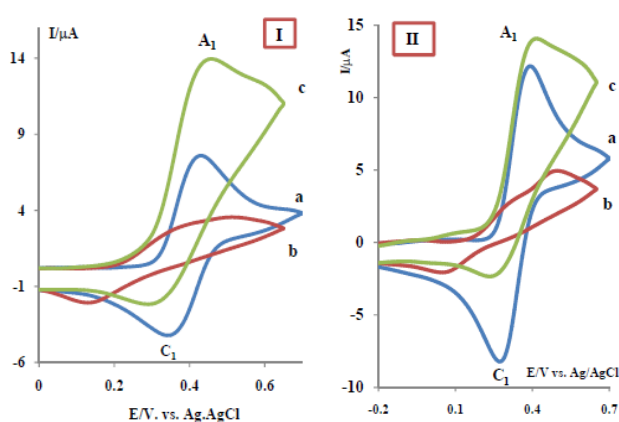

Fig. 2: Cyclic voltammograms of (a) 1.0 mM 3,4-Dihydroxy-cinnamic acid (**1**), (b) 1.0 mM 1 in the presence of 2-Mercaptobenzimidazole (**3**) (c) 1.0 mM **3** in the absence of **1**. (I) in water (phosphate buffer, $c = 0.2$ M, pH = 3.0)/acetonitrile (80/20) solution. (II) in water (phosphate buffer, $c = 0.2$ M, pH = 5.0)/acetonitrile (80/20) solution. Scan rate 100 mV s^{-1}. $t = 25 \pm 1$ ℃.

As can be seen, one anodic (A_1) and cathodic peaks C_1 were obtained. Anodic and cathodic peaks A_1 and C_1 are counterpart and are correspond to the transformation of **1** to *0*-quinone **2** (Scheme 1) and *vice versa* within a quasi-reversible two-electron process.[15] The peak current ratio (I_p^{C1}/I_p^{A1}) is related to pH and scan rate. It increases with decreasing pH and increasing scan rate. The cathodic peak C_1 disappears in basic solutions and/or in low potential sweep rates.[15] The oxidation of **1** in the presence of 2-mercaptobenzimidazole (**3**) as a nucleophile was studied in some detail. Figure 2 curve b, shows the cyclic voltammogram obtained for **1** in the presence of **3**. Comparison of this voltammogram with cyclic voltammogram of **1** in the absence of **2** shows that; a) the cathodic peak C_1 decreased intensively and b) The anodic peak A_1 increased slightly In this Figure, curve c is related to irreversible oxidation of **2.**
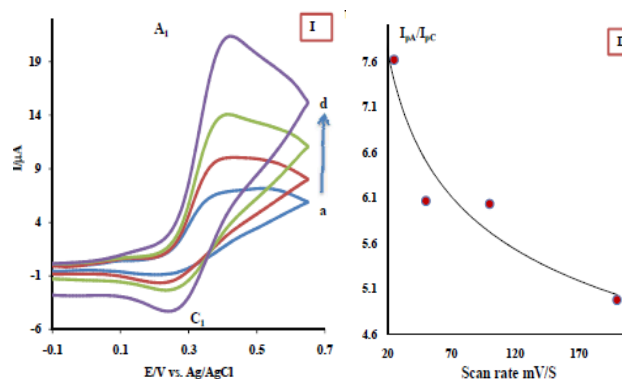
Figure 3. (I) Cyclic voltammograms of **1** (1.0 mM) in the presence of 1.0 mM **3** at various scan rates. Scan rates from a to d are: 25, 50, 100, and 200 mV s^{-1}, respectively. Other conditions are the same as Figure 2, II. (**II**): variation of peak current ratio (I_p^{A1}/I_p^{C1}) versus scan rate.

More studies were performed by varying the potential scan rate in a solution of **1** in the presence of **3** (Figure 3). The results indicate that the peak current ratio (I_p^{C1}/I_p^{A1}) is dependent on the potential scan rate and decreases with increasing it (Figure 3, curve i). The same result was obtained by decreasing the concentration of **3**. The decrease of the peak C_1 and C_2 current in electrochemical oxidation of **1** in the presence of **3** is due to the participation of produced *p*-quinone imine (**2**) in the following chemical reaction. Controlled-potential coulometry was performed in a cell containing 0.25 mmol of **1** and 0.250 mmol of **3** at in water (phosphate buffer, $c = 0.2$ M, pH = 5.0)/acetonitrile (80/20) solution. Cyclic voltammetric analysis was carried out during the coulometry. It is shown that, proportional to the advancement of coulometry, the anodic peak A_1 decreases. This peak disappears when the charge consumption becomes 2e$^-$ per molecule of **1**.

Computational studies:

In order to identify which species is a major product, we have determined the enthalpy change (ΔH) for this reaction. Also, the enthalpy of each of species was obtained using G09 set of programs. Therefore, the structure of all species were optimized at the BP86/6-311+G** level of theory. For the reaction to yield the intermediate **5**, the value of ΔH is negative (-10.04 kcal/mol) that suggests this reaction is energetically favorable. Subsequently, in the next step, for the reaction that produces the major product (**6**), the value of

ΔH is -313.32 kcal/mol. This value reveals that intramolecular cyclization for the formation of the major product energetically is favorable and exothermic.
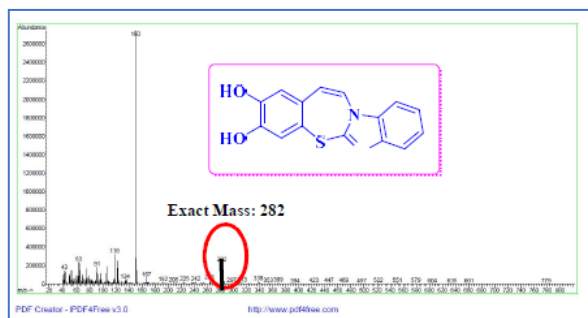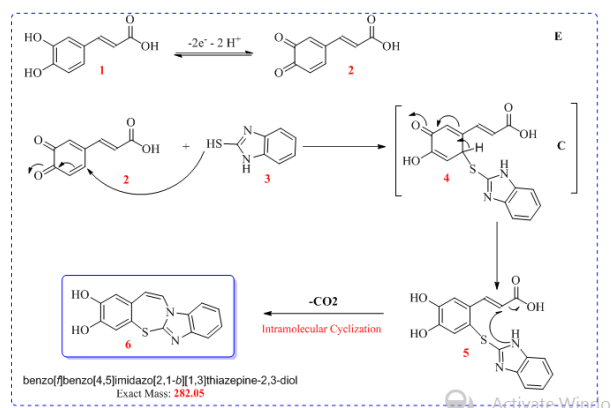

Fig.4

These coulometry and voltammetry results accompanied by the spectroscopic data (Mss, IR) of final product obtained from exhaustive oxidation of **1** in the presence of **2** (Exact Mass 282 for final product, Fig.4) and theoretical analysis allow us to propose the following mechanism for the electrooxidation of **1** in the presence of **3** (Scheme 1).

Scheme 1.

IV. CONCLUSION

In this work we report on a facile electrochemical approach for the synthesis of a new benzothiazepines derivative with the electrochemical oxidation of 3,4-dihydroxy-cinnamic acid in the presence of 2-mercaptobenzimidazole. Also, in order to confirm the synthesis of **6** as the stable product, the calculation of enthalpy change (ΔH) performed and the enthalpy of **5** and **6**

was obtained by DFT calculation, using G09 set of programs. Our results reveals that intramolecular cyclization for the formation of the major product **6**, energetically is favorable and exothermic.

REFERENCES

[1] A.J. Bard and R.L. Fanlkner, Electrochemical Methods, Wiley, New York, **1980**.

[2] M. Touaibia, J. Jean-François and J. Doiron, Mini-Reviews in Medicinal Chemistry, 11, 695-713, **2011**.

[3] T Nagao, S Sato, H Nakajima, A Kiyomoto, Japan J. Pharmacol, 22, 1, **1972.**

[4] A. Amani, D. Nematollahi, J. Iran**.** Chem. Soc., 15, 2669-2674, **2018**.

[5] M. J. Frisch, G. W.Trucks, H. B. Schlegel, G. E. Scuseria, M. A. Robb, J. R. Cheeseman, G. Scalmani, V. Barone, B. Mennucci,G. A. Petersson, et al. Gaussian 09, Revision D.01; Gaussian, Inc.:Wallingford, CT, **2009**.

Direct electron transfers improvement of immobilized tyrosinase using the modified MWCNT-Sp on glassy carbon electrode

Narges Sabbagh Ziarani [a], Hassan Faridnouri [a]*

[a] School of Biology, Damghan University, Damghan 36715-364, Iran.

n.sabbagh@yahoo.com, **Email:* faridnouri@du.ac.ir

Abstract: In this research, tyrosinase (Tyr) was immobilized on the modified multi walled carbon nanotube (MWCNT) by spermine (Sp) on glassy carbon electrode (GCE) and its direct electron transfer rate (DET) was studied using cyclic voltammetry (CV). A pair of well-defined quasi-revesible voltammetric peaks were observed which corresponding to the Cu (II)/ Cu (I) redox couple located in the active site of Tyr. The formal potential of immobilized enzyme was measured to be -51 mV (vs. Ag/AgCl) in phosphate buffer solution at pH 7.0. The apparent heterogeneous electron transfer rate constant and charge-transfer coefficient were estimated to be 1.98 s^{-1} and 0.5, respectively. The surface coverage of Tyr on the surface of the modified electrode was calculated to be 4.32×10^{-10} mol/cm^2.

Keywords: Tyrosinase, Spermine, direct electron transfer, MWCNTs, cyclic voltammetry

I. INTRODUCTION

In recent decades, investigation of direct electron transfer (DET) in proteins has been of great importance through electrochemical techniques. In general, inter-protein ET involves complementary docking sites on each of the redox partners that minimizes the distance between the two redox centers and therefore enhances the ET rate [1]. Since the redox center in proteins is usually located in the interior parts, its distance is far from the electrode surface and resulting in a harder ET. Therefore, any method that leads to an optimum protein immobilization at the electrode surface with a more suitable orientation can lead to acceleration of ET. Therefore, the use of materials such as carbon nanotubes and conductive polymers has improved the quality of new generation biosensors, thereby not only the generated catalytic current can be measured but also the detection of enzyme ET rate becomes facilitate. One of the attractive features of enzyme DET is the possibility of biosensor design using novel

interfacial technologies [2]. The immobilization of Tyr is essential for construction of biosensors to measure phenolic derivatives, especially biological compounds such as Dopa, which is important for identifying certain diseases, such as Alzheimer's. The biocompatible nanomaterials could retain the activity of enzyme well due to the suitable microenvironment, and enhance the DET between the enzyme's active sites and the electrode, so these materials have their unique advantages in enzyme immobilization [3,4]. In this study Tyr was immobilized on the modified carboxylic MWCNT by Sp on the GC electrode and its direct electron transfer rate was investigated using CV method.

II. MATERIALS AND METHODS

The experiments were achieved by using a potentiostat/galvanostat (Radstat 10, Daneshyar Kavosh, Iran) and the PSTrace 4 software was applied for voltammetric analysis. A three-electrode system was employed with a platinum wire as the counter electrode an Ag/AgCl (3M KCl) as the reference electrode, and the modified glassy carbon electrode (GCE) as the working electrode. Prior to modification, GCE was polished with 0.5 μm alumina suspension and then on a filter paper, then Thereafter, it was rinsed with deionized water and sonicated with a Tecno-Gaz ultrasonic cleaner (Italy) in a beaker containing deionized water for 2 min. At first, 10 μl of the dispersion containing MWCNT-COOH-Sp in PBS (0.1M. pH=7.0) was dropped onto the cleaned GCE and was allowed to dry under ambient conditions for 1 h and then, 10 μl of 5mg/ml Tyr solution in 0.1M PBS at pH=7.0 was dropped on modified electrode and allowed to dry under room temperature. The electrode (Tyr/MWCNT-COOH-Sp/GCE) was again rinsed with distilled water, dried and kept in the refrigerator.

III. RESULTS AND DISCUSSION

As can be seen in Fig. 1, there is a pair of well-defined redox peaks for the quasi-reversible DET behavior of immobilized Tyr at various scan rates corresponding to the CU (II)/Cu (I) redox couple located in the active site of Tyr. The cathode and anodic peaks appeared at -0.128 and 0.025 volts, respectively, and the formal-potential value (E°´) was -51 mV compared to the reference electrode. The ratio of the cathode current to the anodic (I_{pc}/Ipa) is also equivalent to one and the peak potential difference is 153 mV. This value shows a decrease of 141 mV compared with our previous work [5], indicating that the presence of carbon nanotubes has increased the reversibility and improved ET rate. The peak-to-peak separation is attributed to this fact that Tyr molecules are probably immobilized in one orientation [6, 7]. As can be seen, there is a linear relationship between the intensity of cathodic and anodic currents with scan rate which is expected from an immobilized enzyme. According to the Laviron theory [8], using the slope of the cathodic current vs. scan rate in Fig. 2 and replacing it in Eq. 1, the amount of surface coating resulting from the immobilization of Tyr on the GCE can be calculated.

$$Ip = \frac{vn^2F^2A\Gamma}{4RT} \tag{1}$$

where Ip is the value of peak reduction, Γ is the electroactive Tyr amount (mol/cm^2), n is the number of electrons transferred, F is the Faraday constant (96,485 C/ mol), A is the surface area of the electrode (cm^2), v is the scan rate (mV/s), R is the gas constant (8.314 J/mol K), and T is the Kelvin temperature (K). Assuming a single electron reaction, the surface coverage of Tyr on the surface of the modified electrode was calculated to be 4.32×10^{-10} mol/cm^2 which is 12.5 times greater than our previous immobilization method [5]. This indicates that carboxylic carbon nanotubes provided much more surface for Tyr immobilization.

The ET kinetic of Tyr was obtained by using the Laviron model [8] from the relationship between redox peak potentials and scan rate. The kinetic parameters of α and heterogeneous transfer rate constant (k_s) are estimated according to the Eq. 2.

$$\log k_s = \alpha \log (1 - \alpha) + (1 - \alpha) \log \alpha$$
$$- \log \frac{RT}{nF\vartheta} - \frac{\alpha (1 - \alpha) nF\Delta E_p}{2.3RT} \tag{2}$$

The ET rate constant (k_s) was obtained 1.98 s^{-1} (for nΔEp≥0.2 V) by using the data for 100 mV/s from Fig. 2. From the k_s value, it can be concluded that in this study, immobilization

Electrochemistry | 33

of Tyr by MWCNT- COOH-Sp, enhanced the rate of ET in comparison to previous work [5].

Furthermore, the slope of log Ipc vs. log ν (Fig. 3) was obtained to be 1.12, which confirms that a thin layer of Tyr molecules is formed at the electrode surface.
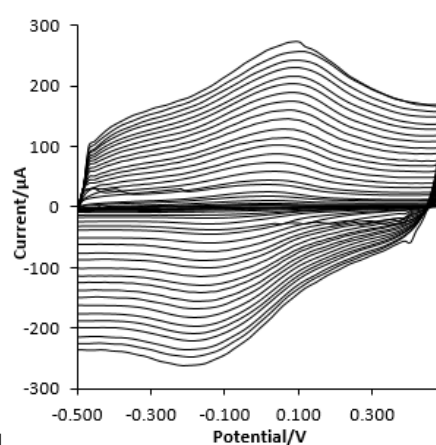

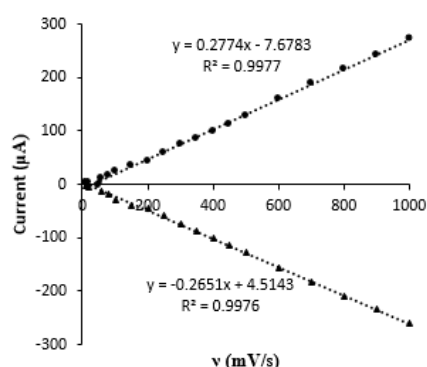Fig.1: Cyclic voltammograms of MWCNT-COOH-Sp/Tyr/GCE at different scan rates in PBS pH=7.0.

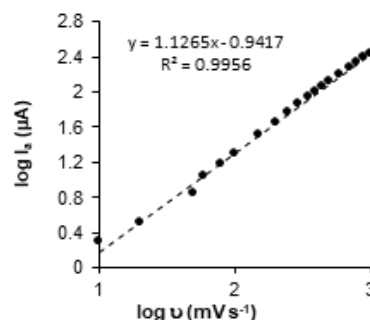Fig 2: plot of the peak current against the scan rate.

Fig.3: log Ipc vs. log ν.

III. CONCLUSION

In summary, electrostatic bonding between the amine groups of Sp and caboxylic groups of amino acids of Tyr cause to stable immobilization of Tyr. Carboxylic carbon nanotubes with spermine has provided a good microenvironment for Tyr immobilization, which has led to an increase in the stability and acceleration of ET. The surface coverage of Tyr on the surface of the modified electrode and The electron transfer rate constant of the biosensor were improved in Compared with the previous immobilization method.

REFERENCES

[1] S. Shleev, J. Tkac, A. Christenson, T. Ruzgas, A.I. Yaropolov, J.W. Whittaker, L. Gorton, Direct electron transfer between copper-containing proteins and electrodes, Biosens. Bioelectron. 20 (2005) 2517–2554.

[2] S. Campuzano, B. Serra, M. Pedrero, F. Javier Manuel de Villena, J.M. Pingarro´ n, Amperometric flow-injection determination of phenolic compounds at self-assembled monolayer-based tyrosinase biosensors, Anal. Chim. Acta 494 (2003) 187–197.

[3] A. Boujakhrout, P. Diez, A. Sanchez, P. Martinez-Ruiz, J.M. Pingarron, R. Villalonga, Gold nanoparticles-decorated silver-bipyridine nanobelts for the construction of mediatorless hydrogen peroxide biosensor, J. Colloid Interface Sci. 482 (2016) 105–111.

[4] Y. Liu, N. Song, Z.Ma, K. Zhou, Z. Gan, Y. Gao, S. Tang, C. Chen, Synthesis of a poly (Nmethylthionine)/ reduced graphene oxide nanocomposite for the detection of hydroquinone, Mater. Chem. Phys. 223 (2019) 548–556.

[5] H. Faridnouri, H. Ghourchian, H. Hashemnia, Direct electron transfer enhancement of covalently bound tyrosinase to glassy carbon via Woodward's reagent K, Bioelectrochemistry, 82 (2011), 1-9.

[6] S. Hashemnia, H. Ghourchian, A.A. Moosavi-Movahedi, H. Faridnouri, Direct electrochemistry of chemically modified catalase immobilized on an oxidatively activated glassy carbon electrode, Journal of Applied Electrochemistry 39 (2009) 7–14.

[7] J. Li, S. Dong, The electrochemical study of oxidation-reduction properties of horseradish peroxidase, J. Electroanal. Chem. 431 (1997) 19–22.

[8] E. Laviron, The use of linear potential sweep voltammetry and of ac voltammetry for the study of the surface electrochemical reaction of strongly adsorbed systems and of redox modified electrodes, J. Electroanal. Chem. Interfacial Electrochem. 100 (1979) 263–270.

Application of Electroless nickel plating on AM60B magnesium alloy via Ti-Zr/sol-gel composite layer as a pretreatment

J. Nazari, D. Seifzadeh*

Department of chemistry, Mohaghegh Ardabili university, Ardabil, Postal code:5619911367, Iran
Email: zhalenazari66@gmail.com

Abstract*:* In order to improve the corrosion resistance of magnesium alloy, Ni-P coating was prepared on the surface of AM60B magnesium alloy by chemical deposition method. In this experiment, morphology, composition and corrosion behaviour of the coatings were investigated by Scanning Electron Microscopy (SEM), Energy Dispersive x-ray Spectroscopy (EDS) and electrochemical impedance spectroscopy (EIS), respectively. The The results showed that Ni-P coatings provide sufficient protection against the corrosion.

Keywords: Sol–gel; Magnesium alloy; Corrosion; Electroless deposition

I. INTRODUCTION

Magnesium alloy has the advantages of high strength, excellent shock absorption performance, good electromagnetic compatibility and recyclability, but its poor corrosion resistance limits its application [1-3]. Electroless Ni-P plating has considered as an effective approach to overcome this problem and improve the corrosion resistance of the magnesium alloys. Traditionally, chromium conversion coating was used as a pretreatment layer but its usage was limited due to the toxicity of the chromium compounds [4, 5]. Other conversion coatings are frequently used as an alternative to chromate conversion coating. The sol-gel coating is another coating which attracted a lot of attention due to its environmentally-friendly nature and good corrosion protection properties [6-8]. The sol-gel process is a chemical synthesis method for preparation of an oxide network by consecutive hydrolysis and condensation of alkoxide precursors. Recently, composite conversion coating/sol-gel layer was used as a corrosion protective coating on magnesium alloys. In this study, electroless Ni-P plating was done on AM60B magnesium alloy via Ti-Zr/sol-gel composite layer as pretreatment. This coating was characterized for its morphology and corrosion protection.

II. METHODS

After abrading and cleaning the substrate surface in acetone (ultrasonically for 15min at 45°C), the sample was immersed

in conversion bath containing 0.5 g/L H_2TiF_6, 1.5 g/L H_2ZrF_6 with pH value of about 2.5 (adjusted by adding NaOH

solution dropwisely). Then, the sample was kept in the solution for 10 min at room temperature. Afterwards, the sol-gel solution was prepared by mixing 0.04 mol TEOS (tetraethylorthosilicate), 0.02 mol GPTMS (γ-glycidyloxypropyltrimethoxysilane) and 1.23 mol acidic water (hydrochloric acid with pH~1.5). The primarily treated samples were then immersed in the sol-gel solution for 5 min using the dip-coater instrument. Then, the samples were withdrawn from the solution with a constant speed of 50 mm/min. The samples were kept at 60 °C for about 2 h in a digital furnace to slow evaporation of the residual water. After that, the samples were subjected to the heat treatment at 130 °C for about 1 h. Surface roughing was carried out by immersion of the samples in a 200 g/L NaOH aqueous solution at 50 C for 15 min. Then, the sample was sensitized in solution containing 20 ml/l HCl and 10 g/l $SnCl_2$ at 30 °C for 8 min. Finally the samples were immersed in plating bath containing $NiSO_4.6H_2O$ (15 g/L), $NaC_2H_3O_2$ (13 g/L), $Na_2H_2PO_2.H_2O$ (14 g/L), HF (12 ml/L), NH_4HF_2 (8 g/L), Thiourea (1ppm), and NH_3 (pH adjusting to 6.4) for 3h at 65 °C.

III. RESULTS AND DISCUSSION

The SEM image (Fig.1) displays that surface of the substrate was covered by the smooth and pore-free Ni-P coating entirely. Furthermore, the grain-boundaries are so compact and inter-granular spacing was not exists between the nodules. The overall reactions of the electroless Ni-P deposition can be expressed as follows [9]:

$$Ni^{2+} + 4H_2PO_2^- + H_2O \rightarrow Ni + 3H_2PO_3^- + P + H^+ + \frac{3}{2}H_2 \quad (1)$$
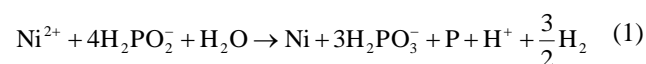
The small amount of the copper sulfate was added to the plating bath to increase the plating rate and so, co-deposition of copper is also possible according to the following reaction:

$$Cu^{2+} + 2H_2PO_2^- + H_2O \rightarrow Cu + 2H_2PO_3^- + 2H^+ + H_2 \quad (2)$$
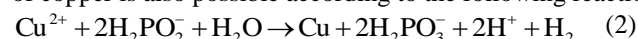
The EDS analysis indicated that the coating consists of Ni, P, and Cu with the averaged amount of 90.88, 8.63, and 0.49 wt.

%, respectively. Based on the P content, this coating has a mixture of amorphous and microcrystalline structure.
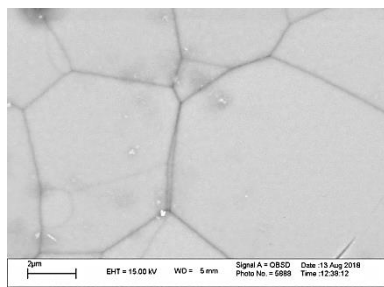

Fig.1

The corrosion protection performance of the Ni-P coating was investigated by EIS test after 30 min exposure in 3.5 wt.%. NaCl solution. The results show that the corrosion resistance of the bare alloy was increased from 1.5 kΩ to about 30 kΩ after applying the Ni-P coating on the sol-gel/Ti-Zr pretreatment layer. This increasing in the corrosion protection performance of the coating indicates that the applied coating is effectively protected the bare alloy from corrosion significantly.

IV. CONCLUSION

1. The alloy surface was completely covered by the compact, pore-free, and smooth Ni-P coating with the fine nodular structure after 3 h electroless plating.
2. The EDS analysis showed that the Ni-P coating has a moderate P content with mixed crystalline-amorphous structure.
3. The EIS results were also indicated that the Ni-P coated sample has much better corrosion resistance than the bare alloy.

The results indicate that the Ni-P coating on Sol−gel can provide good corrosion protection for AM60B magnesium alloy.

REFERENCES

[1] Y. Mao, Z. Li, K. Feng, X. Guo, Z. Zhou, J. Dong, Y. Wu, Preparation, characterization and wear behavior of carbon coated magnesium alloy with electroless plating nickel interlayer, Appl. Surf. Sci. 327 (2015) 100–106.

[2] S. Sadreddini, Z. Salehi, H. Rassaie, Characterization of Ni-P-SiO$_2$nano-composite coating on magnesium, Appl. Surf. Sci. 324 (2015) 393–398.

[3] X.J. Cui, M.T. Li, R.S. Yang, Z.X. Yu, Structure and properties of a duplex coating combining micro-arc oxidation and baking layer on AZ91D Mg alloy, Appl. Surf. Sci. 363 (2016) 91–100.

[4] L. Anicai, R. Masi, M. Santamaria, F. Di Quarto, A photoelectrochemical investigation of conversion coatings on Mg substrates, Corros. Sci. 47 (2005) 2883-2900.

[5] A. Yi, J. Du, J. Wang, S. Mu, G. Zhang, W. Li, Preparation and characterization of colored Ti/Zr conversion coating on AZ91D magnesium alloy, Surf. Coat. Technol. 276 (2015) 239–247.

[6] E. Rocca, C. Juers, J. Steinmetz, Corrosion behaviour of chemical conversion treatments on as-cast Mg-Al alloys: electrochemical and non-electrochemical methods, Corros. Sci. 52 (2010) 2172–2178.

[7] X. Jiang, R. Guo, S. Jiang, Microstructure and corrosion resistance of Ce-Vconversion coating on AZ31 magnesium alloy, Appl. Surf. Sci. 341 (2015)166–174.

[8] L. Lei, J. Shi, X. Wang, D. Liu, H. Xu, Microstructure and electrochemicalbehavior of cerium conversion coating modified with silane agent on magnesium substrates, Appl. Surf. Sci. 376 (2016) 161–171.

[9] T. Zhai, B. Liu, C.H. Ding, L.X. Lu, C. Zhang, K.G. Xue, D.A. Yang, Ni-P electroless deposition directly induced by sodium borohydride at interconnected pores of poly (ether ketone)/multi walled carbon nanotubes composites surface, Surf. Coat. Tech. 272 (2015) 141–148.

Corrosion Behavior of Electrodeposited Ni-W-P-SiO₂ Nanocomposite Coatings in NaCl Solution

M. Abdolmaleki[a]*, G.R. Allahgholipour[a]

Sayyed Jamaleddin Asadabadi University, Asadabad, 6541861841, Iran, Fax: 988133117803; Tel: 988133117804; E-mail: m.abdolmaleki@sjau.ac.ir

Abstract: Nanostructured Ni-W-P-SiO₂ composite coatings were developed on copper sheets using electrolytic tartrate bath. Firstly, the experimental parameters and the composition of the electrolytic bath were optimized. Then, surface morphology and composition of the synthesized coatings were characterized by scanning electron microscopy (SEM) and energy dispersive X-ray (EDX) techniques. Finally, corrosion behavior of the developed Ni-W-P-SiO₂ coatings was evaluated in 3.5wt. % NaCl solution using electrochemical method such as: open circuit potential (E_{OCP}), potentiodynamic polarization and electrochemical impedance spectroscopic (EIS) measurements. Highest corrosion resistance was observed for coating that deposited from bath with concentration of 4 g/L SiO₂.

Keywords: Ni-W-P-SiO₂, Electrodeposition, Nanocomposite, Electrochemical impedance spectroscopy

I. INTRODUCTION

The electrodeposition method is widely used and growing at industrial electronics; this technique involves depositing a thin layer of coating on a substrate [1-3]. The surface of a metal can be reinforced using composite coatings. Co-W-P coatings have useful metallurgical properties such as hardness, high wear and corrosion resistance [4-6]. In fact, the composites are second phase particle that reinforce matrix metal [4-6]. In this work, the SiO₂ nanoparticles deposited into Ni-W-P can lead to refinement in metallurgical properties. The anti-corrosion performances of the Ni-W-P-SiO₂ coatings were studied by various electrochemical tests in a corrosive medium containing 3.5% NaCl solution.

II. METHODS

The analytical reagents with purity grade and double distilled water used to prepare the plating bath. The

composite coatings were deposited from tartrate solutions with various concentrations of SiO₂ (0-12 g/L). The surface morphologies and composition of the composite coatings were examined by a field-emission scanning electron microscope and energy-dispersive X-ray (TESCAN MIRA3 model) experiments. The corrosion characteristics of Ni-W-P-SiO₂ composite coatings were performed by using a vertex potentiostat/galvanostat (Ivium Technology) electrochemical analyzer run by the IviumSoft software.

III. RESULTS AND DISCUSSION

A. SEM and EDX studies

The surface morphology and elemental analysis of Ni-W and Ni-W-P-SiO₂ composite coatings analyzed by SEM-EDX were given in Figs 1 and 2, respectively. The surface of the Ni-W alloy coating was rough with some cracks (Fig. 1a). The nanocomposite coatings have a smooth, uniform surface without any cracks, imperfections and so on (Fig. 1b). These desirable structural properties ensure a good adherence to the substrate. The EDX spectra confirm the presence of silica particles in the structure of composite coatings successfully.
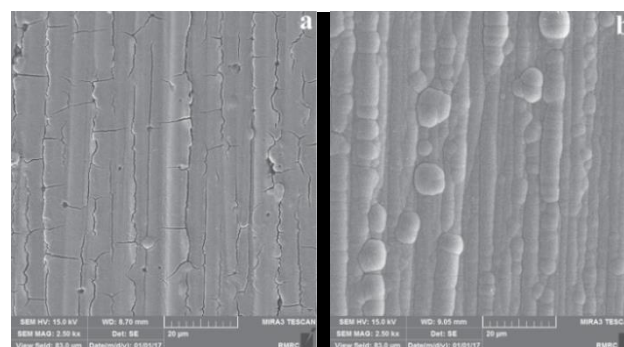

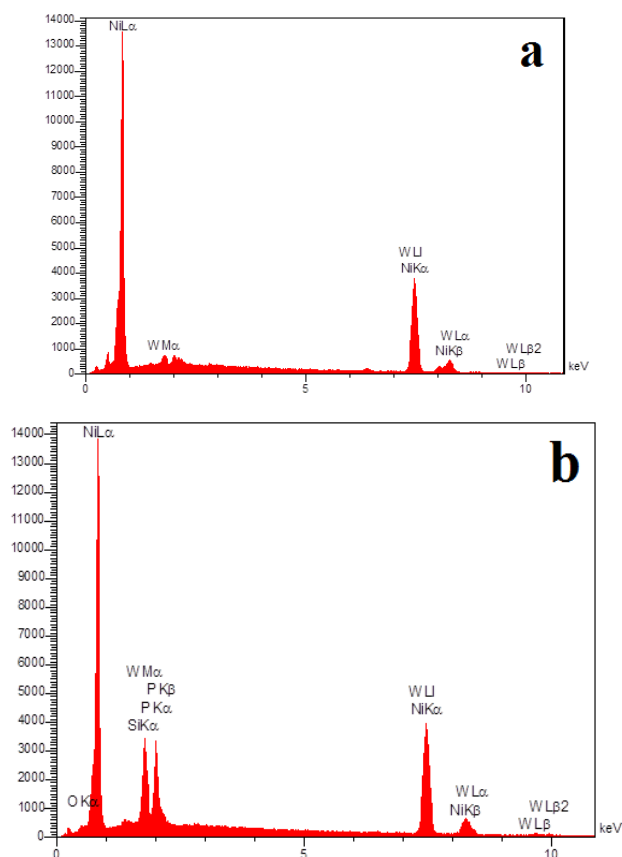Fig. 1: SEM images of the pure Ni-W (a) and optimum Ni-W-P-SiO₂ coating (4 g/L SiO₂) (b).

Fig. 2: EDX spectra of components Ni, W, P, Si and O of the pure Ni-W (a) and optimum Ni-W-P-SiO₂ coating (4 g/L SiO₂) (b).
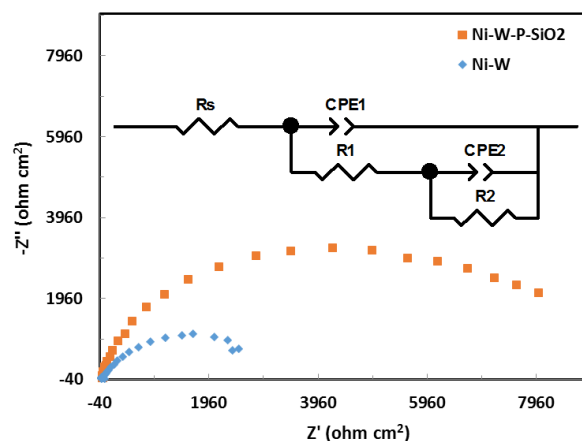

Fig. 3: Comparison of Nyquist plots of the pure Ni-W and optimum Ni-W-P-SiO₂ coatings (4 g/L SiO₂).
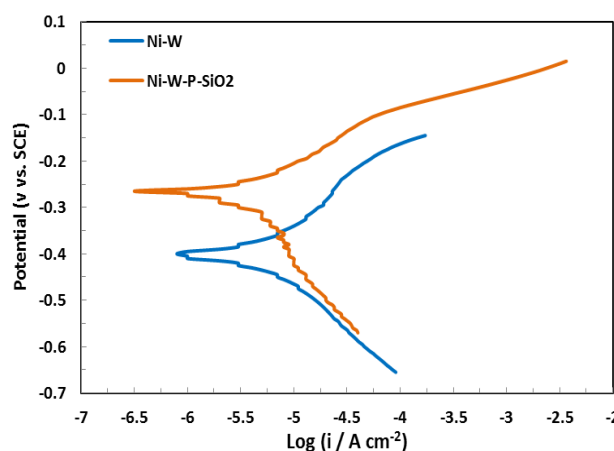
Fig. 4: Comparison of polarization curves of the pure Ni-W and optimum Ni-W-P-SiO₂ coatings.

B. Corrosion tests

The Nyquist plots of EIS and the polarization curves of electrodeposited Ni-W and Ni-W-P-SiO₂ coatings, in 3.5% sodium chloride solution, at their respective open circuit potentials, are shown in Figs 3 and 4, respectively. It can be seen that he presence of SiO₂ particles in composite coatings causes significant shift in the direction of more positive potentials and a significant reduction in the corrosion current density. Therefore, the corrosion resistance of nanocomposite coatings will be much higher than pure nickel-tungsten alloy coating (Fig. 3). The reason for increasing the corrosion resistance of Ni-W-P-SiO₂ composite compared to pure Ni-W alloy coating could have resulted from enhance the surface of these composite coatings with SiO₂ particles.

IV. CONCLUSIONS

Ni-W-P-SiO₂ nanocomposite coatings are synthesized by electrodeposition method from solutions with various concentrations of SiO₂ particle. The SEM results showed that the nanocomposite coatings are smoother, more even; high metallic luster and lack any apparent defects compared to Ni-W alloy coatings. The EIS results indicated high corrosion resistance for Ni-W-P-SiO₂ composite coatings. The results of polarization studies showed a significant reduction in the corrosion density for nanocomposite coatings. In other words, the polarization results in agreement with the EIS measurements.

REFERENCES

[1] X. Zhang, B. Li, H. X. Liu, G. H. Zhao, Q. L. Yang, X. M. Cheng, C. H. Wong, Y. M. Zhang, and C. W. J. Lim, Applied Surface Science vol. 465, pp. 871-879, **2019**.

[2] S. Pouladi, M. H. Shariat, and M. E. Bahrololoom, Surface and Coatings Technology, vol. 213, pp. 33-40, **2012**.

[3] V. A. Safonov, O. V. Safonov, L. A. Fishgoit, K. Kvashnina, and P. Glatzel, Surface and Coatings Technology, vol. 275, pp. 239-244, **2015**.

[4] S. K. Tien, J. G. Duh, and Y. I. Chen, Surface and Coatings Technology, vol. 177-178, pp. 532−536, **2004**.

[5] C. N. Panagopoulos, V. D. Papachristos, U. Wahlstrom, P. Leisner, and L. W. Cheristofersen, Scripta Materialia, vol 43(7), pp. 677-683, **2000**.

[6] M. G. Hosseini, M. Abdolmaleki, and J. Ghahremani, Corrosion Engineering, Science and Technology, vol. 49, pp. 247-253, **2014**.

Direct electron transfers study of immobilized tyrosinase using the modified glassy carbon electrode by MWCNT/ poly (aniline-co-metha phenylene diamine) composite

Samira Seyed Somarin [a], *Hassan Faridnouri* [a*], *Ehsan Nazarzadeh Zare* [b]

aSchool of Biology, Damghan University, Damghan, Iran.
bSchool of Chemistry, Damghan University, Damghan, Iran.
Email: faridnouri@du.ac.ir

Abstract: In this research, tyrosinase (Tyr) was immobilized on the modified glassy carbon electrode (GCE) by carboxylated multi walled carbon nanotube (MWCNT)/ poly (aniline-co-metha phenylene diamine) (PAN-Pd) and its direct electron transfer rate (DET) was studied using cyclic voltammetry (CV). A pair of well-defined quasi-revesible voltammetric peaks were observed which corresponding to the Cu (II)/ Cu (I) redox couple located in the active site of Tyr. The formal potential of immobilized enzyme was measured to be -42 mV (vs. Ag/AgCl) in phosphate buffer solution at pH 7.0. The apparent heterogeneous electron transfer rate constant and charge-transfer coefficient were estimated to be 2.2 s^{-1} and 0.5, respectively. The surface coverage of Tyr on the surface of the modified electrode was calculated to be 1.3×10^{-10} mol/cm^2.

Keywords: Tyrosinase, poly (aniline-co-metha phenylene diamine), direct electron transfer, MWCNTs, cyclic voltammetry

I. INTRODUCTION

Investigation of direct electron transfer (DET) in proteins has been of great importance through electrochemical techniques in recent decades. Since the redox center in proteins is usually located in the interior parts, any method that leads to an optimum protein immobilization at the electrode surface with a more suitable orientation can lead to acceleration of ET [1]. Therefore, the use of materials such as carbon nanotubes and conductive polymers has improved the quality of new generation biosensors [2]. Among various conducting polymers, polyaniline has acquired much attention due to its unique conduction mechanism, easy producibility and high environmental stability [3]. The immobilization of Tyr is essential for construction of biosensors to measure phenolic derivatives, especially biological compounds such as Dopa, which is important for identifying certain diseases, such as Alzheimer's. The biocompatible nanomaterials could retain the activity of enzyme well due to the suitable microenvironment, and enhance the DET between the enzyme's active sites and the electrode, so these materials have their unique advantages in enzyme immobilization [4,5].

In this study Tyr was immobilized on the modified GC electrode by carboxylic MWCNT/ PAN-Pd and its direct electron transfer rate was investigated using CV method.

II. MATERIALS AND METHODS

The experiments were achieved by using a potentiostat/galvanostat (Radstat 10, Daneshyar Kavosh, Iran) and the PSTrace 4 software was applied for voltammetric analysis. A three-electrode system was employed with a platinum wire as the counter electrode an Ag/AgCl (3M KCl) as the reference electrode, and the modified glassy carbon electrode (GCE) as the working electrode. Prior to modification, GCE was polished with 0.5 μm alumina suspension and then on a filter paper, then Thereafter, it was rinsed with deionized water and sonicated with a Tecno-Gaz ultrasonic cleaner (Italy) in a beaker containing deionized water for 2 min. At first, 10 μl of the dispersion containing MWCNT-COOH/PAN-Pd (each of them 1 mg/ml) in PBS (0.1M. pH=7.0) was dropped onto the cleaned GCE and was allowed to dry under ambient conditions for 1 h and then, 10 μl of 5mg/ml Tyr solution in 0.1M PBS at pH=7.0 was dropped on modified electrode and allowed to dry under room temperature. The electrode (Tyr/MWCNT-COOH/ PAN-Pd /GCE) was again rinsed with distilled water, dried and kept in the refrigerator.

III. RESULTS AND DISCUSSION

As can be seen in Fig. 1, there is a pair of well-defined redox peaks for the quasi-reversible DET behavior of immobilized Tyr at various scan rates corresponding to the CU (II)/Cu (I) redox couple located in the active site of Tyr. The cathode and anodic peaks appeared at -0.11 and 0.025 volts, respectively, and the formal-potential value (E°´) was -42 mV compared to the reference electrode. The ratio of the cathode current to the anodic (I_{pc}/Ipa) is also equivalent to one and the peak potential difference is 135 mV. This value shows a decrease of 132 mV and 67 mV, respectively compared to our previous work [6], indicating that the presence of carbon nanotubes and polymer

composite has increased the reversibility of immobilized Tyr. The peak-to-peak separation is attributed to this fact that Tyr molecules are probably immobilized in one orientation [7, 8]. As can be seen, there is a linear relationship between the intensity of cathodic and anodic currents with scan rate which is expected from an immobilized enzyme. According to the Laviron theory [9], using the slope of the cathodic current vs. scan rate in Fig. 2 and replacing it in Eq. 1, the amount of surface coating resulting from the immobilization of Tyr on the GCE can be calculated.

$$Ip = \frac{v n^2 F^2 A \Gamma}{4RT} \tag{1}$$

where Ip is the value of peak reduction, Γ is the electroactive Tyr amount (mol/cm^2), n is the number of electrons transferred, F is the Faraday constant (96,485 C/ mol), A is the surface area of the electrode (cm^2), v is the scan rate (mV/s), R is the gas constant (8.314 J/mol K), and T is the Kelvin temperature (K). Assuming a double electron reaction, the surface coverage of Tyr on the surface of the modified electrode was calculated to be 1.3×10^{-10} mol/cm^2 which is 38 times greater than our previous immobilization method [6]. This indicates that carboxylic carbon nanotubes/polymer composite provided much more surface for Tyr immobilization.

The ET kinetic of Tyr was obtained by using the Laviron model [9] from the relationship between redox peak potentials and scan rate. The kinetic parameters of α and heterogeneous transfer rate constant (k_s) are estimated according to the Eq. 2.

$$\log k_s = \alpha \log (1 - \alpha) + (1 - \alpha) \log \alpha - \log \frac{RT}{nF\vartheta} - \frac{\alpha (1 - \alpha) nF\Delta E_p}{2.3RT} \tag{2}$$

The ET rate constant (k_s) was obtained 2.2 s^{-1} (for nΔEp≥0.2 V) by using the data for 100 mV/s from Fig. 2. From the k_s value, it can be concluded that in this study, immobilization of Tyr by MWCNT- COOH/ PAN-Pd, enhanced the rate of ET 2.4 times in comparison to previous work [6].

Furthermore, the slope of log Ipc vs. log ν (Fig. 3) was obtained to be 1.02, which confirms that a thin layer of Tyr molecules is formed at the electrode surface.

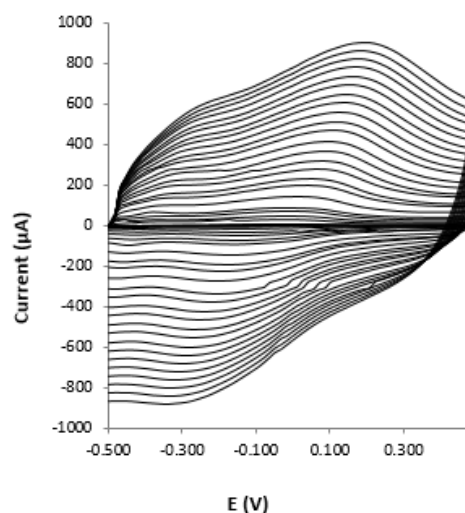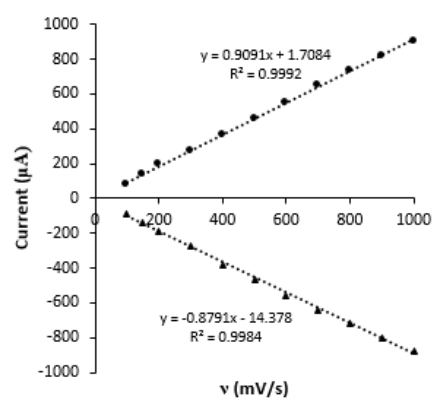Fig.1: Cyclic voltammograms of MWCNT-COOH-polymer/Tyr/GCE at different scan rates in PBS pH=7.0.

y = 0.9091x + 1.7084
R² = 0.9992

y = -0.8791x - 14.378
R² = 0.9984

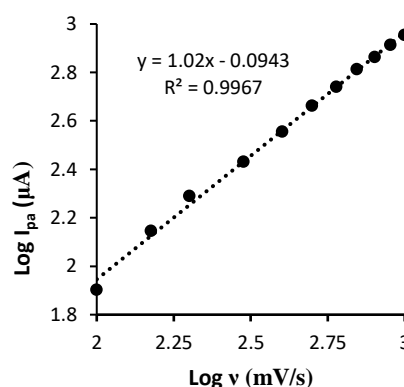Fig 2: plot of the peak current against the scan rate.

y = 1.02x - 0.0943
R² = 0.9967

Fig.3: log Ipc vs. log ν.

III. CONCLUSION

In summary, electrostatic bonding between the amine groups of polymer and caboxylic groups of amino acids of Tyr and MWCNT cause to stable immobilization of Tyr. Carboxylic carbon nanotubes with PAN-Pd has provided a good microenvironment for Tyr immobilization, which has led to an increase in the stability and acceleration of ET. The surface coverage of Tyr on the surface of the modified electrode and The electron transfer rate constant of the biosensor were improved in Compared with the previous immobilization method.

REFERENCES

[1] S. Shleev, J. Tkac, A. Christenson, T. Ruzgas, A.I. Yaropolov, J.W. Whittaker, L. Gorton, Direct electron transfer between copper-containing proteins and electrodes, Biosens. Bioelectron. 20 (2005) 2517–2554.

[2] B. Wanga, J. Zhenga, Y. Hea, Q. Sheng, A sandwich-type phenolic biosensor based on tyrosinase embedding into single-wall carbon nanotubes and polyaniline nanocomposites, Sensors and Actuators B 186 (2013) 417–422.

[3] C. Dhand, M. Das, M. Datta, B.D. Malhotra, Recent advances in polyaniline based biosensors, Biosensors and Bioelectronics 26 (2011) 2811–2821.

[4] A. Boujakhrout, P. Diez, A. Sanchez, P. Martinez-Ruiz, J.M. Pingarron, R. Villalonga, Gold nanoparticles-decorated silver-bipyridine nanobelts for the construction of mediatorless hydrogen peroxide biosensor, J. Colloid Interface Sci. 482 (2016) 105–111.

[5] Y. Liu, N. Song, Z.Ma, K. Zhou, Z. Gan, Y. Gao, S. Tang, C. Chen, Synthesis of a poly (Nmethylthionine)/ reduced graphene oxide nanocomposite for the detection of hydroquinone, Mater. Chem. Phys. 223 (2019) 548–556.

[6] H. Faridnouri, H. Ghourchian, H. Hashemnia, Direct electron transfer enhancement of covalently bound tyrosinase to glassy carbon via Woodward's reagent K, Bioelectrochemistry, 82 (2011), 1-9.

[7] S. Hashemnia, H. Ghourchian, A.A. Moosavi-Movahedi, H. Faridnouri, Direct electrochemistry of chemically modified catalase immobilized on an oxidatively activated glassy carbon electrode, Journal of Applied Electrochemistry 39 (2009) 7–14.

[8] J. Li, S. Dong, The electrochemical study of oxidation-reduction properties of horseradish peroxidase, J. Electroanal. Chem. 431 (1997) 19–22.

[9] E. Laviron, The use of linear potential sweep voltammetry and of ac voltammetry for the study of the surface electrochemical reaction of strongly adsorbed systems and of redox modified electrodes, J. Electroanal. Chem. Interfacial Electrochem. 100 (1979) 263–270.

Synthesize and Electrocatalytic Investigation of CuFe₂O₄ Nanostructures

M. Shaterian*, R. Mohammadi, M. Shaghaghi, S.Z. Hosseini, A. Hajiahmadi

Department of Chemistry, Faculty of Science, University of Zanjan, 451561319, Zanjan, Iran

Email: shaterian@znu.ac.ir

Abstract: $CuFe_2O_4$ nanostructures are synthesized by a sol-gel auto-combustion method. Characterization and study of the nanostructures are performed using various techniques such as X-ray diffraction, scanning electron microscopy and energy dispersive X-Ray spectroscopy. Also, the electrocatalytic sensing behavior of $CuFe_2O_4$ are investigated using cyclic voltammetry technique in the presence of a redox couple probe. Using the method, the $CuFe_2O_4$ nanoparticles show an excellent electrocatalytic activity by acceleration electron transfer between the electrode and probe solution. Therefore, the electrochemical experiments suggest that the nanostructures will become a potential candidate in the field of electrochemical sensors.

Keywords: $CuFe_2O_4$, Nanostructures, Sol-gel auto-combustion, Electrocatalytic properties

I. INTRODUCTION

Spinel ferrite materials have been investigated for approximately four decades, due to their technological applications. $CuFe_2O_4$, are considered as a cubic close-packed arrangement of oxygen, Cu(II) and Fe(III) ions with two crystallographic sites [1]. There are various procedures for synthesis of the nanostructured materials that create various structures. The structural features contain grain boundary junctions, surface pores and also other crystal lattice defects. Some of the methods cotain co-precipitation [2], hydrothermal [3], thermal decomposition [4], and ball milling [5]. The methods have some drawbacks, such as, energy consuming and too long duration. The sol-gel auto-combustion route is proved to be a very commonly applied chemical procedure for preparation of uniform large area thin films and synthesizing powders of micrometer to nanometer size with high purity and homogeneity.

In the present study, the preparation of $CuFe_2O_4$ nanostructures using sol-gel auto-combustion method is reported. Then, their structural and electrocatalytic characterizations are investigated.

II. METHODS

All solutions were freshly prepared by deionized water and chemicals used were of analytical grade. $Cu(NO_3)_2 \cdot 6H_2O$, $Fe(NO_3)_3 \cdot 9H_2O$, NaOH, H_3PO_4, and other chemicals were purchased from Merck and used without any further purification. The sol-gel auto-combustion method was used for synthesize of the $CuFe_2O_4$ nanostructures.

The X-ray diffraction (XRD) patterns of the $CuFe_2O_4$ were recorded by a Model PI TS 3003 of SEIFERT diffractometer using Cu Kα radiation (k = 1.5418 Å) to examine the crystallization and structural properties of the nanopowders. Scanning electron microscopy (SEM) micrographs were recorded using a KYKYEM3200. Electrochemical experiments were carried out by a SAMA potentiostat-galvanostat equipped with SAMA software.

III. RESULTS AND DISCUSSION

XRD result of the synthesized $CuFe_2O_4$ nanostructures is shown in Fig. 1. The crystallite size (D) of the nanopowders can be achieved by the Scherrer's equation (Eq.1):

$$D = 0.9 \, \lambda / \beta \cos\theta \qquad (1)$$

In the Eq. 1, λ is X-ray wavelength, β is the line broadening at half the maximum intensity and θ describes the Bragg angle. Therefore, the crystallite size of the $CuFe_2O_4$ is obtained 30.4 nm.
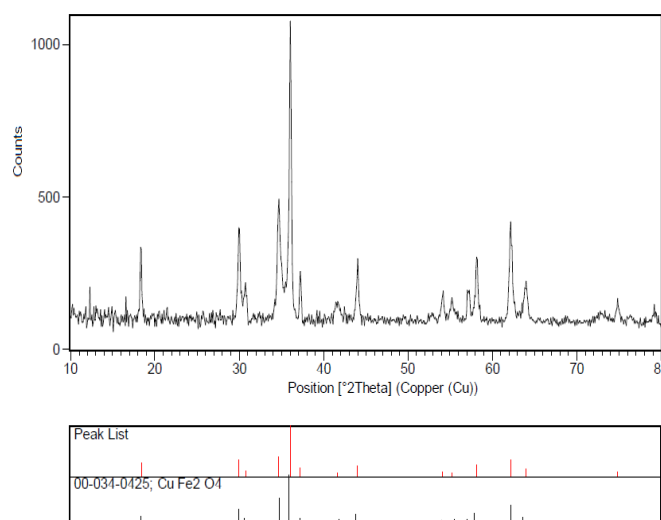

Fig. 1: XRD pattern of $CuFe_2O_4$ nanostructures.

Also, for examination the catalytic activity of the $CuFe_2O_4$ nanostructures, cyclic voltammetry (CV) technique was applied. The cyclic voltammograms of $[Fe(CN)_6]^{3-/4-}$ as a redox couple at the surface of a bare carbon paste electrode (CPE) and modified CPE with $CuFe_2O_4$ nanostructures ($CuFe_2O_4$/CPE) were recorded and presented in Fig. 2. As can be seen, $CuFe_2O_4$/CPE displays a well-defined oxidation peak with magnification of about 3.5 times greater than the CPE. An improvement in electrochemical response is clear evidence of the catalytic effect of the $CuFe_2O_4$. The results confirm a potential applicability of the as-synthesized nanoparticles in electrochemical fields.
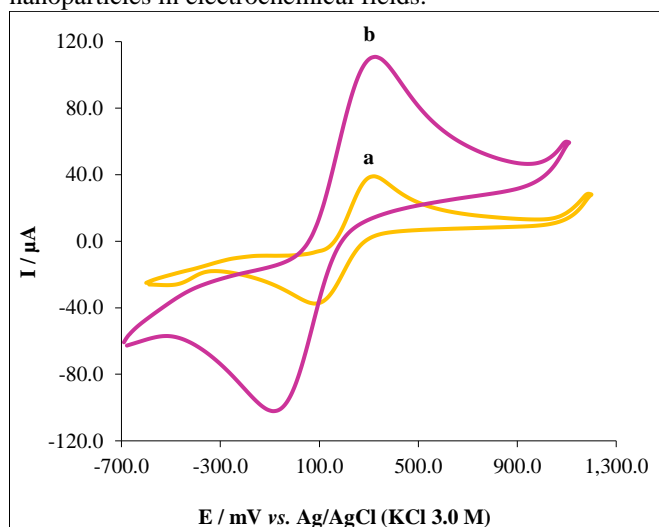

Fig. 2: Cyclic voltammograms of $[Fe(CN)_6]^{3-/4-}$ at the surface of (a) CPE and (b) $CuFe_2O_4$/CPE.

IV. CONCLUSION

$CuFe_2O_4$ were synthesized via sol-gel auto-combustion method. Characterization mechanisms showed that the nanostructures were actually formed without any impurity. Also, voltammetric studies exhibited highly catalytic effects of the $CuFe_2O_4$ for sensing applications.

REFERENCES

[1] G. Raja, S.Gopinath, R. A. Raj, A.K. Shukla, M.S. Alhoshan, K. Sivakumar, Physica E, 83, 69-73, **2016**.

[2] Y. Koseoglu, M.I.O. Oleiwi, R. Yilgin, A.N. Kocbay, Ceram. Int. 38, 6671-6676, **2012**.

[3] L. Zhuang, W. Zhang,Y. Zhao, D. Li, W. Wu, H. Shen, Powder Technol. 217, 46-49, **2012**.

[4] M.J. Akhtar, M. Younas, Solid State Sci. 14, 1536-1542, **2012**.

[5] J. Chen, Y. Wang, Y. Deng, J. Alloy.Compd. 552, 65-69, **2013**.

Sol-gel auto-combustion synthesis of SnO₂ Nanopowders: Application in Electrochemical Studies

M. Shaterian*, A. Babaei, A. Gulmohammad, A. Khwaja-Mohammad, H. Sadiqi

Department of Chemistry, Faculty of Science, University of Zanjan, 451561319, Zanjan, Iran

Email: shaterian@znu.ac.ir

Abstract: SnO_2 with nanosized structures are facilely synthesized by sol-gel auto-combustion method, and their electrochemical properties are investigated. Different techniques contain X-ray diffraction, scanning electron microscopy and energy dispersive X-Ray spectroscopy are applied for study of the nanostructures. Using the techniques crystallization procedure, morphology and particle size of the powders are characterized. For electrochemical studies, a carbon paste electrode is modified with SnO_2 nanostructures. Characterization of the nanostructured electrode is performed by voltammetric techniques. Using the techniques electrocatalytic activity of the SnO_2 in the presence of a probe solution is studied. The voltammetric data are confirmed that the SnO_2 nanostructures are a potential candidate for electrocatalytic analysis in complex samples.

Keywords: SnO_2, Nanomaterials, Sol-gel auto-combustion method, Nanostructured sensor, Electrocatalyst

I. INTRODUCTION

Synthesis of nanomaterials with organized size and morphology is a main step in nano-technological fields. SnO_2 is a key material that has been widely applied in sensors and optoelectronic areas [1,2]. SnO_2 with different morphologies, containing nano hollow spheres, nano-sheets, nano-rods, nano-diskettes, nanoparticles and etc. have been reported and applied in various fields [3-5].

In the present study, a sol-gel auto-combustion method was used for synthesis of nanosized SnO_2. After structural characterizations, a sensitive and simple SnO_2 nanostructured modified carbon paste electrode (SnO_2/CPE) was designed for electrocatalytic investigations of the nanostructures.

II. METHODS

$Sn(NO_3)_2.4H_2O$, NaOH, H_3PO_4, carbon graphite powder and other reagents were purchased from Merck Co. with analytical grade and without further purification. SnO_2 nanostructures were synthesized by a sol-gel auto-combustion route. The X-ray diffraction (XRD) patterns of the nanopowders were recorded by a Model PI TS 3003 of SEIFERT diffractometer using Cu Kα radiation (k = 1.5418 Å) to obtain the structural and crystallization properties of SnO_2 nanostructures. Scanning electron microscopy (SEM) micrographs were achieved using a KYKYEM3200. Electrochemical tests were followed using a SAMA potentiostat-galvanostat. The electrochemical cell was equipped with a three-electrode system containing a working electrode (carbon paste), a counter electrode (platinum wire) and a reference electrode (Ag/AgCl/KCl). A digital pH meter (Metrohm model 691) was used for preparation of buffer materials that served as a supporting electrolyte in the electrochemical studies. A carbon paste electrode (CPE) was modified by SnO_2 nanostructures to design a modified electrode (SnO_2/CPE).

III. RESULTS AND DISCUSSION

Fig. 1 displays the XRD patterns of the as-synthesized SnO_2 nanostructures prepared using sol-gel auto-combustion method. The diffraction peaks indicate tetragonal structure without any impurity peaks. Using the data and Scherrer's equation the crystal size of the SnO_2 nanostructures was obtained about 28.2 nm.
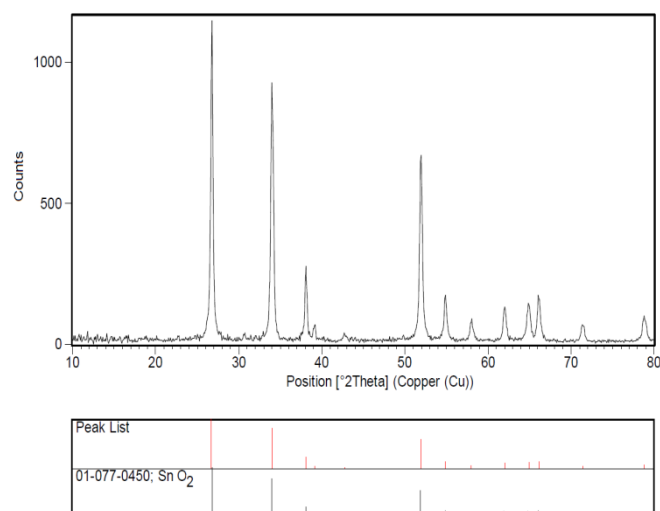

Fig. 1: XRD pattern of SnO_2 nanostructures.

After synthesize and characterization steps, the nanostructures were applied in electrochemical experiments as elecrocatalyst. Therefore, a solution containing $[Fe(CN)_6]^{3-/4-}$ was used as a redox couple probe. The experiments were performed at the surface of a bare CPE and a modified SnO_2/CPE. Cyclic voltammetry (CV) technique was applied for electrochemical experiment. Using CV, SnO_2 nanostructures showed excellent electrocatalytic properties. Also, cyclic voltammograms of SnO_2/CPE in different scan rates indicated that the nanostructures can be a good electrocatalyst for analyzing of environmental and biological samples.

IV. CONCLUSION

A simple sol-gel auto-combustion method was used for synthesize of SnO_2 in nanosized scale. Structural and morphological studies were performed using different spectroscopic and microscopic techniques. The SnO_2 nanostructures were applied as an excellent electrocatalyst in electrochemistry studies.

REFERENCES

[1] T. Sahm, W. Rong, N. Barsan, L. Madler, U. Weimar, Sens Actuators, B, 127, 63-68. **2007**.

[2] N.N. Samotaev, A.A. Vasiliev, B.I. Podlepetsky, A.V. Sokolov, A.V. Pisliakov. Sens Actuators, B, 127, 242-247, **2007**.

[3] W.-S. Kim, Y. Hwa, J.-H. Jeun, H.-Sohn, S.-H. Hong, J. Power Sources 225, 108-112, **2013**.

[4] Y. Li, Y. Guo, R. Tan, P. Cui, Y. Li, W. Song, Mater. Lett. 63, 2085-2088, **2009**.

[5] V.S. Jahnavi, S. Tripathy, A.V.N. R. Rao, Physica B: Condensed Matter, 565, 61-72, **2019**.

Electrochemical performance stability of Pd-Co/rGO nano-catalyst in Ethanol electro-oxidation reaction

Somayeh Majidi[a], Hamidreza Asgari[b]*
[a]Department of Chemistry, Najafabad Branch, Islamic Azad University, Najafabad, Iran.
[b]Department of Chemical Engineering- Health, Safety & Environment, Najafabad Branch, Islamic Azad University, Najafabad, Iran.
Email: Somaye.majidi2010@gmail.com

Abstract: The prepared Pd-Co/rGO nano-particles were used as electro-catalysts for the ethanol (EtOH) oxidation reaction in alkaline media. The performance stability of Pd-Co/rGO was evaluated in the Half-cell by electrochemical techniques such as cyclic voltammetry (CV) and chronoamperometry (CA) techniques. Results indicate that Pd-Co/rGO nano-catalyst show high stability toward EtOH oxidation reaction and is still active even after 150 CV cycles.

Keywords: Pd-Co/rGO electro-catalyst, EtOH oxidation reaction, Performance stability, Alkaline media, Electrochemical technique.

I. INTRODUCTION

The development of catalysts with high electro-catalytic activity for direct alcohol fuel cells application is a central issue to accelerate the clean energy technology in an affordable manner [1,2].

Pd is more abundant in nature, less expensive, and could more efficiently promote EtOH oxidation in alkaline media. Zhang showed that Pd exhibits a peak current density almost four times larger than that of Pt in CV experiment [3]. Therefore, it is considered to be a promising electro-catalyst for EtOH oxidation.

Binary alloyed catalysts, which have been proved to be an effective mean for further improving the electro-catalytic activity of Pd-based electro-catalysts [4]. As confirmed by previous reports, Pd-Co catalysts exhibited higher electro-catalytic activity and stability for alcohol oxidation compared with the Pd electro-catalyst [5,6].

In addition, the desirable selection of support materials is an important index to decrease the Pd metal loading. Reduced graphene oxide (rGO) has emerged as an electro-catalyst support that helps the effective dispersion of nano-catalyst.

In this study, Pd-Co/rGO nano-particles were employed as the electro-catalyst for EtOH electro-oxidation in alkaline electrolyte. The electro-chemical performance stability of Pd-Co/rGO electro-catalyst was evaluated by CV and CA techniques. It is found that the Pd-Co/rGO electro-catalysts exhibits high stability toward EtOH electro-oxidation reaction.

II. METHODS

The electro-chemical performance of electro-catalysts was investigated through a conventional three-electrode electrochemical cell with the potentiostat-galvanostat workstation (SAMA, Iran) at room temperature. A glassy carbon (GC), platinum foil and Ag/AgCl in saturated KCl was used as the working electrode, counter electrode and reference electrode, respectively.

The catalyst ink was prepared by well-dispersing 1 mg of powdered catalyst in a solution of 0.05 ml of Nafion solution in isopropyl alcohol (5 wt.%), 0.5 ml of DI water and 0.5 ml of EtOH. The required amount of the catalyst ink was pipetted on the pre-polished GC electrode surface (area: 0.0314 cm2) and dried at room temperature. The catalyst loading on the pre-polished GC electrode surface was 0.033 mg cm^{-2}.

All electro-chemical measurements were carried out in the basic solution containing 1M KOH and 1M EtOH. For the electro-chemical measurements, CV and CA were performed. CV tests were carried out by scanning of the potential between -0.7 and 0.4 V vs. Ag/AgCl electrode with scan rate of 50 mV/s. CA tests were also carried out at potential which is set in the low potential range.

All potential values have been reported vs. Ag/AgCl potential.

III. RESULTS AND DISCUSSION

Stability of electro-chemical performance of the Pd-Co/rGO electro-catalyst was investigated by CV experiment during 150 CV cycles. Fig. 1 shows consecutive CV patterns for EtOH on the Pd-Co/rGO.

The EtOH oxidation on the surface of Pd-Co/rGO is characterized by two well defined current peaks on the forward and reverse scan. The forward peak at -0.15V is corresponding to the oxidation EtOH. The reverse peak at -0.4V is associated with removal of carbonaceous species not completely oxidized in the forward scan.

IV. CONCLUSION

The electrochemical performance stability of the Pd-Co/rGO was investigated by CV and CA techniques. Results showed an excellent catalytic activity and stability of Pd-Co/rGO. The I_p value of EtOH oxidation on the Pd-Co/rGO declined approximately 61% under 150 CV cycle. The result demonstrated that Pd-Co/rGO electro-catalyst is still active in EtOH oxidation reaction even after 150 CV cycles. The stability of the catalysts was also determined from the long-term poisoning rate in chronoamperometric test.

REFERENCES

[1] Z. Guo, X. Zhang, H. Sun, X. Dai, Y. Yang, X. Li and et al., Electrochim Acta, vol. 134, pp. 411-7, **2014**.
[2] S. Ha, R. Larsen and R. Masel, Journal of Power Sources, vol. 144, pp. 28-34, **2005**.
[3] Z. Zhang, L. Xin, K. Sun and W. Li. International Journal of Hydrogen Energy, vol. 36, pp. 12686-97, **2011**.
[4] Z. Zhang, J. Ge, L. Ma, J. Liao, T. Lu and W. Xing, Fuel Cells, vol. 9, pp. 114-20, **2009**.
[5] Y. Wang, X. Wang and C.M. Li, Applied Catalyst B, vol. 99, pp. 229-34, **2010**.
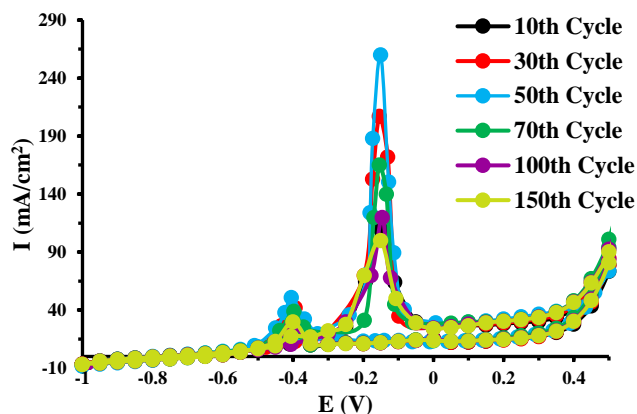[6] Z.S. Yang, J.J. Wu, Fuel Cells, vol. 12, pp. 420-5, **2012**.

Fig. 1: Consecutive CVs of Pd-Co/rGO in the solution containing 1M KOH and 1M EtOH

As shown in Fig. 1, the I_P value was increased during the time up to 50th CV cycle, exhibiting the Pd-Co/rGO activation period. After 50th CV cycle, as shown in Fig. 1, I_p value was decreased with increasing of the CV cycle number because EtOH was consumed and the catalyst was poisoned by the intermediate. However, Pd-Co/rGO catalyst still exhibits peaks for the EtOH oxidation reaction after 150 CV cycle. The I_p value of EtOH oxidation on the Pd-Co/rGO declined 61% under 150 CV cycle.

The long-term electro-catalytic performance of Pd-Co/rGO in the EtOH xidation has also been investigated by CA experiment in the solution containing 1M KOH and 1M EtOH at the potential of -0.2V. The time of CA experiment was 1000s. Fig. 2 shows chronoamperograms of Pd-Co/rGO in the EtOH oxidation reaction. The curve displayed the decay of current during the time, which would be related to the remaining of the adsorbed intermediate products of EtOH oxidation on the surface of electro-catalyst.
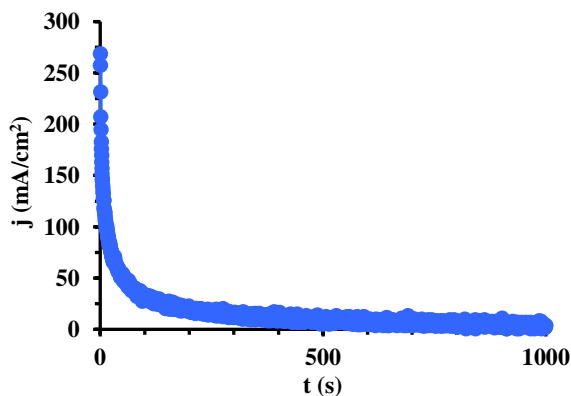

Fig.2: Chronoamperometric curve for Pd-Co/rGO using 1 M KOH and 1M of EtOH with an applied potential of -0.2V

Long-Term Activity of Pd-Co/rGO Nano-Catalyst in Ethylene Glycol Electro-oxidation Reaction in Alkaline Media

Somayeh Majidi[a]*, Hamidreza Asgari[b]

[a]Department of Chemistry, Najafabad Branch, Islamic Azad University, Najafabad, Iran.
[b]Department of Chemical Engineering- Health, Safety & Environment, Najafabad Branch, Islamic Azad University, Najafabad, Iran.
Email: Somaye.majidi2010@gmail.com

Abstract: The Pd-Co/rGO nano-catalysts were used as electro-catalysts for the ethylene glycol (EG) oxidation reaction in alkaline media. The long-term activity of Pd-Co/rGO was investigated in the Half-cell by electrochemical techniques such as cyclic voltammetry (CV) and chronoamperometry (CA) techniques. CV results of EG electro-oxidation reaction on the Pd-Co/rGO were compared to the reported results in the literature. E_{onset} and S_{ap} were -0.3 V and 450 (mA/ mg$_{Pd}$), respectively, suggesting an excellent activity of Pd-Co/rGO in EG oxidation reaction in alkaline media. The low long term poisoning rate (0.018) of Pd-Co/rGO resulted from CA test determines high long-term activity and stability of Pd-Co/rGO in EG electro-oxidation reaction.

Keywords: Pd-Co/rGO, Ethylene glycol, Electro- oxidation, Long-term activity, Alkaline media.

I. INTRODUCTION

Direct alcohol fuel cells (DAFCs) employ a wide range of alcohol fuels such as ethylene glycol (EG). EG has the following advantages: 1) major renewable bio-fuels from the biomass fermentation 2) low toxicity compared to methanol (MeOH), 3) high theoretical mass energy density (5.2 kWh kg^{-1}) [1], 4) high-efficiency energy conversion, 5) easy to store and carry and 6) cheap and wide sources. Therefore, it is desirable to develop such green, low-cost and high-efficiency anodic fuel for DAFCs. The design and employment of new catalysts with high electro-catalytic activity is a central challenge to DAFC development.

In general, three types of electro-catalyst (i.e., Pt-based, Pd-based and Au-based catalysts) have been regarded as electro-catalysts for the electro-oxidation of EG in alkaline media as follow: 1) Pt-based catalysts such as Pt-Co/rGO [2], 2) Pd-based catalysts such as Pd-M bimetallic electro-catalysts (M: Ni or Sn) supported on sulfonated multi-walled carbon nanotubes [3], 3) Au-based catalysts such as Au-Bi/C, Pd-Au/C and Pd-Au-Bi/C [4]. Pd is more abundant in nature, less expensive, and could more efficiently promote alcohol oxidation in alkaline media. Alloying Pd-based catalysts, which have been proved to be an effective mean for further improving the electro-catalytic activity. Therefore, it is

expected that Pd-Co catalysts exhibits higher electro-catalytic activity and stability for alcohol oxidation compared with the Pd electro-catalyst. Reduced graphene oxide (rGO) has selected as an electro-catalyst support that helps the effective dispersion of nano-catalyst. To the best of our knowledge, Pd-Co/rGO electro-catalyst for EG oxidation reaction has not been reported so far in the literature. The novelty of this work is evaluation of long-term activity of Pd-Co/rGO nano-particles as the electro-catalyst for EG electro-oxidation in alkaline medium. The electro-chemical performance of Pd-Co/rGO electro-catalyst was evaluated by CV and CA techniques.

II. METHODS

The activity of Pd-Co/rGO was investigated by a conventional three-electrode electrochemical cell with the potentiostat-galvanostat workstation (SAMA, Iran) at room temperature. A glassy carbon (GC), platinum foil and Ag/AgCl in saturated KCl were used as the working electrode, counter electrode and reference electrode, respectively. The catalyst ink was prepared by well-dispersing 1 mg of powdered catalyst in a solution of 0.05 ml of Nafion solution in isopropyl alcohol (5 wt.%), 0.5 ml of DI water and 0.5 ml of EtOH. The catalyst ink was pipetted on the pre-polished GC electrode surface and dried at room temperature. The catalyst loading was 0.033 mg cm^{-2}. All electro-chemical measurements were carried out in the solution containing 1M KOH and 1M EG. For the electro-chemical measurements, CV and CA were performed. CV tests were carried out by scanning of the potential between -0.7 and 0.4 V vs. Ag/AgCl electrode with scan rate of 50 mV/s. CA tests were also carried out at potential of -0.1V.

III. RESULTS AND DISCUSSION

The performance of electro-catalysts in EG oxidation reaction was evaluated in terms of two aspects: (1) Onset potential (E_{onset}); electro-catalytic activity and (2) Specific current density (S_{ap}); electro-catalyst maximum performance. Electrochemical parameters obtained from CV pattern of Pd-Co/rGO were presented in Table 1 and compared with other

reported electro-catalysts Pd-based and Pt-based which are employed for EG oxidation reaction [3, 5, 6]. Results show that Pd-Co/rGO electro-catalyst has higher and lower performance compared to alloyed-based Pd and Pt electro-catalysts, respectively.

Fig. 1 shows products obtained for electro-oxidation of EG, in the alkaline medium. As shown in Fig. 1, the oxidation of EG is more mechanistically complicated and different intermediates were produced [1]. EG oxidation intermediates can be gradually adsorbed on the nano-catalyst surface and blocked the active sites of catalyst resulted in reducing the electro-catalyst activity along the time.

HOCH$_2$CH$_2$OH
Ethylene glycol

↓

OHCCH$_2$OH
Glycolaldehyde

↙ ↘

HOOCCH$_2$OH   OHCCHO
Glycolic acid   Glyoxal

↘ ↙

HOOCCHO
Glyoxylic acid
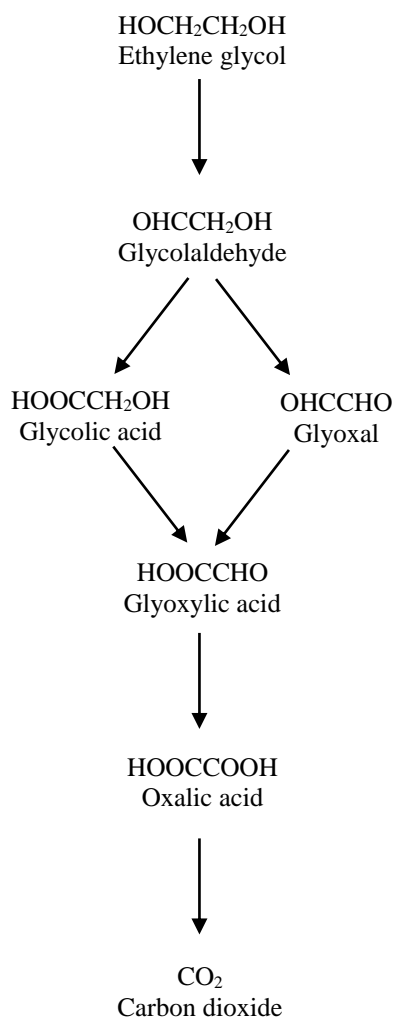
↓

HOOCCOOH
Oxalic acid

↓

CO$_2$
Carbon dioxide

Fig. 1: Products obtained by electro-oxidation of EG [1].

The long-term electro-catalytic activity of Pd-Co/rGO in the EG oxidation reaction has also been investigated by CA experiment in the solution containing 1M KOH and 1M EG,

Table 1: Comparative CV properties of the Pd-based and Pt-based nano-catalysts toward EG oxidation reaction in the alkaline medium

Catalyst	E_{onset} (V)	Sa_p (mA/ mg$_{Pd}$)	[Ref]
Pd-Sn/MWCNT	-0.44	247	[3]
Pd-Ni/MWCNT	-0.39	168	[3]
Pd-NiO/C	-0.48	347	[5]
Pd-Co$_3$O$_4$/C	-0.55	327	[5]
Pd/C	-0.45	352	[5]
Pd-CeO$_2$/C	-0.46	227	[5]
Pd-Mn$_3$O$_4$/C	-0.5	240	[5]
Pt-Pd/rGO	-0.46	1582	[6]
Pt-Ru/C	-0.56	703	[6]
Pt/C	-0.54	709	[6]
Pt/rGO	-0.48	623	[6]
Pd/rGO	-0.3	125	[6]
Pd-Co/rGO	-0.3	450	Current

with an applied potential of -0.1V, which is approximately set with peak potential of EG oxidation in CV test. The time of CA test was set 1000s. The stability of the catalysts was determined from the long-term poisoning rate (δ) in chronoamperometric results. The δ was computed based on the steady decaying rate of potentiostatic curves (dI/dt) according to the following relationship [1]:

$$\delta = -100/I_0 \times (dI/dt)_{(t>150)} \quad (1)$$

Where δ is the long term poisoning rate (% s^{-1}), I_0 is the current at the start of polarization back-extrapolated from the linear current decay and (dI/dt) t >150 is the average slope of the curve from 150th s to 1000th s. To calculate the average slope of the CA curve, the linear range of the curve was used. The CA parameters are presented in Table 2. The results show that the I_0 value for EG is resulting from high activity of Pd-Co/rGO in EG oxidation reaction. In addition, the δ value of Pd-Co/rGO was 0.018 for EG. It can be concluded that the Pd-Co/rGO electro-catalyst has high resistance toward poisoning in EG. The results indicate that Pd-Co/rGO was more active and stable (low δ) for EG electro-oxidation reaction in alkaline media.

Alcohol	I_0 (mA cm^{-2})	δ (% s^{-1})
EG	186	0.018

IV. CONCLUSION

The long-term performance of the Pd-Co/rGO was investigated by CV and CA technique. Results showed an excellent catalytic activity of Pd-Co/rGO in terms of specific peak current density and on-set potential compared to the reported results in literatures for EG electro-oxidation in alkaline media. The stability of the catalysts was also determined from the long-term poisoning rate in chronoamperometric test. This rate was low for EG electro-oxidation reaction. The results indicate that Pd-Co/rGO was high active and stable for EG electro-oxidation reaction in alkaline media while the amount of EG oxidation intermediates is high.

REFERENCES

[1] M. Zhiani, S. Majidi, H. Rostami, M.M. Taghiabadi, International Journal of Hydrogen Energy, vol. 40, pp. 568-76, **2015**.

[2] R. Baronia, J. Goel, V. Kataria, S. Basu, S. K. Singhal, International Journal of Hydrogen Energy, vol. 44, pp. 10023-32, **2019**.

[3] T. Ramulifho, K. I. Ozoemena, R. M. Modibedi, C. J. Jafta, M. K. Mathe. Journal of electroanalytical chemistry, vol 692, pp. 26-30, **2013**.

[4] M. Brandalise, M. M. Tusi, R. M. Piasentin, M. Santos, E. V. Spinace, A. O. Neto, International Journal of Electrochemical Science, vol. 7, pp. 9609-12, **2012**.

[5] C. Xu, Z. Tian, P. Shen, S. P. Jiang, Electrochimica Acta, vol. 53, pp. 2610-8, **2008**.

[6] K. J. Ju , L. Liu, J. J. Feng, Q. L. Zhang, J. Wei, A. J. Wang. Electrochim Acta, vol.188, pp. 696-703, **2016**.

Synthesize of bimetallic nanocomposite on the polymeric substrate for the electrochemical oxidation of methanol

S. Jadali, J. Azizi, L. Sharifi Khangheshlaghi, M. A. Kamyabi*

Department of Chemistry, Colleges of Science, University of Zanjan 45195-313, Iran

E-mail: Kamyabi@znu.ac.ir

Abstract: In this study, different bimetallic nanocomposites were synthesized and their electrochemical performances were investigated towards methanol oxidation reaction (MOR). The electropolymerization of 4-methyl-1,2-diaminobenzene (MDAB) on the MWCNT/GCE produced the proper substrate for electrodeposition of bimetallic nanoparticles. The consideration of synthesized nanocomposites exhibited that Ni-Cu is the best bimetallic for electrochemical oxidation of methanol in alkaline media.

Keywords: methanol oxidation reaction (MOR), bimetallic nanocomposite, 4-methyl- 1,2-diaminobenzene (MDAB)

I. INTRODUCTION

Direct methanol fuel cells (DMFCs) are introduced as a green energy power sources for the replacement of fossil fuels [1]. The properties of methanol such as ease of handling, high activity in low temperature and high energy density turns it into a good power sources for the portable devices. The selection of electrocatalyst is the most important step in the commercialization of DMFCs. The kind of supporting electrolyte is effective on this selection [2]. In this aspect, alkaline media has the promising features over acidic media. The usability of the low cost electrocatalysts and high energy density in the alkaline media are the reasons for the superiority of the alkaline media [3]. In the other part, the utilization of conducting polymers along with carbonaceous materials leads to the increase of conductivity and electrochemical activity [4]. In this study, we have reported the synthesis of the non-noble bimetallic nanocomposites for electrocatalytic oxidation of methanol in alkaline media. The efficiency of the synthesized nanocomposites towards methanol oxidation are studied by cyclic voltammetry (CV) and chronoamperometry (CA) methods. The morphological and physical characterizations of the synthesized nanocomposites are considered by field emission scanning electron microscopy (FESEM) and electrochemical impedance spectroscopy (EIS).

II. METHODS

All of the chemicals were analytical grade and used without additional purification. The electrochemical experiments were performed on the three configuration system (ZIVE LAB, South Korea) controlled by ZMAN 2.3 software including saturated Ag/AgCl, Pt wire, and glassy carbon electrode (GCE, 2 mm in diameter) as a reference, counter, and working electrode. The modification of GCE was performed with the following steps: 1) Drop casting of the MWCNT suspension onto the surface of cleaned GCE, 2) Electropolymerization of MDAB on the MWCNT/GCE by CV method in the optimum condition, and 3) Adsorption of bimetallic nanoparticles on the p-MDAB-MWCNT/GCE by CA method.

III. RESULTS AND DISCUSSION

The electrochemical activity of synthesized nanocomposites towards methanol oxidation was studied by CV method in a solution of 0.1 M NaOH containing 0.5 M methanol at a scan rate of 0.1 $V.s^{-1}$. Fig. 1(A) compares electrochemical activity of different nanocomposites for MOR. Onset potential and current density are the important parameters for the examination of synthesized nanocomposites [5]. As it is seen, Ni-Cu/p-MDAB/MWCNT nanocomposite exhibits the best performance for methanol oxidation. The best performance of Ni-Cu bimetallic nanocomposite can be attributed to the higher conductivity and better dispersion of these bimetallic nanoparticles on the polymeric substrate [6]. The betterment of Ni-Cu in the aspect of conductivity and surface morphology has been exhibited in the Fig. 1 (B) and Fig. 2 respectively.
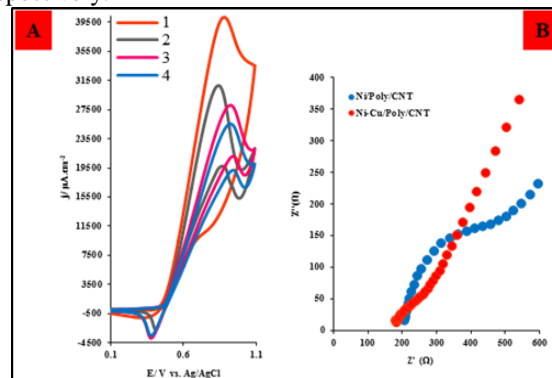

Fig. 1. (A) Cyclic voltammograms of modified p-MDAB-MWCNT/GCE with 1: Ni-Cu, 2: Ni-Ag, 3: Ni-Co, and 4: Ni in 0.1M NaOH + 0.5M MeOH at a scan rate of 0.05 $V.s^{-1}$. (B) The Nyquist plot of the Ni-Cu/p-MDAB-MWCNT/GCE and Ni/p-MDAB-MWCNT/GCE in 0.1 M KCl + 5 mM K3[Fe(CN)6].

The advantages of the proposed method are decreasing the resistance and fast kinetics of MOR on the mentioned nanocomposite [7]. This can be the results of appropriate of bimetallic nanoparticles on the polymeric substrate.
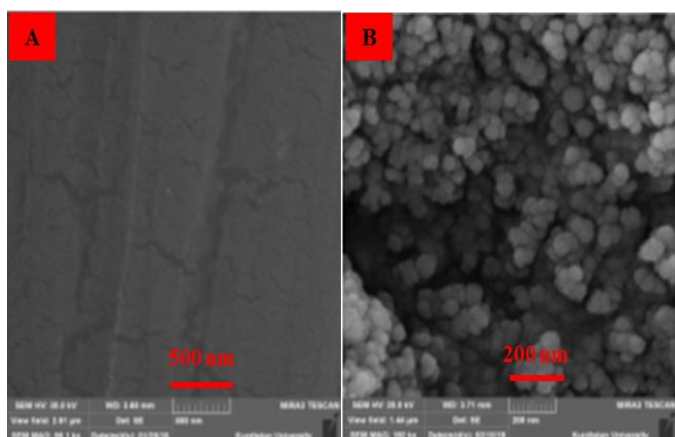

Fig. 2. FESEM images of modified GCE with (A) p-MDAB/MWCNT and (B) Ni-Cu/p-MDAB/MWCNT

IV. CONCLUSION

In this study, we accessed to the following results:

   i. Bimetallic nanocomposites in comparison with monometallic nanocomposites exhibit the distinguished electrochemical activity for methanol oxidation.

   ii. The EIS analysis indicates that the decrease of charge transfer resistance on the bimetallic nanocomposites is the reason for the improvement in electrochemical activity.

   iii. The appropriate performance of synthesized nanocomposites is due to bi-functional effect of polymeric substrate and metallic nanoparticles.

REFERENCES

[1] S. Mondal, and S. Malik, Journal of Power Sources, vol. 328, pp. 271-279, **2016**.

[2] A. A. Shaha, N. Yasmeena, G. Rahmana, S. Bilal, Electrochimica Acta, vol. 224, pp. 468–474, **2017**.

[3] K. Matsuoka, Y. Iriyama, T. Abe, M. Matsuoka, and Z. Ogumi, Electrochimica Acta, vol. 51, pp. 1085-1090, **2005**.

[4] P.Pattanayak, N. Pramanik, P. Kumar, and P. P. Kundu, International Journal of Hydrogen Energy, vol. 43, pp. 11505-11519, **2018**.

[5] X. Huang, Zh. Li, X. Zhang, and X. He, Journal of Colloid and Interface Science, vol. 393, pp. 300–305, **2013**.

[6] D. Y. Zhai, B. R. Liu, Y. Shi, L. J. Pan, Y. Q. Wang, W. B. Li, R. Zhang, and G. H. Yu, ACS Nano, vol. 7, pp. 3540–3546, **2013**.

[7] D. B. Gorle, V. V. Kumman, M. A. Kulandainathan, International Journal of Hydrogen Energy, vol. 42, pp. 16258-16268, **2017**.

Enhancement electrochemical activity of Pt nanoparticles toward methanol oxidation by using a new substrate

J. Azizi, S. Jadali, K. Ebrahimi Qaratapeh, M.A. Kamyabi*
Department of Chemistry, College of Science, Zanjan 45371-38791, Iran
E-mail: Kamyabi@znu.ac.ir

Abstract: Herein, the carbon felt (CF) after modification by poly 4-methyl-1,2-diaminobenzene (p-MDAB) and Pt nanoparticles is used as the anode for methanol oxidation. The electrochemical examination of the modified CF proves the excellent cooperation between polymeric film and carbonaceous substrate for accession of the electrochemical efficiency of Pt nanoparticles in acidic media.

Keywords: carbon felt (CF), methanol, electrochemical efficiency, poly 4-methyl-1,2-diaminobenzene (p-MDAB)

I. INTRODUCTION

The use of direct alcohol fuel cells (DAFCs) is an excellent remedy for solve the energy crisis [1]. From among the DAFCs, direct methanol fuel cells (DMFCs) that convert chemical energy of methanol into electrical energy, are the appropriate selection [2]. Until now, Pt-based catalysts had been taking into consideration for electrochemical oxidation of methanol [3]. The poisoning of Pt-based catalysts with the intermediates such as CO that adsorbed on the catalyst surface is a critical problem. The use of porous materials for deposition of Pt nanoparticles inhibits them from the agglomeration and increases their electrochemical efficiency [4]. The utilization of polymeric layer for electrodeposition of Pt nanoparticles is another way for inhibition against their agglomeration [5]. In this study, the modified CF with a polymeric layer and Pt nanoparticles was used as the anode for methanol oxidation. The effect of polymeric film on the Pt nanoparticles activity was considered by comparison between electrochemical efficiency of Pt nanoparticles that had been deposited on the bare CF and p-MDAB/ CF. Finally; the electrochemical studies of the modified CF (Pt/p-MDAB/CF) suggested it for the excellent candidate of the anode in DMFCs.

II. METHODS

Before modification of CF, it was cleaned ultrasonically with HCl, acetone, and double distilled water respectively. The covering of CF surface with a thin layer of p-MDAB was performed by cyclic voltammetry (CV) in the acidic solution of monomer. Pt nanoparticles were electrodeposited on the p-MDAB/CF by CV method in the 7 mM acidic solution of K_2PtCl_6. After drying, Pt/p-MDAB/CF was used as the anode in three-electrode system that saturated Ag/AgCl and Pt wire were the reference and counter electrode respectively. The surface morphology of Pt/p-PDAB modified CF electrode was considered by field emission scanning electron Microscopy (FESEM) and energy-dispersive X-ray spectra (EDX) analysis. Cyclic voltammetry (CV) and chronoamperometry (CA) were performed for consideration of the electrochemical activity of the modified CF.

III. RESULTS AND DISCUSSION

The electrochemical surface area (ECSA) as a valuable parameter that expresses the number of electrochemically active sites was calculated by CV experiment in 0.5 M H_2SO_4 saturated with N_2 gas and the potential range of −0.2 V to 1 V vs Ag/AgCl at the scan rate of 20 mV.s^{-1} (Fig. 1(A)). By using the Eq. 1, the ECSA value for Pt/p-MDAB/CF was calculated 84.5 m^2. g^{-1}$_{pt}$.

$$ECSA = \frac{Q_1}{m_{Pt} \times Q_2} \qquad (1)$$

Where Q_1 (mC. cm^{-2}) is the coulombic charge that is determined by the integration of the hydrogen adsorption-desorption region in the CV curve, m_{Pt} (g. cm^{-2}) is the loading of Pt nanoparticles on the electrode surface, and Q_2 (0.21 mC.cm^{-2}) is the coulombic charge required for the oxidation of the single layer of hydrogen coverage on Pt surface area [6].

The electrochemical performance of the modified CF towards methanol oxidation was considered by the performing of CV in a solution containing 0.5 M H_2SO_4 + 1 M MeOH in the potential range of 0 V to 1 V and at the scan rate of 50 mV.s^{-1}. The voltammograms of Pt/CF and Pt/p-MDAB/CF have been shown in Fig. 1(B). The ratio of the forward to the backward current (I_f /I_b) is one of the significant parameters obtained from CV studies. The forward peak current is related to the methanol oxidation and the backward peak current corresponds to the oxidation of poisoned intermediate [7].
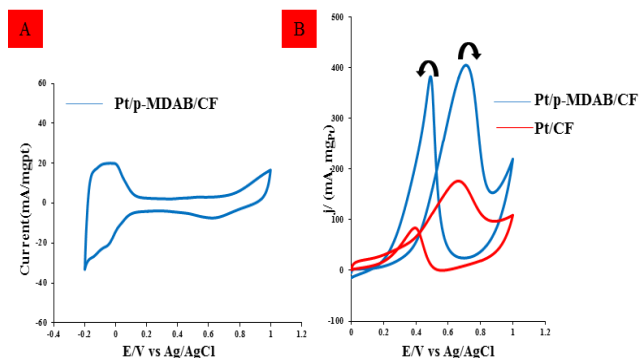
Fig. 1. CV of modified CF in (A) 0.5M H_2SO_4 at a scan rate of 0.02 $V.s^{-1}$ and (B) 0.1 H_2SO_4 + 1M MeOH at a scan rate of 0.05 $V.s^{-1}$.

The higher value of I_f /I_b for Pt/p-MDAB/CF than Pt/CF indicates the wealthy methanol oxidation and high tolerance towards poisoning phenomenon on the surface of Pt/p-MDAB/CF in the acidic media. Although the consideration of stability by chronoamperometery (CA) method exhibits the still decay of current for both the Pt-based catalysts (Fig. 2(A)), the more moderate current density and the higher current density in the steady state condition for Pt/p-MDAB/CF after testing for 3600 s demonstrates the durability and antipoisoning desirability of Pt/p-MDAB/CF[8]. Elemental analysis of the modified CF electrode was exhibited by EDX spectrum. The signal peaks of C and O at 0.2 and 0.5 keV have been shown. The signal peaks of Pt at 2.2, 8.5 and 9.5 keV demonstrate the presence of these nanoparticles on the CF surface. The elemental composition of the Pt/p-MDAB/CF has been reported in the inset of Fig. 2(B).
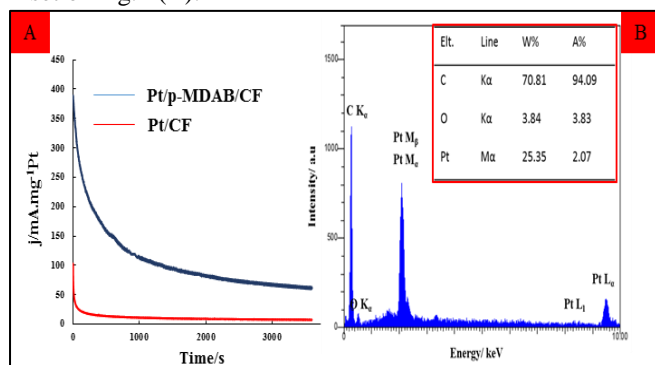

Fig. 2. (A) CA curves of Pt/CF and Pt/p-MDAB/CF in a solution containing 0.1 H_2SO_4 + 1M MeOH. (B) EDX spectrum of Pt/p-MDAB/CF

IV. CONCLUSION

We report the obtained results:

i. The covering of CF surface with the polymeric film was performed through a fast and facile method without an adherent material.

ii. The electrochemical findings indicated that the modification of the CF electrode can enhance the electrochemical efficiency for MOR.

iii. The proper electrochemical parameters of this catalyst is relevant to the cooperation effect of polymeric carbonaceous substrate and Pt nanoparticles for production of the large ECSA.

REFERENCES

[1] J. Wang, N. Cheng, M. N. Banis, B. Xiao, A. Riese A and X. Sun, Electrochimica Acta, vol. 185, pp. 267-275, **2015**.

[2] D. D. Demir, A. Salcı, R. Solmaz, International Journal of Hydrogen Energy, vol. 43, pp. 10540-10548 , **2018**.

[3] Lei F, Z. Li, L. Ye, Y. Wang, and S. Lin, International Journal of Hydrogen Energy, vol. 41, pp. 255-264, **2016**.

[4] R. Solmaz, A. Salcl, International Journal of Hydrogen Energy, vol. **42**, pp. 2464-2475, **2017**.

[5] Y. Li, T. Li, L. Yan, L. An, S. Yao, and Z. Zhang, Electrochimica Acta, vol. 289, pp. 397-406, **2018**.

[6] R. Sha, and S. Badhulika, Journal of Electroanalytical Chemistry, vol. 348, pp. 9-17, **2018**.

[7] C. C. Kung, P. Y. Lin, Y. Xue, R. Akolkar ,L. Dai, X. Yu, and C. C. Liu, Journal of Power Sources, vol. 256, pp. 329-335, **2014**.

[8] J. Cao, Z. Chen , J. Xu , W. Wang, and Z. Chen, Electrochimica Acta, vol. 88, pp. 184-192, **2013**.

Nanocomposite Decorated Glassy Carbon Electrode for Simultaneous Determination of Dopamine and Uric acid

Mohsen Moharramnezhad, Zahra Alipour, Mohammad Ali Kamyabi*

Department of Chemistry, College of Science, University of Zanjan 45195-313, Iran

Email: Kamyabi@znu.ac.ir

Abstract: In this study, a sensitive sensor was constructed based on multi-wall carbon nanotubes and TTF-TCNQ as a conductive organic complex. The complex was fixed on the modified MWCNT/GCE with the droplet method. The modified TTF-TCNQ/MWCNT/GC was used as a sensing probe in a voltammetric system for the determination of dopamine and uric acid. The physical characterization of TTF-TCNQ/MWCNT/GCE was performed with field emission scanning electron microscopy. At the optimum conditions, the modified electrode shows the good electrocatalytic activity for oxidation of dopamine and uric acid in low applied potential in 0.1M PBS solution pH 7. The linear dynamic range for dopamine and uric acid were obtained $5.0 \times 10^{-8} - 3.5 \times 10^{-5}$M and $5.0 \times 10^{-7} - 2.1 \times 10^{-4}$ M, respectively. As well as, the limits of detection were calculated 3.4×10^{-8} M and 4.2×10^{-7}M, respectively. Due to the excellent electrocatalytic performance of the present sensor, the electrode was successfully applied for determination and monitoring the level of dopamine and uric acid in human physiological fluids.

Keywords: dopamine, uric acid, Tetrathiafulvalene-Tetracyanoquinodimethane.

I. INTRODUCTION

Dopamine (DA) plays a vital role in regulating renal function, hormones, and central nerves [1]. Uric acid (UA) is an organic compound, which is removed by the kidneys. As well as, uric acid is an electroactive species found in biologic systems with dopamine and ascorbic acid [2]. Due to the high importance of DA and UA in the biological systems, the accurate and sensitive determination of DA and UA has attracted the attention of many researchers [3]. TTF-TCNQ is a type of organic charge-transfer complex which, due to its high conductivity in electron transfer, has many applications in the field of electrocatalytic and electrochemical biosensors. This complex acts as a conductive species and a redox intermediate in many biosensing probes [4]. In this study, the modification of a glassy carbon electrode with multi-wall carbon nanotubes and TTF-TCNQ salt was proposed as a new probe for the determination of dopamine and uric acid.

II. METHODS

A. Materials and Apparatus

Dopamine, uric acid, and TetrathiafulvaleneTetracyanoquino dimethane were purchased from Sigma Aldrich. As well as, multi-walled carbon nanotubes were purchased from the research institute of the petroleum industry of Iran. The other chemical materials were prepared in analytical grades. The phosphate buffer solutions (PBS) were prepared from H_3PO_4, KH_2PO_4 and K_2HPO_4 and the pH was adjusted to be 7 as natural media. The electrochemical experiments were performed using a potentiostat /galvanostat, PGSTAT 101, controlled by Nova software (Autolab, Switzerland).
A conventional three-electrode system was used for the voltammetric measurements, including the modified glassy carbon as working electrode, a platinum wire as a counter electrode and Ag/AgCl as a reference electrode. Field emission scanning electron microscopy (FESEM) was carried out by using TESCAN/Vega3 (Czech Republic).

B. Preparation of the modified electrode

After polishing the GC electrode surface with 0.05 μm alumina slurry, the electrode was sonicated in acetone and immersed in double distillate water to remove the adsorbed species. The cleaned GCE was coated by casting off 10 μL MWNTs (1 mg/mL in DMSO) and 10 μL of TTF-TCNQ (1 mg/mL in acetonitrile) respectively. After being dried in an oven for 4 h at 40º C to remove the solvent, the TTF-TCNQ/MWCNT/GC was prepared. For comparison, the MWCNTs modified GCE (MWCNTs/GCE) and TTF-TCNQ modified GCE (TTF-TCNQ/GC) can be prepared in the same way. The modified electrode was placed in 0.1 M PBS at 4ºC when not in use.

III. RESULTS AND DISCUSSION

A. Physical characterization of the modified electrode

The surface characterization of the modified electrode surface was performed by FESEM. As shown in Fig.1a, multi-wall carbon nanotubes are well attached to the surface of the GC electrode. Also, Fig. 1b, confirms the formation of needle crystals of TTF-TCNQ on the surface of the MWCNT/GC electrode. These images indicate that the electrode surface has been truly modified with MWCNT and the conductive salt.

B. Determination of dopamine and uric acid

The conductive organic salt of TTF-TCNQ plays the electrocatalytic role in the oxidation of dopamine and uric acid and also facilitates the electron transfer rate due to its excellent conductivity [4]. Thus, the oxidation of these two analytes occurs at the lower potentials. Figure 2, exhibits the cyclic voltammograms and the calibration curves for determination of dopamine and uric acid in 0.1 M PBS buffer solution pH 7.0 under the optimal conditions.
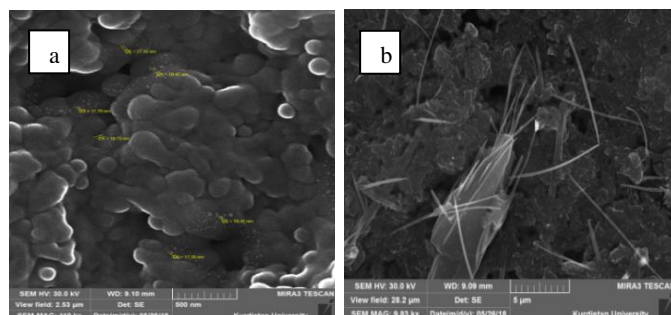

Fig.1. FESEM images of the modified **a)** MWCNT/GCE **b)** TTF-TCNQ/MWCNT/GCE

As shown in Fig. 2a, the current response at the potential of 0.17 V vs. Ag/AgCl, was linear with the concentration of dopamine in the range of $5.0 \times 10^{-8} – 3.5 \times 10^{-5}$ M. The detection limit (signal to noise ratio of 3) was obtained 3.4×10^{-8} M. As well as, in Fig.2b, for determination of uric acid, the linear range and detection limit were calculated $5.0 \times 10^{-7} – 2.1 \times 10^{-4}$ M and 4.2×10^{-7} M respectively. This excellent performance of the sensor can be due to the large active surface of the MWCNT/GC electrode with high conductivity of organic salt which enhances the electrocatalytic oxidation responses of DA and UA.
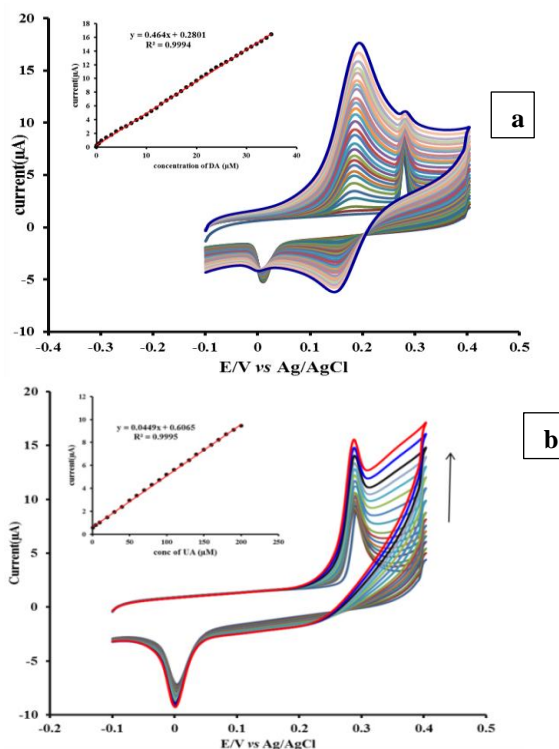

Fig.2. Cyclic voltammogram of TTF-TCNQ/MWCNT/GCE at **(a)** different concentration of dopamine **(b)** different concentration of uric acid; 0.1 M PBS pH=7.0 at scan rate of 50 mV/s.

C. Effect of interference species

The interference effect of foreign species including different ions and coexisting species on the determination of dopamine and uric acid were investigated. The tolerance limit was defined as the concentration which gave an error of 5.0% in the determination of $(1 \times 10^{-5} M)$ of dopamine and uric acid. The results indicated that 20 times of sucrose, lactose, fructose, maltose, glucose, 20 times of ascorbic acid, and 50 times of SO_4^{2-}, Cl^-, Na^+, and Ca^{2+} have no interference in the determination.

D. Real sample analysis

The blood serum samples (from the medical diagnostic laboratory) were diluted with the 0.1 M PBS pH 7.0 to reach the proper concentration range. The results are given in Table 1. The ranges of recoveries from 96% to 99% indicated that the proposed sensor can be successfully applied for clinical usage.

Table 1-DA and UA amounts in real serum sample (diluted 1:1000)

Sample	detect[a] (μM)	Ref[b] (μM)	RSD (%)	Added (μM)	Found (μM)	Recov (%)
DA	5.49	5.5	2.28	2.0	7.47	99
UA	21.98	22	2.27	12.0	33.5	96

a : determined in the Proposed method by average of 3 times of determination.
b : determined in the medical diagnostic laboratory.

IV. CONCLUSION

A simple and novel sensing probe based on TTF-TCNQ/MWCNT/GC electrode was demonstrated for the simultaneous determination of dopamine and uric acid. The conductive organic TTF-TCNQ salt shows the excellent conductivity in electron transfer and the electrocatalytic properties towards electro-oxidation of dopamine and uric acid. Moreover, the high performance of the sensor for the simultaneous determination of dopamine and uric acid demonstrated the development potential of the sensor for biomedical and clinical measurements.

REFERENCES

[1] R. Katai, I. Tsuneyoshi, J. Hamasaki, M. Onomoto, S. Suehiro, R. Sakata, Y. Kanmura, The variable effects of dopamine among human isolated arteries commonly used for coronary bypass grafts, Anesthesia & Analgesia, 98 (2004) 915-920.
[2] J. Fei, K. Wu, Y. Wu, S. Hu, Electrocatalytic oxidation of uric acid at an electrodeposited redox polymer film-modified gold electrode, Journal of Solid State Electrochemistry, 8 (2004) 316-321.
[3] L. Yang, D. Liu, J. Huang, T. You, Simultaneous determination of dopamine, ascorbic acid and uric acid at electrochemically reduced graphene oxide modified electrode, Sensors and Actuators B: Chemical, 193 (2014) 166-172.
[4] G. Sánchez-Obrero, M. Cano, J.L. Ávila, M. Mayén, M.L. Mena, J.M. Pingarrón, R. Rodríguez-Amaro, A gold nanoparticle-modified PVC/TTF-TCNQ composite amperometric biosensor for glucose determination, Journal of Electroanalytical Chemistry, 634 (2009) 59-63.

Electrochemical Behavior Study of Flutamide in Aqueous Solutions

F. Zandiyan, H. Shayani-Jam*, M. R. Yaftian

Phase Equilibria Research Laboratory, Department of Chemistry, Faculty of Science, The University of Zanjan, Zanjan, Postal Code 45371–38791, Iran.

Email: shayan@znu.ac.ir

Abstract: Electrochemical behavior include reduction and then oxidation of flutamide has been studied in various pHs using cyclic voltammetry and controlled-potential coulometry. The obtained results show that the electrochemical behavior of flutamide is pH dependent. The unstable intermediate compound produced by the electrochemical method is hydrolyzed in strong alkaline media and acidic media via a different mechanism. Also, it is dimerized in mild pH conditions. The products were synthesized in aqueous solutions using electro-synthesis. The synthesized products were identified by spectroscopic methods (FT-IR, NMR and MS).

In addition, in this study, a simple method is described for the electrochemical synthesis of flutamide's dimer.

Keywords: Flutamide, Cyclic voltammetry, Electrosynthesis, Dimerization reaction

I. INTRODUCTION

Flutamide is a non-steroidal anti-androgenic compound (NSAA) that is widely used to treat prostate cancer [1,2]. Flutamide acts by inhibiting the binding of androgens in target tissues [3]. The excessive consumption of this drug has several side effects, the most common side effects of which are hot flashes, dry skin, nausea and vomiting, diarrhea, increased appetite or loss of appetite and sleep disorders. Flutamide is rapidly and completely absorbed from the gastrointestinal tract and then rapidly and widely metabolized [4]. It contains about 10 metabolites, including 2-hydroxyflutamide, which have anti-androgenic effects [5].

Since the electrochemical oxidation and reduction of the drugs in the aquatic media is often similar to that of the corresponding catalytic processes in liver microsomes, this was the motive for studying the electrochemical behavior of flutamide at various pH and conditions. .

II. METHODS

Electrochemical experiments included controlled-potential coulometry, cyclic voltammetry and were performed using an OrigaFlex model OGF500 potentiostat/galvanostat.

In commonly, 100 ml of phosphate buffer solution (pH = 7.0, 0.2 M) was pre-electrolyzed at -0.7 V vs. SCE, in an undivided cell. In the next step, 1 mmol of flutamide (**1**) was added to the cell. Electrolysis was cut off when the current reaches below 5% of the initial current. The process was interrupted during the electrolysis and the electrodes were washed in acetone to reactivate them. The precipitated mixture was separated by filtration and recrystallized from methanol. Eventually, products were characterized by IR, ^{1}H NMR, ^{13}C NMR and MS.

The working electrode used in the voltammetry and controlled-potential coulometry experiment was a glassy carbon disk (1.8 mm diameter) and four carbon rods (6 mm diameter and 4 cm length), respectively. A platinum wire was used as the counter electrode. All electrodes were obtained from AZAR Electrodes.

Characterization of Products 3a

2-(trifluoromethyl)benzene-1,4-diamine. MP: 209-210 °C. IR (KBr)=3484, 3375, 1609,1626, 1492, 1146cm^{-1}. ^{1}HNMR (250MHz-DMSO)= 6.754- 7.012 (5.23H, aromatic), 7.957-7.989 (1.85H, aromatic).^{13}CNMR(250MHz-DMSO)= 112.17, 114.87, 120.78, 130.12 (4C, aromatic), 125.12 (CF$_3$), 134.15, 154.82 (C-NH$_2$). MS (EI): m/z): (M$^+$),

III. RESULTS AND DISCUSSION

Fig. 1 shows the cyclic voltammogram of flutamide in buffered phosphate solution (pH = 7, 0.2 M). As it is clear from the voltammogram, flutamide does not initially have the ability to oxidize, but at a potential of -0.68, it has a sharp irreversible cathodic peak (C$_1$) caused by direct reduction of flutamide to hydroxylamine [6].

Also, in the positive-going scan (peak C$_0$), a new anodic and reversible peak (-0.8) is observed.
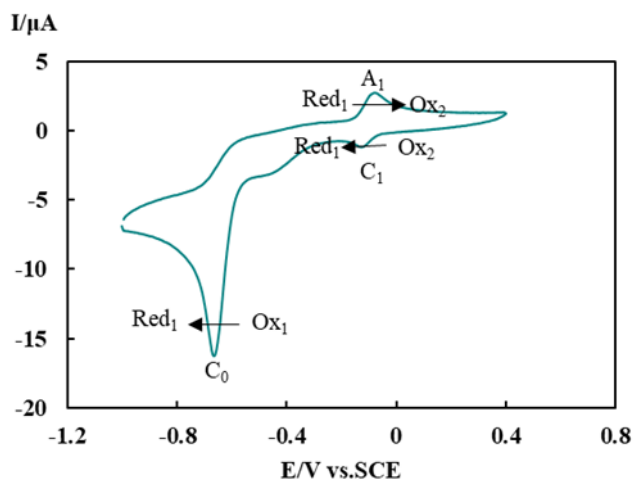
Fig.1: Cyclic voltammograms of 0.5 mM flutamide (**1**) in the at a glassy carbon electrode in phosphate buffer (pH 7.0, 0.2 mol L^{-1}). Scan rate: 25 mVs^{-1}, t = 25 ± 1ºC.

In time scale of our experiments, the variation of peak current ratio (I_{pC1}/I_{pA1}) which can be considered as a criterion for instability of N-((1Z,4E)-4-(hydroxyimino)-3-(trifluoromethyl)cyclohexa-2,5-dien-1-ylidene) isobutyramide (**3**). In acidic (pHs < 4) and alkaline (pHs > 9) conditions, I_{pC1}/I_{pA1} is mostly less than unity. On the other hand, relative stability of **3** was observed in pHs 5 and 9. However, in the range of pH = 5–9, there is considerable instability for **3** that can be attributed to the dimerization process (Scheme 1).

In intermediate pH, the peak current ratio (I_{pC1}/I_{pA1}) is dependent on concentration of flutamide (**1**) and proportional to the augmentation of it, the peak current ratio (I_{pC1}/I_{pA1}) decreases. The dependence of peak current ratio (I_{pC1}/I_{pA1}) on the concentration of flutamide (**1**) is an indication of dimerization reaction after the electron transfer process. Also, cyclic voltammograms show the shift of peak C_1 to negative direction proportional to the increasing of concentration. The negative shift of the peak C_1 which is enhanced proportionally to increasing of concentration of flutamide (**1**) can be due to the formation of a thin film of the product (dimer **3a**) at the surface of the electrode inhibiting to a certain extent the performance of the electrode process.

To obtain more data controlled-potential coulometry (CPC) was performed. Controlled-potential coulometry of aqueous buffer solution containing 1.0 mmol of **1** at -0.7 V vs. SCE was performed. Cyclic voltammetry was used to monitoring the electrolysis progress. The obtained results show that proportional to the advancement of coulometry experiment,

the cathodic peak C_0 decreased and disappears when the charge consumption becomes 5.1e$^-$ per molecule of **1**.
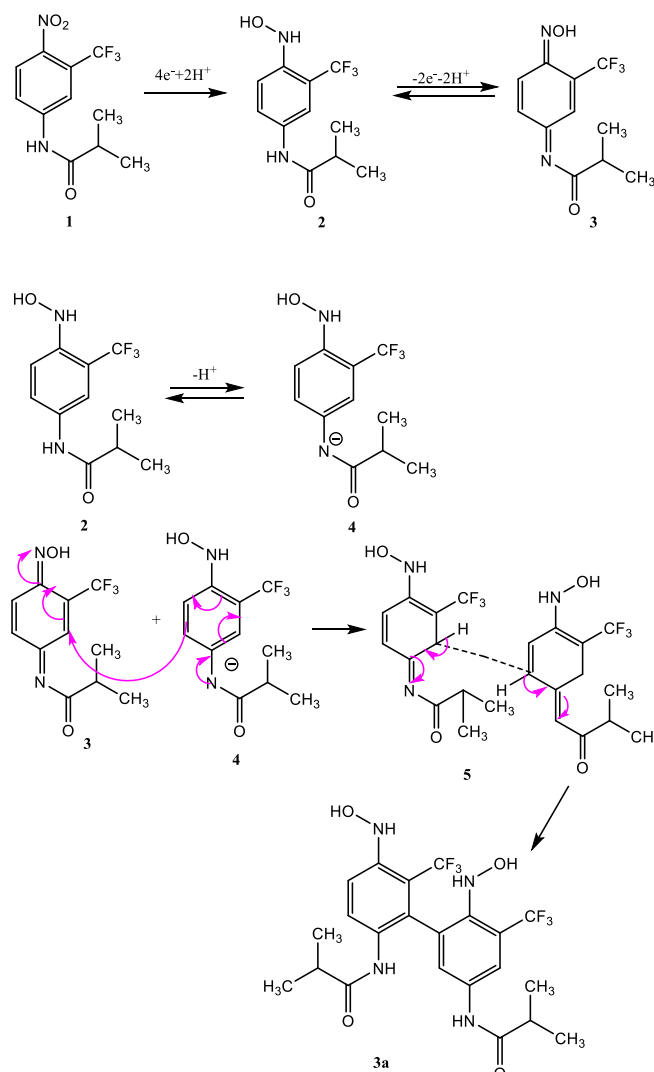
Scheme. 1. Proposed mechanisms for the electrochemical dimerization of flutamide

The final product (**3a**) was analyzed using IR, HNMR, CNMR and MS. The results include the consumption of 5.1 electrons per molecule of **1**, Diagnostic criteria of the cyclic voltammograms and spectroscopic data of the isolated product indicate that the mechanism of the electrochemical reaction of **1** is dimerization reaction.

According to the obtained results, it can be suggested that the Michael addition reaction of anion **4** via C-alkylation to **3**, leading to dimer **3a**.
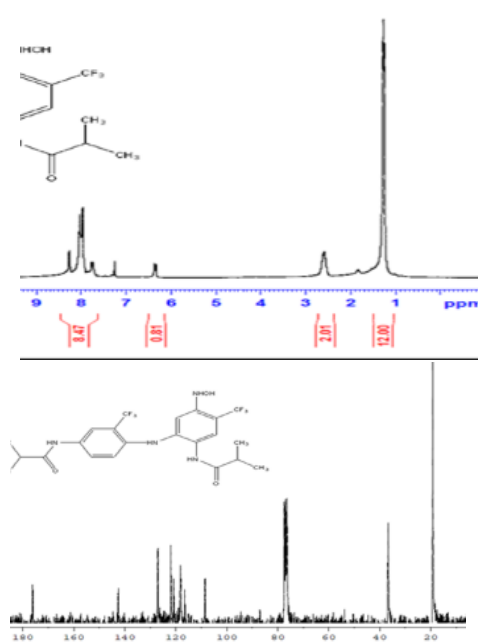
Fig. 2. ^{1}H NMR and ^{13}C NMR of dimer 3a

IV. CONCLUSION

The obtained results show that reduced form of flutamide (**2**) is oxidized in aqueous buffer solutions to **3**. Then, The **2** participates in various reaction such as hydrolyzes dimerization and hydroxylation in solution with different pH. In this study, a simple method is described for the electrochemical synthesis of flutamide's dimer. The product was synthesized in phosphate buffer. The synthesized products were identified by spectroscopic methods (FT-IR, NMR and MS).

REFERENCES

[1] Z. Rezaeifar, G. H. Rounaghi, Z. Es' haghi, M. Chamsaz, Materials Science and Engineering C, 91, 10-18, **2018**.
[2] M. Reddy, T. Murthy, M. D. Reddy, D. Sankar, S Asian Journal of Chemistry, 13, 1261-1268, **2001**.
[3] R. N. Brogden, S. P. Clissold, Drugs, 38, 185-203. **1989**.
[4] F. Lund, F. Rasmussen, British journal of urology, 61, 140-142, **1988**.
[5] M. Schulz, A. Schmoldt, F. Donn, H. Becker, European journal of clinical pharmacology, 34, 633-636. **1988**.
[6] G. S. Reddy, C. L. N. Reddy, V. N. Myreddy, S. J. Reddy, Journal of Clinical Medicine and Research, 3, 35-39, **2011**.

Optimization of deposition voltage for copper electrodeposition on FTO from non-acidic solution

S. Jami[a]*, M. Behboudnia[a], N. Nobari[b]

Department of Physics, Urmia University of Technology, P.O. Box 57155-419, Urmia, Iran
Department of Physics, Mahabad Branch, Islamic Azad University, Mahabad 59135, Iran
Email: siavjami@sci.uut.ac.ir

Abstract: nanostructured copper (Cu) thin films have been electrodeposited on glass/fluorine doped tin oxide (FTO) substrates using the low-cost two-electrode system. The deposition was performed using non-acidic aqueous solutions at low temperatures. Optimal deposition voltages for the growth of adherent shiny copper films were determined. The as-synthesized Cu/FTO samples were characterized by scanning electron microscopy (SEM). The results show that in the non-acidic environment, this layer can be found.

Keywords: Copper, Electrodeposition, Coating, Thin Film, Morphology

I. INTRODUCTION

Copper is one of the most suitable metallization materials and also has high corrosion properties. Among various methods of thin film deposition such as PVD, CVD and sputtering, the electrodeposition is known as a less expensive, highly productive and readily adoptable method [1, 2]. Yusairie Mohd et al. found copper layering on a Stainless Steel substrate, which has a direct relationship with the density of copper particles and the size of the copper particle[3]. The purpose of this work is to compare the copper layers in this paper and the study of Yusairie Mohd and his colleagues.

II. EXPERIMENTAL METHOD

This study was carried out using an electrodes two-electrode electrodeposition device. The chemicals used in the solution at the laboratory temperature include 0.4 mol of $CuSO_4 \cdot 5H_2O$. The important variables in this work are temperature control, concentration, pH, time of the reaction layer and the potential difference between the cathode and the anode.

After preparation, the temperature of the solution was maintained at $30\,^{\circ}$C. The potential difference between the two electrodes was kept at -1.1 v. With the above mentioned above, the layer was made in 250 seconds.

III. RESULTS AND DISCUSSION

In the common methods of thin-layer electrical coatings, typically acids such as MAS[1] are used to improve the electrodeposition[4]. However, soluble acids can affect the corrosion and adhesion properties of the coating layer. In this paper, the electrodeposition process was attempted in a completely non-acidic environment.

The results of the FESEM analysis in figure 1 show that without the use of any additive and acid addition, the coating of nanoparticles can also be achieved by adjusting the coating's improvements.

The optimum voltage was -1.1 volts. However, this coating was tested between voltages -0.85, -0.95 and -1.01. In voltages other than -1.1 volts, the adhesion was very weak.
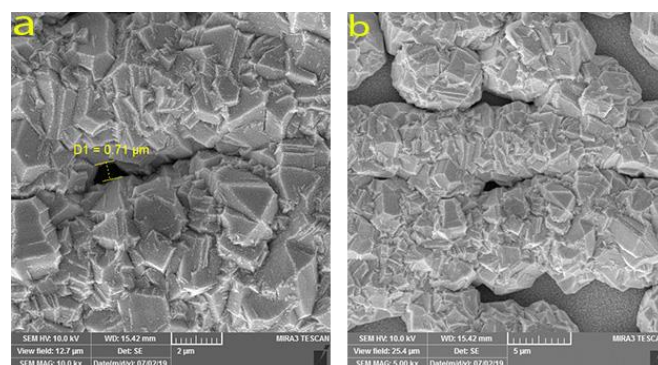

Fig.1: (b) FESEM images of the surface layer copper and (a) with higher magnification

IV. CONCLUSION

In this study, substrate coating was carried out in non-acidic media. Constantly maintaining the variables of temperature, soluble concentration and deposition time, the effect of H_2SO_4 acid in different amounts of pH was investigated. The results show that in the non-acidic environment, this layer can be found.

---

1 - Methanesulfonic acid

[Image of conference header: 22nd Iranian Physical Chemistry Conference]

REFERENCES

[1] Dudin, P.V., O.V. Reva, and T.N. Vorobyova, High rate of copper electrodeposition from the hexafluorosilicate bath. Surface and Coatings Technology, **2010**. 204(20): p. 3141-3146.

[2] Rahman, H.A., A. Moustafa, and S.A. Magid, High rate copper electrodeposition in the presence of inorganic salts. Int. J. Electrochem. Sci, **2012**. **7**: p. 6959-6975.

[3] Isa, N.C., et al., Characterization of copper coating electrodeposited on stainless steel substrate. International Journal of Electrochemical Science, **2017**. 12: p. 6010-6021.

[4] Hasan, M. and J.F. Rohan, Cu electrodeposition from methanesulfonate electrolytes for ULSI and MEMS applications. Journal of The Electrochemical Society, **2010**. 157(5): p. D278-D282.

ZnO Nanoparticles Anchored 3-D Ni-Foam Electrode for Electrochemiluminescence Determination of Amoxicillin

Zahra Alipour, Mohsen Moharramnezhad, Mohammad Ali Kamyabi*
Department of Chemistry, Colleges of Science, University of Zanjan 45195-313, Iran
E-mail: Kamyabi@znu.ac.ir

Abstract: In this work, an electrochemiluminescence (ECL) sensing platform for sensitive determination of amoxicillin has been introduced. The ECL detection procedure was performed on the ZnO nanoparticles modified Ni-foam electrode in the presence of luminol. The size of ZnO nanoparticles was controlled by the silica templates on the electrode surface. The morphological studies were carried out using field emission scanning electron microscopy (FESEM) and electrochemical impedance spectroscopy (EIS). The obtained linear dynamic range of the method was from 4.0×10^{-11} to 6.5×10^{-5} M with a detection limit of 8.3×10^{-12} M (S/N = 3). The proposed modified electrode showed excellent ECL responses with high sensitivity, selectivity and stability for the determination of amoxicillin at the optimal conditions, which makes it a suitable sensor for submicromolar detection of amoxicillin in solutions. The analytical performance of this sensor has been evaluated for the detection of amoxicillin in milk samples with satisfactory results.

Keywords: Nickel foam, ZnO nanoparticles, Electrogenerated chemiluminescence, Amoxicillin, Sensor

I. INTRODUCTION

The β-lactam antibiotic, Amoxicillin (AM), is often used to treat and prevent infections produced by doing surgery or dental work and bacterial infections [1]. Also Low doses of antibiotics are also added to animal feed to promote more production of meat or milk in a short time. Therefore, the Food and Drug Administration (FDA) has recognized regulations to reduce the unnecessary usage of antibiotics in livestock [2, 3]. Thus, the determination of trace amount of antibiotics in biological fluids are crucial. Some of the analytical methods used for the detection of amoxicillin are included spectrophotometry, high-performance liquid chromatography, and chemiluminescence. Among the mentioned methods, Electrochemiluminescence (ECL) is an appealing alternative method, because it is a new technology with a wide dynamic range, high sensitivity and high-quality assay for different analytes [4]. Throughout the electrochemical reaction, ECL luminescent species produce excited states that emit light when returning back to ground

states [5]. These reactions require a chemiluminescent reagent, luminophore, such as luminol, porphyrin, and ruthenium (II) complex. The incorporation of nanomaterials into the ECL sensor not only improve its efficiency but also represent novel species of ECL emitters [6].

II. METHODS

ECL experiments were performed on an electrochemiluminescent analytical system, using a homemade detection system which was equipped with the photomultiplier tube set at 900 V in 0.1 M NaOH solution as supporting electrolyte and luminol as a co-reactant. All solutions were analytical grade and prepared in distilled double water. Electrochemical system was consisted of a three electrodes system including an Ag|AgCl|KCl sat'd and a platinum wire electrode as the reference and counter electrode, respectively.

Electrodeposition of ZnO on the silica/Ni-foam was performed in 0.1 M KCl solution containing 0.1 M $Zn(NO_3)_2.6H_2O$ and one mM CTAB by using the fixed potential of -1.1 V *vs.* Ag/AgCl for 300 s at 70 ° C, then the modified Ni-foam was placed in a furnace at 400°C for 2h. Finally, to remove the silica templates, 35 consecutive cyclic voltammetry scans with a scan rate of 20 mV/s in the potential range of -0.8 up to 0.55 V vs. Ag/AgCl was performed in 3 M NaOH solution.[7]

III. RESULTS AND DISCUSSION

A. Electrochemical impedance spectroscopy and surface characterization of the modified electrode

Figure 1a shows the Nyquist plot of bare Ni-foam and ZnO/Ni-foam electrode in a frequency range from 100 kHz - 100 mHz which consists of two parts; the semicircular part &, the liner part. The semicircular part is related to the charge transfer resistance (R_{ct}) at high frequency and the linear part at low frequency is related to the mass transfer resistance (R_{mt}). It is noteworthy, that the (R_{ct}) decreases when Ni foam was modified with ZnO nanoparticles. The reduction of R_{ct} in ZnO /Ni-foam relative to the Ni foam was confirmed the presence of ZnO nanoparticles that were formed on the nickel foam surface. In the present ECL

process, zinc oxide increases electrical conductivity and accelerates the electron transfer between ZnO and luminol in reaction. The ZnO nanoparticles with the average size of 21.6 nm were regularly formed on the surface of nickel foam and their FESEM image was depicted in Figure 1b.
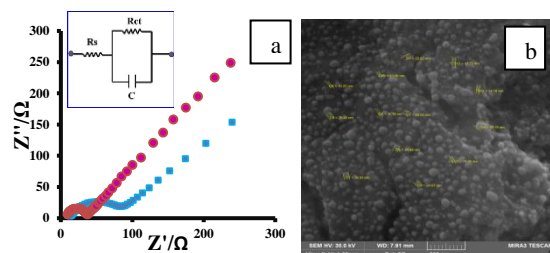

Figure 1. (a) Nyquist plots of bare Ni foam (blue) and ZnO/Ni foam (red), in 0.1 M NaOH containing 1.0 mM $K_3Fe(CN)_6$ at open circuit potential(OCP) with AC amplitude of 10 mV, **(b)** FESEM image of ZnO/Ni foam.

B. ECL determination of amoxicillin

The prepared sensor was applied for the quantitative analysis of amoxicillin in alkaline media. As shown in Figure 2 with increasing of the amoxicillin concentration in 0.1 M NaOH solution contaning, the ECL signals dramatically were increased in the negative potential -0.8 V vs. Ag/AgCl. The inset in Figure2 illustrates a typical logarithmic calibration plot for the detection of amoxicillin at the ZnO/ Ni-foam electrode under the optimal conditions. The obtained of wide linear dynamic range was obtained 4.0×10^{-11}M - 6.5×10^{-5}M. Furthermore, the calculated low detection limit (signal to noise ratio of 3) was 8.3×10^{-11}M, indicates that the modified electrode has a tremendous sensitivity to amoxicillin at very low concentration levels. probably,Enhancing ECL responses is related to the large active surface area of nickel foam and high conductivity of the sensor for electron transfer in the ECL process.
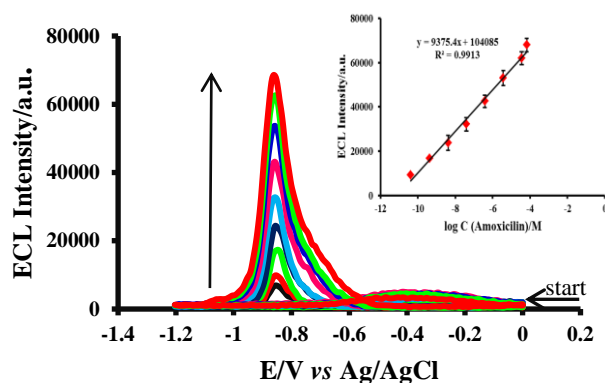

Fig.2. ECL-potential profile of ZnO/Ni foam at different concentration of amoxicillin, luminol: 1.6×10^{-4} M in 0.1M

NaOH solution at the scan rate of 50mV/s, **inset:** calibration curve for amoxicillin.

C. Interference species study and real sample analysis

To assay the selectivity of the proposed method, the impact of the interfering materials such as mineral ions and organic compounds was investigated. In this way, certain amounts of interfering species were added to the solution of 4.0×10^{-9} M amoxicillin and 1.6×10^{-4}M luminol. It is worthy of note that, the species with a relative error of less than 5 % are not considered as interfering agents. As can be seen from Table 1, the presence of beta-lactams such as ampicillin and some anions and cations do not interfere with amoxicillin determination. The cow's milk purchased from the local market was slightly modified according to the literature [8]. The results of amoxicillin determination in different milk samples are shown in Table 2. The data shows that amoxicillin determination is close to the reference value and the range of recoveries is between 95% to 100.8%.

Table1-Tolerable concentrations of interfering species in determining of the amoxicillin

Ca^{2+}, K^+, Na^+, NH_4^+	1000
Cu^{2+}, Ni^{2+}, Zn^{2+}, Co^{2+}	50
SO_4^{2-}, Cl^-, NO_3^-	100
Ampicillin	50
H_2O_2	1

Table2- amoxicillin determination in different milk samples

Sample (%)	Added ($\times 10^{-10}$M) Recovery (%)	Found[a] ($\times 10^{-10}$M)	RSD
1	0.00	1.0	4.2	-
	3.00	3.90	4.5	96.6
	6.00	7.05	4.1	100.8
2	0.00	0.5	3.9	-
	3.00	3.35	4.1	95.0
	6.00	6.42	4.3	98.6

a: determined in the proposed method by average three times of determination

II. CONCLUSION

In conclusion, a ZnO/Ni foam ECL sensor was uniformly made by electrodeposition of ZnO nanoparticles on Ni-foam. ZnO/Ni sensor showed excellent sensitivity, with a detection

limit of 8.3×10^{-12}M at a signal-to-noise ratio of 3 for Amoxicillin determination, likely due to smaller charge-transfer resistance, high conductivity, good mass transfer, and large active surface area on ZnO. Moreover, this sensor exhibited a good linear relationship with the log of amoxicillin concentration in a range of 4.0×10^{-11}- 6.5×10^{-5}M. As well as, good reproducibility and durability of the prepared sensor led to the use of the modified electrode for amoxicillin determination in milk samples.

REFERENCES

[1] T. Rojanarata, P. Opanasopit, T. Ngawhirunpat, C. Saehuan, S. Wiyakrutta, V. Meevootisom, A simple, sensitive and green bienzymatic UV-spectrophotometric assay of amoxicillin formulations, Enzyme and Microbial Technology, 46 (2010) 292-296.

[2] L.-H. Shen, H.-N. Wang, P.-J. Chen, C.-X. Yu, Y.-D. Liang, C.-X. Zhang, The analytical determination and electrochemiluminescence behavior of amoxicillin, journal of food and drug analysis, 24 (2016) 199-205.

[3] D.M. Shlaes, R.C. Moellering Jr, The United States Food and Drug Administration and the end of antibiotics, Clinical Infectious Diseases, 34 (2002) 420-422.

[4] M.M. Richter, Electrochemiluminescence (ecl), Chemical Reviews, 104 (2004) 3003-3036.

[5] F. Mesgari, S.M. Beigi, F. Salehnia, M. Hosseini, M.R. Ganjali, Enhanced electrochemiluminescence of Ru (bpy) 32+ by Sm2O3 nanoparticles decorated graphitic carbon nitride nano-sheets for pyridoxine analysis, Inorganic Chemistry Communications, (2019).

[6] W.-R. Cai, G.-Y. Zhang, K.-K. Lu, H.-B. Zeng, S. Cosnier, X.-J. Zhang, D. Shan, Enhanced electrochemiluminescence of one-dimensional self-assembled porphyrin hexagonal nanoprisms, ACS applied materials & interfaces, 9 (2017) 20904-20912.

[7] Kamyabi, M. A.; Hajari, N.; Babaei, N.; Moharramnezhad, M.; Yahiro, H. Silica template electrodeposition of copper oxide nanostructures on Ni foam as an ultrasensitive non-enzymatic glucose sensor. *J Taiwan Inst Chem Engrs* **2017**, *81*, 21-30.

[8] D. Feng, Y. Wu, X. Tan, Q. Chen, J. Yan, M. Liu, C. Ai, Y. Luo, F. Du, S. Liu, Sensitive detection of melamine by an electrochemiluminescence sensor based on tris (bipyridine) ruthenium (II)-functionalized metal-organic frameworks, Sensors and Actuators B: Chemical, 265 (2018) 378-386.

Electrochemical oxidation of acetaminophen in the presence of metformin

M. Bagheri, H. Shayani-Jam*, M. R. Yaftian

Phase Equilibria Research Laboratory, Department of Chemistry, Faculty of Science, The University of Zanjan, Zanjan, Postal Code 45371–38791, Iran.

Email: shayan@znu.ac.ir

Abstract_:_ In this study, the electrochemical oxidation of acetaminophen in the presence of metformin as an antidiabetic drug in aqueous solution was performed using cyclic voltammetry and controlled potential coulometry techniques. The results show that _N_-acetyl-P-benzoquinone-imine (NAPQI) obtained from electro-oxidation of acetaminophen has been reacted with metformin via the Michael addition reaction. The mechanism of this reaction was suggested as an ECECC pathway using cyclic voltammetry, controlled-potential coulometry and spectroscopic data. In this work, we introduced new compound with good yields through a catalyst-free, environmentally friendly method at room temperature under green conditions.

Keywords: Acetaminophen, Metformin, Cyclic voltammetry, Coulometry, Glassy carbon electrodes.

I. INTRODUCTION

Drug interactions mean the interactions of drugs that can be beneficial or harmful or have no significant effect. For example, the mixing of incompatible chemical drugs can lead to deposition or disabling of intravenous injection [1]. According to studies, 10 to 20 percent of hospital admissions are due to drug problems, of which approximately one percent is due to drug interactions [2]. Elderly people generally use more drugs than young adults, so they face a greater risk of drug interactions. Therefore, as the number of prescription drugs increases, drug interactions also increase [3]. In one of the commonest treatment cases, it is possible to prescribe glucose-lowering drugs with acetaminophen. Therefore, the study of the interaction between these drugs with acetaminophen can be important in terms of drug and treatment. Under normal circumstances, acetaminophen is converted to an unstable intermediate of _N_-acetyl-P-benzoquinone-imine (NAPQI) by cytochrome 2 E1 P450 [4]. NAPQI is effectively deactivated by glutathione (GSH), but when overused, NAPQI reacts with GSH, which results in rapid and extensive depletion of glutathione liver [5]. In this work, we want to use a simple electrochemical approach to study the interaction between acetaminophen and metformin

as a glucose-lowering drug and the synthesis of a new product of acetaminophen oxidation in the presence of metformin.

II. METHODS

Acetaminophen (**1**) was reagent grade material from E. Merck. Metformin (**3**) was obtained from Raha Pharmaceutical Co. All solvents were purchased from E. Merck and were pro-analysis grade. These chemicals were used without further purification.

Electrochemical experiments included controlled-potential coulometry and cyclic voltammetry were performed using an OrigaFlex model OGF500 potentiostat/galvanostat. In commonly controlled-potential coulometry experiment, 100 ml of phosphate buffer solution (pH = 7.0, 0.2 M) was pre-electrolyzed at 0.4 V _vs._ SCE, in a divided cell. In the next step, 0.25 mmol of acetaminophen (**1**) was added to the cell. Electrolysis was cut off when the current reaches below 5% of the initial current. At the end of electrolysis, the precipitated mixture was separated by filtration and it was washed several times with water. Eventually, the product was characterized by spectroscopic methods.

The working electrode used in the voltammetry and controlled-potential coulometry experiment was a glassy carbon disk (1.8 mm diameter) and four carbon rods (6 mm diameter and 4 cm length), respectively. A platinum wire was used as the counter electrode. The working electrode potentials were measured _vs._ a saturated calomel electrode (SCE). All electrodes were obtained from AZAR Electrodes.

III. RESULTS AND DISCUSSION

Cyclic voltammogram of 0.5 mM of acetaminophen (**1**) in aqueous solution containing 0.2 mol L^{-1} phosphate buffer at pH 12.0 showed one anodic (A) and a corresponding cathodic peak (C), which has been attributed to the conversion of acetaminophen to _N_-acetyl-p-benzoquinone-imine (NAPQI) and vice versa through a two-electron quasi-reversible electron process [6] Fig. 1, curve a).

A peak current ratio (I_C/I_A) near to unity shows that NAPQI produced at the electrode surface is stable under the experimental conditions. In other words, any side reactions

such as dimerization, hydrolysis and/or hydroxylation are not observed at the time scale of cyclic voltammetry [7].
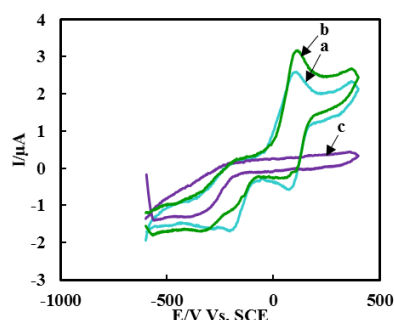

Fig.1: Cyclic voltammograms of 0.5 mM acetaminophen (**1**): (a) in the absence, (b) in the presence of 10 mM metformin (**3**), and (c) 2.5 mM metformin (**3**) in the absence of acetaminophen at a glassy carbon electrode in phosphate buffer (pH 12.0, 0.2 mol L^{-1}). Scan rate: 10 mVs^{-1}, t = 25 ± 1°C.

The electrochemical oxidation of acetaminophen (**1**) was studied in more detail in the presence of metformin (**3**). The Cyclic voltammogram of **1** in the presence of **3** was shown in Fig. 1 curve b. The voltammogram shows one anodic peak (A) at 0.136 V and its cathodic counterpart (C) at 0.076 V *vs.* SCE. The current of peak C and the peak current ratio (I_{pC}/I_{pA}) for acetaminophen decrease in the presence compared with the absence of metformin (**3**). This is related to the chemical reaction between the produced NAPQI as an electrophile and metformin (**3**) as a nucleophile

To obtain more data, controlled-potential coulometry (CPC) was performed in an aqueous solution containing 0.25 mmol of acetaminophen (**1**) and 0.25 mmol of metformin (**3**) at the 0.4 V potential versus SCE. The coulometry progress was monitored using cyclic voltammetry (Fig. 2). It was found that as the electrolysis proceeds, the anodic peak (A) decreased and it was disappeared after the passage of four electrons per molecule of acetaminophen. These observations allowed proposing the mechanism shown in Scheme 1 for electrochemical oxidation of acetaminophen in the presence of metformin.

The produced product was analyzed using IR, HNMR, CNMR and MS.

According to the voltammetric, coulometric and spectroscopic results, the following mechanism can be proposed for the electrochemical oxidation of acetaminophen in the presence of metformin (Scheme 1). As is shown in scheme 1, the electrochemical produced NAPQI is followed

by a Michael type addition reaction with **3**, and 7 as a final product is produced via an ECECC mechanism.
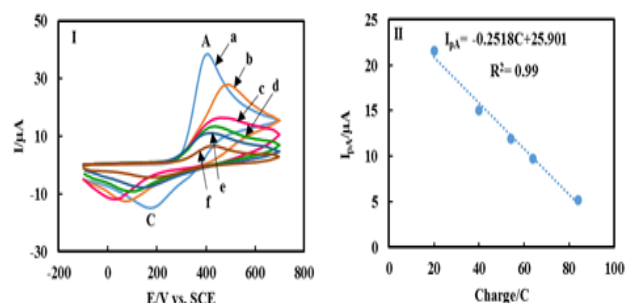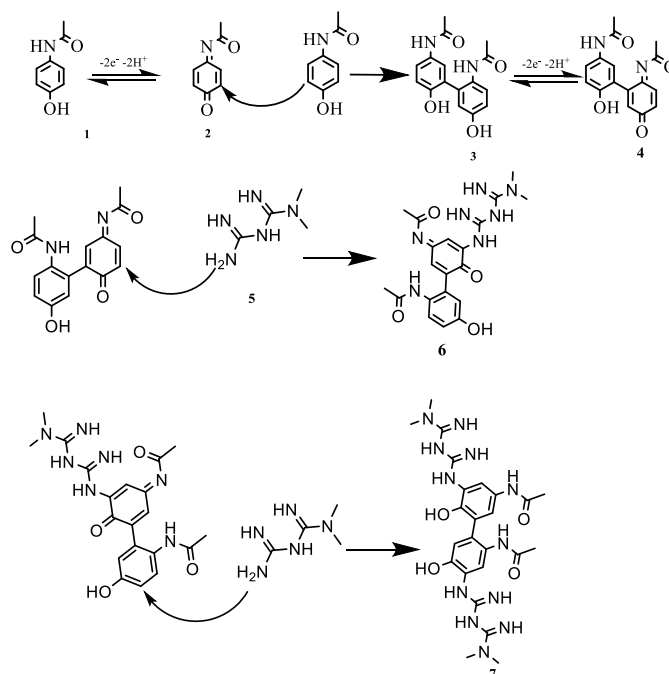

Fig. 2. (I) Cyclic voltammograms of 0.25 mmol acetaminophen (**1**) in the presence of 0.25 mmol metformin (**3**), in water/acetonitrile (90/10) in phosphate buffer (pH 7.0, 0.2 mol L^{-1}), during controlled potential coulometry at 0.4 V *vs.* SCE electrode, after consumption of: (a) 0, (b) 20, (c) 40, (d), 54 , (e) 64 and (f) 84C. Scan rate: 100 mVs^{-1}, (II) Variation of anodic peak current *vs* charge consumed., t = 25 ± 1 °C.

Scheme. 1. Proposed mechanisms for the electrochemical dimerization of acetaminophen

IV. CONCLUSION

This work presents reliable data for the reaction of *N*-acetyl-p-benzoquinone-imine (**2**) produced from the electro-

oxidation of acetaminophen (**1**) in the presence of the anti-diabetic drug (metformin) and synthesis of a new derivative of acetaminophen. On the other hand, it can be said that this reaction of NAPQI in the presence of metformin (**3**) can reduce the toxicity of acetaminophen. Also, this reaction will reduce the effective concentration and performance of the metformin.

REFERENCES

[1]. B. Chadwick, D.G. Waller, and J.G. Edwards, Advances in Psychiatric treatment,11(6), 440-449, **2005.**

[2]. L. Bjerrum, B. Gonzalez Lopez-Valcarcel, and G. Petersen, The European journal of general practice,. 14(1), 23-29, **2008**.

[3]. L. Mallet, A. Spinewine, and A. Huang, The Lancet, 370(9582), 185-191, **2007**.

[4]. El-Sayed, E.S.M., A.M. Mansour, and M.E, Journal of biochemical and molecular toxicology, 29(1), 35-42, **2015**.

[5]. R. Agarwal, et al., Journal of Pharmacology and Experimental Therapeutics, 340(1), 134-142, **2012**.

[6]. D.J. Miner, et al., Analytical chemistry, 53(14), 2258-2263, **1981**.

[7]. D. Nematollahi, et al., Electrochimica Acta, 54(28), 7407-7415, **2009**.